



HAL
open science

Tungsten transport and deposition in magmatic-hydrothermal environments: the example of Panasqueira (Portugal)

Eleonora Carocci

► **To cite this version:**

Eleonora Carocci. Tungsten transport and deposition in magmatic-hydrothermal environments: the example of Panasqueira (Portugal). Earth Sciences. Université de Lorraine, 2019. English. NNT : 2019LORR0315 . tel-02880627

HAL Id: tel-02880627

<https://hal.univ-lorraine.fr/tel-02880627>

Submitted on 25 Jun 2020

HAL is a multi-disciplinary open access archive for the deposit and dissemination of scientific research documents, whether they are published or not. The documents may come from teaching and research institutions in France or abroad, or from public or private research centers.

L'archive ouverte pluridisciplinaire **HAL**, est destinée au dépôt et à la diffusion de documents scientifiques de niveau recherche, publiés ou non, émanant des établissements d'enseignement et de recherche français ou étrangers, des laboratoires publics ou privés.



AVERTISSEMENT

Ce document est le fruit d'un long travail approuvé par le jury de soutenance et mis à disposition de l'ensemble de la communauté universitaire élargie.

Il est soumis à la propriété intellectuelle de l'auteur. Ceci implique une obligation de citation et de référencement lors de l'utilisation de ce document.

D'autre part, toute contrefaçon, plagiat, reproduction illicite encourt une poursuite pénale.

Contact : ddoc-theses-contact@univ-lorraine.fr

LIENS

Code de la Propriété Intellectuelle. articles L 122. 4

Code de la Propriété Intellectuelle. articles L 335.2- L 335.10

http://www.cfcopies.com/V2/leg/leg_droi.php

<http://www.culture.gouv.fr/culture/infos-pratiques/droits/protection.htm>

*« Le cose sono unite da legami invisibili.
Non puoi cogliere un fiore senza turbare una stella. »*

Galileo Galilei

CONTENTS:

Résumé Étendu	12
Abstract	18
Introduction	22
1. STATE OF ART	24
1.1 Genetic Model of Deposits Associated with Veins-Stockworks	25
1.2 W-Sn- (Cu) Panasqueira Deposit	27
1.3 Common Types of Fluids Characterizing Transport and Deposition of W: Fluid Inclusions Data	30
2. SET OF ISSUES AND SUBJECT OF THE THESIS	33
3. OBJECTIVES AND EXPECTED RESULTS	34
4. MATERIALS AND METHODS	36
4.1 Geological Part- Data Collection	36
4.2 Geochemical Collection Data	39
Major elements conditions	39
Trace, Rare Earth elements	39
Dating	39
Fluid Inclusions	40
4.3 Experimental Part- Dataset	41
5. MANUSCRIPT ORGANIZATION	48
Part One	49
First Depositional Stage	49
Paragenetic succession at Panasqueira	50
General characteristics of the paragenetic succession	50
At the pillar scale	50
Later stages	51
At the sample scale	51
Revised Panasqueira paragenetic chart	53

Li-Fe-muscovite	54
Arsenopyrite	56
Topaz	58
Phosphates	61
Siderite	62
CHAPTER ONE	63
INCIPIENT DEPOSITION STAGE OF WOLFRAMITE: W-RUTILE AND TOURMALINE CHEMISTRY AS PROXIES FOR EARLY FLUIDS AT PANASQUEIRA (PORTUGAL)	63
Abstract	63
Introduction	64
Regional background	65
Geological setting and previous work	68
Samples and methods	70
Results	72
Petrography of the tourmalinized wallrocks	72
Tourmaline textures	73
Rutile textures	78
Tourmaline chemical composition	79
Rutile chemical composition:	88
Dating	88
Discussion	91
Age of the early hydrothermal stage	91
Tourmaline evidence for the involvement of two fluids	92
The boron problem and the feasibility of a magmatic source of fluids	95
Metasedimentary source(s) of the fluids: the contribution of REE data	96
Contrasted compositions of F1 and F2 end-members	97
Rutile evidence for short term fluid dynamics and mixing	98
Proposed conceptual model	98
Conclusions	101

CHAPTER TWO	112
RUTILE FROM PANASQUEIRA (CENTRAL PORTUGAL): AN EXCELLENT PATHFINDER FOR WOLFRAMITE DEPOSITION	112
Abstract	112
1. Introduction	113
2. <i>Geological Setting</i>	114
3. <i>Material and Methods</i>	115
4. <i>Results</i>	115
4.1. Petrography	115
4.2. Rutile Chemical Composition	118
5. <i>Interpretation</i>	120
5.1. Crystal Chemistry	120
5.2. Compositional Zoning: Sector Zoning	122
5.3. Compositional Zoning: Oscillatory Zoning	126
6. Discussion	129
6.1. Oscillatory Zoning: External or Internal Control?	129
6.2. Open or Closed System Evolution?	130
6.3. Oscillatory Zoning as a Consequence of Seismic Activity?	131
6.4. Nature of the Fluid(s)	131
7. Conclusions	132
Part Two	141
Panasqueira Chemical Fluid Evolution	141
CHAPTER THREE	142
FLUID EVOLUTION IN THE PANASQUEIRA DEPOSIT: THE ROLE OF EXHUMATION AND MULTIPLE FLUID PULSES IN THE TRANSPORT AND DEPOSITION OF W-Sn-Cu	142
Abstract	142
1 Introduction	143
2 Methods	146

Paragenetic associations	146
Fluid inclusions	147
3 Paragenetic succession at Panasqueira	148
General characteristics of the paragenetic succession	148
Revised Panasqueira paragenetic chart	156
4 Fluid inclusions results	166
Fluid characterization	166
5 Bulk chemical evolution	183
6 P-T estimation	188
Thermal gradients and proximity to magma intrusions: the convective fluid system	189
Long-lived hydrothermal systems likely related to multiple intrusions	189
7 Conclusions	192
Part Three	197
Experimental Part On W-Behaviour	197
CHAPTER FOUR	198
TUNGSTEN (VI) SPECIATION IN HYDROTHERMAL SOLUTION UP TO 400°C AS REVEALED BY IN-SITU RAMAN SPECTROSCOPY	198
Abstract	198
1 Introduction	199
2 Methods	200
2.1 Experiments	200
2.2 Spectroscopic cell and Raman data acquisition	201
2.3 Fitting procedure of Raman spectra	202
3 Results	206
3.1 Effect of temperature and pH on W speciation	206
3.2. Stability and reversible formation of W-species	208
3.3. Effect of carbonate and chloride	209
4 Discussion	211

4.1. Identification of W-species	211
4.2. Tungsten speciation	214
4.3. Geological implications	216
5. Conclusion	216
Part Four	222
Discussion Upon a Possible Panasqueira Model and Open Questions	222
4.1 IMPLICATIONS FROM THE PARAGENETIC SUCCESSION: GEOCHEMICAL INTERPRETATION, PROBLEMS TO BE SOLVED	223
4.2 NATURE AND ORIGIN OF THE FLUIDS	224
A- Fluid origin	224
Predominance of Pseudo-Metamorphic Fluids	224
Introduction of Magmatic Fluids in the System	225
B- Fluid Migration and Exhumation	225
C- Quartz vein formation	226
4.3 METAL SOURCES (W and other RM)	227
A- Granite source of fluids and metals? A connected question: the role of “greisen” and “greisenization”	227
The G1, G2, G3, G4 Granites	229
Greisenization versus Episyenitization	234
Protolithionite (-) and the Silicification Events	235
HYPOTHESIS UPON CONCEALED RMG BODIES	237
B- Metamorphic Source of Metals	238
Magmatic-metamorphic variant:	238
4.4 THE TIME CHART AT PANASQUEIRA	239
4.5 MECHANISMS OF WOLFRAMITE PRECIPITATION	242
A- The Transport of W in Solution, State of the Art	242
B- The New Data on Complexation	243
C- The Potential Mechanisms for W-Species Destabilization	244

4.6	APPLICATION TO PANASQUEIRA CASE	247
A-	Previous Works	247
B-	Constraints Issued from the Present Work/Critics of Previous Works	247
	CONSTRAINTS FROM THE PARAGENETIC SUCCESSION: INCONSISTENCY OF THE LECUMBERRI-SANCHEZ ET AL. (2017) MODEL	247
	CONSTRAINTS FROM THE TOURMALINE STUDY	247
	THE MAIN STAGE OF WOLFRAMITE DEPOSITION: CONSTRAINTS FROM FI DATA	248
	Part Five	250
	Conclusions	250
	250	
	CONCLUSION	251
	THE PANASQUEIRA METALLOGENIC (MINERAL) SYSTEM : THE EVIDENCE FOR A PROTRACTED CRUSTAL-SCALE SYSTEM	251
5.1	Proposition of a Conceptual Model for the Early Stages (I-II)	251
5.3.	A long-lived crustal scale system	257
	Appendix	263
	APPENDIX PART ONE: CHAPTER ONE	264
	Table A1: Operating conditions for the LA-ICP-MS equipment	264
	Appendix A2: Ar-Ar dating of muscovite (methodology)	265
	Appendix A0:	266
1.	Problems in measuring Tur compositions by EPMA	266
2.	Reality and extent of a Si <i>apfu</i> bias in SEM-EDS analyses	266
3.	SEM-EPMA comparison	267
4.	Internal consistency of SEM-EDS analyses	270
5.	The case for F	271
6.	Conclusion	272
	Appendix A3-Table A3: Major element analyses of the early tourmaline from Panasqueira	273
	Appendix A4- Table A4: Major element analyses of the early tourmaline from Panasqueira	273

Appendix A6- Table A6: LA-ICP-MS U-Pb data for the Panasqueira Rutile - All errors are listed at 1 sigma	273
Appendix A7- Table A7: $^{40}\text{Ar}/^{39}\text{Ar}$ dating of a muscovite selvage from Panasqueira	273
Appendix A8:	273
Boron mass balance calculations	273
Volume of magmatic water required for boron transportation	274
Possible water yield by the granite system	274
Appendix A9: Oscillatory zoning: a (micro)seismic connection?	276
APPENDIX PART ONE: CHAPTER TWO	278
Supplementary Data: Table S1	278
APPENDIX PART THREE: CHAPTER FOUR	278
Annex 2: Table 1, k calibration, Table 3, Table 4	278
Annex 1: Table 5, Table 6, Table 7	278
Acknowledgments	280

Résumé Étendu

L'importance accordée aux métaux rares a augmenté considérablement au cours des trois dernières décennies, en raison de la demande croissante provenant de l'industrie, de la technologie et des économies émergentes. Parmi ces métaux rares, le tungstène (W) a été l'objet d'attention puisqu'il est utilisé dans des produits couvrant une large gamme d'objectifs dans l'industrie de haute technologie. En Europe de l'Ouest, la formation des gisements de tungstène s'est principalement déroulée pendant l'orogénèse varisque, avec un total de réserves estimé à ~ 1.1 Mt W. La Zone Ibérique Centrale (ZIC), avec ~ 210 Kt de W, est l'une des principales provinces où ce métal est concentré, avec l'Erzgebirge (~ 270 Kt) et la Cornouailles (425 Kt). Dans la ZIC, la mine de Panasqueira (Covilhã, district de Castelo Branco au centre du Portugal), active pour plus de 100 ans, est depuis longtemps l'un des plus grands gisements de W en Europe occidentale, avec ~ 111 Kt de W produit dont au moins 88 Kt dans la période 1947 – 2014 (correspondant à 110.000 tonnes de concentré de wolframite $(\text{Fe, Mn})\text{WO}_4$). Les réserves restantes sont d'environ 23 Kt. Ce gisement constitue plus d'un tiers des réserves en W de la ZIC. Les résultats présentés dans ce travail portent sur ce gisement.

Panasqueira montre une association, inhabituelle dans la chaîne varisque, composée de veines minéralisées subhorizontales de quartz-wolframite-cassitérite-muscovite-topaze et sulfures. Le système minéralisé couvre une superficie de plus de 10 km² avec une extension verticale d'environ 300 m. Un grand corps granitique en profondeur est révélé par une auréole métamorphique de contact. L'auréole est cependant recoupée par le réseau des veines. Au sommet de cette intrusion, des sills et une coupole de granite à métaux rares sont affectés par la greisenisation et sont également recoupés par le système des veines. L'histoire métallogénique est longue et compliquée, avec une superposition presque systématique des stades tardifs sur les plus précoces. En particulier, des phénomènes généralisés de recristallisation/dissolution du quartz compliquent la mise en place de la séquence paragénetique et l'étude des premiers stades minéralisateurs.

Une connaissance précise et détaillée de la succession paragénetique est la condition préalable à tout travail fiable géochimique ou d'inclusion fluide. Dans cette thèse, on propose une nouvelle succession minéralogique intégrant des observations à toutes les échelles : du niveau de l'« affleurement » (observations à l'échelle du pilier de la galerie dans la mine) au niveau microscopique (compris la microscopie photonique et électronique). Les stades I et II, caractérisés simplement par une association quartz-wolframite (Wfm1-2), sont clairement les principaux événements de dépôt du W. Ni la cassitérite (Cst), ni l'arsenopyrite (Apy), ni la muscovite (Ms), ni la topaze (Toz) ne sont présentes à ces stades. Le dépôt de la Wfm a été immédiatement précédé par un assemblage de tourmaline (Tur) et de rutile (Rt) riche en tungstène, développés dans l'éponte des filons. Le stade IIIa est défini par un

assemblage de Toz-Cst1-wolframite (Wfm3) et marque le début du stade principal à sulfure (stade IIIb), avec la sphalérite (Sph1) - pyrrhotite (Po)-chalcopyrite (Ccp1). Le phosphate rare, wagnerite (Wgn), peut-être synchronique à ce stade et ne semble pas temporellement lié aux autres phosphates. Un premier processus de pyritisation (marcasite) (stade IIIc) suit immédiatement le dépôt du sulfure principal et est indépendant de l'assemblage latéral (Sd)-pyrite (Py) ultérieur. Par la suite, le stade IV est le principal stage de dépôt de Sn (Cst2), avec une Wlf tardive (Wfm4) également présente. Le quartz, la muscovite (Ms1) et l'arsenopyrite (Apy) sont cependant les principaux minéraux de la phase IV, et la panasqueraite et l'apatite (Ap) sont associés. Cette étape est considérée comme la deuxième étape du dépôt du Sn, mais est mineure. C'est à ce stade que se développent les spectaculaires « selvages » d'arsenopyrite et/ou de muscovite, accompagnés par la muscovitisation d'éponte, qui remplace les assemblages quartz-tourmaline antérieurs. Le stade V suivant est marqué par le développement de la sidérite (Sd), pyrite (Py) et de la muscovite tardive (Ms2), puis de la chlorite (Chl). Par la suite, le stade VI est caractérisé par de nouvelles générations de sphalérite (Sp2) et de chalcopyrite (Ccp2) précédant le dernier stade (VII), caractérisé par les minéraux à Bi-Ag-Pb-Sb et Mo. Les principales différences de ce schéma avec les séquences de minéralisation précédentes sont le découplage du dépôt de la wolframite d'autres minéraux (topaze, muscovite, arsenopyrite, apatite) au stade I, et le découplage de la sidérite de la première étape de la pyritisation à la fin du stade III. Contrairement à la muscovite et à la topaze, la tourmaline et le rutile accompagnent toute la succession paragéométrique. L'essentiel de la tourmaline et du rutile sont formés dans les premiers stades de la succession, et précèdent le principal dépôt de tungstène du stade I.

Une partie importante de cette thèse est consacrée à l'étude minéralogique de cette première étape de cristallisation de la Wfm, qui est porteur de tungstène. Il est précédé par un épisode de tourmalinisation généralisé des épontes (micaschistes du complexe de Beira) des veines minéralisées. Les cristaux de tourmaline (50-150 μm , \leq 500 μm) suivent la schistosité de l'encaissant et sont systématiquement zonés, avec un noyau (Tur0) et deux bordures concentriques (Tur1a et Tur1b), pré- et syn- fissuration précoce des veines de quartz, respectivement. En particulier, Tur0 et Tur1a précèdent le dépôt principal de la Wfm, tandis que Tur1b est contemporain de la Wfm et des cristaux de rutile (Rt) riches en W. Ces derniers ont été datés (U/Pb) à 305.2 ± 5.7 Ma, et cet âge correspond, par conséquent, à l'événement principal de dépôt du W. Les cristaux de Rt montrent un zonage sectoriel (SZ) et oscillatoire (OZ). Les données de composition chimique obtenues par microsonde électronique sur ces cristaux, ont été utilisées pour discuter (1) des effets du SZ sur le piégeage différentiel d'éléments en traces, et (2) l'importance du zoning oscillatoire dans la recherche d'indications sur les sources de fluides et leurs mélanges éventuels. Une attention particulière a été donnée aux concentrations de Sn, W (Nb, Ta) dans les rutiles comme traceurs du dépôt de la Wfm. En ce qui concerne le SZ, les résultats indiquent que le W est plus incorporé que Nb et Ta dans des facettes cristallines plus efficaces, tandis que le contenu de Sn n'est presque pas affecté. L'effet du SZ est donc une augmentation progressive de la teneur relative (wt%) en Sn entre la facette de type « pyramide » et la facette de type

« prisme », combinée à une augmentation moins importante des teneur relatives en Nb + Ta. Le ZT concerne la plupart des éléments mineurs : W, Nb (Ta), Fe, V, Cr et Sn. Dans les doublets (bandes claires et foncées) qui caractérisent l'OZ, les bandes claires sont en général enrichies en W par rapport aux bandes foncées, alors que l'inverse est vrai pour Nb et Ta. Les doublets peuvent être considérés comme le résultat de l'afflux successif (1) d'un fluide riche en W, mais pauvre en Nb + Ta, brusquement remplacé par (ou mélangé avec) (2) un fluide riche en Nb+Ta et pauvre en W. Ces doublets pourraient alors être à leur tour liés à une contribution pendant le processus de tourmalinisation de fluides provenant de sills de granite à métaux rares observés au sommet de l'intrusion principale de Panasqueira.

La tourmaline a une gamme de compositions qui la range entre la Fe-dravite et la schorlite avec une tendance de type foitite et oxyfiotite. Du noyau à la bordure plus extérieure de la Tur (de Tur0 à Tur1b), la teneur en F, et le ratio Fe# ($Fe/(Mg+Fe)$) augmentent constamment ($F \leq 1\%$ a.p.f.u. (atom per formula unit)). Les teneurs en éléments en trace (ppm) ont été mesurées par LA-ICP-M : Ti ($\leq 2\,500$), Zn (≤ 931), Mn (≤ 606), Li (≤ 685), V (≤ 472), Cr (≤ 624), Sr (≤ 825), Sn (≤ 92.1), Sc (≤ 92.1), Be (≤ 21.2), Pb (≤ 18.7), Ni (≤ 56.1), Co (≤ 14.3), Y (≤ 20), W (≤ 60), Nb (≤ 52) et Ta (≤ 6). La comparaison des compositions de la tourmaline 1a et 1b suggère que deux fluides sont impliqués dans la tourmalinisation : L1, déjà présent dans le système depuis le début, caractérisé par Co-Cu-Pb-Sc-Sr-V-Cr-W-Nb-Ta ; et L2, injecté plus tard et continuellement mélangé avec L1, et défini par le cortège Li-Zn-Mn-Fe et F. L'appauvrissement du W dans Tur1b peut être le résultat de la compétition avec d'autres phases de W au premier rang desquels, le W-Rutile et la Wolframite précoce. Les résultats de la comparaison entre les tourmalines 1a et tourmaline 1b sont les suivants : 1) l'origine métamorphique de L1, confirmée également par les spectres de Terres Rares dans la tourmaline, et 2) la connexion avec une source granitique pour L2. En outre, les résultats des analyses détaillées des tourmalines et rutiles, ont montré un comportement clairement opposé entre W d'une part, et Nb, Ta, Sn d'autre part, ce qui indique une origine multi-source pour L2. Lors de la tourmalinisation, le système hydrothermal est ouvert et tous les éléments nécessaires au dépôt de la Wfm sont transportés par différents fluides : Fe et Mn clairement par L2, par exemple.

Toutefois, le processus responsable du dépôt de la Wfm reste inexplicable, car il ne peut pas être interprété par l'interaction fluide-roche. En général, la connaissance de la spéciation du W dans les solutions hydrothermales est d'une importance primordiale pour développer les modèles géochimiques décrivant la genèse des gisements à W, et spécialement dans le cas de Panasqueira. A l'heure actuelle, dans la littérature, il y a seulement deux modèles existants pour le transport hydrothermal et le dépôt du W, qui s'appuient sur une spéciation dominée par l'acide tungstique $H_2WO_4^0$, et ses produits de dissociation : HWO_4^- et WO_4^{2-} . Ces modèles démontrent que les espèces polymériques à W peuvent demeurer en solution à T et P élevées à un pH inférieur à 3, mais d'importantes contradictions existent quant à la nature des polymères et leur stabilité thermodynamique. En fait, la spéciation du

W en conditions hydrothermales contraste avec la spéciation du W en conditions ambiantes, où la coexistence de plusieurs polyanions contenant 6, 7, 10 et même 12 atomes du W, selon le pH, a été démontrée. Les modèles négligent également 1) qu'à basse concentration du W, les monomères (HWO_4^- et WO_4^{2-}) deviennent de plus en plus stables, mais qu'au moins un polymère à charge élevée demeure à pH inférieur à 3 ; et (2) l'existence de deux espèces stables de polymères, $\text{W}_{10}\text{O}_{32}^{4-}$ et $\text{H}_3\text{W}_{12}\text{O}_{40}^{5-}$, qui dominent la spéciation du W jusqu'à 200°C dans des conditions acides ou neutre. Fait intéressant, ces polymères de W, censés être présents à une température élevée, ne correspondent pas à ceux clairement identifiés dans des conditions ambiantes comme le *paratungstate* A ($\text{W}_7\text{O}_{24}^{6-}$), le *paratungstate* B ($\text{H}_2\text{W}_{12}\text{O}_{42}^{10-}$) ou le *métatungstate* Y ($\text{H}_2\text{W}_{12}\text{O}_{40}^{6-}$, avec une structure Keggin). Pour combler cette lacune, nous avons effectué des expériences dans le système $\text{Na}_6\text{W}_{12}\text{O}_{39}\cdot\text{H}_2\text{O} + \text{HCl}$ ou NaCl et $\text{Na}_2\text{WO}_4\cdot 2\text{H}_2\text{O} + \text{HCl}$, NaCl ou NaOH en fonction du pH et de la concentration de tungstate et/ou de chlorure. Nous avons utilisé la l'analyses in-situ par spectroscopie Raman à la technique des capillaires pour définir la stabilité des espèces de W mal ou pas encore documentées de 25°C jusqu'à 400°C, afin d'obtenir une vision globale des modes de transport du tungstène. Les résultats indiquent que dans les solutions alcalines, la seule espèce existante est WO_4^{2-} , tandis que dans les solutions acides la spéciation du W est beaucoup plus compliquée avec la coexistence de l'heteropolyanion *paratungstate* A $\text{W}_7\text{O}_{24}^{6-}$, ainsi que d'autres espèces polymériques comme le *décatungstate* $\text{W}_{10}\text{O}_{32}^{4-}$ à basse température, et la prédominance surprenante de la longue chaîne, fortement chargée du *dodeca -métatungstate* $\text{H}_2\text{W}_{12}\text{O}_{40}^{6-}$, espèces à haute température. Même si les espèces de W identifiées peuvent être sujettes à une interprétation différente, toutes celles-ci détectées à température élevée existent à température ambiante ; leur nature est la même, sans formation de nouveaux complexes ou polymères. Par conséquent, le tungstène a une forte tendance à former des complexes, de type hétéropoly-, aquapoly-, et isopoly- caractérisés par des structures Keggin. Ces espèces polymériques jouent probablement un rôle important dans le transport du W dans des solutions hydrothermales acides à neutres, sans carbonate ni chlorure.

Dans la dernière partie de la thèse, les résultats de la partie expérimentale sont combinés avec l'histoire pression-température-composition des fluides de Panasqueira, à travers l'étude des inclusions fluides (IF) piégées dans les minéraux transparents de chaque étape de la séquence paragénétique : le stade à topaze, le dernier stade à quartz-wolframite - cassiterite - aersenopyrite - (riche en Li-Fe) muscovite, ainsi que les stades à apatite et sidérite. Les types d'IF les plus fréquents, tout au long de l'histoire du gisement, sont riches en espèces volatiles et biphasées ($\text{H}_2\text{O}-\text{CO}_2 \gg \text{CH}_4 > \text{N}_2$), homogénéisent en phase liquide à des températures proches de 300 °C. La plupart des IF liées au premier stade de dépôt (grandes veines de QI-II à wolframite, Stade I-IIa) sont malheureusement décrépitées ou déformées. Quelques inclusions de petite taille, non reconnues jusqu'à présent, ont résisté à la déformation dans le quartz. La topaze est sécante sur l'assemblage initial wolframite-quartz, et est antérieure au stade à sulfure. Pour ce stade à topaze (Stade II-b), des inclusions carboniques aqueuses (Lw-c), ainsi que des inclusions denses dominées par la CO_2 Lc-(w) ont été identifiées. Les conditions de pression et température du piégeage, contraintes par

l'intersection entre les isochores des IF Lc-(w), plutôt plates, et les isochores abruptes des IF Lw-c, sont de 2 à 3 kbar et 500°C. Ces conditions de P-T sont cohérentes avec les niveaux structuraux profonds autour de 10 à 11 km et des températures élevées, généralement attendu près des intrusions magmatiques, et sont correspondent au stade de 305 Ma déjà daté par le rutile. Après le stade à sulfures (Stade III-B : pyrrhotite-sphalérite), l'assemblage minéralogique tardif (Stade IV), se compose de quartz IV – wolframite – cassitérite – arsenopyrite – (Li-Fe) muscovite – apatite – sidérite. Il est répandu dans le gisement mais son expression est extrêmement localisée en cavités et géodes, ou comme intercalaires le long de la bordure ouverte entre les épontes et les veines de quartz I-II. Le stade IV à wolframite – cassitérite – arsenopyrite – muscovite Li-Fe est répandu et caractérisé par le développement envahissant de la muscovite Fe-Li au détriment du quartz, qui est dissous en formant de grandes cavités spectaculaires. Ce stade est daté à 296 Ma par K/Ar sur muscovite. Dans le quartz IV, les inclusions les plus fréquentes sont encore une fois les inclusions Lw-c (volatile biphasé, $H_2O-CO_2 \gg CH_4 > N_2$) homogénéisant à l'état liquide (eau) à des températures proches de 300 °C, et semblables à celles décrites dans les travaux précédents. En plus, des IF volatiles presque pures Vc-(w) ($CH_4 > N_2 \gg CO_2$) de haute densité avec de faibles quantités d'eau (T_h de -85°C), apparaissent synchrones à les IF Lw-c. Ainsi, l'intersection des isochores des deux familles permet une estimation robuste des conditions de piégeage qui sont d'environ $500 \pm 25^\circ C$ et 280 ± 20 MPa (considérées lithostatiques, ~ 11±1 km de profondeur). Le stade à quartz-cassitérite suivant est estimé de l'ordre de $400 \pm 50^\circ C$ et 140 MPa. Le stade apatite-sidérite est caractérisé par des couples P-T légèrement inférieurs : 350-400 °C et 30 à 100 MPa. Il est à noter que la plupart des travaux précédents sur les IF de Panasqueira ont probablement porté sur ce stade IV.

Du premier au dernier stade, les fluides sont similaires à ceux généralement présents dans les séries métamorphiques à l'équilibre avec le graphite, $CO_2-CH_4-N_2(H_2O)$. En outre, très peu de preuves de mélange avec un fluide magmatique ont été trouvées, à l'exception des saumures à Li lors du stade le plus tardif à sidérite. Tout au long de l'évolution, des températures très élevées sont enregistrées, indiquant un gradient géothermique élevé (jusqu'à $\sim 75 \pm 10^\circ C \cdot km^{-1}$), alors que pour la pression, des variations considérables ont été estimées : une baisse significative des pressions lithostatiques (240 MPa, pendant le stade principal à oxydes) jusqu'aux pressions hydrostatiques à une profondeur plus superficielle (± 30 Mpa, pendant le stade IV à quartz - wolframite – cassitérite - apatite). Cette chute de pression est liée à une exhumation importante de 10-11 km jusqu'à 3-4 km de profondeur. La persistance de températures élevées, avec des pulses thermiques à faible profondeur, est révélatrice de gradients de température plutôt élevés, probablement liés à l'advection de chaleur produite par une série d'intrusions et/ou par un flux de chaleur locale autour d'un linéament majeur affectant la lithosphère supérieure. Selon les données géochronologiques récentes, un nouveau schéma temporel est proposé entre ~305 Ma à ~296 Ma. Deux stades principaux sont distingués : (1) les stades I-III caractérisés par une exhumation lente (0.1 mm/an), avec le système minéral principal à W(Sn) enraciné profondément autour de 9-12 km de profondeur ; et (2) l'étape IV, avec un

niveau structural beaucoup moins profond d'environ 3 km de profondeur. La nature des fluides ne change pas de manière significative pendant toute l'histoire, ce qui signifie que la contribution des fluides de surface est restée limitée. Du Stade II au Stade IV, une exhumation assez rapide a eu lieu de ~9-10 km (à 303 Ma) à ~3 km (à 296 Ma), soit 6-7 km en 7 Ma correspondant à un taux d'exhumation de 1 mm/an. Ces résultats modifient considérablement le concept génétique de formation du gisement, qui a été considéré pendant plus de 40 ans comme formé près de la surface, comme un dépôt épithermal. Cette dernière hypothèse avait été formulée sur la base d'un concept d'« ébullition » des fluides, sur la base de données d'inclusions fluides qui ne s'applique qu'au stade IV et non au stade principal à W (Qtz I et II).

Abstract

The Panasqueira W-Cu-Sn deposit (Portugal), one of the main W repository in West Variscan Europe, consists of sub-horizontal mineralized veins of quartz-wolframite-cassiterite-muscovite-topaz-sulphides. The deposit history is long and complicated, with nearly systematic superimposition of later stages on the earlier. Therefore, quartz dissolution-recrystallization is the rule, complicating the setting up of the paragenetic sequence and the study of earliest stages. An important part of this thesis is devoted to the mineralogical study of the first wolframite (Wfm) depositional stage, which is the most valuable in terms of ore (W)-quantity. It is preceded by a tourmalinization event spread all around the contact with the ore-veins. Tourmaline (Tur) crystals (50-150 μm , \leq 500 μm) follow the protolith schistosity and are systematically zoned, with a core (Tur0) and two concentric rims (Tur1a and Tur 1b), pre- and syn- early crack-seals, respectively. Tourmaline, coeval with W-Rutile (Rt), is contemporaneous the early wolframite. This event, preceding the main W deposition, has been dated (U/Pb, Rt) at 305.2 ± 5.7 Ma. The rutile crystals display sector (SZ) and oscillatory (OZ) zoning. Compositional data obtained on those crystals (back-scattered electron images and X-ray maps) were used to address (1) the effects of SZ on differential trapping of minor elements, and (2) the significance of the OZ in deciphering fluid sources and fluid circulation dynamics. Particular attention was paid to Sn, W (Nb, Ta) concentrations in rutile as pathfinders of the wolframite deposition. Concerning the SZ, W is more incorporated than Nb and Ta into more efficient crystalline *facies*, whereas Sn contents are nearly not impacted. The net effect of the SZ is thus a progressive increase of the relative weight of Sn from pyramid to prism faces, in combination with a less significant increase in the relative weight of Nb + Ta. The OZ concerns most minor elements: W, Nb (Ta), Fe, V, Cr and Sn. In the doublets (alternate clear and dark bands characterizing the OZ), the clear bands are in general enriched in W relatively to the dark ones, whereas the inverse is true for Nb and Ta. The doublets may be viewed as the result of the successive influx of (1) a W-rich, Nb + Ta poor fluid, abruptly replaced by (or mixed to) (2) a Nb+Ta-rich and W-poor fluid. It could be in turn related to a rare-metal granite layer observed atop of the Panasqueira granite. Tourmaline crystal compositions cover a range between Fe-dravite and schorlite with same foitite and oxy-foitite components. From the core to the external reem of tourmaline crystals (from Tur0 to Tur1b), the amount of F a.p.f.u. (atom per formula unit) and Fe# (Fe/(Mg+Fe)) increases constantly ($F \leq 1\%$). Trace elements contents (ppm) have been measured by LA-ICP-MS: Ti ($\leq 2\ 500$), Zn (≤ 931), Mn (≤ 606), Li (≤ 685), V (≤ 472), Cr (≤ 624), Sr (≤ 825), Sn (≤ 92.1), Sc (≤ 92.1), Be (≤ 21.2), Pb (≤ 18.7), Ni (≤ 56.1), Co (≤ 14.3), Y (≤ 20), W (≤ 60), Nb (≤ 52) and Ta (≤ 6). Quantitative comparison between the two external reems (Tur1a and Tur1b) compositions has shown that two fluids are involved during the tourmalinization: L1, already present in the system from the beginning, characterized by Co-Cu-Pb-Sc-Sr-V-Cr-W-Nb-Ta; and L2, injected later and continually mixed with L1, defined by Li-Zn-Mn-Fe and F. W depletion in the

external reem (Tur1b) may be the result of the concurrency during W-Rt and early Wfm deposition. Results of this comparison are: 1) the metamorphic origin of L1, confirmed also by Tur REEs spectra, and 2) the suspicious connection with a granitic source for L2, as rare metals (W, Sn, Nb, and Ta) are transported by L1. Moreover, the combined results of the detailed analyses of both Tur and Rt, have shown a clear opposite behavior between W and Nb, Ta, Sn which enforce a L2 multi-sources origin. During the tourmalinization event, the hydrothermal system is open and all the elements required for the Wfm deposition are transported by different fluids: Fe and Mn clearly by L2, for instance. However, it remains to find out the reasons for Wfm precipitation, which are not due to the fluid-rock interaction. Only two models exist upon the hydrothermal transport and deposition of W, relying on a speciation dominated by tungstic acid (H_2WO_4)⁰, and the products of its dissociations HWO_4^- and WO_4^{2-} . These models demonstrate that polymeric W-species may remain in solution at elevated T-P and pH below 5 (or 3), but also show important contradictions regarding both the nature of the polymers and their respective stability. To fill this gap, we performed hydrothermal experiments in the $\text{Na}_6\text{W}_{12}\text{O}_{39}, \text{H}_2\text{O} + \text{HCl}$ or NaCl and $\text{Na}_2\text{WO}_4, 2\text{H}_2\text{O} + \text{HCl}$, NaCl , or NaOH system as function of pH and tungstate/chloride content. We use Raman spectroscopy coupled to the fused silica glass capillary technic to define the stability of the undocumented tungsten-species at different temperatures (up to 400°C), to get a global answer upon its transport at different hydrothermal conditions. Results indicate that in alkaline solutions, the only existing species is $(\text{WO}_4)^{2-}$, while in acidic solutions W speciation is far more complicated with the coexistence of the heteropolyanion *paratungstate A* (W_7O_{24})⁶⁻, together with other several polymeric species like *decatungstate Y* ($\text{W}_{10}\text{O}_{32}$)⁴⁻ at low temperature, or the surprising predominance of the long chain, highly charged *dodeca α -metatungstate* ($\text{H}_2\text{W}_{12}\text{O}_{40}$)⁶⁻ species at high temperature. Even if these W-bands identified may be subject to a different interpretation, all W-bearing species detected at elevated T exists at room temperature, and their nature remains the same with no new complex or polymers formation. As a result, tungsten has a strong tendency to form complexes, like heteropoly-, aquapoly-, and isopoly- tungsten compounds characterized by Kegging structures. These polymeric species probably play an important role in the W transport in acidic to neutral hydrothermal solutions, without carbonate or chloride compounds. Also the evolution of P-T-X history has been studied: in particular, the topaz stage, and the later quartz-wolframite-cassiterite-arsenopyrite-(Li-Fe rich) muscovite and apatite-siderite stages. The topaz crosscut initial wolframite-quartz assemblage, and is earlier than the sulphide stage. The wolframite-cassiterite-arsenopyrite-(Li-Fe rich) muscovite stage is widespread and characterized by the pervasive development of (Li-Fe)-muscovite at the expense of dissolved quartz, as spectacular vugs. Most frequent fluid inclusions all along the evolution are two-phase volatile-bearing ($\text{H}_2\text{O}-\text{CO}_2 \gg \text{CH}_4 \gg \text{N}_2$), homogenizing in the liquid (water) phase at temperatures close to 300°C, similar to those described in literature. Unrecognized until now are pure volatile liquid fluid inclusions (with variable amounts $\text{CH}_4 \gg \text{N}_2 \gg \text{CO}_2$ depending on the stages) which appear coeval at each stage with the Lw-c fluid inclusions. The intersection of the two isochore families allows a robust estimation of the trapping conditions from the topaz stage (400±50°C, 300±20 MPa) to the later quartz (wolframite)-apatite-siderite stage characterized by lower pressure and high temperatures (350-420°C,

40 to 120 ± 20 MPa). This indicates that high geothermal gradient affected the studied zones at several stages and are related to heat advection produced by a series of concealed granites from 305 to 295 Ma.

Introduction

Tungsten, W, is a transition metal (group 6, Atomic Number 74, d-block, mass 183.84 g/g atom) and has been considered the most refractory and heaviest metal on Earth, with: the highest melting point (except carbon) of 3422°C, a boiling point of 5930°C, high density (19.25 g/cm³), excellent thermal and electrical conductivity, very high moduli of compression and elasticity and the lowest vapor pressure and expansion coefficient of all metals. Consequently, W is a strategic metal that finds application in different fields of modern science and technology. In a natural environment tungsten has never been found pure, but it exists as oxo-rich tungstate minerals: ([Fe/Mn]WO₄) *wolframite* or (CaWO₄) *scheelite*. The ore-deposits where, wolframite or scheelite are concentrated, are commonly skarns or granite-related vein-type which include also Ta-Nb-Sn- mineralization (Linnen and Cuney, 2005). In particular, W exhibits a clearer affinity for specific geologic and geochemical environments, called metallogenic provinces, which are zones of the Earth in which deposits of an element are unusually abundant (Lehmann, 1990). W-deposits with processes involved in their genesis, have been classified in three main categories by Lehmann, 1990: i) W-deposits associated with igneous rock series, ii) W-deposits originated by the redistribution of tungsten contained in igneous rock bodies through hydrothermal processes, and iii) W-deposits related to pre-magmatic concentration of W. However, in most of the cases, petrological interpretation implies that hydrothermal fluids have the main role in W- transportation and deposition. All significant W deposits have been studied, mainly during the 80s-90s. Since this time, methodological progress has been made, allowing to better constrain the depositional conditions through the improvement of micron-scale analyses of the ore minerals and in-situ measurement of the fluid composition from fluid inclusions microthermometry technique. Consequently, renewed studies have been conducted on selected deposits, with a particular emphasis on the determination of the paleo-ore fluid chemistry (including metal contents), and the detailed characterization of metals in ores in order to identify the behavior of W and other elements, included traces elements, associated in the main solid phases.

This thesis takes part within the framework of the scientific European project ERAMIN "New Ores" and Labex "Ressources 21" on the subject related to the understanding the processes of concentration of strategic metals. It concerns, in particular, the study of rare metals, grouping tungsten (W), tin (Sn), tantalum (Ta) and niobium (Nb), which are, for the European Union, critical metals in term of supply numerous technological applications. Rare metal (W- Ta- Nb- Li- Sn) reserve has taken a major importance in the economic world because of the increasing demand for the new technologies in one hand (Fig. i-1), and the emergence of the new first rank B.R.I.C. (Brazil, Russia, India and China) industrial countries, on the other hand. According to the most recent US Geological Survey report on W, world tungsten production was 88.100 MT in 2016 increasing to 95.000 MT during 2017.

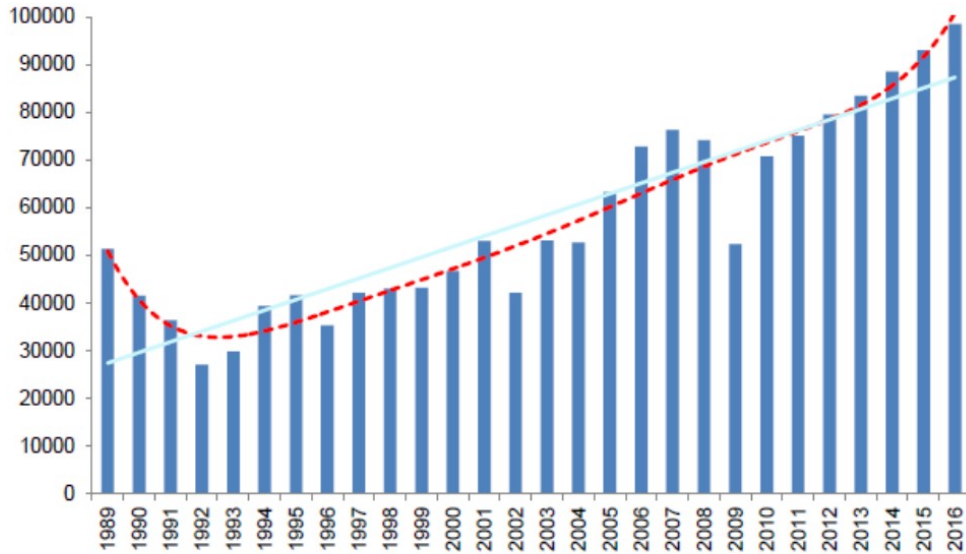


Fig. i-1: W demand in tons from 1986 to 2016. Source: ITIA: Roskill forecast.

In particular, according to SMR GmbH, Steel & Metal Market Research (Reutte, December 2018), there is a real market growth for tungsten due to the high demand, especially from the emerging countries: electronics devices, energy infrastructures, transportation, urbanization, construction, railways, industrial use and chemicals, civil/general aviation etc. Tungsten carbide, for instance, is the dominant requested material also by the defense sector. Tungsten is commonly used to produce electrical wires, for heating and electrical contacts, and is also used in welding, heavy metal alloys, heat sinks, turbine blades and as a substitute for lead in bullets (Koutsospyros et al., 2006). In 2017, the countries with the highest production were (largest to smallest): China (79.000 MT), Vietnam (7.200 MT), Russia (3.100 MT), Bolivia and United Kingdom (1.100 MT), Austria (950 MT), Portugal (680 MT), Rwanda (650 MT) and Spain (570 MT). Clearly, China has a monopoly of world W supply – thus, Europe has to learn how to process low-grade ores and tailings from already mined deposits, and especially to discover new resources.

The Variscan province is the main endowment in rare metals (W- Ta- Nb- Li- Sn) in Europe, with several districts in Germany, United Kingdom, Spain, France, and Portugal. The subject of this thesis is the investigation of one of the largest deposit in Europe: the tin-tungsten deposit of Panasqueira (Portugal). Principally, the aim is to deal with the necessity to better constrain the processes involved with W- deposition at Panasqueira, from the source (hydrothermal, magmatic and/or metamorphic) to its scattered discharge underground. The characterization of W behavior at each stage is required in order to gain an in depth knowledge W sources, transport and deposition. Therefore, the main objective of this thesis is to understand the fluids evolution of Panasqueira hydrothermal system, with a peculiar focus on the main tungsten mineralizing event. The latter is characterized by wolframite (Fe,Mn)WO₄, which is the only W-mineral at Panasqueira. Wolframite is associated together with others

minerals (e.g. quartz, tourmaline and rutile), which have been meticulously analyzed. These results are discussed in Chapters one and two.

To improve geochemical model of W transport and deposition, we have performed an experimental study of W speciation in aqueous fluids up to 400°C. The effects of pH, chloride and carbonate ligands on W speciation under hydrothermal condition have been evaluated. We use Raman spectroscopy coupled to the fused silica glass capillary technic to define the stability of the tungsten-polymers at T up to 400°C. The knowledge of tungsten W-speciation in hydrothermal solutions is of primary importance to develop geochemical models for the genesis of W ore deposits. Currently, W mobility in deep and hot geological fluids is poorly constrained. W in aqueous solution mainly exists as the form of $(\text{WO}_4)^{2-}$ and its protonated forms (Wood S. A. and Vlassopoulos D., 1989) depending on pH. Chloride does not form stable complexes with W (Wood S.A., 1992). However, polymeric W species such as the hexamer $(\text{H}_n\text{W}_6\text{O}_{21})^{n-6}$ or alkali metal complexes such as NaWO_4 or KWO_4 , may also exist, but there is currently no thermodynamic data to predict their abundance (Redkin A.F. and Bondarenko G.V., 2010). In alkaline solutions, the only existing species is $(\text{WO}_4)^{2-}$, while in acidic solutions W speciation is far more complicated with the coexistence of $(\text{HWO}_4)^-$ together with several polymeric species like $(\text{W}_6\text{O}_{19})^{2-}$ at low temperature, or the surprising predominance of the long chain, highly charged $(\text{W}_{10}\text{O}_{32})^{4-}$ species at high temperature. The polymeric species will probably play an important role in the W transport in acidic to neutral hydrothermal solutions. Carbonates complexes with W remain to be demonstrated.

In the following paragraphs an overview regarding the geological setting, previous works, and main scientific questions about Panasqueira genesis ore deposit will be present, together with thesis purposes and methods.

1. STATE OF ART

Sn-W deposits in veins or in stockworks systems are the result of a magmatic-hydrothermal activity linked to the solidification of felsic, peraluminous, up to peralkaline rocks. They occur on a variety of structural settings. They are characterized mainly by: (1) structural control (i.e. veins and fracture), (2) association with highly fractured granitic intrusions, and (3) alteration greisen-type. Hercynian orogeny in Portugal has been accompanied by granitoid, some of them outcropping inside Panasqueira mine. Sn-W deposits are strongly connected to the granitic rock belts which define the spine of the hercynian chain. They consist of a dense network of subhorizontal mineralized quartz veins, intersecting the subvertical foliation of the Beira schists and the greisen cupola (Thadeu, 1951). Mineralized quartz veins emerge from a greisenized granite dome exposed in the deepest galleries of the mine. The hydrothermal ore veins with a greisenized granite dome of the same age, indicates that magmatic fluids may have been an important component. A deep crystallising granite under the vein system would provide a

source for the high overpressures encountered in the quartz layer. These high pressures were able to open the subhorizontal vein system.

1.1 Genetic Model of Deposits Associated with Veins-Stockworks

Granitic rocks associated with Sn-W deposits in veins and stockworks are generally discordant with local and regional structures and are either late orogenic or anorogenic (Sinclair, 1996). The tectonic environments in which these rocks have been placed are typically continental: continental collision zones, continental rifts, and volcanic arcs along continental margins. These deposits of tin-tungsten in the veins and stockworks are found in a wide variety of structures (Fig. i-2), involving individual veins, multiple vein systems, stockworks, breaches and replacement areas in altered rocks adjacent to the veins. They commonly took place in or near granitic intrusions which have been placed at relatively shallow levels (1 to 4 km) in the Earth’s crust. The associated intrusions are highly fractionated and generally enriched with lithophilic elements such as Rb, Li, Be, Sn, W, Mo, Ta, Nb, U, Th and REE, as well as volatile elements such as F and B (Sinclair, 1996).

The hydrothermal alteration associated with the tungsten-tin deposits of veins and stockworks is usually a greisen-type alteration that is characterized by Li, F and/or B-bearing minerals such as topaz, fluorite, tourmaline and/or Li-rich micas (Shcherba, 1970). Many copper tungsten deposits are relatively small, ranging from tens of thousands to hundreds of thousands of tonnes of ore. However, deposits consisting of several veins or stockworks can hold millions to tens of millions of tons. Panasqueira is a deposit of large tonnage (Fig. i-3).

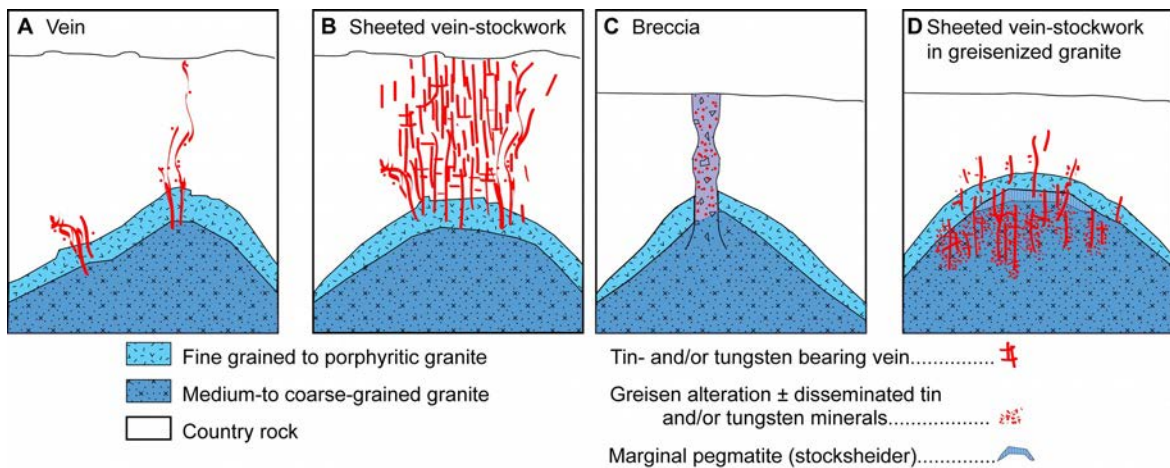


Fig. i-2: Schematic representation of the various forms of tungsten-tin deposits associated with stockworks (after Sinclair, 1996).

The association of tin-tungsten deposits with granitic rocks is well established and a genetic relationship is generally accepted (Sinclair, 1996). These granites are found in various tectonic contexts and their composition

varies from peraluminous to peralkaline. The mineralization style (i.e., vein and stockwork) depends on the containment pressure of the surrounding rocks developed during crystallization by metal-rich fluids. If the containment pressure of the surrounding rocks is low, a metal-containing fluid may escape from the magma, mainly through faults and fractures to form vein deposits (Fig. i-2A). A moderate to high containment pressure, combined with a high fluid pressure in the magma, can lead to significant fracture of surrounding rocks and the development of sigmoid veins and stockworks (Fig. i-2B). An extremely high fluid pressure in the magma leads to the instability of the surrounding rocks and the formation of breccia pipes (Fig. i-2C). If the containment pressure is high and/or if the fluid pressure in the magma is low, fracturing will be limited. In this case, the fluids will mainly be trapped in the magma during crystallization, which will lead to the formation of pegmatites or marginal stockscheider. Trapped fluids will also react with previously crystallized granite to form large areas of greisen alteration (Fig. i-2D) (Sinclair, 1996).

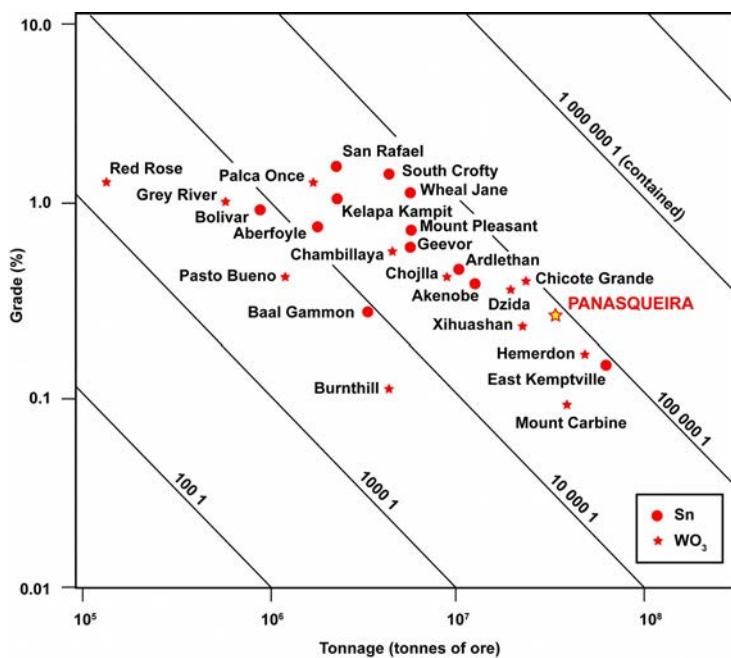


Fig. i-3: Concentration vs tonnage diagram for tungsten tin deposits of stockworks (Sn and WO₃) (modified after Sinclair, 1996).

Many of the tungsten-tin deposits associated with veins exhibit vertical zonation with respect to the morphology of the veins and the distribution of minerals. Nevertheless, Panasqueira deposit is made up of subhorizontal quartz veins that are linked to a greisenized granite dome (Fig. 4) (Thadeu, 1951). The historical models for Panasqueira are those described by Kelly and Rye (1979), Bussink (1984) and Polya (1989), which show that veins were mineralized at temperatures between 300 and 350°C. This deposit has several characteristics, such as the increasing tin content of veins and the increasing abundance of CO₂-rich fluid inclusions in quartz veins

approaching granitic dome, suggest that the same structural conduits of these intrusions were used for fluid introduction. All mineralization is enclosed in metasedimentary rocks which give a significant input for wolframite deposition, according to Lecumberri-Sanchez (2017). Launay (2018) proposes a model with the key role of the greisenized granite dome in focusing fluids and the role of overpressure of fluids when opening veins.

1.2 W-Sn- (Cu) Panasqueira Deposit

Panasqueira W-Sn-(Cu) deposit is located in the Central Iberian Zone (CIZ), which constitutes the axial zone of the Iberian belt (Fig. i-4a) (Julivert et al., 1972). The Variscan history of the CIZ begins in the Early Carboniferous and ends in the Early Permian. The tectono-thermal sequence is conveniently subdivided into five events, D1 to D5 (Diez-Fernandez et al. 2016, and references therein; Diez-Fernandez and Pereira 2017). D1 is coeval with the stacking of the allochthon and is characterized by E- or NE-verging recumbent folding, a penetrative axial plane S1 sub-parallel to S0, and the development of a Barrovian low-grade M1 metamorphism (Qtz+Chl+Pl±Ms±Cal in the more pelitic rocks (Diez Fernandez et al. 2013). It corresponds to crustal thickening, and is dated at ca. 354-347 Ma (e.g., Rubio Pascual et al. 2013).

The Iberian Central Zone consists of a complex called «Schist-Greywacke» characterized by a large amount of granitoid intrusions resulting from a major intrusion event during the last stages of Varischian orogeny (Dias et al., 1998). Numerous mineralized systems were active in the CIZ in close association with the Late Carboniferous tectonics and granitoid emplacement. More than 150 deposits are known, corresponding to both peri- and intra-granitic rare metal (Nb-Ta, Li, W, Sn) and shear-zone hosted (Au-Ag-As-Sb-Pb-Zn-Cu) systems (Tornos et al. 2000; Neiva 2002; Mateus and Noronha 2010; Noronha 2017).

At the crustal scale, the emplacement of late Carboniferous granites was accompanied by the mobilization of “metamorphic” C-O-H-N fluids which, through interaction with either magmatic-hydrothermal fluids or subsolidus (HT) granites, were at the beginning responsible of the Sn-W quartz vein systems. Later, these metamorphic fluids were mixed with massive meteoric water, yielded during the extensional regime, giving as a result the shear-zone hosted Au-Sb deposits (Mateus and Noronha 2010; Noronha 2017).

At ca.280-275 Ma, this late stage fluid event is the result of Permian extension (Lopez-Moro et al. 2017). This upper neoproterozoic age complex is affected by regional metamorphism (green schist facies). The deformation of this complex consists of straight folds (Fig. i-4a and i-4b) with subvertical axial planes NW – SE, produced by a NE – SW shortening associated with the first compressive stage of Varischian orogeny (Dias and Ribeiro, 1995).

The Iberian Central Zone has many Sn–W deposits linked to granite intrusions and formed by magmatic-hydrothermal processes (Derré, 1982). Significant rare metal deposits include:

- rare metal granites like the Argemela granite (Charoy and Noronha 1996),
- Li-Sn, e.g. Feli granite (Robles et al. 1991),

- Sn-Ta-Nb as, Forcarei Sur granite (Fuerte-Fuentes et al. 2000),
- pegmatite fields with Qtz-Cst like Argemela granite (Inverno et al. 2009), and
- Qtz-Wfm-(Cst)±Cu (Panasqueira) vein systems, Qtz-Wfm-polymetallic breccia pipe (Borralha: Noronha 1984; Lima 2015), Qtz-Sch vein systems (Barruecopardo: Sanderson et al. 2008), and skarns (Los Santos: Tornos et al. 2008). Panasqueira granite is a hercynian granite with two micas (fine to medium grain). Clarke (1970) dated the muscovite of this granite using the K-Ar method and obtained 290 ± 10 Ma. Panasqueira deposit is located in the province of Beira Baixa, on the southern side of the Serra da Estrela massif consisting of late to post-tectonic granite intrusions. It is the result of the continental collision during the Hercynian orogeny that involved subduction-related high-pressure low-temperature metamorphism (430 Ma to 400 Ma), followed by nappe intrusion, Barrovian metamorphism, crustal thickening (380 Ma to 340 Ma), and by crustal anatexis and granite emplacement (380 Ma to 280 Ma) (Thadeu, 1951; Clark, 1964; Clark, 1970; Kelly and Rye, 1979; Marignac, 1982; Snee et al., 1988 ; Bussink, 1984 ; Bussink et al., 1984 ; Poly, 1988-1989 ; Foxford et al., 1991; and Noronha et al., 1992).

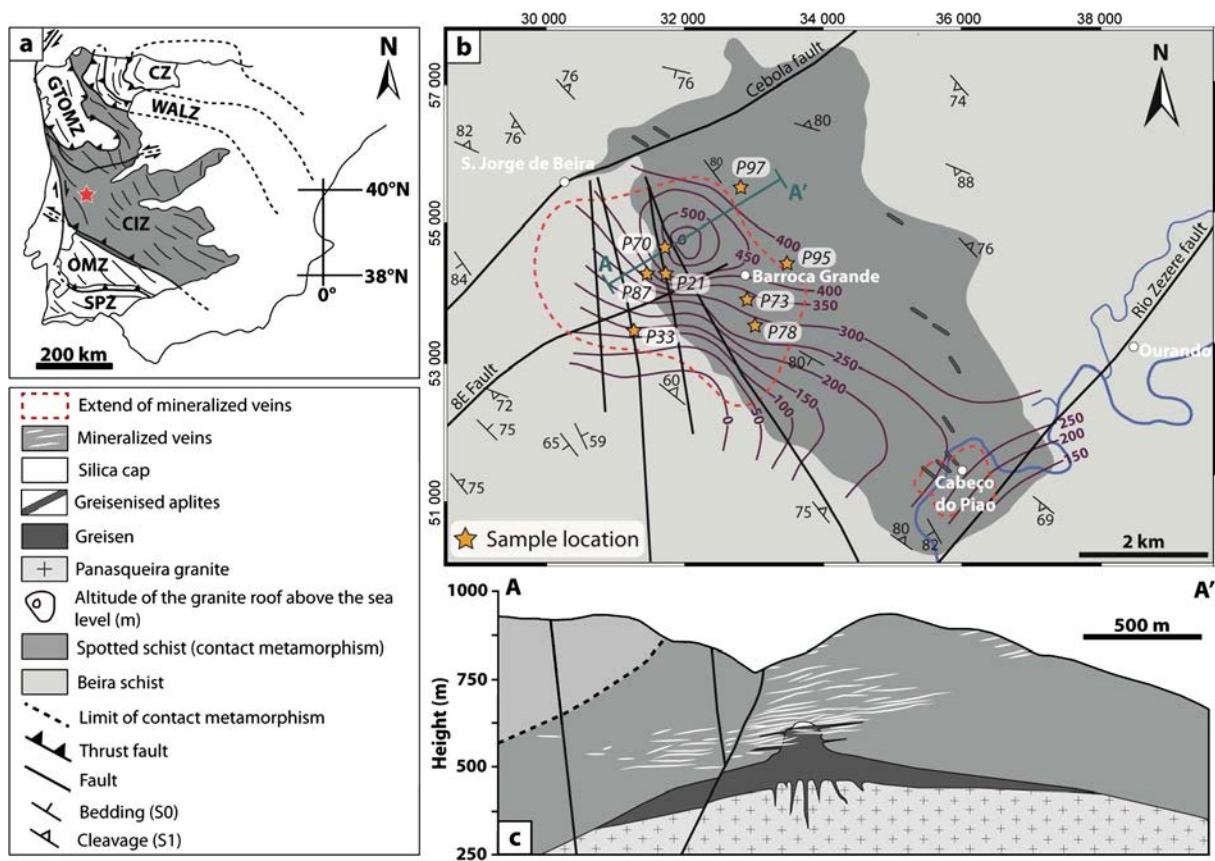


Fig. 1-4: a) Tectonic map of the Iberian Varischan Massif showing the main tectono-stratigraphic domains defined by Julivert et al. (1972). The location of the Panasqueira deposit is marked by a red star. CZ: Cantabrian zone, WALZ: Asturian western zone - Leon, GTOMZ: Trís-os-Montes de Galice zone, CIZ: Central Iberian zone, OMZ: Ossa-Morena zone and SPZ: Southern Portugal zone. (b) Geological map of the Panasqueira deposit showing the elevation of the granite roof. (c) Geological cross-section (A – A') showing the spatial relationship between mineralized veins and greisen dome (modified from Launay, 2018).

The deposit is composed by an intricate network of sub-horizontal mineralized quartz veins that are concentrated at the proximity of a greisen cupola and directly observable underground in the mine. The wall rock is the schist-greywacke complex of the Upper Neoproterozoic pleated and metamorphized, locally called the Beira schist. According to Clark (1964) Panasqueira's spotted shales indicate the presence of a metamorphic thermal aureole bound to an underlying S-type granite. The intrusive body is limited by the Cebola fault to the north and the Rio Zêzere fault to the south (Fig. i-4b). The upper part of this granite consists of a greisenised quartz-muscovite dome formed by an interaction between granitic rocks and acid fluids rich in F, B and Li (Bishop 1989) (Fig. i-4c). The system of veins is centered above the greisen dome and extends over an area of 6 km² for a depth of about 200 to 300 m (Fig. i-4b and i-4c) (Kelly and Rye, 1979; Polyá et al., 2000). This unusual flat orientation of the mineralized veins is compatible with the regional stress field, which implies a NE-SW shortening with a vertical σ_3 stress leading to the formation of tight straight folds, accompanied by the development of NW-SE regional subvertic foliation (Dias and Ribeiro, 1995). The structural study of vein swarms by Foxford et al. (2000) shows a system of late-oriented subvertic faults NNW-SSE and ENE-WSW intersecting veins and granite intrusion (Fig. i-4c). According to Thadeu (1951) these faults are post-mineralization and did not control fluid flow during mineralization at W– (Sn).

The W>Sn-bearing quartz veins are mainly characterized by quartz, tourmaline, muscovite, topaz, apatite, cassiterite, wolframite, arsenopyrite, pyrrhotite, pyrite, sphalerite, chalcopyrite, stannite, galena and carbonates, with less rutile and ilmenite. At the deposit scale, the veins have variable widths (from 0.01 to 1.5 m) and their spatial extension covers an area of over 6 km² and a vertical distance of several hundred meters. They are infilled in complicated mineral assemblages in which the more or less complete succession of this stages is recorded. A simplified paragenetic succession for the entire deposit has been constructed by Polyá et al., 2000 (Fig. i-5) on the base of observations (at the pillar scale) joined with literature data: 1-QS= quartz seam (earliest), 2-MSF= muscovite selvage formation, 3-MOSS= main oxide silicate stage, 4- MSS= main sulfide stage, 5-PAS= pyrrhotite alteration stage, and 6-LCS= late carbonate stage (latest).

The first main stage, characterized by crack-seal textures of quartz and tourmaline is overgrown by fibrous textured muscovite with variable lesser amounts of quartz, arsenopyrite, topaz, apatite and tourmaline. The MOSS stage is volumetrically the most important stage (about 60% of the vein system volume) and comprises early fibrous textured quartz, muscovite and arsenopyrite and later largely cavity-filling quartz with lesser muscovite, arsenopyrite, wolframite, cassiterite, apatite and tourmaline. These three stages formed contemporaneously in different parts of the vein system (Foxford et al., 1991). The MOSS is overgrown or crosscut by the MSS stage that is the second volumetrically largest stage and it is dominated by Zn-, Fe-, Cu- and As-bearing sulfides and quartz with significant muscovite, apatite, complex secondary phosphates, cassiterite and widespread but volumetrically minor tourmaline. This stage, from petrographic and field evidence, unequivocally post-dates the MOSS. An extensive replacement of MSS pyrrhotine in pyrite and marcasite takes place where sub-vertical veins and veinlets intersect the main sub-horizontal vein system. This stage, PAS, is younger than previous stages by about 18 Ma

(Snee et al., 1988 through $^{40}\text{Ar}/^{39}\text{Ar}$ data). The progression from oxide-dominated to base-metal sulphide succession is partially attributed to the increasing of importance of metasedimentary sources for the ore-forming components over time. Finally, the late carbonate stage (LCS), is characterized by minor dolomite-calcite dominated sub-vertical veins that crosscut the main vein system and in part fill the remaining cavities.

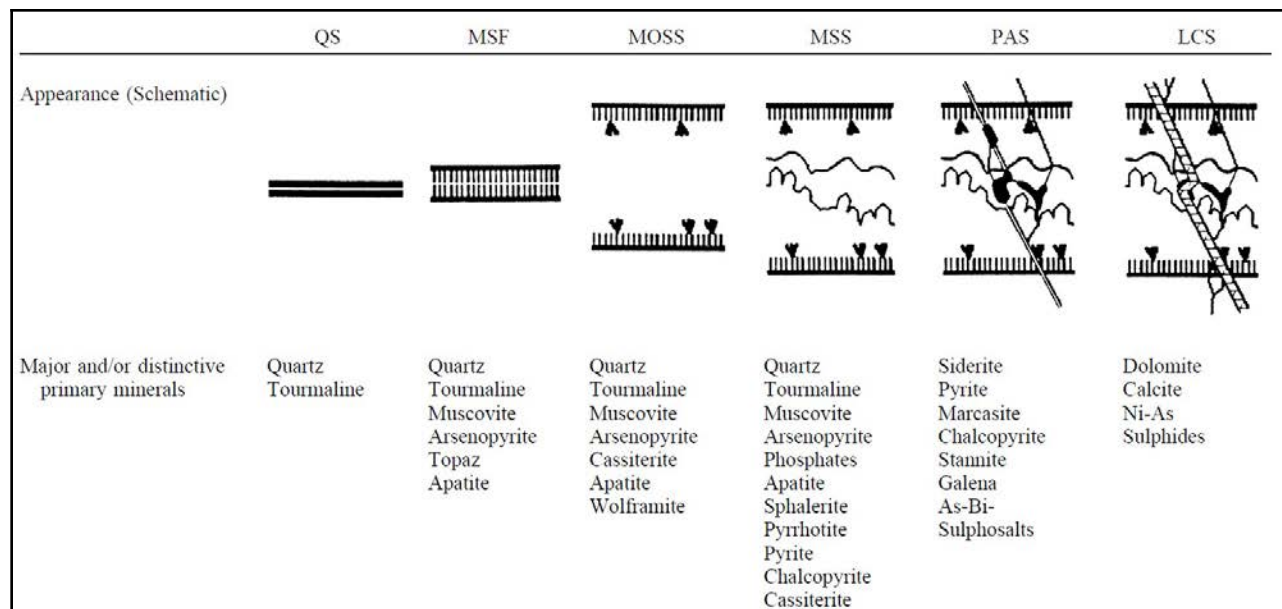


Fig. i-1.5: Paragenetic stages defined by Polya et al., 2000

1.3 Common Types of Fluids Characterizing Transport and Deposition of W: Fluid Inclusions Data

Due to its chemically “hard” nature (Pearson, 1963), W is transported in aqueous solution as an oxyanion, WO_4^{2-} , that can be complexed with Na^+ , K^+ , or H^+ (Wood and Samson, 2000). Precipitation of tungstate minerals requires Fe, Mn and Ca to form ferberite, hübnerite and scheelite, respectively. Nevertheless, clarification about the geological processes and sources involved is needed. W mineralization is typically associated with particular magmas, resulting from: (1) the melting of sedimentary rocks which may have been enriched with W through weathering (Romer and Kroner, 2014, 2016); (2) the magmatic fractionation giving a residual silicate melt enriched with W (Candela, 1992); (3) the saturation of a hydrothermal W-rich fluid with alkali-rich magmatic volatiles (Manning and Henderson, 1984; Zajacz et al., 2008); and (4) the precipitation of tungsten minerals in sedimentary host rocks surrounding granitic bodies (Audétat et al., 2000 and Lecumberri-Sanchez et al., 2017). There is a considerable uncertainty about the nature of fluids and sources responsible for W transportation and deposition and magmatic processes are not the only responsible in W-ore formation. Rare-metal granites developed during a final hydrothermal stage host disseminated mineralization as well as stockworks, for instance (e.g. Beauvoir; Cuney et al., 1992). According to Eugster (1984), if a hydrothermal deposit is granite-related, there are at least three main

sources: (1) Magmatic and hydrothermal fluid interactions accompanied by boiling of the latter and processes like cooling, crystallization, pressure changes and permeability; (2) reactions between magmatic or meteoric hydrothermal fluids with a solidified granite; and (3) reactions of hydrothermal fluids with the wall-rock minerals. The same sources have been described in Marignac and Cathelineau (2009): (1) MH, magmatic-hydrothermal systems; (2) HTH, Non-magmatic high temperature hydrothermal systems, in which externally derived fluids are equilibrated with metamorphic rocks; and (3), HTH, Non-magmatic high temperature hydrothermal systems, as well, in which fluids are in equilibria with granitic rocks. In conclusion, there are specific hydrothermal fluids associated with granite-related W-ore deposits, but the idea widely accepted is that they are composed of variable amount of magmatic, meteoric, and other different types of waters. In particular, according to Whitney (1975), the separation process of a fluid phase from a melt could explain this variety if fluid pressure exceeds the confining pressure. However, magmas have an important role in terms of chemistry, because the relative proportion of CO₂ and Cl present in the early formed hydrothermal fluids (Wyllie and Tuttle, 1961; Burnham, 1967; Holland, 1972; Kilink and Burnham, 1972) depends on their initial concentrations in the melt, and on pressure.

In such hydrothermal fluids, various transport mechanisms of W have been suggested, although currently, transport and speciation of W in deep and hot geological fluids is poorly constrained. Despite a general consensus that W is predominantly transported in the ore-forming fluids as W(VI) anions with negligible chloride complexation, there are only two existing models. Based on tungsten-speciation dominated by tungstic acid (H₂WO₄)⁰, and the products of its dissociations HWO₄⁻ and WO₄²⁻ (Heinrich, 1990; Gibert et al., 1992), such models at elevated temperature (T) and pressure (P) mostly relies on the interpretation of data on W minerals solubility from quench experiments available at that time (Eugster and Wilson, 1985; Wood and Vlassopoulos, 1989; Wood, 1992). This view of W speciation under hydrothermal condition contrasts with the already well studied W speciation at ambient temperature, where the coexistence of several polyanions containing 6, 7, 10, or even 12 W-atoms depending on pH was demonstrated (Duncan and Kepert, 1961; Aveston, 1964; Arnek and Sasaki, 1974; Haufe, 1982; Simon and Gulari, 1984; Cruywagen and van der Merwe, 1987). Moreover, it supports the conclusions of two pioneering studies reporting in-situ measurements of W speciation under hydrothermal conditions. First, Wesolowski et al. (1984) provide the results of potentiometric titrations of tungstate-bearing solution in the range 100-300°C and reveal that polytungstates (H₁₀(WO₄)₆²⁻, H₇(WO₄)₆⁵⁻, H₁₈(WO₄)₁₂⁶⁻) dominate the speciation in the 10⁻² mol.kgH₂O⁻¹ solution below pH 5. At lower W concentration, the monomers (HWO₄⁻ and WO₄²⁻) become increasingly stable, but at least one polymer (H₁₀(WO₄)₆²⁻) remains predominant at pH below 3. Second, thanks to in-situ Raman spectroscopy, Bilal et al. (1986) show the existence of two stable polymeric W-species, W₁₀O₃₂⁴⁻ and H₃W₁₂O₄₀⁵⁻, that prevail in W species at temperatures up to 200°C under acidic and circumneutral conditions. They not succeed to detect HWO₄⁻ over the 3-9 pH range and conclude that the polymerization increases with increasing T and P. Interestingly, the above-mentioned W polymers supposed to be present at elevated temperatures do not correspond to those clearly identified at ambient conditions such as paratungstate A (W₇O₂₄⁶⁻, with a C2v

symmetry), paratungstate B ($\text{H}_2\text{W}_{12}\text{O}_{42}^{10-}$, with a C1 symmetry) or ψ -metatungstate ($\text{H}_2\text{W}_{12}\text{O}_{40}^{6-}$, with a Keggin structure). These two studies are the only one that document W speciation under hydrothermal condition. They demonstrate that polymeric W-species may be stable at elevated temperatures and pH below 5 (or 3), but also show important contradictions regarding both the nature of the polymers and their respective stabilities.

In order to reconstruct the metamorphic /hydrothermal history and the conditions of pressure, temperature and chemical compositions of aqueous solutions in equilibrium with the different parageneses, microthermometric studies and Raman spectroscopy analyses of fluid inclusions have been broadly used. W mineralizing fluids usually exhibit high concentrations of non-polar volatiles such as CO_2 , CH_4 and N_2 (Dubessy et al., 1987). Fluid inclusions evidence from W-ore deposit indicate that CO_2 -rich fluids are strongly involved in the metal transport at high temperatures and pressures (through carbonate/bicarbonate complexation, according to Higgins, 1980) and that a heterogeneous composition characterizes the successive vein deposition. Fluctuations of CO_2 amounts are also responsible for the variation of fluid pH and this could explain wolframite deposition in strong acidic conditions (Higgins, 1985; Liu et al., 2018). Wood and Samson (2000), in their work, conclude that fluids responsible for wolframite deposition are characterized by temperatures from 200° to 500°C, pressure from 200 to 1.500 bars, salinities (NaCl equivalent) generally < 15 wt % (and in some cases, up to 55 wt %), X_{CO_2} < 0.1, and circum-acidic pH, and that ferberite solubility increases strongly with increasing temperature.

2. SET OF ISSUES AND SUBJECT OF THE THESIS

On the basis of paragenetic sequence, fluid inclusion and isotopic (oxygen and hydrogen) works have been elaborated in order to characterize sources and processes involved on the set up of Panasqueira and its chemical evolution. Different possible models for Panasqueira system have been invoked. Kelly and Rye (1979) opted for hot aqueous brines of moderate salinity characterized by dissolution of NaCl and less KCl, on the base of oxygen isotopic data, confirming the meteoric nature of the source, characterizing the last carbonate stage of mineralization. In contrast with the earlier stage which is more dominated by a high (magmatic) fluid equilibrated with the schist and granite host rocks. They do not exclude a mixing between these two different fluid sources. Also, Bussink (1984), interpreted the main mineralizing stage as the results of mixing between meteoric and magmatic water. Campbell et al. (1984), and Poly (1989), agreed with this nature of the source, but in their model, they also add a highly exchanged meteoric water process responsible for the mineralization. Sheppard (1986) proposed an alternative model on the base of deuterium data, invoking organic water (CO₂ from oxidized organic matter in the Beira shales), or deuterium-depleted magmatic waters (Sheppard, 1994). Evidences supporting these models have been confuted by Poly et al., 2000 with a low δ oxygen value of the fluids. In their work, a non-magmatic origin as metal sources for the deposit has been considered. Indeed, low δ oxygen value is indicative of the interaction between non-magmatic meteoric water-dominated ore forming fluids and organic-rich (meta)sedimentary rocks during the evolution of the ore forming hydrothermal system. The low δ oxygen and high Br/Cl observed for the Panasqueira MOSS (main oxide silicate stage) fluids was considered regionally related to the interaction of post magmatic Hercynian or later mineralizing fluids with sedimentary strata, like coals. Idea in accordance with Hoffmann et al. (1988), in which biogenic hydrocarbons in fluid inclusions have been used to prove a non-magmatic ore forming component in Aberfoyle (Tasmania). Thus, according to Poly (1988), Lehmann (1990), and Marignac (1991), metal contents of granitic magmas are, however, unsatisfactory to explain the total metal budgets observed in many granite-related Sn-W deposits, and the only evidence in common, in the majority of the cases, is the progression from oxide- dominated to base metal sulfide-dominated in the evolution of such systems. Recent works on peculiar aspects of the mine deserve to be mentioned: for the mineralogy and paragenesis, contributions came from Neiva (2008), Pinto (2014) and Pinto et al. (2015); the geometry of the veins is well investigated by Foxford et al. (2000); while Jaques and Pascal (2017) focused their attention on the paleostress tensor; the role of tourmaline is reviewed by Neiva et al. (2007) and Codeço et al. (2017); and the permeability of Panasqueira granite has been taken in consideration by Launay et al. (2017). However, the behavior and the sources of mineralizing fluids appear to be in contradiction and full of ambiguity. Even though, we dispose of a large amount of data, from fluid inclusion

information to oxygen and hydrogen isotopic values, there are still unresolved aspects which should play a considerable role in Panasqueira hydrothermal ore-system comprehension:

I) the source of mineralizing fluids containing metals and the source of metals itself

II) how and in which conditions tungsten is transferred from the source(s) to its final localized deposition

III) what are the main processes responsible not only for W transport, but also for the huge amount of W deposition in a specific spot underground and in which lapse of time.

3. OBJECTIVES AND EXPECTED RESULTS

This thesis is aimed to investigate the magmatic-hydrothermal transition that is of primary importance to better understand the current mineralogical expression of Panasqueira rare metal ore deposits. In particular:

1. The discrimination of strictly magmatic processes (partial melting, fractionated crystallization, assimilation, immiscibility) from the hydrothermal processes is necessary to identify the source(s) of the rare metal. This task is achieved through the identification of geochemical and/or mineralogical proxies in both the veins and their surrounding rocks and the identification of specific fluids associated with ore-mineral deposition by direct measuring of fluid compositions (FI) and oxygen isotopes on quartz, where the latter was not possible to investigate.

2- Define the chemical evolution of deposit history with a detailed paragenetic sequence within the complex mineralogical assemblage. This task is achieved through petrological and mineralogical observations at the optic microscope and through the interpretation of geochemical data. Major elements and trace elements concentrations (<1000 ppm: metals, rare Earth elements, Li, Nb, Ta, Sn, W, B, Br...) have been estimated in mineral packages belonging to each depositional stage at the micrometer scale and in selected spatial zones.

3- Reconstruction of the initial conditions (pressure-temperature-composition) and identification of different fluids involved in Panasqueira system, during the main depositional event, through the study of fluid inclusions analyses in transparent minerals. results and the

4- Experimental determination of W speciation of hydrothermal solutions in close-to-natural conditions, through fused silica capillary technique couples with Raman spectroscopy, up to 400°C.

To reach these objectives, it is necessary to know with a high degree of precision the timing of wolframite, cassiterite or chalcopyrite deposition, in a detailed framework of the deposit history. Unfortunately, it appears that in spite of the huge quantity of work already performed at Panasqueira (Kelly and Rye, 1979; Bussink, 1984; Luders, 1996; Polyá, 1988-1989, Foxford et al., 1991) it remains great uncertainty concerning both the timing of vein opening and quartz deposition, and the paragenetic evolution. In particular, the early quartz exhibits far more complexities than realized until now. As a consequence, the timing of the system, and the exact conditions of wolframite, cassiterite, or chalcopyrite deposition, remain poorly constrained.

4. MATERIALS AND METHODS

4.1 Geological Part- Data Collection

In recent years, progresses in the techniques of microanalysis of minerals and their contained fluid inclusions have provided very powerful tools for the unraveling of hydrothermal fluids source and compositions. A precise and detailed paragenetic succession is, however, the prerequisite to any reliable geochemical or fluid inclusion work. Unfortunately, when the hydrothermal history appears, as is usual, multiphase, overprinting phenomena (often implying dissolution and replacement processes) tend to obscure the temporal relationships and the establishment of a robust paragenetic chart. This is precisely the case at Panasqueira.

Around 250 samples have been collected and described from macroscale to microscale. These samples are issued from an extended sampling of level 0 and 1 centered on the historical center of the mine (40 years ago by C. Marignac) and from sampling from different levels, located south-westwards then the historical zones, during this Ph.D (Fig. i-6).

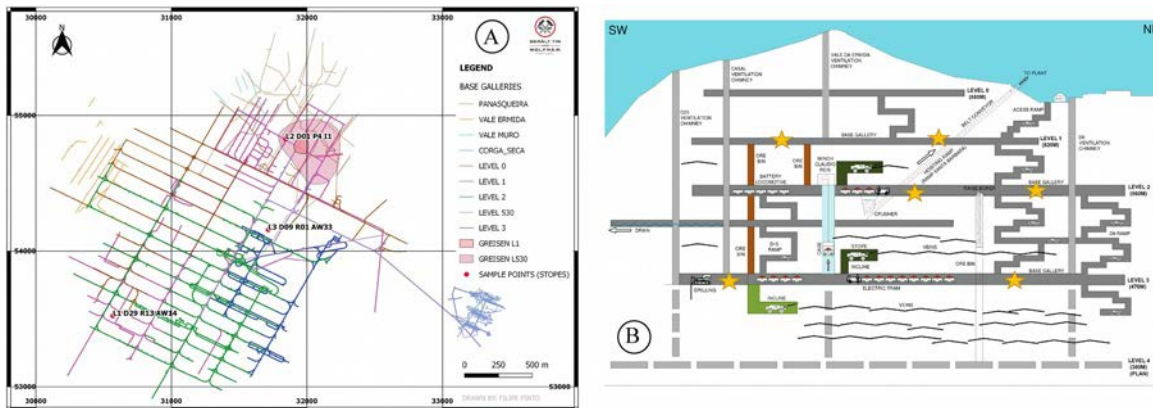


Fig. i-6: A-Samples collected zones. B- Cross section stylized map showing collect samples points (stars). Maps granted by Beralte Tin and Wolfram S.A.

To obtain a reliable paragenetic sequence, observations must be integrated at all scales, from the “outcrop” level (observation works at the scale of the mine gallery pillar) to the microscopic level (including fluorescence and electron microscopy).

At the pillar scale:

A “pulsed” story is marked by the succession of a series of major opening and re-closing events (Fig. i-7), each one characterized by its own mineralogical and structural imprint. On this base, it is possible to distinguish at least four main stages (I to IV) in the evolution of the Panasqueira system with the following characteristics:

the end of every sequence (excepted for the stage IV) is distinguished by a complete infilling, meaning that a new stage is always beginning with the re-opening of an earlier vein system. The mineral assemblage may occur anywhere into this new vein, either at the selvage, or in the central part, or both. Moreover, the successive openings are not necessary parallel, and indeed rarely are, due to the main cause of the problems encountered by earlier workers when dealing with the Panasqueira paragenetic sequence. The stage IV corresponds to the classical giant vugs with spectacular minerals that are so characteristic at Panasqueira (Fig. i-8A-B), and it is practically never found all together in one given place in the mine, with any of the I to III stages (or several of them) possibly lacking. Yet the succession order is invariably the same. Thus, and contrary to 40 years of interpretations following Kelly and Rye (1979), there is a “mineral stratigraphy” at the scale of the Panasqueira mine, and the mineral events may be correlated at the same level, and from one level to another, not only at the “one vein” (≤ 100 m) scale.

At the sample scale:

Distributed crack-sealing is the rule, systematically affecting the earlier parts of the vein system (the “wall-rocks” of the new stages). Combined with generalized dissolution/replacement processes, this lead to potentially complex and intricate mineral assemblages at the sample scale (Fig. i-9). This explains why all previously proposed paragenetic schemes include the repetition of practically all the main minerals in the successive stages.

At the thin section scale:

It is possible to unravel the complexities associated with the above mentioned overprinting effects by paying attention to intersection criteria at the micro scale as the first (and often the only one) way to define temporal successions (Fig. i-10).

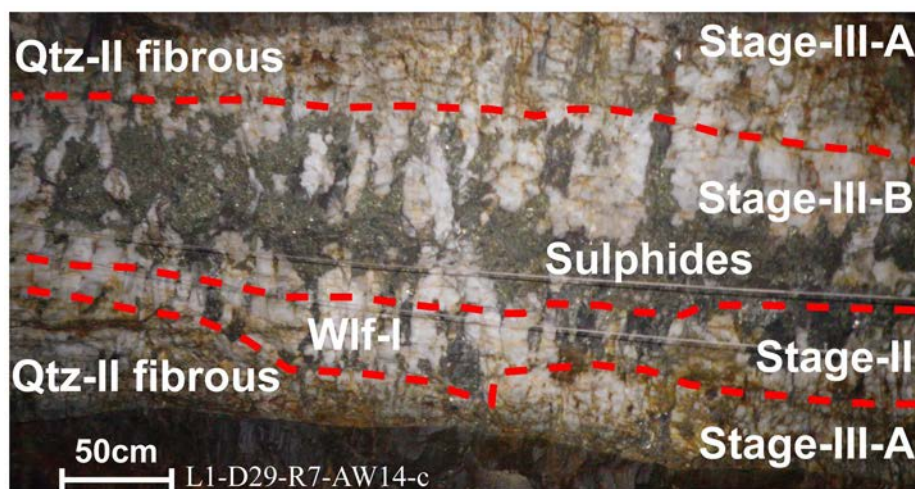


Fig. i-7: Observation at the pillar scale of one single Panasqueira quartz vein showing four main depoitional stages, with different mineral assemblages.



Fig. i-8: A- Quartz vein at the pillar scale showing the stage IV of the paragenetic sequence. B- Larger crystal size concentrated in the vugs

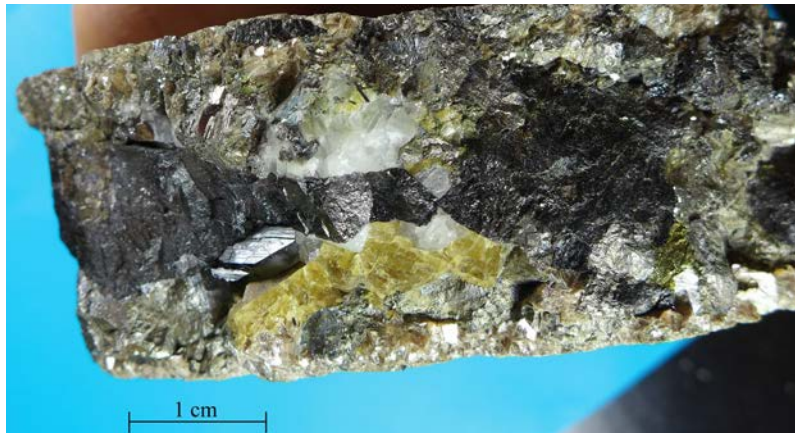


Fig. i-9: Complex and intricate mineral assemblages at the sample scale.

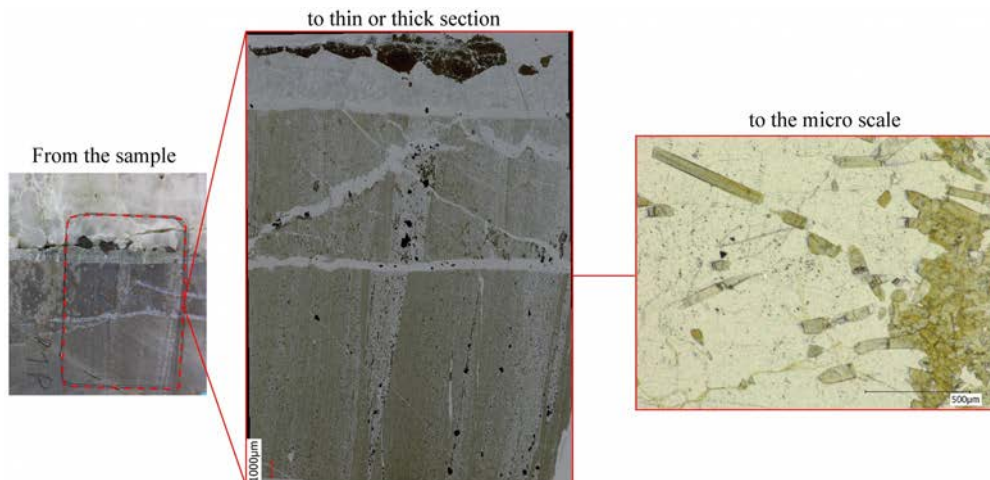


Fig. i-10: Example from the sample scale to the micro scale in order to better understand the complex relationships between different mineral phases.

4.2 Geochemical Collection Data

In order to identify the source(s) of the rare metal, we analyzed around 50 crystals of tourmalines and 34 of rutiles in selected 20 and 9 polished and metallized thin sections, respectively. The instruments available at the GeoRessources Laboratory (Nancy, France) used for mineralogical and textural observations are: an optical microscope polarizing OLYMPUS BX51 (transmitted and reflected light), a microscope (VHX-200, KEYENCE) that allows us to perform 2D cartographies of polished thin and thick sections, a Schottky-FEG (Field Emission Gun) JEOL J7600F scanning electron microscope (SEM) equipped with a SDD-type EDS spectrometer. Backscattered electron (BSE) images were obtained by setting the acceleration voltage at 15 kV.

Major elements conditions

Major-element mineral compositions (Si, Al, Fe, Mg, Ca, Na, Ti, Cr, Nb, W and F) analyses were determined on tourmalines using a CAMECA SX100 Electron microprobe (EPMA). We have used the Schottky-FEG (Field Emission Gun) JEOL J7600F scanning electron microscope (SEM) equipped with an SDD-type EDS spectrometer (Silicon Drift Detector for energy-dispersive x-ray spectroscopy), with a beam current of 1nA, and with an acceleration voltage of 15 kV. Standards for tourmalines major elements quantification were F - topaz, Na - albite, Al - albite, Mg - olivine, Si - orthose, Ca - wallastonite, Ti - MnTiO₃, Fe - Hematite; while for rutiles were Si - albite, Ti - TiO₂, Cr - Cr₂O₃, Fe - hematite, Nb - Nb, Sn - SnO₂, Ta - Ta, and W - CaWO₄.

Trace, Rare Earth elements

Trace and rare earth elements in tourmalines were determined by a 193 nm GeoLas Pro ArF Excimer laser (Microlas®, Göttingen, Germany) at 5 Hz laser frequency and the aerosols were analysed with an Agilent 7500c Quadrupole ICP-MS (Agilent®, Santa Clara, California). The external standards used were the NIST reference glasses 610/612, and to correct differences in ablation behaviour between standard and sample we used the previous electron-microprobe analyses as an internal reference. For REE estimations were normalized against atomic number based on CI carbonaceous chondrites (Anders and Grevesse, 1989). Further details are available in Chapter One.

Dating

The U–Pb ages of rutiles were determined in situ at the Géosciences Rennes laboratory by LA-ICP-MS using an ICP-MS Agilent 7700x coupled with an ESI laser Excimer system producing a radiation with a wavelength of 193 nm (NWR193UC), with ablation spot diameters of 25mm, energy pulses of 7J/cm², and repetition rates of 5 Hz. The resulting ablated material was mixed in a He, N and Ar gas mixture before being transferred into the plasma source of the ICP-MS device. Each analysis lasted 80 s and consisted of a first 20-s background measurement followed by 60-s ablation with measurements of 204(Hg + Pb), 206Pb, 207Pb, 208Pb, 232Th, and 238U, and a 15-s wash-out delay before the next acquisition. More details in Chapter One.

Fluid Inclusions

Microthermometry was carried out on fluid inclusions using a Linkam® MDS600 heating-cooling stage, adapted to an Olympus® microscope at the GeoResources laboratory in Nancy (France). The following microthermometric parameters have been measured: the melting temperatures of ice and hydrohalite ($T_{m_{ice}}$ and $T_{m_{hyd}}$), first melting temperature (T_e), halite dissolution ($T_{S_{NaCl}}$), CO₂ melting and clathrate dissociation ($T_{m_{CO_2}}$ and $T_{m_{Cl}}$), CO₂ homogenization ($T_{h_{CO_2}}$), and total homogenization temperature (T_h). The temperatures of phase changes have a precision of about ± 5 °C for T_e , ± 0.1 °C for $T_{m_{ice}}$, $T_{m_{hyd}}$, $T_{m_{CO_2}}$, $T_{h_{CO_2}}$, and $T_{m_{Cl}}$, and ± 1 °C for $T_{S_{NaCl}}$ and T_h , whereas the accuracy is better than 0.5°C in the low-temperature range, and better than 5°C at high temperatures. Volumetric fraction of the volatile phase (fvp) was estimated by reference to the volumetric chart of Roedder (1979).

The analysis of gas species of the volatile phase was performed with a Dilor-Labram Raman microspectrometer at GeoResources in Nancy (France) on inclusions previously studied by microthermometry above the critical point for carbonic inclusions (Dubessy et al., 1989). Density of the volatile phase (d_v) of carbonic fluid inclusions have been calculated using programs developed by Bakker (1997), Thiery et al. (1994) and Duan et al. (1996). Isochores of fluid inclusions have been calculated using the *ISOC* program developed by Bakker (2003) based on the equations of state from Bowers and Helgeson (1983) reviewed by Bakker (1999).

4.3 Experimental Part- Dataset

A total of 26 experimental aqueous solutions (30 g or of total solution for each run) were prepared using purified water (milli-Q, millipore) with a resistivity of $18.2\text{M}\Omega\cdot\text{cm}$ and different concentrations [0.01] - [0.005] - [0.1] - [0.2] express as $m=\text{mol}/\text{kgH}_2\text{O}$, of the main Na-tungstates (Sigma-Aldrich): $\text{Na}_2\text{WO}_4\cdot 2\text{H}_2\text{O}$, sodium tungstate dihydrate, and $\text{Na}_6\text{W}_{12}\text{O}_{39}\cdot\text{H}_2\text{O}$, sodium metungstate. Four of them were mixed with [0.1] and [1] of HCl, three with [0.1] - [3] of NaCl, five with NaOH [0.1] and one with [1] NH_4Cl . Different compounds like NaHCO_3 , Na_2CO_3 , CO_2 , HCOOH , CH_3COOH , and CH_3COONa have been add into thirteen W-aqueous solutions, in order to investigate the behavior of W with carbonates and in reducing conditions. All of them were loaded in capillaries (Fig. i-11 A) following the protocol (see Chapter Four) described for fused silica capillary in Caumon et al. (2013) (Fig. i-11 B).

The Raman spectra are recorded using a LabRAM HR spectrometer (Horiba Jobin Yvon) equipped with a $600\text{ gr}\cdot\text{mm}^{-1}$ grating and an Edge filter. The confocal hole aperture is of $500\ \mu\text{m}$, the slit aperture is of $100\ \mu\text{m}$ and it gives a spectral resolution of $0.5\ \text{cm}^{-1}$. The excitation beam is provided by a Stabilite 2017 Ar+ laser (Spectra Physics, Newport Corporation) at $514.53\ \text{nm}$ at a power of $200\ \text{mW}$, focused on the sample using a $\times 20$ objective (Olympus). Measurements were performed first at room temperature (21°C) and from 100°C up to 400°C by step of 100°C at a heating rate of $10^\circ\text{C}\cdot\text{min}^{-1}$ for each solution (coexisting with a vapor phase below the critical point). A heating-stage dedicated to capillary heating at saturated vapor pressure (@CAP-500 Linkam) is used to reach the experimental temperature, with an accuracy of $\pm 1\%$ in the range of $20 - 400^\circ\text{C}$ (Fig. i-11 C).

LabSpec 5.64.15 software (@Jobin-Yvon, Horiba) was used to process Raman spectra data at the beginning and in particular to determine precisely the frequency position of the peaks using the baseline-subtraction tool. @OriginPro9 allowed us to calculate peak position, intensity, area, and shape factor for each band W component in the liquid phase.

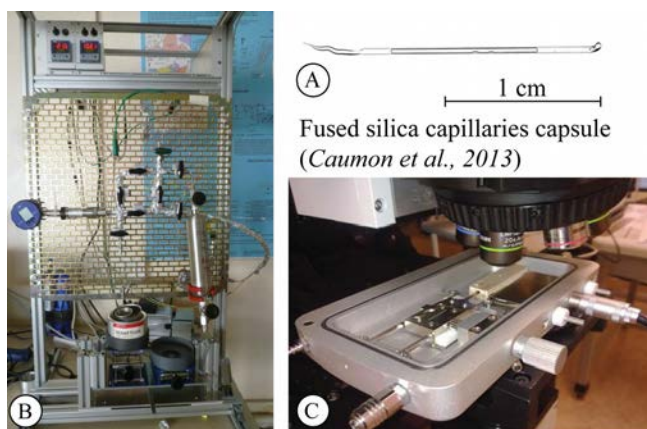


Fig. i-11: A- Schematic picture of a FSCC containing experimental solutions. B- Picture showing the equipment taking part on the capillary loading technique. C- Raman analyses detail: capillary laid down heating-stage dedicated, under the Raman microscope.

References

- Anders, E., & Grevesse, N. (1989). Abundances of the elements: Meteoritic and solar. *Geochimica et Cosmochimica acta*, 53(1), 197-214.
- Arnek, R., & Sasaki, Y. (1974). Equilibrium Studies of Polyanions. 20. A Recalculation of Emf Data on the Reactions of H⁺ and (WO₄)²⁻ in 3 M Na (ClO₄)⁰ at 25 C. *Acta Chemica Scandinavica*, 28(1).
- Aveston, J. (1964). Hydrolysis of tungsten (VI): ultracentrifugation, acidity measurements, and Raman spectra of polytungstates. *Inorganic Chemistry*, 3(7), 981-986.
- Audétat, A., Günther, D., & Heinrich, C. A. (2000). Causes for large-scale metal zonation around mineralized plutons: Fluid inclusion LA-ICP-MS evidence from the Mole Granite, Australia. *Economic Geology*, 95(8), 1563-1581.
- Burnham, C. W. (1967). Hydrothermal fluids at the magmatic stage. *Geochemistry of hydrothermal ore deposits*, 34-76.
- Bussink, R. W., Kreulen, R., & de Jong, A. F. (1984). Gas analyses, fluid inclusions and stable isotopes of the Panasqueira W-Sn deposits, Portugal. *Bulletin de minéralogie*, 107(6), 703-713.
- Campbell, A. R., Rye, D., & Petersen, U. (1984). A hydrogen and oxygen isotope study of the San Cristobal Mine, Peru; implications of the role of water to rock ratio for the genesis of wolframite deposits. *Economic Geology*, 79(8), 1818-1832.
- Caumon, M. C., Dubessy, J., Robert, P., & Tarantola, A. (2013). Fused-silica capillary capsules (FSCCs) as reference synthetic aqueous fluid inclusions to determine chlorinity by Raman spectroscopy. *European Journal of Mineralogy*, 25(5), 755-763.
- Candela, P. A. (1992). Controls on ore metal ratios in granite-related ore systems: an experimental and computational approach. *Earth and Environmental Science Transactions of the Royal Society of Edinburgh*, 83(1-2), 317-326.
- Charoy, B., and Noronha, F.O. (1996). Multistage Growth of a Rare-Element, Volatile-Rich Microgranite at Argemela (Portugal). *Journal of Petrology*, 37, 73-94.
- Clark, A. H. (1964). Preliminary study of the temperatures and confining pressures of granite emplacement and mineralization, Panasqueira, Portugal. *Institute Mining Metallurgy Transactions*, 73, 813-824.
- Clark, A.H. (1970). Potassium-argon ages and regional relationships of the Panasqueira tin-tungsten mineralization, Portugal. *Servicos Geologicos Comunicacoes*, 54, 243-261.
- Codeço, M.S., Weis, P., Trumbull, R.B., Pinto, F., Lecumberri-Sanchez, P., and Wilke, F.D. (2017). Chemical and boron isotopic composition of hydrothermal tourmaline from the Panasqueira W-Sn-Cu deposit, Portugal. *Chemical Geology*, 468, 1-16.
- Cruywagen, J. J., & Van Der Merwe, I. F. (1987). Tungsten (VI) equilibria: a potentiometric and calorimetric investigation. *Journal of the Chemical Society, Dalton Transactions*, (7), 1701-1705.
- Cuney, M., Marignac, C., & Weisbrod, A. (1992). The Beauvoir topaz-lepidolite albite granite (Massif Central, France); the disseminated magmatic Sn-Li-Ta-Nb-Be mineralization. *Economic Geology*, 87(7), 1766-1794.
- Derré, C. (1982). Caractéristiques de la distribution des gisements à étain et tungstène dans l'Ouest de l'Europe. *Mineralium Deposita*, 17(1), 55-77
- Dias, R., & Ribeiro, A. (1993). Porto-Tomar shear zone, a major structure since the beginning of the variscan orogeny. *Comun. Inst. Geol. Min*, 79, 31-40.

- Dias, G., Leterrier, J., Mendes, A., Simões, P. P., & Bertrand, J. M. (1998). U–Pb zircon and monazite geochronology of post-collisional Hercynian granitoids from the Central Iberian Zone (Northern Portugal). *Lithos*, 45(1-4), 349-369.
- Dubessy, J., Ramboz, C., Nguyen-Trung, C., Cathelineau, M., Charoy, B., Cuney, M., ... & Weisbrod, A. (1987). Physical and chemical controls (fO₂, T, pH) of the opposite behaviour of U and Sn-W as exemplified by hydrothermal deposits in France and Great-Britain, and solubility data. *Bulletin de Minéralogie*, 110(2), 261-281.
- Duncan, J. F., & Kepert, D. L. (1961). 1050. Polyanion equilibria in aqueous solution. Part I. The quantitative analysis of acidified tungstate solutions. *Journal of the Chemical Society (Resumed)*, 5317-5325.
- Eckstrand, O. R., Sinclair, W. D., Thorpe, R. I., & Barton, P. S. (1996). Geology of Canadian Mineral Deposit Types. Geological Survey of Canada, Geology of Canada, no. 8, and Geological Society of America, The Geology of North America, v. P-1. *Economic Geology and the Bulletin of the Society of Economic Geologists*, 91(8), 1470-1471.
- Eugster H. P. and Wilson G. A. (1985). Transport and deposition of ore-forming elements in hydrothermal systems associated with granites. In High Heat Production Granites, Hydrothermal Circulation and Ore Genesis. *Inst. Min. Metall., London*, pp. 87-98.
- Fernández, R. D., Foster, D. A., Barreiro, J. G., & Alonso-García, M. (2013). Rheological control on the tectonic evolution of a continental suture zone: the Variscan example from NW Iberia (Spain). *International Journal of Earth Sciences*, 102(5), 1305-1319.
- Fernández, R. D., Arenas, R., Pereira, M. F., Sánchez-Martínez, S., Albert, R., Parra, L. M. M., ... & Matas, J. (2016). Tectonic evolution of Variscan Iberia: gondwana–Laurussia collision revisited. *Earth-Science Reviews*, 162, 269-292.
- Fernández, R. D., & Pereira, M. F. (2017). Strike-slip shear zones of the Iberian Massif: Are they coeval?. *Lithosphere*, 9(5), 726-744.
- Foxford, K.A., Nicholson, R., and Polya, D.A. (1991). Textural evolution of W–Cu–Sn bearing hydrothermal quartz veins at Minas da Panasqueira, Portugal. *Mineralogical Magazine*, 55, 435–445.
- Foxford, K.A., Nicholson, R., Polya, D.A., and Hebblethwaite, R.P.B. (2000). Extensional failure and hydraulic valving at Minas da Panasqueira, Portugal: evidence from vein spatial distributions, displacements and geometries. *Journal of Structural Geology*, 22, 1065–1086. [http://dx.doi.org/10.1016/S0191-8141\(00\)00029-8](http://dx.doi.org/10.1016/S0191-8141(00)00029-8).
- Fuertes-Fuente, M., Martin-Izard, A., Boiron, M-C., and Mangas, J. (2000). Fluid evolution of rare-element and muscovite granitic pegmatites from central Galicia, NW Spain. *Mineralium Deposita*, 35, 332-345.
- Gibert, F., Moine, B., Schott, J., & Dandurand, J. L. (1992). Modeling of the transport and deposition of tungsten in the scheelite-bearing calc-silicate gneisses of the Montagne Noire, France. *Contributions to Mineralogy and Petrology*, 112(2-3), 371-384.
- Häufe, P. (1982). Raman-spectrophotometric determination of the tungstate anion and its isopolyanions in aqueous systems. *Fresenius' Zeitschrift für analytische Chemie*, 310(5), 388-391.
- Heinrich, C. A. (1990). The chemistry of hydrothermal tin (-tungsten) ore deposition. *Economic Geology*, 85(3), 457-481.
- Higgins, N. C. (1980). Fluid inclusion evidence for the transport of tungsten by carbonate complexes in hydrothermal solutions. *Canadian Journal of Earth Sciences*, 17(7), 823-830.

- Higgins, N. C. (1985). Wolframite deposition in a hydrothermal vein system; the Grey River tungsten prospect, Newfoundland, Canada. *Economic Geology*, 80(5), 1297-1327.
- Holland, H. D. (1972). Granites, solutions, and base metal deposits. *Economic Geology*, 67(3), 281-301.
- Inverno, C.M.C., Ferraz, P.J.V., and Moreira, E. (2009). Argemela, a high-tonnage Sn-Li deposit in Central Portugal. *Geological Society of America Annual Meeting, Portland, 2009, Abstracts 41*, p. 680.
- Jaques, L., and Pascal, C. (2017). Full paleostress tensor reconstruction using quartz veins of Panasqueira Mine, central Portugal; part I: Paleopressure determination. *Journal of Structural Geology*, 102, 58-74.
- Julivert, M., & Ribeiro, A. (1972). *MAPA TECTONICO DE LA PENINSULA IBERICA Y BALEARES 1: 1 000 000*. Instituto geologico y minero.
- Kelly, W. C., & Rye, R. O. (1979). Geologic, fluid inclusion, and stable isotope studies of the tin-tungsten deposits of Panasqueira, Portugal. *Economic Geology*, 74(8), 1721-1822.
- Kilinc, I. A., & Burnham, C. W. (1972). Partitioning of chloride between a silicate melt and coexisting aqueous phase from 2 to 8 kilobars. *Economic geology*, 67(2), 231-235.
- Koutsospyros, A., Braida, W., Christodoulatos, C., Dermatas, D., & Strigul, N. (2006). A review of tungsten: from environmental obscurity to scrutiny. *Journal of hazardous materials*, 136(1), 1-19.
- Launay, G., Sizaret, S., Guillou-Frottier, L., Gloaguen, E., & Pinto, F. (2018). Deciphering fluid flow at the magmatic-hydrothermal transition: A case study from the world-class Panasqueira W-Sn-(Cu) ore deposit (Portugal). *Earth and Planetary Science Letters*, 499, 1-12.
- Lecumberri-Sanchez, P., Vieira, R., Heinrich, C. A., Pinto, F., & Wälle, M. (2017). Fluid-rock interaction is decisive for the formation of tungsten deposits. *Geology*, 45(7), 579-582.
- Lehmann, B. (2006). *Metallogeny of tin* (Vol. 32). Springer.
- Lima, L.A.S. (2015). Contribuição para o estudo da mineralogia da brecha de Sta. Helena - Minas da Borralha. *PhD thesis, Porto Universidad*, 103 p.
- Linnen, R. L., & Cuney, M. (2005). Granite-related rare-element deposits and experimental constraints on Ta-Nb-W-Sn-Zr-Hf mineralization, in Linnen RL and Samson IM, eds., rare-element geochemistry and mineral deposits. In *Geological Association of Canada, GAC, Short Course*.
- López-Moro, F. J., Romer, R. L., López-Plaza, M., & Sánchez, M. G. (2017). Zircon and allanite U-Pb ID-TIMS ages of vaugnerites from the Calzadilla pluton, Salamanca (Spain): dating mantle-derived magmatism and post-magmatic subsolidus overprint. *Geologica Acta: an international earth science journal*, 15(4), 395-408.
- Manning, D. A., & Henderson, P. (1984). The behaviour of tungsten in granitic melt-vapour systems. *Contributions to Mineralogy and Petrology*, 86(3), 286-293.
- Marignac, C. (1982). Geologic, fluid inclusions, and stable isotope studies of the tin-tungsten deposits of Panasqueira, Portugal; discussion. *Economic Geology*, 77(5), 1263-1266.
- Marignac, C., Cuney, M., Pagel, M., & Leroy, J. L. (1991). What is the meaning of granite specialization for Sn, W deposit genesis. *Source, transport and deposition of metals. Balkema, Rotterdam*, 771-774.

- Marignac, C., & Cathelineau, M. (2009). The nature of ore-forming fluids in peri-batholithic Sn-W deposits and a classification. In *Smart science for exploration and mining, Proceedings Xth Biennial SGA Meeting, Townsville* (pp. 245-247).
- Mateus, A., and Noronha, F. (2010). Sistemas mineralizantes epigenéticos na Zona Centro-Ibérica; expressão da estruturação orogénica meso- a tardi-varisca (Epigenetic ore-forming systems in Central-Iberian Zone; products of an evolving orogenic framework in meso- to late-Variscan times): *Ciências Geológicas, Ensino, Investigação e sua História (Geologia Aplicada)*. 2, 47-61.
- Neiva, A.M.R. (2002). Portuguese granites associated with Sn-W and Au mineralizations: *Bulletin of the Geological Society of Finland*, 74, 79-101.
- Ng, K. Y. S., & Gulari, E. (1984). Spectroscopic and scattering investigation of isopoly-molybdate and tungstate solutions. *Polyhedron*, 3(8), 1001-1011.
- Negga, H. S., Sheppard, S. M. F., Rosenbaum, J. M., & Cuney, M. (1986). Late Hercynian U-vein mineralization in the Alps: fluid inclusion and C, O, H isotopic evidence for mixing between two externally derived fluids. *Contributions to Mineralogy and Petrology*, 93(2), 179-186.
- Noronha, F. (1984). Caractéristiques physico-chimiques des fluides associés à la genèse du gisement de tungstène de Borralha - Nord du Portugal. *Bulletin de Minéralogie (Paris)*, 107, 273-284.
- Noronha, F. (2017). Fluids and Variscan metallogenesis in granite related systems in Portugal: Water-Rock Interaction International Symposium, 15th: *Procedia Earth and Planetary Science*. 1, p. 1-4.
- Noronha, F., Dória, F., Dubessy, J., and Charoy, B. (1992), Characterization and timing of the different types of fluids present in the barren and ore veins of the W-Sn deposit of Panasqueira, central Portugal. *Mineralium Deposita*, 27, 72-79.
- Pascual, F. J. R., Arenas, R., Catalán, J. R. M., Fernández, L. R. R., & Wijbrans, J. R. (2013). Thickening and exhumation of the Variscan roots in the Iberian Central System: Tectonothermal processes and ⁴⁰Ar/³⁹Ar ages. *Tectonophysics*, 587, 207-221.
- Pearson, R. G. (1963). Hard and soft acids and bases. *Journal of the American Chemical society*, 85(22), 3533-3539.
- Polya, D. A. (1988). Efficiency of hydrothermal ore formation and the Panasqueira W-Cu (Ag)-Sn vein deposit. *Nature*, 333(6176), 838.
- Polya, D. A. (1989). Chemistry of the main-stage ore-forming fluids of the Panasqueira W-Cu (Ag)-Sn deposit, Portugal; implications for models of ore genesis. *Economic Geology*, 84(5), 1134-1152.
- Polya, D.A., Foxford, K.A., Stuart, F., Boyce, A., and Fallick, A.E. (2000). Evolution and paragenetic context of low δD hydrothermal fluids from the Panasqueira W-Sn deposit, Portugal: new evidence from microthermometric, stable isotope, noble gas and halogen analyses of primary fluid inclusions.
- Redkin, A. F., & Bondarenko, G. V. (2010). Raman spectra of tungsten-bearing solutions. *Journal of solution chemistry*, 39(10), 1549-1561.
- Robles, E.R., Perez, A.P., Roldan, F.V., and Fontan, F. (1991). The granitic pegmatites of the Fregeneda area (Salamanca, Spain): characteristics and petrogenesis. *Mineralogical Magazine*, 67, 535-558.

- Romer, R. L., & Kroner, U. (2015). Sediment and weathering control on the distribution of Paleozoic magmatic tin-tungsten mineralization. *Mineralium Deposita*, 50(3), 327-338.
- Romer, R. L., & Kroner, U. (2016). Phanerozoic tin and tungsten mineralization—tectonic controls on the distribution of enriched protoliths and heat sources for crustal melting. *Gondwana Research*, 31, 60-95.
- Sanderson, D.J., Roberts, S., Gumiel, P., and Greenfield, C. (2008). Quantitative analysis of tin- and tungsten-bearing sheeted vein systems. *Economic Geology*, 103, 1043-1056.
- Shcherba, G. N. (1970). Greisens. *International Geology Review*, 12(2), 114-150.
- Sheppard, S. M. F. (1994). Stable isotope and fluid inclusion evidence for the origin and evolution of Hercynian mineralizing fluids. *Metallogeny of collisional orogens. Czech Geological Survey, Prague*, 49-60.
- Sinclair, W. D. (1996). Vein-stockwork tin, tungsten. *Geology of Canadian Mineral Deposit Types*, (ed.) Eckstrand, OR, Sinclair, WD, Thorpe, RI, *Geological Survey of Canada*, 8, 409-420.
- Snee, L.W., Sutter, J.F., and Kelly, W.C. (1988). Thermochronology of economic mineral deposits: dating the stages of mineralisation at Panasqueira, Portugal, by high-precision ^{40}Ar - ^{39}Ar age spectrum techniques on muscovite. *Economic Geology*, 83, 335-354.
- Tadeu, D. (1951). Geologia do couro mineiro da Panasqueira.
- Tornos, F., Delgado, A., Casquet, C., and Galindo, C. (2000). 300 Million years of episodic hydrothermal activity: stable isotope evidence from hydrothermal rocks of the eastern Iberian Central System: *Mineralium Deposita*, 35, 551-569.
- Tornos, F., Galindo, C., Crespo, J.L., and Spiro B.F. (2008). Geochemistry and origin of calcic tungsten-bearing skarns, Los Santos, Central Iberian Zone, Spain. *The Canadian Mineralogist*, 46, 87-109.
- Wesolowski, D., Drummond, S. E., Mesmer, R. E., & Ohmoto, H. (1984). Hydrolysis equilibria of tungsten (VI) in aqueous sodium chloride solutions to 300. degree. C. *Inorganic Chemistry*, 23(8), 1120-1132.
- Whitney, J. A. (1975). The effects of pressure, temperature, and XH_2O on phase assemblage in four synthetic rock compositions. *The Journal of Geology*, 83(1), 1-31.
- Wyllie, P. J., & Tuttle, O. F. (1961). Experimental investigation of silicate systems containing two volatile components; Part 2, The effects of NH_3 and HF , in addition to H_2O on the melting temperatures of albite and granite. *American Journal of Science*, 259(2), 128-143.
- Wood, S. A., & Vlassopoulos, D. (1989). Experimental determination of the hydrothermal solubility and speciation of tungsten at 500° C and 1 kbar, 2. *Geochimica et Cosmochimica Acta*, 53(2), 303-312.
- Wood, S. A. (1990). The aqueous geochemistry of the rare-earth elements and yttrium: 2. Theoretical predictions of speciation in hydrothermal solutions to 350 C at saturation water vapor pressure. *Chemical Geology*, 88(1-2), 99-125.
- Wood, S. A. (1992). Experimental determination of the solubility of WO_3 (s) and the thermodynamic properties of H_2WO_4 (aq) in the range 300–600 C at 1 kbar: calculation of scheelite solubility. *Geochimica et Cosmochimica Acta*, 56(5), 1827-1836.

- Wood, S. A., & Vlassopoulos, D. (1989). Experimental determination of the hydrothermal solubility and speciation of tungsten at 500° C and 1 kbar¹, 2. *Geochimica et Cosmochimica Acta*, 53(2), 303-312.
- Wood, S. A., & Samson, I. M. (2000). The hydrothermal geochemistry of tungsten in granitoid environments: I. Relative solubilities of ferberite and scheelite as a function of T, P, pH, and m NaCl. *Economic Geology*, 95(1), 143-182.
- Zajacz, Z., Seo, J. H., Candela, P. A., Piccoli, P. M., Heinrich, C. A., & Guillong, M. (2010). Alkali metals control the release of gold from volatile-rich magmas. *Earth and Planetary Science Letters*, 297(1-2), 50-56

5. MANUSCRIPT ORGANIZATION

The structure of the manuscript is organized in four main parts, sub-divided in:

PART ONE: FIRST DEPOSITIONAL STAGE

INTRODUCTION: A New Paragenetic Sequence

CHAPTER ONE - Incipient Deposition Stage of Wolframite: W-Rutile and Tourmaline Chemistry as Proxies for Early Fluids at Panasqueira (Portugal)

CHAPTER TWO - Rutile From Panasqueira (Central Portugal): an Excellent Pathfinder for Wolframite Deposition

PART TWO: PANASQUEIRA CHEMICAL FLUID EVOLUTION

CHAPTER THREE - Panasqueira Fluid Inclusion Study

PART THREE: EXPERIMENTAL PART ON W BEHAVIOUR

CHAPTER FOUR - Tungsten (VI) Speciation in Hydrothermal Solution up to 400°C As Revealed By In-Situ Raman Spectroscopy

PART FOUR: DISCUSSION UPON A POSSIBLE PANASQUEIRA MODEL AND OPEN QUESTIONS

Part One

First Depositional Stage

Paragenetic succession at Panasqueira

A precise and detailed paragenetic succession is the prerequisite to any reliable geochemical or fluid inclusion study. At Panasqueira, the paragenetic succession established by Kelly and Rye (1979) remained the basis of the paragenetic scheme for all successive workers, with, however, several corrections and additions in particular by Polya et al. (2000), Lourenço (2004) and Pinto et al. (2015), (see the Introduction Part).

It is however based on debatable criteria and tenets. For instance, selvages, such as the spectacular muscovite or arsenopyrite selvages at the quartz vein contacts, are considered without discussion as evidence for the early deposition of the selvage mineral. In the same way, mineral inclusions are usually interpreted as evidence of the earlier occurrence of the included mineral, and corrosion features are often taken as a reliable criterion of relative age. Unfortunately, when the hydrothermal history is evidently multiphase, as is the case at Panasqueira, overprinting phenomena (often implying dissolution and replacement processes) tend to obscure the temporal relationships, thus making difficult the establishment of a robust paragenetic chart. In the present work, we base our reconstruction of the paragenetic sequence on two criteria: (i) intersection of veins (or veinlets or microcracks), each bearing a well-defined mineral assemblage (ideally - and fortunately frequently encountered- a monomineral one), and (ii) infilling sequence in a *demonstrably open* space, the two criteria being possibly fruitfully simultaneously used, for instance in the crack-seal occurrences. Finally, a methodological criterion is of paramount importance: the parsimony, or Ockham Razor, principle (ORP), specifying that the number of hypotheses must be kept at the minimum compatible with factual observations, meaning in our case of search for a robust paragenetic scheme, the reduction of the number of stages to the minimum consistent with all the observed relationships.

These criteria apply to each scale of observation, from the “outcrop” level (mining works observations, scale of the pillar) to the microscopic level (including fluorescence and electron microscopy). At the sample scale, the required scale of observation may often be larger than the thin section dimensions, a difficulty obviously related to the endowment of the deposit, but which can be alleviated by using sample-scale scanning systems (micro-XRF).

General characteristics of the paragenetic succession

At the pillar scale

A “pulsed” vein evolution is evident, marked by the succession of a series of major opening/closing events, each one with its own mineralogical and structural imprint, defining a series of four main stages (I to IV) in the evolution of the Panasqueira system (Figure P.O.1).

- Each of the first three stages (I-III) represents a full cycle of opening-complete infilling by a specific set of minerals.

- Although new sets of dry joints may be opened at each stage, stages II and III most often correspond to the re-opening of earlier vein systems. The re-opening may occur anywhere, either at the selvages, or in the central part, or both, of the earlier vein. The successive openings are not necessary parallel, and indeed rarely are. This is particularly evident at the stage III.

- Stage IV is characterized by the development of a system of vugs which remained open until now and provide the spectacular crystals that are so characteristic at Panasqueira. These vugs, which range from a few 10 cm to several m (up to 10 m), often occupy the whole width of the vein, overprinting the earlier stages, and usually present a tubular morphology, without clear orientation.

- The four stages are practically never found all together in one given place in the mine, with any of the I to IV stages (or several of them) possibly lacking. Yet the (partial) succession order is invariably the same. Thus, and contrary to 40 years of interpretations following Kelly and Rye (1979), there is a “mineral stratigraphy” at the scale of the Panasqueira mine, and the mineral events may be time-correlated at the same level, and from one level to another, not only at the “one vein” (≤ 100 m) scale.

- Stages I and II are very similar, differing nevertheless by the comb quartz habitus, with blocky prisms in stage I (“Alpine style”) compared to more elongated crystals in stage II, the latter being in addition associated with intense crack-seal processes.

- Stages III and IV are characterized by the intense dissolution/replacement processes that accompany the opening. Thus, stage III sulphide-dominated assemblages are the result of the sealing of series of giant vugs developed along fracture zones, generally oblique to the main vein elongation. The stage IV vugs, for their part, seem to result from the dissolution enlarging of vertical tension joints.

Later stages

At the sample scale, several stages (V to VII) may be defined following stage IV. They differ from the earlier stages by being not related to a large-scale tectonic event accompanied by new opening episodes.

At the sample scale

Distributed crack-sealing is the rule, systematically affecting the earlier parts of the vein system (the “wall-rocks” of the new stages). Combined with generalized dissolution/replacement processes, this lead to potentially complex and intricate mineral assemblages at the sample scale. This may explain why all previously proposed paragenetic charts include the repetition of practically all the main minerals in the successive stages.

Topochemical effects are equally the rule, and are a supplementary factor of complication. For instance, it seems clear that, out from the stage IV vugs, siderite is for a large part restricted to the previously pyritized pyrrhotite. In the same way, chlorite is mainly present as the alteration product of topaz. It would seem that the

main process was the reaction of a former mineral with a new component, CO₂ in the first case, Fe-Mg in the second.

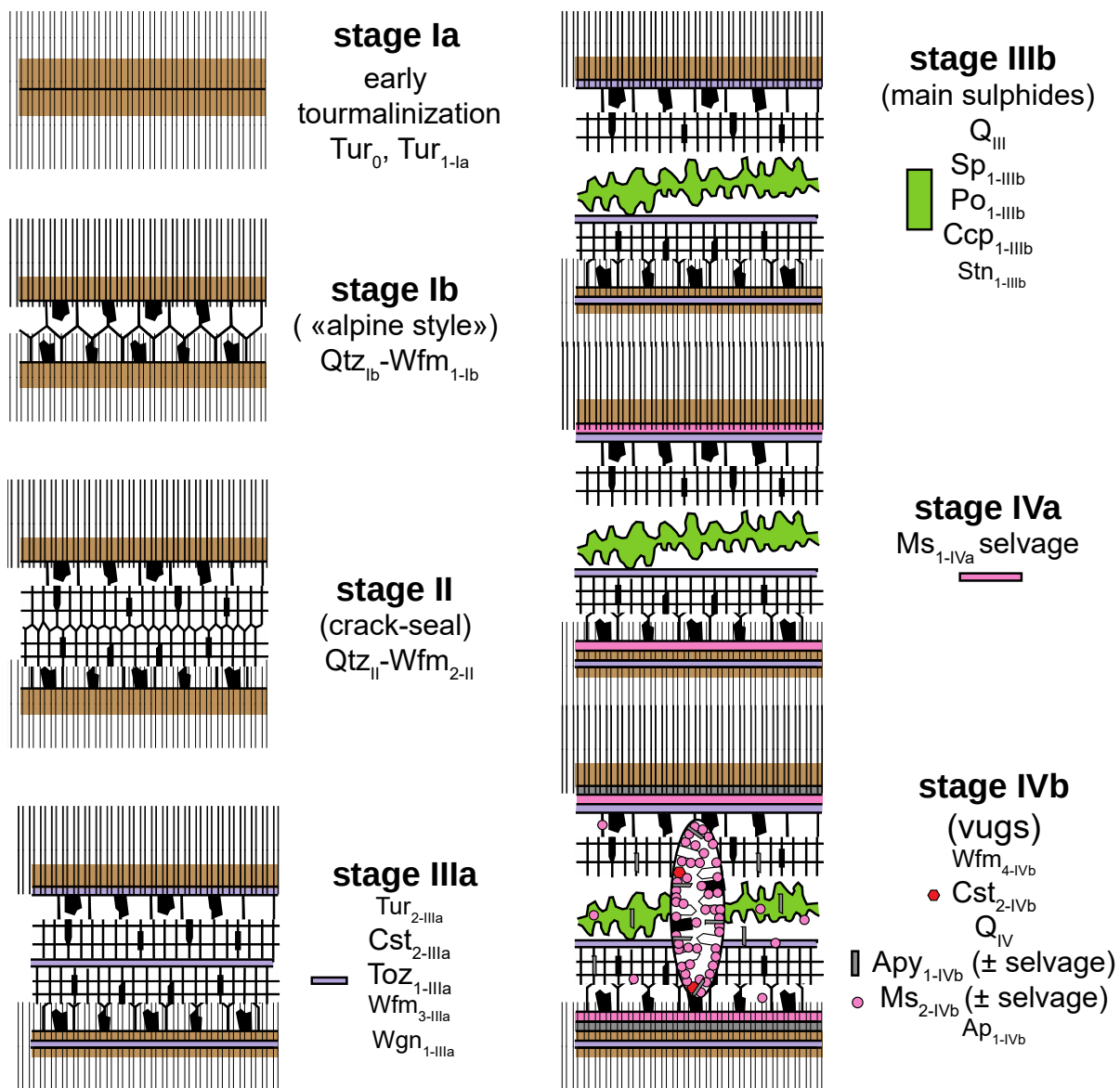


Figure P.O.1: Schematic representation of the multi-stage building of the Panasqueira vein system. Only stages associated with significant reworking of the architecture are presented (hence the absence of IIIc and post-IV stages).

Revised Panasqueira paragenetic chart

Integrating all observation scales, a revised paragenetic chart was obtained (Figure P.O.2). One major difference with the preceding charts (Kelly and Rye, 1979; Polya et al., 2000; Lourenço, 2004) is the decoupling of wolframite from other minerals (topaz, muscovite, arsenopyrite, apatite) at the main ore deposition stage (Oxide Silicate Stage of these authors). Another one is the decoupling of siderite from the first stage of pyritization at the end of stage III. We present in the following the main evidence in favour of the present chart.

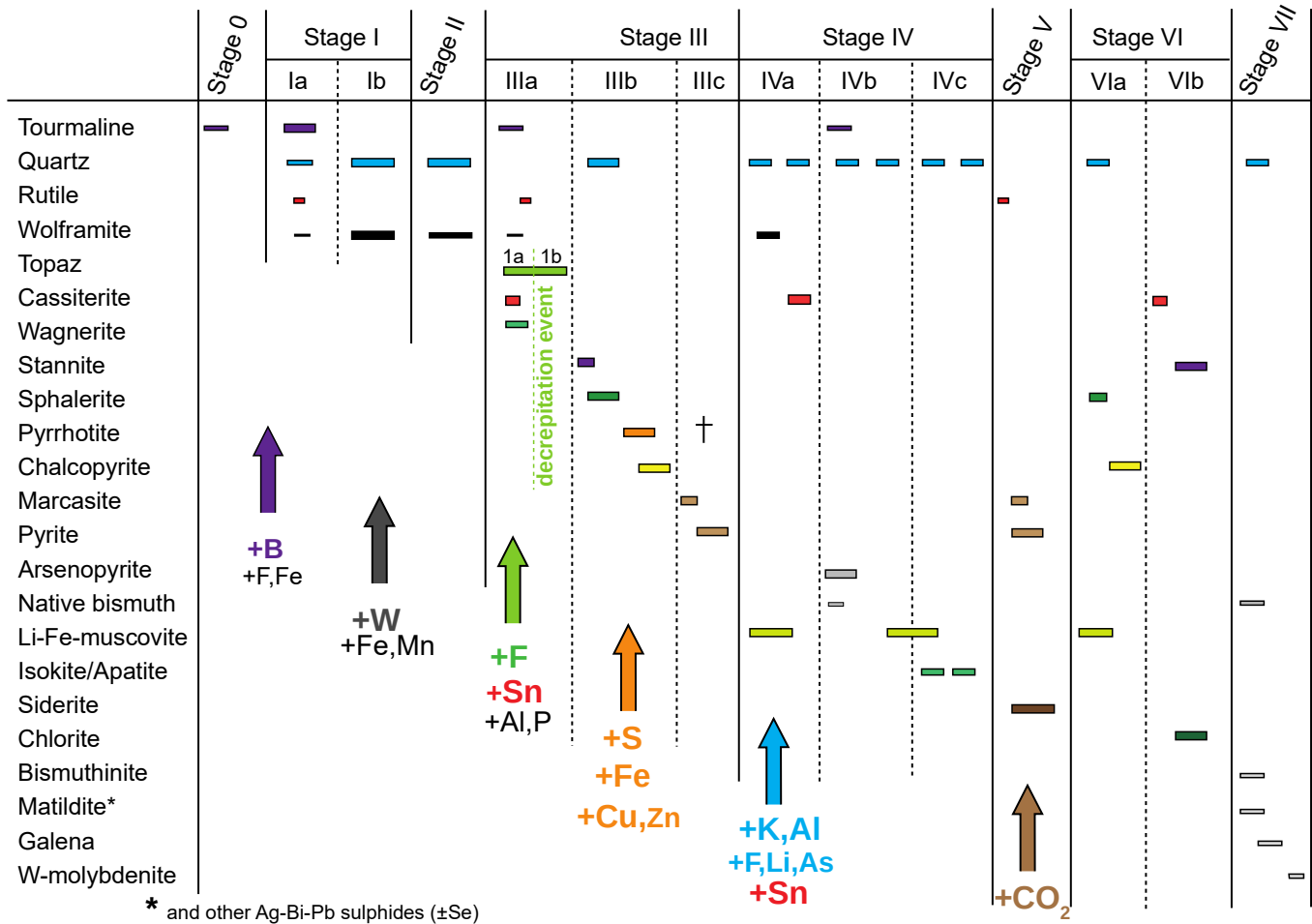


Figure P.O.2. Revised paragenetic chart for the Late Carboniferous Panasqueira vein system. Also indicated are the successive elemental inputs in the system, deduced from mineral assemblages.

Li-Fe-muscovite

Two types of muscovite selvage are observed at Panasqueira. The first, most spectacular, type (Ms1) consists of large fan-shaped crystals (up to c. 5 cm) radiating normally to the vein boundary and lining most often quartz I or II, but also wolframite or arsenopyrite. The second type, with the same mineral association, consists of aggregates of fine grained muscovite crystals. When occurring together with Ms1, this second type appears distinctly later (Ms2). Both muscovite types are seen corroding topaz, and appear therefore to postdate it.

(i) Two textural evidences constrain the relative timing of formation for the Ms1 selvages. In the first place, a remarkable feature of the earlier Panasqueira quartz (stages I and II), is that their fluid inclusions (FI) were decrepitated prior to the inception of stage III quartz, as described in a following section devoted to FI petrology. Everywhere, at the contact between Ms1 and these early quartz, the latter are reworked, showing obliteration of the pristine decrepitated FI, in relation with quartz recrystallization ("bleaching"), in fringes ranging from a few 10 μm to several mm (Fig. P.O.3-A). That this is not the simple result of fluid recirculation at the Ms1-quartz interface is demonstrated by such occurrences as in Figure P.O.3-B. There, QI recrystallization is strictly associated with Ms1 even where it is disconnected from the main selvage (and here, growing onto early wolframite and consequently post-dating it). In the second place, privileged occurrences, such as in Figure P.O.3-C, allow the observation of the progressive decollement of an early QI-Wfm_{1-I} assemblage from the wall-rock, due to the development of Ms1 in staggered rows (crack-seal).

(ii) The age of the Ms1 selvage was set at 296.3 ± 1.2 Ma ($^{40}\text{Ar}/^{39}\text{Ar}$ dating) by Snee et al. (1987) and appears younger of at least 2 Myr than the main wolframite depositing stage (stage I), dated at 305.2 ± 5.7 Ma (U-Pb, rutile) (Carocci et al., 2018).

(iii) Micro-XRF imaging shows that Ms2 selvages are systematically associated to overprinting of the early wolframite (Wfm_{1-I} and Wfm_{2-II}) by a more hübneritic component (Fig. P.O.3-D). In the stage IV vugs, muscovite growing onto neoformed Wfm_{4-IV} prisms is equally associated to Mn-overprinting, thus demonstrating that Ms2 is a stage IV mineral.

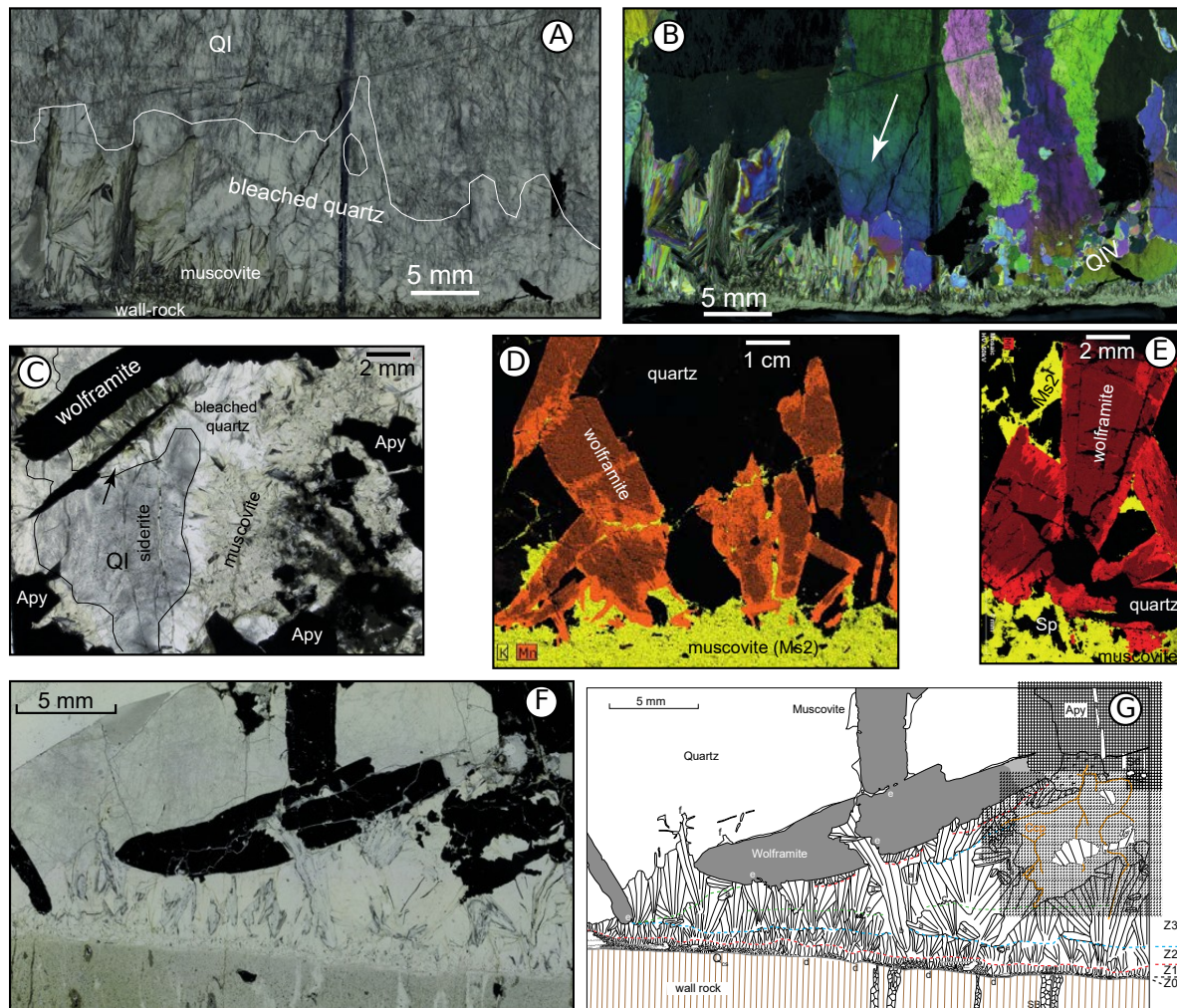


Figure P.O.3. A, B. Muscovite selvage, with bleaching and recrystallization (arrow in B) of QI quartz at the muscovite-quartz boundary (sample PAN-XIV-181-1, level L1, stope D5R7AW15-181, A, natural light, B analysed plane polarized light). C. Selective bleaching of QI quartz at the muscovite-quartz boundary of a muscovite selvage. Note that the muscovite is coating the wolframite (i.e., is definitely later), and that the bleaching stops where coating is absent (arrow) (sample PAN-IV-1b, level 0, stope D9WR17AW13, natural light). D, E. Mn metasomatism in early wolframite as a consequence of the late muscovite (Ms2) overprinting (sample PAN-V-16, level L0, stope D15WR15I2, false-coloured μ -XRF maps). F, G. Development of a muscovite selvage by crack-seal opening in staggered rows; Z1, 2, 3: successive opening increments. The wolframite-quartz assemblage was earlier, as demonstrated by (i) the relics of Z1 and Z2 rows at the wolframite hanging-wall, and (ii) the evident corrosion of both wolframite (e) and quartz (f) by the muscovite. a: falling crystals issued from earlier opening increments; b, c: protracted crystallization through discontinuities. Before the main crack-seal, a first edge of fine-grained muscovite (Z0) overprinted (dissolution/replacement) a Qcs veinlet (opening of which preceded the main stage I quartz), and relics are still visible (d) (sample PAN-XVI-6a-b1, F natural light, G drawing from A).

Arsenopyrite

Arsenopyrite is present in a great variety of settings: small euhedral crystals in the tourmalinized wall-rock, large euhedral to subhedral crystals in selvages or dispersed within quartz I-II or the massive sulphides or in the stage IV vugs, in association with wolframite, topaz or muscovite. Such is the origin of the definition of several arsenopyrite generations in previous works

Nonetheless, whatever the setting, all arsenopyrite crystals display one and the same zoning pattern under SEM examination, with a sequence of zones from a core zone A (with A1 and A2 subzones) to an inner rim B and ending with an outer rim R (Fig. P.O.4-A, B). This sequence is characterized by a secular decrease of the As/As+S ratio, from up to 0.586 down to 0.482, (Fig. P.O.5). There is never “going back”, but discontinuities may be marked, at each A1 → A2, A2 → B and B → R transition, by corrosion and replacement of the earlier arsenopyrite components by the following one. In the same way, some zones may be lacking. In addition, clouds of Bi^o minute crystal inclusions are commonly present and are restricted to the first part of this sequence (i.e., coeval with core zone A) (Fig. P.O.4-A, B).

It seems highly unlikely that such a complicated sequence be more than one time repeated (as indeed implied by all preceding authors who define several stages of arsenopyrite deposition), and the best interpretation is then that there was only one (more or less protracted) arsenopyrite deposition event.

Owing to the presence of arsenopyrite in the stage IV vugs fillings, it results that arsenopyrite is a stage IV mineral, and as arsenopyrite is observed to overprint Ms1 (Fig. P.O.3-C) but to be buried by Ms2 in the vugs, its paragenetic position is well constrained. This conclusion is reinforced by the systematic observation of bleaching of the QI or QII quartz at the contact of disseminated arsenopyrite (Fig. P.O.4-C). As a consequence, the (sometimes spectacular) arsenopyrite selvages must be interpreted as resulting from the re-opening at the vein boundary. Indeed, in the case of arsenopyrite selvages bordering early wolframite, it is clearly observed the corrosion of wolframite by arsenopyrite (Fig. P.O.4-D).

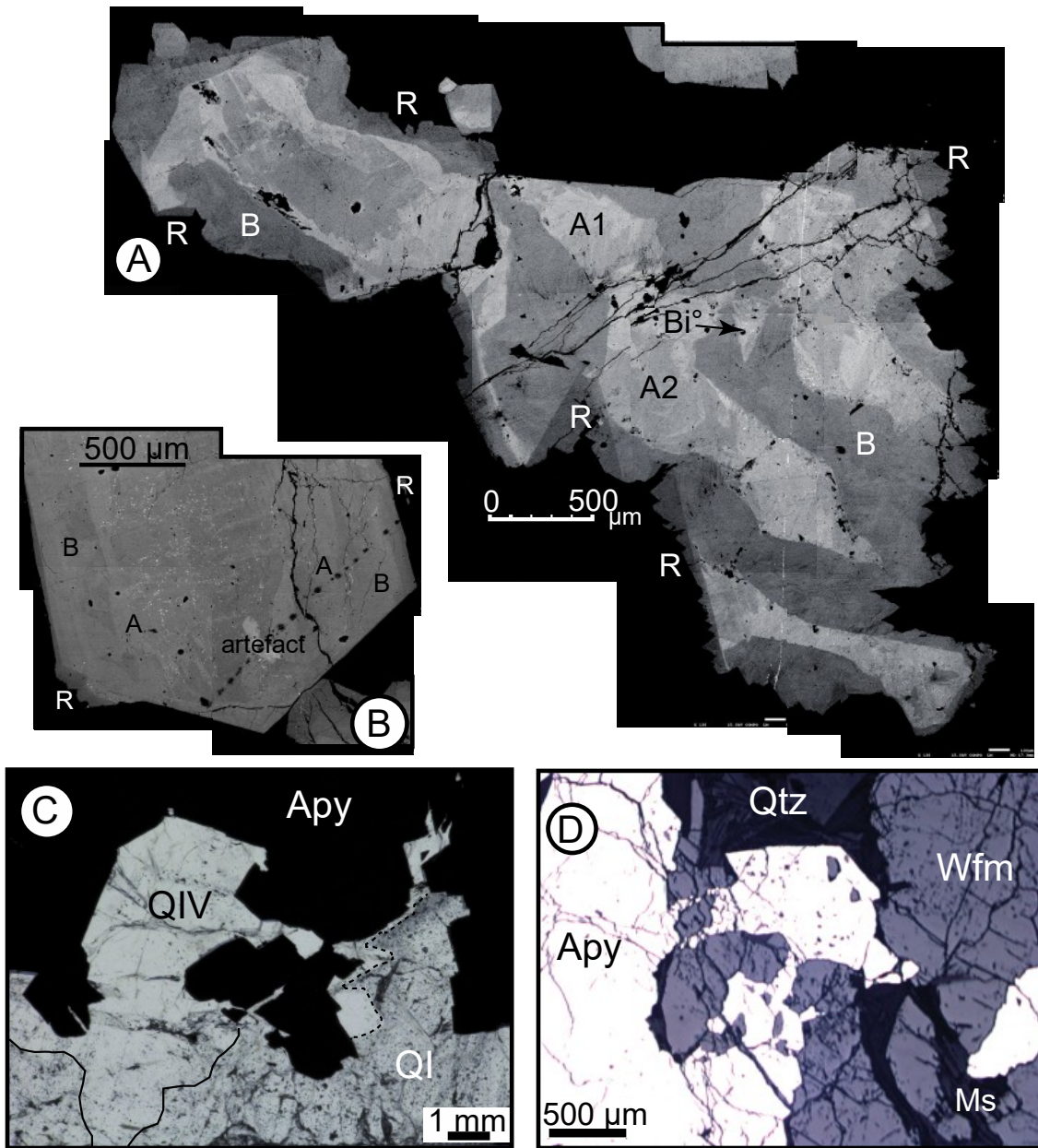


Figure P.O.4. Evidence for the arsenopyrite timing at Panasqueira. **A.** Typical zoning pattern. The crystal comprises: a core zone (A), subdivided into inner (A1) and outer (A2) subzones, an inner rim (B) and an outer rim (R). Several clouds of minute Bi° crystals characterize the core zone. Note that the zone boundaries testify for several overprinting episodes of an earlier zone by a later zone. (sample PAN-IV-5, level L0, stope D15WR15AW10, BSE composite image). **B.** Typical zoning pattern, with a core (A), rich in Bi°, an inner rim (B) and an outer rim (R) (sample PAN-III-8-c2, level L0, stope D15R15WI2, BSE composite image). **C.** Bleached QI quartz (then, QIV) at the QI-arsenopyrite (Apy) contact (sample PAN-III-3b, natural light). **D.** Arsenopyrite selvage of a quartz-wolframite vein: wolframite (Wfm) is clearly overprinted by arsenopyrite (Apy); Ms muscovite (sample PAN-XVIII-11A, level L1, stope D13R10AW17, reflected light).

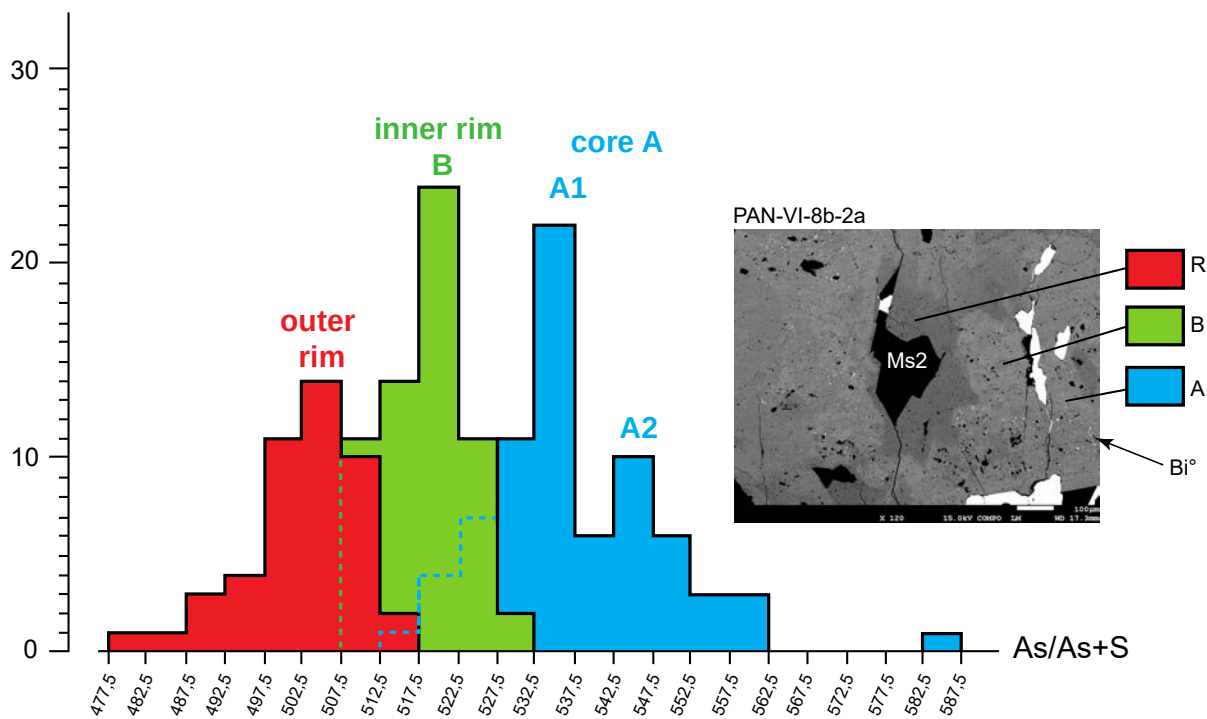


Figure P.O.5. Statistics of Panasqueira arsenopyrite compositions (SEM-EDS analyses). The As/(As+S) ratio varies regularly from As-high values in the core A (in the 0.517 to 0.562 range), to medium values in the inner rim B (in the 0.507 to 0.532 range) and to As-low values in the outer rim R (lower than 0.507).

Topaz

Independent veins or veinlets are currently found in some stopes, that are made of comb topaz followed by sulphide infilling (sphalerite, then pyrrhotite) (Fig. P.O.6-A). Similar veins or veinlets are found within the ore veins, overprinting quartz-wolframite assemblages (Fig. P.O.6-B) or lining massive sulphides (Fig. P.O.6-C). Whereas topaz veins are never observed to overprint massive sulphides, euhedral topaz crystals are commonly found encapsulated into massive pyrrhotite (Fig. P.O.6-D). On the other hand, topaz from topaz selvage in contact with early wolframite is always seen to overprinting it at the thin section scale (Fig. P.O.6-E).

All these observations point to a single topaz episode, post-dating stage I and II wolframite, and preceding the massive sulphide deposition which characterizes the stage III. This conclusion is comforted by several observations: (i) where topaz is associated with muscovite, either Ms1 or Ms2, it is observed to be partially replaced by the latter (Fig. P.O.6-F), (ii) topaz is overprinted by arsenopyrite (Fig. P.O.6-G), and (iii) topaz is never found in the stage IV vugs.

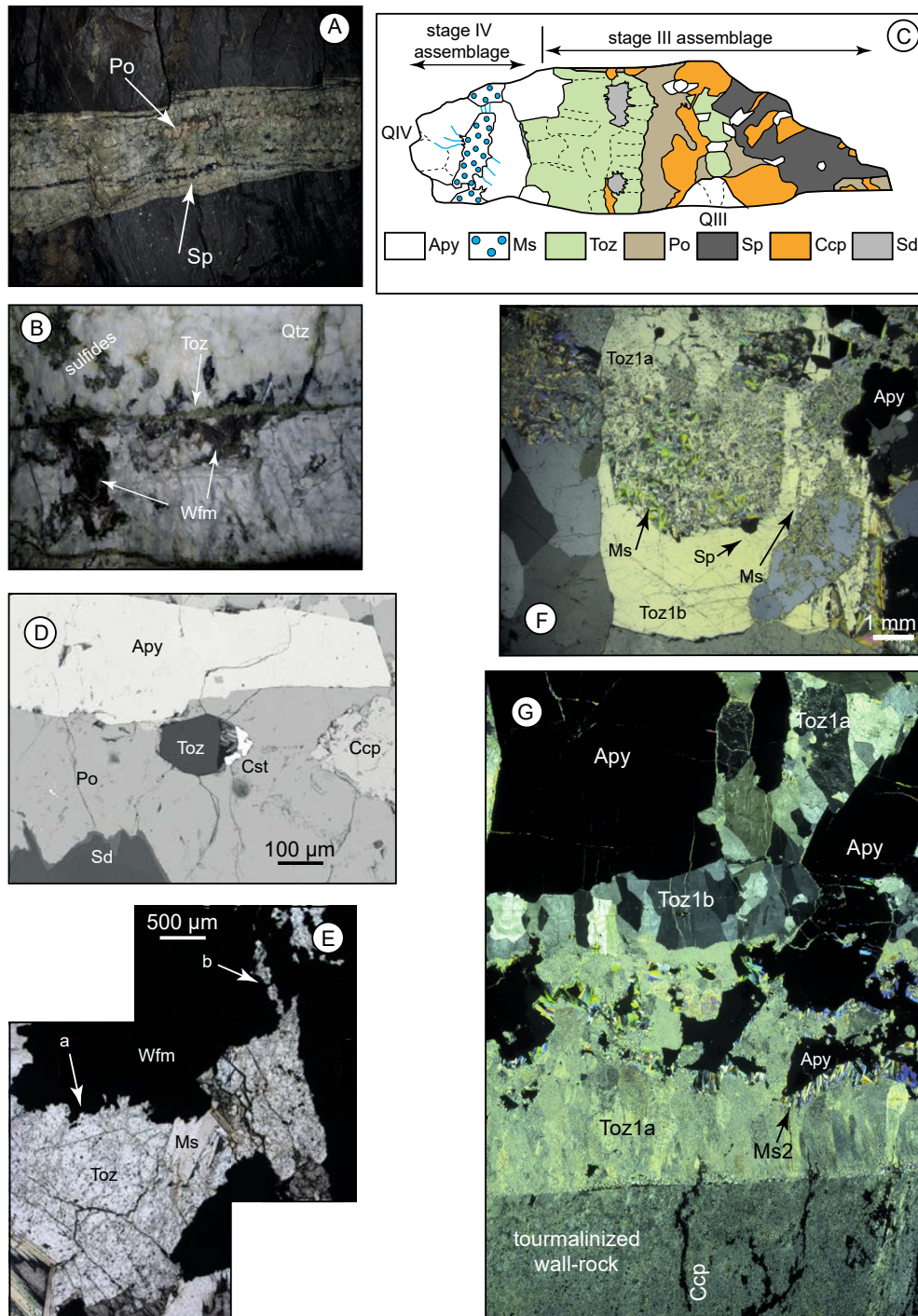


Figure P.O.6. Evidence for the topaz timing at Panasqueira. **A.** Independent topaz vein, showing comb topaz layers and fillings by either sphalerite (Sp) or pyrrhotite (Po) (level L1, stope D29R13AW14E). **B.** Topaz (Toz) veinlet overprinting wolframite (Wfm) from a stage I quartz-wolframite assemblage (level L1, stope D29R13AW24). **C.** Topaz vein lining massive sulphides. Note the crack-seal in topaz vein and topaz crystals included in the sulphide mass. A stage IV Qtz-Apy assemblage overprinted the topaz vein, and was in turn overprinted by later muscovite (drawing from sample PAN-V-10, level L1, stope D15ER3I25). **D.** Topaz (Toz) inclusions in Pyrrhotite (Po) (sample PAN-VI-6a, level L0, stope D9WR17AW13, BSE). **E.** Topaz (Toz) invading wolframite (Wfm) (transmitted light image). **F.** Partial replacement of topaz by muscovite. Note the existence of two topaz generations Toz_{1a} and Toz_{1b} (separated by sphalerite deposition), and the fact that Toz_{1a} is by far more affected than Toz_{1b}. (sample PAN-V-8a, level L0, stope D15R17, analysed plane polarized light). **G.** Topaz (Toz)-arsenopyrite (Apy)-muscovite (Ms) assemblage in a selvage position. Comb topaz developed in several stages (crack-seal), with two generations Toz_{1a} and Toz_{1b}, which are differently affected by muscovitization (Toz_{1a} being up to completely replaced). Arsenopyrite clearly overprints topaz, and is in turn rimmed by crack-seal muscovite (Ms₂). On the base of chemical composition evidence, the latter is coeval with the topaz alteration (sample PAN-XIX-6a-b2, level L1, stope D29R13AW14E, transmitted light, crossed polarizers).

Phosphates

There are two phosphate generations at Panasqueira. The more obvious is the late F-apatite, well exposed in the stage IV vugs, where it is more or less coeval with muscovite Ms2. An earlier fluorophosphate, a Mg-Fe-Mn member of the triplite family with $Mg \geq Fe + Mn$, and consequently named here wagnerite, is systematically replaced by F-apatite, in a majority of occurrences with the intermediate formation of isokite (although defined at Panasqueira, panasqueiraite and thadeuite could not be found again in the present work). At the macroscopic scales, wagnerite is systematically associated with topaz. Microscopic observations confirm that wagnerite is intimately associated with topaz and pyrrhotite, being therefore part of the stage IIIa (Fig. P.O.7-A). Rare occurrences of alumino-phosphates of the goyazite family (with nevertheless a significant F content), being constantly associated with tourmaline (Tur2) of the stage III and with topaz, are equally part of the stage III.

F-apatite may be encountered outside from stage IV vugs, and was for this reason commonly attributed to various earlier stages (Kelly and Rye, 1979; Polya et al., 2000; Lourenço, 2004), depending upon the associated mineral phase. Yet, observations of F-apatite overprinting earlier phases are common (Fig. P.O.7-B). F-Apatite is commonly zoned, either patchy or oscillatory zoning, in many cases with spectacular textures (Fig. P.O.7-C). Zoning is marked on one hand by varying Mn/Fe+Mn ratios, with MnO comprised between 0.05 and 3.27 wt%, and on the other hand, by periodic addition of meaningful Sr contents (up to 6.56 wt% SrO).

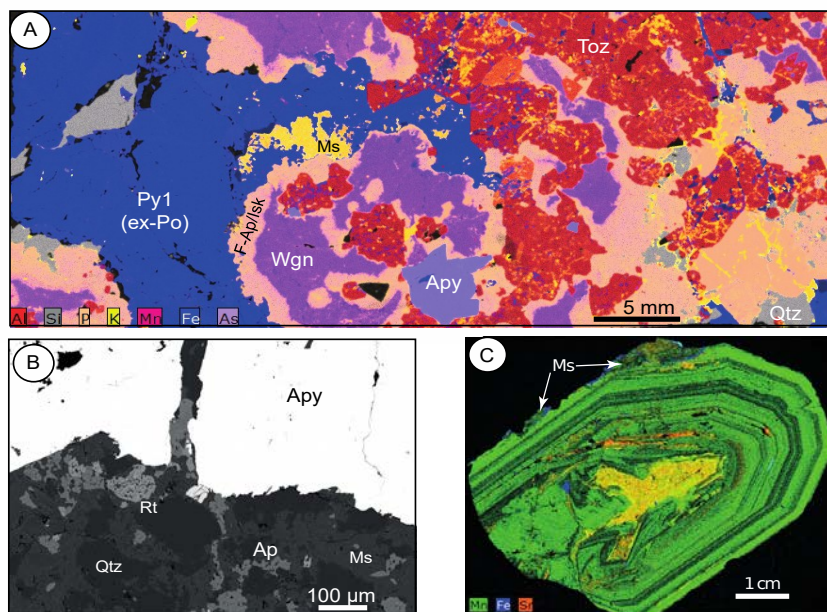


Figure P.O.7. Panasqueira phosphates. **A.** Overprinting of primary stage III assemblage topaz (Toz)-wagnerite (Wgn)-pyrrhotite (Po) (now, pyritized: Py1) by isokite (Isk) and F-Apatite, arsenopyrite (Apy), and late muscovite (Ms) (sample PAN-VII-5a, level L0, intersection D3/D19, false-coloured μ -XRF map). **B.** Late F-apatite (Ap) overprinting the boundary between the arsenopyrite (Apy) selvage of a quartz-wolframite vein and the muscovitized wall rock (Ms) (sample PAN-IV-1a, level L0, stope D9WR17AW13, BSE). **C.** Zoned apatite from a stage IV vug; Ms muscovite (sample *, false-coloured μ -XRF map).

Siderite

At the macroscopic scale, siderite is obviously a late phase, being observed in stage IV vugs, in which it clearly post-dates stage IV assemblages. Outside the vugs, siderite is most commonly found as networks of cracks, equally post-dating all minerals from stage I to stage IV (Fig. P.O.8-A, B). It was nevertheless considered that the siderite which is ubiquitously present in the marcasite-pyrite (Pyr1) assemblage resulting of stage IIIc sulfurization of pyrrhotite is an intrinsic part of the assemblage (PAS of Kelly and Rye, 1979, and subsequent workers). Yet, it may be observed: (i) that in the PAS assemblage, siderite is present as a network of cracks (Fig. P.O.8-C), associated with dissolution/replacement of Py1 leading to a series of vuggy siderite patches (Fig. N+8-D). At the same time, recrystallization of Py1 and growth of a new pyrite (Py2) lead to spectacular symplectic association of siderite and Py2 (Fig. P.O.8-D, E) and growth of euhedral Py2 lining siderite vugs (Fig. P.O.8, F). Given these evidences, and applying the OR principle, it seems clear that the first appearance of siderite in the Panasqueira sequence post-dated stage IV, hence the definition of a stage V in Figure P.O. 8.

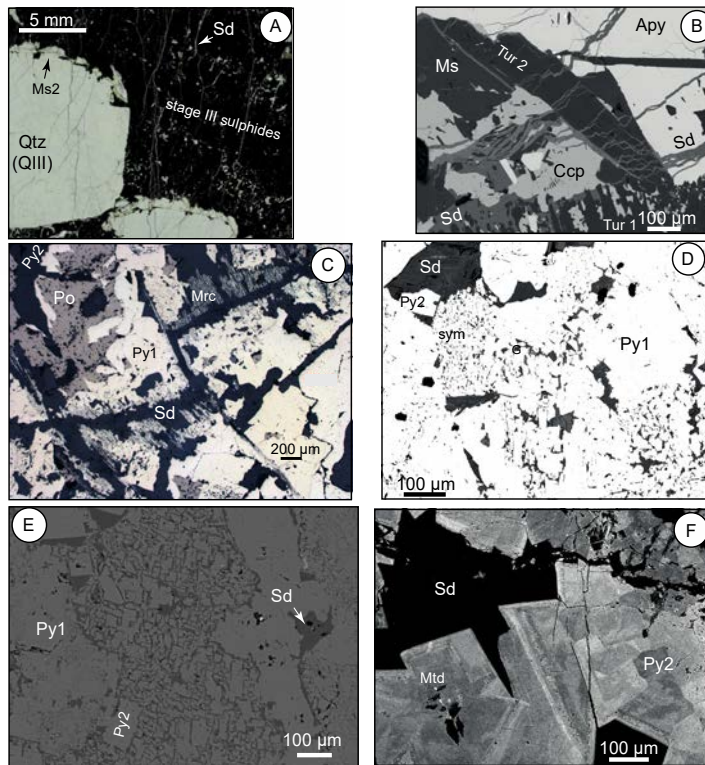


Figure P.O.8. Evidence for siderite timing at Panasqueira. **A.** Network of thin siderite (Sd) veinlets overprinting a QIII-sulphides (stage III pyrrhotite+sphalerite+chalcopyrite assemblage)-muscovite (Ms2) assemblage. Note the numerous inclusions of muscovite or siderite within the sulphides (sample PAN-XV-1c, level L0, natural light). **B.** Siderite microcracks overprinting a composite selvage of muscovite (Ms1), chalcopyrite and arsenopyrite (sample PAN-III-8-c2, level L0, stope D15R15W12, BSE). **C.** Network of siderite (Sd) overprinting the marcasite (Mrc)-pyrite (Py1) assemblage developed at the expense of pyrrhotite (Po) during stage IIIc (sample II-5-2a, level L0, stope D9WR17AW13, reflected light). **D.** Overprinting of primary pyrite (Py1) by dissolution vugs with siderite (Sd) infilling and coeval Py2, the latter forming symplectic associations with Sd (sym) (sample PAN-V-6-c, level L0, stope D15WR15I2, BSE). **E.** Symplectic association of siderite (Sd) and pyrite (Py2) (sample PAN-II-5-2a, level L0, stope D9WR17AW13, BSE). **F.** Zoned euhedral pyrite (Py2) lining a siderite (Sd) vug; zoning is revealed by oxidation of the thin section surface. Here present as microinclusions in pyrite, mathildite (Mtd) is observed to form microcracks in other parts of the same sample, being consequently a late phase (sample PAN-VI-11, level L0-D3, BSE).

CHAPTER ONE

INCIPIENT DEPOSITION STAGE OF WOLFRAMITE: W-RUTILE AND TOURMALINE CHEMISTRY AS PROXIES FOR EARLY FLUIDS AT PANASQUEIRA (PORTUGAL)

Article submitted *in Economic Geology* review

Abstract

At Panasqueira, the main event responsible for the deposition of W follows the strong tourmalinization of the wall-rocks. Tourmaline is coeval with a W-rich rutile (up to 8-10 wt% W) and both minerals record an early introduction of W in the system. U-Pb dating of the rutile by LA-ICP-MS yields an age of 305.2 ± 5.7 Ma, which is 6-10 Ma older than the K-Ar age of 296.3 ± 1.2 Ma obtained by analysis of muscovite. To date, the latter age was considered as the W-ore deposition age. Major and trace element concentration variations in tourmaline record fluid mixing between two end-members, both considered to be of metamorphic origin on the basis of REE patterns. We find evidence for a fluid enriched in Co-Cu-Pb-Sc-Sr-V-Cr-Nb-Ta-Sn, interpreted to be of "local" origin, and a fluid rich in Li-F-Fe-Mn-W inferred to be of deep origin and related to biotite dehydration. The second fluid carried the metals (in particular Fe and Mn) necessary for wolframite deposition, which were not necessarily inherited from the wall-rocks through fluid-rock interaction. Micrometer scale variations in tourmaline and rutile crystal-chemistry are indicative of pulsatory fluid input during the tourmalinization process. In particular, rutile zonation records short term variations in Nb content that may be interpreted as related to a minor fluid contribution from a rare-metal granite.

Introduction

In western Europe, tungsten (W) was mainly concentrated during the Variscan orogeny. The total endowment is estimated to be 1.1 Mt W. The Central Iberian Zone (CIZ), concentrating 210 kt W, is therefore one of the main provinces. Others include Erzgebirge (270 kt W) and Cornwall (≥ 425 kt W; Marignac and Cuney, 2013). In the CIZ the Panasqueira mine, active for more than 100 years, is one of the largest W deposits in western Europe, with a total production of 88 kt W since 1947 and estimated reserves of ~ 23 kt W (Almonty, 2016; Vigne et al., 2018).

Since the 1970s, numerous mineralogical, geochemical and fluid inclusion studies report on the genesis of the Panasqueira deposit (e.g., Kelly and Rye, 1979; Bussink, 1984; Snee et al., 1988; Polyá, 1989; Noronha et al., 1992; Lüders, 1996; Foxford et al., 2000; Polyá et al., 2000; Lecumberri-Sanchez et al., 2017; Launay et al., 2018). Within the Beira schist series, and overlying an inferred contact with a granite pluton (inferred from the presence of a muscovite cupola), the deposit is characterized by thousands of sub-horizontal veins filled by wolframite and quartz. Following Kelly and Rye (1979), most studies conclude that the granite intrusion played a major role in controlling a unique hydrothermal megacycle. Snee et al. (1988) dated muscovites at 296.3 ± 1.2 Ma (2σ), using the $^{40}\text{Ar}/^{39}\text{Ar}$ age step-heating method, and considered this age to represent the approximate timing of the main W depositional stage at Panasqueira on the basis of coeval crystallization of wolframite and muscovite.

Recent investigations carried out on the scale of the whole deposit brought new detailed observations of the mineral sequences synchronous with the incipient opening of the W veins. The fluid inclusion record of the event in which wolframite was deposited (OSS stage of Polyá et al., 2000) was lost due to decrepitation and/or deformation after wolframite crystallization (Cathelineau et al., 2017; 2018), a fact which is not accounted for in most previous work, a fact which was unfortunately overlooked by all previous studies. As a consequence, there is no reliable record of the fluids responsible for wolframite crystallization. A potential way to constrain the composition of these early fluids is to study the crystal-chemistry and trace element concentrations in minerals coeval with incipient wolframite deposition. Here, we demonstrate that tourmaline in the wall-rock, and an associated rutile, are indeed coeval with wolframite. Both minerals display chemical zoning, taken as proxy of the fluid chemistry evolution during their growth. Tourmaline is known to be “ultra-stable” under a wide range of physico-chemical conditions (Van Hinsberg et al., 2011). Its complex structure inhibits significant element diffusion on available timescales (Hawthorne and Dirlam, 2011) and records changes in fluid chemistry all along the crystal growth (Marschall and Jiang, 2011; Sluck and Trumbull, 2011; van Hinsberg et al., 2011; van Hinsberg and Schumacher, 2011). Despite several studies of the Panasqueira tourmalines, based mostly on major elements and boron isotope data (Neiva et al., 2007; Codeço et al., 2017; Launay et al., 2018), none have looked at the detailed variation in trace element concentrations as a potential tracer of the fluid chemistry evolution or of change(s) in the fluid source(s).

The first main objective to be addressed in this study is therefore the detailed analysis by EPMA, SEM-EDS and then LA-ICP-MS of tourmaline and rutile in order to constrain the nature of the ore forming fluids. This results

in a modified conceptual model of the early hydrothermal system at Panasqueira. The second objective is to date the rutile using the in situ U-Pb method, in order to constrain the onset of the hydrothermal system and to compare with the known ^{40}Ar muscovite age.

Regional background

Panasqueira is located in the Iberian Massif, southern branch of the so-called Iberian-Armorican Arc (IAA), which stem from the western termination of the Variscan belt. The latter is currently thought to result from the protracted collision between Gondwana and Laurussia in the late Paleozoic (e.g., Matte, 2001; Franke et al., 2005; Martinez Catalan et al., 2007; and Faure et al., 2009). The IAA is an orocline (Cantabrian Orocline) formed in about 10 Ma at the end of the Carboniferous (Gzhelian)-beginning of the Permian (Asselian) (Weil et al., 2013).

The Iberian Massif is subdivided into a number of tectonostratigraphic units (or Zones) (Julivert et al., 1972) delimited by tectonic boundaries (major fault systems, often reactivated as extensional and/or strike-slip faults at the end of the Variscan orogeny) (Fig. 1). With the exception of the South Portuguese Zone, which is thought to have an Avalonian (Laurussian) affinity (Arenas et al., 2016), all these terranes are considered to be Gondwanian in origin. Some of these terranes are allochthonous, including ophiolites and high-pressure rocks: Galicia-Tras-os-Montes Zone in the NW, Ossa Morena Zone in the south, and both zones are the remnants of a unique nappe stack, which once constituted the tectonic cover of the autochthonous terranes (Pérez-Caceres et al., 2017). The latter are derived from the Paleozoic Gondwanian passive margin, represented by three terranes (Cantabrian, West Asturian-Leonese and Central Iberic Zones), which differ by their Lower Paleozoic sequences.

The main autochthonous terrane is the Central Iberian Zone (CIZ), and comprises a thick sequence of late Ediacarian-Cambrian metasedimentary rocks (the Schist-Greywacke Complex, or Beira Group) overlain unconformably by the Early Ordovician Armorican Quartzite (Diez-Fernandez et al., 2013). The metasedimentary package is divided into three units (Diez-Fernandez et al., 2013): (1) a lower unit (≥ 2000 m thick), monotonous alternation of slates and sandstones (Ediacarian), with at the top intercalation of a thick carbonate levels and several black slate layers (encompassing the upper Ediacarian and lower Cambrian); (2) a middle unit (~500 m thick), characterized by abundant sandstones and conglomerates; and (3) an upper unit (~1000 m thick), mostly composed of greenish-grey slates, with sandstone and conglomerate layers.

The tectono-thermal Variscan history of the CIZ, which begins in the Early Carboniferous and ends in the Early Permian, is subdivided into five events, D1 to D5 (Diez-Fernandez et al., 2016, and references therein; Diez-Fernandez and Pereira, 2017). D1 crustal thickening, characterized by the stacking of the allochthon, E- or NE-verging recumbent folding, a penetrative axial plane S1 sub-parallel to S₀, and the development of a Barrovian low-grade M1 metamorphism (Diez Fernandez et al., 2013) is dated at c. 354-347 Ma (e.g., Rubio Pascual et al., 2013). The subsequent D2-D5 evolution is characterized by large-scale crustal melting, resulting from a combination of

mid-crustal post-thickening heating and mantle-derived heat input at the base of the continental crust (Pereira et al., 2017). The D2 (c. 327-316 Ma) event records the first episode of heat input and mid-crustal melting, with the development of migmatitic (metatexites, water-present partial melting) domes (Fig. 1.3), a flat-lying S2 schistosity and syn-migmatitic detachment shear zones, demonstrating extensional flowing in the middle crust (e.g., Llana-Fúnez and Marcos, 2007; Diez Fernandez et al., 2012; Rubio-Pascual et al., 2013; Pereira et al., 2017). Mafic syn-migmatitic sills and sheet-like bodies of late-kinematic monzogranite and granodiorite (319-316 Ma) are widespread (e.g., Castro et al., 2003; Pereira et al., 2017). The D3 to D5 evolution responds to a protracted series of episodic intra-crustal transcurrent deformation, initiated at ca. 315-310 Ma by the development of km- to 10 km-sized NW-SE to N-S upright F3 folds, with a S3 axial-plane schistosity, and followed by D4 (c. 309-305 Ma) left-lateral and D5 (c. 304-295 Ma) dextral faulting (Diez Fernandez et al., 2017; and references therein). Crustal melting and concomitant mantle-derived heat input were continued throughout D3 to D5, with the pervasive emplacement of syn- to post-kinematic granite plutons, in three pulses roughly coincident with the D3 to D5 events: syn-kinematic porphyritic biotite monzogranites and leucogranites (c. 315-310 Ma); late-kinematic D3 (c. 309-301 Ma) and post-kinematic (c. 295-287 Ma) biotite±cordierite monzogranites and granodiorites, with in addition ferro-potassic subalkaline granites at c. 295-290 Ma (e.g., Dias et al., 1998; Mateus and Noronha, 2010; Sant'Ovaia et al., 2010; Fernandez-Suarez et al., 2011). Water-absent dehydration melting (biotite incongruent melting) produced cordierite-bearing diatexites in the cores of D2 migmatitic domes (Pereira Gomez et al., 2011). Late localized swarms of medium potassic calc-alkaline to shoshonitic E-W dikes at ca 290 Ma, and of NW-SE Late Permian (ca 265 Ma) lamprophyre dikes (camptonite, bostonite) (Orejana et al., 2009; Scarrow et al., 2011) testify to the permanence of mantle influence at the very end of the collision.

Numerous mineralized systems were active in the CIZ in close association with the Late Carboniferous tectonics and granitoid emplacement. More than 150 deposits are known, corresponding to both peri- and intra-granitic rare metal (Nb-Ta, Li, W, Sn) and shear-zone hosted (Au-Ag-As-Sb-Pb-Zn-Cu) systems (Tornos et al., 2000; Neiva, 2002; Mateus and Noronha, 2010; Noronha, 2017). Significant rare metal deposits (Fig. 1.3) include rare metal granites (e.g., Argemela: Charoy and Noronha, 1996), Li-Sn-(Feli: Robles et al., 1991) and Sn-Ta-Nb (Forcarei Sur: Fuertes-Fuente et al., 2000) pegmatite fields, Qtz-cassiterite (Argemela: Inverno et al., 2009) and Qtz-wolframite-(cassiterite)±chalcopyrite (Panasqueira) vein systems, Qtz-wolframite-polymetallic breccia pipe (Borralha: Noronha, 1984; Lima, 2015), Qtz-scheelite vein systems (Barruecopardo: Sanderson et al., 2008), and skarns (Los Santos: Tornos et al., 2008).

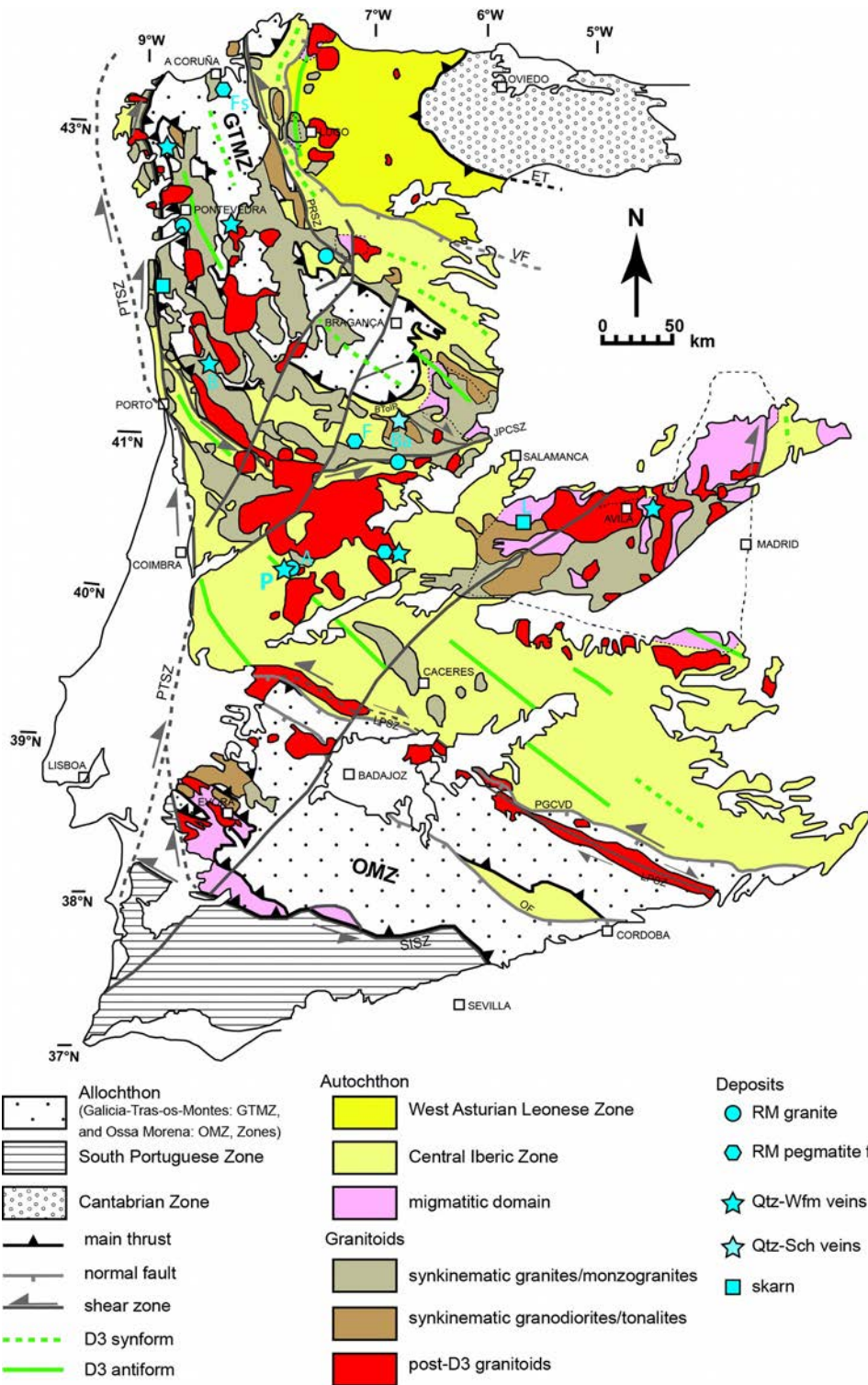


Figure 1.3: Geologic map of the Iberian Massif, with Panasqueira location. The map is adapted and simplified from Diez Fernandez et al. (2016), with complementary data from Alcock et al. (2015), Llana-Furez and Marcos (2007), Rubio Pascual et al. (2013) and Rubio-Pascual et al. (2016). BTolP: basal thrust of the Iberian Parautochthon; ET: Espina thrust, JPCSZ: D4 Jusbado-Perralva do Castelo shear zone; LPSZ: Los Pedroches shear zone; OF: Onza fault; PGCVD: Puente Genave-Castelo Vide detachment fault; PRSZ: Palas de Rei shear zone; PTSZ: Porto-Tomar D5 shear zone; SISZ: South Iberian shear zone; VF: Viveiro fault.

Geological setting and previous work

The Panasqueira W-Cu (Ag)-Sn deposit in central Portugal lies within the Central Iberian Zone (CIZ) (Fig.1.3), in the core of a late Carboniferous anticlinorium bordered by narrow synclines of Ordovician Armorican Quartzite (Fig. 1.4-A). The deposit consists in a dense network of sub-horizontal mineralized quartz veins, crosscutting the subvertical foliation of the greenschist facies micaschists belonging to the Beira Schists (Fig. 1.4-B). The quartz veins crosscut through numerous pods and vein-like masses of barren quartz locally named “seixo-bravo” which are probably late kinematic. Their spatial extent covers an area of over 6 km² for a vertical extent of several hundred meters (Polya, 1989). The deposit is mined using the room and pillar method, allowing detailed 3D-observations to be made.

Concealed beneath the deposit (Fig. 1.4-B), a granite body is responsible for a 6x3 km metamorphic contact aureole of spotted schists, marked by cordierite-biotite spots and cordierite-andalusite assemblages, constraining the pressure to less than 300 MPa at the time of emplacement of the Panasqueira granite (Pattison, 2001; Kuhn, 2018). At the top of the granite body, a greisenized cupola is still observed in some of the galleries. This cupola was described as being overlain by a quartz cap by Kelly and Rye (1979), although this has not been corroborated since. The greisenized cupola sits atop of a sheet-like body of evolved granites that are mainly evidenced in a few drill holes (Bussink, 1984; De Amorin, 2017), but have been encountered locally in some of the deepest galleries of the mine (LB level, Barroca Grande sector: Lourenço, 2002). The cupola sends out several sill-like apophyses, and towards its base, a matrix-supported breccia formed with large (up to 2 m) joint-bounded hornfels clasts (Kelly and Rye, 1979). The greisenized cupola is overprinted by the quartz-wolframite veins. The evolved granites are typical members of the peraluminous rare metal granite (RMG) family (Linnen and Cuney, 2005), and are albite-rich, displaying typical “snowball” quartz textures. They contain (rare) cassiterite and columbo-tantalite as accessory minerals (Lourenço, 2002; De Amorin, 2017). There are at least three superposed layers with distinct granite compositions (De Amorin, 2017), which are greisenized upwards. Below this RMG layer, a few deep drill holes encountered a porphyritic (K-feldspar megacrysts) biotite-(muscovite) granite (Bussink, 1984), which is likely representative of the main granite body responsible for the metamorphic aureole and could be related to the late D3 granites from the nearby Serra de Estrela (Sant'Ovaia et al., 2010) and Serra de Gardunha (Fig. 1.4-A). According to recent gravimetric data (Ribeiro, 2017), the main Panasqueira granite display the shape of a laccolith, with a flattened top, a NNE striking elongated trend (~6.3x3.8 km) and an average thickness of 1 km, but with a 2 km thick keel. The evolved granites are dated at c. 290 Ma, by whole-rock K-Ar (Clark, 1970) or Rb-Sr (Priem and Den Tex, 1984) methods. Close to the deposit, the Fundão granodiorite (Garcia, 2004) and the small Argemela RMG intrusion (Charoy and Noronha, 1986), dated (K/Ar) at 303±6 Ma (Portugal Ferreira and Noronha, 1981, unpublished data) and associated with a quartz-cassiterite vein system (Inverno et al., 2009), are also present.

The Panasqueira deposit attracted attention since the late XXth century (Polya et al., 2000, and references therein; Lourenço, 2002; Burnard and Polya, 2004). According to ³⁹Ar/⁴⁰Ar dating (Snee et al., 1988), the whole paragenesis has been constrained between c. 296 and c. 292 Ma.

More recently, the Panasqueira deposit has been revisited and studied further. Lecumberri-Sanchez et al. (2017) analysed the trace element content of many fluid inclusions and concluded that although the W had been provided by magmatic fluids, wolframite deposition was controlled by fluid-rock interaction with the wallrocks that provided the necessary Fe. Jaques and Pascal (2017) constrained the fluid pressure during vein opening to be 300 MPa (c. 10 km depth). Jacques et al. (2018) proposed that the set of joints opened by fluid overpressure at the main ore stages was created during a folding event characterized by vertical fold axes and related to the oroclinal buckling of the Ibero-Armorican arm. Studying the tourmalinized vein wall-rocks, Codeço et al. (2017) use B-isotope data to conclude that the boron-bearing fluids were of magmatic origin. Cathelineau et al. (2017, 2018) show that most of the early fluid inclusions (FI) in quartz associated with the main wolframite deposition event were decrepitated, implying that all the FI data reported in earlier work were in fact representative of later mineralizing stages. From the pristine FI, they estimate the early conditions at c. 450 ± 50 °C and c. 270 MPa (i.e., at 10 km depth). Launay et al. (2018) deduced fluid flow vectors and rates from tourmaline growth features at the vein margins, and showed that fluid flow was radially structured around the greisenized cupola, hence they concluded a magmatic origin for the fluid.

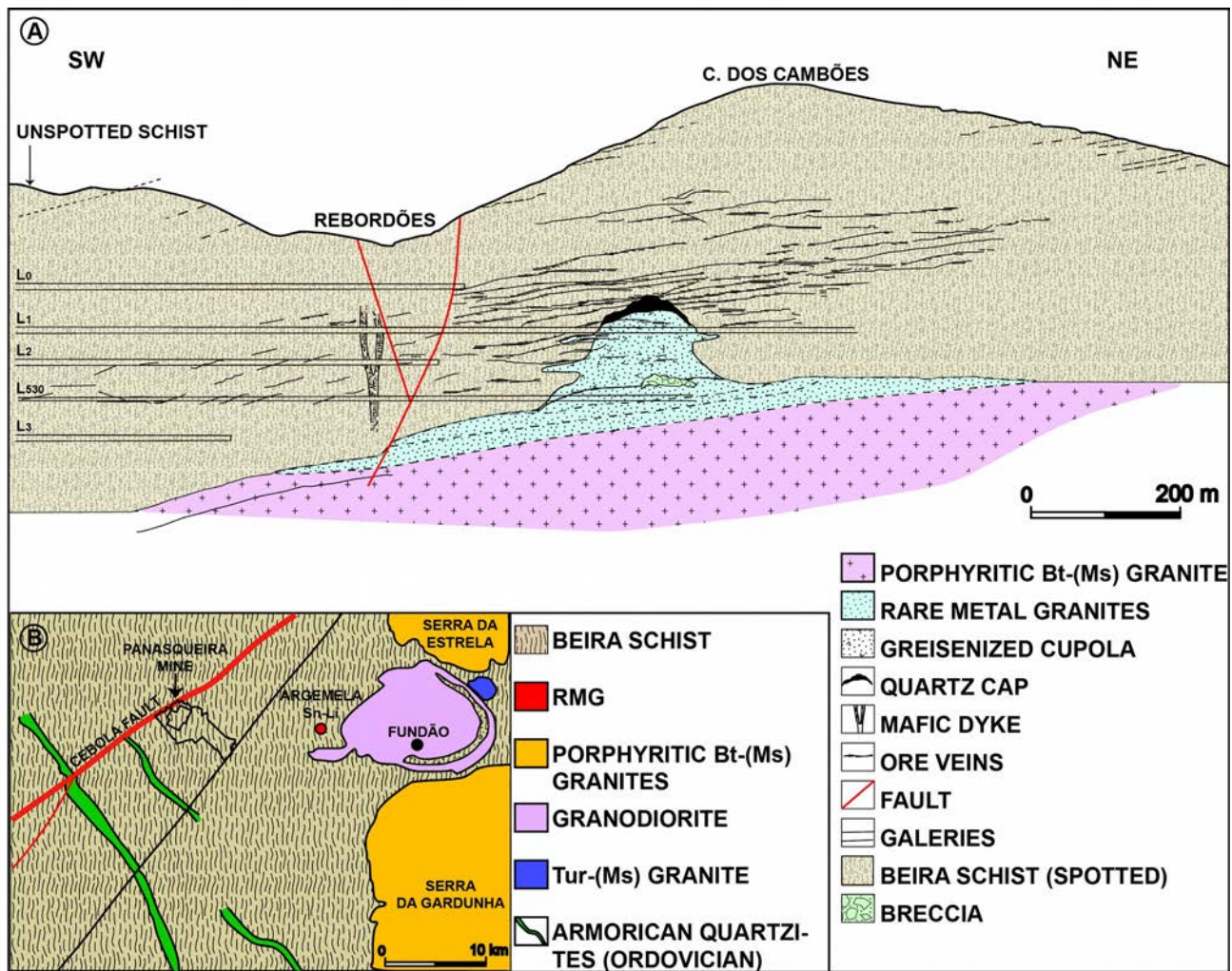


Figure 1.4: Panasqueira geological setting. A. Cross section of the Panasqueira deposit (adapted from Bussink, 1984 and De Amorin, 2017). B. Geologic map of the Panasqueira area (redrawn from Ribeiro, 2017), with location of the cross section. Note the tight synform roots picked out by Ordovician quartzites.

Samples and methods

Our work is based on analyses of >250 samples collected in the late 1970s at levels 0 and 1, in the historical centre of the mine, and in 2015-2016 at the levels 0 to 3, to the south-west of the historical zones.

Following petrographic examination with an OLYMPUS BX51 (transmitted and reflected light) optical microscope and a VHX-200 KEYENCE numeric microscope, selected samples were studied with a Schottky-FEG (Field Emission Gun) JEOL J7600F scanning electron microscope (SEM) equipped with an SDD-type EDS spectrometer at the GeoRessources Laboratory (Nancy, France). Backscattered electron (BSE) images were obtained by setting the acceleration voltage at 15 kV.

Major-element mineral compositions were determined in tourmaline and in rutile using both a CAMECA SX100 Electron microprobe (EPMA) equipped with a wavelength dispersive spectrometer (WDS) and a Schottky-FEG (Field Emission Gun) JEOL J7600F scanning electron microscope (SEM) equipped with a SDD-type EDS

spectrometer at the GeoRessources Laboratory (Nancy, France). Analytical conditions were a 12 nA current and an accelerating voltage of 15 kV for the EPMA, and a 1 nA current and an acceleration voltage of 15 kV for the SEM, with a counting time of 10 s. The same natural and synthetic oxides and silicate standards were used for the two types of analyses. For tourmaline analysis, these standards were topaz (F), albite (Na), olivine (Mg), orthoclase (Si, K), wollastonite (Ca), MnTiO₃ (Ti, Mn) and hematite (Fe). For rutile analysis, the standards were TiO₂ (Ti), Cr₂O₃ (Cr), vanadinite (V), hematite (Fe), LiNbO₃ (Nb), LiTaO₃ (Ta), cassiterite (Sn) and scheelite (W).

Trace and rare earth elements in tourmaline were determined at the Georessource Laboratory, using a 193 nm GeoLas Pro ArF Excimer laser at 5 Hz laser frequency, the aerosols being analyzed with an Agilent 7500c Quadrupole ICP-MS. Analytical settings for laser ablation are detailed in Leisen et al. (2012) and Lach et al. (2013). Laser ablations were performed with a constant fluence of 10 mJ.cm⁻² and a constant repetition rate of 5 Hz. Helium was used as a carrier gas to transport the laser generated aerosols from the ablation cell to ICP-MS. A typical flow rate of 0.5 l.min⁻¹ for He was mixed with Argon before entering the ICP torch. The hole produced by the laser was 24 µm in diameter, except for the REE measurement for which it was 120 µm in diameter. Peak hopping ablation mode began around 20 s after the beginning of signal acquisition, in order to sample the background signal before ablation (used for data reduction), and was stopped after 200 pulses. Return of the background signal to its initial value was checked before ablating a new zone. The external standards used were the NIST reference glasses 610/612, and Si, previously analysed by EPMA, was used as an internal reference. The data were processed using the Iolite software (Paton et al., 2011).

Rutile U-Pb geochronology was conducted by in-situ laser ablation inductively coupled plasma mass spectrometry (LA-ICP-MS) at Géosciences Rennes using an ESI NWR193UC Excimer laser coupled to a quadrupole Agilent 7700x ICP-MS equipped with a dual pumping system to enhance sensitivity (Paquette et al. 2014). The instrumental conditions are reported in Appendix A1, Table A1.

The ablated material is carried into helium, and then mixed with nitrogen and argon, before injection into the plasma source. The alignment of the instrument and mass calibration was performed before each analytical session using the NIST SRM 612 reference glass, by inspecting the ²³⁸U signal and by minimizing the ThO⁺/Th⁺ ratio (<0.5%). During the course of an analysis, the signals of ²⁰⁴(Pb+Hg), ²⁰⁶Pb, ²⁰⁷Pb, ²⁰⁸Pb, ²³²Th and ²³⁸U masses are acquired.

Single analyses consisted of 20 s of background integration followed by 60 s integration with the laser firing and then a minimum of 10 s delay to wash out the previous sample. Ablation spot diameters of 45 µm with repetition rates of 5 Hz were used for all the analyses.

For each analytical session, we used the following standard bracketing procedure. Two analyses of the R10 rutile standard (Luvizotto et al., 2009) used as the primary rutile reference material, one analysis of the R19 rutile standard (489.5 ± 0.9 Ma, Zack et al., 2011) used as quality control, followed by 6 analyses of the rutile grains. This

sequence was then repeated 3 times with one analysis of the R19 and two analyses of the R10 standards at the end of the session.

Data were corrected for U–Pb fractionation and for mass bias by the repeated measurements of the R10 rutile standard. The R19 rutile standard measurements treated as unknowns were used to control the reproducibility and accuracy of the corrections. During the course of the analyses, it provided ages of 490 ± 3 Ma (MSWD = 1.11; n=13) during the April 2016 session and 493 ± 12 Ma (MSWD=2; n=12) during the December 2017 session respectively.

Data reduction was carried out with the data reduction scheme *VizualAge_UcomPbine*, a set of *Iolite* procedures that work with *Igor Pro* (Chew et al. 2014). All data were plotted at 2 sigma in Tera-Wasserburg Concordia diagrams using the *Isoplot 3.75* software (Ludwig, 2012).

$^{40}\text{Ar}/^{39}\text{Ar}$ analytical work was performed at the University of Manitoba (Canada) using a multi-collector Thermo Fisher Scientific ARGUS VI mass spectrometer, linked to a stainless steel Thermo Fisher Scientific extraction/purification line, Photon Machines (55 W) Fusions 10.6 CO₂ laser, and Photon Machines (Analyte Excite) 193 nm laser. Isotope abundances were corrected for extraction-line blanks, which were determined before every sample analysis. Line blanks in both the Excimer and CO₂ system averaged ~3 fA for mass 40 and ~0.013 fA for mass 36. Mass discrimination was monitored by online analysis of air pipettes based on a power law relationship (Renne et al., 2009), which gave $D = 1.0081 \pm 0.0002$ per amu, based on 71 aliquots interspersed with the unknowns. A value of 295.5 was used for the atmospheric $^{40}\text{Ar}/^{36}\text{Ar}$ ratio (Steiger and Jäger, 1977) for the purpose of routine measurement of mass spectrometer discrimination using air aliquots, and correction for atmospheric argon in the $^{40}\text{Ar}/^{39}\text{Ar}$ age calculation. Corrections are made for neutron-induced ^{40}Ar from potassium, ^{39}Ar and ^{36}Ar from calcium, and ^{36}Ar from chlorine (Roddick, 1983; Renne et al., 1998; Renne and Norman, 2001). Data were plotted using *DensityPlotter* (Vermeesch, 2012). Complementary information is given in Appendix A2.

Results

Petrography of the tourmalinized wallrocks

In Panasqueira, tourmaline is a widespread mineral in the vein wallrocks, but it may also be observed at the surface, far from the mineralized envelope, bordering either barren quartz veins or even “dry” joints. The tourmaline-bearing rocks extend to variable distances from the vein/joint boundaries, from a few cm (≤ 10) at the surface up to 1 m in the mine, with a rough estimated average of 25 cm (rather than the 15 cm proposed by Kelly and Rye, 1979).

As recognized first by Bussink (1984), then by Foxford et al. (1991), thin quartz veinlets (1-5 mm in average) are often found in the tourmaline-bearing wallrocks, usually paralleling the main veins boundaries, and in many cases

also underlining the boundary. They display clear evidence for a crack-seal mechanism of opening, and are labelled Qcs in the following (Fig. 1.5-A).

Tourmaline abundance is variable, with a clear organization in bands parallel to S_0 , from nearly tourmalinite to scattered tourmaline in a matrix of quartz. These features evidently inherit the protolith fabric, as already pointed out by Codeço et al. (2017). Owing to the predominance of metashale facies in the local Beira schists package, most of the tourmalinized wallrocks contain more than 50 vol.% tourmaline. Tourmaline is always associated with quartz, and with muscovite in the most pelitic protoliths, where the mica may still underline the schistosity. Together with abundant rutile (see below), frequent zircon, F-apatite and sporadic monazite or xenotime crystals, usually no more than 10-20 μm , often only a few μm in size, are scattered throughout the wall rock. Aggregates of micrometre-scale crystals including zircon and xenotime or zircon and monazite are not exceptional.

In addition to these ubiquitous companions of the tourmaline, a number of other hydrothermal minerals are in place involved in the alteration of the Panasqueira wallrocks, defining specific alteration styles, and including quartz (silicification), topaz (up to topazification), muscovite (up to muscovitization), sulfides (pyrrhotite, sphalerite, chalcopyrite, arsenopyrite), apatite and siderite.

Tourmaline textures

Tourmaline habit and zoning: The tourmaline habit may be either acicular, with length between 500 μm and 1 mm as an average, for diameters no more than 20-50 μm , or, more commonly, more or less stocky prismatic, with length between 50 and 150 μm , for diameters of 10-20 μm (Fig. 1.6-A, B). The prisms are essentially sub-parallel, evidently mimicking the schistosity of the Beira schists (Fig. 1.6-A), but they may be perpendicular, displaying basal prism sections, whereas oblique sections appear to be less common. As recognized previously the contact metamorphic spots are obliterated by tourmaline (Bloot and de Wolf, 1953).

Tourmaline crystals are of brown color in thin section, with a faint color zoning (Fig. 1.5-B), but display in SEM imaging (Fig.1.5-C and 1.6-C,D) a well characterized growth zoning expressed as nearly homogenous zones of variable grey intensity, with rather sharp boundaries. A dark core is commonly present, although not systematically, with usually irregular shapes. Careful examination of the SEM imaging was unable to find evidence for sector zoning. Thus, these cores are best interpreted as relicts of a pristine state of the tourmaline, and are labelled Tur0 in the following. The main body of the tourmaline prisms consist in a medium grey zone, labelled Tur1a, with a clearer rim, labelled Tur1b, showing in rare instances an outermost rim characterized by the recurrence of a darker hue. Some changes in the relative proportions of the different zones may be observed in relation to the distance to the vein boundary. Far from the vein, there is a tendency to see more Tur0 zones, which are on average larger, and sometimes may display regular (prismatic) shapes, and the development of Tur1b rims is

concomitantly less pronounced, the Tur1b rim being in some cases absent in the more distal parts. To the contrary, closer to the vein, there is sometimes a tendency to a greater development of the Tur1b zone, whereas the Tur0 cores are less common, seem corroded, and tend to represent only a comparatively smaller proportion of the crystal volume. On the basis of a limited number of examples, it would appear that this tendency is roughly correlated with the presence of abundant wolframite in the nearby vein. This is corroborated by another set of limited observations, concerning the wallrocks of barren quartz veins, either at the outcrop or in the deeper levels of the mine (L3), where the Tur1b rim is usually absent.

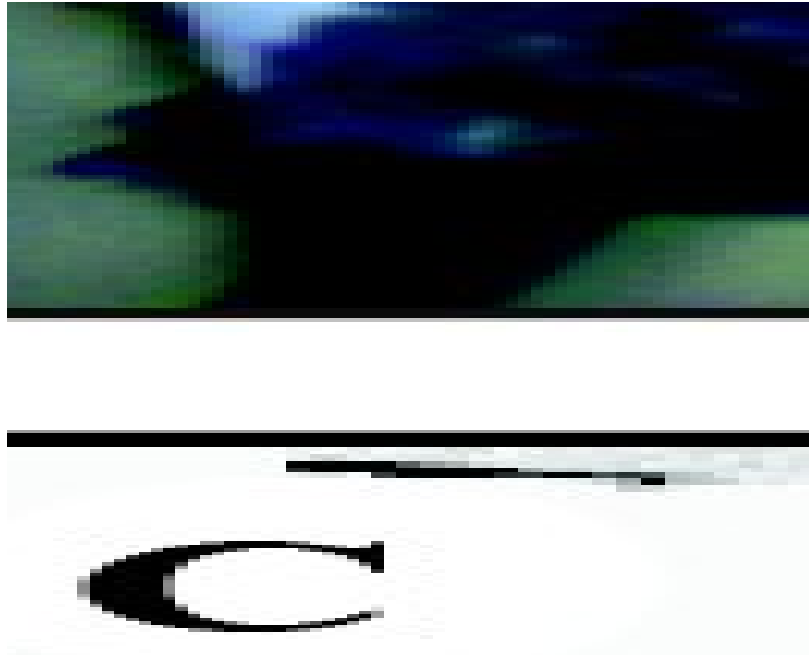


Figure 1.5. A. Typical tourmalinized wall-rock, with Qcs quartz veinlets. S_n regional schistosity. Note the numerous overprinting arsenopyrite (Apy) crystals. Sample PAN-III-8-c1 (NL). B. Poorly zoned tourmaline 1 seen in natural light. Sample PAN-II-8. C. Typical zoning of tourmaline 1(BSE), showing the three Tur0, Tur1a and Tur1b zones. Sample PAN-I-3-1.

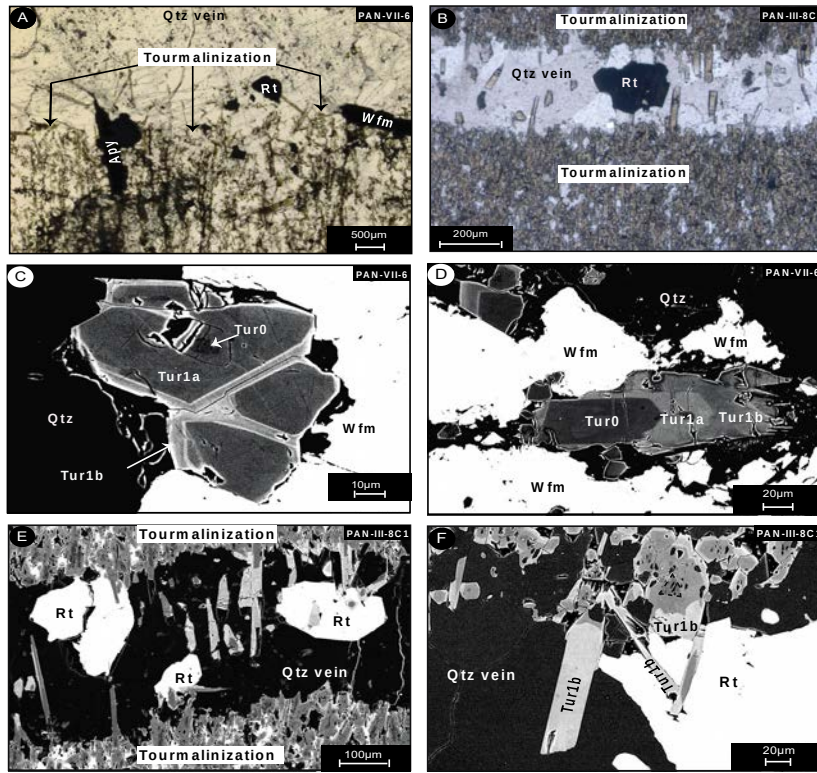


Figure 1.6. A. Typical early assemblage in the tourmalinized wall-rock, with Tur1 elongated along (erased) schistosity and disseminated rutile. Sample PAN-III-8-c1 (SEM). B. Acicular tourmaline in a silicified wall-rock. Sample PAN-VII-6-b1 (NL). C-D. Evidence for coeval growth of Tur1b and early wolframite: C. Wolframite growth inhibited the development of Tur1b zones; D. Wolframite growth was progressively inhibiting first Tur1a, then Tur1b growth. Sample PAN-VII-6-b1 (SEM). E-F. Evidence for coeval growth of Tur1b and the W-rich rutile in a Qcs veinlet. Sample PAN-III-8-c1 (SEM).

Micro-inclusions are common in tourmaline, although not systematic. By order of importance, they are: zircon, rutile, quartz, and rare monazite, pyrite, and apatite. Most often, inclusions “overprint” the zone boundaries, and in most occurrences, the amount of inclusions is basically the same in Tur1a or Tur1b zones, the Tur0 cores being usually poorer, excepted for quartz. Zircon may be zoned, with varying U-Th contents (SEM-EDS characterization). In addition, microanalysis reveals the likely presence of concealed microinclusions (see below).

Tourmaline and Qcs quartz veinlets: Tourmaline prisms are systematically present at the walls of the Qcs veinlets, displaying both Tur1a and Tur1b zones, the latter usually developed to a far higher extent than in the

wallrocks (Fig. 1.6-E, F). Thus, as already pointed out by Foxford et al. (1991), the development of both the main Tur1a tourmaline prisms and the Tur1b rims are coeval with the first increments of vein opening testified by the Qcs veinlets. This is schematically pictured in Fig. 1.7. Yet, even if Tur1a evidently corresponds to the main step of the tourmalinization process, the existence of Tur0, which is typically absent from the Qcs veinlets, demonstrates that the initialization of the tourmalinization process was indeed earlier than these veinlets (stage A in Fig. 1.7).

Tourmaline and other alteration minerals: Whatever the nature and the number of hydrothermal minerals in the wallrocks, the tourmaline crystals invariably display the same pattern of Tur0-Tur1a,b sequential crystallization and appear to be the earliest mineral. For instance, in correlation with topaz and/or muscovite development, appearance of distinct overgrowth onto Tur1b rims may be locally observed. In the same way, when apatite-bearing vugs are created in the wallrocks, incorporating undissolved tourmaline crystals retaining their pristine zonation, distinct overgrowth may also be observed. As sulphides (chalcopyrite, sphalerite, pyrrhotite) and siderite are mainly present as stringers in the wallrocks, it is easy to recognize that these stringers overprint tourmaline prisms and their characteristic zoning.

Small euhedral arsenopyrite crystals, a few 100 μm in size, are frequently found scattered in the wallrocks (Fig. 1.6-A), sometimes (but not commonly) including zoned tourmaline prisms. They have been considered “clearly coeval with early tourmaline” by Codeço et al. (2017). Several features are however in conflict with this assertion. First, arsenopyrite most often overprints tourmaline prisms, rather than incorporating them. Second, arsenopyrite may be seen overprinting Qcs veinlets (Fig. 1.6-A). Third, in 3-D, arsenopyrite is commonly observed to abound along thin joints, otherwise “dry”, that parallel the wallrock schistosity. These observations converge to prove that arsenopyrite grew after the Tur0-Tur1a,b sequence.

Tourmaline and wolframite: Wolframite from the mineralized veins is not, as a rule, associated with tourmaline but develops as large crystals along the wall of the open fractures. There are rare occurrences of development of wolframite crystals in the wallrock, close to the mineralized veins (Fig. 1.6-B). These crystals include zoned tourmaline, and detailed observations show that wolframite growth was coeval with Tur1b rim development (Fig.1.6-C, D). This wolframite is in turn reworked in relation with the main opening and deposition of the main wolframite (stages E and F in Fig. 1.7).

Figure 1.7. Synthesis of the stage Ia tourmalinization. A. Initialization of alteration (Tur0) in relation with simple “dry” joints. B. Main tourmaline development (Tur1a) and first increments of opening in Qcs veinlets. C. Growth of Tur1b tourmaline in relation with new increments of Qcs opening and coeval rutile growth. D. Localized variant with early wolframite growing in the wall-rock coevally with Tur1b. E. Transition to the main wolframite deposition stage.

Rutile textures

Rutile is systematically associated with tourmaline, being present both in the wallrocks, as small (less to 10 μm up to 80-100 μm) crystals, scattered or densely disseminated, or as large (up to 500 μm or more) isolated crystals in the Qcs veinlets, where they are clearly coeval with Tur1b growth (Fig. 1.6-E, F). Micro- to nano-inclusions (from about 1 μm , down to less than 100 nm) of wolframite are not rare. They are usually located at crystallographic boundaries (e.g., faces intersections, twin planes, quartz inclusion boundary) showing that they are coeval with the hosting rutile (Fig. 1.8-A-F). Their compositions, estimated from SEM-EDS measurement, are ferberitic, with Fe/Fe+Mn ratios between 0.67 and 0.83.

In the barren wall-rocks at the surface or underground at the deeper L3 level, rutile crystals are less abundant and are characterized by the presence of inclusions of ilmenite lamellae (Fig. 1.8-F).

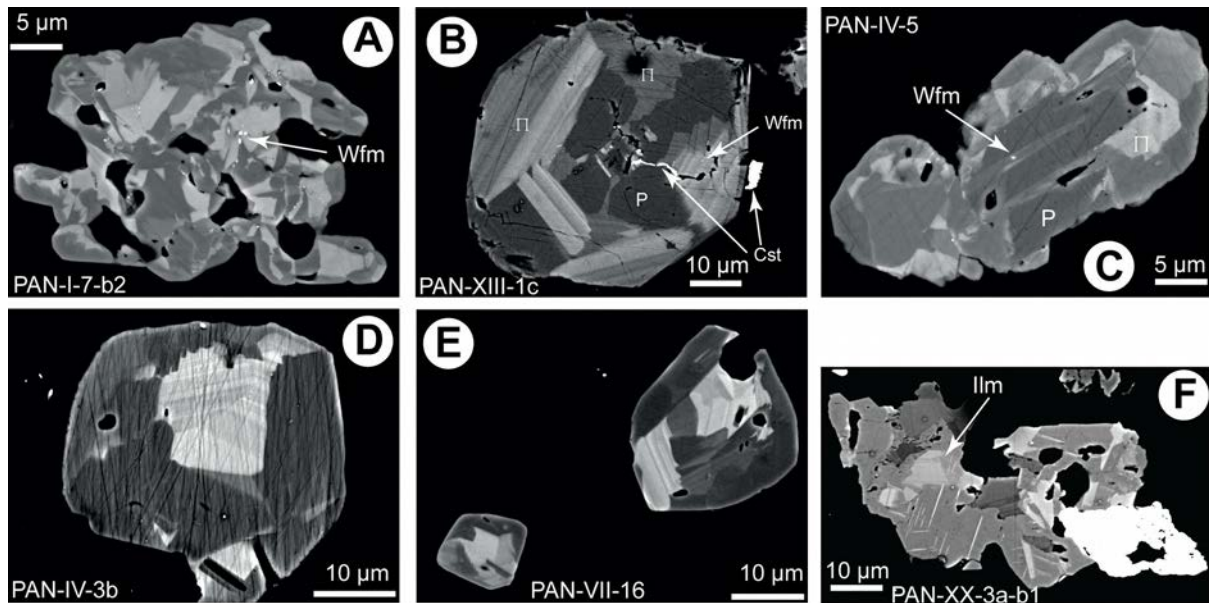


Figure 1.8. Back-scattered SEM images of Panasqueira rutile. **A, B and C.** Crystal aggregate from the wall-rock of a wolframite-bearing vein. Note the primary wolframite nano-inclusions (Wfm). **D and E.** Asymmetric crystal from a Qcs vein in the wall-rock of a wolframite-bearing vein. Note the superimposition of sector zoning (SZ) to the compositional (oscillatory) zoning. **F.** Crystal from the wallrock of a barren vein from the deep L3 level. Note the ilmenite lamellae (Ilm) and the late apatite (Ap), overprinting the rutile crystal.

Tourmaline chemical composition

Major element crystal chemistry: For reasons made explicit in Appendix A0, most analyses were performed using SEM-EDS. A total of 86 crystals from 19 representative samples were analyzed (Appendix A3: Table A3). As a first result, no systematic variation in the zone compositions is perceptible, neither in relation to the distance to the vein boundary, nor between tourmaline from different settings (wallrock, Qcs veinlet, inclusions in early wolframite).

The structural formulae were calculated using normalization to 26.5 (O, OH, F), which (with the assumption of boron stoichiometry) allows us to take into consideration the fluorine content and does not presume the filling of the Y site, which may contain Li, and is otherwise known to possibly contain a vacancy (Bosi, 2018).

The generalized structural formula of the tourmaline super-group is $XY_3Z_6(T_6O_{18})(BO_3)_3V_3W$ (Bosi, 2018). The T site is primarily occupied by Si, which may be replaced by minor Ti, Al or B. In the nine-coordinated site X enter Na^+ , Ca^{2+} , or minor K^+ , but vacancies (X^{\ominus}) may be present, defining the main chemical groups of tourmaline: alkali, calcic and alkali-deficient groups (Henry et al. 2011). The site V, or (O)3, is mainly occupied by OH (with possibly O) while the site W, or (O)1, is occupied by OH, F or O, defining the hydroxy, fluor, and oxy groups, according to the dominant anion in the site. The six-coordinated Z site is mainly occupied by trivalent cations (essentially, Al^{3+} , but also Fe^{3+} , Cr^{3+}), but may contain divalent cations (mainly Mg), (Bosi, 2018). The six-coordinated Y site is occupied by mono- (Li^+), bi- (Mg^{2+} , Fe^{2+} , Mn^{2+}) and tri-valent (mainly Al^{3+} , and possibly Fe^{3+} , Cr^{3+}) cations, but vacancies (Y^{\ominus}) may also be present (Bosi, 2018). Following the criteria of Henry and Dutrow (2011), the obtained tourmaline formulae must be rejected if either $Si > 6.15$ atoms per formula unit (apfu), or the sum of the $Y + Z + T$ cations > 15.5 apfu, or the sum of the X-site cations exceeds 1.1 apfu. These criteria are met by Panasqueira tourmaline, except for Si apfu, which may be in excess of 6.15 in some analyses. For reasons given in Appendix A0, all analyses yielding Si apfu > 6.12 were rejected. Using the empirical formula given by Bosi (2018) to estimate the ZAl apfu content in the Z site, it is found that in Panasqueira tourmaline ZAl is rather constant, around 5.23 apfu, whatever the zone, and that, whereas there is sufficient Mg to fill the site in Tur0 and Tur1a, a small complementary content of ZFe is necessary in Tur1b (Table A3, Appendix A3).

In the classification diagram opposing the normalized X-vacancy to the Mg# ($Mg/(Mg+Fe)$) ratio (Henry et al., 2011), the Panasqueira tourmalines appear to be mainly schorl, with however a clear systematic shift from Mg-rich (ferro-dravite) to Fe-rich compositions in the Tur0 to Tur1a to Tur1b sequence, and a neat tendency towards foitite compositions (Fig. 1.9-A). Indeed, as shown in Fig. 1.9-B, the X-site vacancy is comprised between ~ 0.2 and ~ 0.6 pfu (and thus, the Panasqueira tourmalines trend toward alkali-deficient species) corresponding to the operation of the $Al_{+1}\Delta_{+1}Na_{-1}R^{2+}_{-1}$ vector, leading to the solid solution between schorl-dravite and foitite-Mg-foitite. Consideration of Fig. 1.9-C, E and G shows that other vectors are acting to deviate the observed trends from the preceding one. Of particular importance seems to be the $Al_{+1}O_{+1}(OH)_{-1}(Mg, Fe)_{-1}$ vector, implying an oxy-schorl (or oxy-dravite)

component, but the intervention of another exchange vector ${}^Y_{+1}\text{Al}_2\text{R}^{2+}_{-3}$, responsible for an Y-site vacancy (Bosi, 2011), seems to be equally real. In fact, an Y-site vacancy is observed in our analyses of the Panasqueira tourmaline, often larger than 0.1 apfu, as well as in the works of Codeço et al. (2017) and Launay et al. (2018) (Table 3, Appendix 3). It cannot be due to overlooked Li, because the LA-ICP-MS results (see below) show that the Li content is negligible, being at most of ~330 ppm and averaging ~170 ppm (Tur1a) or ~290 ppm (Tur 1b): this would be reflected by Li contents in the structural formulae of no more than 0.05 apfu, more often in the 0.02-0.04 apfu range.

Contrary to Tur0, which appears to be essentially free of fluorine, there is a distinct fluorine enrichment (up to ~1% F) in Tur1a and Tur1b, without any clear difference between 1a and 1b zones, and there is a clear trend of increasing F apfu with X-site charge (Fig.1.9-D), i.e., with the X-site Na content, most of the Panasqueira tourmaline being practically devoid of Ca, to the exception of Tur0 (which, in turn, explains the higher X-site charge of Tur0 in Fig. 1.9-D).

The complex covariations between aluminium, iron and magnesium that are depicted in Fig. 1.9 are conveniently summarized in the AFM diagram of Figure 1.10, in which it is also possible to illustrate the most common compositional paths from Tur0 to Tur1a and then Tur1b at the crystal scale (Fig. 1.10-B). This figure illustrates an apparently continuous variation of the Fe to Fe+Mg ratio (Fe#) from Tur0 to Tur1b. Yet, realization of detailed profiles along tourmaline crystal axis demonstrates the existence of small scale modulations of the Fe# during crystal growth (Fig. 1.11).

Trace element contents: As LA-ICP-MS measurement implies laser pits with a diameter of at least 24 μm to reach the desired detection limits, and owing to the small size of the Tur1 crystal zones, analysis was only possible on the largest representatives, and in a limited number of samples. What is worse, tourmaline core (Tur0) dimensions were too small to be properly investigated, so attention was restricted to the two external rims, Tur1a and Tur1b. A total of 77 spots, in 47 crystals from 7 samples could be measured for a set of trace elements. REE were also investigated but to get significant signal, a laser beam of 120 μm in diameter was necessary, and therefore only two crystals, from two samples, could be measured. This implied acquisition of only an average composition of Tur1a and Tur1b zones, in equal proportion of both zones however. Results are summarized in Table 1 and given in Appendix A4 (Table A4).

Trace element analyses of the early tourmaline from Panasqueira

	Tur1a (n=29)				Tur1b (n=43)			
	min	max	average	2σ	min	max	average	2σ
Li	22	156	76	4	45	330	130	6
Be	1	21	7	2	0.3	25	7	2
Sc	7	47	20	1	7	31	13	1
Ti	1039	10110	2425	177	849	9300	2184	149
V	104	613	354	11	11	742	301	12
Cr	16	1027	272	18	9	601	176	13
Mn	135	528	418	14	310	2600	543	42
Co	0.2	24	3	0.4	0.1	3	1	0.2
Ni	3	56	17	3	1	21	6	2
Cu	0.6	29	3	1	0.4	23	1	1
Zn	237	756	611	27	161	925	645	27
Sr	13	285	91	4	7	131	44	2
Y	0.2	7	1	0.4	0.1	5	0.4	0.2
Nb	0.1	12	1	1	0.1	52	2	0.4
Ta	0.1	2	0.1	0.1	0.1	7	0.2	0.0
Ta+Nb	0.1	14	1	1	0.1	59	2	0.4
Sn	4	54	24	4	4	157	25	4
W	0.3	52	8	3	0.4	245	11	2
ΣPb	3	232	22	3	1	85	6	2

Table 1. Summary of LA-ICP-MS trace element analyses for the Panasqueira tourmalines. For the purpose of average calculations, the bdl (below detection level) in Table A4 were taken at half the detection level values (i.e., the without bias best estimates) when needed. As a result, the averages for Nb (0.2 ppm) and Ta (0.2 ppm) are not provided in the table.

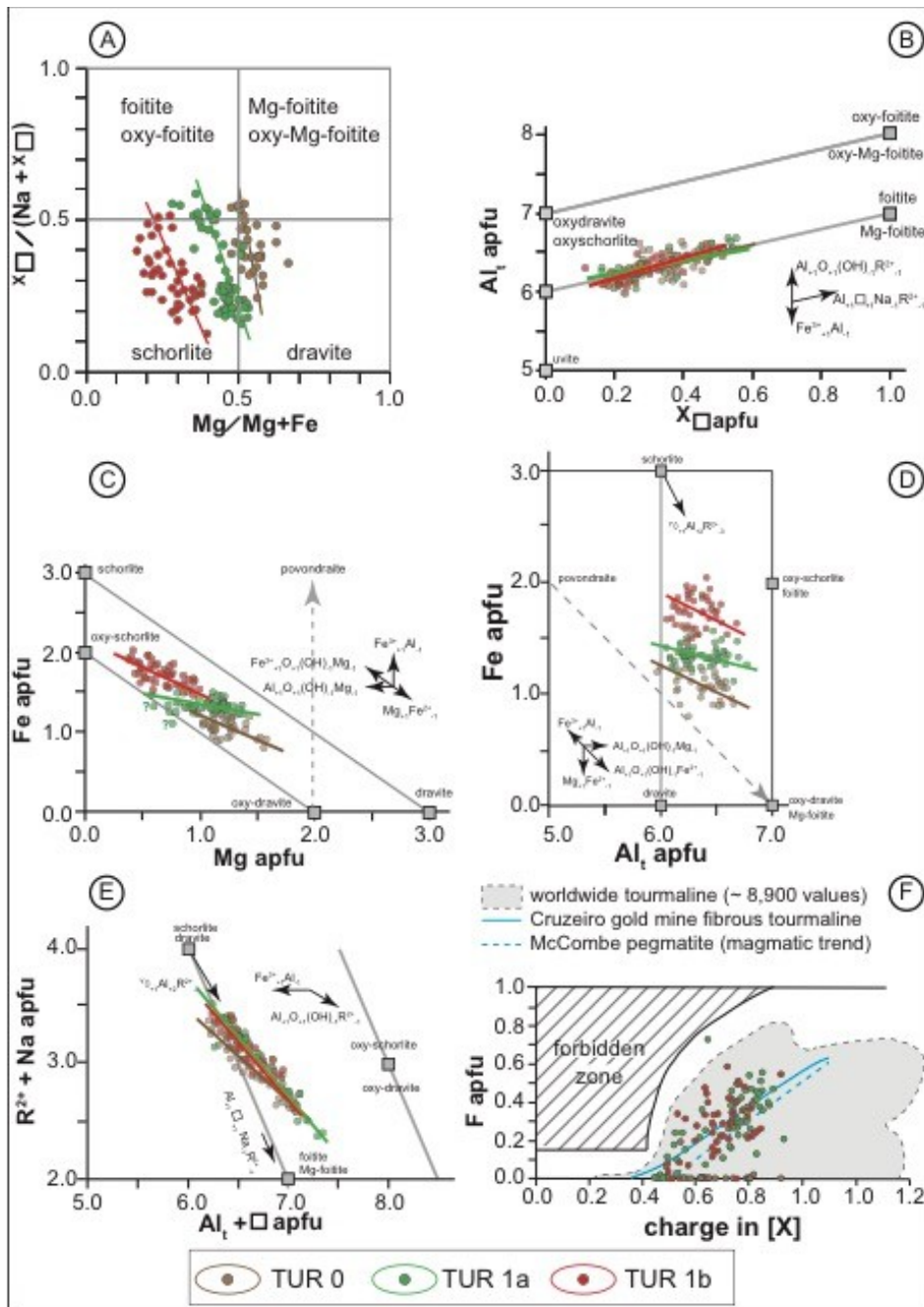


Figure 1.9: Crystal chemistry of the Panasqueira tourmaline, illustrating the characteristics of the three Tur0, Tur1a and Tur1b zones. Note in all the diagrams the continuity of composition variations between the three zones. A. Classification diagram. B. Al vs. X-site vacancy diagram, demonstrating the presence of a foitite component. C. Fe vs. Mg diagram, illustrating the presence of an oxy-schorl component, together with the classical schorl-dravite exchange vector. D. Fe vs. Al diagram, showing the combination of all exchange vectors involved in the Panasqueira tourmaline. E. Na + R²⁺ vs. Al+X-site vacancy diagram, illustrating the deviation from the schorl (dravite)-foitite (Mg-foitite) exchange line due to a combination of the oxy-schorl (dravite) exchange vector and a vector responsible for the creation of Y-site. F. Linear relationships between F and the X-site charge; forbidden zone and references are from Henry and Dutrow (2011): grey domain, worldwide tourmaline (~ 8,900 values); light blue line: Cruzeiro gold mine fibrous tourmaline; dashed blue line: McCombe pegmatite tourmaline (magmatic trend).

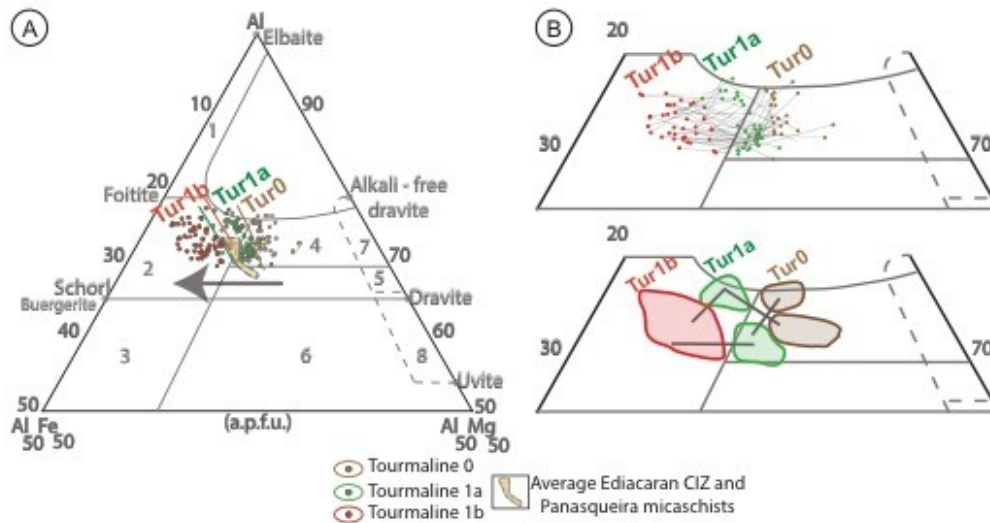


Figure 1.10: A. AFM diagram for the Panasqueira tourmaline, with location of the main tourmaline end-members. (1)-(8) reference fields from Henry and Guidotti (1985): (1) Li-rich granitoids, (2) Li-poor granitoids, (3) Fe³⁺-rich quartz-tourmaline rocks (hydrothermally altered granites), (4) Al-buffered metapelites, (5) not Al-buffered metapelites, (6) Fe³⁺-rich quartz-tourmaline rocks, calc-silicate rocks, and metapelites, (7) low-Ca meta-ultramafics and Cr,V-rich metasediments, and (8) metacarbonates and meta-pyroxenites. Compositions of CIZ schists from Oosterom et al. (1984) and De Amorin (2017). The grey arrow emphasizes the global increase in Fe/Fe+Mg ratio from Tur0 to Tur1b. B. Enlargement of A, illustrating the sequence Tur0-Tur1a-Tur1b: (a) individual paths, (b) synthesis. Note that, if there is always a jump from a zone to another, the starting and final compositions differ for each individual crystal.

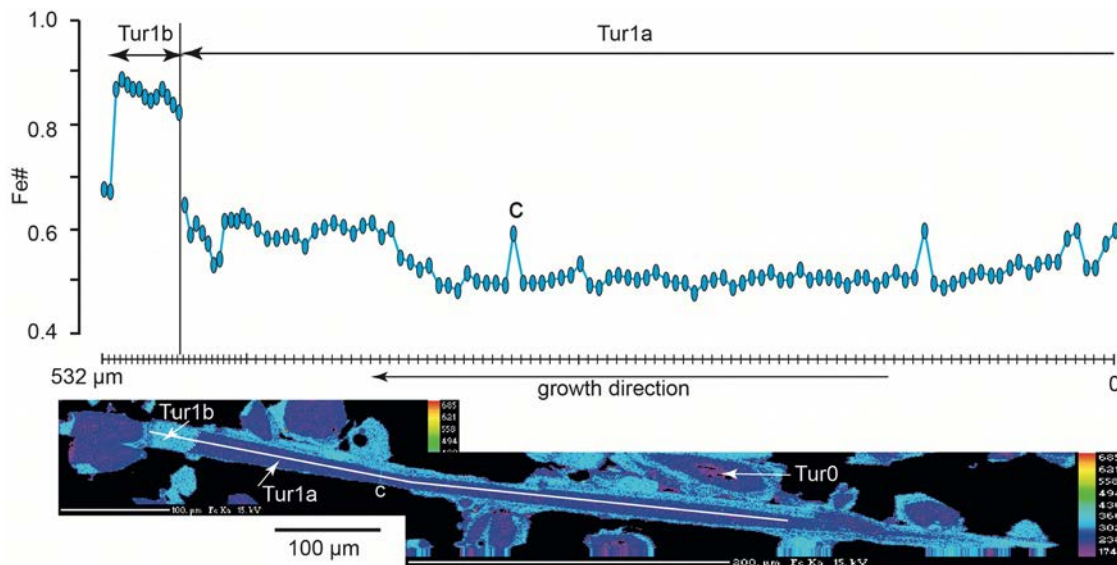


Figure 1.11: Profile of the Fe# ratio (Fe/Fe+Mg) along an acicular prism of tourmaline 1 (EPMA analyses), compared to the false color X-image of the same crystal (sample PAN-VII-6-b2). The major axis of the elliptical symbol corresponds to the estimated error on Fe#. Of the three zones (Tur0, Tur1a, Tur1b) seen on the X-image, only the two latter are documented in the profile. At the rim of Tur1b zone, a recurrence of low Fe# is observed. Note the second and third order modulations of the Fe# ratio along the profile. c: microcrack filled by Tur1b.

For some elements, several LA-ICP-MS spectra display anomalous peaks (anomalous values in Table A4), readily interpreted as recording the presence of concealed micro- to nano-inclusions. A Mn outlier at 2,600 ppm is likely due to siderite, and a Zn outlier at 8,500 ppm is interpreted as due to sphalerite. Several W anomalies record the presence of several W-bearing minerals: W-bearing rutile, when correlated with both Ti and Nb-Ta-Sn

anomalies; cuprotungstite, when correlated with a Cu anomaly (a rare occurrence); and wolframite, when no correlation is observed with neither Ti nor Cu. Most of these W anomalies are found in the Tur1b zones.

The results are presented in Figure 1.12 (trace elements excepting REE, and to the exclusion of the anomalies) and Figure 11 (REE patterns). As seen in Figure 9, titanium, between 530 and 4,360 ppm, together with zinc, between 160 and 930 ppm, and Mn, between 135 and 600 ppm, are the most abundant, followed by lithium (between 40 and 330 ppm), vanadium (between 10 and 740 ppm) and chromium (between 10 and 1,000 ppm). Strontium, between 7 and 285 ppm, and tin, between 4 and 160 ppm, are the following by abundance order. Then come scandium (between 5 and 30 ppm), beryllium (between 3 and 20 ppm), and lead, between 1 and 18 ppm. Other elements are often below detection level (bdl); such as: nickel (up to 56 ppm), cobalt (up to 13 ppm) and yttrium (up to 7 ppm). Most measured tungsten values are between 0.4 and 30 ppm, but for ~25 % of the spots in Tur1a and 50 % in Tur1b, W was found below the detection level of 0.4 ppm. The measured values for niobium are between 0.1 and 3.2 ppm, but for ~75% of the spots are below the detection level of 0.3 ppm; and whereas the few measured Ta values are between 0.3 and 1.6 ppm, the overwhelming majority of the spots were found to be lower than the detection level of 0.3 ppm. From the limited REE data, Σ REE is low (between 1.2 and 12 ppm), and the REE patterns are characterized by high La_N to Yb_N ratios of 6.37 to 6.77, and slightly negative Eu_N/Eu^*_N anomalies (0.65 to 0.83) (Fig. 1.13).

As seen in Fig. 1.12, Tur1a and Tur1b compositions are quite similar at the first order of observation, there are nevertheless minor but significant differences, most of the trace elements appearing depleted in Tur1b relatively to Tur1a, to the notable exception of Li, Mn and Zn (Fig. 1.12).

A principal component analysis was performed on the trace element data (using the JM Pro software), and the results are presented in Figure 1.14. Four axes (PC1-4) explain 61.6 % of the variance. The first axis (PC1) clearly opposes Tur 1a and 1b, as well as two groups of elements: a group A (Li-Mn-Zn) and a group B (nearly all other elements) reproducing as expected the opposition already observed in Figure 10. The PC2, PC3 and PC4 axes variously display correlations within the group B, evidencing several subgroups, namely: Co-Ni-Sr-Y-Sn, Cr-V-Sc, Nb-Ta and Pb-Be. Cu, Ti, and W behave independently, and W appears uncorrelated to Nb-Ta.

In binary plots, elements of the group A display rough linear trends expressing positive correlations (when excluding outliers), as seen for instance in Figures 1.15-A to C, as expected from the principal component analysis. In the same way, elements of the group A display negative correlations with elements of the group B, as seen for instance in Figures 1.15-D to H. Less expected is the existence of linear relationships between elements from the various B subgroups, as seen for instance in Figures 13-I to K. The rare metals (W, Nb, Ta) behave differently. Whereas Nb-Ta are very loosely negatively correlated with Li (Fig.1.15-L), there is no correlation at all between W and Li (Fig. 1.15-M), nor between W and Nb-Ta (Fig. 1.15-N). Finally, Sn is not correlated, neither with Nb-Ta (Fig. 1.15-O) nor with W (Fig. 1.15-P).

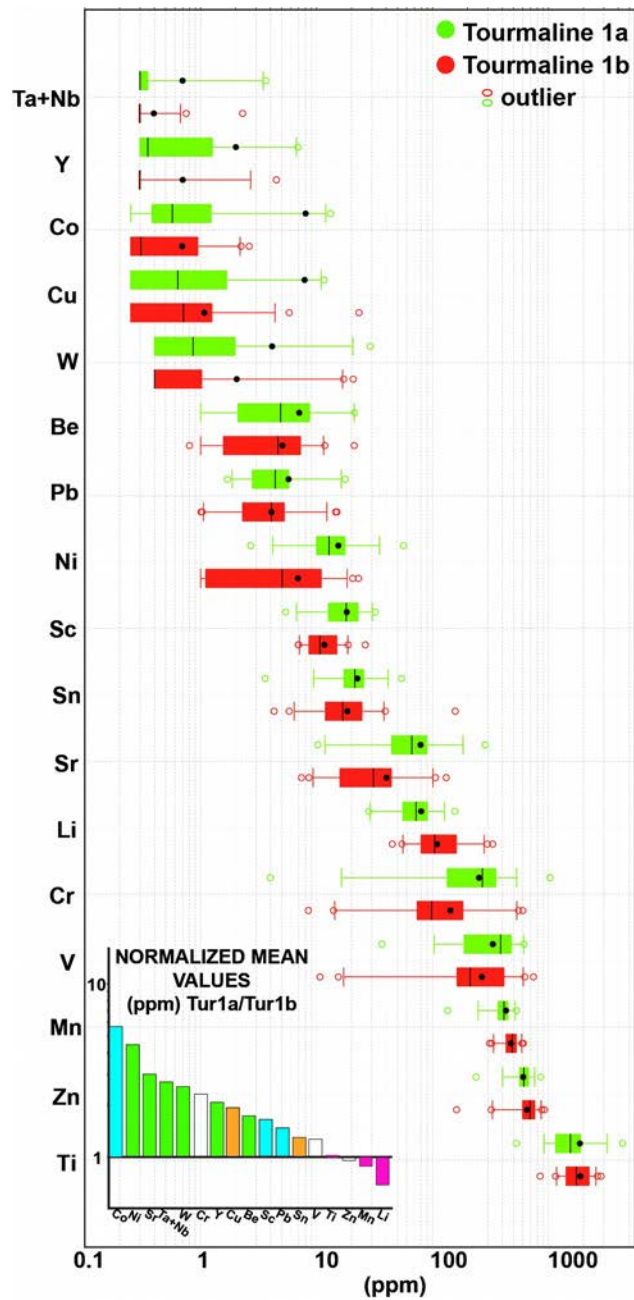


Figure 1.12: Box plots of LA-ICP-MS results for tourmaline 1a and 1b. The box represents the lower quartile to upper quartile interval. The whiskers represent the 5%-95% interval. Black circle: average value, black vertical line: median value. Open circle: outlier value, comprised in the 5% lowest or highest data. Inset: normalization of average values of Tur1a to the Tur1b reference.

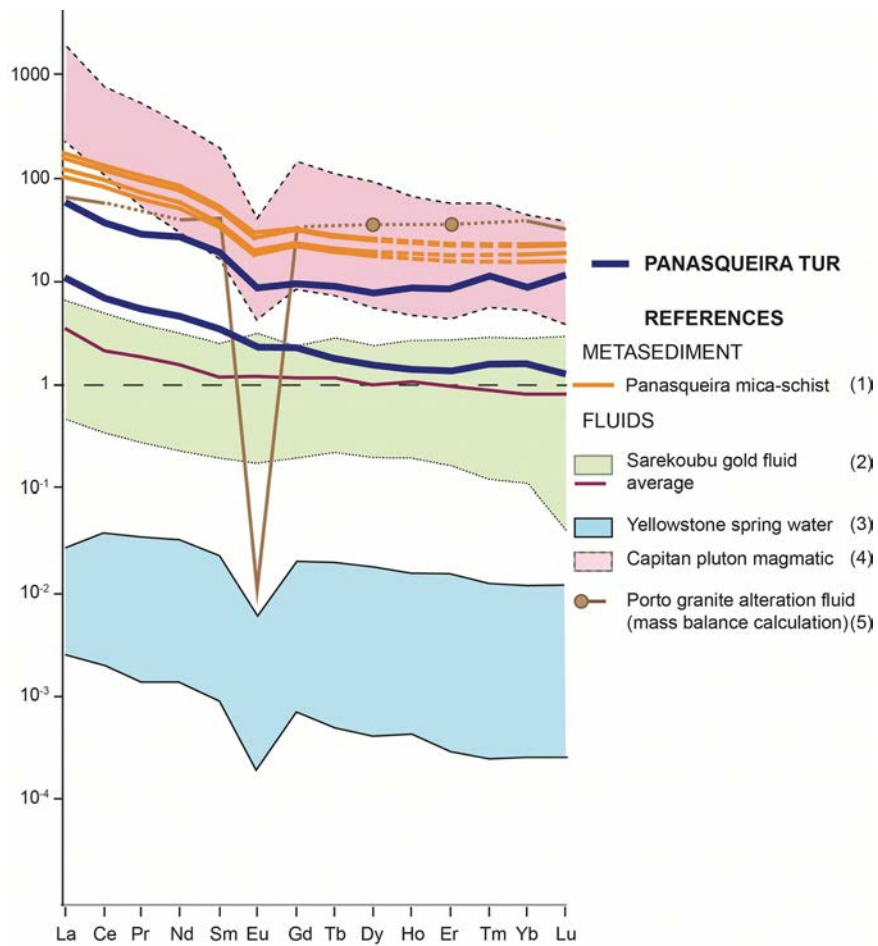


Figure 1.13: Two REE patterns from Panasqueira tourmaline (samples PAN-I-3-c2 and PAN-III-8-c1). They are compared to the patterns of the Panasqueira metasediments (1: De Amorin, 2017), the fluids associated to the Sarekoubu orogenic gold deposit (2: Xu et al., 2008), the Yellowstone spring water (3: Lewis et al., 1997) and to magmatic-derived fluids (4: Banks et al., 1994; 5: Poitrasson et al., 1995) (explanations in the text).

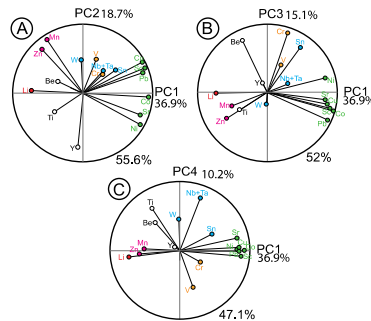


Figure 1.14: PCA analysis of the trace element composition in Panasqueira tourmaline, allowing the definition of several groups of trace elements, namely: Mn-Zn-Li, Cr-V-Sc, Co-Ni-Sr-Y-Sn, Be-Pb, and Nb-Ta (explanations in the text).

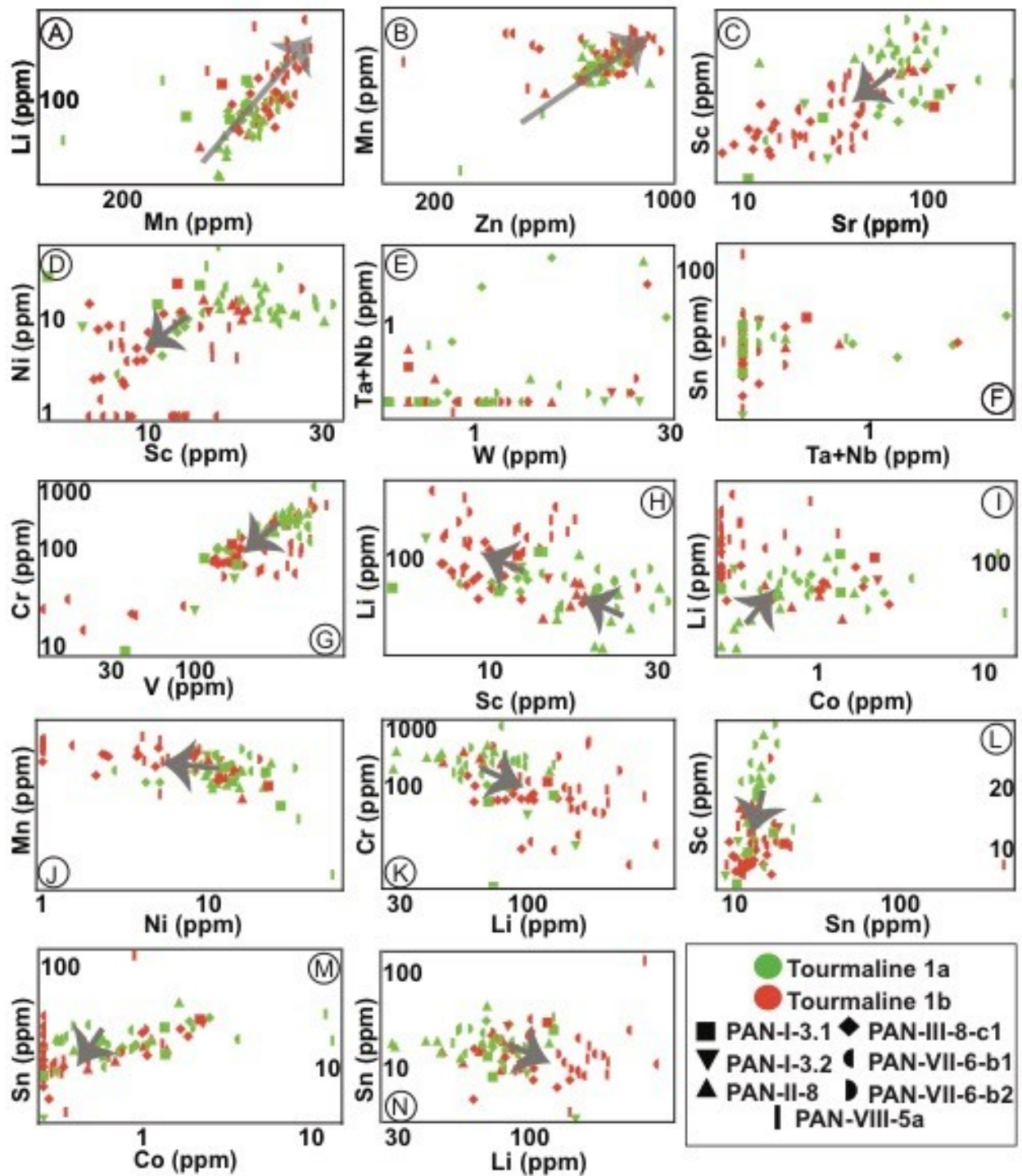


Figure 1.15: Binary plots of selected trace elements from Panasqueira tourmaline, showing contrasting behaviour, including positive, negative and null correlations, depending on the elements (explanation in the text).

Rutile chemical composition:

Panasqueira rutile composition and zoning are described in great detail in Carocci et al. (2019) and only a summary is given here. The Panasqueira rutile systematically contains Fe, V, Sn, Nb, Ta and W, all with highly variable contents, in part because of sector zoning effects: Fe from 0.18 to 2.95 wt%, V from <1000 ppm to 3.48 wt%, Cr from <1000 ppm to 2.41 wt%, Nb from <1000 ppm to 1.64 wt%, Ta from <1000 ppm to 2.17 wt%, and W from 0.20 to 10.7 wt%. Despite the highest reported values, Nb and Ta are usually poorly concentrated, and Nb+Ta is usually lower than 0.5 wt% and the Nb/Nb+Ta ratio varies from 0.05 to 0.97, being in average 0.6.

The crystals display a marked sector zoning, exhibited mostly by W and Fe and, although to a lesser extent, by Nb and Ta, whereas Sn, V (and Cr) are less systematically affected (Fig. 1.8- C to G). Depending on the samples, the maximum W concentration is found to be of 1.12 to 10.7 wt% in the metal-rich sectors, contrasting with 0.26 to 1.40 wt% in the metal-poor sectors.

From a limited number of observations, it would appear that the W enrichment in rutile is somehow correlated to the wolframite endowment in the nearby veins. On the one hand, there is a tendency to a greater development of metal-rich sectors, reaching the highest W contents, in proximal wallrocks when wolframite is significantly present in the adjacent vein. On the other hand, in barren wallrocks, the metal-rich sectors are less endowed in W (no more than 3.5 wt% W).

Sector zoning is superimposed to a conspicuous compositional zoning, expressed from the crystal scale down to the 10 μm to μm scale of the doublets characteristic of oscillatory zoning (Fig. 1.8-C). Excepted for the crystal size, zoning characteristics are qualitatively and quantitatively the same whatever the rutile setting.

All the minor elements, W, Nb(Ta), Fe, V, Cr and Sn, are involved in the compositional zoning. At all scales, W and Nb(Ta) are anti-correlated, whereas tin and vanadium are less variable, and display contradictory behavior, being either correlated with Nb(Ta) and anti-correlated to W or the contrary.

Intercomparison of rutile crystals from different settings, even at the sample scale, shows that there are no general correlations: crystals may exhibit evolution from a Nb-rich and W-poor core to a W-rich and Nb-poor rim, or the inverse, or show moderate variations around middle W contents, the latter seeming to be the commonest case

Dating

Dating the rutile: Results from the petrography study suggest that rutile from both the tourmalinized wallrocks and the Qcs veinlets were coeval with the early tourmaline and the earliest wolframite deposition. Therefore, finding an accurate date for the rutile crystallization is desirable. Unfortunately, the number of rutile crystals available for U-Pb dating is limited by the size of the laser spot (45 μm). Some large crystals from Qcs crack-seal

veins meet the required dimensions, but among the scattered crystals in the wallrocks, only very few exhibit size larger than 50 μm . Thus, only 22 crystals from 5 samples were eligible for U-Pb dating.

The analyzed crystals present various amounts of common lead, yielding low radiogenic compositions (Appendix 6, Table A6). In the Tera-Wasserburg diagram they plot in a discordant to very discordant position, except for one sample (PAN-III-8-c1), plotting close to the Concordia curve. Figure 14 provides three regression lines: i) using all the data, the regression line results in a discordia with a lower intercept at 302.7 ± 8.9 Ma (2 σ , MSWD = 5.3) (Fig. 1.16-A). This poorly constrained date is evidently due to the importance of lead losses. ii) a discordia where the data corresponding to the greater lead losses are ignored (Fig. 1.16-B), passing through the concordant data and yielding a lower intercept at 305.2 ± 5.7 Ma (2 σ , MSWD = 1.9). In that case, the upper intercept yields a common lead $^{207}\text{Pb}/^{206}\text{Pb}$ ratio of 0.906, slightly higher than the 0.855 value expected from the Stacey and Kramers (1975) model at the same age. iii) a discordia, anchored to the Stacey and Kramers composition at 305 Ma, which yields a lower intercept at 303.7 ± 6.6 Ma (2 σ , MSWD = 3.9) (Fig. 11.16-C).

Complementary dating: It was considered useful in the present work to check the $^{39}\text{Ar}/^{40}\text{Ar}$ age of 296.3 ± 0.6 Ma (1 σ) obtained by Snee et al. (1988) on muscovite selvages, which are deemed to have been coeval with the main wolframite deposition (OSS I sub-stage of Snee et al., 1988). A typical muscovite selvage (sample PAN-XIV-181-1) was dated by the $^{39}\text{Ar}/^{40}\text{Ar}$ method at the University of Manitoba (Canada) and yielded a good plateau age of 296 ± 2 (1 σ) Ma, which is indiscernible from the preceding age in the limits of error (Appendix A7-Table A7).

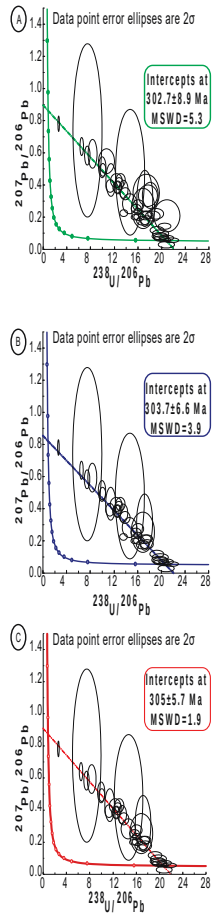


Figure 1.16: U-Pb dating of wall-rock Panasqueira rutile (Tera-Wasserburg Concordia diagrams). Note the highly discordant behaviour of the rutile. A. All data, showing the importance of lead loss in the considered rutile crystals. B. After elimination of the more affected by lead loss data. C. Idem, with constraining the data to consistency with the common lead value of Stacey and Kramers (1975) at c. 300 Ma. Explanations in the text.

Discussion

Age of the early hydrothermal stage

The best regression obtained on the Panasqueira rutile, at 305.2 ± 5.7 Ma with MSWD of 1.9 provides a common lead value ($^{207}\text{Pb}/^{206}\text{Pb}$ ratio = 0.906) slightly different from the Stacey and Kramers (1975) reference value at the same age ($^{207}\text{Pb}/^{206}\text{Pb}$ ratio = 0.855). Constraining the regression by the Stacey and Kramers (1975) common lead composition yields a similar date of 303.7 ± 6.6 Ma, with a slightly higher MSWD value of 3.9. One critical issue relies on the $^{207}\text{Pb}/^{206}\text{Pb}$ value of the common lead in the CIZ at c 305 Ma. At c. 320 Ma, the $^{207}\text{Pb}/^{206}\text{Pb}$ ratio of the Ediacaran and Tremadocian metasediments was between 0.885 and 0.96 (calculated from Nagler et al. 1993, 1995 data). It thus becomes evident that the 0.906 value for the common lead in the Panasqueira rutile is in accordance with the regional values, and, consequently, the date of 305.2 ± 5.7 Ma is interpreted as the best estimate for the crystallization age of the rutile.

The rutile is coeval with the early tourmalinization event and the appearance of the earliest wolframite, and therefore, the latter are of the same age. In addition, as Polya et al. (2000) demonstrated that this event (their QT stage) just preceded the main opening of the quartz vein system and wolframite deposition, it follows that this age of c. 305 Ma is also the maximum age of the main wolframite deposition at Panasqueira.

As seen in Figure 1.17, the obtained age is significantly older than the $^{39}\text{Ar}/^{40}\text{Ar}$ age derived from the Panasqueira selvage muscovite, which is constrained at c. 296 Ma (Snee et al., 1988; our new data). Until now, this age was considered to be the main mineralization age (OSS stage of Polya et al., 2000), under the assumption that this muscovite preceded wolframite deposition. The new results show however that the muscovite selvages are younger by at least 2 Ma.

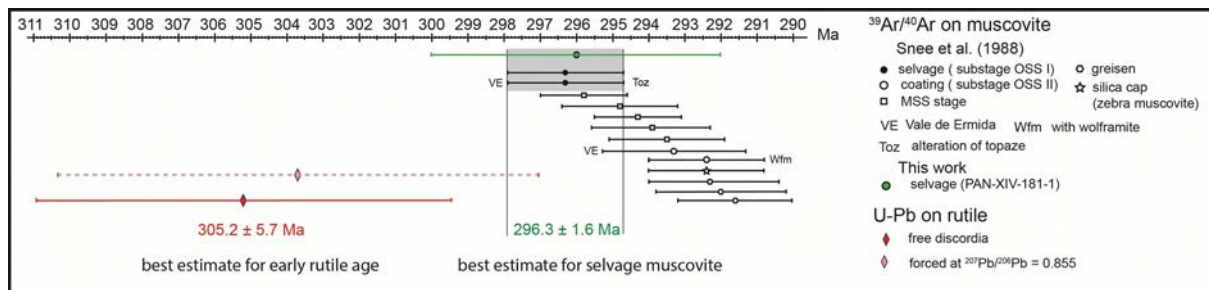


Figure 1.17: Synthesis of radiometric ages for the Panasqueira deposit, comparing results of the present work with Snee et al. (1988) data. Explanation in the text.

Tourmaline evidence for the involvement of two fluids

Owing to the lack of measurable fluid inclusions (FI) in the tourmalinized wallrocks, knowledge of the nature of the fluids responsible for the tourmalinization may be gained indirectly, using the tourmaline composition. On one hand, because the rates of diffusion of major and trace elements in tourmaline are negligible, this mineral may preserve initial composition through later hydrothermal events (e.g., Hawthorn and Dirlam, 2011). On the other hand, there is evidence that tourmaline has the ability to directly record the composition of the medium from which it crystallizes. Experiments at high pressure and temperature by Van Hinsberg (2011) tend to show that trace element partition coefficients between tourmaline and a borosilicate melt are systematically close to 1. The considered trace elements encompass those found in Panasqueira tourmaline, with the notable exception of W, Sn, Nb and Ta. The diversity of lattice sites in the tourmaline structure would render the mineral able to incorporate trace elements of widely different charge and radius (Van Hinsberg, 2011): if true, this would likely be transferable to the partitioning between trace elements and tourmaline in hydrothermal environments, as already proposed by von Goerne et al. (2001). Indeed, recent experimental work confirms that trace elements may enter the the tourmaline lattice without the control of crystallographic constraints (Vereshchagin et al., 2018). As for major elements, there is direct experimental evidence that the content in X-site elements (Na, Ca) is a good record of the fluid composition (von Goerne et al., 2001; Berryman et al., 2016). By contrast, fluorine is submitted to crystallographic constraints, F in the structural formula being broadly correlated with the X-charge in natural tourmalines (Henry and Dutrow, 2011). Within these constraints, however, the entrance of F in the tourmaline structure is nevertheless controlled by external factors, in particular the F availability.

Recent studies on the Panasqueira fluid system conclude that a single fluid was responsible for both the wall-rock alteration and the wolframite deposition (Codeço et al., 2017; Lecumberri-Sanchez et al., 2017; Launay et al., 2018). This fluid would have been of magmatic origin, would have brought the boron (Codeço et al., 2017) and its interaction with the wall-rock would have yielded the iron and manganese demanded by wolframite deposition (Lecumberri-Sanchez et al., 2017). However, the latter interpretation is based on data that appear to be open to interpretation. On the one hand, Lecumberri-Sanchez et al. (2017) consider that the muscovitized areas which commonly (but not systematically) fringe the mineralized quartz veins are coeval with the more external tourmalinized zone. We conclude that this is not the case because (1) muscovite is demonstrably later than the wolframite, as shown in a preceding section, and (2) the muscovitized fringe is synchronous with the muscovite selvages of the mineralized quartz veins, and the new ages obtained in this study ensure that it cannot be coeval with the earlier wall-rock tourmalinization. Thus, mass balance calculations based on the global composition of the altered rocks, as done by Lecumberri-Sanchez et al. (2017) is not informative. On the other hand, Lecumberri-Sanchez et al. (2017) use analyses of fluid inclusions (FI) deemed to be representative of the tungsten mineralizing fluid, to conclude that this fluid was deprived from iron and therefore that an external source of iron was needed.

Lecumberri-Sanchez et al. (2017) overlooked the fact that early FI recording wolframite deposition were all decrepitated and that easily measurable FI (such as those they studied) are later and trapped in relation with recrystallization, affecting the early quartz (Cathelineau et al., 2017, 2018).

Single fluid theory is difficult to reconcile with the data presented in our results section. Among these data, the regular increase in the Fe# from Tur0 to Tu1b, and the contrasting behavior of trace elements concentrated in either Tur1a or Tur1b (as seen in Fig. 1.12 and 1.15) are particularly significant. It is an established fact that the Fe# ratio may increase with decreasing temperature, and Codeço et al. (2017) explicitly use this property to conclude to the existence of a single fluid. However, their demonstration of a temperature decrease at Panasqueira relies on the FI data of Lecumberri-Sanchez et al. (2017; and of other workers, who all overlooked the early FI decrepitation). Based on the Ti-in-quartz thermometer, the median temperature estimates from Codeço et al. (2017) for tourmalinization is around c. 460°-480°C, which is very similar to the temperature of 450°±50°C estimated for the wolframite deposition stage by Cathelineau et al (2018). Thus, a strong temperature decrease at the end of the early tourmaline growth seems excluded, and therefore, the compositional zoning of the Panasqueira tourmaline could not have been controlled by temperature.

Explaining the Fe# increase by simply invoking fractional crystallization would imply permanent closed system conditions, but this is contradicted by the crack-seal behaviour of the Qcs veinlets associated with (and likely responsible for) the fluid influx into the wall-rocks. Also, fractional crystallization cannot explain the fluctuations in Al contents that occur concurrently with the variations in Fe# during the tourmaline crystallization (Fig. 1.10-B).

A process by which a single fluid would continuously evolve from low (wall-rock controlled: Tur0) toward high (fluid controlled: Tur1) water-rock ratios during its interaction with the wallrocks could be considered. This would be consistent with the absence of compositional differences between Tur1a and b zones whatever the tourmaline position in the system (contained in Qcs veinlets or making the tourmalinized wall-rock, close to or far from the veins boundaries), a fact pointing toward high water-rock ratios at the time of Tur1 growth, but not necessarily at the Tur0 time. If such a process was going on, it would be expected that the Tur0 composition would reflect the host-rock composition prior to the alteration. In this regard, major elements in the tourmaline could on one hand seem to give substance to the single fluid process, because it is likely that some constituents for tourmaline precipitation have been found locally. In particular, the calcium which is commonly encountered in Tur0 cores (average 0.26 wt% CaO, up to 0.8 wt%) may come from the altered rocks, and the fact that later Tur1a and mainly Tur1b zones are depleted in calcium may be explained by the total consumption of the low initial Ca content (≤ 0.4 wt% CaO: Bussink, 1984) in the protolith. In the same way, as neither biotite nor cordierite may no longer be seen in the tourmaline-bearing wallrocks, and tourmaline prisms are most frequently elongated in one and the same direction, evidently mimicking the schistosity, the main components of tourmaline may have been provided by the replaced ferro-magnesian minerals. Yet, the Fe# of Tur0 cores is distinct from the average

composition of the Beira schists, well constrained at 0.59 (between 0.52 and 0.66) (Bussink, 1984; De Amorin, 2017), and plotting in the AFM diagram inside the Tur1a field, thus clearly distinct from both Tur0 and Tur1b (Fig. 1.10-A). Despite the high Ti content (0.6 to 1.0 wt% TiO₂) of the Beira schists (Bussink, 1984), the tourmaline is rather Ti poor, a fact which may be however ascribed to a competition with the coeval rutile. Muscovite from the protolith would have contributed to buffer the activity of Al₂O₃ at high values (London, 2011), thus favouring Al entrance in the tourmaline structure. On the other hand, the lack of F in Tur0 is in strong contrast with the high F content in the Beira schists (average 570 ppm: Oosterom et al., 1984).

It is unfortunate that the trace element contents in Tur0 remain unknown. Yet, an interpretation of the trace element assemblages in the single fluid model remains possible, by assuming that Tur1a retains more of the protolith composition than Tur1b. As seen in Figure 10, the Tur1a assemblage is, by decreasing order of abundance: Zn-Mn-V-Cr-Li-Sr-Sn-Sc-Ni-Pb-Be-W-Cu-Co-Y-Nb-Ta. A compilation of regional and local data (Oosterom et al., 1984; Villaseca et al., 2009; Ugidos et al., 2003-2010; Fuelanbrada et al., 2016; De Amorin, 2017) shows that all these elements are equally available in the Beira schists, with however the following decrease in order of abundance: Mn-V-(Cr, Zn)-(Li, Sr)- (Ni, Cu, Y)-(Co, Nb, Pb, Sc, Sn)-W-Be-Ta. It is clearly seen that the only part of the Tur1a assemblage which may favourably be compared with the schists is the V-Cr-Li-Sr one. By all other aspects, the lack of similarity is striking, in particular when considering Y and the rare metals (Sn, W, Nb, Ta, Be), as to preclude direct inheritance of the trace element assemblage from the host rocks.

Taken together with the common occurrence of corrosion of the Tur0 cores, strongly suggesting that Tur0 was no more stable at the onset of Tur1 growth, and the small scale oscillations of Fe# during crystal growth, as well as the existence of a recurrence of low Fe# at the end of Tur1b crystallization (Fig. 1.11), that are both difficult to interpret in a single fluid evolution path controlled by variations of the water-rock ratio, a single-fluid origin seems unlikely.

The facts that cannot be explained by the single fluid theory are on the other hand all consistent with the involvement of two fluids end-members (F1 and F2) and a mixing process. In particular, the partition in two groups of elements, exhibiting positive correlations inside the group, but negative correlations from one group to the other (Fig. 1.15), is exactly the behaviour to be expected in a mixing process.

In the course of this mixing process, the earliest Tur0 tourmaline would have been formed from F1, while the Tur1a to Tur1b sequence would record the more or less progressive addition of the F2 fluid to the initial F1 fluid. In this framework, Tur1a records an F1-dominated fluid mixture, whereas Tur1b records an F2-dominated fluid mixture. Therefore, comparison of the element assemblages in Tur1a (most representative of F1) and in Tur1b (most representative of F2) allows us to infer the chemical characteristics of the two end-members. The assemblage Co-Cu-Pb-Sc-Sr-V-Cr is characteristic of the fluid F1, while the assemblage Li-Mn-Zn is characteristic of the fluid F2. In addition, the Fe# increase recorded by the sequence Tur0 to Tur1b (Fig. 1.10-A) would mean that F2 is iron-rich

relatively to F1, i.e., that iron is imported in the system, and in the same way, owing to the fact that Tur0 is F-poor, and Tur1a and Tur1b are rich, the F behaviour would indicate that F2 is by far richer in fluorine than F1.

The boron problem and the feasibility of a magmatic source of fluids

Based on ^{11}B isotope composition (Codeço et al., 2017) or a reconstruction of the fluid pathflow (Launay et al., 2018), recent workers conclude that tourmalinization was the result of the circulation of a magmatic fluid issued from the "Panasqueira granite" and in particular from the greisenized cupola. In the first place, it must be recognized that the large concealed granite body recently modelled by Ribeiro (2017) is evidently responsible for the conspicuous thermal aureole hosting the Panasqueira deposit. Tourmaline clearly replaced the contact metamorphism minerals; it results that the tourmalinization was later than the emplacement of the main granite body. As a consequence, this large body was unable to yield the fluids responsible for the tourmalinization.

However, the greisenized cupola, and the subjacent more or less altered granite layers, which are representative of the rare metal granite (RMG) family (De Amorin, 2017), are likely to have been emplaced later, and could be considered as a possible source of fluids and, in particular, of boron.

It is possible to estimate by mass balance calculation what was the B yield from the RMG and to compare with the B mass demanded by the tourmalinization process. Detailed calculation is presented in Appendix A8. It appears that the cupola was unable to deliver by itself a significant part of the boron needed for the wall-rock tourmalinization at the deposit scale. However, the subjacent RMG could have supplied a large part, but not all, of the required amount of boron, provided a significant B enrichment of the melt, which remains speculative. Tourmaline is typically absent of either the cupola or the subjacent RMG, and direct observation of the cupola/schist contact fails to reveal tourmalinization of the wallrock (observation at the L2 level).

Another problem is the volume of fluids which is needed to perform tourmalinization (Appendix A8). It is found that, whereas a volume of fluid between $2.2 \cdot 10^8 \text{ m}^3$ and $4.5 \cdot 10^8 \text{ m}^3$ was required for the tourmalinization, the Panasqueira RMG sheet-like body could have expelled $\sim 1.8 \cdot 10^7 \text{ m}^3$ of fluid, e.g., a volume of an order of magnitude below the required fluid quantity.

The $\delta^{11}\text{B}$ values of the Panasqueira tourmaline, between -4‰ and -13‰ (with however 90% of the data between -7‰ and -11‰) and displaying a Gaussian distribution (Codeço et al., 2017) are consistent with both a magmatic boron source or a regional metasediment signature. Codeço et al. (2017) prefer the magmatic source, arguing that the boron concentration in the regional schists is too low ($\sim 100 \text{ ppm B}$; Oosterom et al., 1984). This of course would be constraining in the case of a rock-dominated system, which is not the case here. But if, as demonstrated above, the granitic source is not feasible, the metasedimentary connection becomes unavoidable (making in addition a further argument in favour of a high water-rock ratio during the Panasqueira tourmalinization).

With a schist density of 2.77 t.m^{-3} (Ribeiro, 2017), and a B content of 100 ppm, a volume of $\sim 3800 \text{ m}^3$ will contain 1 t of B. Thus, to yield the 470 kt to 950 kt of B that are concentrated in the tourmalinized wall-rocks (Appendix A8), a schist volume of 1.7 km^3 to 3.4 km^3 is required (allowing for a 100% efficient extraction, which is not so likely). However, with a 10% extraction efficiency, the volumes required become $17\text{-}34 \text{ km}^3$. Such volumes are able to yield the volume needed for tourmalinization: in fact (assuming a water productivity of about 3 wt%: Fyfe et al., 1978) between 5 km^3 and 10 km^3 of schist are sufficient to provide the required volume of fluid.

According to the experimental data of Weisbrod et al. (1986), the solubility of tourmaline in aqueous fluids buffered in aluminium is dramatically increased when temperature increases above c. 500°C (at 100 MPa), and at tourmaline saturation, the wt% B_2O_3 of the fluid varies by more than an order of magnitude for every 100°C (London, 2011). Consequently, a metamorphic origin of the boron supposes (1) a source of the fluid at greater depth than the deposit, at a place where temperatures of 600°C or more could have been attained, allowing incorporation of significant boron contents, and (2) a fast transfer towards the deposit level, where rapid cooling would cause boron to be precipitated as tourmaline (discussed later).

The involvement of large quantities of fluids of metamorphic origin in the early tourmalinization process is all the more likely as the earlier preserved FI at Panasqueira, which may be considered as remnants of the pristine fluid inclusions less affected by post-trapping modifications, are members of the C-H-O-N-NaCl system (Cathelineau et al., 2017, 2018). These fluids, associated with the main wolframite deposition following the tourmalinization event, are also consistent with a metamorphic origin.

Metasedimentary source(s) of the fluids: the contribution of REE data

Tur1 exhibits REE patterns very similar to those of the Beira schists (Fig. 1.12) suggesting that Beira schists are the REE source and reinforcing the conclusions of the previous section. This similarity is readily interpreted as an indication that fluids involved in the tourmalinization process are effectively fluids of metamorphic origin equilibrated at high temperature with metasediments. A similar conclusion was reached by Xu et al. (2008) in the case of the Sarekoubu orogenic gold deposit (Hunnan), where tourmaline and host rocks also display similar REE patterns (Fig. 1.11).

By contrast, owing to the fact that magmatic-hydrothermal fluids issued from evolved felsic magmatic sources as well as fluids equilibrated at high subsolidus temperature with a granite display a pronounced negative europium anomaly (e.g., Banks et al., 1994; Poitrasson et al., 1995), the lack of such an anomaly in the Panasqueira tourmaline patterns in Figure 11 is an argument against a significant contribution of a magmatic-related component to the hydrothermal fluid. It is however known that, similar to the behaviour in plagioclase, Eu^{2+} may be incorporated in tourmaline in place of calcium (e.g., Berryman et al., 2017). In Tur1, Ca contents are low, commonly

lower than the detection limit (~ 600 ppm). However, the Σ REE are equally very low, and therefore it remains possible that significant Eu^{2+} may be present, which may in turn overprint a negative anomaly. It seems unlikely that, if present in the fluid, a strong negative Eu^{2+} anomaly be erased in the tourmaline as a consequence of Eu^{2+} incorporation.

Contrasted compositions of F1 and F2 end-members

Observation of Figure 13 shows that in tourmaline, Nb, Ta and Sn forms a distinct subset, which is more concentrated in Tur1a zones, and was consequently more abundant in the F1 fluid, having suffered dilution in the mixing process.

Tungsten being clearly disconnected from Nb, Ta and Sn, it should be part of the F2 package. Yet, as shown in Figure 10, most Tur1b are depleted in W relative to Tur1a, although high W contents are measured in some Tur1b zones. The competition for tungsten between Tur1b and the coeval W-rich rutile is the likely explanation of this apparent contradiction. That the F2 end-member was a significant carrier of tungsten may also be deduced from the abundant W-bearing nano-inclusions found in the Tur1b zones (as inferred from tungsten anomalies in the LA-ICP-MS record, see above). If true, this means that W in Tur1a records the influence of the F2 component in the mixed fluid responsible for Tur1a crystallization.

Summarizing, the trace element signature of the F1 fluid end-member would be (by decreasing order of abundance) Ti-V-Cr-Sr-Sn-Sc-Pb-Ni-Co-Cu-Y-Nb-Ta. This is a package consistent with a metamorphic origin. The F2 fluid end-member signature (Fe-F-Zn-Mn-Li-W) is quite different and could indeed be suggestive of a granite connection. For instance, it may be contrasted with the composition of magmatic fluids issued from Li-rich granitic melts, as recently determined on the example of the Beauvoir granite (France) (Harlaux et al., 2017). Beside their elevated F and Li contents, these fluids are characterized by rather high contents in Fe, Mn, and rare metals. They however contain typically more Sn than W, and rather similar W and Nb-Ta contents, and are deprived from Zn. These discrepancies seem significant, and could point to difference in the source, as indeed indicated by the REE data. A possible source for the F2 fluid could be the partial melting processes occurring in the CIZ middle crust at the end of the Carboniferous. Dehydration-melting migmatites, involving biotite breakdown and formation of granitic melts with cordierite restites, are observed in the migmatite domains (Pereira Gomez et al., 2000) and were likely formed at the end of the Carboniferous, as in equivalent domains of the Variscan belt at the same time (e.g., Barbey et al., 2015). Biotite breakdown is a likely source for Li, F, Fe, Mn, Zn, and rare metals. Quantitative data are scarce in the CIZ; yet a few data on the Peña Negra migmatites (Acosta-Vigil et al., 2011) confirm that biotites from the high-grade (unmelted) metasediments contain significant proportions of F, Li and are a likely source of Fe, Mn, Zn and W. On the other hand, there is evidence for the mobilization of B (and Li) from such migmatitic domains in the CIZ. In the Peña Negra migmatitic complex, the high grade metasediments are already depleted in B (35 ppm),

but not in Li (79 ppm) relative to the average Beira schists (100 ppm B, 75 ppm Li), whereas the diatexites are depleted in both (67 ppm Li, 20 ppm B: Acosta-Vigil et al., 2011). This is in accordance with experimental data showing that tourmaline breakdown occurs at temperatures between 725° and 775°C, at pressures of 200 MPa (London, 2011, and references therein). Thus, a hypothetical diatexite domain beneath Panasqueira at c. 305 Ma could have provided both the components of the F2 end-member, and part of the B needed for the tourmalinization process, whereas the high temperature of the F2 fluid environment would have guaranteed elevated boron contents in the fluid and the possibility of delivering huge boron quantities, provided a quick cooling of the F2 fluid be achieved.

Rutile evidence for short term fluid dynamics and mixing

For reasons discussed in detail in Carocci et al. (2019), it is concluded that the Panasqueira rutile mainly grew under open-system conditions. The minor element package (Fe, V, Sn, W, Nb, Ta) is consistent with the data from tourmaline and with an interpretation in terms of metamorphic fluids. In particular, the variations observed at the full crystal scale, between Nb-dominated and W-dominated growth zones, with all intermediaries (Fig. 1.8), are likely to record changes in the F1 to F2 ratios, with short range modulations as in the tourmaline.

However, at the scale of the "light band/dark band" doublets from the OZ, the observed composition changes (sharp jumps from light W-rich bands to dark Nb-rich bands) are interpreted as recording the successive influx of a W-rich, Nb-Ta poor fluid, abruptly replaced by (or mixed to) a Nb-Ta-rich and W-poor fluid (Carocci et al., 2019). This abrupt oscillatory change in concentrations could be interpreted as related to short timescale fluid events such as those described in relation with microseismic events (Charmoille et al., 2005) (Appendix A9). A (micro)seismic event would allow the influx in the growing environment of the main fluid circulating at this time at the deposit scale, which should be a F2-dominated, W-rich, F1-F2 mixture, and a "light band" would grow. After a short time-lag, a new fluid (F3), coming from a low permeability reservoir, would in turn invade the growing environment, provoking the growth of the succeeding "dark band". In the latter bands, the predominance of Nb-Ta on W and, as well, the lack of systematic relationships between Nb-Ta and Sn or V, could indicate that F3 association is distinct from either F1 or F2 fluids. F3 is likely to have been related to a Nb-Ta-rich granite, such as the RMG layer observed at the top of the Panasqueira granite. As described by De Amorin (2017), the RMG is characterized by abundant Nb-rich columbo-tantalite (Nb# in the 0.74-0.93 range), but is poor in cassiterite, yielding to a rather low Sn content of the granite (≤ 75 ppm).

Proposed conceptual model

In order to integrate the preceding results into a workable model for the tourmalinization process at Panasqueira, a starting point is to consider the upward transfer of the boron-rich F2 fluid from the inferred source at depth up to the deposit level. Here, the concept of a mid-crustal channelized fluid flow (Connolly, 1989) may be

called for. According to the modelling by Connolly (1989), deep fluids issued from biotite dehydration may be gathered into a collection zone, then focused and channelized in a mid-crustal fault zone, ascending at high rates up to a dispersion region in cooler rocks. The half-width of both collection and dispersion zones is typically in the 3-5 km range, and the height of the system is on the order of 10 to 15 km. The flow results in upward heat advection, with a c. 10^4 yr time-scale, inducing a temperature increase of several 10s °C at the 100 kyr time-scale in the dispersion region.

Applied to the Panasqueira system, the collection domain of this model could have been located at depths of 15-20 km, where F2 fluids could have been generated by biotite dehydration. With a total width of 10 km, such a collection domain would have been large enough to provide both the required boron quantity and fluid volume for the tourmalinization process. The fault zone necessary for the channelling process is thought to have been related to the emplacement of the main Panasqueira granite: owing to the NNW-SSE elongation of the body (Ribeiro, 2017), this postulated fault should have a similar direction. In addition, fluid ascent was facilitated by the vertical permeability (S_0 and schistosity) in the core of the Panasqueira anticline.

At a level corresponding roughly to the bottom of the dispersion level of Connolly (1989), the ascending F2 fluid encountered the Panasqueira granite body and was forced to contour it. Launay et al. (2018) reconstructed the pattern of fluid circulation at the time of tourmaline growth, and interpreted the result as proving a radiating flow issued from the "greisen cupola". This remarkable pattern may instead record the deflection of the flowing metamorphic fluids around the cupola - as indeed admitted by Launay et al. (2018) for a part of the flowing fluids.

When arriving at the level of the deposit, the F2 fluid was able to mix with the residing fluids. As seen in Figure 16, at c. 305 Ma, a continuous cap of thick impermeable Ordovician quartzite (Armorican Quartzite) was extended upon the Beira schists, defining a reservoir for the metamorphic fluids issued from either the first LP-HT event in the CIZ or the contact metamorphism of the main Panasqueira granite or both. These fluids may readily be associated with the F1 end-member. The mixing of F1 with F2 is associated with main tourmaline deposition. The mixing was the cause of tourmaline deposition by allowing a strong cooling of the incoming F2 end-member and the concomitant liberation of its contained boron. The continuous transfer of heat by F2 and the resulting heating of the dispersion zone (Connolly, 1989) must have driven a convective flow in the Panasqueira reservoir, allowing continuous renewal of the F1 fluid and of tourmaline growth. Depending on the (unknown) precise timing of the main Panasqueira granite emplacement, cooling of this pluton may also have contributed to the inception of this convective flow, as envisaged by Launay et al. (2018).

As far as the F2 input may well vary with time, the model in Fig. 1.18 is consistent with the short term variations in the F1 to F2 ratios that are inferred from the rutile zoning and tourmaline profiling. The model is also consistent with the alternation of retention and liberation of limited volume of the mixed fluids in the RMG layer at the top of the Panasqueira granite, triggered by a seismic activity which may tentatively be related to the operations of the regional Cebola wrench-fault (Fig. 1.4).

Finally, it appears that the flat top of the Panasqueira granite system and the associated set of dense flat joints (Fig. 1.4) are likely to have focused the flow of the multiple fluids the existence of which is inferred from the mineral composition, and to have favoured the complex mixing patterns revealed by the detailed mineral chemistry interpretation.

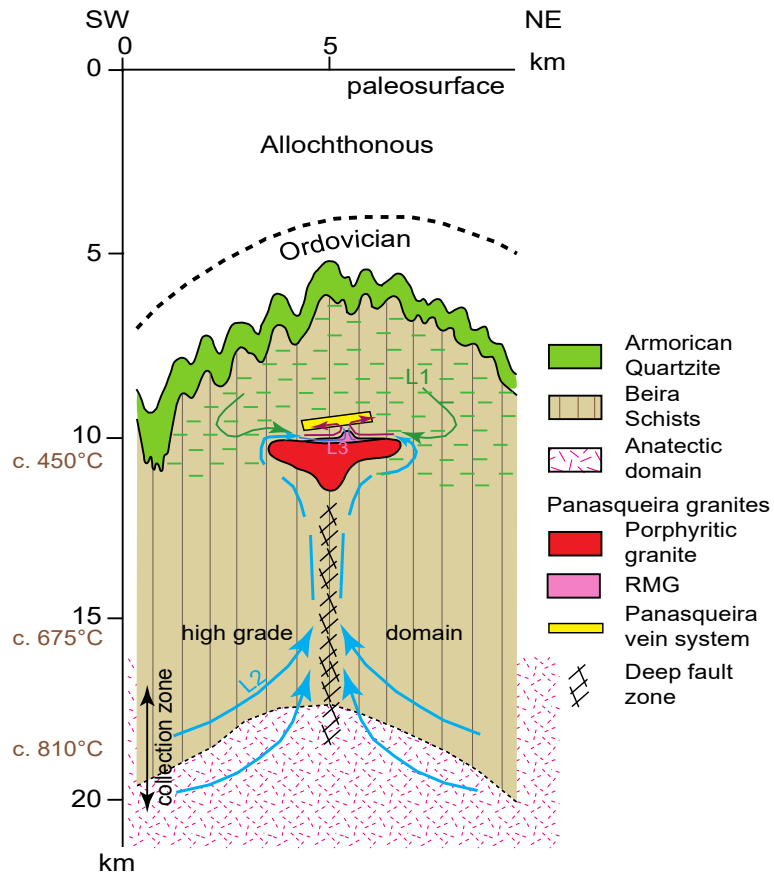


Figure 1.18: Conceptual model of the crustal scale hydrothermal system at the onset of the main wolframite stage at Panasqueira. A geothermal gradient of $c. 40^{\circ}\text{C.km}^{-1}$ is adopted (Cathelineau et al., 2018). The model involves two sources of metamorphic fluids at different structural levels (F1 and F2), and their mixing prior to enter the Panasqueira vein system. A minor contribution of a F3 fluid resulting from interaction with the granite cupola is added. Explanations in the text.

Conclusions

1. Replacement of protolith ferro-magnesian minerals by tourmaline prisms mimicking schistosity and crystallizing according to the Tur0-Tur1a,b sequence is the earliest hydrothermal event in the Panasqueira system. It was correlated to the first increments of crack-seal openings under overpressuring (Qcs veinlets).

2. The early Tur1 tourmaline, and in particular, the development of Tur1b rims, was coeval with the formation of W-bearing rutiles (which are among the richest in W worldwide) and the first appearance of wolframite. Such a combination of tourmaline, W-rutile and wolframite is also observed in the Puy-les-Vignes breccia-pipe tungsten deposit (Harlaux, 2016) and could well appear to be a characteristic of a class of peribatholithic quartz-wolframite vein systems.

3. On the basis of a limited number of observations, it seems that a correlation exists between the presence/abundance of wolframite in quartz veins and the relative importance in the adjacent altered wallrock of Tur1b rim development in tourmaline prisms, and high tungsten content in rutile crystals, correlated with the presence of wolframite nano-inclusions. Reciprocally, on the same limited basis, poor development of the Tur1b rim, and limited W enrichment in the rutile, correlated with the presence of ilmenite lamellae, may indicate barren veins. Such correlations should be investigated further in the future.

4. The age of formation of the early rutile was obtained by U-Pb dating (LA-ICP-MS) and found to be of 305.2 ± 5.7 Ma. It is therefore the age of the early tourmalinization and first appearance of wolframite. This new age is older than the age currently accepted of c. 296 Ma, which was obtained on muscovite selvages which therefore must definitely be considered as representative of processes after wolframite deposition.

5. This new age yields a rather distinct model than those previously published: the Panasqueira system appears as a long-lived hydrothermal system over more than 6-8 Ma developed along a rather significant crustal anomaly probably along a much deeper crustal system than the simple and unique system linked to a single granite intrusion.

6. Two fluids, both of metamorphic origin, were involved through mixing in the tourmaline growth in a fluid-dominated hydrothermal system. The first one, rich in Ti-V-Cr Sr-Sn-Sc-Pb-Ni-Co-Cu-Y-Nb-Ta, and of "local" derivation, was progressively replaced by the second, rich in Li-F-Fe-Mn-W, of deeper origin (biotite dehydration). This second fluid carried the metals necessary to wolframite deposition and in particular Fe and Mn, which were thus not necessarily inherited from the wall-rocks through fluid-rock interaction, contrary to the conclusions of Lecumberri-Sanchez et al. (2017). Yet, the reasons why the start of wolframite deposition occurred only at the end of the tourmalinization process remain unclear.

7. A minor contribution of a Nb-rich fluid is perceptible during the rutile growth, and was likely sourced in the rare metal granite from the top of the Panasqueira granite body.

Acknowledgements

This work benefited from the analytical capabilities of the GeoResources Laboratory (Université de Lorraine, CNRS, CREGU), and the authors gratefully acknowledge Olivier Rouer, Andrei Lecomte, Lise Salsi and Chantal Peiffert for their technical help. LA-ICP-MS equipment was financed by CPER program (National Funds – Lorraine region – FEDER). Reviewers, E.J. Berryman and A.E. Williams-Jones, are warmly acknowledged for their constructive remarks.

This work was financed by the ERAMIN project NewOres financed by ANR (ANR-14-EMIN-0001), and Labex Ressources 21 (supported by the French National Research Agency through the national program “Investissements d’avenir”) with reference ANR – 10 – LABX 21 –LABEX RESSOURCES 21.

Fabian B. Wadsworth (Durham University) is warmly thanked for his thorough review of the English.

We are most grateful to Beralt Tin and Wolfram S.A. for permitting access to the Panasqueira underground mine.

References

- Acosta-Vigil, A., Pereira, M.D., Shaw, D.M., and London, D., 2011, Contrasting behaviour of boron during crustal anatexis: *Lithos*, v. 56, p. 15-31.
- Alcock, J.E., Martínez Catalán, J.R., Rubio Pascual F.-J., Díez Montes, A., Díez Fernández, R., Gómez Barreiro, J., Arenas, R., Dias da Silva, I., and Clavijo, E.G., 2015, 2-D thermal modeling of HT–LP metamorphism in NW and Central Iberia: Implications for Variscan magmatism, rheology of the lithosphere and orogenic evolution: *Tectonophysics*, v. 657, p. 21-37.
- Almonty Industries, 2016, Report NI 43-101. Technical report on the mineral resources and reserves of the Panasqueira mine, Portugal: http://www.almonty.com/_resources/Panasqueira_43-101_Tech_Rep_Dec16_SEDAR.PDF.
- Arenas, R., Díez Fernández, R., Rubio Pascual, F.J., Sánchez Martínez, S., Martín Parra, L.M., Matas, J., González del Tánago, J., Jiménez-Díaz, A., Fuenlabrada, J.M., Andonaegui, P., and Garcia-Casco, A., 2016, The Galicia–Ossa-Morena Zone: Proposal for a new zone of the Iberian Massif. Variscan implications: *Tectonophysics*, v. 681, p. 135-143.
- Banks, D.A., Yardley, B.W.D., Campbell, A.R., and Jarvis, K.E., 1994, REE composition of an aqueous magmatic fluid: A fluid inclusion study from the Capitan Pluton, New Mexico, U.S.A: *Chemical Geology*, v. 113, p. 259-272.
- Barbey, P., Villaros, A., Marignac, C., and Montel, J.M., 2015, Multiphase melting, magma emplacement and P-T-time path in late-collisional context: the Velay example (Massif Central, France): *Bulletin de la Société Géologique de France*, v. 186, p. 93–116.
- Berryman, E.J., Wunder, B., Rhede, D., Schettler, G., Franz, G., and Heinrich, W., 2016, P–T–X controls on Ca and Na distribution between Mg–Al tourmaline and fluid: *Contributions to Mineralogy and Petrology*, v. 171, p. 31-43.

- Berryman, E.J., Kutzschbach, M., Trumbull, R.B., Meixner, A., van Hinsberg, V., Kasemann, S.A., and Frantz, G., 2017, Tourmaline as a petrogenetic indicator in the Pfitsch Formation, Western Tauern Window, Eastern Alps: *Lithos*, v. 284-285, p. 138-155.
- Bloot, C., and De Wolf, L.C.M., 1953, Geological features of the Panasqueira tin-tungsten ore-occurrence (Portugal): *Boletim da Sociedade Geologica de Portugal*, v. XI, p. 1-57.
- Bosi, F., 2011, Stereochemical constraints in tourmaline: from a short-range to a long-range structure: *The Canadian Mineralogist*, v. 49, p. 17-27.
- Bosi, F., 2018, Tourmaline crystal chemistry: *American Mineralogist*, v.103, p. 298-306.
- Burnard, P.G., and Polya, D.A., 2004, Importance of mantle derived fluids during granite associated hydrothermal circulation: He and Ar isotopes of ore minerals from Panasqueira: *Geochimica et Cosmochimica Acta*, v. 68, p. 1607–1615. doi:10.1016/j.gca.2003.10.008.
- Bussink, R.W., 1984, Geochemistry of the Panasqueira tungsten-tin deposit, Portugal: *Geologia Ultraiectina*, v. 33, p. 1-159.
- Carocci E., Marignac C., Cathelineau M., Truche L., Lecomte A., Pinto F. (2019) - Rutile from Panasqueira (Central Portugal) : an excellent pathfinder for wolframite deposition. *Minerals*, v. 9, 9; <https://doi.org/10.3390/min9010009>.
- Castro, A., Corretge, L.G., de la Rosa, J.D., Fernández, C., López, S., García-Moreno, O., and Chacón, H., 2003. The appinite–migmatite complex of Sanabria, NW Iberian Massif, Spain: *Journal of Petrology*, v. 44, p. 1309–1344.
- Cathelineau, M., Marignac, C., Rolland, J.-M., Boiron, M.-C., and Dejean, M., 2017, Are we sure to know the fluids responsible for W mineralization at Panasqueira (Portugal): the case for loss of information due to intense quartz recrystallization and FI natural decrepitation: *European Current Research on Fluid Inclusions (ECROFI) Biennial Meeting, 24th, Nancy, France, Abstracts*, p. 98.
- Cathelineau, M., Marignac, C., Boiron, M.-C, Carocci, E., Rolland, J.-M., Dejean, M, Dourk, M., and Pinto, F., 2018, Nouvelle approche du chemin P-T-t des fluides dans le gisement à W-Sn-Cu de Panasqueira (Portugal): persistence d'une anomalie thermique d'origine profonde en cours d'exhumation: *Earth Science Meeting (RST), 26th, Lille, France, 2018, Abstracts*, p. 694.
- Charmoille, A., Fabbri, O., Mudry, J., Guglielmi, Y., and Bertrand, C., 2005, Post-seismic permeability change in a shallow fractured aquifer following a ML 5.1 earthquake (Fourbanne karst aquifer, Jura outermost thrust unit, eastern France): *Geophysical Research Letters*, v. 32: LA8406, doi:10.1029/2005GL023859.
- Charoy, B., and Noronha, F.O., 1996, Multistage Growth of a Rare-Element, Volatile-Rich Microgranite at Argemela (Portugal): *Journal of Petrology*, v. 37, p. 73-94.
- Chew, D.M., Petrus, J.A., and Kamber, B.S., 2014, U-Pb LA-ICPMS dating using accessory mineral standards with variable common Pb: *Chemical Geology*, v. 363, p. 185-199.
- Clark, A.H., 1970, Potassium-argon ages and regional relationships of the Panasqueira tin-tungsten mineralization, Portugal: *Servicos Geologicos Comunicacoes*, v. 54, p. 243-261.

- Codeço, M.S., Weis, P., Trumbull, R.B., Pinto, F., Lecumberri-Sanchez, P., and Wilke, F.D., 2017, Chemical and boron isotopic composition of hydrothermal tourmaline from the Panasqueira W-Sn-Cu deposit, Portugal: *Chemical Geology*, v. 468, p. 1-16.
- Connolly, J.A.D., 1989, Mid-crustal focused fluid movement: thermal consequences and silica transport, in Jamtveit, B., Yardley, B.W.D., eds, *Fluid flow and transport in rocks, mechanisms and effects*: Chapman & Hall, London, p. 235-250.
- De Amorin, A., 2017, *Pétrographie géochimie des granitoides de la mine de W de Panasqueira (Portugal): Rôle dans la genèse des minéralisations*: Unpublished M.Sc. thesis, Université de Lorraine (France), Laboratoire Géoressources, 37 p.
- Dias, G., Leterrier, J., Mendes, A., Simões, P.P., and Bertrand J.M., 1998, U-Pb zircon and monazite geochronology of post-collisional Hercynian granitoids from the Central Iberian Zone (Northern Portugal): *Lithos*, v. 45, p. 349-369.
- Díez Fernández, R., and Pereira, M.F., 2016, Extensional orogenic collapse captured by strike-slip tectonics: Constraints from structural geology and U-Pb geochronology of the Pinhel shear zone (Variscan orogen, Iberian Massif): *Tectonophysics*, v. 691, p. 290-310.
- Díez Fernández, R., and Pereira, M.F., 2017, Strike-slip shear zones of the Iberian Massif: Are they coeval?: *Lithosphere*, v. 9, p. 726-744.
- Díez Fernández, R., Martínez Catalán, J.R., Barreiro, J.G., and Arenas, R., 2012, Extensional Flow during Gravitational Collapse: A Tool for Setting Plate Convergence (Padrón Migmatitic Dome, Variscan Belt, NW Iberia): *The Journal of Geology*, v. 120, p. 83-103.
- Díez Fernández, R., Barreiro, J.G., Martínez Catalán, J.R., and Ayarza, P., 2013, Crustal thickening and attenuation as revealed by regional fold interference patterns: Ciudad Rodrigo basement area (Salamanca, Spain): *Journal of Structural Geology*, v. 46, p.115-128.
- Díez Fernández, R., Arenas, R., Pereira, M.F., Sánchez-Martínez, S., Albert, R., Martín Parra, L.M., Rubio Pascual, F.J., and Matas, J., 2016, Tectonic evolution of Variscan Iberia: Gondwana–Laurussia collision revisited: *Earth-Science Reviews*, v. 162, p. 269-292.
- Faure, M., Lardeaux, J.M., and Ledru, P., 2009, A review of the pre-Permian geology of the Variscan French Massif Central: *Comptes Rendus Geosciences*, v. 341, p. 202–213.
- Fernández-Suárez, J., G. Gutiérrez-Alonso, S. T. Johnston, T. E. Jeffries, D. Pastor-Galan, G. A. Jenner, and Murphy, J.B., 2011, Iberian late- Variscan granitoids: Some considerations on crustal sources and the significance of “mantle extraction ages”: *Lithos*, v. 123, p. 121–132, doi:10.1016/j.lithos.2010.09.010.
- Foxford, K.A., Nicholson, R., and Polya, D.A., 1991, Textural evolution of W–Cu–Sn bearing hydrothermal quartz veins at Minas da Panasqueira, Portugal: *Mineralogical Magazine*, v. 55, p. 435–445.
- Foxford, K.A., Nicholson, R., Polya, D.A., and Hebblethwaite, R.P.B., 2000, Extensional failure and hydraulic valving at Minas da Panasqueira, Portugal: evidence from vein spatial distributions, displacements and geometries: *Journal of Structural Geology*, v. 22, p. 1065–1086, [http://dx.doi.org/10.1016/S0191-8141\(00\)00029-8](http://dx.doi.org/10.1016/S0191-8141(00)00029-8).
- Franke, W., Matte, P., and Tait, J., 2005, Europe: Variscan orogeny: *Encyclopedia of Geology*, Oxford, Elsevier, v. 2., p. 75–85.

- Frikken, P.H., Cooke, D.R., Walshe, J.L., Archibald, D., Skarmeta, J., Serrano, L., and Vargas, R., 2005, Mineralogical and isotopic zonation in the Sur-Sur tourmaline breccia, Río Blanco-Los Bronces Cu-Mo deposit, Chile—implications for ore genesis: *ECONOMIC GEOLOGY*, vol. 100, p. 935–961.
- Fuertes-Fuente, M., Martin-Izard, A., Boiron, M-C., and Mangas, J., 2000, Fluid evolution of rare-element and muscovite granitic pegmatites from central Galicia, NW Spain: *Mineralium Deposita*, v. 35, p. 332-345.
- Fyfe, W.S., Price, N.J., and Thompson, A.B., 1978, *Fluids in the earth's crust*. Amsterdam: Elsevier, 389 p.
- Garcia, D., 2004, *Travaux présentés pour l'obtention du diplôme Habilitation à Diriger les Recherches en Sciences de la Terre et de l'Univers, Espace: Génie des procédés, Université Jean Monnet; Ecole Nationale Supérieure des Mines de Saint-Etienne*, 87 p.
- Harlaux, M., 2016, *Les systèmes métallogéniques hydrothermaux à tungstène et métaux rares (Nb, Ta, Sn) dans le contexte orogénique fini-varisque : exemple du Massif Central Français (Tungsten and rare-metal (Nb, Ta, Sn) hydrothermal metallogenic systems in the late-Variscan orogenic context: example of the French Massif Central)*: PhD thesis, Université de Lorraine (France), Laboratoire Géoressources, 451 p.
- Harlaux, M., Mercadier, J., Bonzi, W.M.-E., Kremer, V., Maignac, C., and Cuney, M., 2017, Geochemical signature of magmatic-hydrothermal fluids exsolved from the Beauvoir rare-metal granite (Massif Central, France): insights from LA-ICPMS analysis of primary fluid inclusions: *Geofluids*, v. 2017, Article ID 1925817, 25 p. <https://doi.org/10.1155/2017/1925817>.
- Hawthorne, F.C., and Dirlam, D.M., 2011, Tourmaline the indicator mineral: From atomic arrangement to Viking navigation: *Elements*, v. 7, p. 307-312.
- Henry, D.J., and Dutrow, B.L., 2011, The incorporation of fluorine in tourmaline: internal crystallographic controls or external environmental influence?: *The Canadian Mineralogist*, v. 49, p. 41-56.
- Henry, D.J., and Guidotti, C.V., 1985, Tourmaline as a petrogenetic indicator mineral: an example from the staurolite-grade metapelites of NW Maine: *American Mineralogist*, v. 70, p. 1-15.
- Henry, D.J., Novák, M., Hawthorne, F.C., Ertl, A., Dutrow, B.L., Uher, P., and Pezzotta, F., 2011, Nomenclature of the tourmaline supergroup minerals: *American Mineralogist*, v. 96, p. 895–913.
- Inverno, C.M.C., Ferraz, P.J.V., and Moreira, E., 2009, Argemela, a high-tonnage Sn-Li deposit in Central Portugal: *Geological Society of America Annual Meeting, Portland, 2009, Abstracts* 41, p. 680.
- Jackson, S.E., Pearson, N.J., Griffin, W.L., and Belousova, E.A., 2004, The application of laser ablation-inductively coupled plasma-mass spectrometry to in situ U-Pb zircon geochronology: *Chemical Geology*, v. 211, p. 47-69.
- Jacques, D., Vieira, R., Muchez, P., and Sintubin, M., 2018, Transpressional folding and associated cross-fold jointing controlling the geometry of post-orogenic vein-type W-Sn mineralization: examples from Minas da Panasqueira, Portugal: *Mineralium Deposita*, v. 53, p. 171-194.
- Jacques, L., and Pascal, C., 2017, Full paleostress tensor reconstruction using quartz veins of Panasqueira Mine, central Portugal; part I: Paleopressure determination: *Journal of Structural Geology*, v. 102, p. 58-74.
- Julivert, M., Fontboté, J.M., Ribeiro, A., and Nabais-Conce, L.E., 1972, Mapa tectónico de la Península Ibérica y Baleares, 1:1.000.000: IGME, Memoria explicativa, p. 113.

- Kelly, W.C., and Rye, R.O., 1979, Geologic, fluid inclusion, and stable isotope studies of the tin-tungsten deposits of Panasqueira, Portugal: *ECONOMIC GEOLOGY*, v. 74, p. 1721–1822.
- Kuhn, T., 2018, Al-in-Hornblende barometry of Southern New England intrusions and comparison with metamorphic bathograds: Senior Thesis, Department of Geology and Geophysics, Yale University, 25 p.
- Lach P, Mercadier J., Dubessy J., Boiron M.C., and Cuney M., 2013, In-situ quantitative measurement of rare earth elements in uranium oxides by Laser Ablation-Inductively Coupled Plasma-Mass Spectrometry. *Geostandards and Geoanalytical Research*. 37, 277-296
- Launay, G., Sizaret, S., Guillou-Frottier, L., Gloaguen, E., and Pinto, F., 2018. Deciphering fluid flow at the magmatic-hydrothermal transition: A case study from the world-class Panasqueira W–Sn–(Cu) ore deposit (Portugal): *Earth and Planetary Science Letters*, v. 499, p. 1-12.
- Lecumberri-Sanchez, P., Vieira, R., Heinrich, C., Pinto, F., and Walle, M., 2017, Fluid-rock interaction is decisive for the formation of tungsten deposits: *Geology*, v. 45, p. 579–582.
- Leisen M., Dubessy J., Boiron M.C., Lach P., 2012. Improvement of the determination of element concentrations in quartz-hosted fluid inclusions by LA-ICP-MS and Pitzer thermodynamic modeling of ice melting temperature. *Geochim. Cosmochim. Acta*, 90, 110-125.
- Lewis, A.J., Palmer, M.R., Sturchio, N.C., and Kemp, A.J., 1997, The rare earth element geochemistry of acid-sulphate and acid-sulphate-chloride geothermal systems from Yellowstone National Park, Wyoming, USA: *Geochimica et Cosmochimica Acta*, v. 61, p. 695-706.
- Lima, L.A.S., 2015, Contribuição para o estudo da mineralogia da brecha de Sta. Helena - Minas da Borralha: PhD thesis, Porto Universidad, 103 p.
- Linnen, R.L., and Cuney, M., 2005, Granite-related rare-element deposits and experimental constraints on Ta-Nb-W-Sn-Zr-Hf mineralization, in Linnen, R.L. and Samson, I.M., eds., rare-element geochemistry and mineral deposits, Geological Association of Canada, Short Course Notes, v. 17, p. 45-67.
- Llana-Funez, S., and Marcos, A., 2007, Convergence in a thermally softened thick crust: Variscan intracontinental tectonics in Iberian plate rocks: *Terra Nova*, v. 19, p. 1-8.
- London, D., 2011, Experimental synthesis and stability of tourmaline: a historical overview: *The Canadian Mineralogist*, v. 49, p. 117-136.
- Lourenço, A., 2002, Paleofluidos e mineralizações associadas às fases tardias da Orogenia Hercínica: Unpublished PhD, Universidade do Porto, 326 p.
- Lüders, V., 1996, Contribution of infrared microscopy to fluid inclusion studies in some opaque minerals (wolframite, stibnite, bournonite): Metallogenic implications: *ECONOMIC GEOLOGY*, v. 91, p. 1462–1468.
- Ludwig, K.R., 2012, User's Manual for Isoplot 3.75, A Geochronological Toolkit for Microsoft Excel: Berkeley Geochronology Center, Special Publication No. 5.
- Maner, J.L., London, D., and Morgan, G.B., 2014, Elemental partitioning and zoning in tourmaline: An experimental investigation: Goldschmidt Conference Abstracts, Sacramento, California, 2014, p. 1583.

- Manzotti, P., Poujol, M., and Ballèvre, M., 2015, Detrital zircon geochronology in blueschist-facies metaconglomerates from the Western Alps: implications for the late Carboniferous to early Permian palaeogeography: *International Journal of Earth Sciences*, v. 104, p. 703–731.
- Marignac, C., Cuney, M. (2013) Past and present rare metal potential of Western Europe: In: PDAC 2013 (Toronto) Short Course "New Mines in the Old World: the untapped potential of Europe".
- Marschall, H.R., and Jiang, S-Y., 2011, Tourmaline isotopes: No element left behind: *Elements*, v. 7, p. 313-319.
- Martínez Catalán, J.R., Arenas, R., Díaz García, F., Gómez Barreiro, J., González Cuadra, P., Abati, J., Castiñeiras, P., Fernández-Suárez, J., Sánchez Martínez, S., Andonaegui, P., González Clavijo, E., Díez Montes, A., Rubio Pascual, F.J., and Valle Aguado, B., 2007, Space and time in the tectonic evolution of the northwestern Iberian Massif. Implications for the Variscan belt. In: Hatcher RD, Carlson MP, McBride JH, Martínez Catalán JR (eds) 4-D framework of continental crust: *Geological Society of America Memoir*, Boulder, p. 403–423.
- Mateus, A., and Noronha, F., 2010, Sistemas mineralizantes epigenéticos na Zona Centro-Ibérica; expressão da estruturação orogénica meso- a tardi-varisca (Epigenetic ore-forming systems in Central-Iberian Zone; products of an evolving orogenic framework in meso- to late-Variscan times): *Ciências Geológicas, Ensino, Investigação e sua História (Geologia Aplicada)*, v. 2, p. 47-61.
- Matte, P., 2001, The Variscan collage and orogeny (480 ± 290 Ma) and the tectonic definition of the Armorica microplate: a review: *Terra Nova*, v. 13, p. 122–128.
- Mello Mendes, F., Correia De Sa, A., Ferreira, E., and Silva, J., 1987, The geomechanics of Panasqueira Mine, Portugal: *International Society for Rock Mechanics Congress, 6th, Montreal, 1987, Extended Abstracts*, p. 1145-1152.
- Nägler, T.F., Schäfer, H-J., and Gebauer, D., 1993, A new approach for the determination of the age of partial or complete homogenization of Pb isotopes Example: anchimetamorphic, detrital sediments of the Central Iberian Zone, Spain: *Chemical Geology*, v. 107, p. 191-199.
- Nägler, T.F., Schäfer, H-J., and Gebauer, D., 1995, Evolution of the Western European continental crust: implications from Nd and Pb isotopes in Iberian sediments: *Chemical Geology*, v. 121, p. 345-357.
- Neiva, A.M.R., 2002, Portuguese granites associated with Sn-W and Au mineralizations: *Bulletin of the Geological Society of Finland*, v. 74, p. 79-101.
- Neiva, A.M.R., Silva, M.M.V.G., and Gomes, M.E.P., 2007, Crystal chemistry of tourmaline from Variscan granites, associated tin-tungsten- and gold deposits, and associated metamorphic and metasomatic rocks from northern Portugal: *Neues Jahrbuch für Mineralogie Abhandlungen*, v. 184, p. 45-76.
- Noronha, F., 1984, Caractéristiques physico-chimiques des fluides associés à la genèse du gisement de tungstène de Borralha - Nord du Portugal: *Bulletin de Minéralogie (Paris)*, v. 107, p. 273-284.
- Noronha, F., 2017, Fluids and Variscan metallogenesis in granite related systems in Portugal: *Water-Rock Interaction International Symposium, 15th: Procedia Earth and Planetary Science*, v. 1, p. 1-4.
- Noronha, F., Dória, F., Dubessy, J., and Charoy, B., 1992, Characterization and timing of the different types of fluids present in the barren and ore veins of the W-Sn deposit of Panasqueira, central Portugal: *Mineralium Deposita*, v. 27, p. 72–79.

- Noronha, F., Ribeiro, M.A., Almeida, A., Dória, A., Guedes, A., Lima, A., Martins, H.C., Sant'Ovaia, H., Nogueira, P., Martins, T., Ramos, R., and Vieira, R., 2013, II.1.8. Jazigos filonianos hidrotermais e aplitopegmatíticos espacialmente associados a granitos (norte de Portugal), in Dias, R., Araujo, P., Terrinha, P., Kullberg, J.P., eds, *Geologia Pré-Mesozoica de Portugal: Escolar Editora*, v. 2, p. 403-438.
- Orejana, D., Villaseca, C., Pérez-Soba, C., López-García, J.A., and Billström, K., 2009, The Variscan gabbros from the Spanish Central System: A case for crustal recycling in the sub-continental lithospheric mantle?: *Lithos*, v. 110, p. 262-276.
- Paquette, J.L., Piro, J.-L., Devidal, J.-L., Bosse, V., Didier, A., Sannac, S., and Abdelhour, Y., 2014, Sensitivity enhancement in LA-ICP-MS by N₂ addition to carrier gas: application to radiometric dating of U-Th - bearing minerals: *Agilent ICP-MS Journal*, v. 58, p. 4-5.
- Paton, C., Hellstrom, J., Bence, P., Woodhead, J., and Herg, J., 2011, Iolite: Freeware for the visualisation and processing of mass spectrometric data: *Journal of Analytical Atomic Spectrometry*, v. 26, p. 2508-2518.
- Pattison, D.R.M., 2001, Instability of Al₂O₅ 'triple point' assemblages in muscovite+biotite+quartz bearing metapelites, with implications: *American Mineralogist*, v. 86, p. 1414-1422.
- Pereira, M.F., Díez Fernández, R., Gama, C., Hofmann, M., Gärtner, A., and Linnemann, U., 2017, S-type granite generation and emplacement during a regional switch from extensional to contractional deformation (Central Iberian Zone, Iberian autochthonous domain, Variscan Orogeny): *International Journal of Earth Sciences (Geologische Rundschau)*, DOI 10.1007/s00531-017-1488-3.
- Pereira Gómez, M.D., and Rodríguez Alonso, M.D., 2000, Duality of cordierite granites related to melt-restite segregation in the Peña Negra anatectic complex, central Spain: *Canadian Mineralogy*, v. 38, p. 1329-1346.
- Pérez-Cáceres, I., Martínez Poyatos, D., Fernando Simancas, J., and Azor, A., 2017, Testing the Avalonian affinity of the South Portuguese Zone and the Neoproterozoic evolution of SW Iberia through detrital zircon populations: *Gondwana Research*, v. 42, p. 177-192.
- Poitrasson, F., Pin, C., and Duthou, J.-L., 1995, Hydrothermal remobilization of rare earth elements and its effect on Nd isotopes in rhyolite and granite: *Earth and Planetary Science Letters*, v. 130, p. 1-11.
- Polya, D.A., 1989, Chemistry of the main-stage ore-forming fluids of the Panasqueira W-Cu(Ag)-Sn deposit, Portugal: implications for models of ore genesis: *ECONOMIC GEOLOGY*, v. 84, p. 1134-1152.
- Polya, D.A., Foxford, K.A., Stuart, F., Boyce, A., and Fallick, A.E., 2000, Evolution and paragenetic context of low δ D hydrothermal fluids from the Panasqueira W-Sn deposit, Portugal: new evidence from microthermometric, stable isotope, noble gas and halogen analyses of primary fluid inclusions: *Geochimica et Cosmochimica Acta*, v. 64, p. 3357-3371.
- Priem, H.N.A., and Den Tex, E., 1984, Tracing crustal evolution in the NW Iberian Peninsula through the Rb-Sr and U-Pb systematics of Paleozoic granitoids: a review: *Physics of the Earth and Planetary Interiors*, v. 35, p. 121-130.
- Renne, P.R., and Norman, E.B., 2001, Determination of the half-life of Ar-37 by mass spectrometry: *Physical Review*, v. C, p. 6304-7302.
- Renne, P.R., Swisher, C.C., Deino, A.L., Karner, D.B., Owens, T.L., and DePaolo, D.J., 1998, Inter-calibration of standards, absolute ages and uncertainties in ⁴⁰Ar/³⁹Ar dating: *Chemical Geology*, v. 145, p. 117-152.

- Renne, P.R., Cassata, W.S., and Morgan, L.E., 2009. The isotopic composition of atmospheric argon and $^{40}\text{Ar}/^{39}\text{Ar}$ geochronology: Time for a change?: *Quaternary Geochronology*, v. 4, p. 288–298.
- Ribeiro, R.F., 2017, Gravimetric Modelling and Geological Interpretation of Argemela-Panasqueira Area: PhD Thesis, Porto Universidad, 61 p.
- Robles, E.R., Perez, A.P., Roldan, F.V., and Fontan, F., 1991, The granitic pegmatites of the Fregeneda area (Salamanca, Spain): characteristics and petrogenesis: *Mineralogical Magazine*, v. 67, p. 535-558.
- Roddick, J.C., 1983, High precision intercalibration of $^{40}\text{Ar}/^{39}\text{Ar}$ standards: *Geochimica et Cosmochimica Acta*, v. 47, p. 887-898.
- Rubio Pascual, F.J., Arenas, R., Martínez Catalán, J.R., Rodríguez Fernández, L.R., and Wijbrans, J.R., 2013, Thickening and exhumation of the Variscan roots in the Iberian Central System: Tectonothermal processes and $^{40}\text{Ar}/^{39}\text{Ar}$ ages: *Tectonophysics*, v. 587, p. 207-221.
- Rubio Pascual, F.J., López-Carmona, A., and Arenas, R., 2016, Thickening vs. extension in the Variscan belt: P–T modelling in the Central Iberian autochthon: *Tectonophysics*, v. 681, p. 144-158.
- Sanderson, D.J., Roberts, S., Gumiel, P., and Greenfield, C., 2008, Quantitative analysis of tin- and tungsten-bearing sheeted vein systems: *ECONOMIC GEOLOGY*, v. 103, p. 1043-1056.
- Sant’Ovaia, H., Olivier, P., Ferreira, N., Noronha, F., and Leblanc, D., 2010, Magmatic structures and kinematics emplacement of the Variscan granites from Central Portugal (Serra da Estrela and Castro Daire areas): *Journal of Structural Geology*, v. 32, p. 1450-1465.
- Scarrow, J.H., Molina, J.F., Bea, F., and Montero, P., 2009, Within-plate calc-alkaline rocks: Insights from alkaline mafic magma–peraluminous crustal melt hybrid appinites of the Central Iberian Variscan continental collision: *Lithos*, v. 110, p. 50-64.
- Scarrow, J.H., Molina, J.F., Bea, F., Montero, P., and Vaughan, A.P.M., 2011, Lamprophyre dikes as tectonic markers of late orogenic transtension timing and kinematics: A case study from the Central Iberian Zone: *Tectonics*, v. 30(4): TC4007.
- Sláma, J., Košler, J., Condon, D.J., Crowley, J.L., Gerdes, A., Hanchar, J.M., Horstwood, M.S.A., Morris, G.A., Nasdala, L., Norberg, N., Schaltegger, U., Schoene, B., Tubrett, M.N., and Whitehouse, M.J., 2008, Plešovice zircon—a new natural reference material for U–Pb and Hf isotopic microanalysis: *Chemical Geology*, v. 249 (1–2), p. 1–35.
- Snee, L.W., Sutter, J.F., and Kelly, W.C., 1988, Thermochronology of economic mineral deposits: dating the stages of mineralisation at Panasqueira, Portugal, by high-precision ^{40}Ar - ^{39}Ar age spectrum techniques on muscovite: *ECONOMIC GEOLOGY*, v. 83, p. 335-354.
- Stacey, J.S., and Kramers, J.D., 1975, Approximation of terrestrial lead isotope evolution by a two-stage model: *Earth and Planetary Science Letters*, v. 26, p. 207–221.
- Steiger, R.H., and Jäger, E., 1977, Subcommittee on geochronology: Convention on the use of decay constants in geo- and cosmochronology: *Earth and Planetary Science Letters*, v. 36, p. 359–362, doi: 10.1016/0012-821X(77)90060-7.

- Tornos, F., Delgado, A., Casquet, C., and Galindo, C., 2000, 300 Million years of episodic hydrothermal activity: stable isotope evidence from hydrothermal rocks of the eastern Iberian Central System: *Mineralium Deposita*, v. 35, p. 551–569.
- Tornos, F., Galindo, C., Crespo, J.L., and Spiro B.F., 2008, Geochemistry and origin of calcic tungsten-bearing skarns, Los Santos, Central Iberian Zone, Spain: *The Canadian Mineralogist*, v. 46, p. 87-109.
- van Achterbergh, E., Ryan, C.G., Jackson, S.E., and Griffin, W.L., 2001, Data reduction software for LA-ICP-MS, in Sylvester, P., ed., *Laser-Ablation-ICPMS in the Earth Sciences. Principles and Applications*: Mineralogical Association of Canada, St. John's, Newfoundland, p. 239–243.
- van Hinsberg, V.J., 2011, Preliminary experimental data on trace-element partitioning between tourmaline and silicate melt: *The Canadian Mineralogist*, v. 49, p. 153-163
- van Hinsberg, V.J., Henry, D.J., and Marschall, H.R., 2011, Tourmaline: an ideal indicator of its host environment: *The Canadian Mineralogist*, v. 49, p.1-16.
- Vereshchagin, O.S., Frank-Kamenetskaya, O.V., Rozhdestvenskaya, I.V., and Zolotariev, A.A., 2018, Incorporation of 3d elements in tourmalines: structural adjustments and stability: *European Journal of Mineralogy*, v. 30, p. 917-928.
- Vermeesch, P., 2012, On the visualisation of detrital age distributions: *Chemical Geology*, v. 312-313, p. 190-194, doi: 10.1016/j.chemgeo.2012.04.021.
- Vigne, J-L., André, G., and Kapal, F., 2018, Données industrielles, économiques, géographiques sur les principaux produits chimiques, métaux, matériaux (11ème edition). <http://www.societechimiquedefrance.fr/extras/Donnees/acc.htm>
- von Goerne, G., Franz, G., and Heinrich, W., 2001, Synthesis of tourmaline solid solutions in the system $\text{Na}_2\text{O} \pm \text{MgO} \pm \text{Al}_2\text{O}_3 \pm \text{SiO}_2 \pm \text{B}_2\text{O}_3 \pm \text{H}_2\text{O} \pm \text{HCl}$ and the distribution of Na between tourmaline and fluid at 300 to 700 °C and 200 MPa: *Contributions to Mineralogy and Petrology*, v. 141, p. 160-173.
- von Goerne, G., Franz, G., and van Hinsberg, V.J., 2011, Experimental determination of Na–Ca distribution between tourmaline and fluid in the system $\text{CaO}–\text{Na}_2\text{O}–\text{MgO}–\text{Al}_2\text{O}_3–\text{SiO}_2–\text{B}_2\text{O}_3–\text{H}_2\text{O}$: *The Canadian Mineralogist*, v. 49, p. 137-152.
- Weil, A.B., Gutiérrez-Alonso, G., Johnston, S.T., Pastor-Galán, D., 2013, Kinematic constraints on buckling a lithospheric-scale orocline along the northern margin of Gondwana: A geologic synthesis: *Tectonophysics*, v. 582, p. 25-49.
- Weisbrod, A., Polak, C., and Roy, D., 1986, Experimental study of tourmaline solubility in the system Na–Mg–Al–Si–B–O–H. Applications to the boron content of natural hydrothermal fluids and tourmalinization processes: *International Symposium on Experimental Mineralogy and Geochemistry, Nancy, 1986, Abstracts*, v. 140-141.
- Xu, J., Ding, R., Xie, Y., Zhong C., and Shan L., 2008, The source of hydrothermal fluids for the Sarekoubu gold deposit in the southern Altai, Xinjiang, China: Evidence from fluid inclusions and geochemistry: *Journal of Asian Earth Sciences*, v. 32, p. 247-258.
- Zack, T., Stockli, D.F., Luvizotto, G.L., Barth, M.G., Belousova, E., Wolfe, M.R., and Hinton, R.W., 2011, In situ U-Pb rutile dating by LA-ICP-MS: ^{208}Pb correction and prospects for geological applications: *Contributions to Mineralogy and Petrology*, DOI 10.1007/s00410-011-0609-4

CHAPTER TWO

RUTILE FROM PANASQUEIRA (CENTRAL PORTUGAL): AN EXCELLENT PATHFINDER FOR WOLFRAMITE DEPOSITION

Article published in Minerals 2019, 9(1), 9; <https://doi.org/10.3390/min9010009>

Received: 31 October 2018; Accepted: 18 December 2018; Published: 24 December 2018

Abstract

Abundant W-rich rutile in the tourmalinized wall-rocks from the Panasqueira W-deposit appears to be a marker of the onset of the main wolframite depositing event. Rutile displays spectacular zoning, both sector (SZ) and oscillatory (OZ). An extensive set of compositional data obtained on crystals, beforehand studied using back-scattered electron images and X-ray maps, was used to address (i) the effects of SZ on differential trapping of minor elements, and (ii) the significance of the OZ in deciphering fluid sources and fluid circulation dynamics. Particular attention was paid to Sn, W (Nb, Ta) concentrations in rutile as pathfinders of the W deposition. Concerning the sector zoning, W is more incorporated than (Nb, Ta) onto more efficient faces, whereas Sn contents are nearly not impacted. The net effect of the sector zoning is thus a progressive increase of the relative weight of Sn from pyramid to prism faces, in combination with a less significant increase in the relative weight of Nb + Ta. The oscillatory zoning concerns most minor elements: W, Nb (Ta), Fe, V, Cr and Sn. In the frequent doublets, the clear bands are in general enriched in W relatively to the dark ones, whereas the inverse is true for Nb and Ta. The doublets may be viewed as the result of the successive influx of (i) a W-rich, Nb + Ta poor fluid, abruptly replaced by (or mixed to) (ii) a Nb + Ta-rich and W-poor fluid. The Nb + Ta-rich fluid could be in turn related to a rare-metal granite layer observed atop of the Panasqueira granite.

Keywords: W-rich Rutile; sector zoning; oscillatory zoning; fluid source signature; wolframite; Panasqueira

1. Introduction

Rutile is the most abundant Ti-bearing mineral and a very common accessory mineral stable in a wide range of geological environments from igneous to sedimentary settings [1]. Rutile may incorporate a variety of elements, and in particular Al, V, Cr, Fe, Zr, Nb, Sn, Sb, Hf, Ta, W and U [2–10]. Trace elements in rutile may be used as marker of sediment sources, e.g., [11,12], or to probe subduction and magmatic processes, e.g., [1,13–15]. Rutile is also widely used to date (U/Pb) metamorphic events [1,16], and references therein], less commonly magmatic events, e.g., [17], or ore deposition, e.g., [18–21]. Zr content in rutile may also be used as a geo-thermometer [22].

Rutile is common in felsic magmatic rocks, and an extensive literature deals with Nb and Ta-bearing rutile in rare-metal granites and pegmatites as a marker of magmatic processes such as fractionation or mixing, e.g., [23–31]. Rutile is also found in a variety of ore deposit types, including orogenic gold, porphyry copper [32], VHMS (Volcanic-Hosted Massive Sulfide), skarns, and hydrothermal W–Sn veins [33]. HFSE (High Field Strength Elements) spectra in rutile may be used to discriminate different stages of ore deposition or different types of deposits [33].

W-rich rutile (i.e., rutile with ≥ 1 wt % W) is comparatively rare, and is mainly found in epithermal deposits [6], orogenic gold deposits [34–36], rare metal pegmatites [37], and W-bearing deposits, e.g., [33,38]. In such occurrences, W content in rutile may be as high as, for instance: 7.2 wt % in a Mo-bearing aplite [39]; 8 wt % in some W-skarn deposits [40]; 9.5 wt % in orogenic gold deposit of Kalgoorlie [36]; 9.6 wt % at Puy-Les-Vignes (W-deposit) [38]. Rutile is also known to display zoning textures, most commonly sector zoning, e.g., [6], but also oscillatory zoning, e.g., [10]. Yet, detailed studies of rutile zoning aimed to interpretation of the rutile growth environment are surprisingly rare.

In this paper, we explore W-rich rutile from the Panasqueira W–Sn–Cu deposit (Central Portugal), that is found to be abundant accessory phase in tourmalinized wall-rock. Both tourmaline and rutile are involved at the main wolframite depositing event [21] which has made Panasqueira one of the largest W deposit in Western Europe. This W-rich rutile displays spectacular zoning, both sector (SZ) and oscillatory (OZ). We use an extensive set of composition data to address (i) the differential trapping of minor elements in SZ, and (ii) the significance of the OZ in terms of fluid sources and fluid circulation dynamics. Particular attention was paid to Sn, W (Nb, Ta) concentrations in rutile as the latter may be considered as a pathfinder of the W deposition.

2. Geological Setting

Panasqueira is located in the Variscan Central Iberian Zone (CIZ) (Figure 1.19B). The Panasqueira W–Sn–Cu mine, active more than 100 years, was for long one of the largest tungsten deposits in Western Europe, amounting for at least c. 111 kt W (the sum of a past production of at least 88 kt W in 1947–2014 [41], and of remaining reserves + resources of ~ 23 kt W [42]), and thus contributing for more than one third to the CIZ tungsten endowment. The deposit is hosted in greenschist facies micaschists belonging to the Beira Schists Complex [43] and consists of a swarm of sub-horizontal W–Sn–Cu bearing quartz veins extending for over 10 km² with a vertical extent of around 300 m (Figure 1.19A). A large concealed granite body with a laccolith shape [44] is associated with a metamorphic contact spotted aureole, crosscut by the vein swarm. Atop of this body, layers and a cupola of rare metal granites [45–47] are more or less affected by greisenization and also overprinted by the vein system. This deposit has been the subject of many studies, e.g., [45,46,48,49,50–65]. The deposit experienced a protracted history, beginning with a strong tourmalinization of the wall-rocks [63,65], heralding the main wolframite deposition event. Rutilites are systematically associated with tourmaline and are dated using U–Pb method at 305.2 ± 5.7 Ma [65]

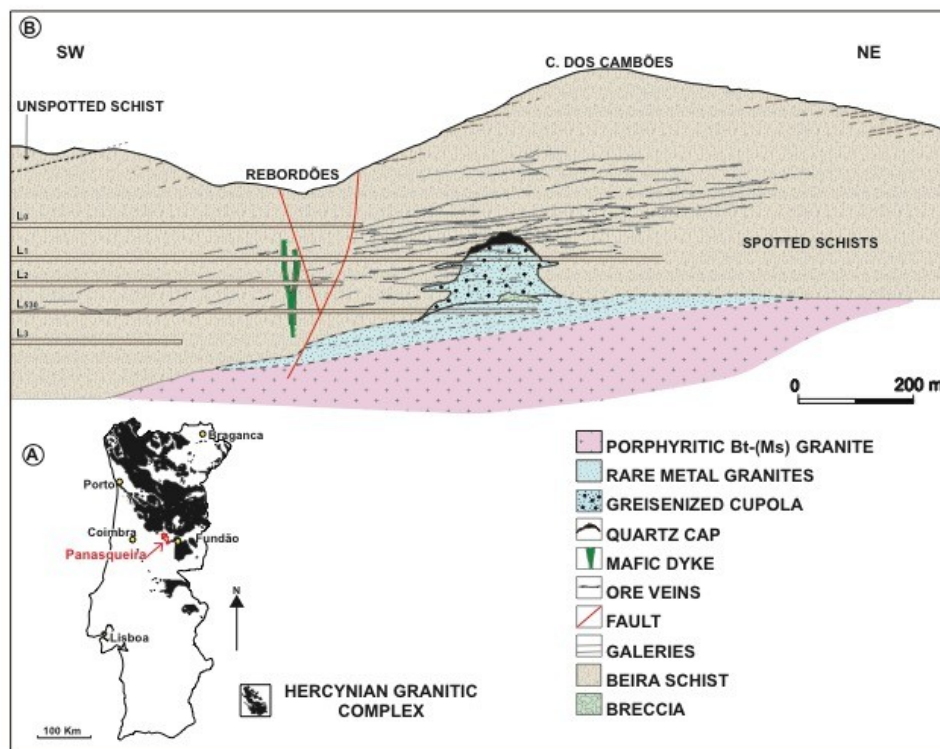


Figure 1.19. (A) Distribution of Hercynian granitic rocks and the Panasqueira location (modified after [45]). (B) Schematic cross section of the Panasqueira deposit, showing the concealed granites and greisenized cupola with a silica cap, and the gently dipping quartz–wolframite vein system (modified after [46,47]).

3. Material and Methods

Classical petrographic examinations have been carried out using an Olympus BX51 (transmitted and reflected light) optical microscope and a VHX-200 Keyence numeric microscope. Selected polished thin sections were studied with a JEOL J7600F scanning electron microscope (SEM) equipped with a Silicon Drift Detector (SDD)-type EDS spectrometer at the GeoRessources Laboratory (Nancy, France). Backscattered electron (BSE) images were obtained by setting the acceleration voltage at 15 kV. X-ray mapping was done using a CAMECA SX100 Electron microprobe (EPMA) equipped with a wavelength dispersive spectrometer (WDS), with a 12 nA current and an accelerating voltage of 15 kV. Micro-XRF mapping was done using the Bruker-Nano M4 Tornado instrument. This system has a Rh X-ray tube with a Be side window and polycapillary optics giving an X-ray beam with a diameter of 25–30 μm on the sample. The X-ray tube was operated at 50 kV and 200 μA . X-rays are detected by a 30 mm² XFlash® SDD with an energy resolution of <135 eV at 250,000 cps. All analyses were carried out at 2 kPa vacuum. Main elements such as Fe, Ti, Cl, Al, and Si were mapped, and composite images were generated. Major-element mineral compositions were determined using a JEOL J7600F SEM at the GeoRessources Laboratory (Nancy, France). Analytical conditions were a 1 nA current and an acceleration voltage of 15 kV, with a counting time of 60 s. Natural and synthetic oxides and silicate standards were used: MnTiO₃ (Ti), Cr₂O₃ (Cr), vanadinite (V), hematite (Fe), LiNbO₃ (Nb), LiTaO₃ (Ta), cassiterite (Sn) and scheelite (W). Detection levels were taken at ~1000 ppm for all elements, except Ta. Due to overlap with the W peak, Ta detection level is set at ~3000 ppm. However, in many cases, although a clear shouldering on the W peak testifies for the presence of Ta, disentangling is not feasible. In such instances, we arbitrarily set a Ta value at 1500 ppm, i.e., at the best estimate without bias.

4. Results

4.1. Petrography

Rutile crystals are found either scattered or densely disseminated in the tourmalinized wall rocks, or associated with tourmaline in thin early quartz veinlets (Qcs) resulting from a crack-seal process [58] (Figure 1.20A,B). In the wall rocks, they occur either as single crystals (Figure 1.21C,D) or aggregates (Figure 1.21B), sometimes chain of crystals, with a size from less than 10 μm up to 80–100 μm , varying from sample to sample. They locally may be associated with zircon or Th-rich monazite. In the Qcs veinlets, they form isolated larger crystals (Figure 1.21E,F), up to 500 μm or more in diameter. Rutile crystals commonly contain euhedral quartz or muscovite inclusions.

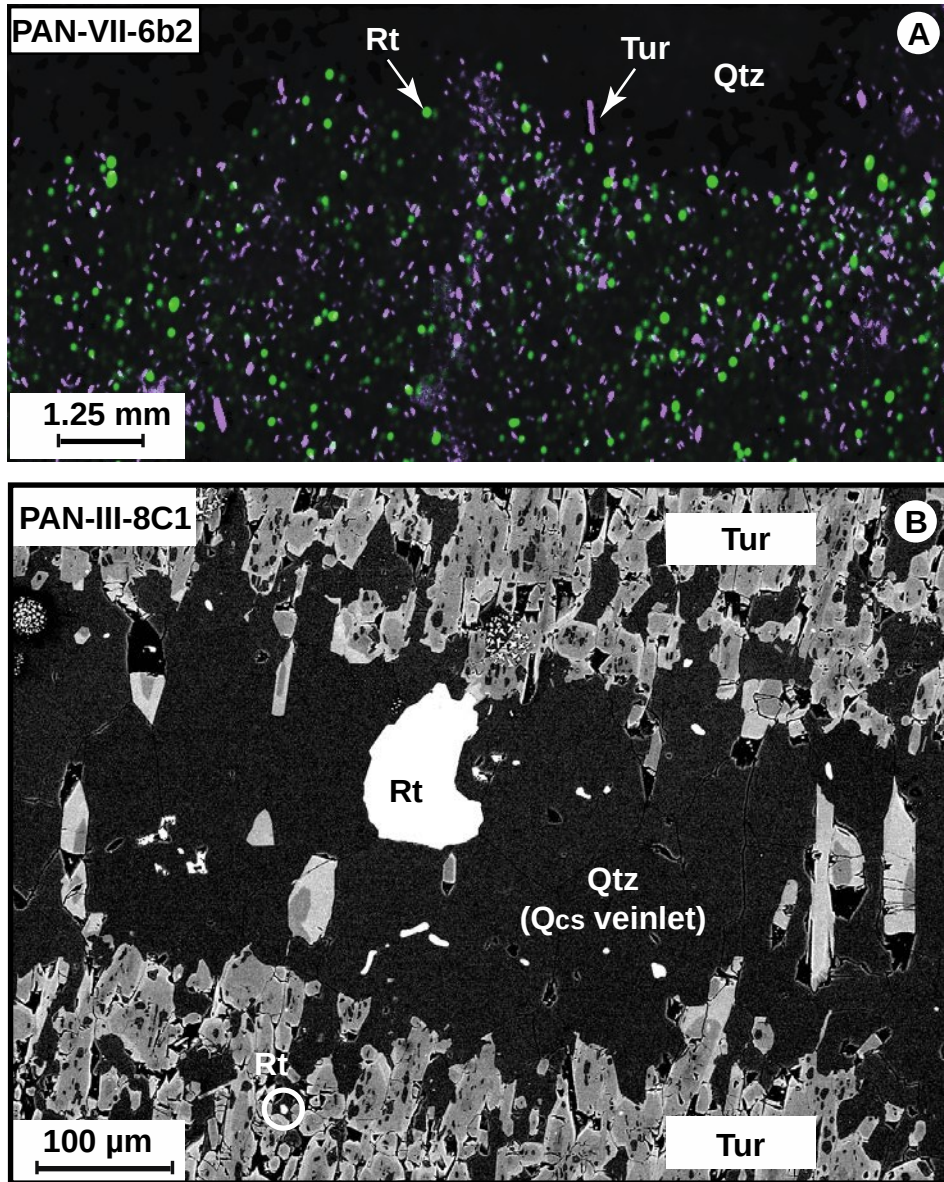


Figure 1.20. (A) A false-colored μ -XRF composite map of the wall rock from a wolframite-bearing quartz vein. Tourmaline (Tur) is imaged by chlorine and rutile (Rt) by titanium, Qtz = quartz. (B) BSE image of an early quartz veinlet (Qcs) bearing rutile. Tourmalinization in the wall rock is coeval with the Qcs, as shown by the tourmaline crystals protruding into the veinlet.

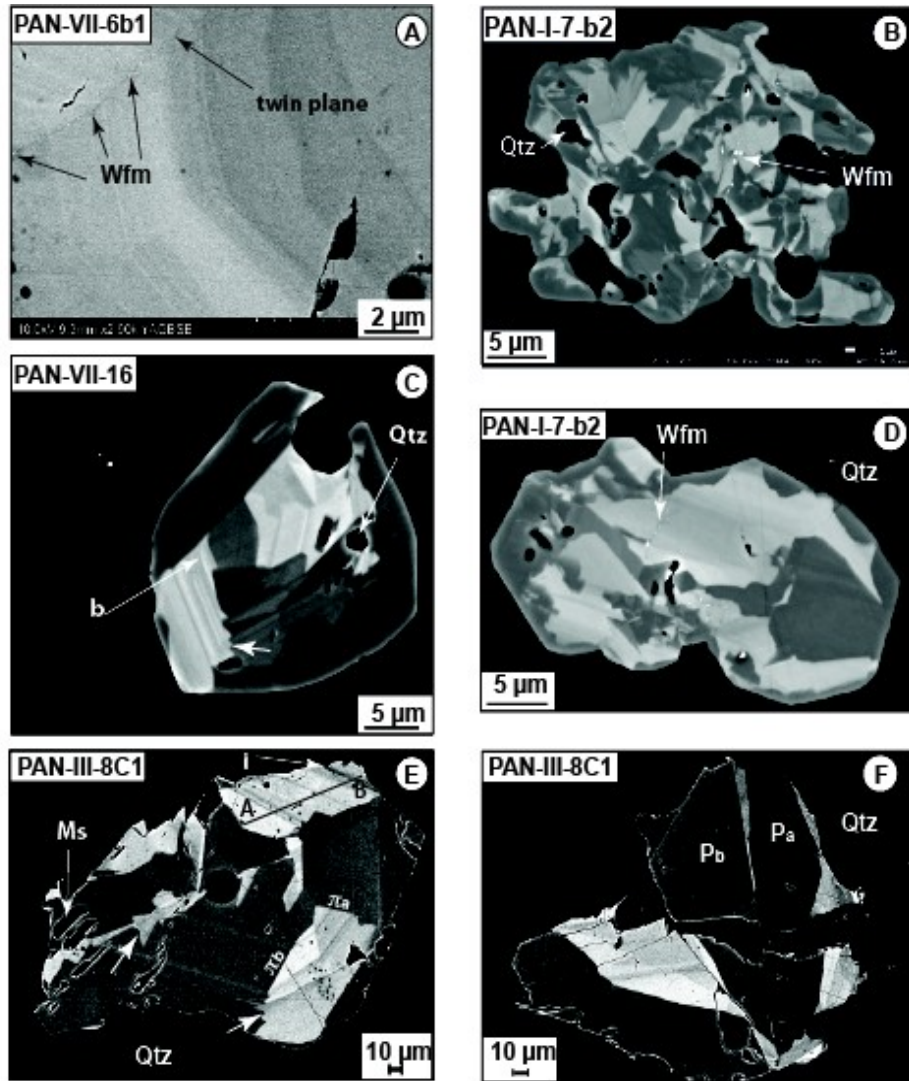


Figure 1.21. Aspects of the Panasqueira rutile crystals (SEM-BSE). Note the ubiquitous sector zoning, marked by the strong contrast in BSE images, and the well-expressed oscillatory zoning (OS), particularly in metal-rich pyramidal sectors (A, F–G crystals from Qcs veinlets, B–D crystals from tourmalinized wall rock). (A) Location of wolframite nano-inclusions along a twin plane. (B) Aggregate of crystals, with abundant wolframite (Wfm) as nano-inclusions. (C) Small isometric crystal; note the "fir-tree" texture (arrow) typical of the sector zoning, and the beveling (b) in the OS. (D) Composite crystal, rich in wolframite (Wfm) nano-inclusions; note the "fir-tree" texture (arrow). (E) Particularly well-expressed oscillatory zoning in a large crystal; note the inversion in the OS trends in i, and the "fir-tree" texture (arrows); π_a and π_b , two types of pyramid faces (see text for definition); Ms muscovite; A–B: profile in Figure 1.28. (F) Twinned crystal; P_a and P_b , two types of prism faces (see text for definition).

Micro- to nano-inclusions (1–100 nm) of zircon or wolframite are not rare, and up to 10 or more nano-crystals may be contained in a single crystal. Wolframite nano-inclusions are usually located at crystallographic boundaries (such as faces intersections, twin planes, and quartz inclusion boundary) (Figure 1.21A,B,D), suggesting that their growth was coeval with the host rutile. Compositions estimated from SEM-EDS are ferberitic, with a Fe/Fe + Mn ratio between 0.67 and 0.83. From detailed relationships between rutile, tourmaline and early wolframite, it is inferred that rutile deposition was coeval with the inception of the main wolframite depositing event [21].

4.2. Rutile Chemical Composition

The crystals are typically zoned on a scale of the order of 10 μm or less, precluding measurement of their chemical composition by EPMA. For this reason, the chemical composition was measured (including oxygen) by SEM-EDS on the basis of the back-scattered images. Sixty-one crystals from 12 samples were studied in great detail, and a selection of results is presented in Table 1 (the whole set of data is provided in Supplementary Data Table S1). Structural formulae were calculated on a 3 cation basis, to conform to the general formula AB_2O_6 . With an average 6.04 apfu (Atom Per Formula Unit) the calculated structural O is found to be very close to 6, attesting to the good quality of the analyses. The Panasqueira rutile systematically contains Fe, V, Sn, Nb, Ta and W, all with highly variable contents, in part because of sector zoning effects (see below): Fe from 0.18 to 2.95 wt %, V from below detection level (bdl) to 3.48 wt %, Cr from bdl to 2.41 wt %, Nb from bdl to 1.64 wt %, Ta from bdl to 2.17 wt %, and W from 0.20 to 9.45 wt %. Nb + Ta is usually lower than 0.5 wt %, and the Nb/Nb + Ta ratio varies from 0.05 to 0.97, being on average 0.6.

The crystals display a marked sector zoning, often combined with typical oscillatory zoning (Figure 1.21). All the minor elements, W, Nb (Ta), Fe, V, Cr and Sn, are equally involved in the zoning (Figure 1.22). Sector zoning is exhibited mostly by W and Fe, a fact already mentioned by [6], and, although to a lesser extent, by Nb and Ta (Figure 1.22B,F-K), whereas Sn, V (and Cr) are less systematically affected: compare Sn or V in Figure 1.22D-H, and Figure 1.22J-M.

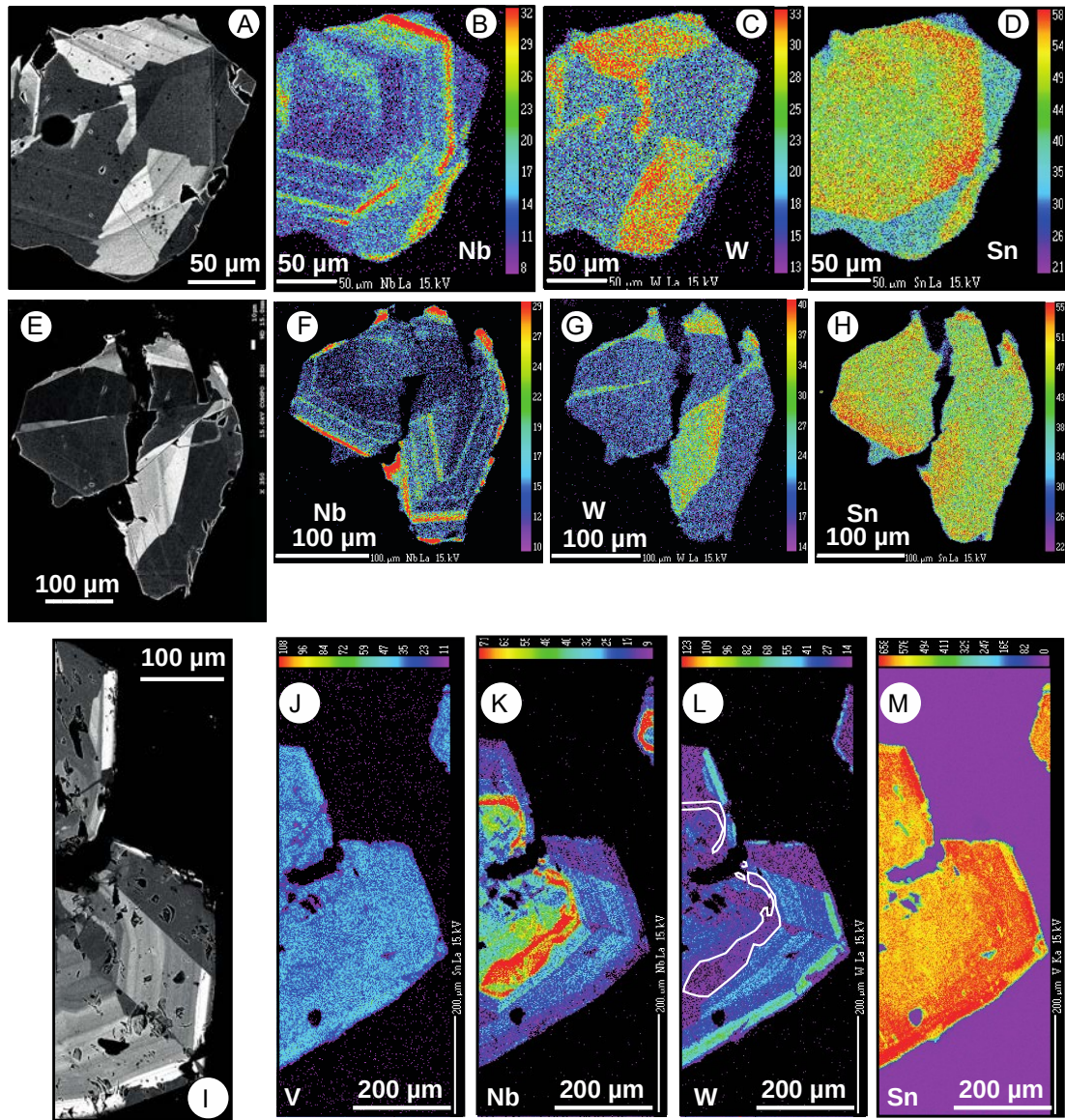


Figure 1.22. Characterization of the zonation in Panasqueira rutiles by coupling BSE images and false-color coded X-ray (EPMA) maps. Warmer colors correspond to higher concentrations. All crystals are from Qcs veinlets. Note the combination of conspicuous sector and oscillatory zonation. (A) to (D): a crystal from sample PAN-III-8-c1. (A) BSE image, (B) to (D) X-ray maps. (E) to (H): a twinned crystal from the same sample. (E) BSE image, (F) to (H) X-ray maps. (I) to (M): part of a very large crystal from sample PAN-VII-6-b1. (I) BSE image, (J) to (M) X-ray maps; in (L) white lines underline the areas with the highest Nb concentrations in (K).

5. Interpretation

5.1. Crystal Chemistry

In the general AB_2O_6 structure, in which TiO_2 may be seen as an end-member, entrance of W^{6+} or $R(Nb, Ta)^{5+}$ is generally thought to be due to coupling with a R^{3+} cation, according to the exchange vectors:

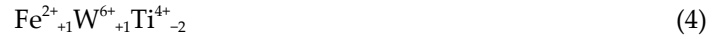


Exchange between W^{6+} and R^{5+} is also possible, equally involving coupling with a R^{3+} cation, according to:



The R^{3+} cation could be Al^{3+} , not documented at Panasqueira, and Cr^{3+} , V^{3+} or Fe^{3+} .

Iron is commonly thought to enter the rutile structure as Fe^{3+} , e.g., [66], but Fe^{2+} is sometimes considered [37], entering the structure according to the vectors:



Tin (Sn^{4+}) directly replaces Ti. Among the three possible V valences, V^{4+} is the more prone to replacing Ti, followed by V^{3+} and then V^{5+} , according to [67]. V^{4+} will directly replace Ti, and V^{5+} will exchange with R^{5+} .

The valences of Fe and V in the rutile structure may be discriminated according to the following considerations. When all vectors are considered, and both Fe^{2+} and Fe^{3+} are supposed to be present, the following relationship is valid (in apfu):

$$2Fe^{2+} + (2a + b - c) + Cr + V^{3+} = 2W + Nb + Ta \quad (6)$$

where all V is considered V^{3+} and a, b, and c are respective coefficients (between 0 and 1) of the vectors (1), (2) and (3) where $R^{3+} = Fe^{3+}$. With $Fe^{2+} = X$ and consequently $Fe^{3+} = 1 - X$ (i.e., $2a + b - c = 1 - X$), equation (6) reduces to:

$$X + 1 = 2W + Nb + Ta \quad (7)$$

It follows that in a $Fe + Cr + V$ vs. $2W + Nb + Ta$ diagram, when all V is considered to be V^{3+} , all the rutile analyses should plot between two lines corresponding to two extreme cases:

$$2Fe^{2+} + Cr + V = 2W + Nb + Ta \quad (\text{all Fe as } Fe^{2+}) \quad (8)$$

$$Fe^{3+} + Cr + V = 2W + Nb + Ta \quad (\text{all Fe as } Fe^{3+}) \quad (9)$$

thus, theoretically allowing a qualitative evaluation of the Fe^{2+} to Fe^{3+} proportion. In the Panasqueira case, owing to the fact that as a rule $2W \gg Nb + Ta$, the slopes of lines (8) and (9) will be close to 1 and 0.5, respectively. If, nevertheless, other V valences are involved, they will be expressed by shifts of the plotted analyses in the preceding diagram, i.e., vertically if V^{4+} is present, and horizontally if V^{5+} is present. If the analyses plot above line (8), the involvement of V^{4+} is likely, and in the same way, if they plot below line (9),

the presence of V^{5+} may be envisaged. However, if they plot in between the two lines (8) and (9), the effects of valence changes in Fe and V will be indiscernible.

Nevertheless, replacing Fe + Cr + V by Fe + Cr in the testing diagram may allow an independent evaluation of the possible effect of the V^{3+} to V^{4+} shift. As seen in Figure 1.23A, when plotted in the Fe + Cr + V (apfu) vs. 2W + Nb + Ta (apfu) diagram (i.e., assuming all V as V^{3+}), the Panasqueira rutile crystals predominantly occupy the whole interval between the two (8) and (9) lines, with a neat tendency to overlap the " V^{4+} domain" and with trends which are not rooted at zero. By contrast, when plotted in the Fe + Cr (apfu) vs. 2W + Nb + Ta (apfu) diagram (i.e., assuming all V as V^{4+}), the Panasqueira rutile crystals are in their great majority on (or close to) the (9) line (Figure 1.23B). This behavior is readily explained if in the crystals (i) Fe is predominantly present as Fe^{3+} , and (ii) concomitantly V is predominantly present as V^{4+} . In a few occurrences, however, distinct shifts from the (9) line are still present in the diagram of Figure 1.23B. In one case (sample II-10a), vertical shifts may be interpreted as recording the presence of Fe-rich nano-inclusions, most likely, ilmenite. In sample XIII-1c, most analyses are under the (9) line, meaning that in this sample, a higher proportion of vanadium is present as V^{3+} .

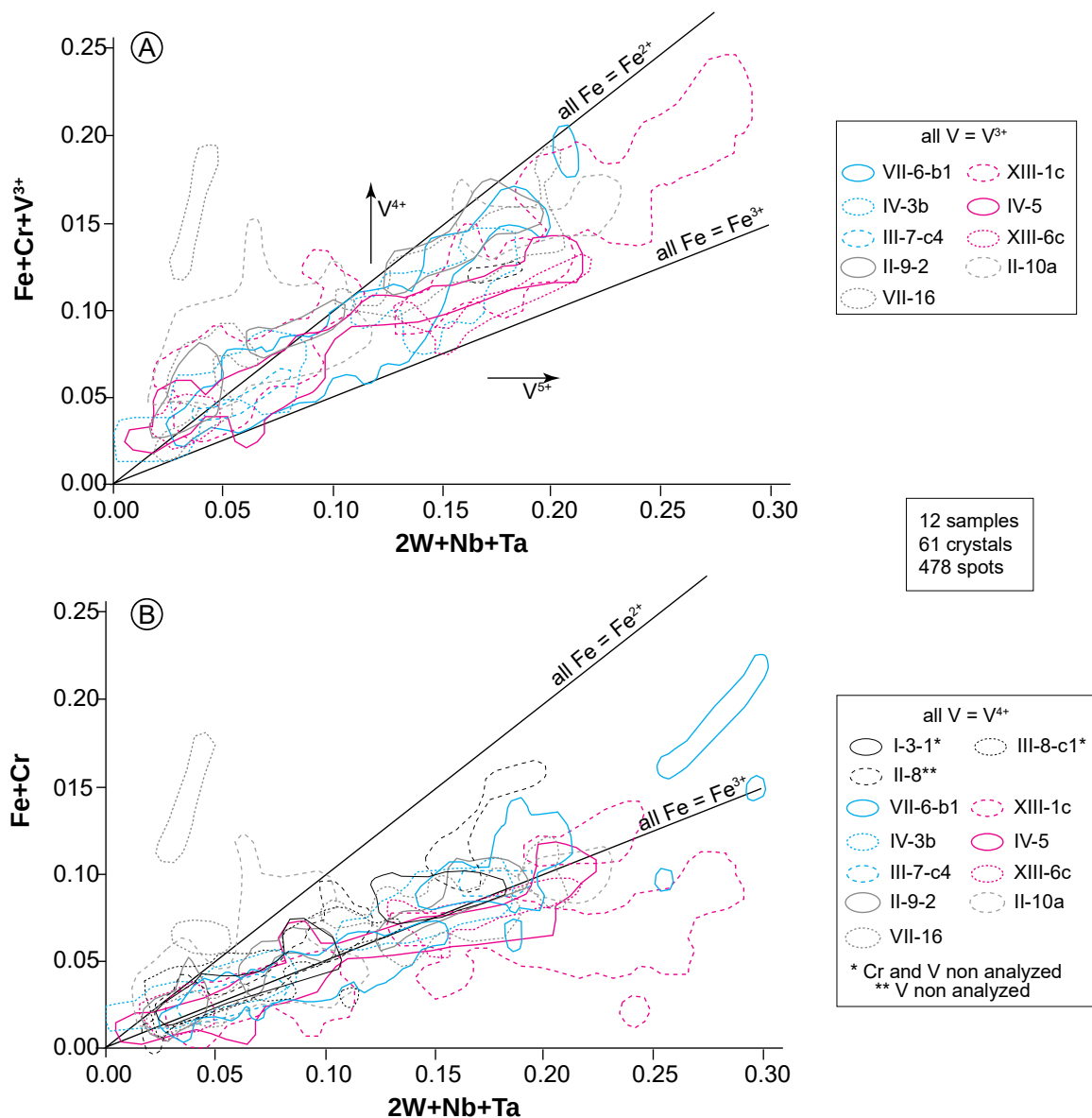


Figure 1.23. Unravelling Fe and V valences in the Panasqueira rutile: plot of trivalent cations vs. $2W + Nb + Ta$. (A). All V is assumed to be present as V^{3+} . (B) All V is assumed to be present as V^{4+} . When present in a sample, outliers are drawn as isolated from the main field for this sample. Explanations in the text.

5.2. Compositional Zoning: Sector Zoning

Patterns of sector zoning are said to be "a function of both crystal habit and how it changes with progressive growth", commonly leading to typical "fir-tree" shaped sectors [68]. BSE images of rutile sections may therefore be complicated and difficult to interpret, in particular, where crystals are aggregated, which is a common case at Panasqueira (e.g., Figure 1.21B). On favorable sections, seemingly close to being parallel, or orthogonal, to the prism axis, comparison of BSE images with ideal rutile form shows that we are apparently dealing with two tetragonal prisms ($a = \{100\}$ and $m = \{110\}$) and two dipyrramids ($e = \{101\}$, and $s = \{111\}$) (Figure 1.24). It appears that the crystal sectors that more efficiently concentrate metals are associated with pyramid faces (Figure 1.24). This is at variance with the opinion of [6], who thought that this role was

taken by the prism faces in the W-rich rutile crystals at Kori Kollo gold mine (Bolivia). It also appears that the two sets of prisms or the two sets of pyramids are not equivalent, one of them being systematically more efficient in concentrating minor elements than the other, as seen by the contrasting grey hues in BSE images (Figure 1.24). Unfortunately, it was not possible to properly index the faces, and consequently we choose to label π_a and π_b the two sets of tetragonal pyramid faces, with π_b the more efficient, and P_a and P_b the two sets of tetragonal prism faces, with P_b the more efficient (Figure 1.24). The different forms are variably combined, with apparently all the possibilities between prism-dominated or pyramid-dominated habits, nearly isometric habits being seemingly the more common. Otherwise, P_a and π_b are by far the most common faces.

Quantitatively, systematic measurement of rutile composition as a function of the face shows that W and Fe are preferentially concentrated in the pyramid faces, as do Nb and Ta in a lesser proportion, whereas V, (Cr) and Sn are almost not affected by the differential trapping (Table 1). The maximum W concentration in a given type of face is variable, depending on the samples: 1.12 to 10.7 wt % in π_b , 1.07 to 7.62 wt % in π_a , 0.64 to 3.92 wt % in P_b and 0.26 to 1.40 wt % in P_a . In π_b and π_a , the Panasqueira rutile appears as one of the richest in W worldwide. The partitioning of the four types of faces is well displayed in the W-Sn-(Nb + Ta) diagram in Figure 1.25. As seen in Figure 1.25, W is more incorporated than Nb and Ta onto the more efficient faces, whereas Sn contents are nearly not impacted. As a consequence, the net effect of the sector zoning is a progressive increase of the relative weight of Sn from π_b to π_a then to P_b and finally to P_a . This effect combines with a less significant increase of the relative weight of Nb + Ta.

Figure 1.24. Interpretative identification of the crystallographic faces involved in the sector zoning (SEM-BSE). Prism faces: P_a and P_b;

crystal face	Qcs veinlet					wall rock					
	A Pa	A Pb	A π_a	A π_b	A π_b	B Pa	C Pb	D π_a	E π_a	F π_b	G π_b
W	0.99	1.75	3.92	5.01	9.13	0.33	1.64	2.59	4.37	5.97	6.37
Sn	0.51	0.62	0.75	0.45	0.71	0.67	0.75	0.84	0.95	1.66	0.79
Nb	1.24	0.16	0.21	0.26	0.22	0.23	0.12	0.16	0.21	1.48	<i>bdl</i>
Ta	0.15	0.34	0.15	0.15	0.15	0.43	0.36	0.32	0.15	0.58	0.33
Cr	<i>bdl</i>	<i>bdl</i>	0.27	0.15	1.39	<i>bdl</i>	0.18	<i>bdl</i>	1.56	<i>bdl</i>	<i>bdl</i>
V	0.58	0.5	0.96	0.74	0.66	0.19	0.67	0.56	0.55	0.60	0.56
Fe	0.59	0.58	0.96	1.29	1.40	0.42	0.36	0.95	0.20	2.05	1.91
Ti	56.22	57.28	54.11	53.46	50.08	58.24	57.09	55.75	53.28	50.72	51.85
O	39.28	39.68	38.79	38.5	37.92	39.70	39.67	39.13	38.39	38.00	37.85
Σ	99.65	100.91	100.12	100.01	101.66	100.21	100.84	100.30	99.80	101.06	99.67
base 3 cations											
W	0.013	0.023	0.053	0.069	0.127	0.004	0.022	0.035	0.060	0.083	0.089
Sn	0.011	0.013	0.016	0.010	0.015	0.014	0.015	0.017	0.020	0.036	0.017
Nb	0.033	0.004	0.006	0.007	0.006	0.006	0.003	0.004	0.006	0.41	
Ta	0.003	0.005	0.002	0.003	0.002	0.006	0.005	0.004	0.003	0.008	0.005
Cr			0.013	0.007	0.069		0.008	0.000	0.075		
V	0.028	0.024	0.047	0.037	0.033	0.009	0.032	0.027	0.027	0.030	0.028
Fe	0.026	0.025	0.043	0.058	0.064	0.018	0.016	0.042	0.009	0.094	0.088
Ti	2.882	2.906	2.820	2.810	2.683	2.943	2.899	2.870	2.799	2.708	2.773
O	6.025	6.023	6.049	6.054	6.078	6.002	6.026	6.027	6.035	6.071	6.057
Nb+Ta	0.04	0.01	0.01	0.02	0.01	0.01	0.01	0.01	0.01	0.05	0.01
Nb#	0.92	0.43	0.72	0.74	0.75	0.51	0.39	0.49	0.630	0.83	0

Table 1. Selected EDS analyses of different faces of rutile crystals; for labeling of faces, see text; *bdl* below detection level; for Ta, 0.15 is set as the best estimate value when disentangling from the W peak was not feasible (see chapter "Methods"). A: sample PAN-VII-6-b1; B: sample PAN-II-10a; C: sample PAN-IV-5; D: sample PAN-IV-3b; E: sample PAN-VII-16; F: sample PAN-XIII-6-c2; G: sample PAN-IV-5.

pyramid faces: π_a and π_b (see text for definitions). All crystals are from tourmalinized wall rock, except D, taken from a Qcs veinlet. (A) Theoretical rutile crystal combining two tetragonal prisms (a and m) and two tetragonal dipyrramids (e and s). In the figure is also shown one of the two possible connections between the indexed crystallographic faces and the P_a, P_b, π_a , π_b notation. (B) Crystal with a prismatic habitus; Ms muscovite, Wfm wolframite. (C) Section near to perpendicular to A4 axis. Sector zoning is well defined, with typical "fir-tree" texture (arrow). Note the contrast between the syn-rutile growth wolframite (Wfm) nano-inclusions, located at the OS boundaries, and the cassiterite (Cst), post-dating rutile growth. (D) Isometric crystal, seemingly showing a greater development of the pyramid faces. (E) Two large crystals displaying a morphology controlled by the dipyrramids, with a flattened prism: crystal 1 would be cut near to perpendicular, and crystal 2, near to parallel, to the A4 axis. Both crystals are earlier than the arsenopyrite (Apy) (corrosion: arrows). (F) The two types of prism face are well discriminated in a section oblique onto the A4 axis; Ms muscovite. (G). The two types of pyramid face are well identified. (H). Example of a nondescript section in which face identification is not easy and may remain subjective; Ms muscovite, Zrn zircon.

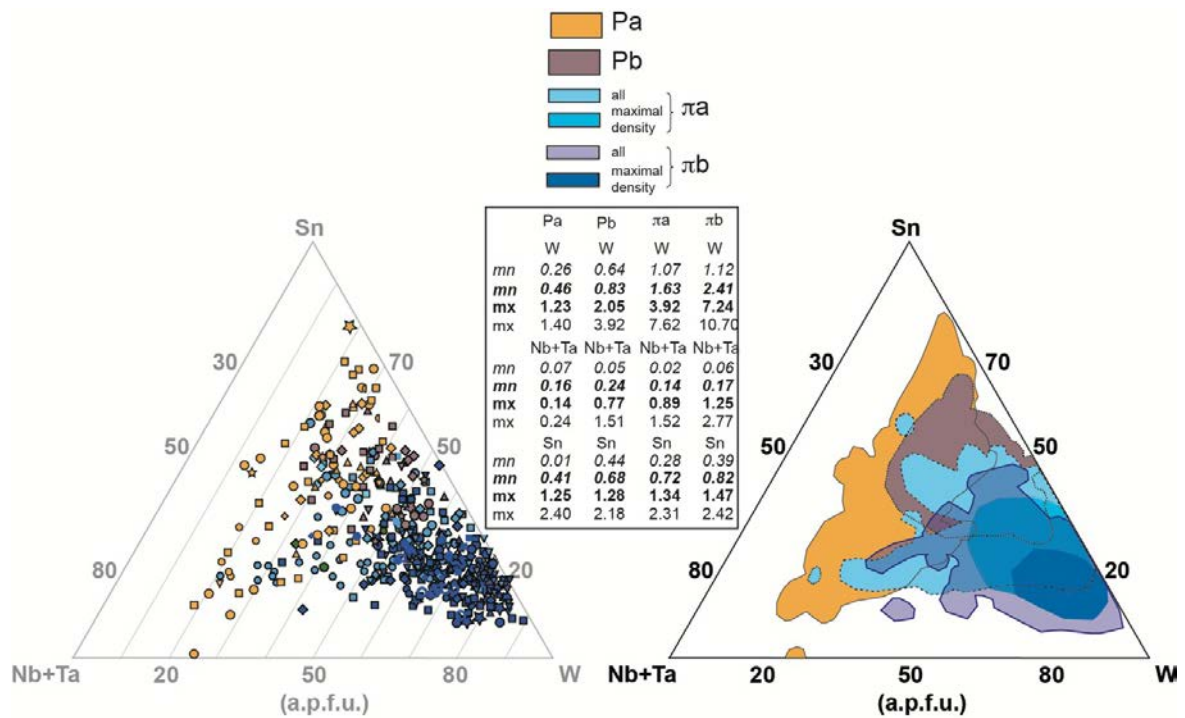


Figure 1.25. Demonstration of the sector zoning compositional effects in the W–Sn–(Nb + Ta) triangular diagram. Insert: minimal and maximal values (wt %) for W, Nb + Ta and W according to the type of faces. Both absolute (*italics*) and average (**bold**) values are given. Not the regular changes from the less to the more efficient faces.

5.3. Compositional Zoning: Oscillatory Zoning

Superimposed to sector zoning, oscillatory zoning is conspicuous, in particular in the pyramid sections (π_a and π_b). In most of the large crystals from Qcs veinlets, and in many of the smaller crystals in the wall rocks, oscillatory zoning is characterized by alternation of “clear” and “dark” bands in BSE images (Figure 1.26). Zoning characteristics are the same regardless of the rutile setting. The band boundaries appear as clear-cut, although in many instances the boundary is marked by a short-range but continuous variation of the grey hues, from the clear to the dark band. In the latter case, it thus appears that the two bands form a doublet, limited by abrupt boundaries. In a limited number of occurrences, the doublet is inverted, starting from the dark band (Figure 1.26A).

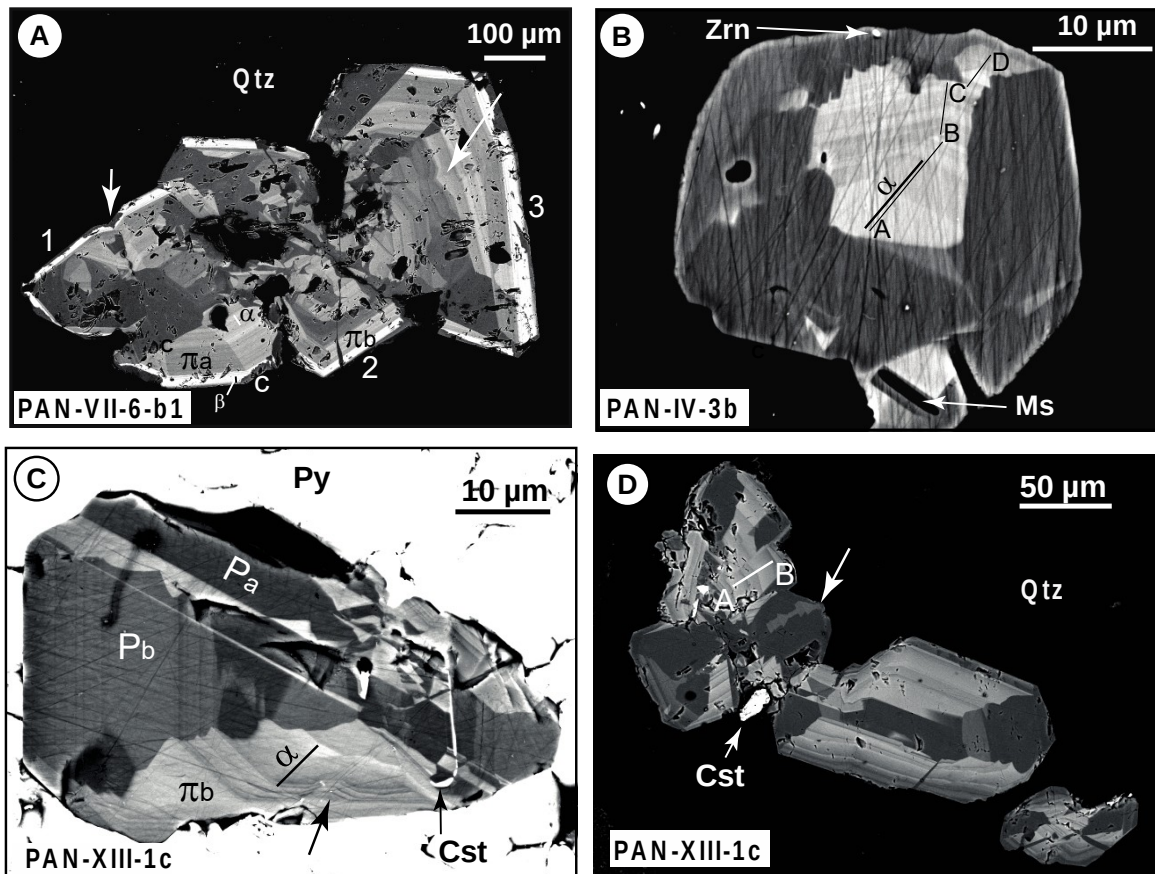


Figure 1.26. Rutile crystals with well-organized oscillatory zoning, in which are implanted the profiles of Figures 1.27 and 1.28 (SEM-BSE). (A) Three aggregated large crystals (1, 2, 3) from a Qcs veinlet. Profiles α and β in Figure 1.27 are from crystal 1. The two dipyrramids (π_a and π_b) are well displayed. Note the late corrosion (c) and the presence of twins (arrows, cf. Figure 1.21A). (B) Small crystal from a tourmalinized wall rock. Profile α is presented in Figure 1.27, and profile ABCD in Figure 1.28. Zrn zircon (C) Large crystal from a Qcs veinlet that we named Rt 5. The crystal is encapsulated in a late pyrite (Py), and crosscut by cassiterite (Cst). Note the convoluted oscillatory zoning (arrow). Profile α is presented in Figure 1.27. (D) Group of crystals from the same Qcs veinlet. Note the well expressed "fir-tree" texture (arrow). Profile AB is presented in Figure 1.28 where is noted as Rt7. Cst cassiterite.

Careful examination at high resolution suggests that doublets may in reality be the rule, the transition between the clear and dark bands being however extremely fast, in the micrometer range. The size of the bands is highly variable, in the 10–25 μm range (with possible intercalations of smaller 1–5 μm ribbons) in the larger crystals, down to 1–5 μm in the smaller crystals from the wall rocks (e.g., Figure 1.21C and Figure 1.26B). At the crystal scale, zoning is expressed as succession of large strips, in the 50–150 μm range in the larger crystals, and 5–15 μm in the smaller. Each strip groups several elementary bands or doublets. The strips are characterized by major compositional changes as revealed in both SEM imaging and X-ray (EPMA) mapping (Figure 1.24).

All the minor elements, W, Nb + Ta, Fe, V, Cr and Sn, are involved in the compositional zoning. Three zoning scales must be considered. (i) At the band scale, owing to their small size, only in a very limited number of cases was construction of a profile possible. The results (Figure 1.27) did not provide a systematic organisation of the data. (ii) At the doublet scale (Figures 1.27,1.28) it appears that the clear bands are in general enriched in W relatively to the dark ones, whereas the inverse is true for Nb and Ta, which are most commonly conspicuously enriched in the latter. The clear/dark sharp boundary is always well reflected

into jumps in these minor element contents. Tin and vanadium behavior is more erratic, these elements being either correlated or anti-correlated with Nb and Ta. (iii) At the crystal scale, some regularity is observed.

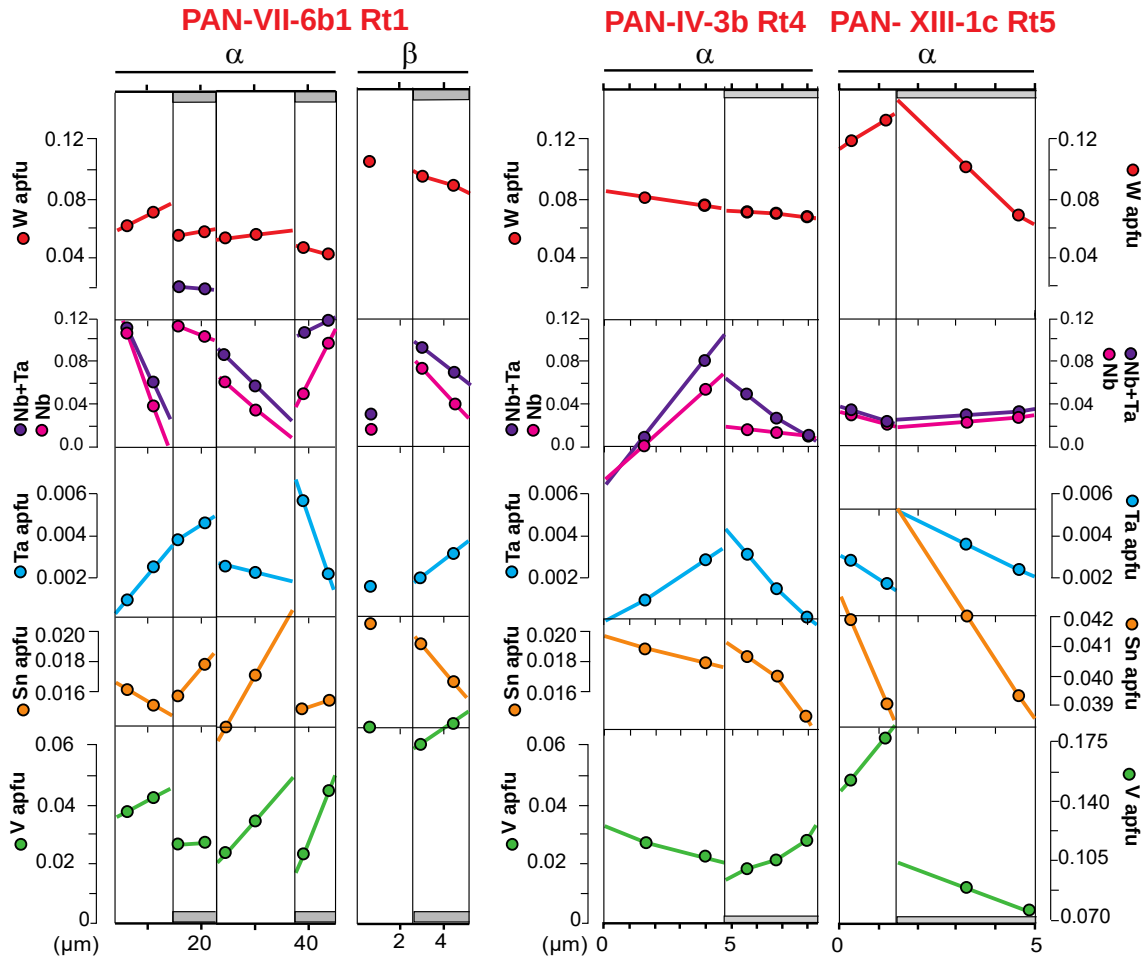


Figure 1.27. A selection of doublet profiles. The profiles are located in Figure 1.26 (PAN-VII-6-b1: Figure 1.26A; PAN-IV-3b: Figure 1.26B; PAN-XIII-1c: Figure 1.26C). Explanations in the text.

As seen in Figures 1.22 and 1.28, there is a clear tendency of Nb to be anti-correlated with W, and element contents are modulated at the scale of a few doublets (Figure 1.28). Tin and vanadium are less variable, and display contradictory behavior, being either correlated with Nb + Ta and anti-correlated with W (Figure 1.22J,K,L,M) or the contrary (Figure 1.22B,C,D and Figure 1.22F,G,H), just as in the doublet cases. Comparison of rutile crystals from different settings, even at the sample scale, shows that there are no general correlations: crystals may exhibit evolution from a Nb-rich and W-poor core to a W-rich and Nb-poor rim (PAN-VII-6-b1, Figure 1.22K,L), or the inverse (Figure 1.22F,G), or show moderate variations around middle W contents, which seems the most common case (Figure 1.22C).

6. Discussion

6.1. Oscillatory Zoning: External or Internal Control?

Several theoretical and experimental works, concerning either silicate growth in a magmatic medium [69–72], or the hydrothermal growth of barite [73], or calcite [74,75], have shown that oscillatory zoning (OZ) may be due to internal factors. The competition between the growth speed and the elemental diffusion rates leads, in some conditions, to a self-organized process resulting in oscillatory zoning (OZ) without need for a change in the generating medium. Some workers emphasize the role of “impurities” in the appearance of self-organization, e.g., [76,77]. The self-organization point of view has been however challenged, some workers pointing out that oscillatory zoning may be related to both internal and external factors, e.g., [6], and others showing that oscillatory zoning may be entirely controlled by external factors, e.g., [78,79]. Experiments on calcite growth lead [75] to conclude that whereas large scale elemental variations reflect the overall changes of the growth solution, the finer scale modulations (OZ) are caused by growth-rate controlled incorporation of trace elements.

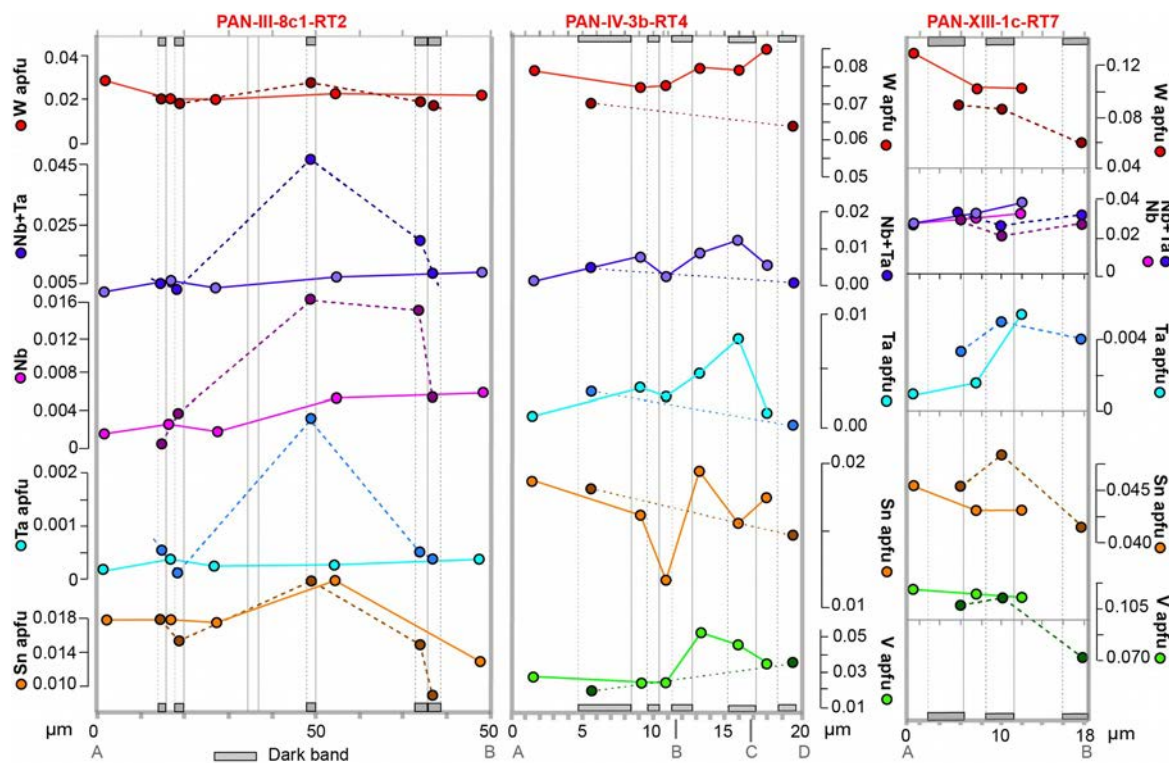


Figure 1.28. Minor element profiles in a selection of doublets from Panasqueira rutile, showing the time-controlled modulation of the minor element contents. Continuous tie-lines rely the onset of clear bands, whereas dotted tie-lines rely the onset of dark bands. The profiles are located in Figure 1.21 (PAN-III-8-c1-Rt2: Figure 1.21E, line AB) and in Figure 1.26 (PAN-IV-3b-Rt4: Figure 1.26B, line ABCD; PAN-XIII-1c-Rt7: Figure 1.26D, line AB). Explanations in the text.

All the self-organization models yield stationary theoretical profiles characterized by more or less pronounced asymmetry, quasi-periodical evolution of the composition, regular size of the bands with oscillation between constant bounds. Nevertheless, very strong gradients may be produced, mimicking discontinuities. These characteristics are poorly matched by the doublets characterizing OZ in the Panasqueira rutile crystals (Figure 1.26): (i) the successive doublets are of various size, (ii) there is no real oscillation of the contents between fixed bounds from one doublet to the other, (iii) the internal structure of the doublets is not regular, the clear and dark bands being variously large or narrow between adjacent doublets (Figure 1.27), and (iv) elemental variations within doublets are not constrained to one and the same pattern. Therefore, to the possible exception of the narrower banding in the large crystals (which could well be explained by self-organization), it must be concluded that the oscillatory zoning in the Panasqueira rutile crystals was essentially developed under external constraints. As crystallization temperature is not expected to have much varied [63], and unless pressure variations exert a major control on element partitioning into the rutile, which is thought to be unlikely, it results that the zoning reflects variations in the composition of the hydrothermal fluid.

Owing to sector zoning, interpretation must be based on homogeneous data, i.e., on data from the same kind of crystal forms, namely on the pyramid data, in particular, from the π_b faces. With this restriction, the rutile data may help to further enlighten the fluid characteristics. Yet, the information the rutile can yield must be considered to cover shorter time ranges than in the tourmaline case. This is shown by the absence of global correlation in the zoning features, suggesting that the crystallization of a given rutile crystal spanned less time than the coeval tourmaline. This is consistent with the fact that well-zoned rutile crystals may be included in tourmaline.

6.2. Open or Closed System Evolution?

Compositional variations may be controlled by either close- or open-system conditions of growth. There are no experimental data to constrain the W behavior in the course of fractional crystallization of a W-bearing rutile. According to [80], Nb being more compatible than Ta in a rutile crystal, a decrease of the Nb to Nb + Ta ratio is expected during crystallization of a Nb–Ta rutile in a closed system. As seen in Figure 1.27, a decrease of this ratio is not systematic, and when occurring, it is not associated with a correlative systematic variation of neither W nor Nb + Ta contents. In addition, the strong compositional changes at the clear/dark boundary in the OZ doublets is difficult to reconcile with fractional crystallization, which is on the contrary expected to yield rather continuous compositional variations. It is thus thought that the Panasqueira rutile grew under open-system conditions. Yet, in the context of sector zoning, it must be recalled that, according to [68], within-sector compositional changes may be induced by simply changing the normal growth rates of the corresponding faces, these changes being however difficult to separate from those in fluid chemistry. In the present case, it is thought that this effect may in part explain the apparently

chaotic aspects of the minor elements behavior in the profiles of Fig.1.28. In an open-system perspective, most of the doublets may be viewed as the result of the successive influx of (i) a W-rich, Nb-Ta poor fluid, abruptly replaced by (or mixed to) (ii) a Nb-Ta-rich and W-poor fluid.

6.3. Oscillatory Zoning as a Consequence of Seismic Activity?

To go further in the interpretation, we must now consider the timescale of growth for a given doublet. For a large spectrum of mineral species, and in a large temperature (25–450 °C) and pressure (0.1–200 MPa) range, experimentally measured crystal growth rates are comprised between a few 10^{-1} nm·s⁻¹ and 10–20 (up to 100) nm·s⁻¹ (ZnO [81]; berlinite [82]; quartz [83,84]; fluorite and AgCl [85]; vaterite [86]; calcite [87–89]). As a rule, the rates increase with the concentration of the solution and the temperature of crystallization. For the Panasqueira rutile, growing at c. 450 °C, it seems then reasonable to bracket the growth rates between 1 and 10 nm·s⁻¹, as a first order of magnitude. With such values, the time growth of a 20 µm-large band in a rutile crystal would be in the order of $2 \cdot 10^3$ to $2 \cdot 10^5$ s, i.e., from less than 1 h to ~2 days, meaning that it should be also the time scale for the turning over the flow feeding at the doublet growth scale. This, in turn, is reminiscent of seismically controlled fluid flow processes. It has been shown that seismic events have the capacity to activate micro-permeability in the affected rock volume, allowing the incorporation of otherwise captive fluids in the circulating fluid flow [90,91]. The time constant of the process is in the order of a few hours to a few days, consistent with the estimated growth rates for the rutile. An experimental work on apatite [92] confirms that complex zoning patterns may result from short-lived fluid flow events associated with rapid fluid composition fluctuations such as those occurring during a seismic cycle. Thus, the formation of a doublet could be understood as the result of seismic activity. A (micro) seismic event would allow in a first time the influx in the growing environment of the main fluid circulating at this time at the deposit scale, and a light band would grow. After a short time lag, a new fluid, coming from a low permeability reservoir, would in turn invade the growing environment, triggering the growth of the succeeding dark band.

6.4. Nature of the Fluid(s)

At Panasqueira, the early tourmalinization process is demonstrated to result from the progressive mixing between a first fluid F1, characterized by a Co–Cu–Pb–Sc–Sr–V–Cr–Sn–Nb–Ta elemental assemblage, and a second fluid F2, characterized by the F–Li–Fe–Mn–Zn–W elemental assemblage [65]. Both fluids are thought to be of metamorphic origin. At the end of the tourmaline growth, when rutile is crystallizing, F2 is dominant in the mineralizing mixed fluid. This is in agreement with the composition of the clear bands in the rutile doublets, which are characterized by high W contents. It is by contrast impossible to relate to F1 nor to F2 the repetitive infiltrations of a small quantity of fluid during micro-seismic events that are thought to be at the origin of the dark bands. It cannot be F1, owing to the lack of systematic positive correlation

between Nb + Ta and V or Sn in these dark bands. In addition, neither in F1 nor in F2 is observed the high Nb to W ratio found in the dark bands. Consequently, a third fluid F3 seems to be recorded in the rutile growth, and rutile thus appears as a very sensitive marker of fluid evolution.

There is a rare metal granite (RMG) layer atop of the Panasqueira granite (Figure 1.19B), and these RMG are characterized by abundant Nb-rich columbo-tantalite (Nb/Nb + Ta in the 0.74–0.93 range). However, they are poor in cassiterite, a fact which is reflected in rather low Sn contents in the granites (≤ 75 ppm) [47]. It is thus tempting to relate fluid F3 to these Nb-rich granites. Nevertheless, F3 is unlikely to be a magmatic-hydrothermal fluid, because there is no evidence at the RMG-micaschist boundary for an interaction between the wall rock and a fluid issued from the granitic melt, except a limited Rb and Sr enrichment of micaschists on a few meters [47]. On the other hand, the RMG layer could well have acted as the low-permeability reservoir required by the model presented in the previous section. It may thus be proposed that at the favor of seismic events, the main F1/F2 mixture could invade the RMG. During the inter-seismic period of retention, high temperature fluid-rock interaction could cause the F1/F2 mixture to evolve into fluid F3. The latter would be released at the occasion of the next seismic event, causing the growth of a new dark band in the rutile, whereas coeval invasion of F1/F2 into the granite would initiate the following cycle.

7. Conclusions

1. From the crystal-chemistry point of view, iron and vanadium in the Panasqueira rutile crystals are predominantly present as Fe^{3+} and V^{4+} , respectively.

2. The conspicuous sector zoning is due to differential incorporation of minor elements onto pyramidal and prismatic faces, the latter being by far less efficient. Two families of both types are involved, but could not be indexed. W is more strongly incorporated than Nb + Ta onto the more efficient faces, whereas Sn and V contents are nearly not impacted. The net effect of the sector zoning is thus a progressive increase of the relative weight of Sn from the most efficient pyramid family to the less efficient prism family of faces, somewhat in combination with a less significant increase of the relative weight of Nb + Ta.

3. The Panasqueira rutile rank among the richest in tungsten worldwide (up to 10.7 wt % W). This is connected with this rutile heralding the main wolframite deposition event.

4. The conspicuous oscillatory zoning concerns most minor elements: W, Nb + Ta, Fe, V, Cr and Sn. It does not result from a self-organizing process, and records open-system conditions of crystallization. The doublets of "clear" and "dark" bands that make the oscillatory zoning are viewed as the result of the successive influx of (i) a W-rich, Nb + Ta poor fluid, abruptly replaced by (or mixed to) (ii) a Nb-rich and W-poor fluid. Whereas the clear bands likely crystallized from the main fluid associated with the tourmaline growth, the dark bands are thought to record repetitive influxes of another fluid, released from a tight

reservoir in relation to seismic events. This reservoir was likely the rare metal granite layer atop of the Panasqueira granite.

5. Rutile appears to be a very sensitive marker of fluid evolution in hydrothermal systems, in the same way as rutile is a sensitive marker of melt evolution in magmatic systems.

Supplementary Materials: The following are available online at www.mdpi.com/xxx/s1, Table S1: SEM-EDS analyses of the Panasqueira rutile.

Author Contributions: Conceptualization, E.C., C.M. and M.C.; Methodology and Data Curation, A.L.; Validation, L.T. and F.P.; Writing—Original Draft Preparation, E.C.; Writing—Review & Editing, E.C. and C.M.

Funding: This work was funded by the ERAMIN project NewOres financed by ANR (ANR-14-EMIN-0001), and Labex Ressources 21 (supported by the French National Research Agency through the national program “Investissements d’avenir”) with reference ANR-10-LABX 21-LABEX RESSOURCES 21. LA-ICP-MS equipment was financed by CPER program (National Funds - Lorraine region - FEDER).

Acknowledgments:

This work benefited from the analytical capabilities of the GeoRessources Laboratory (Université de Lorraine, CNRS, CREGU), and the authors gratefully acknowledge Olivier Rouer and Lise Salsi for their technical help. We thank Isabella Pignatelli for her assistance in crystallographic approaches. We are most grateful to Beralt Tin and Wolfram S.A. for permitting access to the Panasqueira underground mine. Three anonymous reviewers are warmly thanked for their constructive criticism and help in improving the manuscript.

Conflicts of Interest: The authors declare no conflict of interest.

References

1. Meinhold, G. Rutile and its applications in earth sciences. *Earth-Sci. Rev.* 2010, 102, 1–28.
2. Graham, J.; Morris, R.C. Tungsten- and antimony-substituted rutile. *Mineral. Mag.* 1973, 39, 470–473.
3. Hassan, W.F. Geochemistry and mineralogy of Ta–Nb rutile from Peninsular Malaysia. *J. Asian Earth Sci.* 1994, 10, 11–23.
4. Murad, E.; Cashion, J.D.; Noble, C.J.; Pilbrow, J.R. The chemical state of Fe in rutile from an albitite in Norway. *Mineral. Mag.* 1995, 59, 557–560.
5. Smith, D.; Perseil, E.-A. Sb-rich rutile in the manganese concentrations at St. Marcel-Praborna, Aosta Valley, Italy; petrology and crystal-chemistry. *Mineral. Mag.* 1997, 61, 655–669.
6. Rice, C.; Darke, K.; Still, J. Tungsten-bearing rutile from the Kori Kollo gold mine Bolivia. *Mineral. Mag.* 1998, 62, 421–429.
7. Zack, T.; Kronz, A.; Foley, S.F.; Rivers, T. Trace element abundances in rutiles from eclogites and associated garnet mica schists. *Chem. Geol.* 2002, 184, 97–122.
8. Bromiley, G.D.; Hilairet, N. Hydrogen and minor element incorporation in synthetic rutile. *Mineral. Mag.* 2005, 69, 345–358.
9. Scott, K.M. Rutile geochemistry as a guide to porphyry Cu–Au mineralization, Northparkes, New South Wales, Australia. *Geochem. Explor. Environ. Anal.* 2005, 5, 247–253.
10. Carruzzo, S.; Clarke, D.B.; Pelrine, K.M.; MacDonald, M.A. Texture, composition, and origin of rutile in the South Mountain Batholith, Nova Scotia. *Can. Mineral.* 2006, 44, 715–729.
11. Zack, T.; von Eynatten, H.; Kronz, A. Rutile geochemistry and its potential use in quantitative provenance studies. *Sediment. Geol.* 2004, 171, 37–58.
12. Triebold, S.; von Eynatten, H.; Luvizotto, G.L.; Zack, T. Deducing source rock lithology from detrital rutile geochemistry: An example from the Erzgebirge, Germany. *Chem. Geol.* 2007, 244, 421–436.
13. Plank, T.; Langmuir, C.H. The geochemical composition of subducting sediment and its consequences for the crust and mantle. *Chem. Geol.* 1998, 145, 325–394.
14. La Tourette, T.; Hervig, R.L.; Holloway, J.R. Trace element partitioning between amphibole, phlogopite and basanite melt. *Earth Planet. Sci. Lett.* 1995, 135, 13–30.
15. Barth, M.G.; McDonough, W.F.; Rudnick, R.L. Tracking the budget of Nb and Ta in the continental crust. *Chem. Geol.* 2000, 165, 197–213.
16. Zack, T.; Stockli, D.F.; Luvizotto, G.L.; Barth, M.G.; Belousova, E.; Wolfe, M.R.; Hinton, R.W. In situ U–Pb rutile dating by LA-ICP-MS: 208Pb correction and prospects for geological applications. *Contrib. Mineral. Petrol.* 2011, 162, 515–530.
17. Ferreira-Filho, C.F.; Naldrett, A.J.; Fuck, R.A.; Kamo, S.L.; Krogh, T.E. Zircon and rutile U–Pb geochronology of the Niquelândia layered mafic and ultramafic intrusion, Brazil: Constraints for the timing of magmatism and high grade metamorphism. *Prec. Res.* 1994, 68, 241–255. doi:10.1016/0301-9268(94)90032-9.

18. Richards, J.P.; Krogh, T.E.; Spooner, E.T.C. Fluid inclusion characteristics and U–Pb rutile age of late hydrothermal alteration and veining at the Musoshi stratiform copper deposit, Central African copper belt, Zaire. *Econ. Geol.* 1998, 83, 118–139.
19. Schandl, E.S.; Davis, D.W.; Krogh, T.E. Are the alteration halos of massive sulfide deposits syngenetic? Evidence from U–Pb dating of hydrothermal rutile at the Kidd volcanic center, Abitibi subprovince, Canada. *Geology* 1990, 18, 505–508.
20. Wong, L.; Davis, D.W.; Krogh, T.E.; Robert, F. U–Pb zircon and rutile geochronology of Archean greenstone formation and gold mineralization in the Val d’Or region, Quebec. *Earth Planet. Sci. Lett.* 1991, 104, 325–336.
21. Carocci, E.; Marignac, C.; Cathelineau, M.; Truche, L.; Pinto, F. Trace Elements in Tourmaline: Markers of Incipient W Deposition in Panasqueira Mine. In *Proceedings of the Goldschmidt Conference, Paris, France 13–18 August 2017*.
22. Zack, T.; Moraes, R.; Kronz, A. Temperature dependence of Zr in rutile: Empirical calibration of a rutile thermometer. *Contrib. Mineral. Petrol.* 2004, 148, 471–488.
23. Novák, M.; Černý, P. Niobium–tantalum oxide minerals from complex granitic pegmatites in the Moldanubicum, Czech Republic: Primary versus secondary compositional trends. *Can. Mineral.* 1998, 36, 659–672.
24. Tindle, A.G.; Breaks, F.W. Oxide minerals of the Separation Rapids rare-element granitic pegmatite group, Northwestern Ontario. *Can. Mineral.* 1998, 36, 609–635.
25. Černý P.; Goad, B.E.; Hawthorne, F.C.; Chapman, R. Fractionation trends of the Nb- and Ta-bearing oxide minerals in the Greer Lake pegmatitic granite and its pegmatite aureole, southeastern Manitoba. *Am. Mineral.* 1986, 71, 501–517.
26. Černý, P.; Chapman, R.; Simmons, W.B.; Chackowsky, L.E. Niobian rutile from the McGuire granitic pegmatite, Park County, Colorado; solid solution, exsolution, and oxidation. *Am. Mineral.* 1999, 84, 754–763.
27. Hanson, S.L.; Simmons, W.B.; Falster, A.U. Nb–Ta–Ti oxides in granitic pegmatites from the Topsham pegmatite district, southern Maine. *Can. Mineral.* 1998, 36, 601–608.
28. Uher, P.; Černý, P.; Chapman, R.; Határ, J.; Miko, O. Evolution of Nb, Ta-oxide minerals in the Prašivá granitic pegmatites, Slovakia. I. Primary Fe, Ti-rich assemblage. *Can. Mineral.* 1998, 36, 525–534.
29. Belkasmí, M.; Cuney, M.; Pollard, P.J.; Bastoul, A. Chemistry of the Ta-Nb-Sn-W oxide minerals from the Yichun rare metal granite (SE China): Genetic implications and comparison with Moroccan and French Hercynian examples. *Mineral. Mag.* 2000, 64, doi:10.1180/002646100549391.
30. Aurisicchio, C.; De Vito, C.; Ferrini, V.; Orlandi, P. Nb and Ta oxide minerals in the Fonte Del Prete granitic pegmatite dike, Island of Elba, Italy. *Can. Mineral.* 2002, 40, 799–814.
31. Bouabsa, L.; Marignac, C.; Chabbi, R.; Cuney, M. 2010. The Filfila (NE Algeria) topaz bearing granites and their rare metal minerals: Petrologic and metallogenic implications. *J. Afr. Earth Sci.* 2010, 56, 107–113.
32. Rabbia, O.M.; Hernández, L.B. Mineral chemistry and potential applications of natural-multi-doped hydrothermal rutile from porphyry copper deposits. In *Rutile: Properties, Synthesis and Application*; Low, I.-M., Ed.; Nova Science Publishers, Inc.: Hauppauge, New York, NY, USA, 2012; pp. 209–228.

33. Clark, J.R.; Williams-Jones, A.E. Rutile as a Potential Indicator Mineral for Metamorphosed Metallic ore Minerals Deposits; Rapport Final de DIVEX, Sous-projet SC2; Divex: Montréal, QC, Canada, 2004; 17p.
34. Scott, K.M.; Radford, N.W. Rutile compositions at the Big Bell Au deposit as a guide for exploration. *Geochem. Explor. Environ. Anal.* 2007, 7, 353–361.
35. Dostal, J.; Kontak, D.J.; Chatterjee, A. Trace element geochemistry of scheelite and rutile from metatubidite-hosted quartz vein gold deposits, Meguma Terrane, Nova Scotia, Canada: Genetic implications. *Mineral. Petrol.* 2009, 97, 95–109.
36. Scott, K.M.; Radford, N.; Hough, R.; Reddy, S. Rutile compositions in the Kalgoorlie Goldfields and their implications for exploration. *Aust. J. Earth Sci.* 2011, 58, 803–812.
37. Černý, P.; Novák, M.; Chapman, R.; Ferreira, K.J. Subsolidus behavior of niobian rutile from the Písek region, Czech Republic: A model for exsolution in W- and Fe²⁺ » Fe³⁺-rich phases. *J. Geosci.* 2007, 52, 143–159.
38. Harlaux, M. Tungsten and Rare-Metal (Nb, Ta, Sn) Hydrothermal Metallogenic Systems in the Late Variscan Orogenic Context: Example of the French Massif Central. Ph.D. Thesis, Lorraine University, Lorraine, France, 2016; p. 576.
39. Michailidis, K.M. An EPMA and SEM study of niobian-tungstenian rutile from the Fanos aplitic granite, central Macedonia, northern Greece. *Neues Jahrbuch für Mineralogie-Monatshefte* 1997, 12, 549–563.
40. Baksheev, T.A.; Guseva, E.V.; Spiridonov, E.M. W- rutile from vein post-skarn mineralization of the Bestiube deposit, north Kazakhstan. In *Proceedings of the 16th General Meeting Abstracts International Mineralogical Association (IMA)*, Pisa, Italy, 4–9 September 1994; Volume 16, pp. 25–26.
41. Vigne, J.-L.; André, G.; Kapal, F. Données industrielles, économiques, géographiques sur les principaux produits chimiques, métaux, matériaux, 11th ed.; 2018. Available online: <http://www.societechimiquedefrance.fr/extras/Donnees/acc.htm>.
42. Almonty Industries. Report NI 43-101. Technical Report on the Mineral Resources and Reserves of the Panasqueira Mine, Portugal, 2016. Available online: http://www.almonty.com/_resources/Panasqueira_43-101_Tech_Rep_Dec16_SEDAR.PDF.
43. Díez Fernández, R.; Barreiro, J.G.; Martínez Catalán, J.R.; Ayarza, P. Crustal thickening and attenuation as revealed by regional fold interference patterns: Ciudad Rodrigo basement area (Salamanca, Spain). *J. Struct. Geol.* 2013, 46, 115–128.
44. Ribeiro, R.F. Gravimetric Modelling and Geological Interpretation of Argemela-Panasqueira Area. Ph.D. Thesis, Porto University, Porto, Portugal, 2017; p. 61.
45. Kelly, W.C.; Rye, R.O. Geologic, fluid inclusion, and stable isotope studies of the tin–tungsten deposits of Panasqueira, Portugal. *Econ. Geol.* 1979, 74, 1721–1822.
46. Bussink, R.W. Geochemistry of the Panasqueira tungsten-tin deposit, Portugal. *Geol. Ultraiect.* 1984, 33, 1–159.
47. De Amorin, A. Petrographie géochimie des granitoides de la mine de W de Panasqueira (Portugal): Rôle dans la genèse des minéralisations. Unpublished MSc Thesis, Lorraine University (France), Lorraine, France, 2017; p. 31.

48. Thadeu, D. Geologia e jazigos de chumbo e zinco da Beira Baixa. *Boletim da SGP (Sociedade Geológica de Portugal)* 1951, 9, 1–144.
49. Polyá, D.A. Chemical behaviour of tungsten in hydrothermal fluids and genesis of the Panasqueira W-Cu-Sn deposit, Portugal. Unpublished Ph.D. Thesis, Manchester University, Manchester, UK, 1988; 334p.
50. Polyá, D.A. Compositional variation in wolframites from the Barroca Grande mine, Portugal: Evidence for fault-controlled ore formation. *Mineral. Mag.* 1988, 52, 497–503.
51. Polyá, D.A. Efficiency of hydrothermal ore formation and the Panasqueira W-Cu(Ag)-Sn vein deposit. *Nature* 1988, 333, 838–841.
52. Polyá, D.A. Chemistry of the main-stage ore-forming fluids of the Panasqueira W-Cu(Ag)-Sn deposit, Portugal: Implications for models of ore genesis. *Econ. Geol.* 1989, 84, 1134–1152.
53. Snee, L.W.; Sutter, J.F.; Kelly, W.C. Thermochronology of economic mineral deposits: Dating the stages of mineralisation at Panasqueira, Portugal, by high-precision ^{40}Ar - ^{39}Ar age spectrum techniques on muscovite. *Econ. Geol.* 1988, 83, 335–354.
54. Noronha, F.; Dória, F.; Dubessy, J.; Charoy, B. Characterization and timing of the different types of fluids present in the barren and ore veins of the W-Sn deposit of Panasqueira, central Portugal. *Miner. Depos.* 1992, 27, 72–79.
55. Lüders, V. Contribution of infrared microscopy to fluid inclusion studies in some opaque minerals (wolframite, stibnite, bournonite): Metallogenic implications. *Econ. Geol.* 1996, 91, 1462–1468.
56. Foxford, K.A.; Nicholson, R.; Polyá, D.A. Textural evolution of W-Cu-Sn bearing hydrothermal quartz veins at Minas da Panasqueira, Portugal. *Mineral. Mag.* 1991, 55, 435–445.
57. Foxford, K.A.; Nicholson, R.; Polyá, D.A.; Hebblethwaite, R.P.B. Extensional failure and hydraulic valving at Minas da Panasqueira, Portugal: Evidence from vein spatial distributions, displacements and geometries. *J. Struct. Geol.* 2000, 22, 1065–1086, doi:10.1016/S0191-8141(00)00029-8.
58. Polyá, D.A.; Foxford, K.A.; Stuart, F.; Boyce, A.; Fallick, A.E. Evolution and paragenetic context of low δD hydrothermal fluids from the Panasqueira W-Sn deposit, Portugal: New evidence from microthermometric, stable isotope, noble gas and halogen analyses of primary fluid inclusions. *Geochim. Cosmochim. Acta* 2000, 64, 3357–3371.
59. Lourenço, A. Paleofluidos e mineralizações associadas às fases tardias da Orogenia Hercínica. Unpublished Ph.D. Thesis, Porto University, Porto, Portugal, 2002; 326p.
60. Burnard, P.G.; Polyá, D.A. Importance of mantle derived fluids during granite associated hydrothermal circulation: He and Ar isotopes of ore minerals from Panasqueira. *Geochim. Cosmochim. Acta* 2004, 68, 1607–1615, doi:10.1016/j.gca.2003.10.008.
61. Pinto, F.; Vieira, R.; Noronha, F. Different cassiterite generations at the Panasqueira Deposit (Portugal): Implications for the metal zonation model. In *Mineral Resources in a Sustainable World*; André-Mayer, A.S., Cathelineau, M., Muchez, P., Pirard, E., Sindern, S., Eds.; Proceedings of the Society of Geology Applied to Mineral Deposits (SGA) Biennial Meeting: Nancy, France, 2015, Volume 2, pp. 827–830.
62. Lecumberri-Sanchez, P.; Vieira, R.; Heinrich, C.; Pinto, F.; Walle, M. Fluid-rock interaction is decisive for the formation of tungsten deposits. *Geology* 2017, 45, 579–582.

63. Codeço, M.S.; Weis, P.; Trumbull, R.B.; Pinto, F.; Lecumberri-Sanchez, P.; Wilke, F.D. Chemical and boron isotopic composition of hydrothermal tourmaline from the Panasqueira W-Sn-Cu deposit, Portugal. *Chem. Geol.* 2017, 468, 1–16.
64. Launay, G.; Sizaret, S.; Guillou-Frottier, L.; Gloaguen, E.; Pinto, F. Deciphering fluid flow at the magmatic-hydrothermal transition: A case study from the world-class Panasqueira W–Sn–(Cu) ore deposit (Portugal). *Earth Planet. Sci. Lett.* 2018, 499, 1–12.
65. Carocci, E.; Marignac, C.; Cathelineau, M.; Pinto, F.; Truche, L. Le stade initial du dépôt de la wolframite dans le gisement à W-Sn-Cu de Panasqueira (Portugal): Caractérisation indirecte des fluides par l'étude des tourmalines précoces. In *Proceedings of the 24th Réunion des Sciences de la Terre, Lille, France, 22–26 October 2018*; p. 439.
66. Černý, P.; Ercit, T.S. Mineralogy of niobium and tantalum; crystal chemical relationships, paragenetic aspects and their economic implications. In *Lanthanides, Tantalum and Niobium*; Möller, P., Černý, P., Saupé, F., Eds.; Springer-Verlag: Heidelberg, Germany, 1989; pp. 27–79.
67. Liu, L.; Xiao, Y.; Aulbach, S.; Li, D.; Hou, Z. Vanadium and niobium behavior in rutile as a function of oxygen fugacity: Evidence from natural samples. *Contrib. Mineral. Petrol.* 2014, 167, 1025–1077.
68. Paterson, B.A.; Stephens, W.E. Kinetically induced compositional zoning in titanite: Implications for accessory-phase/melt partitioning of trace elements. *Contrib. Mineral. Petrol.* 1992, 109, 373–385.
69. Allègre, C.J.; Provost, A.; Jaupart, C. Oscillatory zoning: A pathological case of crystal growth. *Nature* 1981, 294, 223–228.
70. Ortoleva, P.; Merino, E.; Moore, C.; Chadam, J. Geochemical self-organization. I: Reaction-transport feedbacks and modeling approach. *Am. J. Sci.* 1987, 287, 979–1007.
71. L'Heureux, I. Oscillatory zoning in crystal growth: A constitutional undercooling mechanism. *Phys. Rev. E* 1993, 48, 4460–4469.
72. Miura, H.; Tsukamoto, K. Role of Impurity on Growth Hysteresis and Oscillatory Growth of Crystals. *Cryst. Growth Des.* 2013, 13, 3588–3595.
73. Katsev, S.; L'Heureux, I. Autocatalytic model of oscillatory zoning in experimentally grown (Ba,Sr)SO₄ solid solution. *Phys. Rev. E* 2002, 66, doi:10.1103/PhysRevE.66.066206.
74. Wang, Y.; Merino, E. Dynamic model of oscillatory zoning of trace elements in calcite: Double layer, inhibition, and self-organization. *Geochim. Cosmochim. Acta* 1992, 56, 587–596.
75. Barker, S.L.L.; Cox, S.F. Oscillatory zoning and trace element incorporation in hydrothermal minerals: Insights from calcite growth experiments. *Geofluids* 2011, 11, 48–56.
76. Guskov, S.S.; Faddeev, M.A.; Chuprunov, E.V. Concentration oscillations at doped crystal growth from solutions. *Crystallogr. Rep.* 2010, 55, 626–631.
77. Shkutenberg, A.G.; Punin, Y.O. Micromorphological instability of a growing face as a source of oscillatory zoning in crystals. *Mineral. Mag.* 2011, 75, 169–183.
78. Ginibre, C.; Wörner, G.; Kronz, A. Minor and trace element zoning in plagioclase: Implications for magma chamber processes at Paríacota Volcano, N. Chile. *Contrib. Mineral. Petrol.* 2002, 143, 300–315.

79. Ginibre, C.; Kronz, A.; Wörner, G. High-resolution quantitative imaging of plagioclase composition using accumulated back-scattered electron image: New constraints on oscillatory zoning. *Contrib. Mineral. Petrol.* 2002, 142, 436–448.
80. Green, T.H.; Pearson, N.J. T-rich accessory phase saturation in hydrous mafic-felsic compositions at high P, T. *Chem. Geol.* 1986, 54, 185–201.
81. Laudise, R.A.; Kolb, E.D.; Caporaso, A.J. Hydrothermal growth of large sound crystals of zinc oxide. *J. Am. Ceram. Soc.* 1964, 47, doi:10.1111/j.1151-2916.1964.tb14632.x.
82. Kolb, E.D.; Grenier, J.-C.; Laudise, R.A. Solubility and growth of AlPO_4 in a hydrothermal solvent: HCl. *J. Cryst. Growth* 1981, 51, 178–182.
83. Hosaka, M.; Taki, S. Hydrothermal growth of quartz crystals at low fillings in NaCl and KCl solutions. *J. Cryst. Growth* 1986, 78, 413–417.
84. Lander, R.H.; Larese, R.E.; Bonnell, L.M. Toward more accurate quartz cement models: The importance of euhedral versus noneuhedral growth rates. *AAPG Bullet.* 2008, 92, 1537–1563.
85. Nielsen, A.E.; Toft, J.M. Electrolyte crystal growth kinetics. *J. Cryst. Growth* 1984, 67, 278–288.
86. Kralj, D.; Brecevic, L.; Nielsen, A.E. Vaterite growth and dissolution in aqueous solution I. Kinetics of crystal growth. *J. Cryst. Growth* 1990, 104, 793–800.
87. Yanagisawa, K.; Feng, Q.; Ioku, N.; Yamasaki, N. Hydrothermal single crystal growth of calcite in ammonium acetate solution. *J. Cryst. Growth* 1996, 163, 285–294.
88. Tai, C.Y.; Chien, W.-C.; Chen, C.-Y. Crystal growth kinetics of calcite in a dense fluidized-bed crystallizer. *AIChE J.* 1999, 45, 1605–1614.
89. Teng, H.H.; Dove, P.M.; De Yoreo, J.J. Kinetics of calcite growth: Surface processes and relationships to macroscopic rate laws. *Geochim. Cosmochim. Acta* 2000, 64, 2255–2266.
90. Charmoille, A. Traçage hydrochimique des interactions hydrauliques et mécaniques entre les volumes perméables et peu perméables au sein des aquifères fracturés carbonatés: Aquifère karstique de Fourbanne (Avant-pays jurassien, 25), Laboratoire naturel de Coaraze (Alpes Méridionales, 06). Ph.D. Thesis, Besançon University, Besançon, France, 2005; 271p.
91. Charmoille, A.; Fabbri, O.; Mudry, J.; Guglielmi, Y.; Bertrand, C. Post-seismic permeability change in a shallow fractured aquifer following a ML 5.1 earthquake (Fourbanne karst aquifer, Jura outermost thrust unit, eastern France). *Geophys. Res. Lett.* 2005, 32, LA8406, doi:10.1029/2005GL023859.
92. Borg, S.; Liu, W.; Pearce, M.; Cleverley, J.; MacRae, C. Complex mineral zoning patterns caused by ultra-local equilibrium at reaction interfaces. *Geology* 2014, 42, 415–418.

Part Two

Panasqueira Chemical Fluid Evolution

CHAPTER THREE

FLUID EVOLUTION IN THE PANASQUEIRA DEPOSIT: THE ROLE OF EXHUMATION AND MULTIPLE FLUID PULSES IN THE TRANSPORT AND DEPOSITION OF W-Sn-Cu

A paper to be submitted to Ore Geology Reviews

Cathelineau M., Marignac C., Boiron M-C, Carocci E., Dour M., Temperville A., Dejean M., Rolland JM

GeoRessources, Vandoeuvre les Nancy, France

Abstract

The Panasqueira deposit, one of the main W deposit in West Variscan Europe, has a long and complicated history with nearly systematic superimposition of later on stages onto the earlier. As a consequence, quartz dissolution-recrystallization is found to be the rule, as is the consecutive disappearance of first-formed fluid inclusions in quartz, the phenomenon being so pervasive as to destroy all traces of the earliest hydrothermal event, either in the earliest quartz containing most of the W reserve, or in the subsequent first generation of topaz. Thus, it appears that most preserved FI from the earliest mineralizing stages (large QI-II veins hosting the main wolframite, Stage I-IIa) were decrepitated or deformed in the deposit history. A few inclusions of small size have resisted to the deformation in quartz and are rather dense aqueous-carbonic inclusions (Lw-c). They display rather similar composition and densities than the inclusions found in second stage of vein infilling by topaz (stage II-b), where aqueous carbonic inclusions (Lw-c) are found, together with dense CO₂ dominated inclusions Lc-(w). The P-T pair of trapping constrained by the intersection between rather flat Lc-(w) isochores and steep Lw-c inclusions isochores, is 2-3kb/500°C. Such a P-T pair is consistent with deep structural levels around 10-11 km and high temperatures generally expected close to magmatic intrusions, and is inferred to correspond to the 305 Ma stage already dated by rutile.

After the sulphide (stage III-B: pyrrhotite-sphalerite) stage, a late mineral assemblage (stage IV) composed of quartz-IV-wolframite-cassiterite-arsenopyrite-Li-Fe-muscovite-apatite-siderite is widespread in the deposit but its expression extremely localized in vugs and geodes, or as infillings all along the re-opened boundary

between host-rocks and quartz I-II veins. Thus, this stage is characterized by the pervasive development of a Li-Fe-muscovite at the expense of dissolved quartz, as spectacular selvages or vugs. Most previous works on Panasqueira FI have been related to this stage. In quartz IV, most frequent inclusions are again Lw-c inclusions (two-phase volatile-bearing, $\text{H}_2\text{O}-\text{CO}_2 \gg \text{CH}_4 \gg \text{N}_2$) FI homogenizing in the liquid (water) state at temperatures close to 300°C, and similar to those described in the cited literature. In addition, nearly pure volatile vapours Vc-(w) FI ($\text{CH}_4 \gg \text{N}_2 \gg \text{CO}_2$) of high density with low amounts of water homogenizing at 85°C, appear coeval to the Lw-c FI. Thus, intersecting the isochores of the two families allow for the first time a robust estimation of the trapping conditions which are around $500 \pm 25^\circ\text{C}$, 280 ± 20 MPa (considered lithostatic, i.e., c. 11±1 km depth). The following stages quartz cassiterite is estimated to occur at $400 \pm 50^\circ\text{C}$, 140 MPa, and then the apatite-siderite stage: 350-400°C- 30 to 100 MPa, a P-T pair close to those proposed in previous works which, the most probably, described only this stage dated around 292-295 Ma.

From the earliest to the latest stage, fluids are similar to those generally found in metamorphic series at equilibrium with graphite, eg $\text{CO}_2\text{-CH}_4\text{-N}_2(\pm\text{H}_2\text{O})$ fluids. Besides, very little evidences of fluid mixing with a magmatic fluid input was found, at the exception of the Li-brines from the late siderite stage. Throughout the entire evolution, very high temperatures are recorded indicating high geothermal gradient (up to c. $75 \pm 10^\circ\text{C}\cdot\text{km}^{-1}$), while for pressure, considerable variations have been estimated: a significant drop-down from lithostatic pressures (240 MPa, during the main oxide stage) down to hydrostatic pressures at shallower depth (± 30 MPa, during the quartz-wolframite IV-cassiterite-apatite stage). This pressure drop is linked to a significant exhumation from 10-11 km down to 3-4 km depth. The persistence of high temperatures or the heat pulses at shallow depth is indicative of rather high temperature gradients, likely related to heat advection produced by series of intrusions and/or local heat flow around a major crustal lineament within the 305-295 Ma.

1 Introduction

The Panasqueira W-Cu-Sn deposit, one of the main W repository in West Variscan Europe, has been for long the subject of many FI studies, intended to reconstruct P-T-X evolution and to reveal ore depositing conditions (Kelly and Rye 1979, Bussink 1984, Noronha et al. 1992, Polya et al. 2000, Lourenço 2002, Lecumberri-Sanchez et al. 2017, Jaques and Pascal 2017). Previous studies by Kelly and Rye (1979) focused primarily on quartz and at a lesser degree on other minerals such as apatite and siderite. Pressure-temperature interpretation is based on a debatable postulate which considers that fluids were trapped close to boiling conditions, this yielding to consider homogenization temperatures as trapping temperatures. Kelly and Rye (1979) conclude therefore that the whole deposit formed at around 230-360°C at low pressures (below 150 bars). They conclude that the burial was very low, in between 600 m and 1300 m at maximum. Bussink (1984) adopts the same of interpretation, e.g. the fact that the presence of both vapour dominated

inclusions and aqueous carbonic liquids is indicative of unmixing, and considers, assuming the veins are connected to the surface, and the ore deposition depth between 1600 and 2000 m with a pressure around 150 bars.

It however comes up against the difficulty of explaining the presence of a few dense fluid inclusions, and is considering as possible a strong overpressure at the very first stage of opening of the deposit. Later, Noronha et al. (1992) consider that fluid pressure was fluctuating below lithostatic pressure but do not provide ranges of temperatures and pressures, except that temperatures could be higher than 350°C. More recently, Codeco et al. (2017) propose a temperature derived from Ti-quartz geo-thermometer applied to wall-rock hydrothermal quartz (earliest stage of tourmalinisation preceding the W deposit): 549–420 °C assuming that alteration occurred at 100 MPa, and/or 530–404°C for 20 MPa, both P-T pairs being by far different than the previous estimates. 500°C is considered by the latter authors as necessarily linked to a hot magmatic fluid. To calculate such temperatures using the Ti-quartz geothermometer which needs a pressure estimate, pressure values were inspired from the model from Foxford et al. (2000). This model does not provide however any pressure values, but suggests in a conceptual drawing that lithostatic pressures were reached under a seal during the early stage at a depth around 3.5 km., e.g. around 90 MPa, without real constrains.

Lourenço (2002) confirms that mineralization is associated with CO₂-CH₄-N₂ aquo-carbonic fluids with low salinity (5 - 10wt%NaCl) and minimum entrapment temperature, close or below 300°C. As Noronha et al. (1992), Lourenço concludes that most fluids are of metamorphic derivation. Finally, IR-study of wolframite-hosted FI (Lüders, 1996) has shown that FI trapped in wolframite differs from those found in surrounding quartz. This result is problematic, as the setting of the studied wolframite is not specified. [in another section?] Judging however from the results in the "surrounding quartz", clearly showing that this quartz is a late QIV quartz from a vug, it is reasonable to infer that the studied wolframite was also a late Wfm4-IV: owing to the fact that Wfm4-IV is demonstrably earlier than the QIV quartz, the result obtained by Lüders (1996) is not so surprising. But it must be noted that this result is by no way related to the main wolframite depositing event. later the main problem being to ensure that the surrounding quartz is coeval of wolframite. Lecumberri-Sanchez et al. (2017), building on these early results, provided LA-ICP-MS analyses of unspecified volatile-bearing FI from the quartz veins and concluded that whereas fluids were magmatic and transported W, wolframite precipitation was entirely dependent of iron ability in the altered wall rocks.

Independent temperature estimates were recently proposed by Codeco et al. (2017), using the Ti-in-quartz geo-thermometer, and Codeço et al. (2019) using B isotopes. The Ti-in-quartz geothermometer, applied to wall-rock hydrothermal quartz (earliest stage of tourmalinisation preceding the W deposit) yields estimates of 550–420 °C, for a pressure of 100 MPa, or 530–404°C, for 20 MPa, far higher than the earlier estimates. To calculate such temperatures using the Ti-quartz geothermometer which needs a pressure estimate, The high pressure estimate is derived from the model of Foxford et al. (2000). Yet, this model does

not provide any pressure values, only suggesting, in a conceptual drawing, that lithostatic pressures were reached under a seal during the early stage at a depth of around 3.5 km., e.g. around 90 MPa, without real constraints. The low pressure estimate is the classical estimate of Kelly and Rye (1979) and following workers. The high temperature of c. 500°C thus obtained is considered by Codeço et al. (2017) as necessarily testifying for a hot magmatic fluid. The B thermometer proposed by Codeço et al. (2019) assumes isotopic equilibrium between tourmaline and muscovite, and yielded a range of temperatures, from a 400-460°C average interval for the formation of the vein selvages down to c. 250°C for the latest stages. The high temperature range was obtained by combining B isotope data from the tourmaline in tourmalinized wall rocks and from muscovite in the vein selvages, considered as having coevally grown and therefore attained equilibrium, which is a disputable assertion.

These estimates are in strong contrast with most of the previously published estimates. It must be however underlined that these previous estimates came from the debatable extremely low P conditions assumed by Kelly and Rye (1979) and Bussink (2004), based on supposed (but not demonstrated) boiling conditions, and that no isochores were drawn. It is only in the work of Jaques and Pascal (2017) that isochores were used, in combination however with a contestable use of the arsenopyrite geothermometer, yielding high T (c.400-470°C) and P (c. 300 MPa).

At the occasion of a new study of the early hydrothermal events at Panasqueira (Carocci et al. 2018, 2019*), we became aware that the Panasqueira vein system experienced a long and complicated history, with nearly systematic superimposition of later on stages onto the earlier. As a consequence, quartz dissolution-recrystallization is found to be the rule, as is the consecutive disappearance of first-formed inclusions, the phenomenon being so pervasive as to destroy all traces of the earliest hydrothermal event. In addition, it appears that a great part of FI from the earliest mineralizing stages (main wolframite stage) were decrepitated or deformed sometimes in the course of the deposit history. In fact, all previous works on Panasqueira FI exclusively concerned later FI, and in particular the easily studied FI found in the nice euhedral quartz crystals from vugs. This observation prompted us to initiate a detailed study of all the fluid inclusion assemblages, with the aim of getting a robust reconstruction of the P-T-X-t evolution of the Panasqueira hydrothermal system, using all available tools. All the mineral stages were thus studied in detail by petrography using both light microscopy and cathodoluminescence, microthermometry, and Raman spectroscopy. FI were found and studied in quartz, topaz, apatite and siderite. Our study was favoured by the existence in recent mine galleries of a new and excellent material, such as topaz veins crosscutting the main oxide (wolframite-quartz) stage assemblages, and yielding exceptionally well-preserved fluid inclusions from rather early stages. We were successful in obtaining a new and complete P-T-X-t path of the hydrothermal fluids throughout the whole story of the deposit, with the main results that (i) very few (if any) magmatic fluids are documented in the FI record, fluids of metamorphic (s.l.) origin being constantly

dominant, and (ii) that temperatures remain very high all along the life of the system, implying the renewal of heat sources at the crustal scale.

As a conclusion, although extensively studied, the P-T-X evolution of ore fluids at Panasqueira during its long history is not solved and most published estimations disagree with each other. One of the possible explanation for this, is the long and complicated history, with nearly systematic superimposition of later on stages onto the earlier. As a consequence, quartz dissolution-recrystallization is found to be the rule, as is the consecutive disappearance of first-formed inclusions, the phenomenon being so pervasive as to destroy all traces of the earliest hydrothermal event. In addition, it appears that a great part of FI from the earliest mineralizing stages (main wolframite stage) were decrepitated or deformed sometimes in the deposit history. Indeed, all previous works on Panasqueira FI exclusively concerned later FI frequently in the nice euhedral quartz crystals from geodes (stage IV), but meaning that the earlier conditions of ore deposition remain in part unknown at present. The overall pressure-temperature evolution is therefore poorly documented. This results in part from the lack of any P-T diagram based on isochores for each stage of mineral infillings, from the debatable extremely low P-T conditions resulting in Kelly and Rye (1979) and Bussink (1984) with supposed boiling conditions, and from the not proven unmix process.

The lack of consensus of P-T estimates has encouraged a detailed study of fluid inclusion assemblages using all available tools necessary for detailed bulk chemistry and density reconstruction for detailed P-T reconstruction. In addition, recent mine galleries have provided new and excellent material, such as topaz veins crosscutting the main oxide (wolframite-quartz) stage assemblages, containing exceptionally well-preserved fluid inclusions. All mineral stages were thus studied in detail by petrography using both light microscopy and cathodoluminescence, microthermometry, and Raman spectroscopy on FI in order to re-evaluate the P-T evolution during the whole story of the deposit.

2 Methods

Paragenetic associations

Following petrographic examination with an OLYMPUS BX51 (transmitted and reflected light) optical microscope and a VHX-200 KEYENCE numeric microscope, selected samples were studied with a Schottky-FEG (Field Emission Gun) JEOL J7600F scanning electron microscope (SEM) equipped with an SDD-type EDS spectrometer at the GeoResources Laboratory (Nancy, France). Backscattered electron (BSE) images were obtained by setting the acceleration voltage at 15 kV.

Micro-XRF mapping was effected using the Bruker-Nano M4 Tornado instrument. This system has a Rh X-ray tube with a Be side window and polycapillary optics giving an x-ray beam with a diameter of 25-30 μm on the sample. The X-ray tube was operated at 50 kV and 200 μA . X-rays are detected by a 30 mm² xflash® SDD with an energy resolution of <135 eV at 250,000 cps. All analyses were carried out at 2 kPa

vacuum. Main elements such as U, Ca, Mg, Mn, Fe, Ti, Al, K, Na and Si were mapped, and composite images were generated.

Fluid inclusions

Fluid evolution has been studied by looking at relationships between fluid inclusions, their host mineral, the geometry of the host microstructures and the location of ore minerals, in quartz veins. Fluid inclusions have been related to the different stages of fluid percolation on the basis of the relative chronology of mineral assemblages and microstructures. Notation of the fluid inclusion types follows nomenclature previously published (Boiron et al., 1992), which takes into account the nature of the dominant chemical phases and phase changes observed. It is based on the total homogenisation Th (L-V to the vapour noted V, L-V to the liquid noted L) and the quantity of C-H-O-(N-S) species detectable by Raman spectroscopy (subscript c, when C-H-O-S species are the only components and water is not visible; c-w, when water and homogenisation of carbonic phase are observable; w-c, when both water, CO₂, CH₄ and N₂ species are present but are detected only by clathrate melting and Raman spectroscopy; and w, when C-H-O- (N- S) species are not detected by any methods). Carbonic inclusions were classified using the nomenclature of Boiron et al. (1992) which is based on the type of CO₂ homogenization at ThCO₂ (CO₂(L)+ CO₂(V) → CO₂(L) noted Lc; CO₂(L)+ CO₂(V) → CO₂(V) noted Vc). The “c” stands for carbonic. “(w)” is added when a water meniscus is observable: Vc(w) inclusions are for example inclusions whose volatile phase homogenize into the vapor phase and with a small water meniscus.

Microthermometry was carried out on fluid inclusions using a Linkam® MDS600 heating-cooling stage, adapted to an Olympus® microscope at the GeoResources laboratory in Nancy (France). The following microthermometric parameters have been measured: the melting temperatures of ice and hydrohalite (T_{m_{ice}} and T_{m_{hyd}}), first melting temperature (Te), halite dissolution (T_{S_{NaCl}}), CO₂ melting and clathrate dissociation (T_{m_{CO2}} and T_{m_{Cl}}), CO₂ homogenization (Th_{CO2}), and total homogenization temperature (Th). The temperatures of phase changes have a precision of about ±5 °C for Te, ±0.1 °C for T_{m_{ice}}, T_{m_{hyd}}, T_{m_{CO2}}, Th_{CO2}, and T_{m_{Cl}}, and ±1 °C for T_{S_{NaCl}} and Th, whereas the accuracy is better than 0.5°C in the low-temperature range, and better than 5°C at high temperatures. Volumetric fraction of the volatile phase (fvp) was estimated by reference to the volumetric chart of Roedder (1979).

The analysis of gas species of the volatile phase was performed with a Dilor-Labram Raman microspectrometer at GeoResources in Nancy (France) on inclusions previously studied by microthermometry above the critical point for carbonic inclusions (Dubessy et al., 1989). Density of the volatile phase (dv) of carbonic fluid inclusions have been calculated using programs developed by Bakker(1997)Thierry et al. (1994) and Duan et al. (1996). Isochores of fluid inclusions have been calculated

using the *ISOC* program developed by Bakker (2003) based on the equations of state from Bowers and Helgeson (1983) reviewed by Bakker (1999).

3 Paragenetic succession at Panasqueira

A precise and detailed paragenetic succession is the prerequisite to any reliable geochemical or fluid inclusion study. At Panasqueira, the paragenetic succession established by Kelly and Rye (1979) remained the basis of the paragenetic scheme for all successive workers, with, however, several corrections and additions in particular by Polya et al. (2000), Lourenço (2002) and Pinto et al. (2015).

It is however based on debatable criteria and tenets. For instance, selvages, such as the spectacular muscovite or arsenopyrite selvages at the quartz vein contacts, are considered without discussion as evidence for the early deposition of the selvage mineral. In the same way, mineral inclusions are usually interpreted as evidence of the earlier occurrence of the included mineral, and corrosion features are often taken as a reliable criterion of relative age. Unfortunately, when the hydrothermal history appears multiphase, as is the case at Panasqueira, overprinting phenomena (often implying dissolution and replacement processes) tend to obscure the temporal relationships, thus rendering difficult the establishment of a robust paragenetic chart. In the present work, we base our reconstruction of the paragenetic sequence on only two criteria: (i) intersection of veins (or veinlets or microcracks), each bearing a well-defined mineral assemblage (ideally - and fortunately frequently encountered- a monomineral one), and (ii) infilling sequence in a *demonstrably open* space. These two criteria are possibly fruitfully simultaneously used, for instance in the crack-seal occurrences. Finally, a methodological criterion is of paramount importance: the parsimony, or Ockham Razor (ORP) principle, specifying that the number of hypotheses must be kept at the minimum compatible with factual observations, meaning in our case of search for a robust paragenetic scheme, the reduction of the number of stages to the minimum consistent with all the observed relationships. These criteria have been applied to each scale of observation, from the “outcrop” level (mining works observations, scale of the pillar) to the microscopic level (including photonic and electronic microscopy). At the sample scale, the required scale of observation may be often larger than the thin section dimensions, a difficulty obviously related to the endowment of the deposit, but which can be alleviated by using sample-scale scanning systems (micro-XRF).

General characteristics of the paragenetic succession

At the pillar scale: A “pulsed” story is evident, marked by the succession of a series of major opening/closing events, each one with its own mineralogical and structural imprint, defining a series of four main stages (I to IV) in the evolution of the Panasqueira system (Fig. 3.1).

- Each of the first three stages (I-III) represents a full cycle of opening-complete infilling by a specific set of minerals.

- Although new sets of dry joints may be opened at each stage, *stages II and III* most often correspond to the re-opening of earlier vein systems. The re-opening may occur anywhere (Fig. 3.2 and 3.3), either at the selvages, or in the central part, or both, of the earlier vein. The successive openings are not necessary parallel, and indeed rarely are. This is particularly evident at the stage III (Fig. 3.4, 3.5 and 3.6).

- *Stage IV* is characterized by the development of a system of vugs which remained open until now and provides the spectacular crystals that are so characteristic at Panasqueira (Fig. 3.7, 3.8, 3.9 and 3.10). These vugs, which range from a few 10 cm to several m (up to 10 m), often occupy the whole width of the vein, overprinting the earlier stages, and usually present a tubular morphology, without clear orientation.

- The four stages are practically never found all together in one given place in the mine, with any of the I to IV stages (or several of them) possibly lacking. Yet the (partial) succession order is invariably the same. Thus, and contrary to 40 years of interpretations following Kelly and Rye (1979), there is a “mineral stratigraphy” at the scale of the Panasqueira mine, and the mineral events may be time-correlated at the same level, and from one level to another, not only at the “one vein” (≤ 100 m) scale.

- *Stages I and II* are very similar, differing nevertheless by the comb quartz habitus, with blocky prisms in stage I (“Alpine style”) compared to more elongated crystals in stage II, the latter being in addition associated with intense crack-seal processes.

- *Stages III and IV* are characterized by intense dissolution/replacement processes that accompany the opening. Thus, stage III sulphide-dominated assemblages are the result of the sealing of series of giant vugs developed along fracture zones, generally oblique to the main vein elongation. The stage IV vugs, for their part, seem the result of the enlarging dissolution of vertical tension joints.

Later stages: At the sample scale, several stages (V to VII) may be defined following stage IV. They differ from the earlier stages by being not related to a large-scale tectonic event accompanied by new opening episodes.

At the sample scale: Distributed crack-sealing is the rule, systematically affecting the earlier parts of the vein system (the “wall-rocks” of the new stages). Combined with generalized dissolution/replacement processes, this lead to potentially complex and intricate mineral assemblages at the sample scale. This may explain why all previously proposed paragenetic charts include the repetition of practically all the main minerals in the successive stages.

Topochemical effects are equally the rule, and are a supplementary factor of complication. For instance, it seems clear that, out from the stage IV vugs, siderite is in large part restricted to the previously pyritized pyrrhotite. In the same way, chlorite is mainly present as the alteration product of topaz. It would seem that the main process was the reaction of a former mineral with a new component, like CO₂ in the first case, and Fe-Mg in the second.

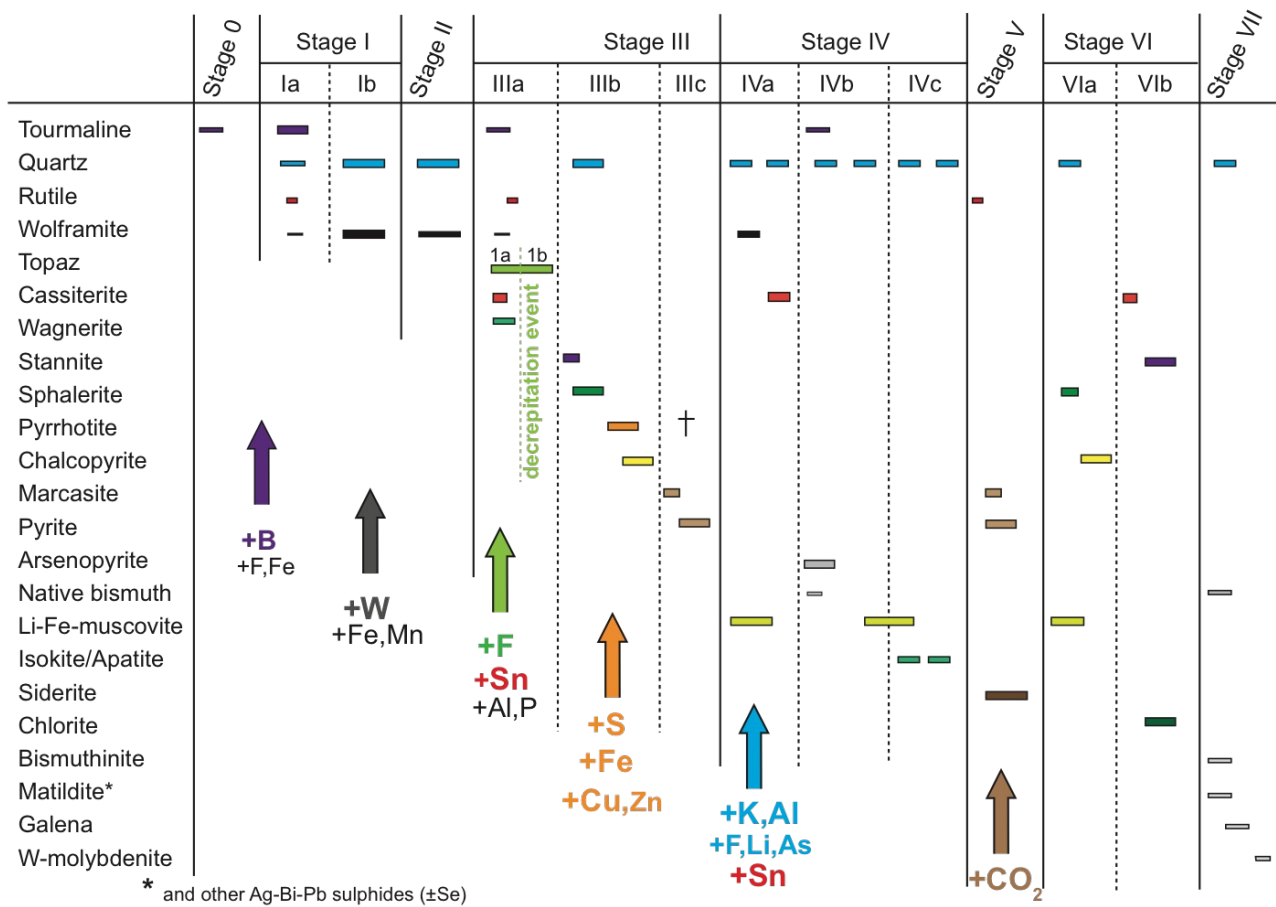


Fig. 3.1: Revised paragenetic sequence for Panasqueira. Wfm: wolframite with two main stages, the first which represents most of the exploited W, and the second one as in-fillings in the middle of veins, and as euhedral crystals in goethes, and vugs together with Qtz IV.

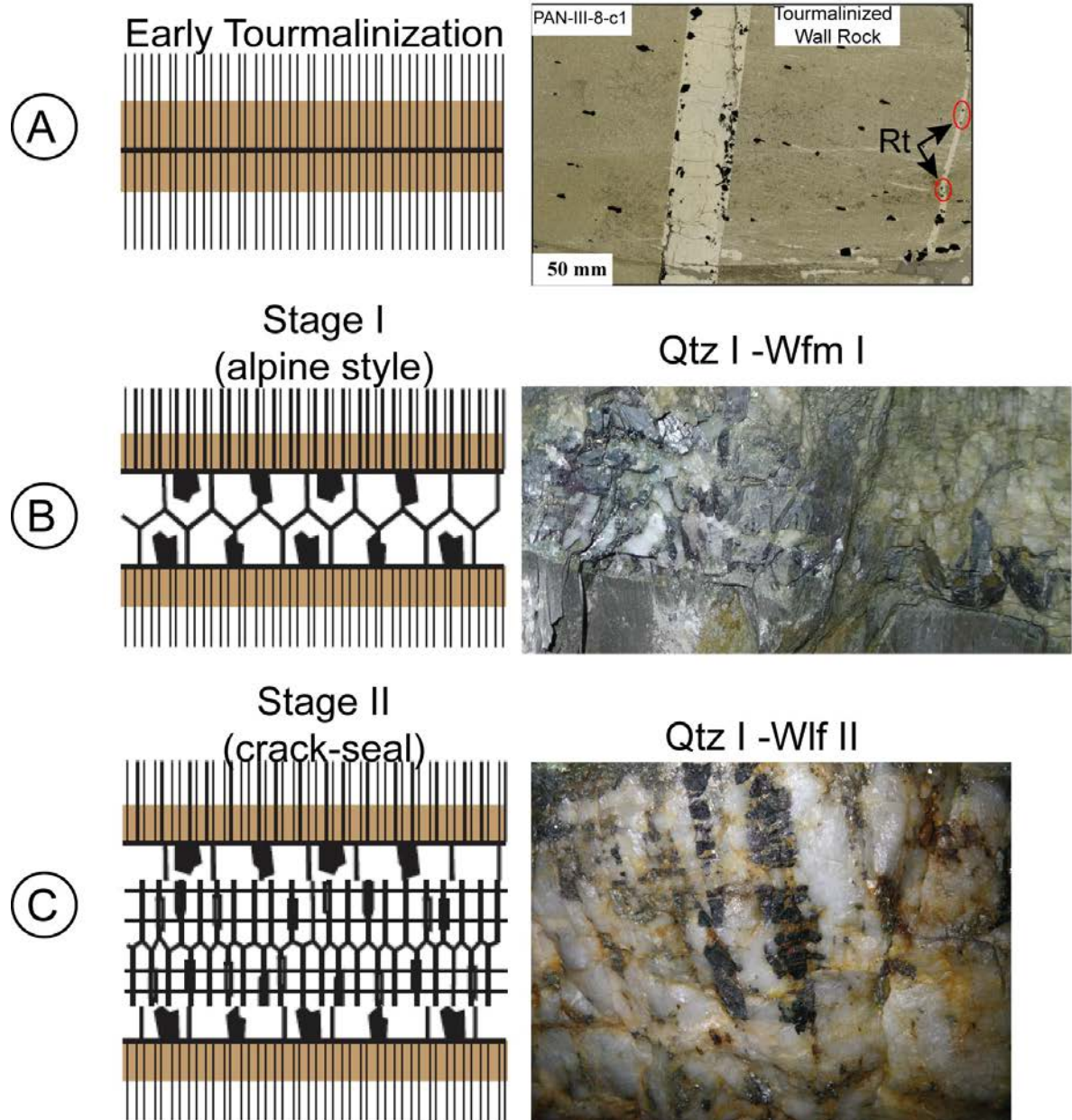


Fig. 3.2: Stage I-II assemblages from the early tourmalinization stage in the wall-rock to the crack-seal episodes which cut the wolframite in small pieces and affects deeply the quartz I and its fluid inclusions.

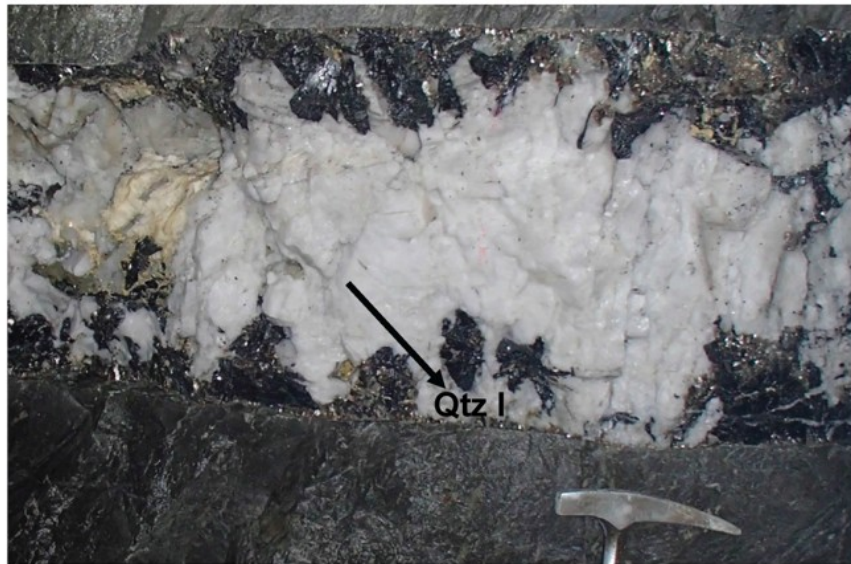
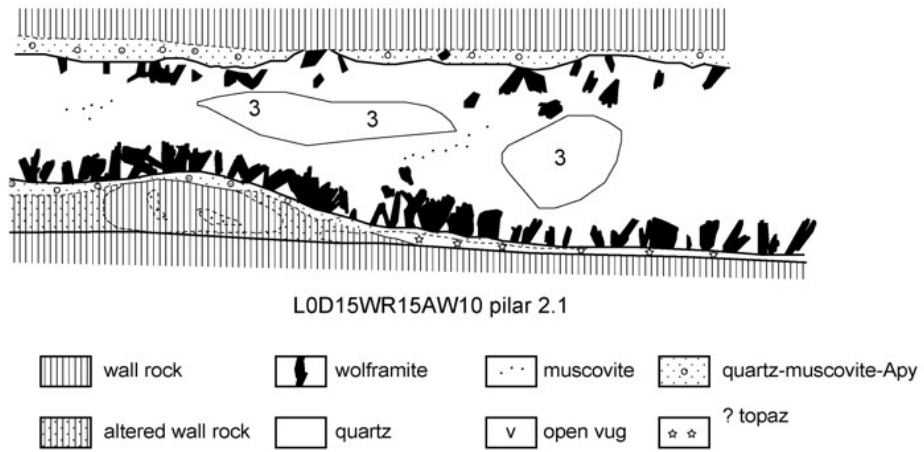


Fig 3.3: The earliest vein infilling: wolframite followed by quartz QI, which represent more than 90 % of the vein infillings observed in galleries.

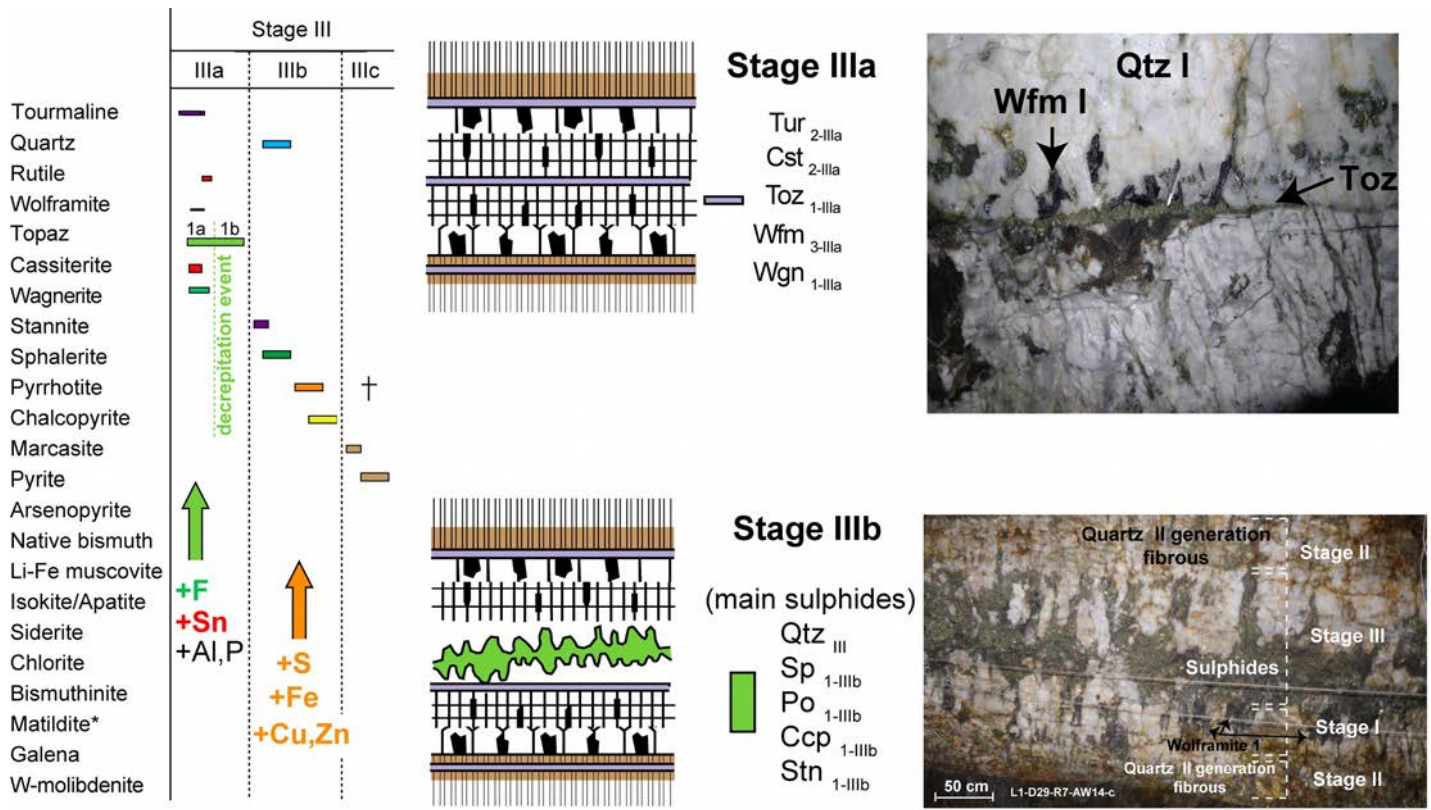


Fig. 3.4: Stage III a and b: Topaz veins crosscut the wolframite–quartz I veins. At stage IIIb- euhedral quartz are then embedded in a sulphide (pyrrhotite, transformed later on in pyrite) cement.

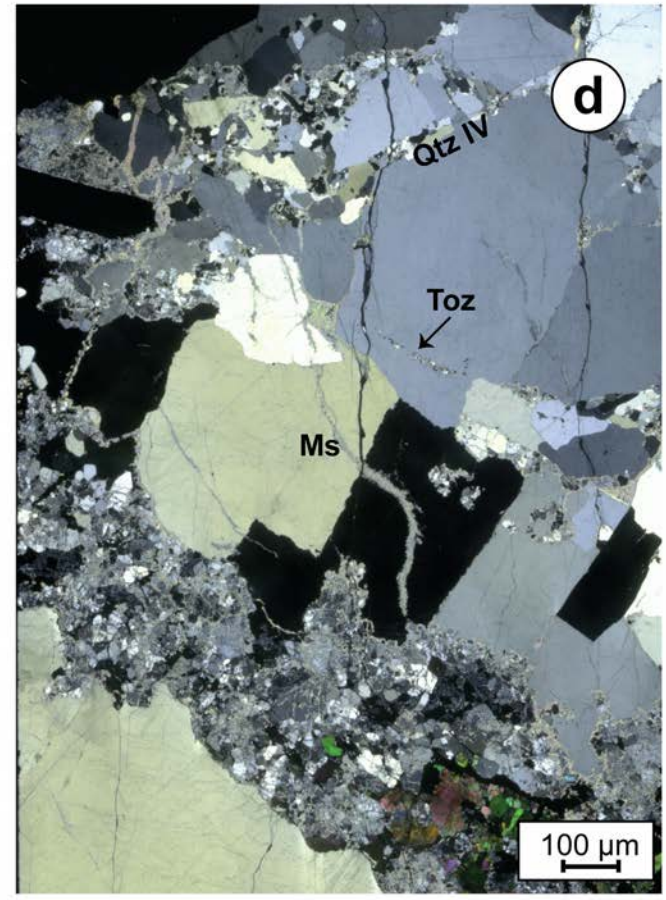
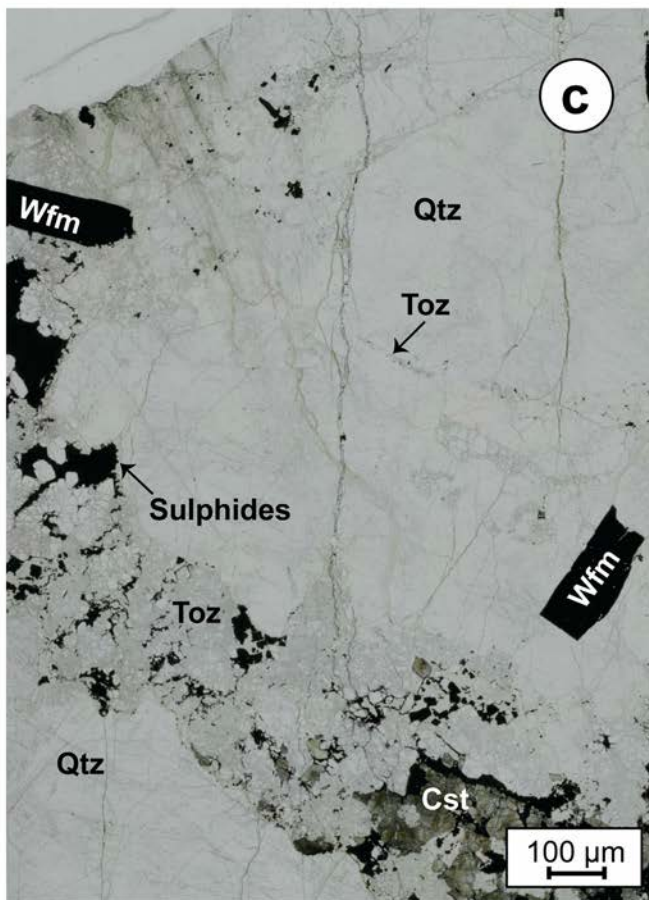


Fig. 3.5: a, b Topaz in veins crosscutting the early Qtz I-wolframite assemblage. c, d Topaz overprinting quartz (micro-crack infilling and corrosion of the earlier quartz).

PAN-III-8b

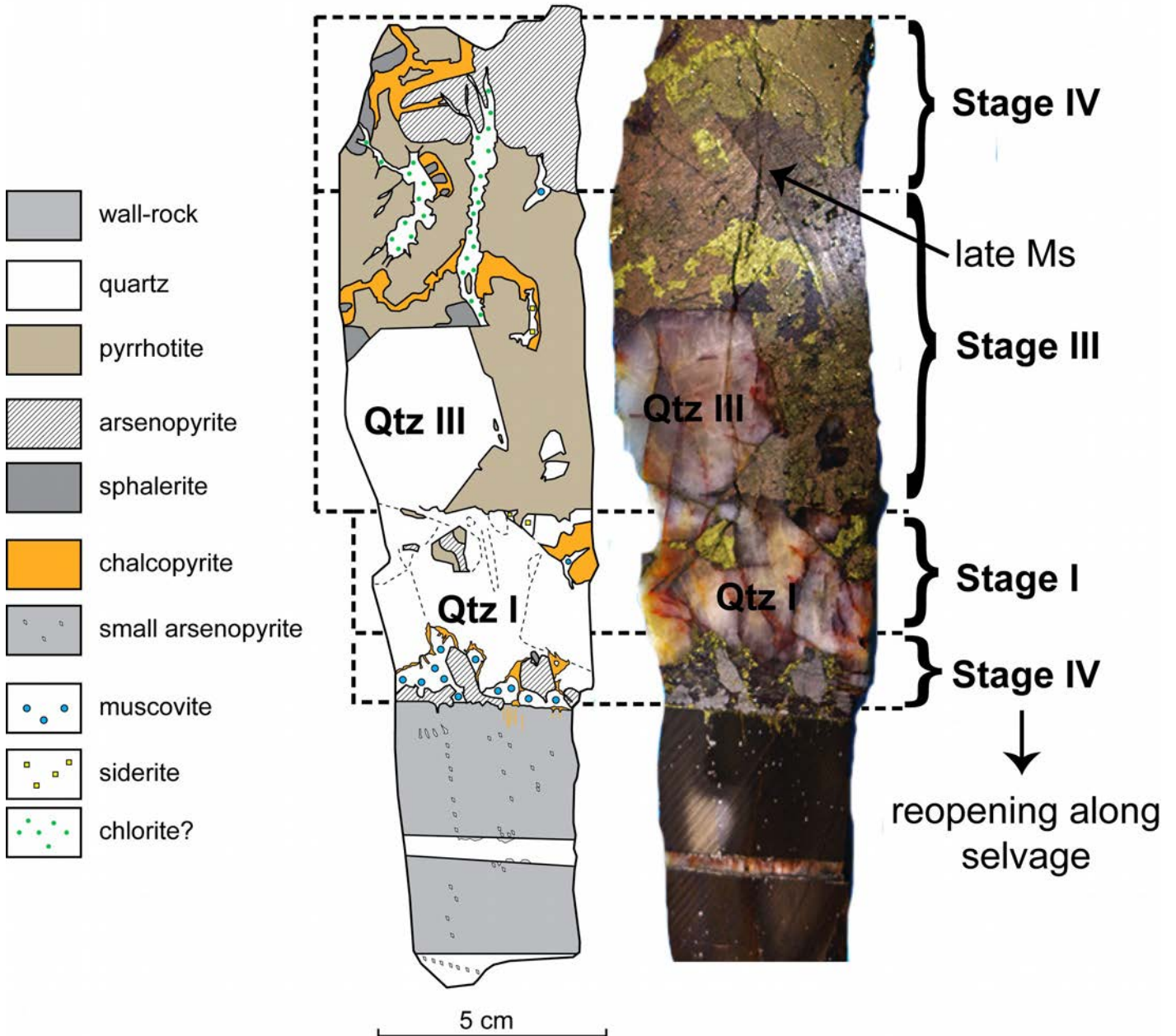


Fig. 3.6: Example of complex relationships between the different mineral assemblages: QI-II: euhedral quartz, then deformed, affected by crack-seal, QIII: euhedral quartz embedded in sulphides, QIV: quartz from geode (euhedral Qtz + Muscovite ± wolframite IV).

Revised Panasqueira paragenetic chart

Integrating all observation scales, a revised paragenetic chart was obtained (Fig. 3.1). One major difference with preceding charts (Kelly and Rye, 1979; Polya et al., 2000; Lourenço, 2002) is the decoupling of wolframite from other minerals (topaz, muscovite, arsenopyrite, apatite) at the main ore depositional stage (Oxide Silicate Stage of these authors). Another one is the decoupling of siderite from the first stage of pyritization at the end of stage III. We present below the main evidences in favour of the present chart.

Li-Fe-muscovite: Two types of muscovite selvage are observed at Panasqueira (Fig. 3.7). The first, most spectacular, type (Ms1) consists of large fan-shaped crystals (up to c. 5 cm) radiating normally to the vein boundary and lining most often quartz I or II, but also wolframite or arsenopyrite. The second type, with the same occurrences, consists of aggregates of fine grained muscovite crystals. When occurring together with Ms1, this second type appears distinctly later (Ms2). Both muscovite types are seen corroding topaz, and appear therefore to postdate it (Fig. 3.8 and 3.9).

(i) Two textural evidences constrain the relative timing of formation for the Ms1 selvages. In the first place, a remarkable feature of the earlier Panasqueira quartz (stages I and II), is that fluid inclusions (FI) in this early stage quartz were decrepitated prior to the inception of stage III quartz, as described in a following section devoted to FI petrology. Everywhere, at the contact between Ms1 and these early quartz, the latter are reworked, showing obliteration of the pristine decrepitated FI, in relation with quartz recrystallization ("bleaching"), in fringes ranging from a few 10 μm to several mm (Fig. 3.8). The simplest result of fluid recirculation at the Ms1-quartz interface is demonstrated by such occurrences in (Fig. 3.10). There, QI recrystallization is strictly associated with Ms1 even where it is disconnected from the main selvage (and here, growing onto early wolframite and consequently post-dating it). In the second place, privileged occurrences, such as in (Fig. 3.10), allow the observation of the progressive decollement of an early QI-Wfm_{1-I} assemblage from the wall-rock, due to the development of Ms1 in staggered rows (crack-seal).

(ii) The age of the Ms1 selvage was fixed at 296.3 ± 1.2 Ma ($^{40}\text{Ar}/^{39}\text{Ar}$ dating) by Snee et al. (1988) and appears by at least 2 Myr later than the main wolframite depositing stage (stage I), dated at 305.2 ± 5.7 Ma (U-Pb, rutile) (Carocci et al., 2018).

(iii) Micro-XRF imaging shows that Ms2 selvages are systematically associated to overprinting of the early wolframite (Wfm_{1-I} and Wfm_{2-II}) by a more hübneritic component (Fig. 3.9). In the stage IV vugs, muscovite growing onto neofomed Wfm_{4-IV} prisms is equally associated to Mn-overprinting, demonstrating that Ms2 is a stage IV mineral.

Arsenopyrite: Arsenopyrite is present in a great variety of settings: small euhedral crystals in the tourmalinized wall-rock, large euhedral to subhedral crystals in selvages or dispersed within quartz I-II or in

massive sulphides or in the stage IV vugs, in association with wolframite, topaz or muscovite. That explains the original definition for several arsenopyrite generations in previous works

Irrespective of the setting, all arsenopyrite crystals display only one and the same zoning pattern under SEM examination, with a sequence of zones from a core zone A (with A1 and A2 subzones) to an inner rim B and ending with an outer rim R (Fig. 3.11). This sequence is characterized by a secular decrease of the As/As+S ratio, from up to 0.586 down to 0.482. There is never "going back", but discontinuities may be marked, at each A1 → A2, A2 → B and B → R transition, by corrosion and replacement of the earlier arsenopyrite components by the following one. In the same way, some zones may be lacking. In addition, clouds of Bi minute crystal inclusions are commonly present and are restricted to the first part of this sequence (i.e., coeval with core zone A) (Fig. 3.11).

It seems highly unlikely that such a complicated sequence is more than one time repeated (as indeed implied by all preceding authors who define several stages of arsenopyrite deposition), and the best interpretation is that there was only one (more or less protracted) arsenopyrite deposition event.

Owing to the presence of arsenopyrite in the stage IV vugs fillings, it results that arsenopyrite is a stage IV mineral, and as arsenopyrite is observed to overprint Ms1 (Fig. 3.9) and covered by Ms2 in the vugs, its paragenetic position is well constrained. This conclusion is reinforced by the systematic observation of bleaching of the QI or QII quartz at the contact of disseminated arsenopyrite. As a consequence, the (sometimes spectacular) arsenopyrite selvages must be interpreted as resulting from the re-opening at the vein boundary. Indeed, in the case of arsenopyrite selvages bordering early wolframite, it is clearly observed the corrosion of wolframite by arsenopyrite.

Topaz: Independent veins or veinlets are currently found in some stopes, that are made of comb topaz followed by sulphide infilling (sphalerite, then pyrrhotite) (Fig. 3.9). Similar veins or veinlets are found within the ore veins, overprinting quartz-wolframite assemblages (Fig. 3.4 and 3.5) or lining massive sulphides. On the other hand, topaz from topaz selvage in contact with early wolframite is always seen to overprinting it at the thin section scale. All these observations point to a single topaz episode, post-dating stage I and II wolframite, and preceding the massive sulphide deposition which characterizes the stage III. This conclusion is comforted by several observations: (i) where topaz is associated with muscovite, either Ms1 or Ms2, it is observed to be partially replaced by the latter, (ii) topaz is overprinted by arsenopyrite, and (iii) topaz is never found in the stage IV vugs.

Phosphates: There are two phosphate generations at Panasqueira. The more obvious is the late F-apatite, well exposed in the stage IV vugs, where it is more or less coeval with muscovite Ms2. An earlier fluorophosphate, a Mg-Fe-Mn member of the triplite family with $Mg \geq Fe + Mn$, and consequently named here wagnerite, is systematically replaced by F-apatite, in a majority of occurrences with the intermediate formation of isokite (although defined at Panasqueira, panasqueiraite and thadeuite could not be found again in the present work). At the macroscopic scales, wagnerite is systematically associated with topaz.

Microscopic observations confirm that wagnerite is intimately associated with topaz and pyrrhotite, being therefore part of the stage IIIa. Rare occurrences of alumino-phosphates of the goyazite family (with nevertheless a significant F content), being constantly associated with tourmaline (Tur2) of the stage III and with topaz, are equally part of the stage III.

F-apatite may be encountered outside from stage IV vugs, and was for this reason commonly attributed to various earlier stages (Kelly and Rye, 1979; Polyá et al., 2000; Lourenço, 2002), depending upon the associated mineral phase. Yet, observations of F-apatite overprinting earlier phases are common. F-apatite is commonly zoned, either patchy or oscillatory zoning, in many cases with spectacular textures. Zoning is marked on one hand by varying Mn/Fe+Mn ratios, with MnO comprised between 0.05 and 3.27 wt %, and on the other hand, by intermittent adjunction of significant Sr contents (up to 6.56 wt% SrO).

Siderite: At the macroscopic scale, siderite is obviously a late phase, being observed in stage IV vugs, in which it clearly post-dates stage IV assemblages. Outside the vugs, siderite is most commonly found as networks of cracks, equally post-dating all minerals from stage I to stage IV (Fig. 3.12 and 3.13). It was nevertheless considered that the siderite, which is ubiquitously present in the marcasite-pyrite (Pyr1) assemblage resulting of stage IIIc sulfurization of pyrrhotite, is an intrinsic part of the assemblage (PAS of Kelly and Rye, 1979, and subsequent workers). Yet, it may be observed: (i) that in the PAS assemblage, siderite is present as a network of cracks, associated with dissolution/replacement of Py1 leading to a series of vuggy siderite patches. At the same time, recrystallization of Py1 and growth of a new pyrite (Py2) lead to spectacular symplectic association of siderite and Py2 and growth of euhedral Py2 lining siderite vugs. Given these evidences, and applying the OR principle, it seems clear that the first appearance of siderite in the Panasqueira sequence post-dated stage IV, hence the definition of a stage V in Figure 3.1.

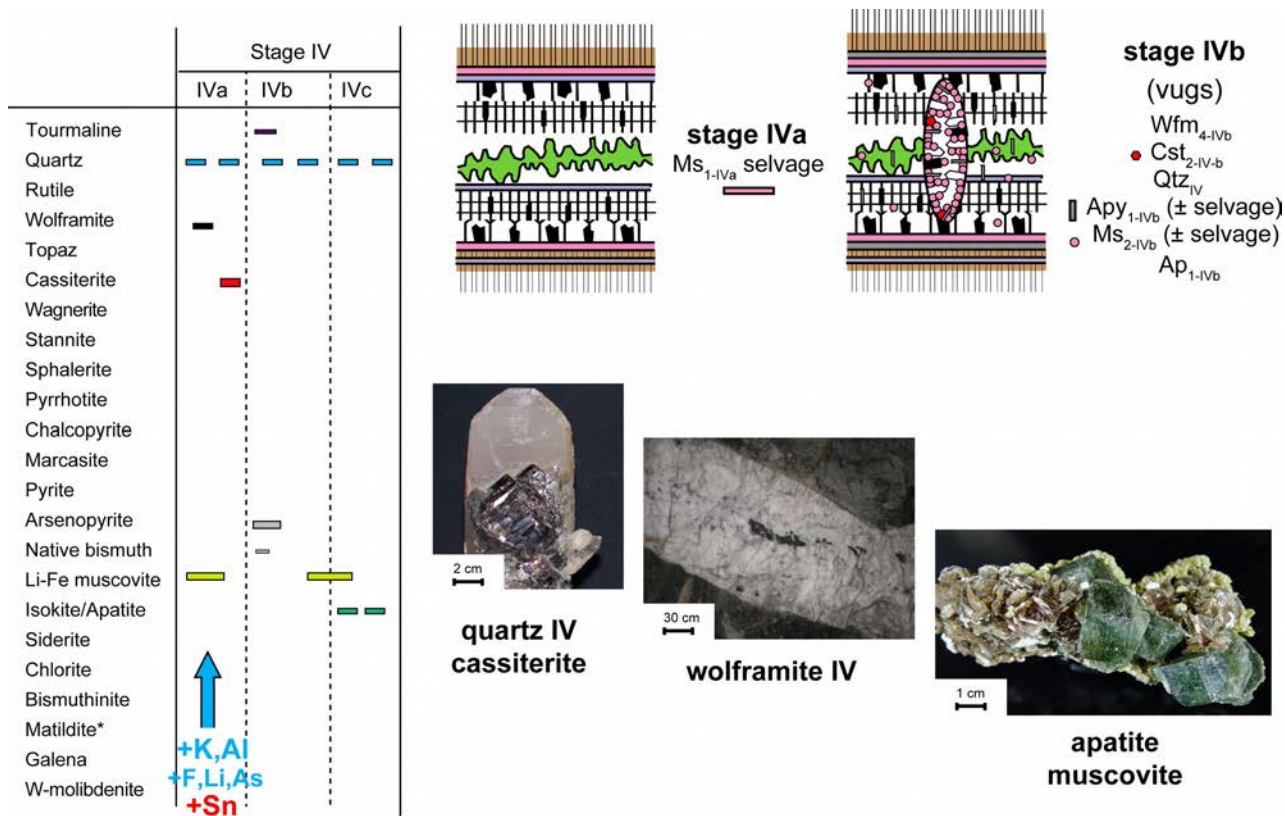


Fig. 3.7: The Stage IV stage is characterized by large vug infillings: euhedral quartz-cassiterite (top)-Wolframite IV (middle), followed by apatite and muscovite (bottom).

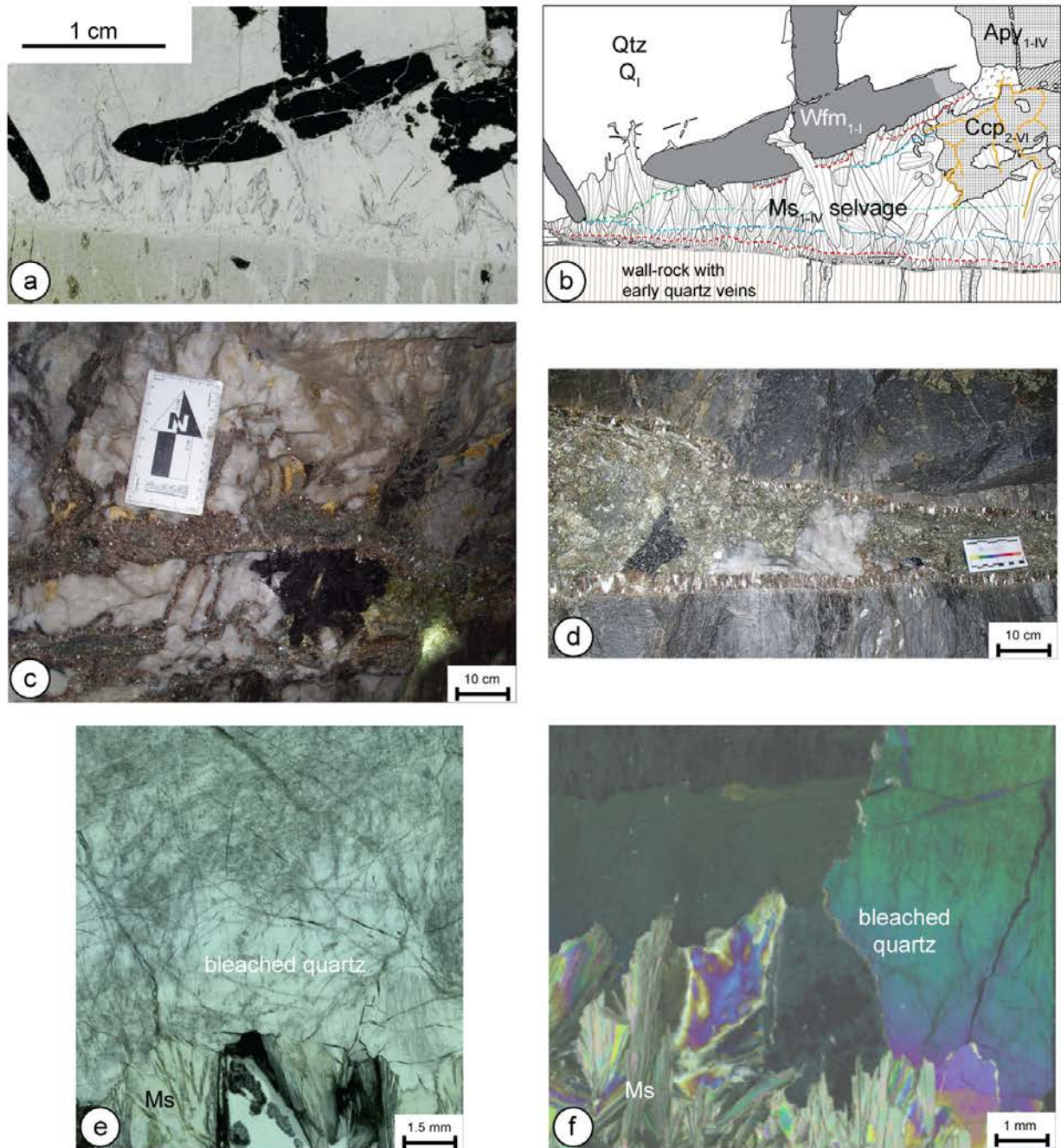
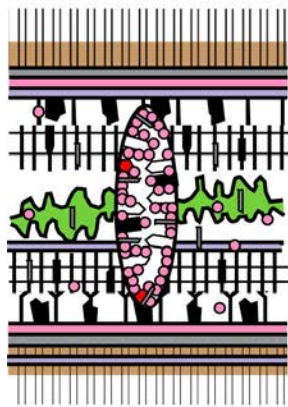


Fig. 3.8: Typical « selvage » of wolframite I vein where muscovite appears as rather late and post-wolframite as it replaces it locally (a and b). The muscovite selvage was evidently later than the wolframite (Wfm1-I)-quartz (Q1) assemblage, whereas arsenopyrite (Apy1-IV) overprinted the muscovite fans from the selvage (Ms1-IV) and siderite (Sd1-V) and chalcopyrite (Ccp2-VI) were evidently still later (c and d). Below truncation of wolframite by muscovite and muscovite invading the quartz vein (photographs, courtesy F. Pinto). At bottom, clear quartz (bleached Q1) in contact with muscovite (e and f).



stage IVb

(vugs)

Wfm_{4-IVb}

● Cst_{2-IV-b}

Qtz_{IV}

▬ Apy_{1-IVb} (± selvage)

○ Ms_{2-IVb} (± selvage)

Ap_{1-IVb}



Fig. 3.9: Arsenopyrite and muscovite from Stage IV are found also as an infilling of the reopened selvage at the vein/ host-rock boundary with significant dissolution processes which allow their crystallization: a) muscovite, b) locally, significant masses of muscovite and /or arsenopyrite may crystallize.

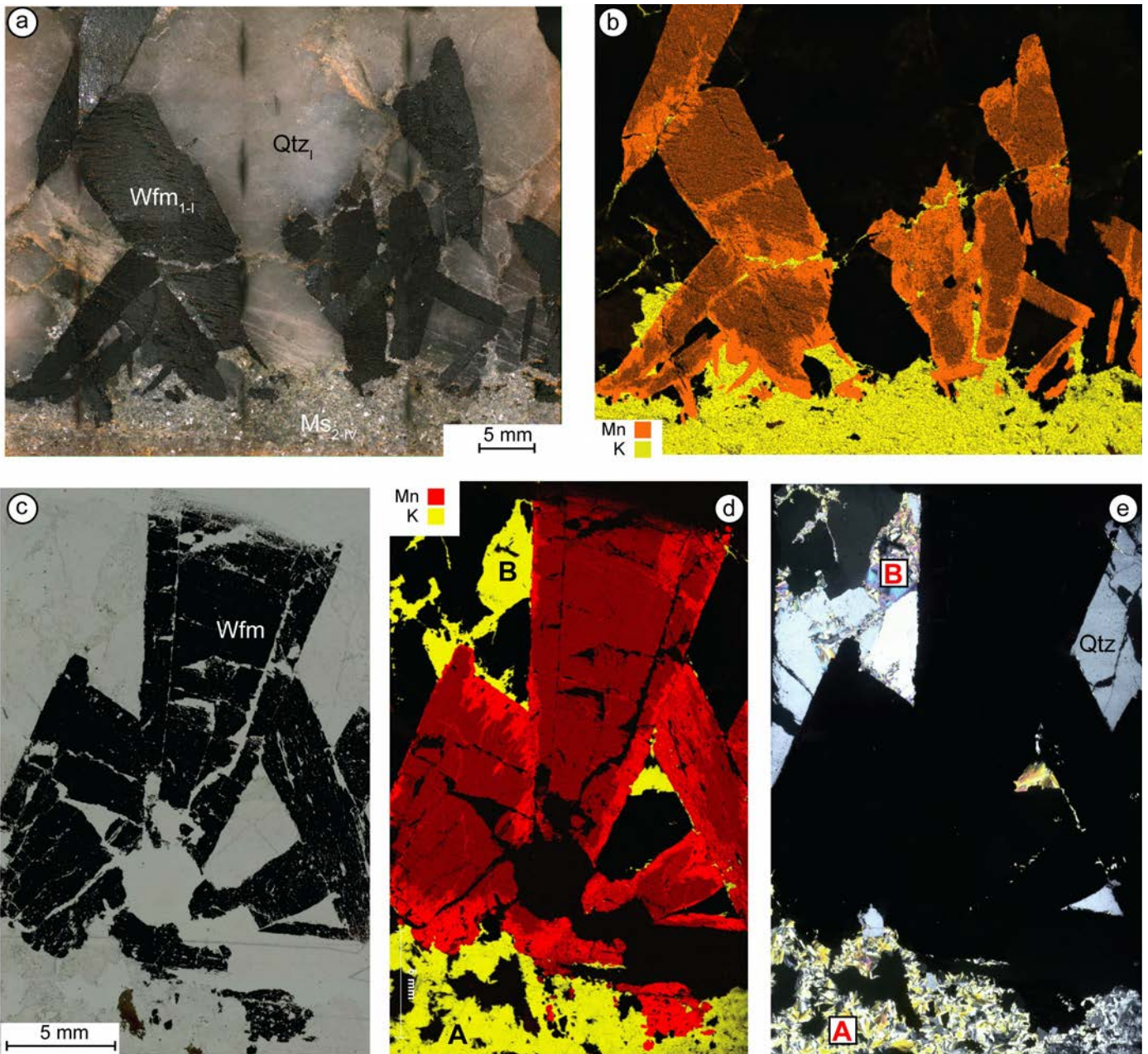


Fig. 3.10: a) Clear recrystallization of wolframite in relation with the muscovite selvage is convincing evidence that wolframite predated muscovite. b) Note also the corrosion of Qtz₁ by muscovite. This fine-grained muscovite is of late stage IV (Ms_{2-IV}). c) Muscovite (Ms_{2-IV}) selvage and replacement in quartz (d-e) is associated to Mn corrosion of the earlier wolframite (Wfm₁₋₁).

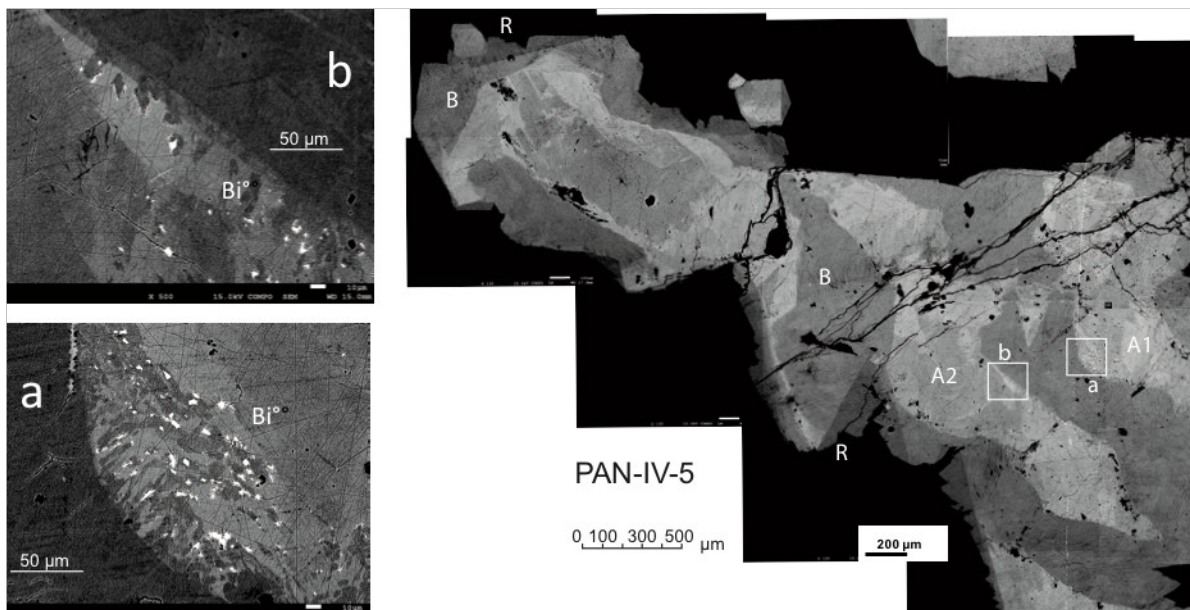
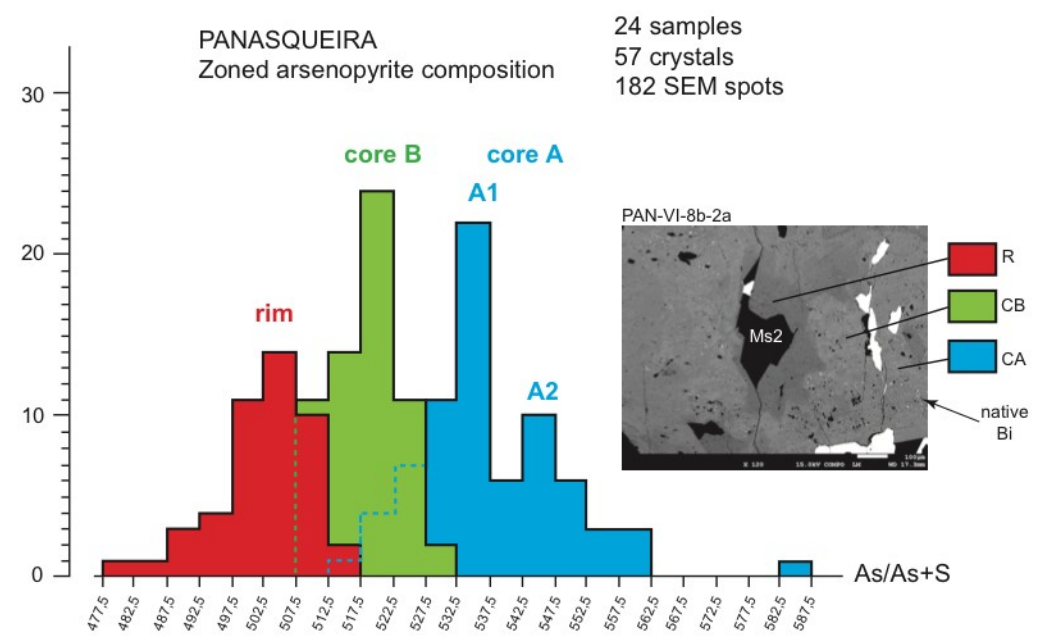


Fig. 3.11: A number of arsenopyrite generations have been recognized by previous workers. Examination of microscopic (SEM) features leads however to reconsider the question. All Panasqueira arsenopyrite crystals display a more or less complex zoned structure, with however a basic distinction between a core divided in two zones (A1, A2 and B) and a rim (R). A prominent feature is that, for most of the analyzed crystals, compositions of CA, CB, and R are essentially constant. Another remarkable feature, is that most crystals contain native Bi° blebs, most commonly included in the core CA.

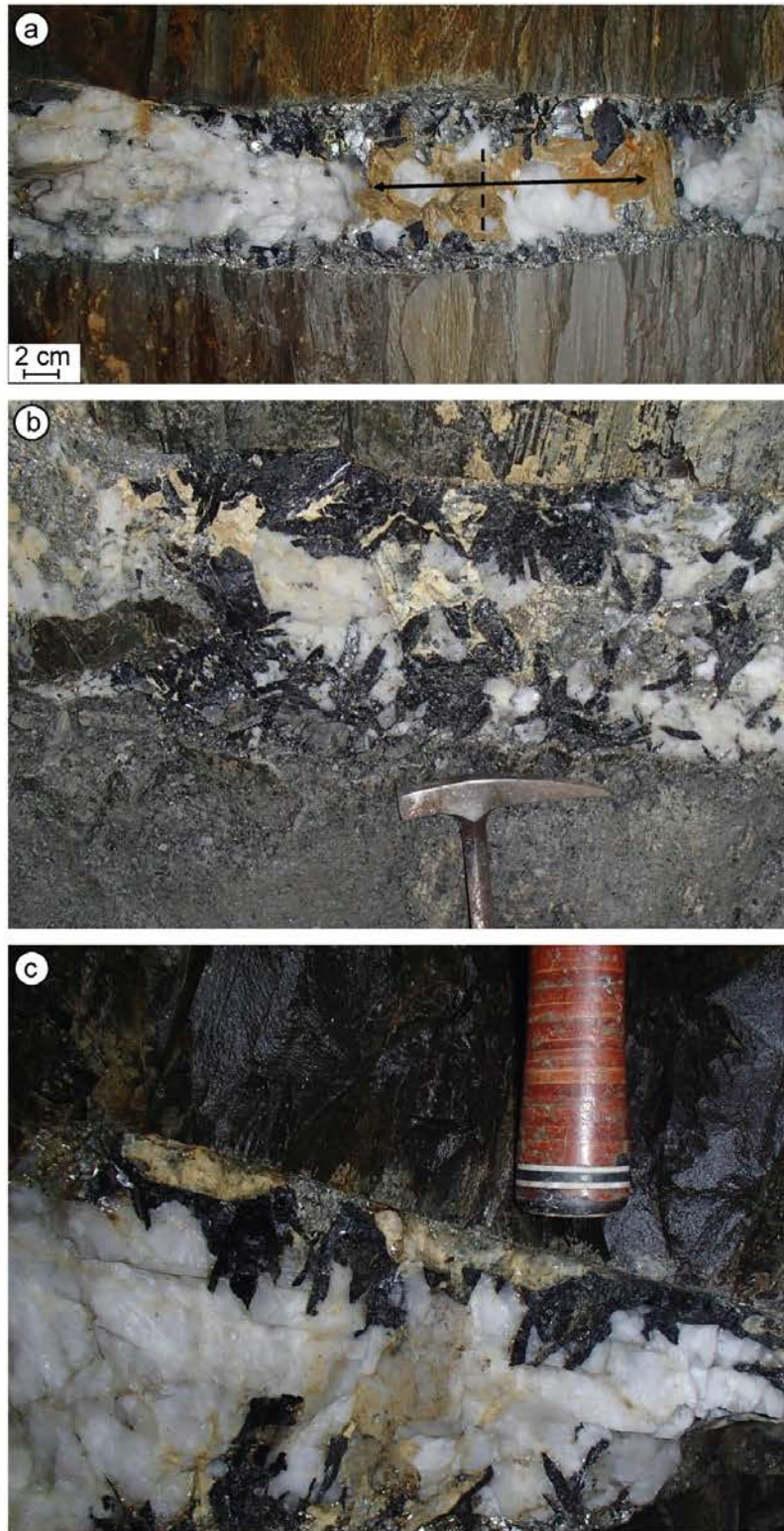
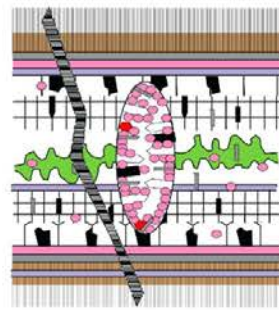
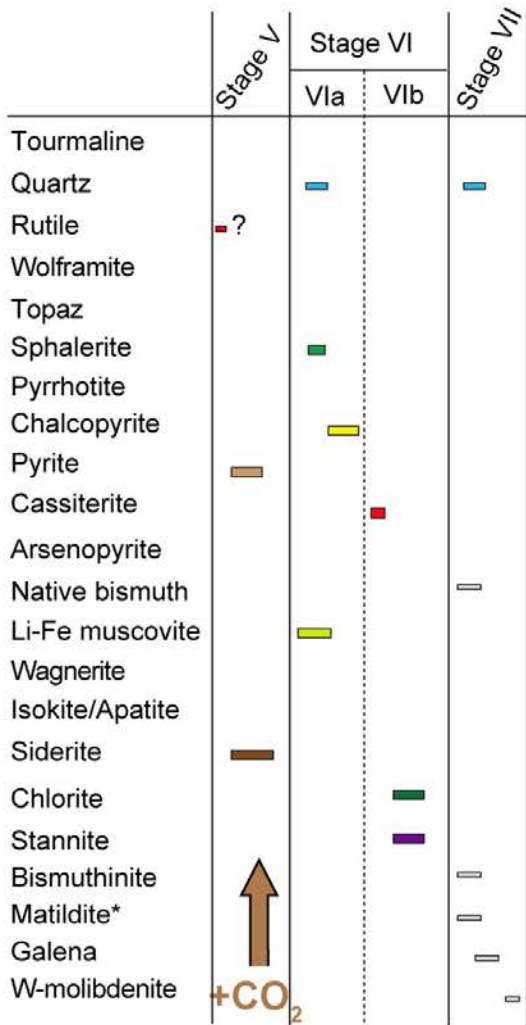


Fig. 3.12.: Expression of siderite out of the vugs, at pillar scale. a) Small (closed) siderite vug. The opening (arrows) seems controlled by extensional conditions. b) Siderite overprinting earlier assemblages in location L3-D25-R2A-AW31 (P3260744, Pinto). c) A particular of siderite “selvage”, in the same area (PB201274, Pinto).



stage V

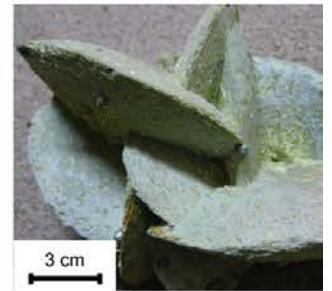
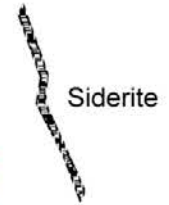


Fig. 3.13: Siderite stage is at the origin of the formation of euhedral large siderite crystals in cavities, the crystallization of xenomorph isolated crystals in the quartz veins, and some crystals at the boundary between host-rock and earliest veins in the cavities created by the muscovite-arsenopyrite stage. Siderite crystallizes onto quartz IV euhedral crystals, and is then covered by chalcopyrite crystals in geodes.

4 Fluid inclusions results

Fluid characterization

Table 1 summarizes the microthermometric and Raman spectroscopy data obtained on fluid inclusions studied in a series of minerals from the whole mineral sequence: QI, Topaz 1 and 2, QIII, Qz IV, Apatite, and Siderite. Table 2 shows the calculated bulk compositions of selected fluid inclusions representative of each inclusion type. Fluid inclusions are grouped in five major types.

The predominant type of fluid inclusions are carbonic-aqueous fluid inclusions that can be further subdivided into 4 sub-types (Fig. 3.14):

- Lc-(w) inclusions are high density carbonic-aqueous inclusions that homogenize into the liquid phase ("L" stands for liquid, "c" stands for carbonic and (w) is present, observed as a small water meniscus, i.e. between 0 and 5-10 vol. %, and by the nucleation of clathrates).

- Vc-(w) inclusions are low density carbonic-aqueous inclusions that homogenize into the vapor phase ("V" stands for vapor, "c" stands for carbonic) .

- Lw-c inclusions are aqueous-carbonic fluid inclusions whose volatile homogenize to the vapor phase at ThCO_2 and whose total homogenization (Th) occurs into the liquid phase, the amount of liquid water being higher than 70%.

- Lw-(g) inclusions. "g" means the passage from inclusions characterized by water and mix volatiles (carbon-nitrogen-methan), to inclusions water-dominated and containing separated coupled volatile phases (carbon-nitrogen, carbon-methan, methan-nitrogen). The density of volatile phase has been only detected by Raman spectroscopy and has low values, although relative amounts of CO_2 , N_2 and CH_4 may cover large ranges.

- Lw-hh are high-salinity aqueous fluid inclusions (>20 % eq. NaCl) (termed Lw for liquid water and Lwh for liquid water + halite when a NaCl cube is observed).

In most stages, carbonic-aqueous fluid inclusions Lc-(w) or Vc-(w) together with Lw-c inclusions were found. The two first types, Lc-(w) or Vc-(w), were poorly described in terms of microthermometric properties, densities and related isochores in the available literature although present in all studied samples. The hypersaline inclusions are described for the first time.

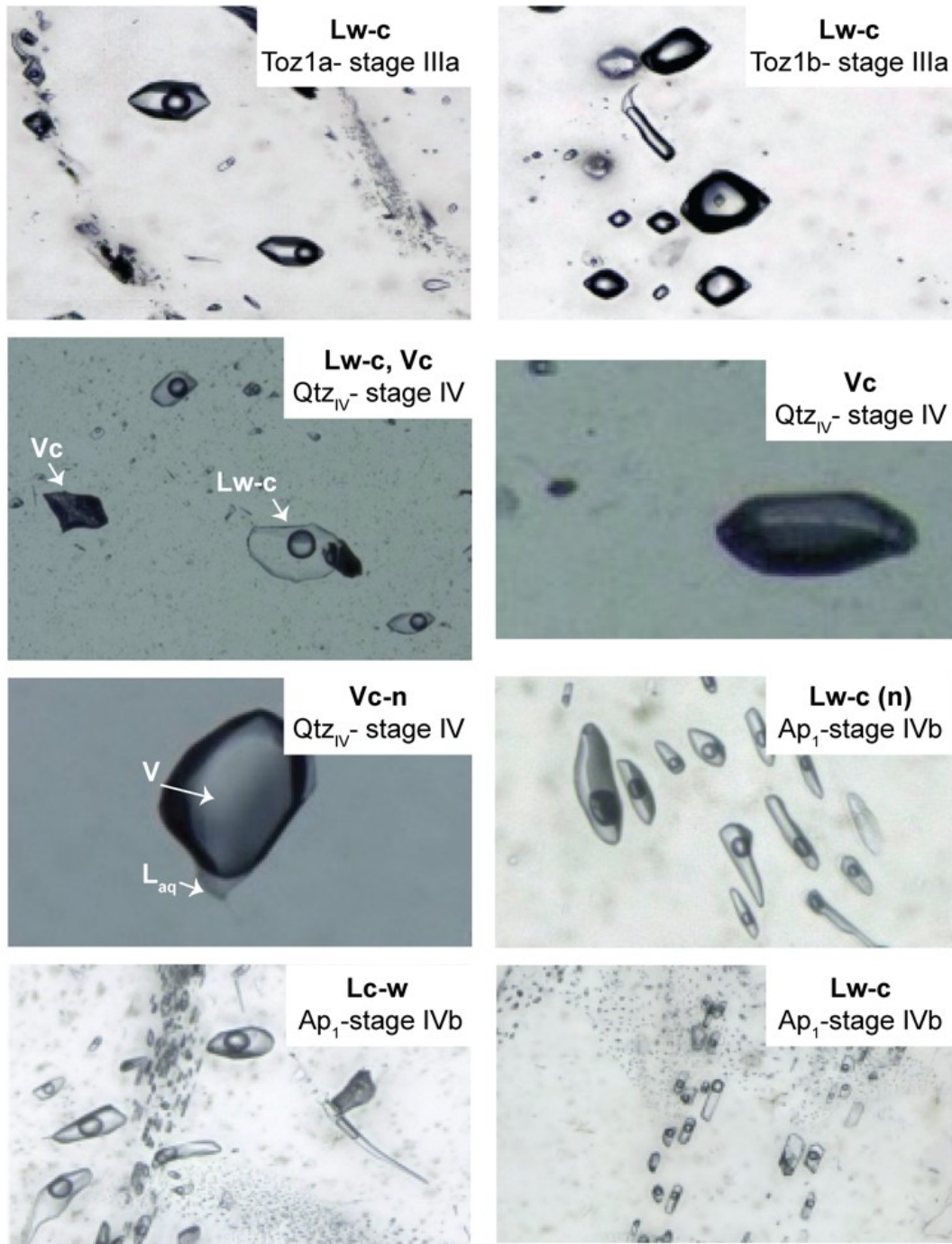


Fig. 3.14: Main fluid inclusions types in the main studied minerals (topaz1a), quartz QtzIV, and apatite. Nomenclature of fluid inclusions is explained in text.

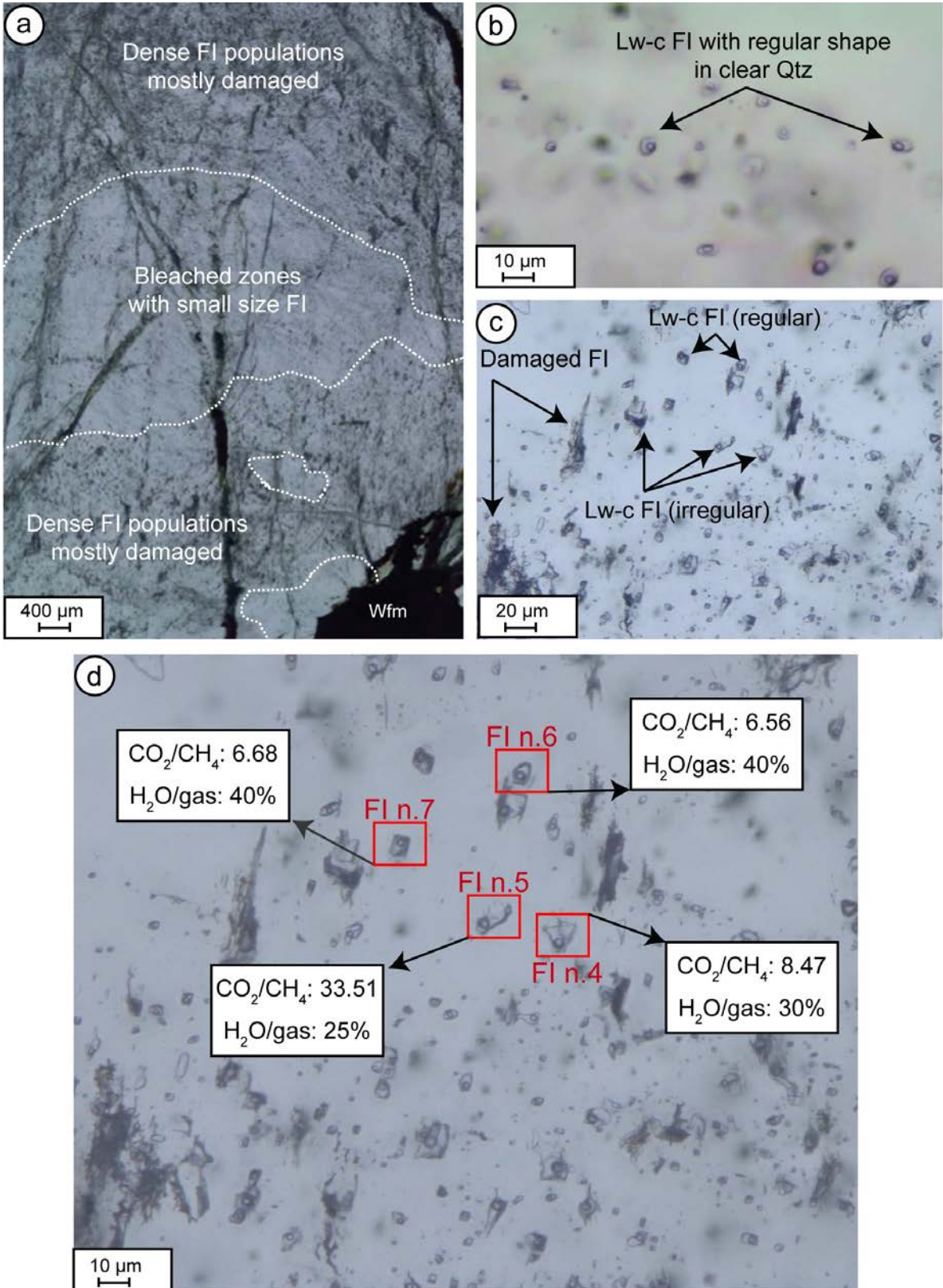


Fig. 3.16: Stage I-II: complex textures in relic quartz Qtz I affected by recrystallization during the stage IV: regular shape FI in clear recrystallized quartz Qtz IV (Lw-c inclusions), and deformed Lw-c inclusions in the earliest quartz Qtz I.

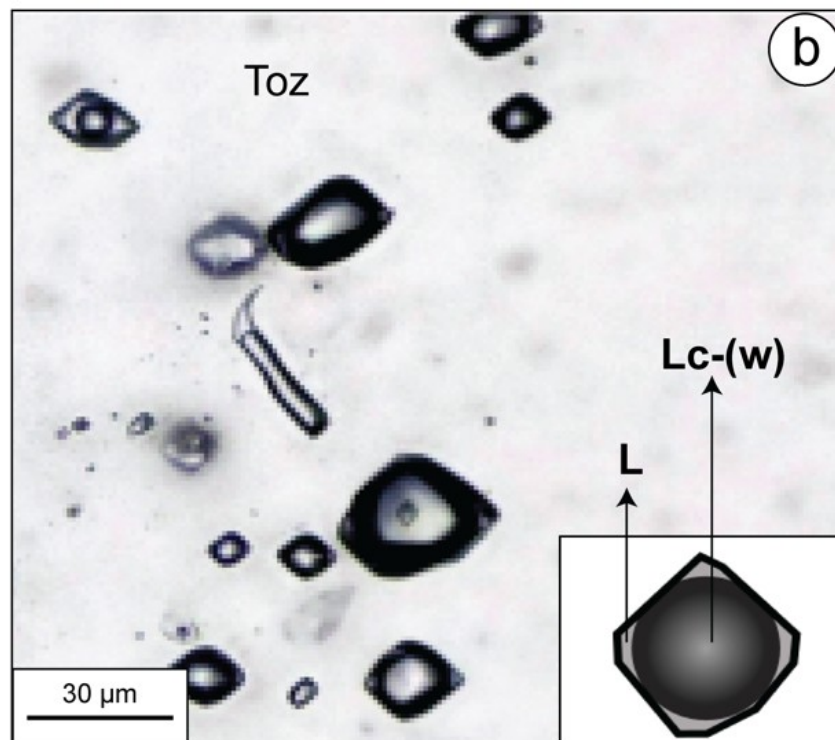
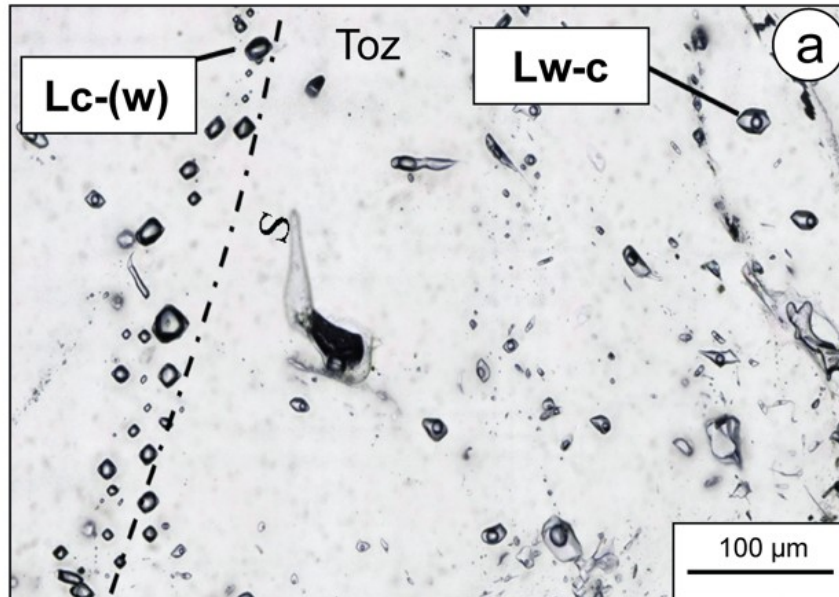


Fig. 3.17: Fluid inclusions in topaz 2. a: cluster of primary inclusions and pseudo-secondary inclusions aligned along FIP, b: detail of volatile rich dense Lc-(w) inclusions with negative crystal shape. Such inclusions were found exclusively in topaz, attesting that they correspond to fluid pulse nearly synchronous of topaz.

Quartz I (Quartz II): Aqueous-carbonic fluid inclusions (Tables 1 and 2) are the predominant inclusions in the quartz veins. They show also abundant decrepitation textures (highly irregular, dendritic textures (Fig. 3.15) **indicating** re-equilibration (Vityk and Bodnar, 1995) and/ or deformation (Diamond, 2003) processes. Such fluid inclusions show strong volatile/water ratio variability; the volatile phase represents the 30–100% of the fluid inclusion volume, and exhibits variations of CO₂/ CH₄ ratio (Fig. 3.16). The melting temperature of CO₂ (T_m CO₂) ranges from - 61.2 to -57.6°C.

Topaz: Toz 1 is characterized by the presence of decrepitated or deformed inclusions yielding to the loss of the fluid content during deformation. In topaz veins, topaz 2 has grown over the topaz 1, and no deformation is observed, all inclusions are well preserved in topaz 2. This could indicate that intense deformation stopped after Toz1 as, no other mineral phase from the overall sequence exhibits decrepitated inclusions except for quartz I-II and Topaz1. Two main types of fluid inclusions are observed: Lc-(w) inclusions and Lw-c inclusions. They occur as clusters of inclusions dispersed in clear topaz and are considered both as primary inclusions, and occur also as pseudo-secondary inclusions (Fig. 3.16).

Carbonic (-aqueous) fluid inclusions, Lc-(w) are 15 to 40 μm in size with a often crystal negative shape. They can form either rare three, most abundant two (Fig. 3.17) or in a few cases apparent one phase inclusions at room temperature. Thus, water can occur either as a thin meniscus up to 10 vol.% of the fluid inclusion volume (Lc(w)) or in smaller inclusions which is not visible (apparent Lc), but water is always present as clathrate are observed in all cases. At room temperature, the fraction of the volatile phase (fvp) thus ranges from 90 to 100 vol.%. T_mCO₂ of these inclusions ranges from -60.0 to -58.7 °C, Th_{CO2 (L+V→L)} ranges from 10.3 to 12.5 °C. Th_{CO2 (L+V→L)} are identical for a given cluster. T_mcl ranges from 8.6 to 10.6 °C and T_mice from -7.1 to -4.9 °C. Total homogenization temperatures (Th) ranges from 289 to 312°C.

Carbonic-aqueous, Lc-w inclusions are of 15 to 30μm in size and showed fvp ranging from 20 to 30 vol.%. T_mCO₂ of these inclusions ranges from -61.7 to -57.4 °C, Th_{CO2 (L+V→V)} ranges from 10.6 to 19.4 °C (Table 1). T_mcl ranges from 5.1 to 9.8 °C and T_mice from -6.9 to -4.3 °C. Total homogenization temperatures for Lc(w) inclusions, Th range from 250 to 295°C.

Several types of secondary fluid inclusions aligned in healed microfissures (fluid inclusions planes, noted FIP) are observed in topaz.

Lw-c inclusions (Fig. 3.18) display neither visible T_mCO₂ nor Th_{CO2} but the presence of CO₂ is attested by T_mcl ranging from 3.0 to 10.2°C, T_mice from -6.5 to -4.2 °C. Th ranges from 150 to 250°C. Other fluid inclusions as FIP are aqueous inclusions presenting traces of gases detected only by Raman spectroscopy. CO₂, CH₄ and N₂ are present in variable amounts.

In both Lc-(w), Lc-w, and Lw-c, the volatile phase is dominated by CO₂ (80 to 95 mol.%). CH₄ ranges from 2 to 9% and N₂ from 2 to 13%. N₂ is the most abundant in Lc-(w) inclusions where it ranges from 10 to 13%. (Table 1). The main features of representative FI bulk compositions are reported in Table 2.

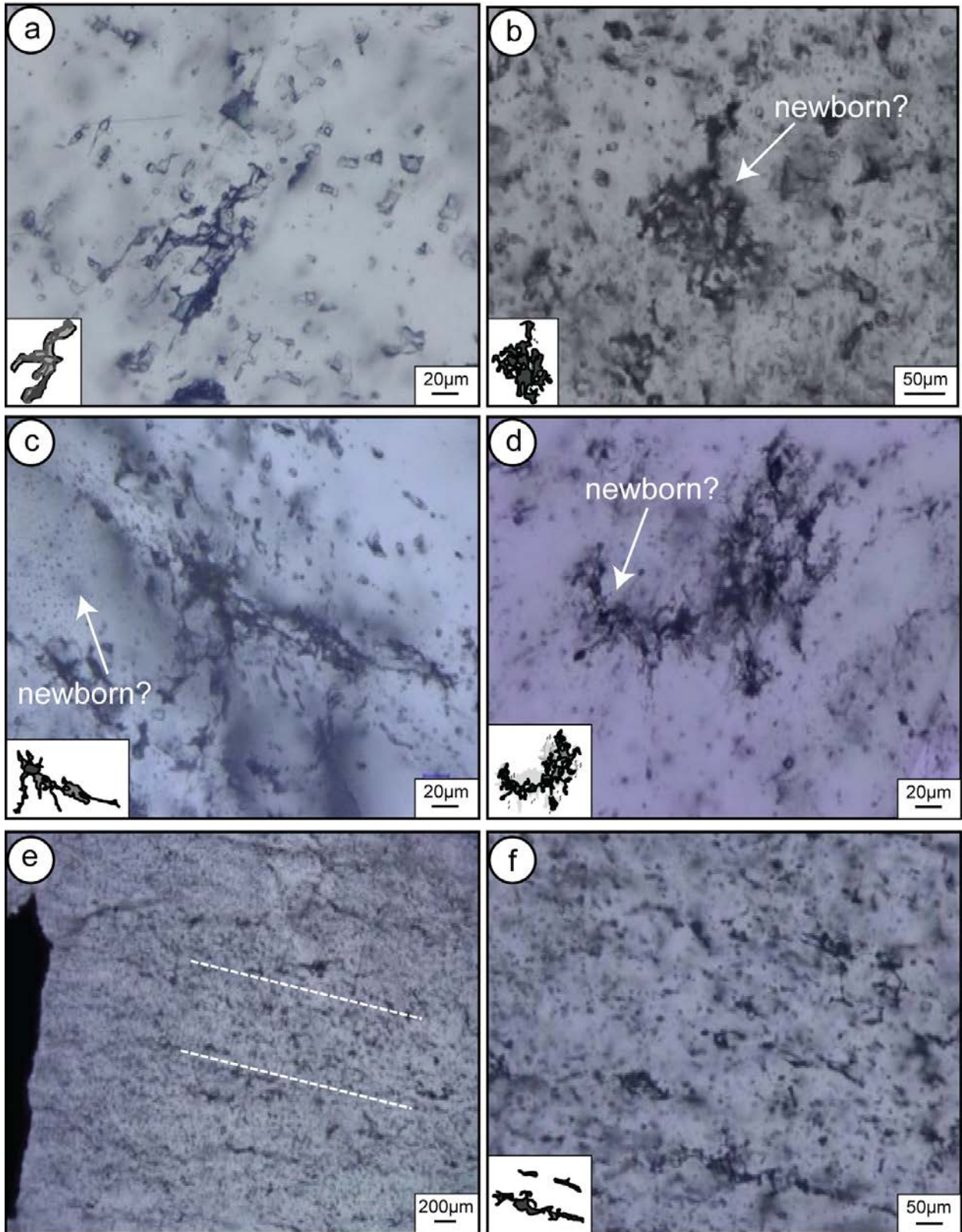


Fig. 3.15: Main features of decrepitated fluid inclusions types in Quartz Qtz I. The largest inclusions are destroyed whilst a few tiny inclusions are in part preserved.

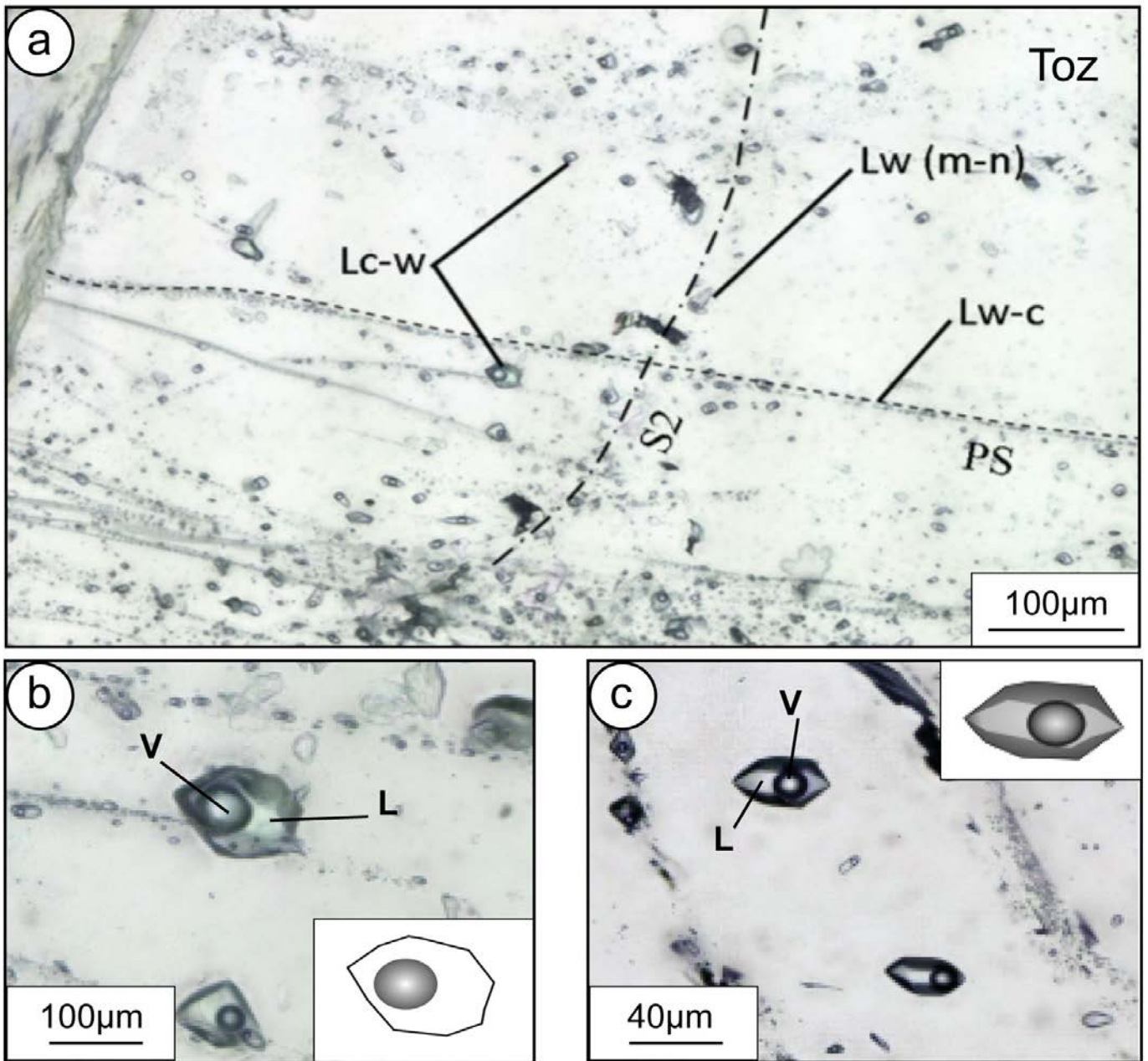


Fig. 3.18: Fluid inclusions in topaz 2. a: isolated primary inclusions and pseudo-secondary inclusions aligned along FIP, b: detail of primary Lw-c inclusions, c: negative crystal shape of the Lw-c inclusions.

Quartz III: No clear primary inclusions were found in euhedral quartz III. Several FIP (Fluid Inclusion Planes) are observed, some of them having similar features than those found in FI from stage IV. Most FI types are thus described together with Quartz IV. Carbonic-aqueous Lc-(w) inclusions show a predominant volatile phase (fvp). $T_{m_{CH_4-CO_2}}$ of these inclusions ranges from -90.6 to -86.7 °C, $T_{h_{CO_2 (L+V \rightarrow V)}}$ ranges from -83.4 to 83.4 °C.

Quartz IV: Quartz IV is clear with no decrepitated or deformed inclusions. In quartz IV, most types of fluid inclusions are observed as isolated clusters of inclusions, and as pseudo-secondary inclusions.

Carbonic-aqueous Lc-w inclusions (Fig. 3.19) isolated and considered as primary (FIP), crosscut all the micro-domains of quartz. Their size ranges between 10 and 100 μ m and show the fraction of the volatile phase (fvp) from 20 to 30 vol.%. $T_{m_{CO_2}}$ of these inclusions ranges from -62.1 to -57.9 °C, $T_{h_{CO_2 (L+V \rightarrow V)}}$ ranges from -10.8 to $+9.8$ °C. $T_{m_{cl}}$ ranges from 4.9 to 11.6 °C and $T_{m_{ice}}$ from -5.6 to -3.4 °C. T_h for Lc(w) inclusions, T_h range from 254 to 305°C.

Carbonic (-aqueous) vapors inclusions, Vc and Vc-(w) (Fig. 3.20) are 15 to 70 μ m in size with most often crystal negative shape. Water can occur as a thin meniscus up to 10 vol.% maximum of the fluid inclusion volume visible in the largest inclusions. At room temperature, their fvp is equal or higher than 95 vol.%. $T_{m_{CO_2}}$ of these inclusions ranges from -57.2 to -62 °C, $T_{h_{CO_2 (L+V \rightarrow V)}}$ ranges from 8.6 to 20.4 °C (Table 1 and Fig. 21). $T_{m_{cl}}$ ranges from 10 to 12.3°C and $T_{m_{ice}}$ around -7.7 . T_h is almost impossible to observe precisely.

Lw-c inclusions do not display $T_{h_{CO_2}}$ but the presence of CO_2 is attested by $T_{m_{CO_2}}$ ranging from -65.5 to -57.8 , and $T_{m_{cl}}$ ranges from -1.7 to 11.1 °C. $T_{m_{ice}}$ from -6.0 to -2.9 °C. T_h ranges from 169 to 311°C. Other fluid inclusions as FIP are aqueous inclusions presenting traces of gases detected only by raman spectroscopy. CO_2 , CH_4 and N_2 are present in variable amounts.

In both Lc-w, and Vc-(w), the volatile phase is dominated by CO_2 , CH_4 , and N_2 . The main features of representative FI bulk compositions are reported in Table 2. Several types of secondary fluid inclusions aligned in healed microfissures (fluid inclusions planes, noted FIP) are also observed in quartz IV.

Apatites are characterized by several growth episodes as revealed by microXRF mapping. Fluid inclusions have been thus reported in each crystal as a function of the stage of crystal growth and development of growth bands. All inclusions are well preserved and no evidence of deformation was found. Aqueous- carbonic Lc-w inclusions are 15 to 50 μ m in size are found within the first growth band of apatite, and show fvp ranging from 20 to 25 vol.%. $T_{m_{CO_2}}$ of these inclusions ranges from -60.5 to -58.5 °C, $T_{h_{CO_2 (L+V \rightarrow V)}}$ ranges from 12.7 to 15.9 °C (Table 1 and Fig. 7A). $T_{m_{cl}}$ ranges from 5.4 to 9.3 °C and $T_{m_{ice}}$ from -5.0 to -7.2 °C. Total homogenization temperatures for Lc(w) inclusions, T_h range from 275 to 296°C.

Carbonic (-aqueous) fluid inclusions, Vc-(w) are 15 to 70 μm in size most often crystal shape. Water can occur as a thin meniscus and at room temperature, the fraction of the volatile phase (fvp) thus is equal or higher than 95 vol.%. $T_{m_{\text{CO}_2}}$ of these inclusions ranges from -56.9 to -56.8 $^{\circ}\text{C}$, $T_{h_{\text{CO}_2}}$ is not observed (Table 1 and Fig.). $T_{m_{\text{cl}}}$ ranges from 2.2 to 2.4 $^{\circ}\text{C}$ and $T_{m_{\text{ice}}}$ is around -7.8 $^{\circ}\text{C}$. $T_{h_{\text{CO}_2 (L+V\rightarrow V)}}$ is above 200 $^{\circ}\text{C}$ but could not be observed precisely.

Vc-w inclusions are synchronous with Lw-c inclusions. Lw-c inclusions have $T_{m_{\text{CO}_2}}$ in between -62.1 and -58.5 $^{\circ}\text{C}$, $T_{h_{\text{CO}_2}}$ is not observed (Table 1). $T_{m_{\text{ice}}}$ ranges from -7.3 to -3.5 $^{\circ}\text{C}$. T_h ranges from 265 to 299 $^{\circ}\text{C}$.

Lw-(c-(n)) inclusions display neither visible $T_{m_{\text{CO}_2}}$ nor $T_{h_{\text{CO}_2}}$ but the presence of CH_4 is attested by Raman spectroscopy data. $T_{m_{\text{ice}}}$ ranges from -6.4 to -3.7 $^{\circ}\text{C}$ and T_h from 240 to 280 $^{\circ}\text{C}$. Besides the main fluid inclusion types, several other types are present in pseudo secondary and secondary fluid inclusions (FIP) in apatite.

Siderite (from stage IV) displays a series of aqueous –carbonic inclusions. In addition, hypersaline inclusions were found in some FIP.

Aqueous- carbonic Lc-w inclusions are of 15 to $50\mu\text{m}$ in size showing a fvp from 20 to 25 vol.%. $T_{m_{\text{CO}_2}}$ of these inclusions ranges from -62.1 to -57.6 $^{\circ}\text{C}$, $T_{h_{\text{CO}_2 (L+V\rightarrow V)}}$ ranges from 10.6 to 17.3 $^{\circ}\text{C}$. $T_{m_{\text{cl}}}$ ranges from 9.0 to 11.1 $^{\circ}\text{C}$ and $T_{m_{\text{ice}}}$ from -7.9 to -3.0 $^{\circ}\text{C}$. Total homogenization temperatures for Lc(w) inclusions, $T_{h (L+V\rightarrow L)}$ ranges from 294 to 298 $^{\circ}\text{C}$.

Carbonic (-aqueous) fluid inclusions, Vc-(w) are 15 to $70\mu\text{m}$ in size with most often crystal negative shape. The volatile phase (fvp) thus is equal or higher than vol.%. $T_{m_{\text{CO}_2}}$ of these inclusions ranges from -61.5 to -58.6 $^{\circ}\text{C}$, $T_{h_{\text{CO}_2}}$ ranges from 13.1 to 17.1 . $T_{m_{\text{cl}}}$ ranges from 9.9 to 13.2 $^{\circ}\text{C}$ and $T_{m_{\text{ice}}}$ ranges from -22.8 to -14.6 $^{\circ}\text{C}$. T_h is around 250 - 260 $^{\circ}\text{C}$.

Several other fluid inclusion types are observed.

Lw-hh inclusions are hypersaline characterized sometimes by the presence of halite cube, $T_{m_{\text{ice}}}$ from -23.2 to -19.3 $^{\circ}\text{C}$ and $T_{m_{\text{h}}}$ is observed in between -29.3 and -4.5 $^{\circ}\text{C}$. T_h are rather scattered with values up to 336 $^{\circ}\text{C}$. Eutetic temperatures are rather low and indicative of the presence of Li (Te difficult to observe precisely in between -80 and -60 $^{\circ}\text{C}$). They contain in some instance and halite cube which melts at 150 $^{\circ}\text{C}$.

Lw-c inclusions do not display $T_{h_{\text{CO}_2}}$ but the presence of CO_2 is attested by $T_{m_{\text{CO}_2}}$ ranging around -57.8 $^{\circ}\text{C}$, and $T_{m_{\text{cl}}}$ ranges from 7.1 to 9.6 $^{\circ}\text{C}$. $T_{m_{\text{ice}}}$ from -4.0 to -2.3 $^{\circ}\text{C}$. T_h is around 276 $^{\circ}\text{C}$. Other fluid inclusions as FIP are aqueous inclusions presenting traces of gases detected only by Raman spectroscopy. CO_2 , CH_4 and N_2 are present in variable amounts.

Other inclusions are Lw-c FI with $T_{m_{\text{cl}}}$ ranging from 7.1 to 9.6 $^{\circ}\text{C}$, $T_{m_{\text{ice}}}$ ranging from -4.0 to -2.3 $^{\circ}\text{C}$ and T_h from 115 to 197 $^{\circ}\text{C}$. Lw FI have $T_{m_{\text{ice}}}$ ranging from -5.9 to -0.6 $^{\circ}\text{C}$ and T_h from 170 to 280 $^{\circ}\text{C}$.

Qtz IV

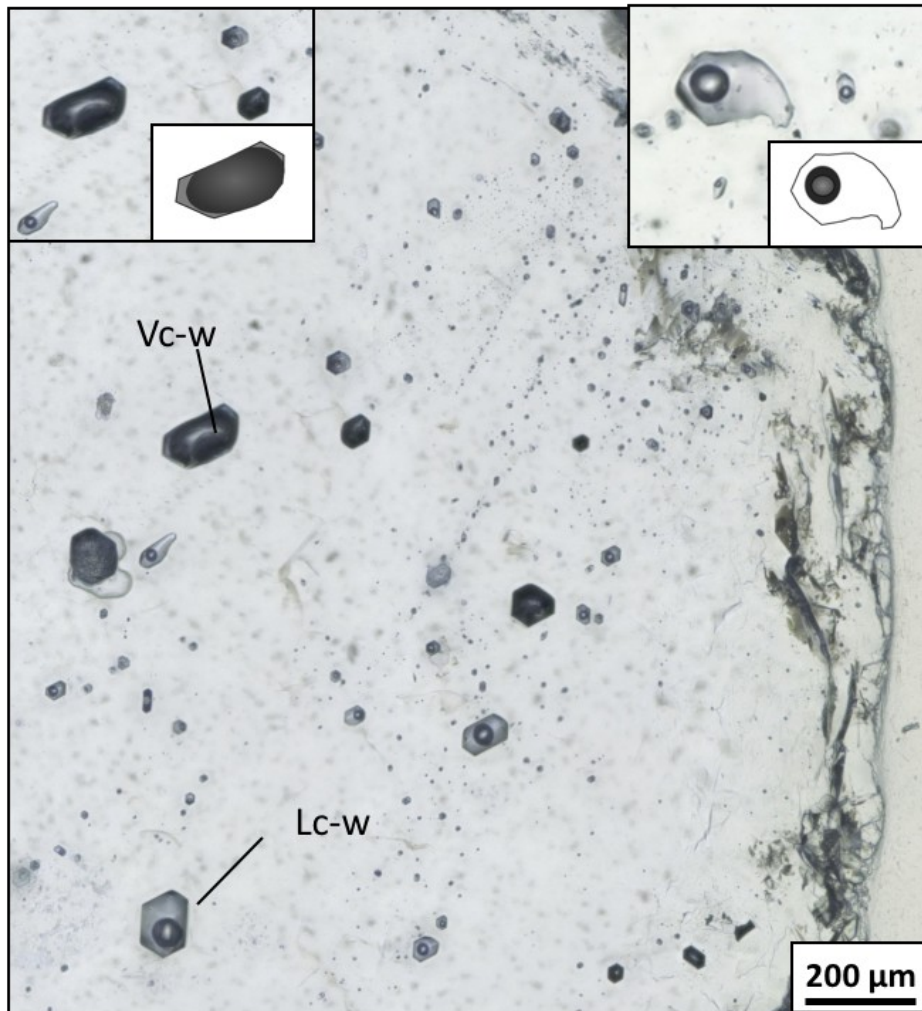


Fig. 3.19: Fluid inclusions in quartz IV: co-existence of primary Lw-c and V-w-c inclusions in quartz IV. This association, coupled with microthermometric and Raman results attests of an episode of unmixing. Thus, both fluid compositions and densities are compatible with unmixing conditions. This is the kind of observation which yields to the conclusions of « boiling » as suggested by Kelly and Rye, 1979, and then Bussink, 2004. This late stage (IV) is the only one for which unmixing occurred.

Quartz QIV

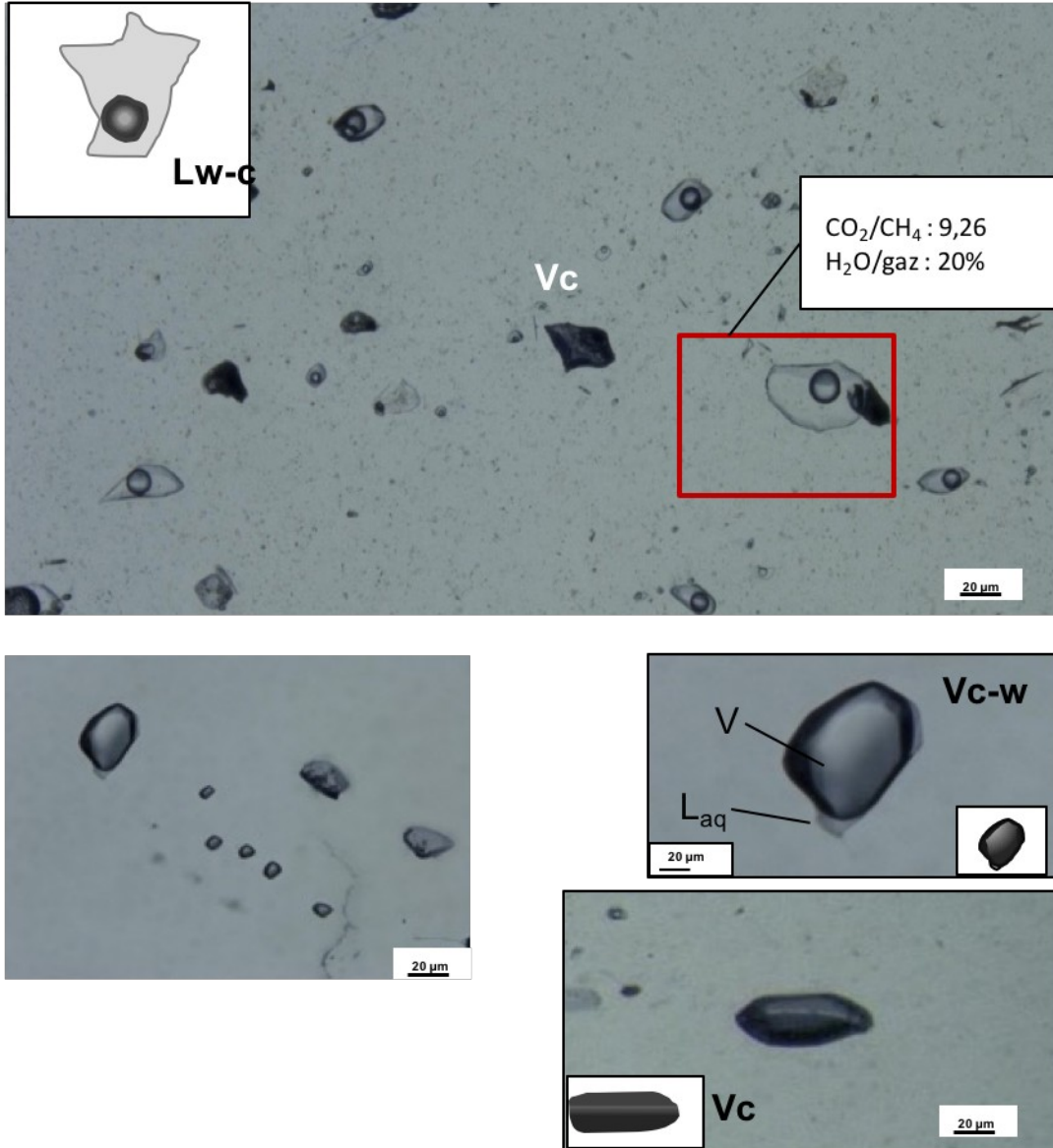


Fig. 3.20: Fluid inclusions in euhedral quartz Qtz IV. A: association of primary inclusions Vc and Vc(w) inclusions and Lw-v inclusions, B: detail of volatile rich dense Lc(w) inclusions with negative crystal shape. Such inclusions were found exclusively in topaz, attesting that they correspond to fluid pulse sub-synchronous of Topaz.

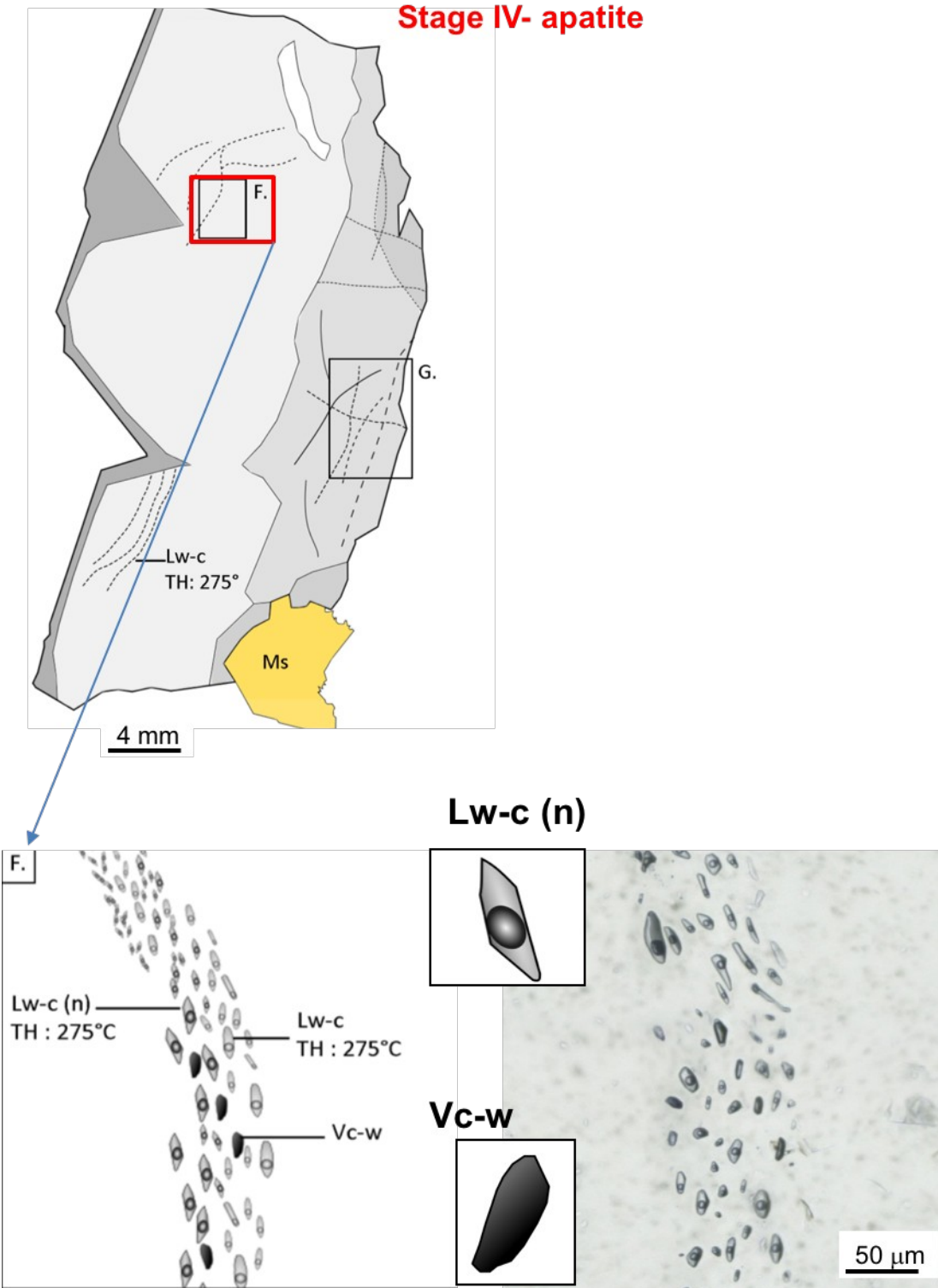


Fig. 3.21: Example of pseudo-secondary fluid inclusion planes containing both Lw-(g) inclusions (with g= CO₂ and N₂) and Vc-w inclusions. The square noted F, is presented below in detail with a sketch drawing and the corresponding microphotograph.

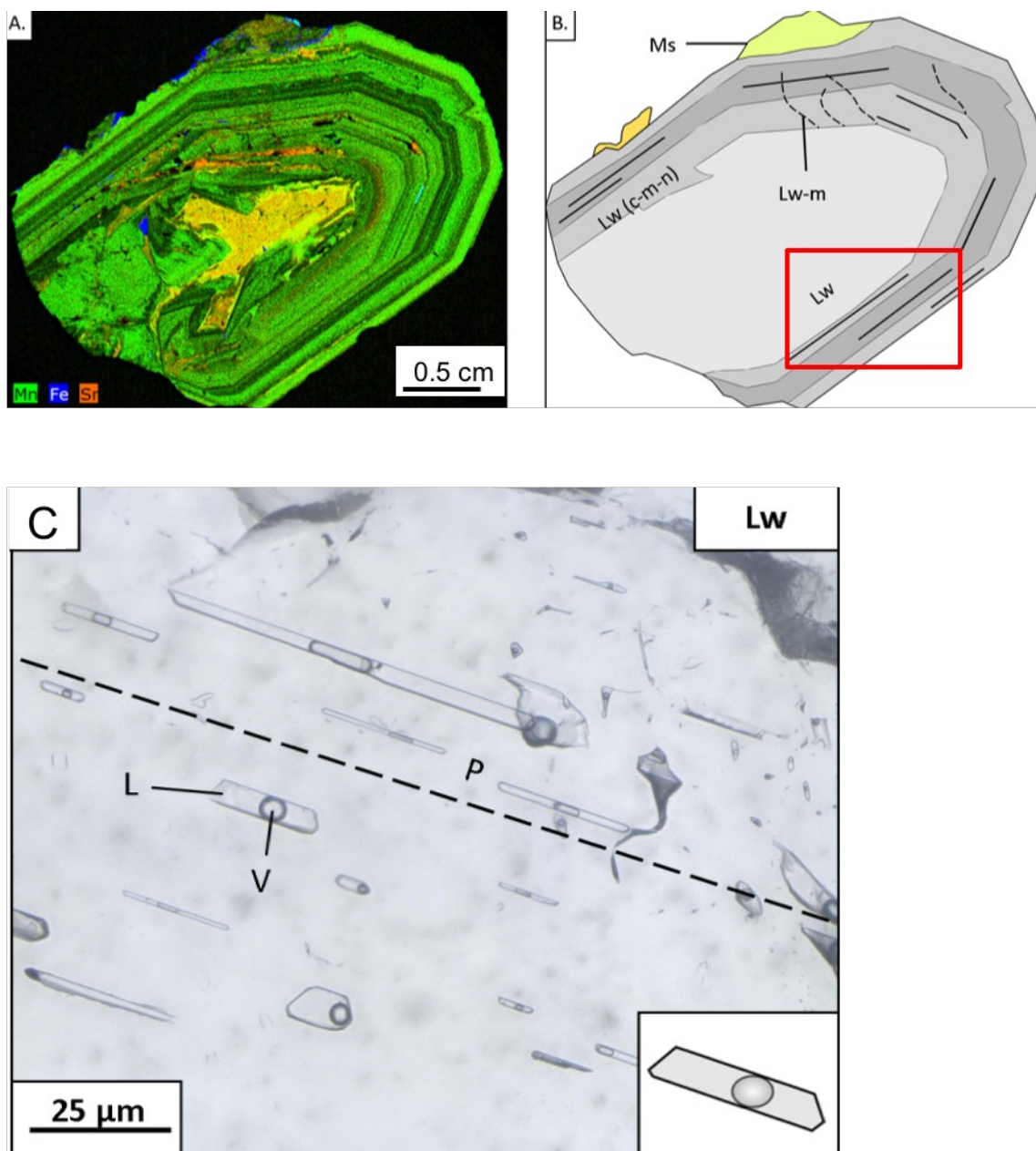


Fig. 3.22: A. Multi-element micro-fluorescence X map of apatite crystal revealing the growth bands. B. On the map of growth bands issued from micro-XRF, the main FI fields are reported: primary inclusions along growth bands and pseudo-secondary inclusions as small healed microfissures. C. Field of primary Lw inclusions in the external growth band of apatite.

Stage	Mineral	IF type	Tm CO2	Th CO2	mode	Tm Cl	Tm ice	Tm hh	Th	mode
I	Quartz I	Lw-c				5.3 to 10.1 13	-4.6 to -7.8 14		198 to 232 6	L
	Topaz	Lc-(w)	-58.7 to -60 9	10.3 to 12.5 9	L	8.6 to 10.6 9	-4.9 to -7.1 7		289 to 312 9	V
		Lc-w	-57.4 to -61.7 16	10.6 to 19.4 9	V	5.1 to 9.8 16	-4.3 to -6.9 16		250 to 295 16	L
IIIa		Lw-c				3 to 10.2 8	-4.2 to -6.5 8		150 to 250 8	L
		Lw-(g)					-2.8 to -5.2 7		160 to 213 6	L
	Quartz III	Lc-(w)	-86.7 to -90.6 4	-83.4 to 84.9 4	L					
III		Lw-c	-57.6 to 61.2 22			9.8 to 13.7 36	-4 to -10 37		205 to 285 14	L
		Lw-(g)					-1.1 to -1.2 5		150 to 191 5	L
		Lw-hh					-20.3 to -26.6 25	2.9 to 16.7 16	105 to 142 11	
	Quartz IV	Lc-w	-57.9 to 62.1 8	-10.8 to 9.8 7	V	4.9 to 11.6 10	-3.4 to -5.6 11		254 to 305 10	L
		Lw-c	-57.8 to -65.5 17			-1.7 to 11.1 28	-2.9 to -6 23		169 to 311 23	
IV		Vc-(w)	-57.2 to -62 10	8.6 and 20.4 2	V	10.6 and 12.3 2	-7.7 1			
		Lw-(g)					-0.3 to -2.6 15		115 to 180 15	
		Lw-(g)-hh					-21.4 8	-8.5 8	118 to 120 8	
	Apatite	Lc-w	-58.5 to -60.5 9	12.7 to 15.9 9	V	5.4 to 9,3 9	-5 to -7.2 9		275 to 296 9	L
IV		Lw-c	-58.5 to -62.1 9			3.1 to 10.7 26	-3.5 to -7.3 32		265 to 299 32	L
		Lw-(g)					-3.7 to -6.4 11		240 to 280 9	L
		Vc-(w)	-56.8 to -56.9 2			2.2 to 2.4 2	-7.8 1		200 2	L
	Siderite	Vc-(w)	-58.6 to -61.5 18	13.1 to 17.1 15	V	9.9 to 13.2 11	-14.6 to -22.8 13		256 1	
V		Lc-w	-57.6 to -62.1 20	10.6 to 17.3 16	V	9 to 11.1 17	-3 to -7.9 15		294 to 298 2	L
		Lw-c	-57.8 4			7.1 to 9.6 11	-2.3 to -4 10		276 2	L
		Lwhh					-19.3 to -23.2 25	-4.5 to -29.3 11	115 to 197 5	L
		Lw					-0.6 to -5.9 53		170 to 280 25	L

Table1: Microthermometric data for all studied stages.

Stage	type	Inclusion N°	Type	Microthermometry						Raman analysis				Bulk composition				
				TmCO ₂	ThCO ₂	Mode	TmCl	Tm Ice	TH	mode	%CO ₂	%CH ₄	%N ₂	H ₂ O	CO ₂	CH ₄	N ₂	NaCl
I	Deformed Qi	5	Lw-c				8,7	-7,8	209	L	97	3	0	93,0	4,6	0,1	2,3	
I	Deformed Qi	8	Lw-c				10,1	-4,7	222	L	93	7	0	93,8	4,9	0,2	1,1	
I	Deformed Qi	9	Lw-c				10,1	-5,1	199	L	94	6	0	94,0	4,3	0,1	1,6	
I	Deformed Qi	16	Lw-c				6,9	-6,1	233	L	84	16	0	94,4	3,4	0,2	2,0	
I	Deformed Qi	6	Lw-c				7,1	-4,8	213	L	82	13	5	94,1	4,2	0,3	1,3	
IIa	Topaz II	1.a	Lc-(w)	-60,0	10,4	L	9,7	-7,1	300	V	88	3	9	13,3	76,6	2,3	7,8	
IIa	Topaz II	1.b	Lc-(w)	-59,9	10,3	L	9,7	-5,1	299	V	87	3	10	23,9	66,3	2,0	7,7	
IIa	Topaz II	1.c	Lc-(w)	-58,8	10,5	L	9,5	-5,5	312	V	85	3	12	13,6	73,1	2,9	10,4	
IIa	Topaz II	1.d	Lc-(w)	-58,7	11,6	L	9,7	-5,2	304	V	85	4	12	13,4	73,3	3,0	10,3	
IIa	Topaz II	IV.1.a	Lc-(w)	-59,4	11,3	L	9,8	-4,9	295	V	85	3	12	24,3	64,6	2,5	8,5	
IIa	Topaz II	2.b	Lc-w	-58,9	18,9	V	8,1	-5,2	250	L	89	3	8	90,6	6,3	0,1	0,3	
IIa	Topaz II	2.d	Lc-w	-57,8	19,4	V	9,8	-4,4	254	L	88	3	9	92,6	5,5	0,1	0,3	
IIa	Topaz II	X.4	Lc-w	-58,3	14,9	V	6,1	-5,5	250	L	91	4	5	94,1	3,4	0,0	0,0	
IIa	Topaz II	IV.1.a	Lc-w	-57,9	18,3	V	9,1	-5,4	290	L	91	3	7	92,9	4,6	0,6	0,1	
IIa	Topaz II	2.b	Lc-w	-58,6	11,2	V	9,2	-4,8	295	L	95	3	2	92,6	5,4	0,1	0,2	
IIa	Topaz II	2.a	Lc-w	-59,3	10,6	V	8,6	-5,2	285	L	87	4	9	92,1	5,2	0,2	0,3	
IIa	Topaz II	3.a	Lw-c				10,2	-4,2	185	L	80	8	12	95,6	3,1	0,1	1,1	
IIa	Topaz II	I.2.a	Lw-c				4,7	-5,3	152	L	1	38	61	96,5	0,1	0,5	0,8	
IIa	Topaz II	IV.2.c	Lw-c				2,9	-4,6	159	L	1	40	59	97,1	0,1	0,4	0,5	
IIa	Topaz II	X.1	Lw-c				5,5	-5,3	248	L	83	5	11	94,9	3,3	0,2	1,6	
IIa	Topaz II	X.3	Lw-c				5,9	-5,6	247	L	88	4	8	94,7	3,6	0,1	0,1	
IIa	Topaz II	III.1.a	Lw-c				8,2	-6,5	255	L	86	6	8	94,2	3,6	0,1	0,1	
IIa	Topaz II	3.b	Lw-(fg)					-3,8	213	L	87	5	8					
IIa	Topaz II	3.c	Lw-(fg)					-3,8	203	L	91	3	6					
IIa	Topaz II	IV.2.b	Lw-(fg)					-5,2	217	L	73	11	16					
IIa	Topaz II	3.b	Lw-(fg)					-4,1	172	L	56	19	25					
III	QIII	A/E D	Lc-(w)	-90,6 *	-84,0	L					10	72	19	0	10	71	19	
III	QIII	A/E E	Lc-(w)		-84,7	L					8	74	18	0	8	74	18	
III	QIII	A/E H	Lc-(w)	-88,7 *	-84,9	L					3	79	19	0	2	78	19	
III	QIII	A/E I	Lc-(w)	-86,7 *	-83,4	L					17	65	19	0	16	65	19	
III																		
III	QIII	B/A B	Lw-c				9,9	-5,8	nd		92	2	6	92	5	0	0	
III	QIII	B/A C	Lw-c				10	-6,5	nd		83	6	11	91	5	0	0	
III	QIII	B/A E	Lw-c				10,2	6,3	nd		77	6	17	91	5	0	1	
III	QIII	B/A F	Lw-c				10,2	-5,7	nd		70	9	20	92	5	0	0	
III	QIII	B/A G	Lw-c				10	-5,4	nd		84	6	10	92	5	0	0	
III	QIII	B/A H	Lw-c				9,9	-5,5	nd		79	7	14	91	6	0	0	
III	QIII	B/A I	Lw-c				9,8	-5,4	nd		88	4	8	92	5	0	0	
III	QIII	B/A J	Lw-c				9,8	-5,4	nd		92	3	5	91	6	0	0	
III	QIII	G/A A	Lw-c				11,8	-4,1	nd		76	7	17	91	7	0	1	
III	QIII	G/A B	Lw-c	-58,3			11,7	-4,4	nd		76	8	17	95	3	0	0	
III	QIII	G/A C	Lw-c	-57,8			11,3	-4,6	nd		82	5	13	92	6	0	2	
III	QIII	G/A D	Lw-c	-59			12	-4,4	nd		80	7	14	92	6	0	2	

Table 2: Microthermometric and Raman data of representative fluid inclusions from all studied stages (continues on the two following pages)

Stage	type	Inclusion N°	Type	Microthermometry						Raman analysis				Bulk composition				
				TmCO2	ThCO2	Mode	TmCl	Tm Ice	TH	mode	%CO2	%CH4	%N2	H2O	CO2	CH4	N2	NaCl
IV	QIV	1	Lc-w	-59,8	-1,3	V	10,8	-5,0	265	V	73	9	19	95,6	3,6	0,2	0,3	0,3
IV	QIV	5	Lc-w	-59,5	1,5	V	8,5	-5,4	254	L	77	12	11	94,0	3,6	0,2	0,2	2,1
IV	QIV	1a	Lc-w	-59,6	9,8	V	11,3	-5,1	289	V	87	5	8	94,1	5,0	0,1	0,2	0,5
IV	QIV	2.a	Lc-w		9,5	V	11,6	-3,8	305	L	86	4	10	94,3	5,0	0,1	0,3	0,3
IV	QIV	2.a	Lc-w	-62,1	-10,6	V	5,7	-5,6	246	L	72	18	10	93,9	2,9	0,2	0,1	2,8
IV	QIV	2	Lc-w	-66,3	0,9	V	8,2	-3,4	259	L	55	18	27	94,5	2,9	0,3	0,5	1,8
IV	QIV	8	Lc-w	-60,5	-1,7	V	9,9	-4,4	298	L	62	10	27	92,9	4,4	0,4	1,0	1,4
IV	QIV	1.a	Vc-(w)	-57,2	8,6	V	10,6	-7,7	200	V	78	13	8	66,5	25,9	4,2	2,7	0,9
IV	QIV	2	Vc-(w)	-57,6	nd		nd	nd	nd		96	4	0	0,0	96,0	4,0	0,0	0,0
IV	QIV	9	Vc-(w)	-57,7	20,4	V	nd	nd	nd		98	2	0	0,0	98,0	2,0	0,0	0,0
IV	QIV	H	Vc-(w)	-60,7	nd		12,3	nd	nd		67	8	25	0,0	67,0	8,4	24,6	0,0
IV	QIV	D	Vc-(w)	-61,0	nd		nd	nd	nd		46	15	39	0,0	46	15	39	0,0
IV	QIV	J	Vc-(w)	-61,8	nd		nd	nd	209	V	46	11	43	0,0	46	11	43	0,0
IV	QIV	2	Vc-(w)	-62,0	nd		nd	nd	nd		46	18	36	0,0	46	18	36	0,0
IV	QIV	B	Vc-(w)	-62,0	-34,0	V	nd	nd	234	V	55	13	32	0,0	55	13	32	0,0
IV	QIV	G	Vc-(w)	-61,5	nd		nd	-5,0	nd		55	11	34	0,0	55	11	34	0,0
IV	QIV	A	Lw-c	-59,3			10,6	-5,2	306	L	91	5	4	91,6	7,0	0,2	0,2	1,0
IV	QIV	F	Lw-c	-59,7			11,7	-5,0	311	L	88	6	6	92,8	5,6	0,2	0,2	1,2
IV	QIV	1.a	Lw-c	-58,7			10,5	-3,8	286	L	65	12	23	95,0	3,4	0,2	0,4	1,0
IV	QIV	6.a	Lw-c	-59,6			8,2	-3,7	305	L	60	13	27	95,6	2,8	0,2	0,4	1,0
IV	QIV	2.b	Lw-c	-63,5			9,2	-3,8	291	L	63	13	25	94,3	3,7	0,3	0,6	0,9
IV	QIV	2.c	Lw-c	-58,5			8,9	-3,2	286	L	72	9	20	94,7	3,8	0,2	0,4	0,8
IV	QIV	1.a	Lw-c	-65,5			8,5	-3,5	278	L	62	15	23	95,7	2,9	0,2	0,3	0,9
IV	QIV	1.b	Lw-c	-65,4			7,4	-3,5	277	L	63	15	22	96,0	2,6	0,2	0,2	1,0
IV	QIV	1.c	Lw-c	-63,5			3,2	-3,8	280	L	70	13	18	96,6	2,1	0,1	0,1	1,1

Stage	type	Inclusion N°	Type	Microthermometry					Raman analysis					Bulk composition				
				TmCO2	ThCO2	Mode	TmCl	Tm Ice	TH	mode	%CO2	%CH4	%N2	H2O	CO2	CH4	N2	NaCl
IV	Apatite	1.a	Lc-w	-58,9	15,9	V	7,7	-6,4	290	L	83	9	83,5	3,6	0,1	0,1	2,7	
IV	Apatite	1.b	Lc-w	-58,9	12,7	V	6,5	-6,0	275	L	81	7	90,9	5,1	0,3	0,4	3,4	
IV	Apatite	1.c	Lc-w	-58,5	14,8	V	7,4	-7,2	278	L	81	7	89,6	6,2	0,3	0,6	3,3	
IV	Apatite	1.d	Lc-w	-58,9	15,8	V	5,4	-5,5	290	L	80	8	91,2	5,0	0,2	0,4	3,2	
IV	Apatite	1.f	Lc-w	-59,0	14,5	V	9,3	-6,6	278	L	82	7	91,2	5,9	0,3	0,5	2,1	
IV	Apatite	3.d	Lc-w	-60,2	14,7	V	7,5	-5,0	295	L	70	7	91,8	4,2	0,2	0,6	3,3	
IV	Apatite	4.b	Lc-w	-60,5	14,2	V	9,0	-6,3	295	L	89	7	93,1	4,5	0,2	0,1	2,1	
IV	Apatite	1.e	Vc-(w)	-56,9			2,2	-7,8	200	V	93	6	77,4	21,0	1,2	0,3	0,1	
IV	Apatite	1.f	Vc-(w)	-56,8			2,4		200	V	100	0	77,6	22,3	0,0	0,0	0,1	
IV	Apatite	1.a	Lw-c				6,3	-6,5	276	L	81	7	94,3	3,4	0,1	0,2	2,1	
IV	Apatite	1.a	Lw-c				3,1	-6,2	298	L	75	11	95,3	2,4	0,1	0,1	2,2	
IV	Apatite	1.c	Lw-c				4,2	-6,3	299	L	81	11	94,6	3,0	0,2	0,1	2,1	
IV	Apatite	1.e	Lw-c				3,9	-6,2	297	L	89	11	95,2	2,6	0,1	0,0	2,1	
IV	Apatite	2.a	Lw-c				7,7	-5,3	271	L	75	15	94,9	3,1	0,2	0,1	1,6	
IV	Apatite	2.b	Lw-c				8,5	-5,5	272	L	70	16	94,6	3,2	0,3	0,2	1,7	
IV	Apatite	1.c	Lw-c	-62,1			6,1	-7,3	277	L	86	6	94,1	3,3	0,1	0,1	2,5	
IV	Apatite	2.a	Lw-c	-58,5			5,3	-6,7	280	L	84	8	94,1	3,5	0,1	0,1	2,2	
IV	Apatite	2.c	Lw-c	-58,5			8,9	-7,1	268	L	83	7	92,9	4,7	0,2	0,2	1,9	
IV	Apatite	2.f	Lw-c	-65,5			4,1	-6,3	277	L	85	8	94,6	3,2	0,1	0,1	2,1	
IV	Apatite	3.a	Lw-c	-60,2			9,2	-5,7	275	L	72	9	94,2	3,6	0,2	0,3	1,7	
IV	Apatite	3.b	Lw-c	-60,5			8,5	-5,9	279	L	68	9	94,3	3,4	0,2	0,4	1,8	
IV	Apatite	3.c	Lw-c	-59,6			9,2	-7,0	275	L	67	9	93,5	3,7	0,2	0,5	2,1	
IV	Apatite	4.a	Lw-c	-58,9			8,5	-6,5	295	L	83	6	93,7	4,1	0,1	0,2	1,9	
IV	Apatite	1.a	Lw-c				10,0	-3,8	283	L	8	85	7	94,8	0,6	3,0	0,2	1,3
IV	Apatite	1.b	Lw-c				10,7	-3,9	276	L	4	93	3	94,6	0,4	3,6	0,1	1,3
IV	Apatite	2.a	Lw-c				9,4	-3,8	286	L	12	77	12	94,8	0,8	2,7	0,4	1,3
IV	Apatite	2.b	Lw-c				10,1	-4,0	291	L	9	74	17	94,5	0,7	2,9	0,6	1,3
V	Siderite	5e	Vc-(w)	-61,2	17,1	V	12,8	-16,6			51,9	13,2	34,9					
V	Siderite	1a	Vc-(w)	-60,8			11,9	-14,6			56,3	12,6	31,1	55,8	25,4	5,4	13,4	0
V	Siderite	1b	Vc-(w)	-60,7	13,8	V		-14,6			56,6	11,5	31,9					
V	Siderite	SB122a	Lc-w	-58,6	14,7	V	10,5				91	5	4	89,7	8,6	0,3	0,3	1,1
V	Siderite	SB121	Lc-w	-59,0	14,2	V	10,3	-7,9			94	0	6	93,6	5,7	0	0,2	0,5
V	Siderite	SB121-2	Lc-w	-59,4	14,3	V	10,2	-6,2			83	7	10	93	4,7	0,2	0,3	1,8
V	Siderite	SB121-3	Lc-w	-58,4			9,0	-7,1			68	16	16	92,6	4,5	0,5	0,5	1,9
V	Siderite	SB121-4	Lc-w	-58,7	14,3	V	10,5	-3,4			85	5	10	92	6	0,2	0,4	1,4
V	Siderite	SB121-5	Lc-w	-58,7	14,2	V		-6,9			81	0	19	91,4	6,1	0	0,8	1,7
V	Siderite	SB121-6	Lc-w	-58,7			9,6	-7,1			85	7	8	92,7	5	0,2	0,2	1,9

5 Bulk chemical evolution

Most fluids are aqueous-carbonic and have H₂O/CO₂/CH₄ ratio close to those predicted by water-graphite equilibrium at high temperatures above 400°C (Huizenga, 2001). The aqueous-carbonic fluids from quartz veins (Qtz I and II) are dominated by water, but contain a volatile phase dominated by CO₂, and a low content in methane and nitrogen. In quartz I-II, the variations in volatile/water ratio ranges may be attributed to the partial resetting of the FI during deformation. In topaz (Stage IIIa), two distinct fluid types of high densities are encountered with well-defined chemical compositions, a water rich aqueous carbonic fluid and a volatile rich liquid, both having a volatile component dominated by CO₂ and a minor CH₄ contribution. The volatile phase rather rich in CO₂ is coherent with the high P-T pair of trapping (see below) at water-graphite equilibrium.

An evolution of the volatile phase is then observed from Stage I-III towards stage IV fluids which display pulses of fluids with lower volatile density but higher relative amounts of CH₄ and N₂ compared to CO₂. Thus, considering the H₂O content and the CO₂/CH₄ ratio (Fig. 3.23 to 3.26), three end-members can be identified: i) the fluids close to equilibrium with graphite dominated by H₂O, and CO₂ in the volatile phase, ii) water rich fluids with traces of gases, with two main end-members for the volatile phase and almost all intermediate compositions in between a N₂ dominated end-member close to N₂ and a CH₄ dominated end-member, close to CH₄.

Volatile rich (CH₄-N₂) fluids may indicate that some lithologies produced significant amounts of CH₄ during thermal events, N₂ being probably produced by the oxidation of ammonium in micas. The presence of meta-sediments rich in graphite although not present in the immediate surroundings is the most probable explanation, as these volatile rich fluids are frequently found in lydites in Portugal (Noronha et al., 1999, Doria, 2000 on Tres Minas district).

The predominance of H₂O-CO₂-CH₄ aqueous-carbonic fluids with moderate salinities (6-10 wt% NaCl) along the whole history of the deposit evolution are also found in other W deposits in northern Portugal (Noronha et al., 1999).

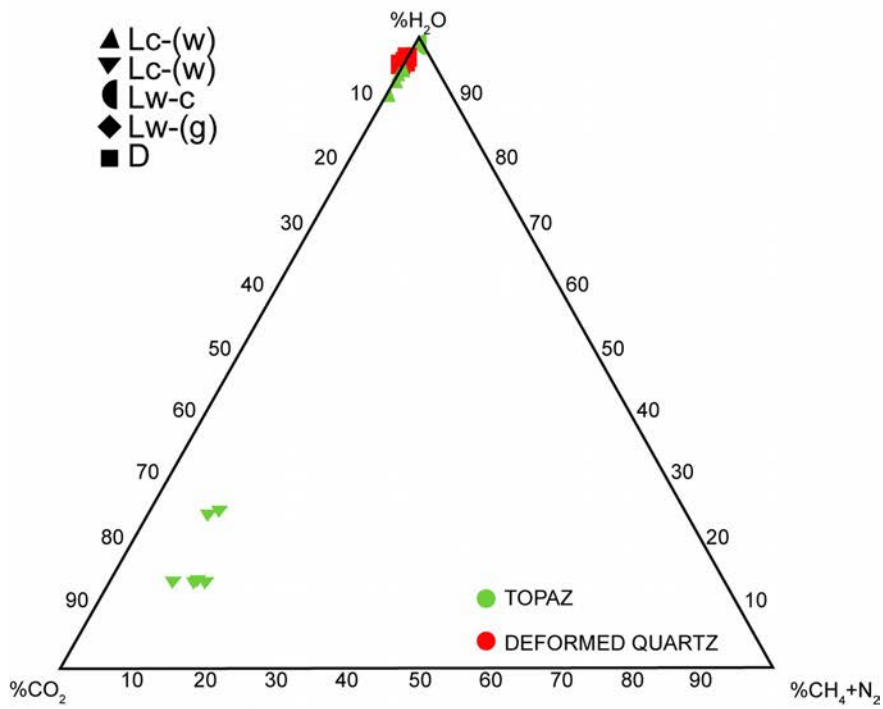
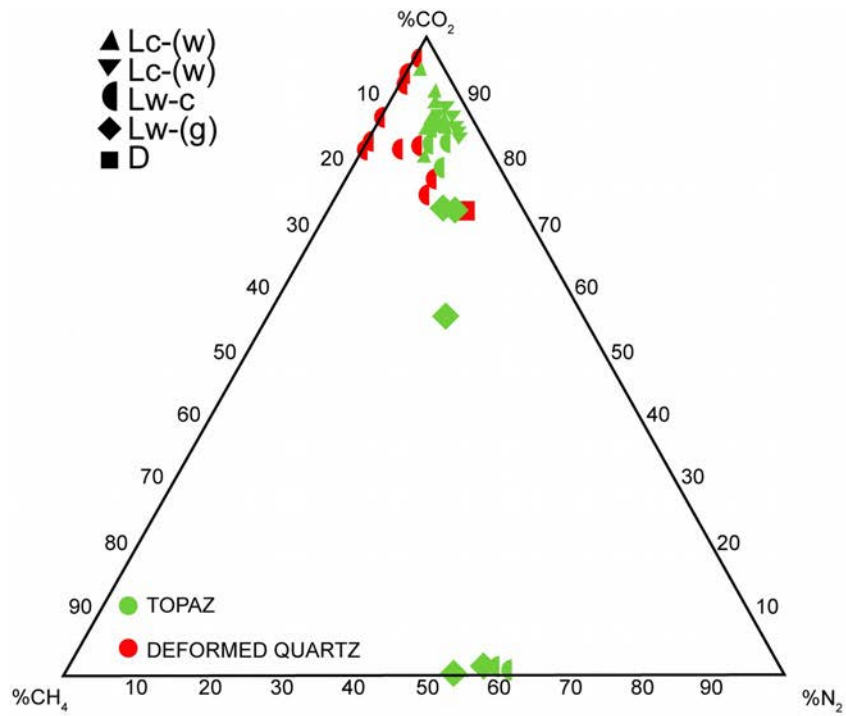


Fig. 3.23: Distribution of CO_2 , CH_4 , and N_2 in the volatile phase of fluid inclusions trapped during the two first stages: Q1-II and Topaz(2).

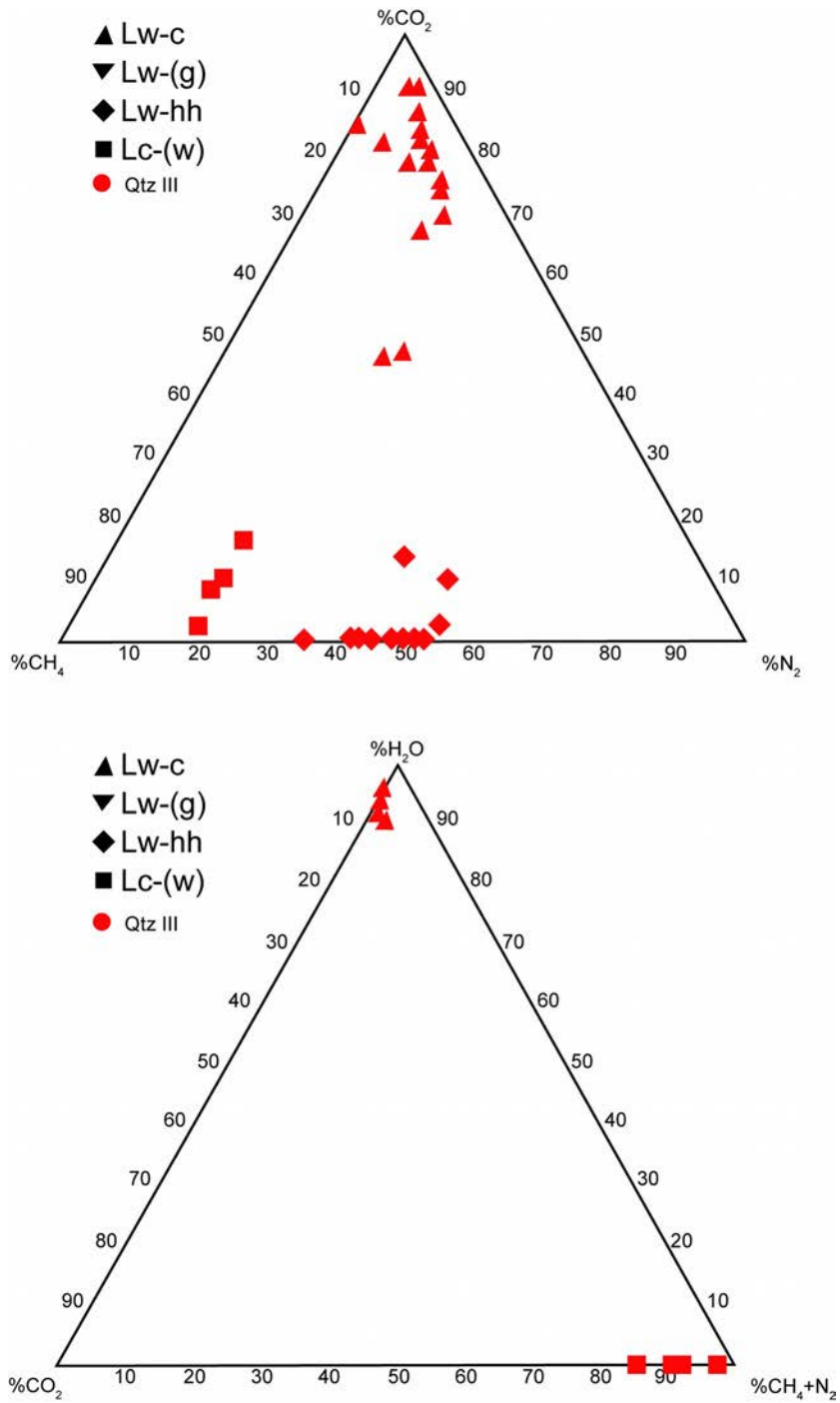


Fig. 3.24: Distribution of CO₂, CH₄, and N₂ in the volatile phase of fluid inclusions trapped during the stage II quartz (QIII) (primary but also secondary fluid inclusions).

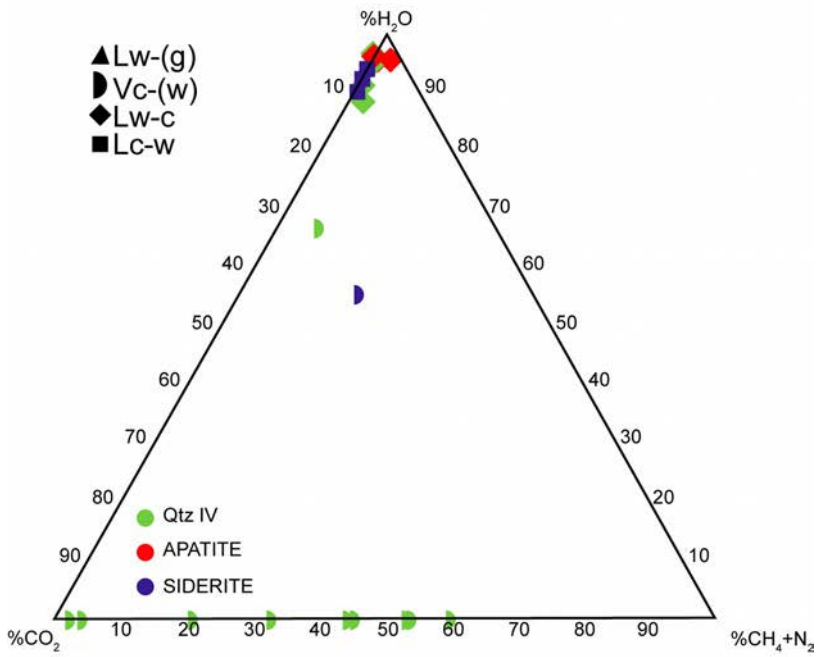
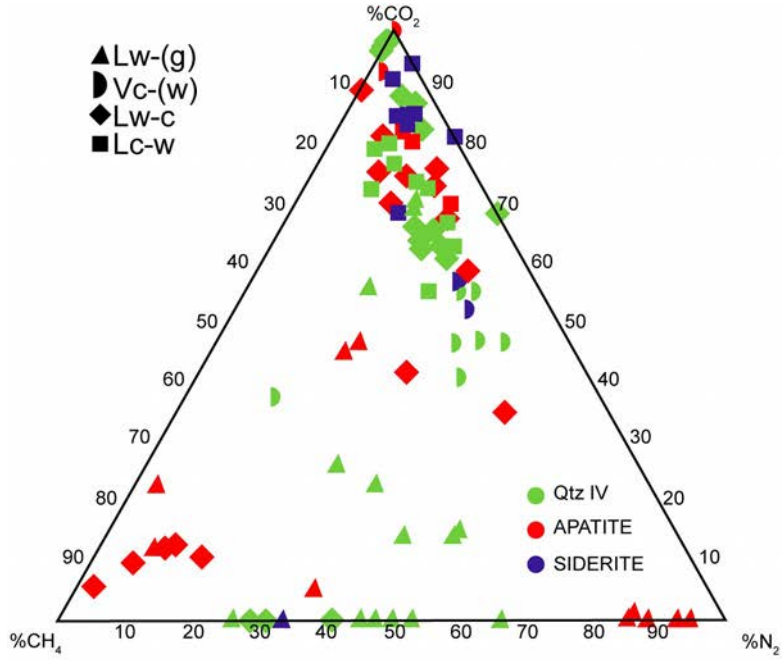


Fig. 3-25: Distribution of CO₂, CH₄, and N₂ in the volatile phase of fluid inclusions trapped during the stage V: quartz QIV -apatite, and stage V (siderite).

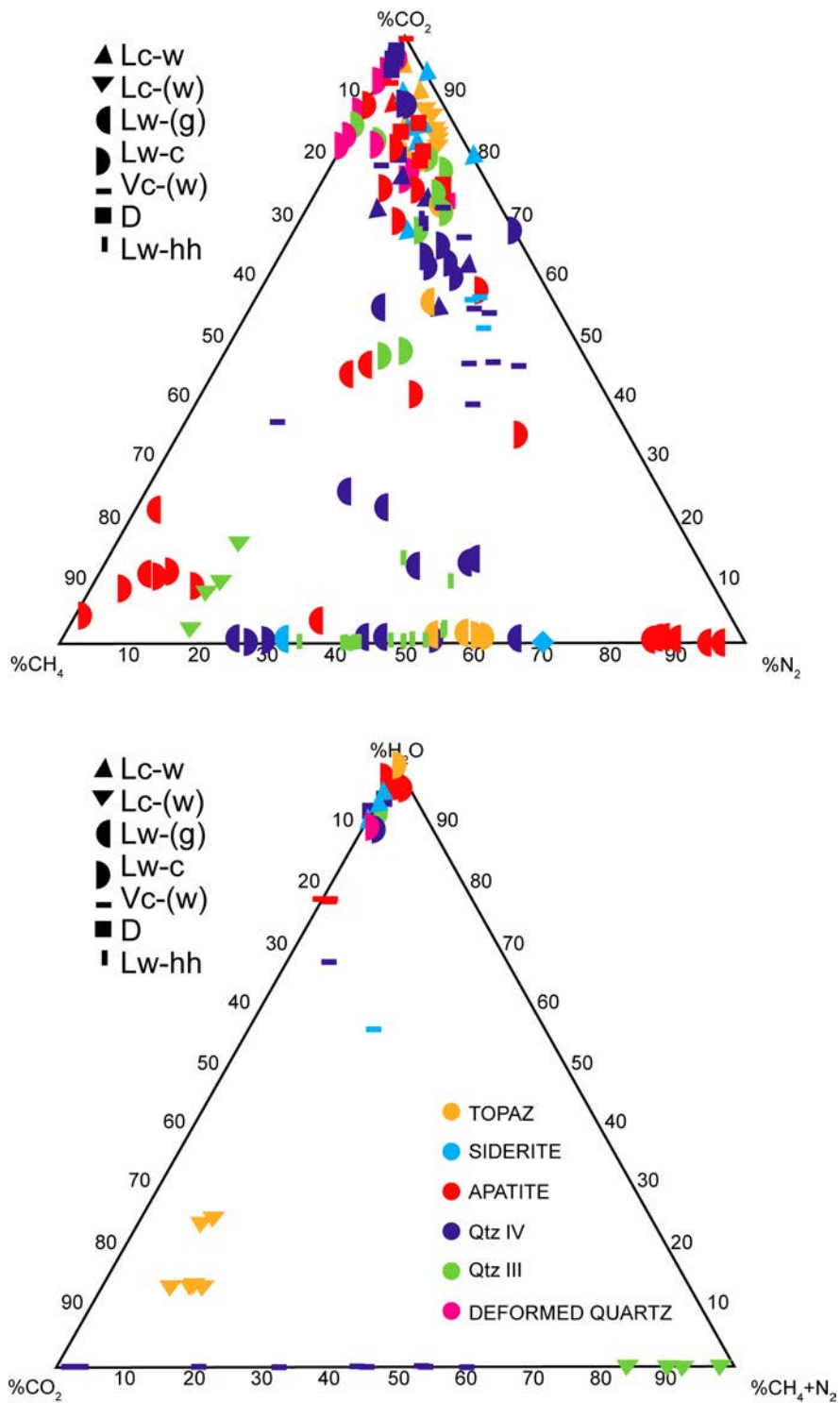


Fig. 3.26: Distribution of CO₂, CH₄, and N₂ in the volatile phase of fluid inclusions trapped in all the studied stages from I to V.

6 P-T estimation

A series of isochores representative of the main fluid types have been calculated from microthermometric and Raman spectroscopy measurements and reported on a pressure–temperature plot (Fig. 3.27).

Topaz (Quartz I-II): The highest densities observed are those of the aqueous-carbonic fluids trapped in topaz, and a few preserved inclusions from stage I quartz. Considering the isochores and trapping in the range 400–500 °C, a pressure of 230–300 MPa is inferred. i.e. slightly below metamorphism conditions (Vallance et al., 2003). These fluids probably record lithostatic pressures during the sealing of the fracture system related to the topaz formation after the Quartz I-II formation.

Between stages I and II and topaz a possible but limited pressure drop of 50 MPa and a cooling of < 50 °C is inferred from the consideration of the few isochores available on quartz Qtz I inclusions. Considering the structural level during the Stage I-II-III (10-11 km), the pressure drop may be explained oscillation around lithostatic pressures.

Quartz IV-apatite: Between topaz2 and quartz-IV-apatite stages, a rather significant pressure drop of 100-150 MPa has occurred, accompanied by a cooling of around 50 to 100°C. Considering the structural level during the Stage I (10-11.5 km), the pressure drop from topaz to quartz-apatite stage cannot be explained simply by a change from lithostatic to hydrostatic regime but implies an uplift of the basement of around 6 km. Pressure drops during stage IV could then be mostly related to changes from lithostatic to hydrostatic conditions.

The consequence of pressure drops at this shallower structural level yield unmixing of the aqueous-carbonic fluids. Lc-w vapour inclusions and water-rich aqueous-carbonic vapours (Vc-w) display similar volatile composition and can, in that case, be interpreted as the result of unmixing at decreasing pressure down to 40–50 MPa at around 285–365 °C. The domain is defined on the basis of the intersection of isochores and isopleths of the most probable parent fluids. These oscillations correspond to tectonic episodes leading to fracturing of rocks and increased porosity, resulting in a rapid drop in fluid pressure. Such P changes were attributed in former works (Kellie and Rye, 1979, Foxford et al, (2000)) to stage I-II but are the most probably restricted to stage IV.

Most data suggest an evolution in an open system with the injection of one or more fluids for each stage. These data are in contradiction with the hypothesis of a closed system evolution over time of the same fluid input as proposed by Lecumberri et al. (2017).

Thermal gradients and proximity to magma intrusions: the convective fluid system

The thermal gradients in both cases are high (50 to 60°C /km for the topaz stage under lithostatic pressure, 60 to 70°C/ km for the quartz-apatite stage). This is in favor both of a quick exhumation of the basement and the presence of magma intrusions at shallow levels acting as strong heat engines. The quick exhumation does not allow rocks to cool down sufficiently quickly to the expected temperature at the uplifted level, and temperatures is maintained through a series of magmatic intrusions likely related to the Variscan granite magmatism.

The main driving forces behind fluid migration are thus the existence of a major discontinuity acting as drainage zones, both for the emplacement of syntectonic and then post-tectonic plutons, and subsequent fluid flows as well the exhumation and general decompression of the rock units. The deep penetration of waters from surface as suggested by stable isotope studies (Polya et al., 2000) during the main exhumation stage of the basement may allow metals to be dissolved from the metamorphic series and/or pre-concentrations and transported within the transport path thanks to the convecting cells centered on hot spot.

Besides the isotopic ratio of helium $^3\text{He}/^4\text{He}$ trapped in FI from wolframite and arsenopyrite (Burnard and Polya, 2004) are 5 times higher than the atmospheric ratio, a data which is inconsistent with a peraluminous granite source. For these authors, these gases come from a deeper source which alternately is an evidence of a deep-seated fluid source, may be linked to migmatization, or drained from mantle.

Long-lived hydrothermal systems likely related to multiple intrusions

De Amorin (2016) who studied the rare earth and trace element signature of Panasqueira granite revealed several injections of peraluminous magmas that intruded between them, as well as in the Beiras shales. These various magma pulses may well explain the persistence of high temperatures of 300 - 400°C for several million years.

The main driving forces behind the fluid migration are therefore major discontinuities acting as drainage zones for both fluids and magmas (Fig. 3.28), the emplacement of series of magmas, uplift and general decompression of the rock units, penetration of meteoric fluids down to rather deep structural levels, and upward migration of fluids produced by the migmatization at depth.

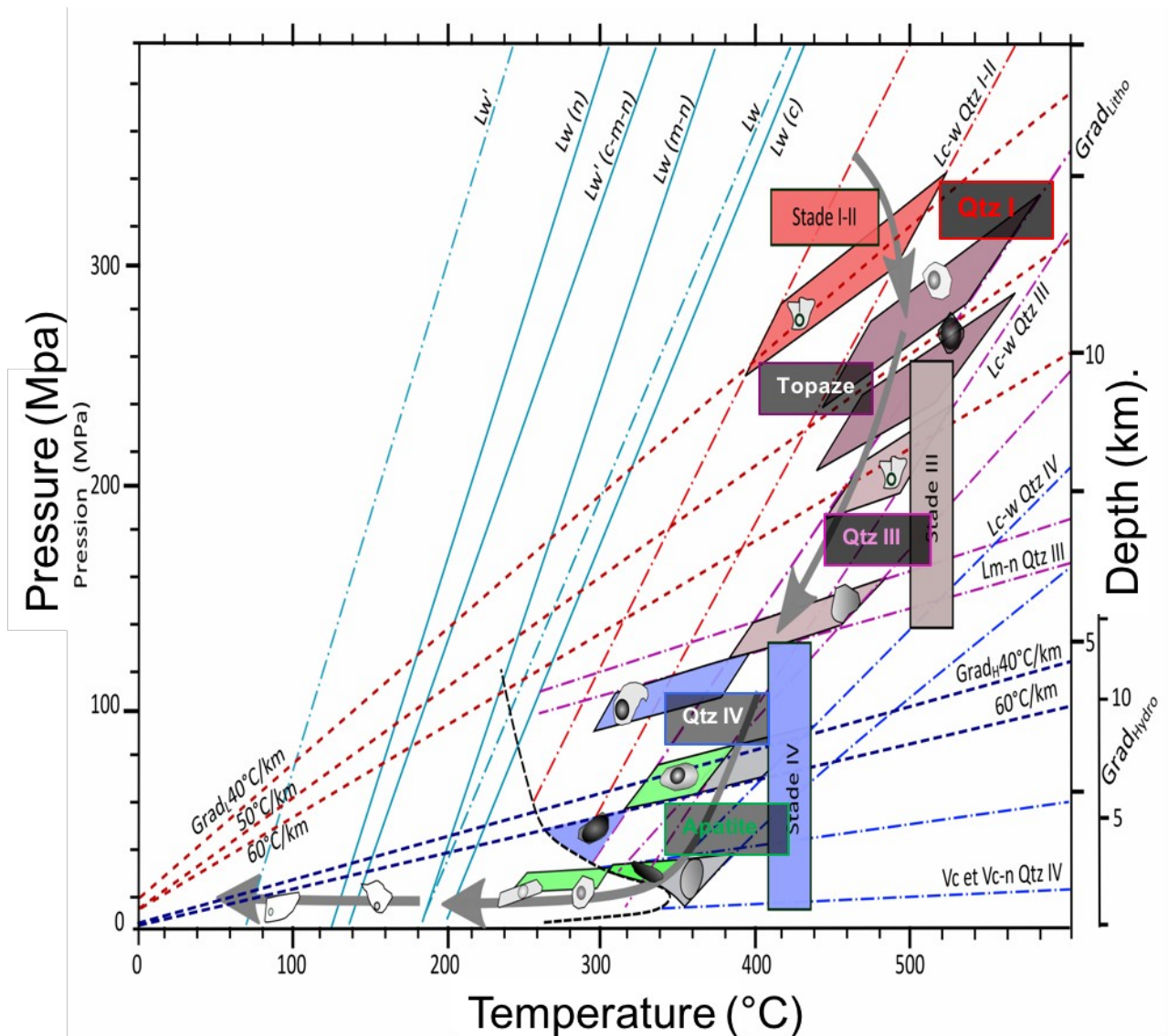


Fig. 3.27: General P-T evolution based on representative isochores of fluid inclusions for each stage of the evolution of the Panasqueira deposit. Lithostic and hydrostatic gradients are reported. Boxes were defined on the basis of representative isochores and their intersection as for almost each stage for which volatile rich inclusions and aqueous-carbonic inclusions are found. For Stage I, the geothermal gradient of 40°C/km has been chosen, and for the unmixing stage (stage IV) the conditions were defined by the intersection of isochores with the CO₂-H₂O isopleth.

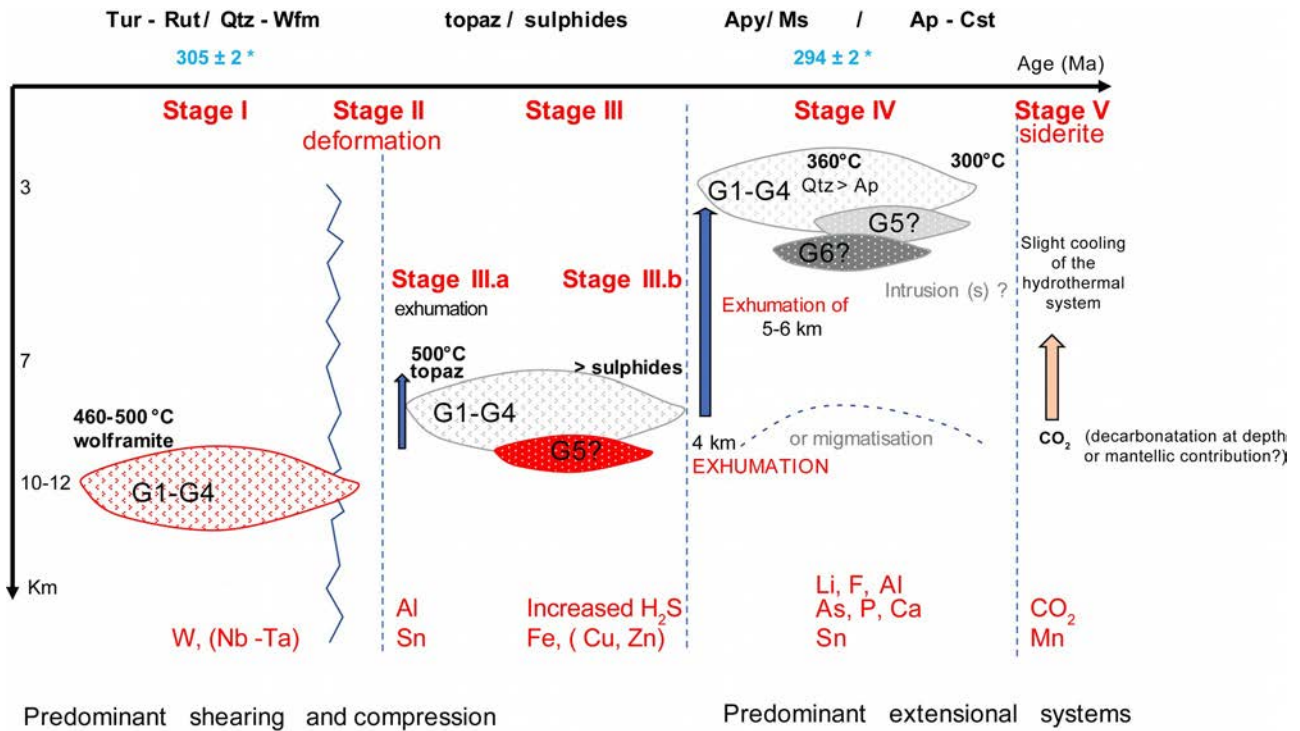


Fig. 3.28: General evolution of the Panasqueira based on P-T data and ages of rutile for the first stage and muscovite for stage IV. The overall exhumation is around 8km in 11 Ma indicating that the mean exhumation rate was 0.7 mm / year, a rather reasonable value as very similar exhumation rate is proposed in Northern Massif central at the same period. The element associations vary with time, this indicating probably different fluid inputs but also several distinct processes for both metal transfer and deposition. Granites are not dated but at least 5 distinct intrusions were recognized in the drill cores (Amorin, 2018).

*Age of Stage I: based on U-Pb data on rutile from tourmalinisation stage preceding the wolframite I – Chapter One

*Age of Stage IV: based on Ar-Ar data (Snee et al, 1981, Carocci et al. submitted) on muscovite; U-Pb on apatite (Launay, 2019).

7 Conclusions

- The paragenetic succession of the Panasqueira deposit has been revised, in particular several significant changes have been proposed: i) muscovite, arsenopyrite, topaz are not considered anymore as pre-W deposition minerals, but as linked to a re-opening stage of the « selvage » during the newly defined stage IV, ii) the oxide stage is consequently redefined as a quasi-monomimeral stage characterized by the predominant deposition of wolframite I, and the sealing of the vein by quartz QtzI.
- The main quartz (Qtz I) underwent crack-seal processes and deformation, yielding to the almost complete loss of the primary fluid inclusions. Quartz QtzI is in addition partly dissolved and re-crystallized as clear quartz (Qtz IV) during stage IV. The latter quartz hosts vapour and liquid aqueous carbonic inclusions which are the most probably products of unmixing, the main process proposed in former works to explain wolframite deposition. Such a process is probably valid for the wolframite IV deposition, which represents a minor contribution to the W stock metal at Panasqueira. Most previous works concern this stage which occurs at rather low pressure and shallow structural level. The FI data yield to pressures of 40 to 80 Mpa, which may correspond to depth of a few kilometres (3 ± 1 km), thus pressures slightly higher than those previously proposed by pioneer works.
- New data on the early stages at Panasqueira were obtained on topaz. The presence of high density liquids either aqueous-carbonic or volatile rich yield to P-T estimate of 500°C-240 Mpa, which may correspond to lithostatic pressures corresponding to deep structural levels in between 8 and 10 km depth. Considering that the early tourmalinisation stage which is pre-Wolframite I is dated by U-Pb on rutile at 305 Ma, the stages I to III may be considered as linked to deep P-T conditions, and deformational stages rather distinct than those prevailing during stage IV. The very high temperature conditions around 500°C during the topaz stage could be related to a magma intrusion. It is however difficult to relate this event to any of the six magmatic facies distinguished on the basis of petrographic and geochemical criteria found in Panasqueira drillings, as none of this facies was dated.
- The consideration of two main structural levels, $10 \pm$ km at 305 Ma and 3 ± 1 km at 296 Ma implies an exhumation of 6-7 km, ad an exhumation rate of 0.7 mm/ year, coherent with those generally considered at the end of the Variscan orogeny.
- From the early to the late stage, main dominant fluids are aqueous-carbonic fluids which display the same features than pseudo-metamorphic fluids defined in most Au deposits from western Europe. Such fluids are strongly equilibrated with metamorphic series, and contain volatiles linked to water-graphite equilibrium and nitrogen related to the oxidation of ammonium contained by micas or feldspars within metamorphic series. Pulses of volatiles may be linked to the devolatilisation of lydites. There are little evidences of magmatic fluid inputs from the study of fluid inclusions, although links between main stages of fluid migration and magma intrusions are likely, considering the persistence of high temperatures during 10

Ma, or at less the succession of hot events likely linked to magma intrusions and/or deep crustal lineament and thermal anomalies. The penetration of waters around a hot spot along a major crustal discontinuity may allow tungsten to be dissolved and transported from the metamorphic series and/or pre-concentrations and redeposited in structural and geochemical traps such as the boundary between the Panasqueira intrusion and its metasedimentary cover, below a quartzite cap.

References

- Bakker, R. J. (1997). Clathrates: Computer programs to calculate fluid inclusion VX properties using clathrate melting temperatures. *Computers & Geosciences*, 23(1), 1-18.
- Bakker, R. J. (1999). Adaptation of the Bowers and Helgeson (1983) equation of state to the H₂O–CO₂–CH₄–N₂–NaCl system. *Chemical Geology*, 154(1-4), 225-236.
- Bakker, R. J. (2003). Package FLUIDS 1. Computer programs for analysis of fluid inclusion data and for modelling bulk fluid properties. *Chemical Geology*, vol.194, 3-23.
- Boiron, M.C., Essarraj, S., Sellier, E., Cathelineau, M., Lespinasse, M., Poty, B. (1992). Identification of fluid inclusions in relation to their host microstructural domains in quartz by cathodoluminescence. *Geochimica et Cosmochimica Acta* 56, 175–185. [https://doi.org/10.1016/0016-7037\(92\)90125-3](https://doi.org/10.1016/0016-7037(92)90125-3)
- Bowers, T.S., Helgeson, H.C. (1983). Calculation of the thermodynamic and geochemical consequences of non-ideal mixing in the system H₂O–CO₂–NaCl on phase relation in geological systems: equation of state for H₂O–CO₂–NaCl fluids at high pressure and temperature. *Geochim. Cosmochim. Acta* 47, 1247– 1275.
- Burnard, P.G., Polya, D.A. (2004). Importance of mantle derived fluids during granite associated hydrothermal circulation: He and Ar isotopes of ore minerals from Panasqueira 1 Associate editor: R. Wieler. *Geochimica et Cosmochimica Acta* 68, 1607–1615. <https://doi.org/10.1016/j.gca.2003.10.008>
- Bussink R. W. (1984). Geochemistry of the Panasqueira tungsten-tin deposit, Portugal. *Geol. Ultraiectina*. 33, 170p.
- Bussink, R. W., Kreulen, R., & de Jong, A. F. (1984). Gas analyses, fluid inclusions and stable isotopes of the Panasqueira W-Sn deposits, Portugal. *Bulletin de minéralogie*, 107(6), 703-713.
- Carocci, E. (2018). Caractérisation indirect des fluides du stade à W-Sn-Cu de Panasqueira (Portugal) : Information tirée de l'étude des tourmalines précoces. RST, Lille.
- Codeço, M.S., Weis, P., Trumbull, R.B., Pinto, F., Lecumberri-Sanchez, P., Wilke, F.D.H. (2017). Chemical and boron isotopic composition of hydrothermal tourmaline from the Panasqueira W-Sn-Cu deposit, Portugal. *Chemical Geology* 468, 1–16. <https://doi.org/10.1016/j.chemgeo.2017.07.011>
- Diamond, L. W. (2003). Introduction to gas-bearing, aqueous fluid inclusions. *Fluid inclusions: analysis and interpretation*, 32, 101-158.
- Duan, Z., Møller, N., Weare, J.H. (1996). A general equation of state for supercritical fluid mixtures and molecular dynamics simulation of mixture PVTX properties. *Geochimica et Cosmochimica Acta* 60, 1209–1216. [https://doi.org/10.1016/0016-7037\(96\)00004-X](https://doi.org/10.1016/0016-7037(96)00004-X)

- Dubessy, J., Poty, B., & Ramboz, C. (1989). Advances in COHNS fluid geochemistry based on micro-Raman spectrometric analysis of fluid inclusions. *European journal of Mineralogy*, 1(4), 517-534.
- Foxford, K., Nicholson, R., Polya, D., Hebblethwaite, R.P. (2000). Extensional failure and hydraulic valving at Minas da Panasqueira, Portugal: evidence from vein spatial distributions, displacements and geometries. *J. Struct. Geol.* 22, 1065–1086. doi:10.1016/S0191-8141(00)00029-8
- Huizenga, J. M. (2001). Thermodynamic modelling of C–O–H fluids. *Lithos*, 55(1-4), 101-114.
- Kelly, W. C. et Rye, R. O. (1979). Geologic, fluid inclusions, and stable isotope studies of the tin tungsten deposits of Panasqueira, Portugal. *Econ. Geol.* 74, 1721–1822.
- Lecumberri-Sanchez, P., Vieira, R., Heinrich, C.A., Pinto, F., Wälle, M. (2017). Fluid-rock interaction is decisive for the formation of tungsten deposits. *Geology*. 45, 579–582. <https://doi.org/10.1130/G38974.1>
- Lourenço, A. (2002). Paleofluidos e mineralizações associadas às fases tardias da Orogenia Hercínica. Thèse de doctorat, Université de Porto. 303p.
- Lüders, V. (1996). Contribution of infrared microscopy to fluid inclusion studies in some opaque minerals (wolframite, stibnite, bournonite); metallogenic implications. *Economic Geology*, 91(8), 1462-1468.
- Noronha, F., Vindel, E., Lopez, J.A., Garcia, E., Boiron, M.C et Cathelineau, M. (1999). Fluids related to tungsten ore deposits in northern Portugal and Spanish central system : a comparative study. *Rev. Soc. Geol. Espana*, 12 (3 –4), 397 – 403.
- Noronha, F., Doria, A., Dubessy, J. et Charoy, B. (1992). Caractérisation and timing of the different types of fluids present in the barren ore-veins of the W-Sn deposit of Panasqueira, Central Portugal. *Mineral Deposita* 27, 72 – 79.
- Pinto, F., Vieira, R., & Noronha, F. (2015). Different cassiterite generations at the Panasqueira Deposit (Portugal): Implications for the metal zonation model. *Mineral Resources in a Sustainable World; André-Mayer, AS, Cathelineau, M., Muchez, P., Pirard, E., Sindern, S., Eds*, 827-830.
- Polya, D. A., Foxford K. A., Stuart F. M., Boyce A., et Fallick A. E. (2000). Evolution and paragenetic context of low δ D hydrothermal fluids from the Panasqueira W-Sn deposit, Portugal; new evidence from microthermometric, stable isotope, noble gas and halogen analyses of primary fluid inclusions. *Geochim. Cosmochim. Acta* 64, 3357–3371.
- Roedder, E., (1979). Fluid inclusions as samples of ore fluids. In: Barnes, H.L (Ed), *Geochemistry of Hydrothermal Ore Deposits*, 2nd edn. Wiley, New-York, 984 – 737.
- Snee, L.W., Sutter, J.F., Kelly, W.C. (1988). Thermochronology of economic deposits: dating the stages of mineralisation at Panasqueira, Portugal, by high precision $^{40}\text{Ar}/^{39}\text{Ar}$ age spectrum techniques on muscovite. *Economic Geology*. 83, 335–354.
- Thiéry, R., Van Den Kerkhof, A. M., Dubessy, J. (1994). vX properties of CH₄-CO₂ and CO₂-N₂ fluid inclusions: modelling for T< 31°C and P<400 bars. *Eur.J.Mineral.*, 6, 753-771
- Thadeu, D. (1951). Geologia do couro mineiro da Panasqueira. *Comunic. Serv. Geol. Portugal.* 32, 5–64.
- Vallance, J., Cathelineau, M., Boiron, M. C., Fourcade, S., Shepherd, T. J., & Naden, J. (2003). Fluid–rock interactions and the role of late Hercynian aplite intrusion in the genesis of the Castromil gold deposit, northern Portugal. *Chemical Geology*, 194(1-3), 201-224.

Vityk, M. O., & Bodnar, R. J. (1995). Textural evolution of synthetic fluid inclusions in quartz during reequilibration, with applications to tectonic reconstruction. *Contributions to Mineralogy and Petrology*, 121(3), 309-323.

Part Three

Experimental Part On W-Behaviour

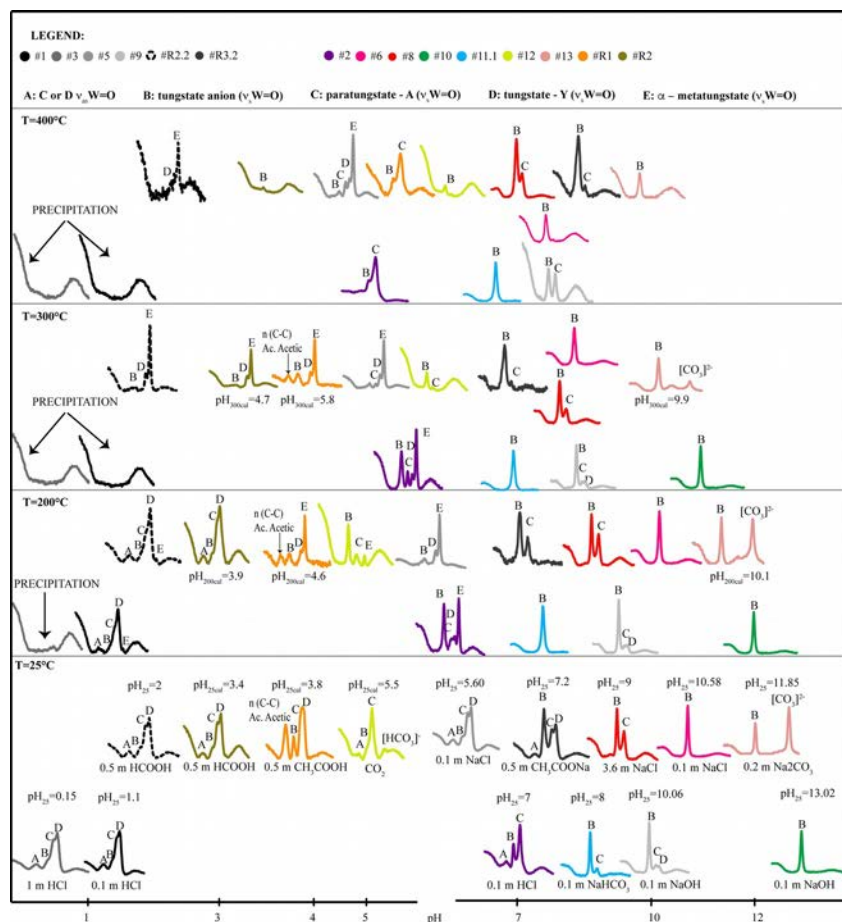
CHAPTER FOUR

TUNGSTEN (VI) SPECIATION IN HYDROTHERMAL SOLUTION UP TO 400°C AS REVEALED BY IN-SITU RAMAN SPECTROSCOPY

In preparation for *Geochimica and Cosmochimica Acta*

Abstract

Tungsten (VI) speciation in hydrothermal solutions has been investigated through in-situ Raman spectroscopy coupled to the fused silica glass capillary technique at temperature up to 400°C. The effect of temperature, pH, chlorinity and carbonate speciation have been evaluated. The tungstate ion WO_4^{2-} is the only W species in solution at $\text{pH} > 10$ and all investigated temperatures. The presence of dissolved carbonates, chloride, acetate and ammonium do not affect the tungsten speciation. We reveal that tungsten polymers are stable up to 400°C under acidic to circum-neutral pH values. Among the 3 observed polymers, namely $[\text{W}_7\text{O}_{24}]^{6-}$ (paratungstate-A), $[\text{W}_{10}\text{O}_{32}]^{4-}$ (tungstate-Y), $\alpha\text{-}[\text{H}_2\text{W}_{12}\text{O}_{40}]^{6-}$ (α -metatungstate), only the hepta and dodeca-tungstate are stable at elevated temperature. These observations imply that the currently



available thermodynamic data to model W speciation and transport in deep and hot geological fluids need to be revised.

1 Introduction

The knowledge of tungsten (W) speciation in hydrothermal solutions is of primary importance to develop geochemical models for the genesis of tungsten ore deposits. Currently, conditions to W mobility in deep and hot geological fluids are poorly identified, despite a general consensus that W is predominantly transported in the ore-forming fluids as anion complexes with W being hexavalent (W(VI)) and with negligible chloride complexation. The few models of hydrothermal transport and deposition of tungsten are based on a speciation of tungsten dominated by tungstic acid (H_2WO_4^0), and the products of its dissociations HWO_4^- and WO_4^{2-} (Heinrich, 1990; Gibert et al., 1992, Wood and Samson, 2000). This rather simple aqueous W speciation model at elevated temperature (T) and pressure (P) mostly relies on the interpretation of data on W-bearing minerals solubility from quench experiments available at that time (Eugster and Wilson, 1985; Wood and Vlassopoulos, 1989; Wood, 1992). Wang et al. (2019a) have recently investigated the solubility and speciation of W in NaCl-bearing solutions up to 350°C through quenched solution analysis. They demonstrate that NaCl concentration do not affect the solubility of tungsten trioxide. They also concur with W speciation dominated by monomeric tungstate species over the entire pH range at $T \geq 250^\circ\text{C}$.

This view of W speciation under hydrothermal condition contrasts with the already well studied W speciation at ambient T-P, where the coexistence of several polyanions containing 6, 7, 10, and even 12 W-atoms depending on pH was demonstrated (Duncan and Kepert, 1961; Aveston, 1964; Arnek and Sasaki, 1974; Häufe, 1982; Ng and Gulari, 1984; Cruywagen and Van Der Merwe, 1987). It also ignores, or simplify the conclusions of two pioneering studies reporting in-situ measurements of W speciation under hydrothermal conditions. First, Wesolowski et al. (1984) provide the results of potentiometric titrations of tungstate-bearing solution in the range 100-300°C and reveal that polytungstates ($\text{H}_{10}(\text{WO}_4)_6^{2-}$, $\text{H}_7(\text{WO}_4)_6^{5-}$, $\text{H}_{18}(\text{WO}_4)_{12}^{6-}$) dominate the speciation into $10^{-2} \text{ mol}\cdot\text{kg}_{\text{H}_2\text{O}}^{-1}$ solution below pH 5. At lower W concentration, the monomers (HWO_4^- and WO_4^{2-}) become increasingly stable, but at least one polymer ($\text{H}_{10}(\text{WO}_4)_6^{2-}$) remains predominant at pH below 3 up to 350°C. Second, thanks to in-situ Raman spectroscopy, Bilal et al. (1986) show the existence of two stable polymeric W-species, $\text{W}_{10}\text{O}_{32}^{4-}$ and $\text{H}_3\text{W}_{12}\text{O}_{40}^{5-}$, that dominate the W speciation at T up to 200°C under acidic and circum-neutral conditions. They did not succeed to detect the presence of HWO_4^- over the 3-9 pH range and conclude that the polymerization degree increases with increasing T and P. Wang et al. (2019b) have recently performed in-situ Raman spectroscopic investigation of the hydrothermal speciation of tungsten under moderately acidic (pH > 4 at room T) to alkaline conditions. Despite the fact that these authors have unambiguously detected polymeric species of W under moderately acidic conditions, at least at $T < 300^\circ\text{C}$, they did not clearly identify them, and even ignore them in their thermodynamic modelling of W transport and mineralization at $T < 300^\circ\text{C}$. Interestingly, the above-mentioned

6	10.58		0.1	0.1				
8	9.56		0.1	3.6				
9	10.06	0.1			0.1			
10	13.02		0.1		0.1			
10.1	13.03		0.01		0.1			
10.2	12.94		0.05		0.1			
10.3	12.98		0.2		0.1			
11	8.90		0.1			1.1		
11.1	7.50		0.1			0.1		
11.2	8.32		0.05			0.1		
11.3	8.31	0.05				0.1		
12	5.5		0.1					151
12.1	7.2	0.1						199
13	11.85		0.1			1.2		
R1	4.00		0.1				0.5	
R1.2	2.75	0.1					0.5	
R2	3.00		0.1					0.5
R2.2	2.00	0.1						0.5
R3	9.00		0.1					0.5
R3.2	7.80	0.1						0.5
N1	7.12		0.10					

2.2 Spectroscopic cell and Raman data acquisition

To obtain high-quality Raman spectra, solutions must be contained in a material that satisfies several conditions. First, the cell material must have sufficient mechanical resistance at the experimental T-P conditions. Second, it must be transparent in the visible spectral region and it must not induce fluorescence. Third, the cell material has to be chemically inert with respect to the aqueous solutions and must not induce catalytic or redox processes. Fused silica capillary capsules (FSCC) satisfy all these requirements (Chou et al., 2008; Caumon et al., 2013; Dargent et al., 2013; Truche et al., 2014). The capillaries were purchased from Polymicro Technologies, LCC, and have internal diameter of 100 μm and an external diameter of 320 μm . The sample loading procedure includes the following steps: (1) the silica tube is sealed at one extremity using a $\text{H}_2\text{-O}_2$ micro torch (Elmaflamme), (2) experimental solutions (Table 1) are loaded from the open end of the tube and centrifuged towards the closed end at 12000 rpm, (3) the open end of the tube is connected to a vacuum line, then immersed into liquid nitrogen to freeze the solution, and the atmosphere above the frozen solution is evacuated, (4) CO_2 gas are loaded cryogenically, and (5) the open end of the capillary is sealed using a hydrogen flame, while the closed end is kept frozen in liquid nitrogen under vacuum. The pressure of CO_2 loaded cryogenically is estimated to be 10 bar at 20°C. Partial gas pressure is calculated from the pressure drop in the source reservoir. The accuracy of this method is considered to be within 20%, based on volume errors and pressure uncertainty.

A heating-stage adapted to capillary heating at saturated vapor pressure (@CAP-500 Linkam) is used to reach the experimental T, with an accuracy of $\pm 1\%$ in the range of 20 - 400°C. The heating-stage is coupled

with a Raman spectrometer (Labram HR, ®Jobin-Yvon, Horiba) and an optical microscope (®Olympus). The best compromise combining the highest intensity of the ν_1 Raman band of the tungstate ion and the best rejection of silica-glass spectrum was obtained using a 20× magnification and a 500 μm diameter for the confocal hole. The grating (1800 grooves per mm), the 800 mm focal distance of the spectrometer and the 100 μm slit width give a spectral resolution of 0.5 cm^{-1} . Raman spectra were obtained with an excitation using the 514.532 nm line of an Ar^+ laser (spectra physics, ®Newport Corporation). The laser power at the sample was 70 mW. Spectra were collected in the spectral interval range between 150 cm^{-1} and 4500 cm^{-1} . High-quality spectra were obtained after 60 s acquisition time per spectral window and four accumulations. Measurements were performed first at room T (21°C) and from 100°C up to 400°C by step of 100°C at a heating rate of 10°C·min⁻¹ for each solution (coexisting with a vapor phase below the critical point).

2.3 Fitting procedure of Raman spectra

We used two commercial softwares, ®LabSpec 5.64.15 and ®OriginPro9, in order to determine peak position, intensity, area, and shape factor for each band component in the liquid phase. The deconvolution has been made using a pseudo-Voigt function (a linear combination of Gaussian and Lorentzian functions) after baseline subtraction. All the observed Raman bands associated to the dissolved W species are localized in the 860-1010 cm^{-1} wavenumbers region. The wavenumbers at maximum intensity of the different band component of the W species in the 860-1010 cm^{-1} region were constrained before the fitting calculation. Figure 4.1 displays a collection of typical raw Raman spectra of W-bearing solution obtained at T ranging from 25 to 400°C. A zoom on the frequency domain corresponding to the symmetric stretching ($\text{W}=\text{O}$) vibrations is also shown on this figure.

Tungstate (WO_4^{2-} , hereafter noted “B₉₃₀”) concentration was calculated using calibration equations establishes from band’s area measurement in four strongly alkaline solutions having total W concentration ranging from 0.01 to 0.2 mol/kgH₂O. In the 860-1010 cm^{-1} spectral region, where the presence of W species may be identified, the Raman spectra collected with these standard solutions display a single symmetric band at around 927 cm^{-1} , without any additional features that might suggest the presence of other complexes (Figs. 4.2A, B).

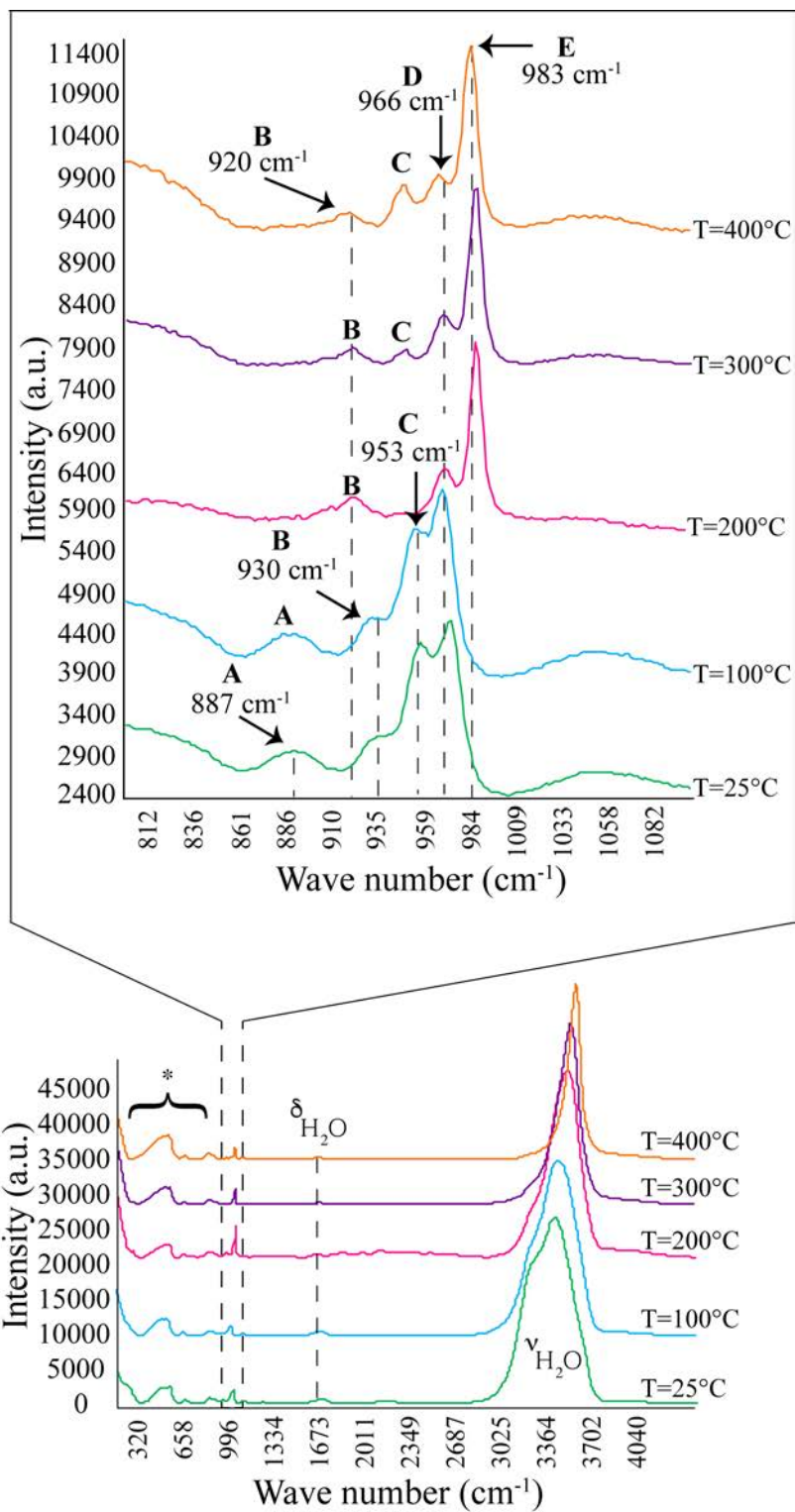


Fig.4.1: Raman spectra of dissolved W-species in hydrothermal solution #5 (with 0.1m NaCl, $\text{pH}_{25^\circ\text{C}}=5.60$) as a function of temperature.

Sol. #10 : 0.1 m $\text{Na}_2\text{WO}_4 \cdot 2\text{H}_2\text{O}$ + 0.1 m NaOH
 $\text{pH}_{T=25^\circ\text{C}} = 13$

Sol. #10.1 : 0.01 m $\text{Na}_2\text{WO}_4 \cdot 2\text{H}_2\text{O}$ + 0.1 m NaOH

Sol. #10.2 : 0.05 m $\text{Na}_2\text{WO}_4 \cdot 2\text{H}_2\text{O}$ + 0.1 m NaOH

Sol. #10.3 : 0.2 m $\text{Na}_2\text{WO}_4 \cdot 2\text{H}_2\text{O}$ + 0.1 m NaOH

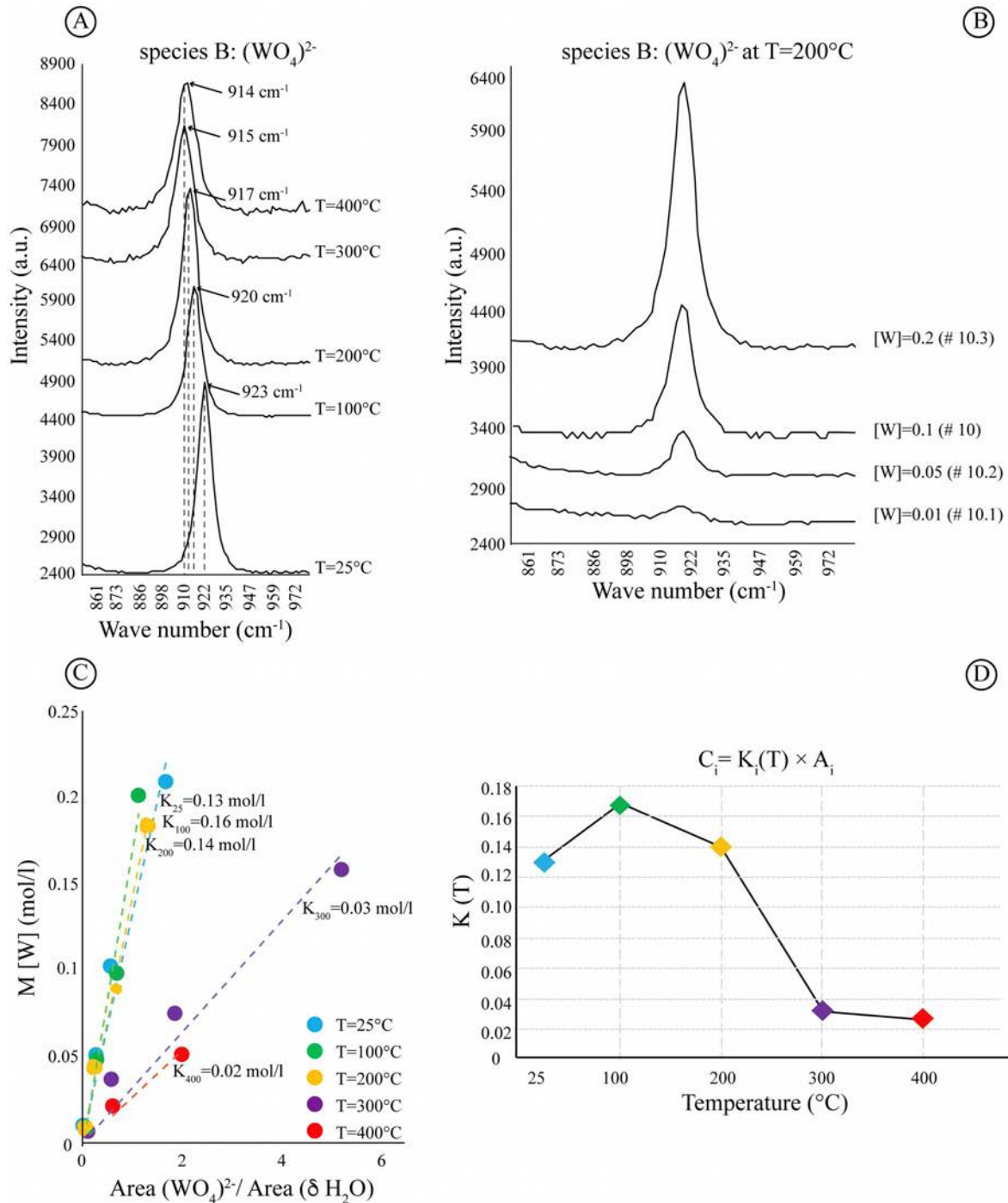


Fig.4.2: (A) Raman spectra between 850 cm^{-1} and 980 cm^{-1} of experimental solution #10 (0.1m $\text{Na}_2\text{WO}_4 \cdot 2\text{H}_2\text{O}$ +0.1m NaOH) from 25 $^\circ\text{C}$ up to 400 $^\circ\text{C}$ showing the band of tungstate ion **B** $(\text{WO}_4)^{2-}$. The shift at lower frequency values with increasing temperature is due to the change of solution density. (B) Raman spectra showing the band of tungstate ion **B** $(\text{WO}_4)^{2-}$ for different tungsten concentrations: 0.01m, 0.05m, 0.1m, 0.2m. Intensity of $(\text{WO}_4)^{2-}$ increases with W-concentration at constant temperature of 200 $^\circ\text{C}$. (C) Linear correlation between **B** W-specie normalized area and its volumetric concentration for all temperatures, shows similarity for $T= 25^\circ\text{C}$, 100 $^\circ\text{C}$ and 200 $^\circ\text{C}$. (D) Relationship between calibration coefficient and temperature for their correlation is barely linear between 100 $^\circ\text{C}$ and 300 $^\circ\text{C}$.

We used a linear relationship (Eq. 1) between the volumetric concentration of tungstate (C_i , mol/l) and its H₂O-normalized Raman band area (A_i) to determine the calibration coefficient (K_i) of this species at a given T (Fig. 4.2C, D):

$$C_i = K_i(T) \times A_i \quad (1)$$

The calibration coefficient depends on both the Raman cross-section of the considered band and the spectrometer response. The tungstate volumetric concentration at each investigated T was previously (Annex 2- Table 1) derived according to Eq. 2

$$C_i = (\rho_{fluid}/F) \times m_i \quad (2)$$

where m_i is the molality of tungstate (mol/kg_{H₂O}), F the molality to molality conversion factor $F = 1000/(1000 - b)$ where b is the mass in grams of total dissolved solutes per 1 kg of liquid, and ρ fluid the density (g/cm³) of aqueous solution at a given T and vapor saturation pressure. The latter has been measured at 25°C and 1 bar by weighing 1 ml of each experimental solution. The knowledge of density for high T necessitates the use of computational models, because we have no control about volumetric variations of solution inside the FSCC during heating. For this purpose, we compare soWat (Sodium Chloride-Water) model (Driesner and Heinrich, 2007; Driesner, 2007) with AqSo-NaCl computer program (Bakker, 2018). These 2 models require (1) the calculation of NaCl mole fraction, according to Eq. 3:

$$x_{NaCl} = \text{mol}_{eqNaCl} / [\text{mol}_{eqNaCl} + (1000 - b)/u_{H_2O}] \quad (3)$$

where b is the mass in grams of total dissolved solutes per 1 kg of liquid and u_{H_2O} is the molecular mass of water, and (2) the pressure value of solution at each investigated T: 1, 0.9, 15, 85.83 and 220 bar for T= 25, 100, 200, 300 and 400°C, respectively. Both methods give the same results at the second decimal position (Annex 2 - Table 1).

The obtained calibration coefficients for species B at T ranging from 25 to 400°C allows us to quantify its concentrations in all experimental solution, but also to estimate the concentration of the other W species through the following procedure. First, in all of the collected Raman spectra, we identify those displaying only one Raman band in addition to that of tungstate (at 927 cm⁻¹) in the 860-1010 cm⁻¹ spectral region. This configuration exists only under circum-neutral to mid-alkaline condition - the C species being the only secondary Raman band contribution. Second, we derive the C species concentration by subtracting the previously calculated concentration of tungstate (B-species) at the total W concentration of the solution. Third, we infer the calibration coefficient (k_c) for the C species at T ranging from 25 to 400°C (in Annex 2 - k calibration – tables B, C, and D and figures B, C, and D), and thus we calculate the C species concentration in all our experimental solutions (Annex 2- Table 2). Finally, we repeat this step by step procedure for Raman spectra displaying 3, and eventually 4 Raman bands in the 860-1010 cm⁻¹ spectral region. Of course, uncertainty increases over the course of this step by step approach because of growing cumulative errors and because some calibration lines are poorly constrained.

3 Results

A total of 5 different Raman bands have been detected in our experimental runs in the 860 - 1010 cm^{-1} spectral region, which corresponds to the symmetric stretching ($\text{W}=\text{O}$) vibration domain. Note that this latter domain is overlapped by the asymmetric stretching ($\text{W}=\text{O}$) vibration domain ranging from 825 to 930 cm^{-1} . In the following sections, these Raman bands are identified with alphabetic letters (A, B, C, D, E), and ranked by increasing wavenumbers. The corresponding W-species include simple dissolved ions, but also clusters and/or polyanion species, like heteropoly acids with Keggin structures known as heteropolytungstates. We discuss their respective attribution in section 4.1.

3.1 Effect of temperature and pH on W speciation

Figure 4.3 shows 4 series of Raman spectra corresponding to 4 different W-bearing aqueous solutions recorded at different pH and at T ranging from 25 to 400°C. Under strongly alkaline condition (Fig. 4.3A), only one single Raman band exists in the 860 - 1010 cm^{-1} spectral region at each investigated T. This band, noted "B" is clearly identified by its intense and sharp shape at $\approx 923 \text{ cm}^{-1}$ at 25°C, which slightly shift toward lower frequency with T increase. Under acidic to circum-neutral condition, W speciation is far more complex, with at least 5 well-identified Raman band over the investigated T range. The relative evolution of the area of these bands reflects the speciation of tungsten.

The Raman band noted "A", is characterized by a broad and weak peak at $\approx 894 \text{ cm}^{-1}$. At room T, this band exists in solution from strongly acidic to neutral condition (Fig. 4.3B-D), and its area normalized to water area (of bending vibrational mode) slightly increases over the 1.1 to 6.9 pH range (Annex 2 - Table 3). The intensity of this "A" band decreases with T and vanishes at T above 200°C. The Raman band noted "B", previously identified under alkaline conditions, exists over all the investigated pH and T ranges, but its intensity decreases abruptly under circum-neutral pH conditions, and remains very low under acidic condition. The Raman band noted "C" is identified by an intense and sharp peak at $\approx 960 \text{ cm}^{-1}$ at room temperature. Its intensity is maximum under circum-neutral condition, it decreases rapidly with increasing pH and disappears at pH around 11. However, the intensity of this "C" band only slightly decreases with decreasing pH and remains significant even at pH below 1 at room T. A slight wavenumber shift toward lower frequency with T increase is also observed for this band. The Raman band noted "D" appears at pH below 7 at room temperature. It is characterized by an intense and sharp peak at $\approx 970 \text{ cm}^{-1}$, downshifting toward slightly lower frequency with T increases. This band is the most intense of all at pH below 7 and at 25°C. It may remain detectable in solution at T up to 400°C, but it is progressively replaced by a fifth band, namely "E" at $T \geq 200^\circ\text{C}$. This latter band is well identified by a sharp intense peak at $\approx 988 \text{ cm}^{-1}$ at 200°C,

downshifting to $\approx 983 \text{ cm}^{-1}$ at 400°C . At pH below 2 and $T > 200^\circ\text{C}$, precipitation occurs and no more dissolved W-species remain detectable.

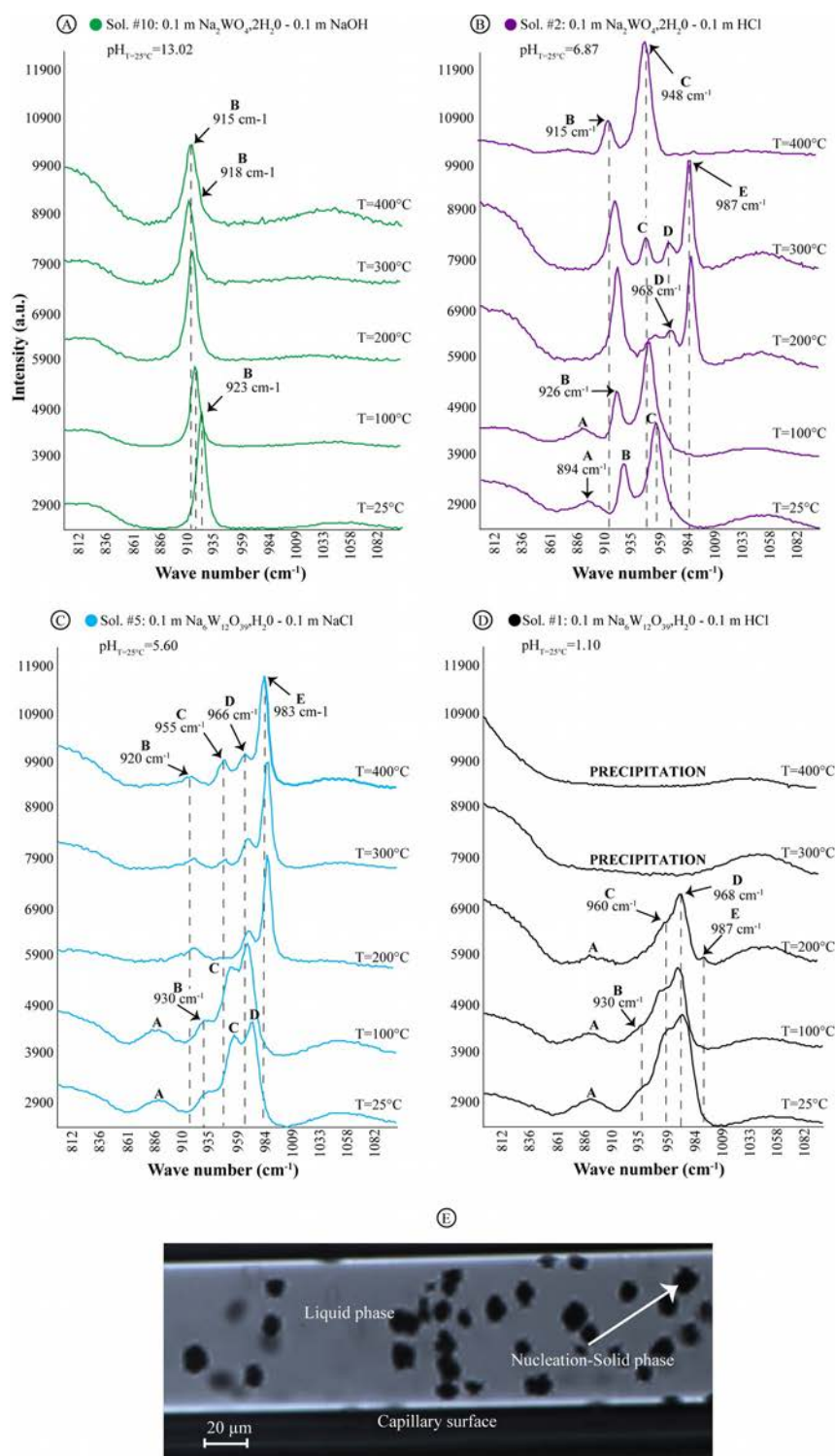


Fig. 4.3: Raman spectra of W-bearing aqueous solution results displaying different W-species dissolved at four different pH conditions and at temperature ranging from 25 to 400°C . (A) describes alkaline systems (solution #10: 0.1m $\text{Na}_2\text{WO}_4 \cdot 2\text{H}_2\text{O}$ +0.1m NaOH) characterized by the dissolution of only one isolated species. (B) Raman spectra of solution #2 having a neutral pH at 25°C . It is made of 0.10m $\text{Na}_2\text{WO}_4 \cdot 2\text{H}_2\text{O}$ plus 0.10m HCl. In (C) W- speciation is referred to solution #5 (0.10m $\text{Na}_6\text{W}_{12}\text{O}_{39} \cdot \text{H}_2\text{O}$ plus 0.10m NaCl) characterized by a room temperature pH of 5.60. (D) shows the W-species dissolved in solution #1 synthesized with 0.10m of $\text{Na}_6\text{W}_{12}\text{O}_{39} \cdot \text{H}_2\text{O}$ plus 0.10m of HCl, having a $\text{pH}_{T=25^\circ\text{C}}=1.10$. (E) Microscopic image of FSCC containing 0.10m $\text{Na}_6\text{W}_{12}\text{O}_{39} \cdot \text{H}_2\text{O}$ plus 0.10m NaCl at $T=300^\circ\text{C}$. Both liquid and solid phases coexist at the same temperature.

3.2. Stability and reversible formation of W-species

The question of the stability and reversibility of the characterized W speciation was addressed three different ways: 1) by comparing Raman spectra acquired immediately after heating the capillary at 200, 300 and 400°C with those obtained at the same temperature after 48 hours heating at 350°C, 2) by performing heating and cooling cycles, and 3) by measuring W speciation at 25°C two months after having heated the capillary up to 400°C and by comparing the obtained Raman spectra to both, fresh and aged (after 6 month) unheated solutions.

Figure 4.4 shows one example of these tests performed on a capillary containing a solution at 0.1m Na_2WO_4 and 0.5m acetic acid (#R1), having a pH = 4 at 25°C, and thus being demonstrative of the evolution of the 5 previously described Raman bands. First, the comparison of the Raman spectra obtained at 200, 300, and 400 °C immediately after loading the capillary (Fig. 4.4A, lower part) and after 48 hours heating at 350°C (Fig. 4B) are perfectly identical in terms of peak feature and peak intensities (when normalize to water bending, Annex 2 - Table 4). Second, W speciation is fully reversible upon heating-cooling cycles over the 200-400°C T range. The D and E Raman bands observed at 200 and 300°C disappear in favor species C at 400°C. These two first tests demonstrate that the 4 Raman bands B, C, D and E belong to 4 different W species. They also demonstrate that these 4 species are stable and that the equilibrium is achieved within minutes under hydrothermal condition. However, the third test, which consists in comparing Raman spectra obtained at room T with i) freshly prepared, ii) aged, and iii) heated up to 400°C solutions, shows a clearly different picture (Fig. 4.4A). In particular, the species E, not present in the fresh solution, remains abundant in solution immediately as well as 2 months after cooling. Species C, which was present in the fresh solution, is absent after cooling, and the abundance of species D is different before and after heating/cooling. Note that W speciation at 25°C in unheated solution remains nearly identical in freshly prepared solution and after 6 months aging. This latter comparative test demonstrate that W-speciation as observed in fresh solution does not reflect equilibrium, or at least that W-solution is in a metastable equilibrium state. Equilibrium requires a very long time to be reached at 25°C (> 6 months), species E being the thermodynamically stable byproduct of the D (and probably C) W-bearing compound in solution.

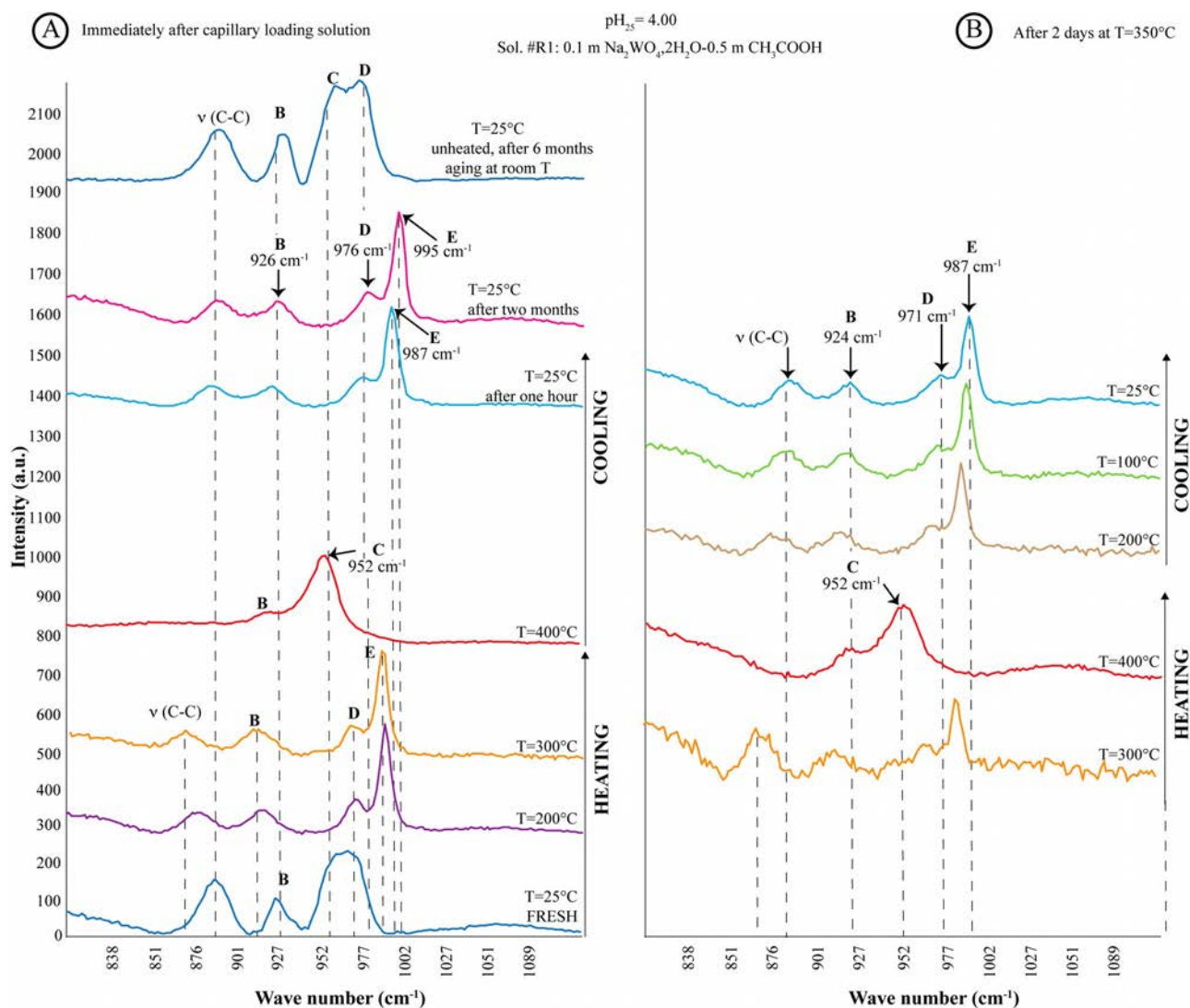


Fig. 4.4: Raman spectra for the solution R1 (0.1065mNa₂WO₄·2H₂O-0.5155mCH₃COOH; pH_{T=25°C}= 4.00). (A) showing W-speciation for fresh solution at T= 25°C (blue), during heating at 300°C (orange)- 400°C (red) from below; and at T=25°C (light blue) during cooling and after two months (fuchsia). The blue spectrum (T=25°C) on the upper part is representative of W-speciation of the not-heated solution after six months. (B) shows Raman results of the same solution after heated at 350°C for two days.

3.3. Effect of carbonate and chloride

The effect of carbonate on W-speciation was studied using three well known carbonate-bearing systems, where CO₂(aq) (experiment #12, pH_{25°C} ≈ 7.2), HCO₃⁻ (experiment #11, pH_{25°C} = 8.3), and CO₃²⁻ (experiment #13, pH_{25°C} = 11.9) were the dominant dissolved carbonate species. At room T, the in-situ pH value of the W-bearing solution (0.1 m Na₂WO₄) in equilibrium with 0.15 bar CO₂(g) has been estimated using the Phreeqc software package (V3.0; Parkurst and Apello, 1999) together with the Ilnl database (Johnson et al., 2000), based on the relative abundance of HCO₃⁻ and CO₂(aq). The Raman spectra shown in Figure 4.5 are strictly identical to those obtained under similar pH and T conditions without carbonate (see Fig. 4.3). Thus, the presence of dissolved carbonate in substantial amount (> 0.1 m) has no effect on W speciation over the 6 < pH < 12, and 25 ≤ T ≤ 400 °C ranges.

The effect of chloride on W speciation was examined through 3 experiments with 0.1 to 3.6m NaCl. Figure 4.6 shows the Raman spectra collected for two different W-bearing solutions containing 0.1 m, and 3.6m NaCl, at $\text{pH}_{25^\circ\text{C}}$ 5.6 and 9.6 respectively. In both systems chloride complexation with dissolved W species does not take place, as no new species are detected in solution compared to those already described. At low salinity (Fig. 4.6A), W speciation is identical to the one measured under similar pH condition (i.e. $\text{pH}_{25^\circ\text{C}} = 5.6$). At high salinity, the presence of the species "C" seems to be promoted in comparison to salt-free experiments conducted under similar pH condition (i.e. $\text{pH}_{25^\circ\text{C}} = 9.6$).

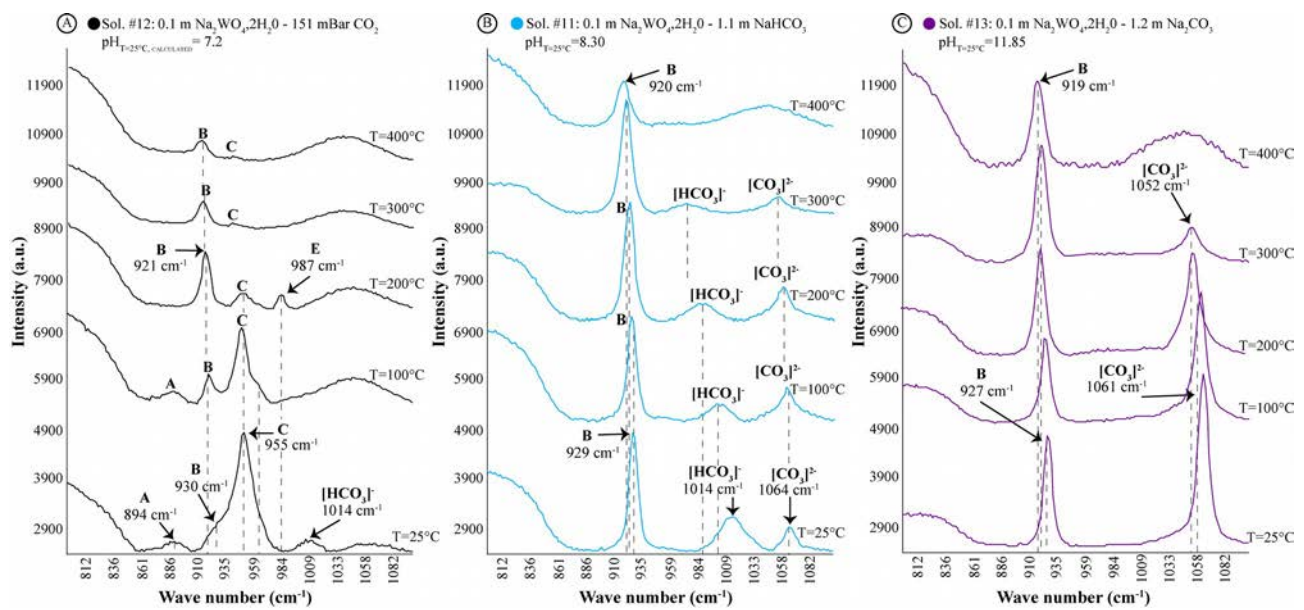


Fig. 4.5: Raman spectra results of W-bearing aqueous solutions, displaying W-speciation characterising 3 different carbonate-systems at temperature ranging from 25 to 400°C. (A) shows the W-species dissolved in solution #12 synthesized with 0.10m $\text{Na}_2\text{WO}_4 \cdot 2\text{H}_2\text{O}$ plus CO_2 , having a calculated $\text{pH}_{T=25^\circ\text{C}} = 3-4$. D-species does not occur. In (B) W-speciation is referred to solution #11 (0.10m $\text{Na}_2\text{WO}_4 \cdot 2\text{H}_2\text{O}$ plus 1.1m NaHCO_3) characterized by a room temperature pH of 8.30. (C) Raman spectra of solution #13 having an alkaline pH at 25°C. It is made of 0.10m $\text{Na}_2\text{WO}_4 \cdot 2\text{H}_2\text{O}$ plus 1.2m Na_2CO_3 . B-species predominates the (B) and (C) systems.

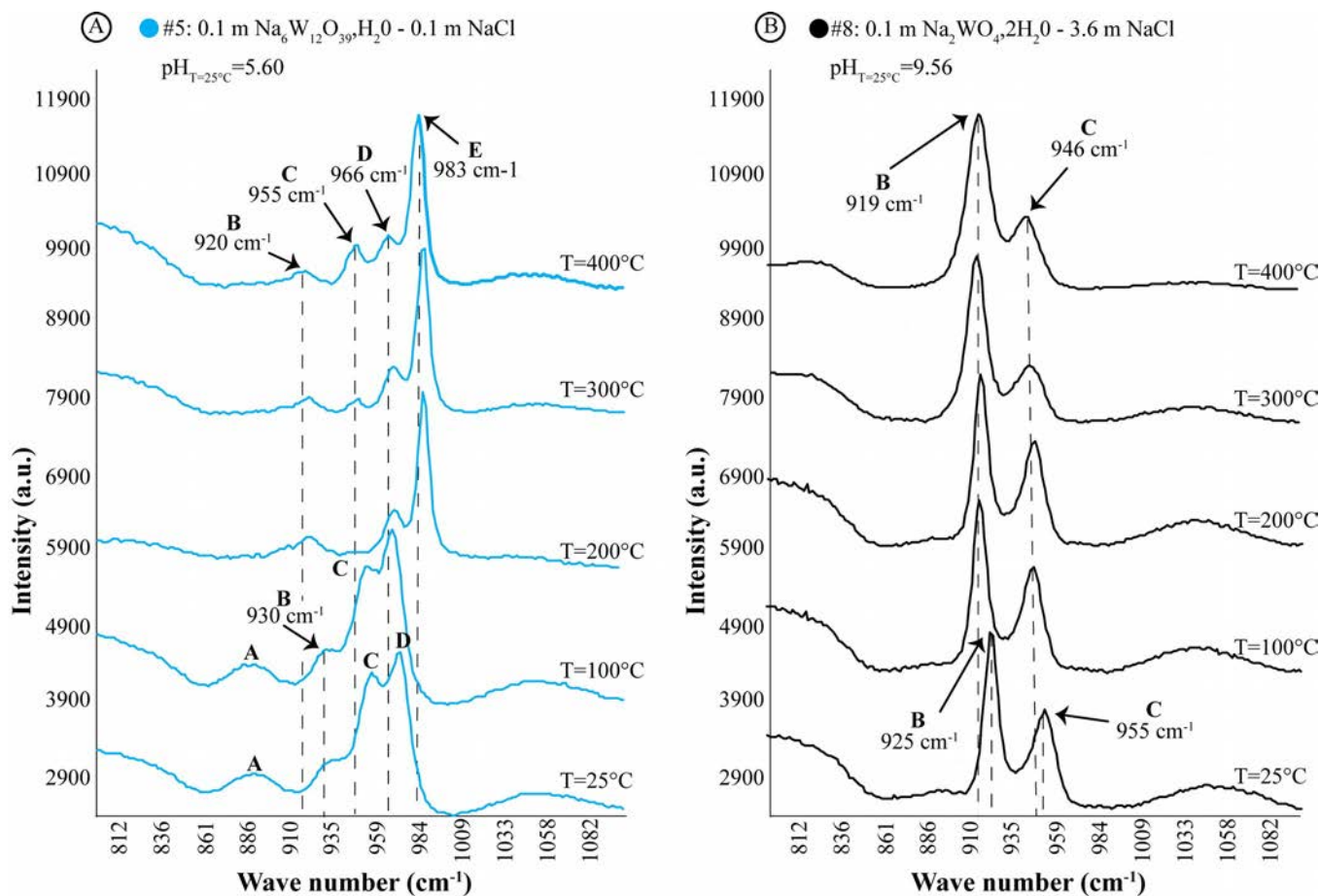


Fig. 4.6: Raman spectra of W-bearing aqueous solution results displaying W-species dissolved in NaCl system, from 25 to 400°C. (A) shows the W-species B and C dissolved in solution #8 synthesized with 0.10m $\text{Na}_2\text{WO}_4\cdot 2\text{H}_2\text{O}$ plus 3.6 NaCl, having a $\text{pH}_{T=25^\circ\text{C}}= 9.56$. In (B) Raman spectra of solution #5 (0.10m $\text{Na}_6\text{W}_{12}\text{O}_{39}\cdot\text{H}_2\text{O}$ plus 0.10m NaCl) at the same temperatures, with a $\text{pH}_{T=25^\circ\text{C}}= 5.60$, reflecting the complexity of W-speciation.

4 Discussion

4.1. Identification of W-species

Among the 5 detected Raman band, only the one at 927 cm^{-1} belonging to species “B”, may be attributed with certainty to the $\nu_s(\text{W}=\text{O})$ symmetric stretching vibration of the WO_4^{2-} anion (Ng and Gulari, 1984; Bilal et al., 1986; Vigasina et al., 2000; Barré et al., 2005; and Redkin and Bondarenko, 2010). Note that the $\nu_{as}(\text{W}=\text{O})$ asymmetric stretching mode at 834 cm^{-1} and the $\delta(\text{W}=\text{O})$ bending mode at 326 cm^{-1} of WO_4^{2-} interfere with Raman bands of the silica-glass of the FSCC. The other 4 observed bands (at ~890, 955, 970 and 985 cm^{-1}) are far more difficult to attribute to a specific W species as there is no consensus in the literature. However, one important finding of this study is that all the detected species under hydrothermal condition exist in solution at room T, even species “E” that forms upon heating at $T \geq 200^\circ\text{C}$ but remains stable 2 months after cooling at room T. Thus, the observed W-species are not specific to hydrothermal condition and must have been described in the plethora of studies dedicated to W speciation at ambient T-P.

In an attempt to propose a first comprehensible identification of these W-species, we cross-compare the published Raman spectroscopic studies (Annex 1 - Table 5) with other sources of W speciation data (e.g. potentiometric titration, solubility experiments, ultracentrifugation, mass spectrometry, and Nuclear Magnetic Resonance; Annex 1 - Table 6), and with thermodynamic calculations (Annex 1 - Table 7). This exercise allows us to infer the most probable W species associated to each Raman peak previously observed.

Species "A" - Raman band at 888-892 cm^{-1} . The morphology of this Raman band is very different from the others: low intensity and very large full-width at half maximum (averaged FWHM are 24, 18 and 4 cm^{-1} at 25, 100 and 200°C, respectively). This Raman band is only detected at $T \leq 200^\circ\text{C}$ and $\text{pH} < 8$. It is always associated to the presence of the "D" and/or "C" bands and its normalized intensity varies accordingly with these latter bands (see Annex 2 – Table 3). Thus, this later behavior leaves us thinking that the "A" band corresponds to the weak asymmetric stretching (W=O) vibration mode of species "D" and/or "C". The Raman spectra of Keggin heteropolytungstate anions exhibit bands between 950 and 1015 cm^{-1} ($\nu_s(\text{W}=\text{O})$ symmetric stretching mode) and 825-930 cm^{-1} ($\nu_{as}(\text{W}=\text{O})$ asymmetric stretching mode) as well as bands at lower wavenumbers arising from the bridging W-O-W bonds (Ross-Medgaarden and Wachs, 2007).

Species "C" – Raman band at 950-960 cm^{-1} . This band is sharp and intense. It is located next to the one of WO_4^{2-} (species "B"), with a slight upshift in frequency. It exists at all investigated T and at $\text{pH}_{25^\circ\text{C}} < 10.5$. Its maximum intensity is reached at $\text{pH}_{25^\circ\text{C}} \approx 7$ and room T. The species "C" may coexists alone with WO_4^{2-} at $7 < \text{pH}_{25^\circ\text{C}} < 10.5$ and at T up to 400°C (Fig. 4.3C). At $T > 300^\circ\text{C}$, it forms at the expense of species E (and D in a lesser extent) and its formation at elevated T is fully reversible upon cooling. Redkin and Bondarenko (2010) have assumed this band to be related to the vibration of $[\text{HW}_6\text{O}_{21}]^{5-}$, by analogy with thermodynamic simulations relying on data reported by Baes and Mesmer (1976) and Wesolowski et al. (1984). In their extensive potentiometric investigation of W(VI) speciation to 300°C, Wesolowski et al. (1984) considered several criteria to select 3 speciation schemes compatible with their data. Among the 3 speciation schemes, two including $[\text{W}_7\text{O}_{24}]^{6-}$ were proposed, but slight preference was given to the scheme comprising the two hexamers $[\text{HW}_6\text{O}_{21}]^{5-}$ and $[\text{W}_6\text{O}_{19}]^{2-}$ in addition to monomers and the dodecamer $[\text{H}_2\text{W}_{12}\text{O}_{40}]^{6-}$. The ambiguity of the choice concerned the inclusion of hexameric or heptameric species in their speciation scheme under weakly acidic conditions. Indeed, since the pioneering work of Jander et al. (1929) the hexameric anion had been included in nearly all speciation models. However, this ambiguity has been subsequently unequivocally removed by the combined results of NMR (Maksimovskaya and Burtseva, 1985; Hasting and Howarth, 1992), potentiometric (Cruywagen and Van Der Merwe, 1987) cyclic voltammetric (Himeno et al., 2000), and Raman (Fuchs and Flindt, 1979; Himeno et al., 2000) studies. All these works concur to the existence and stability of $[\text{W}_7\text{O}_{24}]^{6-}$ in this pH domain. This species display a strong $\nu_s(\text{W}=\text{O})$ symmetric stretching Raman band at $\sim 953 \text{ cm}^{-1}$ at room temperature (Fuchs and Flindt, 1979; Himeno et al., 2000; Weiner et al., 2005). Despite all these line of evidence, Wang et al (2019b) have attributed this Raman band to HWO_4^- , in order to comply with the thermodynamic predictions made by Wesolowsky et al (1984) or Wood and

Samson (2000). Even if we recognize that this choice is tempting, particularly because it satisfies the classical view of W speciation at elevated T and the fact that neutral or weakly charged species are favored under hydrothermal condition due to the decrease of the dielectric constant of water (e.g. Crerar et al. 1985; Brimhall and Crerar, 1987), we cannot ignore the vast Raman spectroscopy literature that clearly assign the vibration at 950 cm^{-1} to $[\text{W}_7\text{O}_{24}]^{6-}$ (paratungstate-A). In our experiments, this band is observed at room T over a wide pH range (from pH = 1 to nearly 10), and its main features (e.e. position, and FWHM) do not really change with T.

Therefore, we have attributed the Raman band at $\sim 955\text{ cm}^{-1}$ to $[\text{W}_7\text{O}_{24}]^{6-}$ (paratungstate-A).

Species "D" – Raman band at 970-979 cm^{-1} . At room temperature and pH < 6, this band is the most intense of all. Its intensity strongly decreases at $T \geq 200^\circ\text{C}$, but remains detectable up to 400°C under acidic conditions (pH < 5). The disappearance of this band at elevated T is not reversible upon cooling (Fig. 4.4). Therefore, the species "D" is metastable. Bilal et al. (1986) have attributed this band to the $[\text{W}_{10}\text{O}_{32}]^{4-}$ species (tungstate-Y) in their Raman spectra recorded at 150°C , 1 kbar and $\text{pH}_{150^\circ\text{C}} = 6$. These authors also observed the complete disappearance of this band at $T = 200^\circ\text{C}$. This behavior is in good agreement with our observations. Tungstate-Y is known to be kinetically unstable in aqueous solution. Upon prolonged heating at 80°C it yields the thermodynamically stable true α -metatungstate $\alpha\text{-}[\text{H}_2\text{W}_{12}\text{O}_{40}]^{6-}$ (Hasting and Howarth, 1992; Himeno and Kitazumi, 2003). Thus, we have attributed the Raman band at $970\text{-}979\text{ cm}^{-1}$ to $[\text{W}_{10}\text{O}_{32}]^{4-}$ (tungstate-Y).

Species "E" – Raman band at 983-995 cm^{-1} . This band is very sharp (FWHM(200°C) = 7, FWHM(300°C) = 6, and FWHM(400°C) = 2) and intense. It only appears at pH ≤ 7 and $T \geq 200^\circ\text{C}$ upon heating. It forms at the expense of species "D". The behavior of the species belonging to this band is very surprising since its formation is reversible upon heating and cooling in the $200 - 400^\circ\text{C}$ T range, but once formed at elevated T, it remains stable at room T even after 2 months (Fig. 4.4). This band has been assigned to the $[\text{W}_{10}\text{O}_{32}]^{4-}$ by Himeno et al., (2000), in their Raman spectra obtained at room T and pH < 4, without heating. They observed a disappearance of this band upon increasing pH above 3 or after heating at 80°C for 3 days. This behavior is not consistent with our observation: species E forms upon heating preferentially under slightly acidic conditions. Thus, we rule out the possibility for $[\text{W}_{10}\text{O}_{32}]^{4-}$ to belong to the Raman band at $983\text{-}995\text{ cm}^{-1}$. This band has been assigned to $[\text{H}_3\text{W}_{12}\text{O}_{40}]^{5-}$ by Bilal et al. (1986) in their spectra recorded at 150°C , 1 kbar and $\text{pH}_{150^\circ\text{C}} = 6$. These authors also observed that this complex is the only stable polymeric species at pH < 5, $T = 200^\circ\text{C}$ and $P = 1\text{ kbar}$. Again, this observation is in very good agreement with our measurements, even if other minor species are also detected (mainly B and D) either because of the higher pressure applied in Bilal et al. (1986) study or to the better sensitivity of our modern spectrometer. Wang et al. (2019b) have also detected this band in their experiments performed from 0.03 to 0.1 mol.kg_{H₂O}⁻¹ of W in the presence of CO₂, but they do not attribute it to a particular polymeric species. In their thorough and comprehensive NMR spectroscopy (183W, 17O and 1H) study of tungstate solution in the pH range 1.5 to 8,

Hasting and Howarth (1992) give an in-depth perspective on the formation of W species in solution in relation to polyoxoanions already characterized in the solid state. The $[\text{H}_3\text{W}_{12}\text{O}_{40}]^{5-}$ complex is a protonated form of paratungstate-B ($[\text{H}_2\text{W}_{12}\text{O}_{42}]^{10-}$), that forms at $\text{pH} < 2$. This description does not correspond to our observations because the species E appears at $T > 100^\circ\text{C}$ and slightly acidic conditions. Thus, $[\text{H}_3\text{W}_{12}\text{O}_{40}]^{5-}$ and $[\text{W}_{10}\text{O}_{32}]^{4-}$ complexes cannot be assigned to the Raman band at $983\text{-}995\text{ cm}^{-1}$. Instead, the well-known behavior of α -metatungstate ($\alpha\text{-}[\text{H}_2\text{W}_{12}\text{O}_{40}]^{6-}$) which is the dominant and thermodynamically stable W-species that from upon prolonged heating (70°C) below $\text{pH} 6$ (Hasting and Howarth, 1992; Himeno et al., 2000, Himeno et Kitazumi, 2003), satisfies all our observation. Therefore, we have attributed the Raman band at $983\text{-}995\text{ cm}^{-1}$ to $\alpha\text{-}[\text{H}_2\text{W}_{12}\text{O}_{40}]^{6-}$ (α -metatungstate).

4.2. Tungsten speciation

Based on our calibration procedure, we have been able to derive the concentration of WO_4^{2-} and to estimate step by step the concentration of the 3 other identified species namely, $[\text{W}_7\text{O}_{24}]^{6-}$, $[\text{W}_{10}\text{O}_{32}]^{4-}$, and $\alpha\text{-}[\text{H}_2\text{W}_{12}\text{O}_{40}]^{6-}$ in all our experimental solution at every temperature up to 400°C . The value of the obtained calibration coefficients (k) are comprised within the 0.01 to 0.2 mol/l range. Surprisingly, the tungsten polymerization does not have a significant effect on the value of the Raman scattering coefficient. These coefficients tend to decrease with temperature starting from about 0.15 mol/l at 25°C and decreasing abruptly to $0.02 - 0.04\text{ mol/l}$ at $T > 200^\circ\text{C}$. Only the calibration coefficient of the $[\text{W}_7\text{O}_{24}]^{6-}$ species display a significantly different behavior, a slight increase with T, from 0.15 to 0.2 mol/l , over the $25\text{-}400^\circ\text{C}$ T range. The pH of the experimental solution has been measured at room T, and calculated at elevated T using the Phreeqc geochemical code together with the llnl thermodynamic database. This approach is rather safe under extreme pH condition ($\text{pH} < 3$ or $\text{pH} > 10$) or in the presence of concentrated pH buffers (acetic acid, formic acid, carbonate/bi-carbonate solutions) because the evolving tungsten speciation weakly impact H^+ activity. However, for a small number of solutions (e.g. sol.#2, #2.2 and #5), where the circum-neutral pH values measured at room T were not buffered, our calculation have been made for indicative purpose as there is no thermodynamic data for the observed complex at elevated T. The resulting tungsten speciation as a function of pH is shown in Figure 4.7 at $25, 100, 200,$ and 300°C .

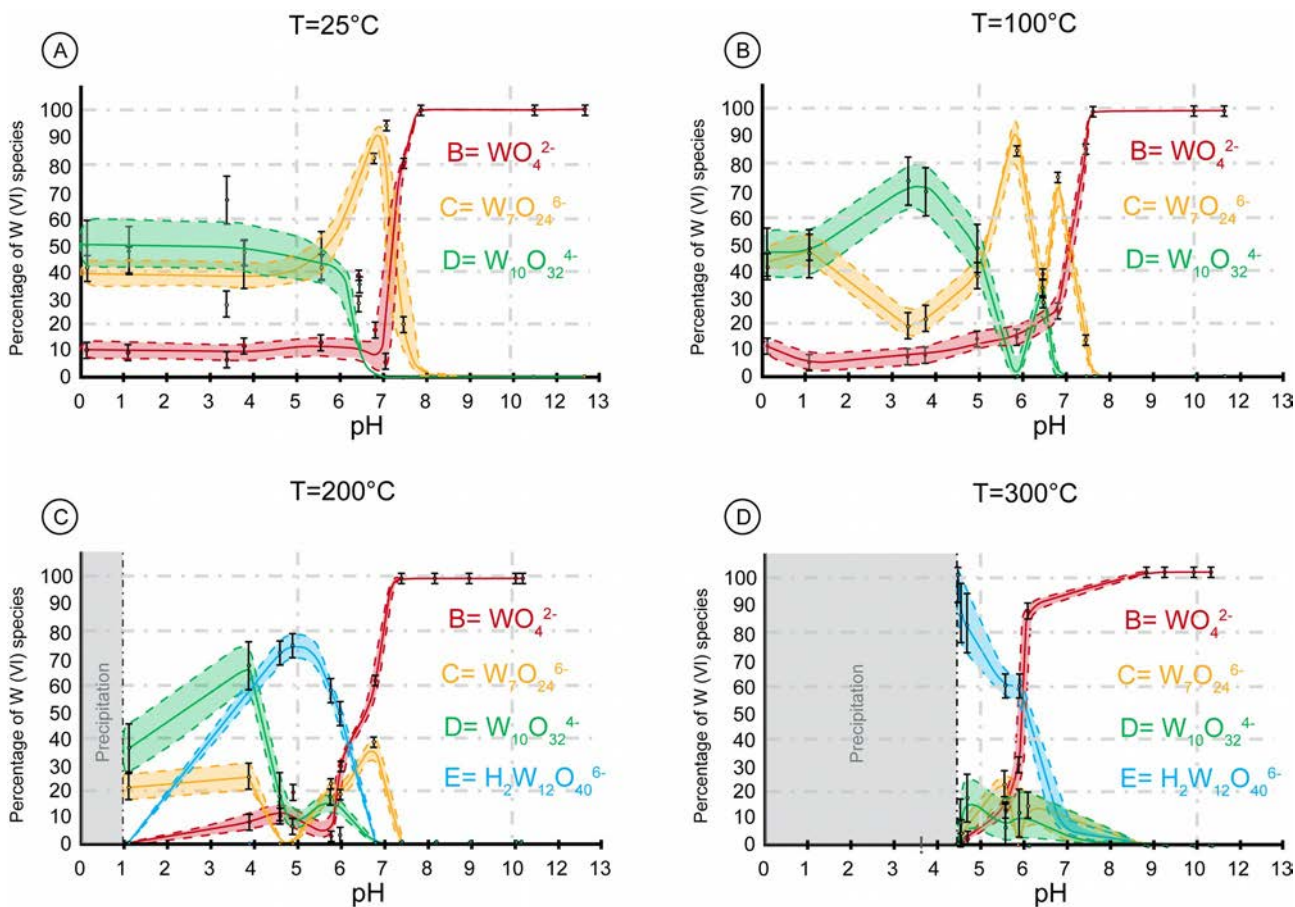


Fig. 4.7: Tungsten speciation as a function of pH and temperature: A (25°C), B (100°C), C (200°C), D (300°C).

The WO_4^{2-} anion is the predominant species at pH above 7.5 at 25°C. Its predominance domain is slightly shifted toward lower pH value with T increase. Interestingly, we have been able to detect and quantify the presence of WO_4^{2-} even under strongly acidic condition, where it still represents between 5 to 10% of the total dissolved W concentration. The $[\text{W}_7\text{O}_{24}]^{6-}$ polyanion is the predominant species under circum-neutral condition ($6 < \text{pH} < 7$) at T up to 100°C. At lower pH, it still represents an important contribution to the W speciation (20 to 40%). At higher T, its concentration in solution drastically decreases, and it only represents 10 to 20% of the total dissolved W concentration. The $[\text{W}_{10}\text{O}_{32}]^{4-}$ polyanion, which is metastable, dominates the W speciation at $\text{pH} < 5$ and T up to 200°C upon heating. Under these conditions its concentration represents 40 to 80% of the total W speciation. Upon further heating it progressively disappears in favor of $\alpha\text{-}[\text{H}_2\text{W}_{12}\text{O}_{40}]^{6-}$. Its disappearance is not reversible upon cooling. Finally, the $\alpha\text{-}[\text{H}_2\text{W}_{12}\text{O}_{40}]^{6-}$ polyanion is the most abundant and stable specie at $\text{pH} < 6$ and $T \geq 300^\circ\text{C}$. Once formed, it remains in solution upon cooling, which is not the case of $[\text{W}_{10}\text{O}_{32}]^{4-}$.

4.3. Geological implications

This new view of W speciation has important consequences for W transport and deposition by hydrothermal aqueous fluids. Polymeric tungstates are important species for the transport of W in mineralizing fluids. Even if their definitive identification may be subject to caution, the fact remains that they predominate in solution under acidic to circumneutral conditions at T up to 400°C. The existence of stable highly charge polymeric species at T up to 400°C is a major discovery as it definitively shifts the long-standing paradigm that only neutral or weakly charged species predominate under hydrothermal conditions because of the decrease of the dielectric constant of water with T increase (Crerar et al., 1985; Mei et al., 2014; Brugger et al., 2016).

Tungsten does not form complexes with carbonates species over the whole pH and T range investigated here. This observation does not preclude the important role of CO₂/carbonate in the transport and deposition of W. The existence of CO₂-rich fluids is documented in fluid inclusions associated to numerous W deposits. First, the presence of dissolved CO₂, may buffer the pH in the range 5-6 and thus favors a W speciation dominated by polymeric species. Second, CO₂/water immiscibility, may result in CO₂ degassing and trigger wolframite precipitation due to pH increase (Wood and Samson, Liu et al., 2018; Wang et al., 2019a). Unmixing is recognized in some cases such as at Panasqueira (Portugal), where aqueous-carbonic fluids produce both liquids and vapors enriched in CO₂ and other volatiles in minor amounts. The pressure drop coupled with moderate temperature yield thus the system to reach the two phase fluid domain. In such a case, unmixing could have a role on W speciation, and subsequently on the W precipitation.

Therefore, although pressure has a secondary effect on transport and deposition of W-ore minerals, unmixing of CO₂ may indirectly promote the instability of W species by decreasing the water activity and modifying the dielectric constant of the solvent which controls ion paring (Kokh et al., 2017) at temperature in excess of 100°C.

5. Conclusion

Important findings from this study are summarized below.

- 1) Tungsten does not for complexes with chlorides and carbonates ions over the whole pH (0-13) and T (25°C-400°C) range investigated here.
- 2) Tungsten polymers form reversibly under acidic to circum-neutral conditions and T up to 400°C.
- 3) The W polymers identified under hydrothermal conditions are exactly the same as those already well characterized at room T.

4) This work challenges the long-standing paradigm that highly charged polymers cannot exist under hydrothermal conditions because of the decrease of the dielectric constant of water with T increase.

Especially for this last conclusion, it could be inferred that localized fluid circulation along a major crustal discontinuity in relation with a hot spot has favored tungsten to be dissolved and transported as stable highly charged polymers. Thus, a hypothetical scenario would be to consider that W-kegging structures may have been the main carrier of W, as their formation and stability are possible in the considered environments.

In general, W ore minerals deposition requires the availability of Fe and Mn (or Ca) depending of the nature of the precipitate (wolframite or scheelite). To reach, for instance, wolframite oversaturation, sufficient amounts of Fe (Mn) and W are required and their concentrations in solution are defined by the solubility product of wolframite. Fe may have been provided by another fluid, by the rocks present in the deposits, or by the minerals already deposited (Fe sulfides for instance, which may be altered). Fe needs to be present in solution, this requiring low redox conditions, and an active source which could be related to a process of Fe-mineral destabilization. Besides, the availability of W may have been favored by the destabilization of W-complexes caused by the unmixing of volatiles in solution. This is known to have occurred in a significant number of W deposits.

A perspective from this study would be to investigate more deeply W precipitation process in hydrothermal conditions, adding experimental solutions ad hoc with different amount of Fe and/or Ca, for instance. Raman spectroscopy coupled with capillary technique has proven to be a perfect tool in the study of tungstate speciation, and in a micro dimension, it allows to better understand what could happen in a very large scale.

Acknowledgements

We are grateful to Maria A. Kokh for constructive discussion and precious competence during the developing of starting results. Pascal Robert and Aurélien Randi are warmly thanked for their help during the experimental solution set up. Guillaume Barre and Julien Boulliung are thanked for shearing their

experiences and useful suggestions on capillary loading technique. Financial support for this work was provided by Grant Labex Ressources21 and NewOre project (Lorraine University).

References

- Arnek, R., & Sasaki, Y. (1974). Equilibrium Studies of Polyanions. 20. A Recalculation of Emf Data on the Reactions of H⁺ and WO₄²⁻ in 3 M Na (ClO₄) at 25 C. *Acta Chem. Scand. A*, 28(1).
- Aveston, J. (1964). Hydrolysis of tungsten (VI): ultracentrifugation, acidity measurements, and Raman spectra of polytungstates. *Inorganic Chemistry*, 3(7), 981-986.
- Baes, C. F., & Mesmer, R. E. (1976). *The Hydrolysis of Cations* Wiley. New York, 177-182.
- Bakker, R. J. (2018). AqSo_NaCl: Computer program to calculate pTVx properties in the H₂O-NaCl fluid system applied to fluid inclusion research and pore fluid calculation. *Computers & geosciences*, 115, 122-133.
- Barré, T., Arurault, L., & Sauvage, F. X. (2005). Chemical behavior of tungstate solutions: Part 1. A spectroscopic survey of the species involved. *Spectrochimica Acta Part A: Molecular and Biomolecular Spectroscopy*, 61(4), 551-557.
- Bilal, B. A., Haufe, P., & Möller, P. (1986). Raman spectroscopic and electrochemical study of polymerization of tungsten (VI) in a hydrothermal solution up to 1 kbar and 200 C. *Physica B+ C*, 139, 721-724.
- Caumon, M. C., Dubessy, J., Robert, P., & Tarantola, A. (2013). Fused-silica capillary capsules (FSCCs) as reference synthetic aqueous fluid inclusions to determine chlorinity by Raman spectroscopy. *European Journal of Mineralogy*, 25(5), 755-763.
- Chou I.-M., Song Y. and Burruss R. C. (2008). A new method for synthesizing fluid inclusions in fused silica capillaries containing organic and inorganic material. *Geochim. Cosmochim. Acta* 72, 5217–5231.
- Cruywagen, J. J., & Van Der Merwe, I. F. (1987). Tungsten (VI) equilibria: a potentiometric and calorimetric investigation. *Journal of the Chemical Society, Dalton Transactions*, (7), 1701-1705.
- Dargent, M., Dubessy, J., Truche, L., Bazarkina, E. F., Nguyen-Trung, C., & Robert, P. (2013). Experimental study of uranyl (VI) chloride complex formation in acidic LiCl aqueous solutions under hydrothermal conditions (T= 21 C–350 C, Psat) using Raman spectroscopy. *European Journal of Mineralogy*, 25(5), 765-775.
- Driesner, T. (2007). The system H₂O–NaCl. Part II: Correlations for molar volume, enthalpy, and isobaric heat capacity from 0 to 1000 C, 1 to 5000 bar, and 0 to 1 XNaCl. *Geochimica et Cosmochimica Acta*, 71(20), 4902-4919.
- Driesner, T., & Heinrich, C. A. (2007). The system H₂O–NaCl. Part I: Correlation formulae for phase relations in temperature–pressure–composition space from 0 to 1000 C, 0 to 5000 bar, and 0 to 1 XNaCl. *Geochimica et Cosmochimica Acta*, 71(20), 4880-4901.
- Duncan, J. F., & Kepert, D. L. (1961). 1050. Polyanion equilibria in aqueous solution. Part I. The quantitative analysis of acidified tungstate solutions. *Journal of the Chemical Society (Resumed)*, 5317-5325.
- Eugster H. P. and Wilson G. A. (1985). Transport and deposition of ore-forming elements in hydrothermal systems associated with granites. In *High Heat Production Granites, Hydrothermal Circulation and Ore Genesis*. *Inst. Min. Metall., London*, pp. 87-98.
- Fuchs, J., & Flindt, E. P. (1979). Preparation and structure investigation of polytungstates-contribution to the paratungstate-a problem. *Zeitschrift für Naturforschung Section Ba Journal of Chemical Sciences*, 34(3), 412-422.

- Gibert, F., Moine, B., Schott, J., & Dandurand, J. L. (1992). Modeling of the transport and deposition of tungsten in the scheelite-bearing calc-silicate gneisses of the Montagne Noire, France. *Contributions to Mineralogy and Petrology*, 112(2-3), 371-384.
- Hastings, J. J., & Howarth, O. W. (1992). A ^{183}W , $^{1\text{H}}$ and ^{17}O nuclear magnetic resonance study of aqueous isopolytungstates. *Journal of the Chemical Society, Dalton Transactions*, (2), 209-215.
- Häufe, P. (1982). Raman-spectrophotometric determination of the tungstate anion and its isopolyanions in aqueous systems. *Fresenius' Zeitschrift für analytische Chemie*, 310(5), 388-391.
- Heinrich, C. A. (1990). The chemistry of hydrothermal tin (-tungsten) ore deposition. *Economic Geology*, 85(3), 457-481.
- Himeno, S., Yoshihara, M., & Maekawa, M. (2000). Formation of voltammetrically-active isopolyoxotungstate complexes in aqueous CH_3CN media. *Inorganica Chimica Acta*, 298(2), 165-171.
- Himeno, S., & Kitazumi, I. (2003). Capillary electrophoretic study on the formation and transformation of isopolyoxotungstates in aqueous and aqueous- CH_3CN media. *Inorganica chimica acta*, 355, 81-86.
- Jander, G., Mojert, D., & Aden, T. (1929). Über amphotere Oxydhydrate, deren wäßrige Lösungen und kristallisierende Verbindungen. VIII. Mitteilung. Über Wolframate, Isopoly- und Heteropoly-Wolframsäuren. *Zeitschrift für anorganische und allgemeine Chemie*, 180(1), 129-149.
- Johnson, J., Anderson, G., & Parkhurst, D. (2000). Database "thermo. com. V8. R6. 230," Rev. 1-11. *Lawrence Livermore Natl. Lab., Livermore, California*.
- Kokh, M. A., Akinfiyev, N. N., Pokrovski, G. S., Salvi, S., & Guillaume, D. (2017). The role of carbon dioxide in the transport and fractionation of metals by geological fluids. *Geochimica et Cosmochimica Acta*, 197, 433-466.
- Maksimovskaya, R. I., & Burtseva, K. G. (1985). ^{17}O and ^{183}W NMR studies of the paratungstate anions in aqueous solutions. *Polyhedron*, 4(9), 1559-1562.
- Ng, K. Y. S., & Gulari, E. (1984). Spectroscopic and scattering investigation of isopoly-molybdate and tungstate solutions. *Polyhedron*, 3(8), 1001-1011.
- Parkhurst, D. L., & Appelo, C. A. J. (1999). User's guide to PHREEQC (Version 2): A computer program for speciation, batch-reaction, one-dimensional transport, and inverse geochemical calculations. *Water-resources investigations report*, 99(4259), 312.
- Redkin, A. F., & Bondarenko, G. V. (2010). Raman spectra of tungsten-bearing solutions. *Journal of solution chemistry*, 39(10), 1549-1561.
- Ross-Medgaarden, E. I., & Wachs, I. E. (2007). Structural determination of bulk and surface tungsten oxides with UV- vis diffuse reflectance spectroscopy and raman spectroscopy. *The Journal of Physical Chemistry C*, 111(41), 15089-15099.
- Truche, L., Bazarkina, E. F., Barré, G., Thomassot, E., Berger, G., Dubessy, J., & Robert, P. (2014). The role of S^{3-} ion in thermochemical sulphate reduction: Geological and geochemical implications. *Earth and Planetary Science Letters*, 396, 190-200.
- Vigasina, M. F., Orlov, R. Y., Dadze, T. P., & Kashirtseva, G. A. (2000). Determination of thermodynamic parameters of water-dissolved complexes at $T < 360^\circ\text{C}$ with the help of Raman spectroscopy: methods

and equipment. In *Raman Scattering* (Vol. 4069, pp. 103-108). International Society for Optics and Photonics.

- Wang, X., Qiu, Y., Lu, J., Chou, I. M., Zhang, W., Li, G., & Zhong, R. (2019a). In situ Raman spectroscopic investigation of the hydrothermal speciation of tungsten: Implications for the ore-forming process. *Chemical Geology*, 119299.
- Wang, X. S., Timofeev, A., Williams-Jones, A. E., Shang, L. B., & Bi, X. W. (2019b). An experimental study of the solubility and speciation of tungsten in NaCl-bearing aqueous solutions at 250, 300, and 350° C. *Geochimica et Cosmochimica Acta*.
- Wesolowski, D., Drummond, S. E., Mesmer, R. E., & Ohmoto, H. (1984). Hydrolysis equilibria of tungsten (VI) in aqueous sodium chloride solutions to 300. degree. C. *Inorganic Chemistry*, 23(8), 1120-1132.
- Wood, S. A., & Vlassopoulos, D. (1989). Experimental determination of the hydrothermal solubility and speciation of tungsten at 500° C and 1 kbar^{1, 2}. *Geochimica et Cosmochimica Acta*, 53(2), 303-312.
- Wood, S. A. (1992). Experimental determination of the solubility of WO₃ (s) and the thermodynamic properties of H₂WO₄ (aq) in the range 300–600 C at 1 kbar: calculation of scheelite solubility. *Geochimica et Cosmochimica Acta*, 56(5), 1827-1836.
- Wood, S. A., & Samson, I. M. (2000). The hydrothermal geochemistry of tungsten in granitoid environments: I. Relative solubilities of ferberite and scheelite as a function of T, P, pH, and m NaCl. *Economic Geology*, 95(1), 143-182.

Part Four

*Discussion Upon a Possible Panasqueira Model and
Open Questions*

4.1 IMPLICATIONS FROM THE PARAGENETIC SUCCESSION: GEOCHEMICAL INTERPRETATION, PROBLEMS TO BE SOLVED

From a geochemical point of view, Panasqueira is not only a major repository of W, Sn, and Cu, but also a *Si and Fe deposit* owing to the abundance of quartz and Fe-bearing minerals at all stages. Iron is indeed a major component of all the minerals forming the bulk of the veins infilling (wolframite, pyrrhotite, chalcopyrite, arsenopyrite). Another important feature of the Panasqueira deposit is the recurrent activity of *reducing fluids*. This is consistent with the ubiquitous presence at all quartz stages of C-O-H-N volatiles, likely equilibrated with graphite through interaction with (initially) organic-rich sedimentary rocks.

Intermittent oxidative events are however testified at the stage scale:

- PAS (IIIC) stage (Po → Py)

- cassiterite or chalcopyrite deposition (oxidation required to turn the valence of Cu or Sn in the fluid to the one in the crystal)

or at the mineral scale:

- oxy-foitite component in the tourmaline

- Fe and V valences in rutile (evidence for V⁴⁺ in the early rutile).

Panasqueira is also a *sulphur deposit*, mainly produced during the stage III, with massive pyrrhotite deposition. It may be speculated that Fe (and possibly S) was reincorporated in a later iron-bearing phases, which appear to have been preferentially concentrated within, or closely, to the main pyrrhotite masses, according to reactions such as:

- FeS+As, yielding arsenopyrite (which indeed is often seen replacing the pyrrhotite)

- FeS+Cu, yielding chalcopyrite

- FeS+CO₂, yielding the stage V symplectites of siderite and pyrite, expansion of the earlier (PAS) pyritization of Po.

It is a striking fact that, in the “greisen” of L2-level, development of siderite seems to be controlled by the presence of earlier Fe-facies (Po or Py), as well as the development of late sulphides (Gn in particular) seems to be conditioned by the presence of earlier S-bearing phases (Py).

In summary, it seems that, in the same way as W which was principally introduced in stage I (and II), or F and Sn which were supplied in stage III-A, Fe and S were principally introduced in the system in a single stage (III-B).

Significant are also the *missing* elements at the main to minor levels of abundance:

- owing to the Bi abundance, in particular the Bi⁰ associated to arsenopyrite (likely trapped from dissolved bismuth), *gold absence* is noticeable, as is also the paucity in tellurium (a very rare Te-canfieldite is

mentioned by Wimmers 1985, likely belonging to stage VI; new observations were done in the present work, but Te remains very rare).

- Se is rare, and apparently restricted to the latest stages (as a minor substituted element only), as is also Sb.

- Mo is practically absent (only a few occurrences in our data base, all significantly W-bearing, pointing again to severe reducing conditions).

Except apatite, the REE are poorly concentrated, and, seemingly, only at a late stage, being sporadically encountered as monazite or xenotime (in stage IV), as are also U and Th, restricted to monazite.

Finally, it is noteworthy that a temporal disjunction is observed between wolframite and cassiterite deposition at Panasqueira: the main wolframite stage is not associated with cassiterite, and in further stages (III and IV), not only wolframite occurs earlier than cassiterite, but it is at these latter stages a minor phase. Thus, different sources and/or deposition mechanisms must be sought for W and Sn.

From these considerations, it results that a complete understanding of the formation of the Panasqueira deposit must comprise deciphering the sources not only of W, Sn and Cu, but also of Fe and S (and accessory elements, such as As), and understanding under what conditions the corresponding minerals were deposited, and why the deposition followed the sequential order testified by the paragenetic succession.

4.2 NATURE AND ORIGIN OF THE FLUIDS

A- Fluid origin

Predominance of Pseudo-Metamorphic Fluids

From the early to the late stage, main dominant fluids are aqueous-carbonic fluids with a moderate salinity (5 to 10 %eq. NaCl). They display the same features than pseudo-metamorphic fluids defined in most Au deposits from the same period (Boiron et al., 2003), but also in W deposits from western Europe (Noronha et al., 2000, Harlaux et al., 2018). Such fluids are considered as equilibrated with metamorphic facies, the markers of the pristine origin being lost. They contain volatiles linked to water-graphite equilibrium (CO_2 , CH_4) and nitrogen probably related to the oxidation of ammonium contained by micas or feldspars from metamorphic series. Pulses of predominant volatiles may be linked to the devolatilisation of lydites.

From these characteristics, it appears that Panasqueira fluids share a part of their history with late Hercynian Au deposits (Boiron et al., 2003) and Au mesothermal deposits worldwide (Groves et al., 1998; Dugdale and Hagemann, 2001).

Introduction of Magmatic Fluids in the System

There are little evidences of magmatic fluid inputs from the study of fluid inclusions, although links between main stages of fluid migration and/or magma intrusions are reasonable, considering the persistence of high temperatures during 10 Ma, or at less the succession of hot events related to magma intrusions and/or deep crustal lineament and thermal anomalies.

Only metamorphic fluids? On the basis of tourmaline (Tur₁₋₁) microchemistry, it has been concluded that involvement of fluids equilibrated with a granite was limited to small Nb-bearing inputs. Most fluids would be of metamorphic origin (sourced in the large contact metamorphism aureole) or of deeper-seated migmatitic origin. Based on microthermometric data it seems that this conclusion could be extended to the whole hydrothermal system.

The magmatic fluid inputs: A recent crucial observation was made in siderite (Temperville, 2019). It is the only evidence of brines at Panasqueira, that was found together with aqueous carbonic fluid inclusions in siderite (late mineral in the sequence), which contains however Lw-c fluids very similar to those characterizing all the preceding stages. In these brines, clear evidence of the presence of Li (very low eutectic temperatures of the fluid inclusions at around -70°C) could indicate the presence of a magmatic fluid pulse. Such a Li enrichment is typically expected for fluids evolved from RMG (see Harlaux et al. 2018). Interestingly, although there is no evidence for rare metal deposition at the time of siderite crystallization (stage V), a very late stage of cassiterite and stannite crystallization is documented in the deposit. Thus, owing to the fact that only RMG are expected to be involved in the Panasqueira general system starting from the inception of mineralizing fluids, this may imply that magmatic fluids are not systematically involved in the system.

However, other evidences of magmatic fluid introduction in the system are: i) the F-bearing phases (topaz), ii) the Li, F-bearing micas, iii) the Li-Nb-Ta association signature in tourmalines. In the cases of (F-Al-Sn) (stage III-A) and (Al-Li-Fe-Sn) (stage IV), magmatic fluid inputs could be envisaged despite the fact that (i) no late RMG is observed in our observations, unless Argemela but the only available age is a K/Ar date of 303±6 Ma (Portugal Ferreira and Noronha 1981, in Chapter One), and ii) the trace elements record is of difficult interpretation because of the numerous sources involved in all cases. Finally, the very high thermal gradients especially for stage IV suggest an intrusion proximity.

B- Fluid Migration and Exhumation

At Panasqueira, new data obtained on stage III-A are crucial for the P-T-depth evolution. The presence of high density liquids either aqueous-carbonic or volatile rich yield to P-T estimatimations of 500°C-240 Mpa, which may correspond to lithostatic pressures corresponding to deep structural levels in between 8 and 10 km depth. Considering that the early tourmalinisation stage, which is pre-Wolframite I is

dated by U-Pb on rutile at 305 Ma, the stages from I to III may be considered as linked to deep P-T conditions, and as deformational stages rather distinct than those prevailing during stage IV.

From stage I-II to stage III there is a limited but distinct increase in temperature, up to 500°C, correlated with a small pressure decrease. This event could be correlated with the intrusion of a RMG melt in the appearance of topaz. Indeed, the inception of stage III has been associated with the intrusion of a variety of RMG. Although identification of the G2-3 granites found in the SCB2 drill hole with this speculative RMG is a distinct possibility, to go further is difficult and will have to wait accurate dating of the Panasqueira granite suite.

The consideration of two main structural levels, ca. 10-12 km at 305 Ma and ca. 3 km at 296 Ma implies an exhumation of 6-7 km, and an exhumation rate of 0.7 mm/ year, coherent with those generally considered at the end of the Variscan orogeny. These findings modify considerably the concept of formation of the deposit which has been considered during more than 40 years as formed close to the surface, as an epithermal deposit (Taylor, 2007). The latter hypothesis was formulated on the basis of the “boiling” of fluids, based on fluid inclusions which are more probably related to stage IV, on the of the latest stage, and not to the main W stage (Qtz I and II).

It is in the course of the stage III-A, during the topaz growth, that the decrepitation/deformation of the earlier FI is demonstrated to have occurred. This event has evidently to do with the temperature increase documented in stage III-A. Yet, it seems clear that a transition from lithostatic to hydrostatic conditions would simultaneously occurred, aiding decrepitation.

C- Quartz vein formation

The main driving process responsible for fracture sealing was the ascending flow of waters, equilibrated with the metamorphic pile, along and into fracture/fault network, developed at the top of the concealed granite. The mechanism to precipitate silica from those hydrothermal aqueous solutions was a drop in fluid pressure, as quartz solubility is highly dependant on pressure in the 400–500 °C range (Walther and Helgeson, 1977; Cox et al., 1991). It is possible that those early fluids experienced a moderate increase in chlorinity linked to the hydration of minerals such as biotite, alteration of feldspars in phengite during the fluid–rock interaction around their migration through faults.

4.3 METAL SOURCES (W and other RM)

As shown by our findings on tourmaline, W seems disconnected from the other rare metals, in particular from Sn. Excluding the Stempok et al., 2003 concept of a mantle source, there are three possibilities:

(i) W comes from a granite melt (magmatic-hydrothermal system); like the Mole granite (Audtat et al., 2000). This is the dominant point of view world-wide (Černý et al. 2005 and references therein).

(ii) W comes from sub-solidus leaching of a granite body: like the example in Cornwall (for both W and Sn), but this is controversial; arguments in Marignac and Cathelineau (2009).

(iii) W comes from metamorphic rocks, as envisaged for the scheelite disseminations in Gasc by Gibert and Moine (1992). A specific role could be played by the devolatilization in a magmatic context, as apparently demonstrated by the La Favière peri-anatectic scheelite deposit (Marignac, 2004).

In the first case, the fluids are magmatic in origin, while in the second and third cases, their origin is metamorphic or migmatitic.

A variant, first proposed by Marignac and Cathelineau (2009), and then demonstrated in a specific case by Harlaux (2019), considers a two-stage model, with first extraction of W from a granite melt by a magmatic fluid, followed by its trapping in the surrounding rocks; and second, remobilization of this stock by metamorphic (or pseudo-metamorphic) fluids. This variant is particularly appealing for the schist-hosted peri-batholithic Qtz-Wfm vein deposit class, from which Panasqueira is a preeminent example.

A- Granite source of fluids and metals? A connected question: the role of “greisen” and “greisenization”

Until recently, the only information on the Panasqueira granite came from underground works (observations limited to the “greisen cupola”) and a few exploration drill holes. However, a recent gravity survey allowed Ribeiro (2017) to propose a 3D model of the Panasqueira pluton. It appears that the main granite body is a rather thin laccolith, with a large keel striking NE-SW (Fig.5.1). Unexpectedly, the greisen cupola appears offset from this keel, although seemingly equally striking NE-SW.

The Panasqueira laccolith intrusion is evidently the cause of the thermal aureole which is well-documented in the mineralized area by clear cordierite spots. They are replaced, during the wall rocks tourmalinization, by the vein system formation preceding the development of the main quartz-wolframite veins. Thus, it seems evident that the emplacement of the main granite mass imaged by Ribeiro (2017) precedes the onset of the Panasqueira hydrothermal system, and, consequently, that the magmatic fluids issued from this body could not be directly involved in this system.

There are only a few published petrographical data on the Panasqueira granite, most of them coming from the exploration drill holes. Bussink (1984) gives very succinct descriptions, concentrating on a geochemical approach. Some glimpses are provided by Lourenço (2002). A new drill hole (SCB2) was sampled by both Orleans and Nancy teams, and De Amorin (2017) and Launay (2018) give descriptions and a new set of analyses. Very recently, a new gallery at the L2 level crosscut through the greisen cupola. A first description of samples from this gallery is given by Keita (2019).

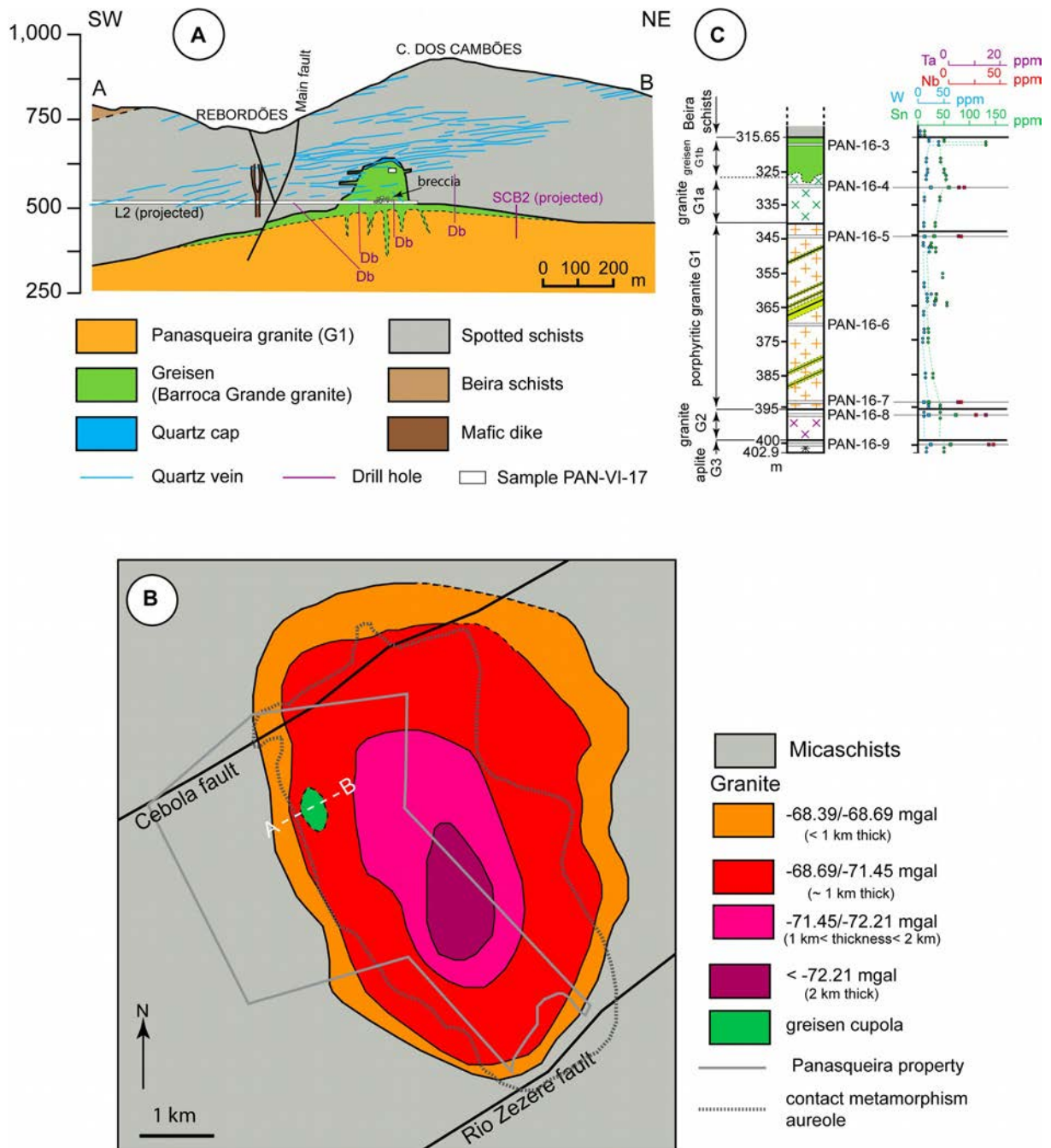


Fig. 5.1: Panasqueira granite architecture. A. Upper part of the granite body, according to Kelly and Rye (1979) and Bussink (1984). Location of the old drill holes as well as the recent SCP2 hole and L2 gallery, are indicated. The vertical greisen roots are proposed by Bussink (1984), but without any observational base (no intersection by the figured drill holes). B. A 3-D model of the granite body according to the gravimetric survey of Ribeiro (2017). C. The SCP2 drill hole profile, adapted and reinterpreted from De Antonin (2017) and Launay (2019). Samples from the present study are located (* analysed sample).

The G1, G2, G3, G4 Granites

Launay et al. (2018), following Bussink (1984), considered that there is only one G1 granite, and its altered derivatives. They consider the greisenization an “auto-hydrothermal process” linking Panasqueira magma to the vein system, in the form of the muscovite selvages, deemed to be coeval with wolframite. This contradicts with Lourenço (2006) observations, and they conclude with a second granite type, belonging to the RMG family, situated in the cupola (the Barroca Grande granite).

In reality, the De Amorin (2017) and Keita (2019) works concur with our personal results to conclude that a serie of granites is present in and under the cupola. We are apparently dealing with a Beauvoir-type differentiation suite (Cuney et al. 1992; Raimbault et al. 1995) (Fig. 5.2). The more primitive (homologous to the Colette granite in the Beauvoir suite) is the G1 two-mica porphyritic granite suite (G1, G1a, G1b) documented in the SCB2 drill hole (Fig.5.3), in which the black mica is a Fe-protolithionite. We do not know if the bulk of the Panasqueira granite (the laccolith imaged by Ribeiro 2017) has the same composition (or less evolved and more akin) in respect with the regional granites.

Two other granite types (G2 and G3), located at the bottom of the SCB2 drill hole, were likely intruded in the G1 granite. It seems that they apparently escaped the first alteration stage in G1 (see below). The G2 and G3 types differ from the G1 suite by being equigranular and containing Nb-Ta-W phases (rutile and columbotantalite).

A fourth facies (G4) is representative of the very top of the SCB2 hole, like all the rocks encountered at the L2 level or higher in the cupola, and may be equated to the Barroca Grande granite of Lourenço (2002). This G4 facies is strongly altered (see below), but may be identified on the basis of the “snowball” morphology of the magmatic quartz, and of the P-enrichment (up to 1% wt P) of the microlithes (otherwise pure albite and Kfs) characteristic of the snowball texture.

At the L2 level, it was possible to observe the boundary between the (greisenized) granite (G4) and the wall rock. It is characterized by:

i) a very thin (a few mm thick) aplitic rim which runs along this contact is spread into the silification, and by

ii) a thin fringe, no more than a few cm thick, made of a black mica with protolithionite to zinnwaldite compositions (Fig. 5.4). It has been regularly found in the schists along the contact. Also, small flakes with the same composition have been observed in the quartz enclaves of the greisen cupola, as incorporated and dilacerated seixo bravo veins. It seems reasonable to assign the development of these Li-rich micas to the effects of fluid-rock interaction between the magmatic-hydrothermal fluids issued from the G4 cupola and the surrounding schists. It is interesting to note that, excepted for Rb and Cs, there is no marked effect of this interaction in the schist. There is in particular no significant enrichment in neither W, nor Sn, nor Nb-Ta (Fig. 5.1c).

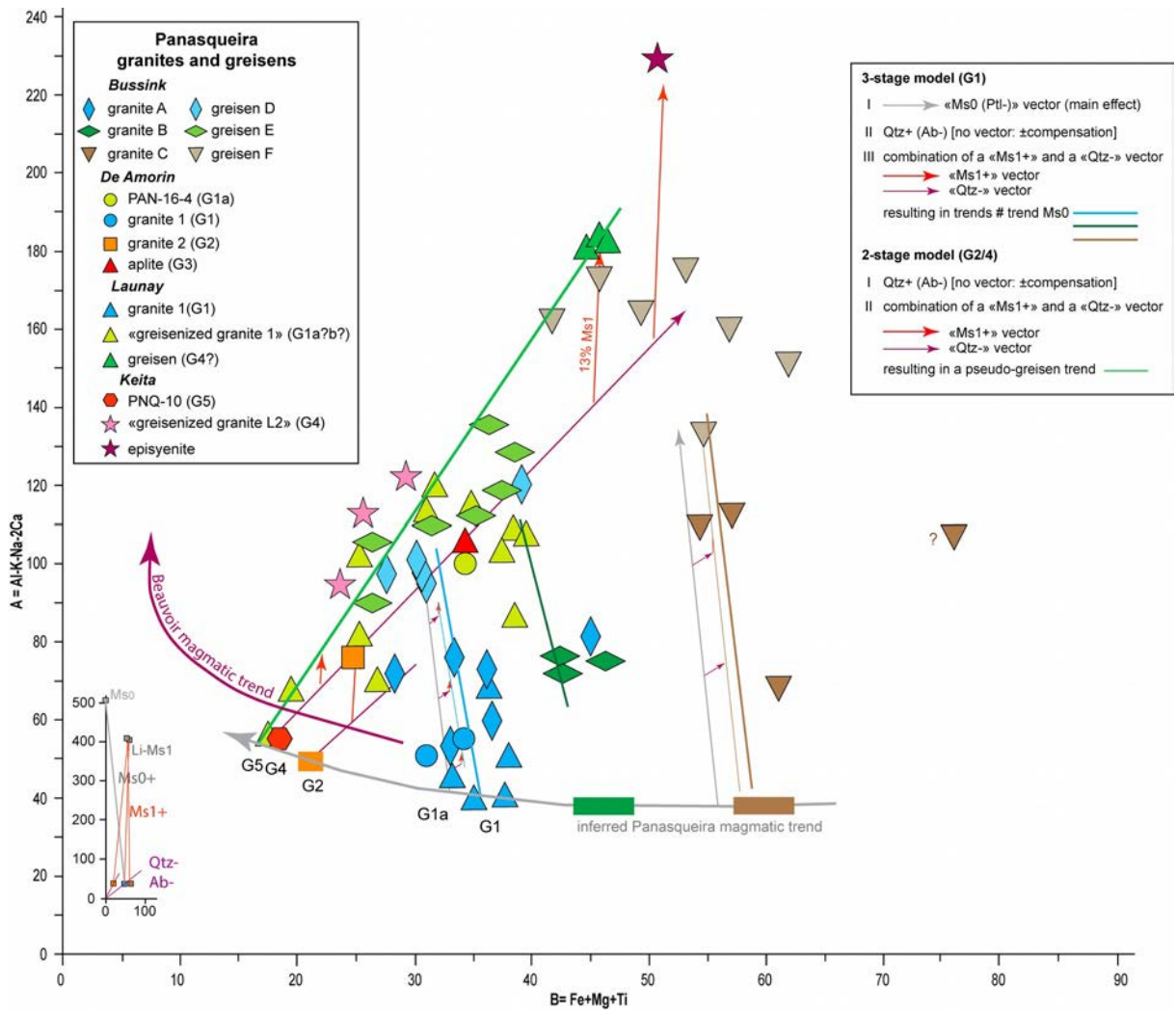


Fig. 5.2: Interpretation of the Panasqueira granites and greisens compositions in the AB diagram (La Roche et al., 1980). Two different alteration histories explain the contrasted trends exhibited by the G1 suite, on one hand, and the G2-G4 suite, on the other hand. The difference is based on the fact that protolithionite vanishing (Ptl- vector) was the main process in the G1 suite granites, whereas the succession of quartzification and episyenitization (muscovization) prevailed in the G2-G4 suite. Disentangling the alteration effects allows to infer the magmatic evolution displayed by the Panasqueira granites. It appears that it is very similar to the Beauvoir trend of RMG, although not leading to such evolved melts as in the Beauvoir case. Insert: definition of the various alteration vectors.

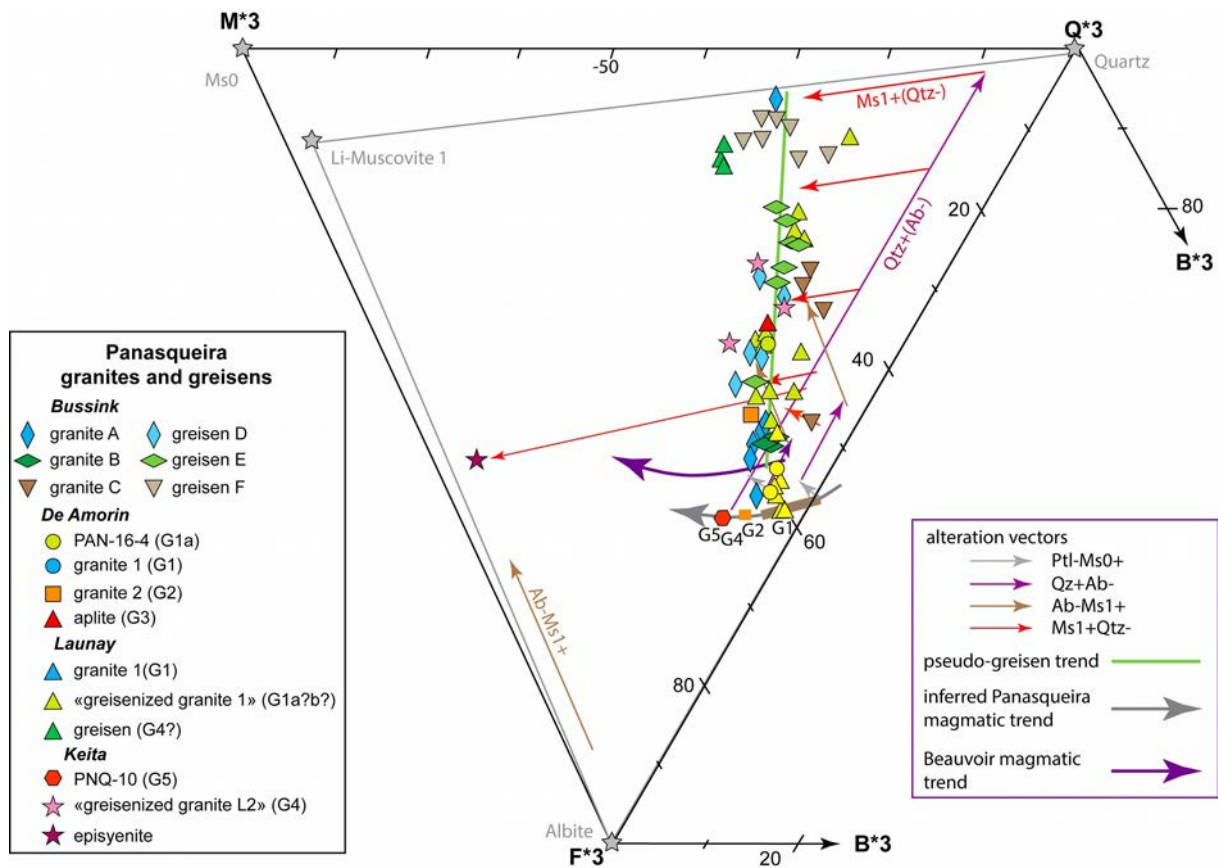


Fig. 5.3: Interpretation of the Panasqueira granites and greisens compositions in the $Q^*_3B^*_3F^*_3$ diagram. As in Figure 5.2 two different alteration histories are displayed by the data. But to the contrary of Fig. 5.2 the alteration trends of both the G1 and the G2-G4 suites are here similar and follow the same "pseudo-greisen" trend. This is because, in the G1 suite, the effects of the albite transformation into Li-Ms1 become sensitive, whereas the effects of successive quartzification and episyenitization (muscovitization) remain prevalent in the G2-G4 suite. In the same way as in Figure 5.2, disentangling the alteration effects allow to reconstruct the Panasqueira magmatic trend, which here also, appears similar to the classical Beauvoir trend.

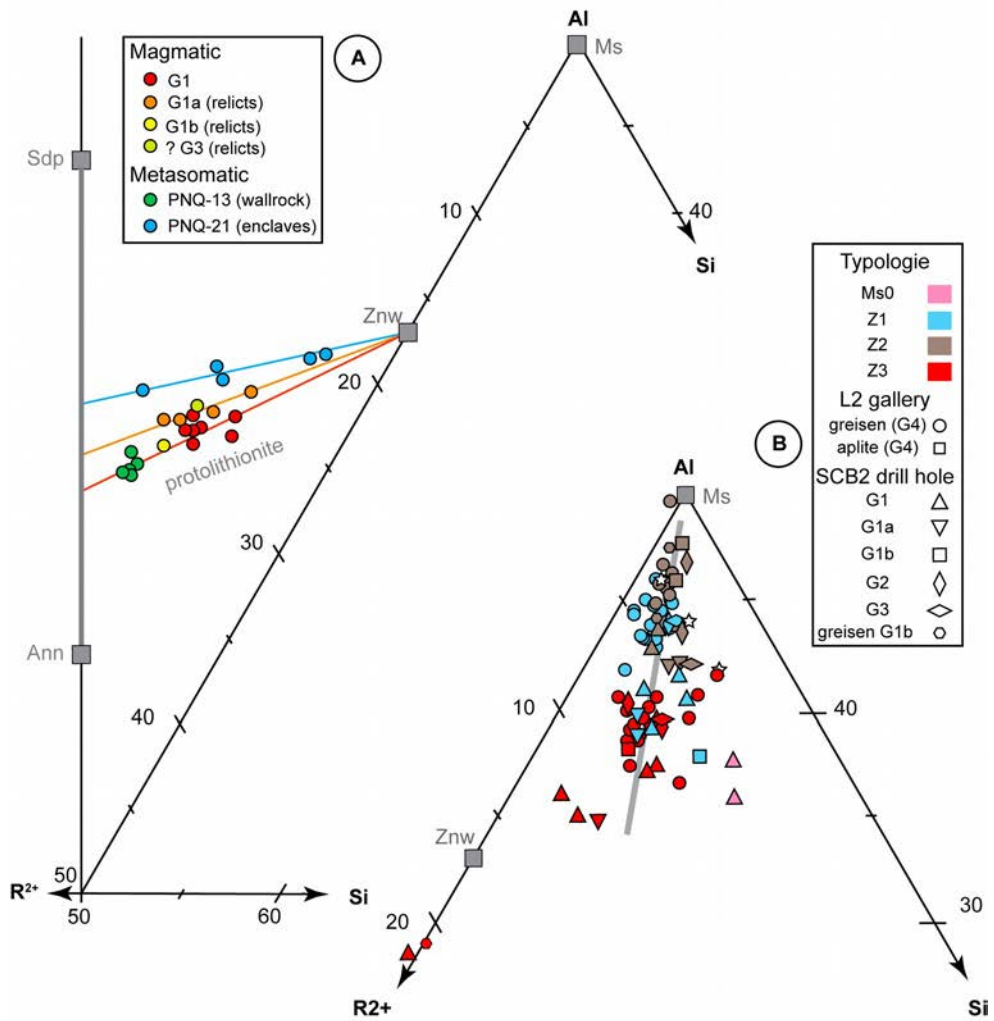


Fig. 5.4: Mica from Panasqueira granites in the $Al-R^{2+}-Si$ diagram (Robert and Monier, 1987). A. Trioctahedral micas: protholitionite from the granite suite and metasomatic zinwaldite resulting from magmatic fluid inprint on to the granite wall-rock. B. Li-Fe muscovite from the greisen Ms0: early muscovitization of protholitionite in G1, Z1, 2, 3 zoning of the greisen muscovite. It is clearly seen that the Z1, 2, 3 compositions are similar in all the granite.

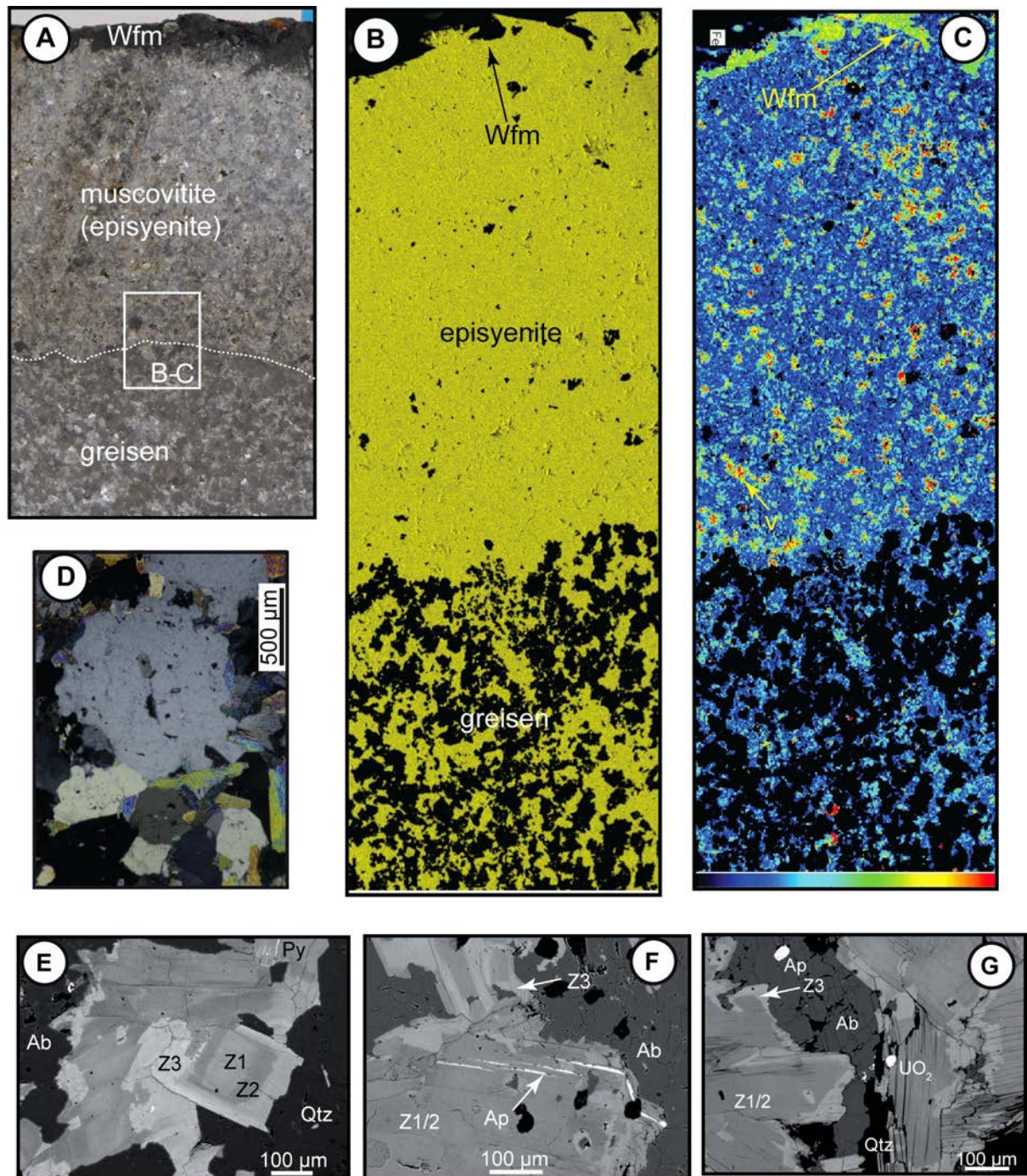


Fig. 5.5: Evidence for a late muscovitisation of the quartzified G4 facies. **A.** Transition from of a muscovite-only rock (muscovite) to a greisen (sample PAN-VI-17, L0 level). Note the wolframite fringe in the muscovite. **B** and **C.** False-colored μ -XRF maps of the greisen/muscovite contact in **A.** **B.** $K K\alpha$ map; note the digitate shapes of the muscovite patches in the greisen and their apparent aggregation at the level of the quite sharp transition from the greisen to the muscovite. **C.** $Fe K\alpha$ map; whatever the location, "greisen" or muscovite, most of the muscovite displays the same iron content, i.e., there is no appearance of a compositional zoning, although the Fe-rich fringes are more developed in the muscovite body." **D.** Relic quartz magmatic quartz in the L0 greisen (sample PAN-VI-17). Note the embryonic snowball texture. **E** to **G.** BSE imaging of muscovite zoning in the greisenized G4 facies at the L2 level. The zoning pattern consists in three zones with a grey core (Z1), a darker first rim (Z2) and a bright second rim (Z3). **E.** Compositional zoning (sample PNQ-19a). A clear succession of the three zones (Z1 to Z3) is visible, although patchy zoning features are also evident. **F.** Patchy zoning in the muscovite from the greisenized G4 granite near the wall-rock boundary (sample PNQ-13a). The Z3 zone is evidently encroaching the earlier muscovite. Note the clear overprinting by apatite (Ap). **G.** Conspicuous Z3 Fe-enriched rim at the albite edge (sample PNQ-17a).

Greisenization versus Episyenitization

In the course of the study of the tourmalinized wall rocks, it was not uncommon to observe in the quartz matrix of the rocks the presence of small euhedral flakes of crystals with a protolithionite-zinnwaldite composition similar to that in the contact rocks, and associated to small euhedral apatite. It seems logical to attribute the development of these crystals to the same magmatic-hydrothermal fluid/rock interaction process as at the L2 level. It is noteworthy that never was observed the superimposition of this protolithionite-zinnwaldite neither on the tourmaline crystals, nor on the thin crack-seal quartz veinlets associated to the tourmalinization process (see Chapter One). It must therefore be concluded that the emplacement of the G4 cupola equally preceded the inception of the Panasqueira hydrothermal system, and that consequently, the G4 magmatic-hydrothermal fluids could not be involved in this system, not more than for the G1 suite.

Observations in the new L2 level gallery show without ambiguity that the “greisen” is the result of a two-stage process:

- (i) silicification (“quartz greisen”), and
- (ii) muscovitization (episyenitization).

During the first stage, most of the pristine minerals were dissolved: the only remaining crystals are delicately lace-shaped albite and the magmatic quartz (micro)-phenocrysts (Qm). In the upper L0 level, only Qm (with the characteristic microliths) is preserved. This is very likely the origin of the “quartz cap” described by Kelly and Rye (1979) (and no more accessible since this date).

A downwards decreasing intensity of the quartz greisenization event is evident in the SCB2 hole. During the second stage, muscovite (more or less Fe-Li enriched) invaded the quartz greisen, replacing quartz as connected patches of flexuous crystals, until a total replacement as a characteristic porous muscovitite. The process is clearly a variety of episyenitization, as quartz is no more stable, and marked by a potassic alteration, owing to the association between potassium input with muscovite crystallization. Muscovite crystals are systematically zoned with the succession (often as patchy superimposition due to replacement processes) of three zones characterized by their grey hues in BSE images (clear Z1, darker Z2 and ultra-clear Z3) due to variable Fe contents (Fig. 5.5 E, F and G). Albite remnants of the first stage are preserved, and seem to have experienced recrystallization to some extent (Albite II of Lourenço, 2002). Cassiterite is occasionally observed in association with the muscovitization event. The “greisen” at Panasqueira is therefore a pseudo-greisen, resulting from the superimposition of two processes acting in opposite directions. The name “greisen” being currently used at Panasqueira, it will continue to be used in the following sections.

Contrary to the quartz greisenization, the episyenitization affects the totality of the granite body in its upper part, being still well seen down to the G3 facies. The same process is demonstrated not only by the

ubiquitous presence of the same zoning pattern (Z1-2-3) as in the upper greisen, but also by the consistency of the zone compositions throughout from the top of the greisen cupola down to the G3 facies (Fig.5.4).

Protolithionite (-) and the Silicification Events

The quartz greisen contains typical decrepitated FI, with all identical characters of those in the QI quartz of the Panasqueira vein system. Thus, the greisenization is earlier than the FI decrepitation event, which is at the moment assigned to the onset of stage III-B in the vein system. By contrast, recrystallized quartz surrounding the muscovite patches in the greisen, does not show decrepitated FI, but contains typical FI of the late stages. For this reason, the episyenitization stage may be equated with the beginning of stage IV (Ms1 of the muscovite selvages). This interpretation is consistent with the great similarity in composition between the greisen and the selvage muscovites.

In the G1 granite suite, which is affected by the same alterations (silicification, muscovitization) as the more evolved granites (see above), another set of subsolidus modifications affect the protolithionite, which is transformed into an assemblage of muscovite, siderite, chlorite and a moderately Nb-Ta-enriched rutile. The latter would have trapped, together with the titanium released from the altered protolithionite, at least a part of the rare metals which were likely also released from it. Yet, these observations are suggestive of the possibility of sourcing rare metals, and in particular tungsten, in this early fluid-rock interaction affecting the G1 body.

It is not possible to assess the time relationships between this protolithionite (-) event and the silicification process, because the latter is poorly developed in the G1 facies. On the other hand, there is consistent evidence that the protolithionite (-) event was overprinted by the muscovitization. This negates the conclusion of Launay et al. (2019) that the muscovite development (true greisenization process to them) was due to an auto-metasomatic magmatic-hydrothermal process and that it was linked to the main wolframite deposition event, through the coeval development of the muscovite selvages in the veins.

The silicification event was apparently responsible for the erasing of all the rare-metal minerals which could have been present in the G4 facies: by comparison with G2-G3, it seems more probable that Nb-Ta-W-rich minerals (either rutile, or niobo-tantalate or both) were indeed present in the G4 facies. Therefore, the quartz greisenization process could be responsible for the significant content in rare metals release. In fact, it has been observed in the vein-system that the earliest wolframite was linked with a silicification of the already tourmalinized wall rocks (see Chapter One).

The quartz greisenization event may be a clue to the interpretation of the enigmatic "quartz cap" described at the top of the greisen cupola by Kelly and Rye (1979), the only workers to have seen it. In reality, a massive white quartz clouded with muscovite and affected by subhorizontal sheeting with "muscovite metasomatism", could well be the result of quartzification. Indeed, Kelly and Rye (1979, p.1741), mention that there was a continuity between the quartz cap and some quartz veins of the main system. But it

is probable that these "veins" are indeed quartzified sills issued from the cupola, emphasizing then its initial magmatic nature. Another observation of Kelly and Rye (1979) is that "At some spots along the accessible edges of the cap, large euhedral quartz crystals, some more than 20 cm long, can be seen along the hanging-wall contact. These appear to have perched on the schist and grown inward toward the cap interior. Such crystals are most easily seen where later quartz filling in around them, is rich in fine-grained muscovite" (p.1741) and that "At one location, these big crystals continue out a short distance as a lining of the hanging wall of a thick vein that joins the cap" (p. 1741). Contrary to the opinion of Kelly and Rye (1979), who thought the cap to be of hydrothermal origin, and these giant quartz representative of the earlier crystals of this quartz infilling, it seems clear that these observations reinforce the present interpretation of the quartz cap, pointing to these giant quartz being the only preserved remnants of a now destroyed pegmatite, possibly a stockscheider. In this connection, Kelly and Rye (1979) underlined that the "quartz cap", a thin body (14 m thick) with a very limited development (53x73 m in plan), had "a flat floor and an arching roof", and that the contact with the underlying greisen was sharp. All these data point to an interpretation of the quartz cap as the witness of a now quartzified border pegmatite at the top of the cupola.

The G4 facies contributed to some extent to the formation of the main wolframite stock, as well. Indeed, several W_{fm1-1} crystals display a spectacular compositional oscillatory zoning (OZ), characterized by strong variations of Nb content. This may be interpreted in the same way as for rutile, i.e., in terms of "periodic" addition of a Nb-rich fluid from the main W-depositing fluid. This could be explained if the source of this Nb-fluid is the result of the RMG cupola leaching, distinguished from that of W.

A provisional conclusion of all this discussion is that if a granite source for tungsten must be sought, only the G1 granite (not magma) may have had the demanded potential, through the earlier alteration process, i.e., the protolithionite (-) event. The age of this interaction is unknown, being only constrained to be earlier than the stage IV. But, a contribution of G1 to the very beginning of Panasqueira system should be recorded by the REE patterns in Tur1 (see Chapter One), which exclude any granite. Thus, the role of this G1 granite may be envisaged under two (mutually not compatible) possibilities. As a first possibility, the protolithionite (-) alteration could be older than the beginning of tourmalinization in the same zone of the future vein system. In this scenario, it could have been responsible for the very large anomaly in rare metals demonstrated by Polya (1988, 1989), and provided the initial stock of W for the deposit, according to the models of Marignac and Cathelineau (2009) and Harlaux (2016), through a further leaching. As a second possibility, the protolithionite (-) event was more or less coeval with the silicification. Then, it would have directly provided the W amount for the main wolframite stage. In this scenario, the external fluids progressively invade the granite body, causing its alteration. Indeed, being CO_2 -rich fluids, they would have had the potential for the acid leaching (and fixation of iron as siderite) of the protolithionite.

In any case, it is difficult to consider a magmatic source for the fluids responsible for the acid alterations. In fact, the problem would be to explain how a magmatic fluid equilibrated with granitic

feldspars may become able to dissolve them. To the contrary, external fluids with metamorphic origin, or equilibrated with graphite in metamorphic rocks, would be rich in CO₂ (Fischer-Torpf reaction) and potentially aggressive. In fact, it has been demonstrated that greisenization in the Skiddaw granite (Bebout et al., 1999) was due to ingress from fluids coming from the thermal aureole. In the same way, Zouhair and Marignac (1990) provided evidence that CO₂-bearing fluids were involved in the greisenization of the Ment massif (Morocco). In both cases, however, a true Qtz-Ms greisen was the result.

By contrast, it may be speculated that the fluids responsible for the episyenitization have a magmatic origin. For instance, in the case of the Variscan episyenites in Limousin (French Massif Central), the causative fluids were simply water equilibrated with a granite at HT (under a vapour or supercritical state) and enduring condensation by uprising along a decreasing thermal gradient. The key point here is not the quartz dissolution, but is the muscovitization because of the K (potassic alteration) and Al inputs by a fluid which is also silica under-saturated. At the moment, only F-rich fluids issued from evolved RMG seem to have the potential to meet these prerequisites. Similar considerations may also be applied to the topazification in quartz veins which characterize the stage III-A in the evolution of the hydrothermal system.

HYPOTHESIS UPON CONCEALED RMG BODIES

Owing to the pervasive occurrence of both topaz and Li-muscovite in the Panasqueira hydrothermal system, the presence at depth of until now concealed RMG bodies must be assumed. At least two such intrusions (or intrusion suites) are required, one responsible for the topaz-cassiterite assemblage (stage III-A), and the other responsible for the muscovite-(cassiterite) assemblage (stage IV).

There are indeed indications that such intrusions may be present in the Panasqueira system. *In primis*, the G2-3 granites, found at depth in the SCB2 drill hole, seem to have escaped the protolithionite (-zinnwaldite) event. That is because the G2-3 granite shows no products of such alteration. In particular, there is total absence of the characteristic Nb-rutile produced in the G1 suite by the protolithionite destabilization. Secondly, a highly evolved granite sample (GS) was found by us in the wastes of the old works at Cabeço da Piu. The composition of GS matches properly with that of the Panasqueira-Barroca Grande granite suite (Fig. 5.2-3). Thus, this GS is well representative of a granite body at depth which would have been encountered by the old works. It characterized by the absence of alterations, contrasting with those affecting aplite dykes in the area (Launay et al., 2019) and possibly testifying a late emplacement. Finally, there is the Argemela RMG body at only ca. 10 km from Panasqueira. The Argemela age is however not precisely known. A K/Ar age of 306±4 has however been obtained by Portugal Ferreira and Noronha (1981), in chapter One, and would it be confirmed, would rather be consistent with the early date envisaged for the G4 facies.

Therefore, it is not unreasonable to envisage that in the course of the evolution of the Panasqueira hydrothermal system, several pulses of RMG intrusions may have contributed magmatic fluids to the total

fluid mix circulating in the vein system. Indeed, nothing prevents us from considering that the imaged Panasqueira body is in reality composite, and that another (or several others) suites of the G1 to G4 style are present at depth. This remains nevertheless speculative.

B- Metamorphic Source of Metals

At the time of the deposit formation, a renewal of deep mantle-crust interaction leading to dehydration melting (biotite breakdown) is highly probable on the basis of what is known at the scale of the CIZ. This is a possible long-lived source for W (and B-Li-F-Fe-Mn), provided that:

(i) The thermal front is displacing towards shallower and shallower levels (protracted production of fluids). This is possible through continuous heat input from the mantle

(ii) The ascent fluid is sufficiently fast to preclude significant fluid/rock interaction inducing "en route" sequestration of the RM. This is included in the model presented for tourmalinization.

A strong consequence of these considerations is that the persistency of a deep-seated source of hydrothermal flow is required.

Magmatic-metamorphic variant:

Finding of RM-rich rutile in the wallrocks could have been an argument for this model. Unfortunately: (i) it is demonstrated that these Rt were coeval with the pervasive tourmalinization process, and (ii) there is no evidence for their destruction (and consequently, no evidence for RM release) at the time of incipient Wfm deposition (to the exclusion of sporadic finding of a late, corrosive, external RM-depleted rims affecting the larger Rt crystals).

Yet, Polya (1998) argues for a large (several km in diameter) halo of W-enrichment (several 10 ppm) around the Panasqueira deposit. This halo contains a much larger W stock than the deposit itself (from 3 to 6 times the Panasqueira endowment). The question remains open: do this halo precede or, to the contrary, was a consequence of the W-mineralizing activity? See above the corresponding discussion.

4.4 THE TIME CHART AT PANASQUEIRA

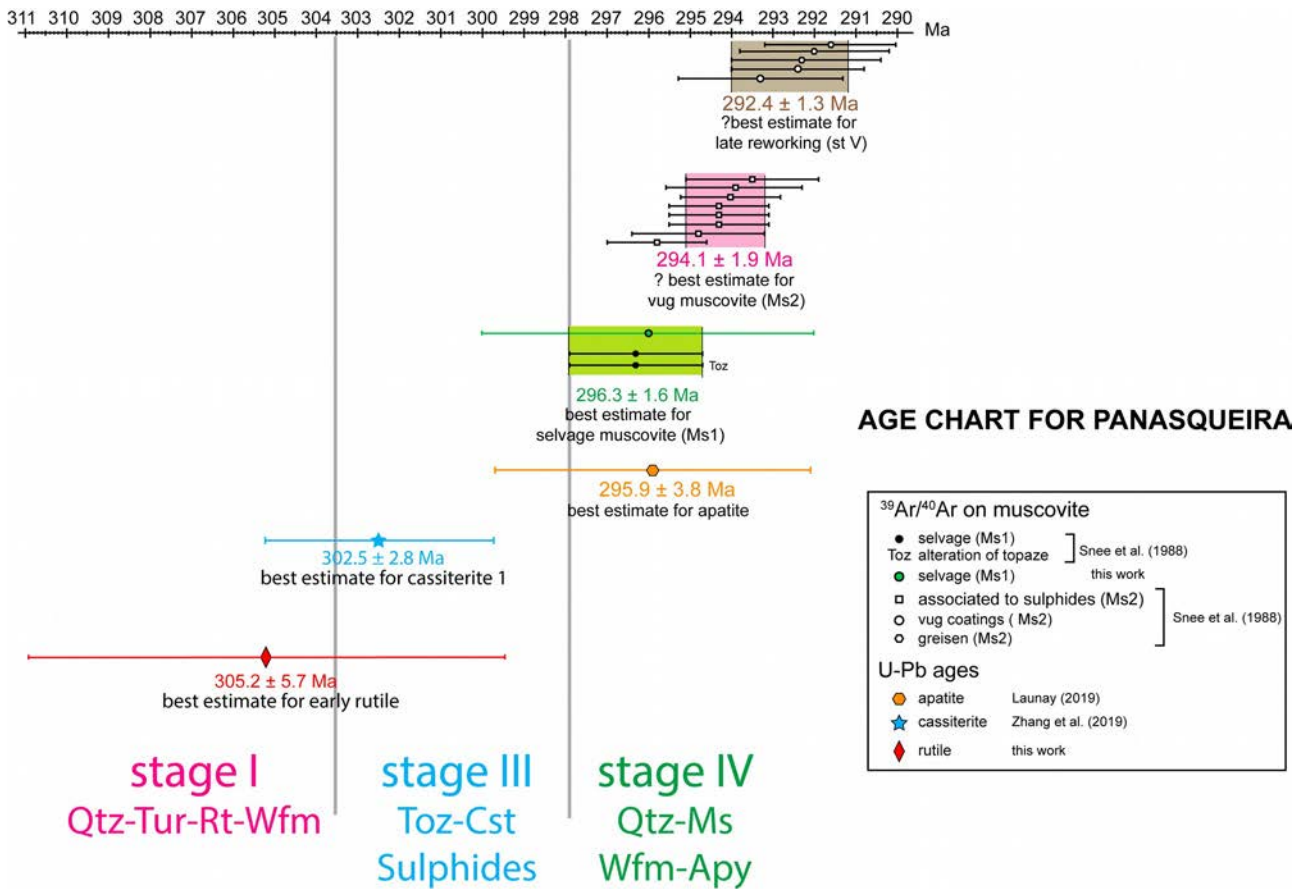


Fig. 5.6: Panasqueira time chart.

Until recently, the age data base at Panasqueira was rather limited, consisting of (i) a K-Ar age on the Panasqueira granite of 290 ± 10 Ma Clarke (1070) and (ii) a series of a $^{39}\text{Ar}/^{40}\text{Ar}$ ages on muscovite of different settings (Snee et al. 1988), spreading from c.296 to c. 292 Ma. Both the ages record the muscovite selvages (Ms1), well constrained at 296.3 ± 1.6 Ma and being until now the accepted age for the main wolframite event (at ca. 292 Ma).

Four new ages have been produced in recent times (Fig. 5.6):

(i) A 305.2 ± 5.7 Ma age obtained (U/Pb) on the early rutile associated with early tourmalinization (see Chapter One). This is consequently the age of the inception of tungsten deposition and precisely the age of the main wolframite deposition stages (I, II). Unfortunately, the U contents in Panasqueira wolframite are too low to authorize direct U/Pb dating.

(ii) A new $^{39}\text{Ar}/^{40}\text{Ar}$ age on a muscovite selvage (Ms_{1-IV}), dated at 296 ± 4 Ma*, i.e., indiscernible from the Snee et al. (1988) age in the limits of errors. This confirms the new paragenetic chart, showing that the muscovite selvages were formed long after the wolframite deposition.

(iii) A 303 ± 3.3 Ma and 301 ± 4.2 Ma age obtained (U/Pb) on cassiterite by Zhang et al. (2019). Although not specified, this cassiterite most probably corresponds to the main cassiterite (until now deemed to have been coeval with the main wolframite). These new ages therefore provide a constraint for the age of stage III-A, which may consequently be estimated at 302.5 ± 2.8 Ma by matching the two error intervals, and appears significantly younger than the inception of stage I.

(iv) A 296.3 ± 4.2 Ma age obtained (U/Pb) by apatite from the G1 granite, and a 294.5 ± 5.3 Ma age by apatite from the veins (associated to muscovite selvage) by Launay (2019). The vein apatite being a member of the stage IV assemblage, the latter age is consistent with the dating at 296.3 Ma of the stage IV muscovite and confirms that stage IV occurred quite after the W mineralization stage. On the other hand, the former age would point to stage IV timing for the granite emplacement, which is evidently contradicted by the facts at hand. There is no specification by Launay (2019) of the kind of apatite crystals used for G1 dating, except that they comprise “magmatic apatite” from the 2-mica porphyritic granite (=G1), and “altered magmatic apatite” of “the” greisen (presumably, the G1a and/or G1b facies from the present study, see Fig. 5.1, profile SCB2). Indeed, even the apatite in G1 display evidence of recrystallization. Large apatite crystals in G1 are zoned, with a patchy core, more or less loaded with micro-inclusions of monazite and more or less sodic members of the hagedorfite group, and a rim exhibiting oscillatory zoning and being devoid of any inclusions. Overgrowths of small assemblages of alumina-phosphate-sulphates (APS) of Sr and LREE (solid solutions between goyazite and florencite) are commonly associated (Fig. 5.7). All this points to a strong subsolidus reworking of the pristine magmatic apatite, and the U/Pb age obtained by Launay (2019) most probably records this alteration event, which therefore appears to pertain to stage IV. Evidently, the old K/Ar age obtained on G1 must also be interpreted as recording the alteration. A new age estimate for the stage IV may now be settled at 295.9 ± 3.8 Ma by matching the two error intervals, being indiscernible from the Ms1 age. Therefore, the stage IV may be considered as having been of short duration, owing to the fact that Ms1 heralded the stage, whereas apatite marked its closure.

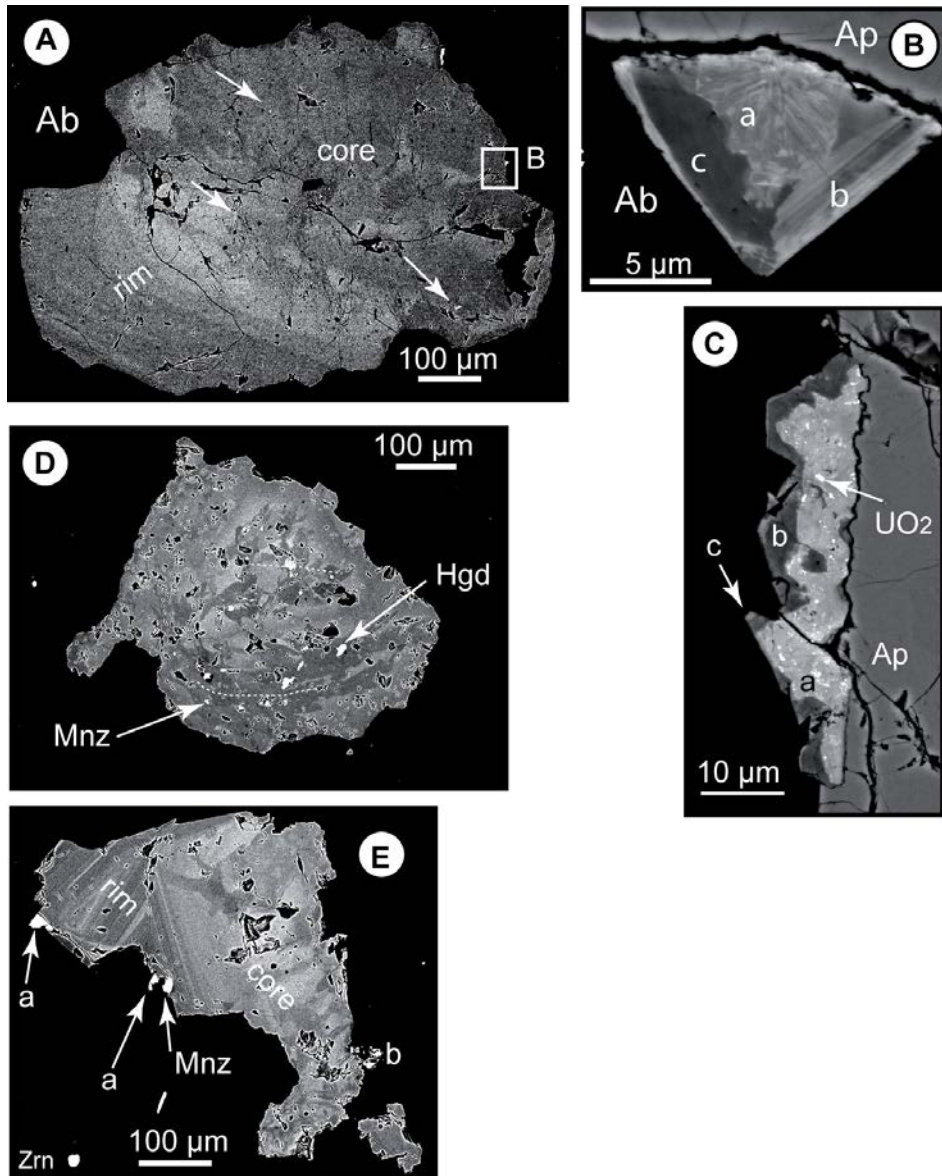


Fig. 5.7: Evidence for subsolidus evolution of magmatic apatite in the Panasqueira granites of the SCP2 drill-hole (BSE images). See Fig.5.2 for sample location. A and B. A large zoned apatite embedded in an albite aureole within the perthitic Kfs (sample PAN-16-5b, G1 facies)). A. Overview of the crystal, showing a core with inclusions of uraninite, monazite and Al-Fe-Mn phosphate (arrows), which is corroded/surrounded by a rim with oscillatory zoning (OZ). B. Overgrowth of an alumino-phosphate-sulphate (APS) assemblage; a: fibrous solid solution goyazite-florencite, b: metal-poor sector of a sector zoned crystal, formed by goyazite, c: metal-rich sector, formed by a solid solution goyazite-florencite (OZ is due to variations in Sr and LREE contents). C. Another occurrence of APS overgrowth on the apatite; a and c: solid solution goyazite-florencite, b: goyazite; note the numerous uraninite micro-inclusions in a (sample PAN-16-4a, G1a facies). D. A large zoned crystal (sample PAN-16-3b, G1b facies); a patchy core is dotted by micro-inclusions of monazite (Mnz) and hagendorfite (Hgd), with Hgd concentrated in a central domain (dashed line separation). E. A large zoned crystal, included in an albite phenocryst invaded by quartz and muscovite (sample PAN-16-3b, G1b facies); a patchy core is surrounded by a zoned rim (OZ). There are no inclusions in the core, but overgrowth of monazite (Mnz) and APS occur on the rim; a: solid solution goyazite-florencite; b: APS succession and uraninite inclusions as in C.

4.5 MECHANISMS OF WOLFRAMITE PRECIPITATION

A- The Transport of W in Solution, State of the Art

Relative to many metals concentrated through hydrothermal processes, tungsten presents characteristics that make it different. Its actual oxidation state is +6, and it forms strong metal-ligands especially with O_2 and OH^- (Wood, 1992 and references therein) because of its “hard” nature in the Pearson (1963) sense. Even if it has been commonly asserted that tungsten is in solution in the form of chloride complexes (Ivanova, 1966; Manning, 1984; Manning and Henderson, 1984; Schooke et al., 1984; Palmer et al., 1987), robust studies on scheelite solubility demonstrate not only the contrary, but also that W concentration is independent of HCl concentration (Eugster and Wilson, 1985; Wood and Vlassopoulos, 1989; and Wood, 1990). Consequently, a great importance is attributed to a class of complexes, called *Kegging structures*, that could play a significant role in tungsten mobility. The metatungstate $(H_2W_{12}O_{40})^{6-}$ is one of such structures, being characterized by four groups of edge-sharing WO_6 octahedra, disposed in the form of a cage around two hydrogen atoms (Keggin 1934). Souchay (1942), Kepert (1973) and Rollinson (1973) proved that these structures, the heteropolytungstates, can accommodate other elements, such as P, As, Si and B, as the central atom.

Indeed, Manning and Henderson (1984) consider that at high temperature tungsten may be transported principally as isopolytungstates and heteropolytungstates. But there is at present very little evidence concerning the thermal stability of the isopolytungstates and heteropolytungstates.

Until recently, there were only two models of hydrothermal transport and deposition of tungsten, both relying on a speciation of tungsten dominated by tungstic acid ($H_2WO_4^0$), and the products of its dissociations HWO_4^- and WO_4^{2-} (Heinrich, 1990; Gibert et al., 1992). These models were based on the experimental data of Eugster and Wilson (1985), Wood and Vlassopoulos (1989) and in particular, Wood (1992). Very recently, Wang et al. (2019) have studied the solubility of tungsten trioxide solid and the speciation of tungsten in NaCl-bearing solutions. Experiments were conducted at 250, 300, and 350 °C under vapour-saturated water pressure. NaCl concentration had no effect on the solubility of tungsten trioxide, which was controlled only by temperature and pH. They observed two tungsten species, $H_2WO_4^0$ at low pH, and HWO_4^- at higher pH. According to their calculations, $H_2WO_4^0$ being only important at low pH values (<2.8), it is HWO_4^- the dominant tungsten species under most common conditions in nature.

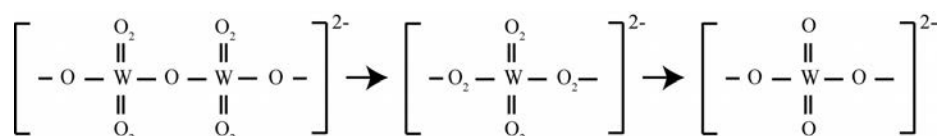
On the other hand, many studies conducted at ambient T-P have consistently shown the coexistence of several polyanions containing 6, 7, 10, and even 12 W-atoms, depending on the pH (Duncan and Kepert, 1961; Aveston, 1964; Arnek and Sasaki, 1974; Haufe, 1982; Simon and Gulari, 1984; Cruywagen and van der Merwe, 1987). Most importantly, two pioneering studies reporting in-situ measurements of W speciation

under hydrothermal conditions have also revealed the presence of polyanions. Wesolowski et al. (1984), interpreting the results of potentiometric titrations of tungstate-bearing solution in the 100-300°C range, conclude that the polytungstates $H_{10}(WO_4)_6^{2-}$, $H_7(WO_4)_6^{5-}$, and $H_{18}(WO_4)_{12}^{6-}$ dominate the speciation in the 10^{-2} mol·kgH₂O⁻¹ solution below pH 5. By contrast, at lower W concentration, the monomers (HWO_4^- and WO_4^{2-}) become increasingly stable, but at least one polymer ($H_{10}(WO_4)_6^{2-}$) remains predominant at pH below 3. Bilal et al. (1986) used in-situ Raman spectroscopy to show the existence of two stable polymeric W-species, $W_{10}O_{32}^{4-}$ and $H_3W_{12}O_{40}^{5-}$, that dominates the W speciation at T up to 200°C under both acidic and circumneutral conditions. They do not succeed to detect the presence of HWO_4^- over the 3-9 pH range and conclude that the polymerization degree increases with increasing T and P. It must be underlined that the above-mentioned W polymers, supposed to be present at elevated T, do not correspond to those clearly identified at ambient conditions such as *paratungstate A* ($W_7O_{24}^{6-}$, with a C_{2v} symmetry), *paratungstate B* ($H_2W_{12}O_{42}^{10-}$, with a C_1 symmetry) or *ψ-metatungstate* ($H_2W_{12}O_{40}^{6-}$, with a Keggin structure). Thus, while it seems demonstrated that polymeric W-species may remain in solution at elevated T-P and pH below 5 (or 3), there is no consistent results regarding both the nature of the polymers and their respective stabilities, although there is a general consensus that W is predominantly transported in the ore-forming fluids as W(VI) anions.

B- The New Data on Complexation

Even if chloride does not form stable complexes with W (Wood, 1992 and references within), polymeric W species such as the hexamer $(H_nW_6O_{21})^{n-6}$ or alkali metal complexes such as $NaWO_4$ or KWO_4 , may also exist, but there is currently no thermodynamic data to predict their abundance. Thus, we performed hydrothermal experiments in the $Na_6W_{12}O_{39}H_2O+HCl$ or $NaCl$ and $Na_2WO_4 \cdot 2H_2O+HCl$, $NaCl$, or $NaOH$ system as function of pH and tungstate/chloride content. We use Raman spectroscopy coupled to the fused silica glass capillary technic to define the stability of the undocumented tungsten-polymers at different temperatures (up to 400°C), to get a global answer upon its transport at different hydrothermal conditions. In alkaline solutions, the main species identified is B: $(WO_4)^{2-}$, while in acidic solutions W speciation is more complicated with the formation of polymeric species like C: $(W_7O_{24})^{6-}$ and D: $(W_{10}O_{32})^{4-}$ at low temperature, and it is dominated by E: $(H_2W_{12}O_{40})^{6-}$ (known as decatungstate by Redkin and Bondarenko, 2010) at high temperature. Thus, the evolution of W-speciation is strongly dependent on T and pH. Moreover, our experimental study strongly demonstrates that W forms highly charged polymers up to 400°C like the *paratungstate A* (C species) $(W_7O_{24})^{6-}$, which is definitely stable at all investigated temperatures, and the *decatungstate ψ* (D species) $(W_{10}O_{32})^{4-}$. This latter species is clearly less stable in respect to the *dodeca α-metatungstate* (E species) $(H_2W_{12}O_{40})^{6-}$ which is formed, starting from 200°C, at the expense of the decatungstate. An important conclusion is that all the W-bearing species that are detected at elevated T, also

exist at room T, with no new complex or polymers formation. This strong tendency of tungsten to form complexes, like heteropoly-, aquapoly-, and isopoly- tungsten compounds, is apparently unique. No other element of the periodic table (not even Mo, the W chemical brother) acts in that way. The Mo-W contrast may be explained (as for other transition elements) by the weakening of bonding of the valence electrons from Mo to W, which results in the stability increase of the higher oxidation states of W and in its tendency to form oxygen compounds, while Mo forms compounds with sulfur. The formulas below, from Barabanov (1971), show the strong affinity of W for oxygen in acid conditions and gradual weakening of this affinity with increase pH values.



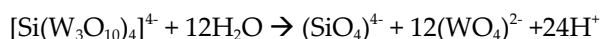
Chemically, this is because the valence electrons of Mo and W are in (n-1)d and-ns - orbitals, but in Mo their energy levels are nearly equal, while in W they are different.

Owing to the common present of CO₂ in the fluids apparently associated to W mineralization, the possible role of carbonates and in particular, of CO₂, in W speciation was also investigated. As a result, neither chloride nor carbonate complexes are involved in W speciation. Tungsten is transported in water, forming complexes and polymers characterized by Kegging structures.

C- The Potential Mechanisms for W-Species Destabilization

More or less based on experimental data and/or empirical observations, many ways of precipitating tungstates have been proposed over the years.

(i) According to Gundlach (1967), the stability of silico-tungstic acid increases with increase in pressure and is preserved in aqueous solutions at T= 250-300°C. Thus, a pressure drop could trigger W deposition. He titrated the silico-tungstic acid with a solution of sodium hydroxide results in the dissociation into SiO₄⁴⁻ and WO₄²⁻ ions:



Gundlach observed that if Fe, Mn, and Ca are present in the solution, the tungstates of these cations are precipitated: FeWO₄ at pH=5.9, MnWO₄ at pH=6.7, and CaWO₄ for pH equal to 7.3. This model allows syn-deposition of quartz and the tungstate.

(ii) Barabanov (1971), based on his study of the ferberite deposit at Barun-Shivey (eastern Transbaykal), is of the opposite point of view that wolframite in the quartz-wolframite veins always crystallized before quartz. He proposed that the tungsten-bearing solutions, poor in iron, manganese, and

calcium, are able to precipitate ferberite through cooling in contact with iron-rich (meta)sedimentary rocks (ferruginous sandstones, shales). In this model, the fluid-rock interaction is the main process in which all compounds for wolframite formation are available. Barabanov (1971) also proposed that wolframite precipitation occurred under weakly acid, nearly neutral conditions. In such a medium, the concentration of hexatungstate ions decreases rapidly because of their transformation into $H(WO_4)^-$ and WO_4^{2-} ions. The increase in activity of the monomer ions WO_4^{2-} into solution, increase in alkalinity, creates the favorable conditions for precipitation of Fe and Mn tungstates (Barabanov, 1971). As shown above, dissociation in B species $(WO_4)^{2-}$, paratungstate A (C species) $(W_7O_{24})^{6-}$, decatungstate ψ (D species) $(W_{10}O_{32})^4$, and in dodeca α -metatungstate (E species) $(H_2W_{12}O_{40})^{6-}$, is in agreement with this conclusion.

(iii) Heinrich (1990) developed a qualitative model for the formation of granite-related cassiterite-wolframite deposits, and concluding that wolframite can be precipitated by the simple (quasi-isobaric) cooling of Fe-W-bearing fluids without wall-rock reactions. Many subsequent workers were of the same opinion (e.g., Campbell and Robinson-Cook, 1987; Campbell and Panter, 1990; Lüders, 1996; O'Reilly et al. (1997); Pei et al., 2015).

(iv) Samson (1990) proposed that dilution (which is, in his work, the progressive fluid mixing of magmatic fluids and meteoric water) is the driving process for wolframite precipitation.

(v) Gibert et Moine (1992) drew attention on the possible role of N_2 , in order to explain the scheelite mineralization in thin layers of calc-silicate gneiss (CSG) belonging to the metamorphic series of the Montagne Noire (French Massif Central). Here, metamorphism of black shales produced abundant nitrogen through the breakdown of NH_4^+ -bearing micas (Kreulen and Schuiling 1982; Duit et al. 1986; Bahdi and Moine 1992), and the metamorphic fluids were aqueous solutions (about 90 mol %) with relatively low salinity (ca. 1 m NaCl) and a N_2 gaseous phase (up to 25 mol % of the gas) (Guillot, 1989). On this basis, Gibert and Moine (1992) modeled the addition of a nonpolar volatile N_2 into ore-forming hydrothermal solutions at pH=4.5-6.5 conditions. Solubility values have been estimated by Gibert and Moine (1992), through empirical calculations of W aqueous species distribution, which originates from the assumption of three main reactions: (1) $H_2WO_4^0 = HWO_4^- + H^+$, (2) $HWO_4^- = WO_4^{2-} + H^+$, and (3) $NaHWO_4^0 = HWO_4^- + Na^+$. The modelling leads to the conclusion that adding N_2 results in the increase of polymeric W species relative to the monomeric W-species, allowing the precipitation of W. Maybe N_2 presence into the system allows the acidification of the aqueous solutions and therefore, a decrease of mineral solubility because of the increase of activity coefficients.

Even if the metal species in the Gibert and Moine (1992) study do not correspond with those which have been identified in the present work as the most stable, their work seems to demonstrate that the addition of N_2 to the mineralizing solutions lead to a strong decrease of scheelite solubility in the solution pH range consistent with common metamorphic assemblages (pH about 5.5-6), and this might explain the frequent association of W (and Sn) deposits with graphitic series generating mixed volatiles fluids.

Further evidence for the role of N_2 in W deposition may be found in literature. At the Olimpiada Au-Sb-W deposit (Prokof'yev et al. 1995), a "skarnoid" deposit, Raman data from FI documented the existence of a " N_2 barrier" coinciding with the scheelite accumulation (Fig. 5.8). In the vein-type Yangjingou scheelite deposit, Wang et al. (2018) observe that a N_2 -rich fluid was closely associated with scheelite precipitation.

(vi) Very recently, Wang et al. (2019) use their experimental data to model the solubility of the main tungstates, scheelite and ferberite. They conclude that to maximize tungsten concentration in geological fluids, high temperature, high salinity, and low concentrations of calcium and iron are required, as well as either very low or high pH. Conversely, temperature and salinity decrease, addition of Fe or Ca, and pH buffering would control tungsten deposition.

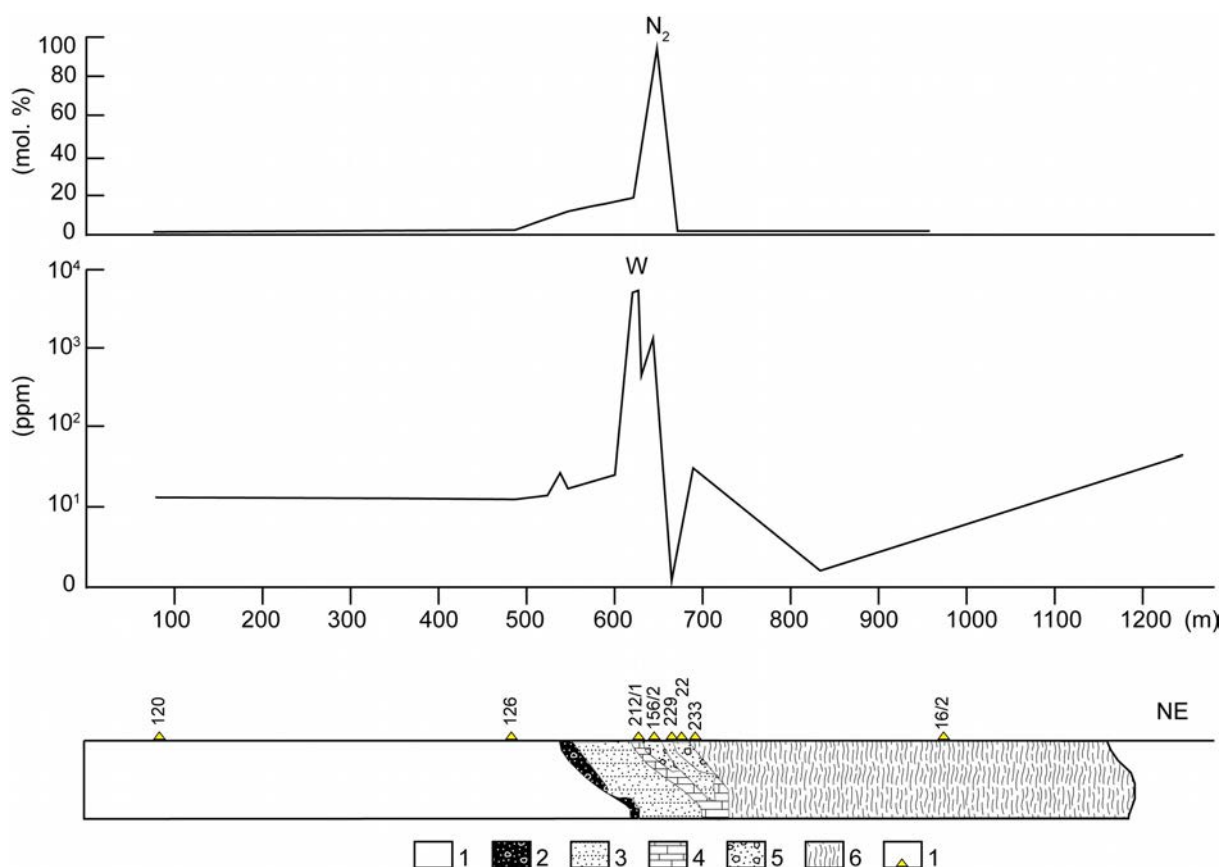


Fig. 5.8: Cross section of the Olimpiada Au-Sb-W deposit (Yenisey Ridge, Russia) (adapted from Prokof'yev et al, 1995), illustrating the N_2 barrier effect on scheelite deposition. The N_2 volatile contents in fluid inclusions from quartz is correlated with the W profile. 1 Quartz-micaschist, 2 skarnoid (CSG), 3 Quartz-carbonate-micaschist, 4 marble (metamorphized limestone), 5 zoisite-bearing CSG, 6 muscovite-quartz-carbonaceous schist, 7 sampling point.

4.6 APPLICATION TO PANASQUEIRA CASE

A- Previous Works

Many ways of precipitating wolframite have been proposed at Panasqueira over the years. Kelly and Rye (1979) proposed a progressive fluid mixing between magmatic fluids and meteoric water, and that dilution process induced wolframite precipitation.

Based on the gap in homogenization temperatures of fluid inclusions from barren and ore-bearing vein quartz (230 to 420 °C), Noronha et al. (1992) proposed that fluid pressure fluctuations below lithostatic pressure could be the main process responsible for tungsten precipitation. Lecumberri-Sanchez et al. (2017) base their model on the FI composition. They observe that salinity remains constant and that assumed W-bearing fluids are poor in Fe. They conclude that wolframite precipitation at Panasqueira was triggered by fluid-rock interaction during tourmalinization and muscovitization, yielding the demanded iron, and allowing alkali depletion and pH neutralization in the fluid. They agree that sudden pulses of pressure change may have contributed to wolframite precipitation, but negate fluid mixing or boiling.

B- Constraints Issued from the Present Work/Critics of Previous Works

CONSTRAINTS FROM THE PARAGENETIC SUCCESSION: INCONSISTENCY OF THE LECUMBERRI-SANCHEZ ET AL. (2017) MODEL

At Panasqueira, tourmalinization preceded/accompanied the beginning of wolframite deposition. As a consequence, the iron in the wall-rock was hosted in tourmaline before the inception of ore deposition. What is more, when wolframite began to grow, tourmaline, not only remained stable, but indeed experienced overgrowth. As a consequence, there is no factual basis for the Lecumberri-Sanchez et al. (2017) model by which iron from the wall-rock was used for triggering wolframite deposition. Indeed, these authors invoke the obvious iron depletion observed in the muscovitisation fringes that are commonly present at the vein boundaries: unfortunately, these fringes, being related to the spectacular muscovite selvages, are obviously far later (stage IV) than the wolframite deposition. At a pinch, the Lecumberri-Sanchez (2017) model may apply to the small quantity of wolframite in the stage IV vugs.

CONSTRAINTS FROM THE TOURMALINE STUDY

Study of trace element distribution in the early tourmaline leads to the conclusion that two fluids are involved at the beginning of stage I, one with a clear “metamorphic” signature, the other, with a F-Fe-Mn-Li-

W signature being more akin to a granite origin. Yet, REE data are against a magmatic-hydrothermal origin, and a sourcing in a deep anatectic domain (biotite dehydration melting) is favoured. Alternatively (or, more likely) concomitantly, fluid-rock interaction with the main Panasqueira granite may be considered.

Another constraint is that fluid-rock interaction at the tourmalinization stage was fluid-dominated (another argument against the Lecumberri-Sanchez et al. (2017) model).

THE MAIN STAGE OF WOLFRAMITE DEPOSITION: CONSTRAINTS FROM FI DATA

A critical point is the recognition that early FI in quartz were decrepitated in the subsequent course of the hydrothermal system. There are indeed numerous non-decrepitated FI, but they are demonstrably associated to recrystallized portions of the early quartz, and most of them only record the latest stages. Unfortunately, these late FI are precisely those which were studied by all previous studies. It follows that whatever conclusion based on these FI and concerning main wolframite deposition must be considered invalid. This is evidently the case for all the deposition models presented in the previous works. This is particularly relevant for the Lecumberri-Sanchez et al. (2017) model, which is based on the low iron content of alleged “syn-wolframite FI”. Thus, their model could be considered for the stage IV, when wall rock muscovitisation could have loaded in iron a Fe-poor incoming fluid, causing the formation of the beautiful (but scarce) wolframite 4 (but a reworking of earlier wolframite may also be considered).

A complication arises when trying to use FI studies to constrain the W-bearing fluid. Following Higgins (1980), many study have documented the presence of CO₂-bearing fluids in wolframite deposits. Yet, since the appearance of infra-red microscopy, allowing FI study in opaque minerals such as wolframite, several authors drew attention to the discrepancy between FI data from wolframite and surrounding quartz, respectively. It is not uncommon that CO₂-bearing FI are observed in quartz, while there are none in wolframite (Pei et al., 2015).

At Panasqueira, it has been claimed that is the same case (Lüders, 1996). Unfortunately, the paragenetic position of the wolframite crystals studied is not specified. Yet, the FI are not decrepitated. Owing to the brittle behavior of wolframite, it seems highly probable that FI included in wolframite would also decrepitate, like in the surrounding quartz (either by pressure drop combined to temperature increase, or deformation, or both). Consequently, it seems very probable that the crystals studied by Lüders (1996) belong to the late stage IV and come from vugs: these Wfm_{4-IV} being clearly earlier than the surrounding vug quartz. It is not so surprising to observe a discrepancy between the FI included in these two minerals.

Although they are all affected by the decrepitation events, some early FI may still carry some information. These are small FI, which were only partially re-equilibrated, allowing access to both fluid composition and P-T conditions. The study leads to the conclusion that neither pressure nor temperature were much variable during stage I. Thus, models based on pressure or temperature drop are not feasible.

On the other hand, these early FI consistently contain a volatile phase, dominated by CO₂, but with significant CH₄ and N₂ contents, and a rather high N₂/CH₄ ratio. This could suggest the relevance of the Gibert and Moine (1992) model. However, this is debatable because of the presence of N₂ throughout the hydrothermal history. Infact, there is no evidence for a “N₂ burst” into data. Yet, the data also show that the volatile component results from a mixing process between a CO₂-rich phase and a CH₄-N₂ mixture. The CO₂ component displays an elevated CO₂ to CH₄ ratio (without N₂), characteristic of water equilibration with graphite (Fischer-Torpf reaction) at temperatures higher than 500°C (i.e., higher than the estimated temperature at the early stage, around 450°C).

Finally, the data may be reconciled with the conclusions of the tourmaline study, with the existence of two distinct fluids, both of metamorphic origin: a deep fluid, related to anatexis, and a more classical metamorphic fluid, possibly related to the thermal effects of the Panasqueira granite. The former could have brought the CO₂ component, the latter the N₂ one. If the fluid composition data from tourmaline composition are adapted to the main wolframite deposition stages (I, II), then, the W-bearing fluid was also (Fe, Mn)-bearing. This is not in agreement with the conclusions of Wang et al. (2019) stating that the W-mineralizing fluids should be iron-poor. A consequence is that pH variation should have been the main control on wolframite deposition in the Panasqueira case.

Part Five
Conclusions

CONCLUSION

THE PANASQUEIRA METALLOGENIC (MINERAL) SYSTEM : THE EVIDENCE FOR A PROTRACTED CRUSTAL-SCALE SYSTEM

5.1 Proposition of a Conceptual Model for the Early Stages (I-II)

From the preceding discussion, it results that the basic tenets of the model adopted for early tourmalinization in Chapter 1 (Fig. 6.1-A) may be kept for the main wolframite stage (Fig. 6.1-B). A major change is however the possibility that the alterations experienced by the main Panasqueira granite (G1) may have been coeval with the wolframite stage. In this perspective, the deep F2 fluid could have been the responsible for these alterations (Fig. 6.2) and could therefore, following the fluid-rock interaction, have been able to transport a significant amount of the W required for the deposit.

Maintaining a flow of deep-sourced fluids is thought possible due to renewal of heat input by the mantle (as mafic melts underplating the crust or intruding the lower crust). Such a renewal is considered to have been effective at the scale of the CIZ during the late Carboniferous (cf. Chapter 1).

As depicted in Figure 6.2, at the level of the G4 cupola complex fluid-rock interaction was responsible for the early quartzification, allowing an additional input of rare metals to the hydrothermal system.

The observed alteration dominated by the nearly complete replacement of albite (and mica) by quartz and the lack of newly formed Al-bearing silicate (neither andalusite, nor topaz as F is present, nor mica) implies a significant oversaturation with respect to quartz. Such an oversaturation is likely the result of pressure decrease at constant temperature, and/or dilution (mixing) with more acidic fluids (Monecke et al. 2018 and reference therein) (Fig. 6.3). Fluids oversaturated with respect to quartz are expected to be in the field of feldspars if pH is not too much acidic. On the other hand, observation indicates that feldspar dissolution provides a part of the SiO₂ implied in quartz precipitation. This apparent contradiction may be considered to be due to kinetic problems in relation to the quartz oversaturation. According to this model, the key process leading to quartzification is the mixing inside the G4 cupola of the F2 fluids passing through G1 (and therefore less acidic due to fluid rock interaction) and of the F1 fluid, more acidic (CO₂-rich and equilibrated with quartz-muscovite).

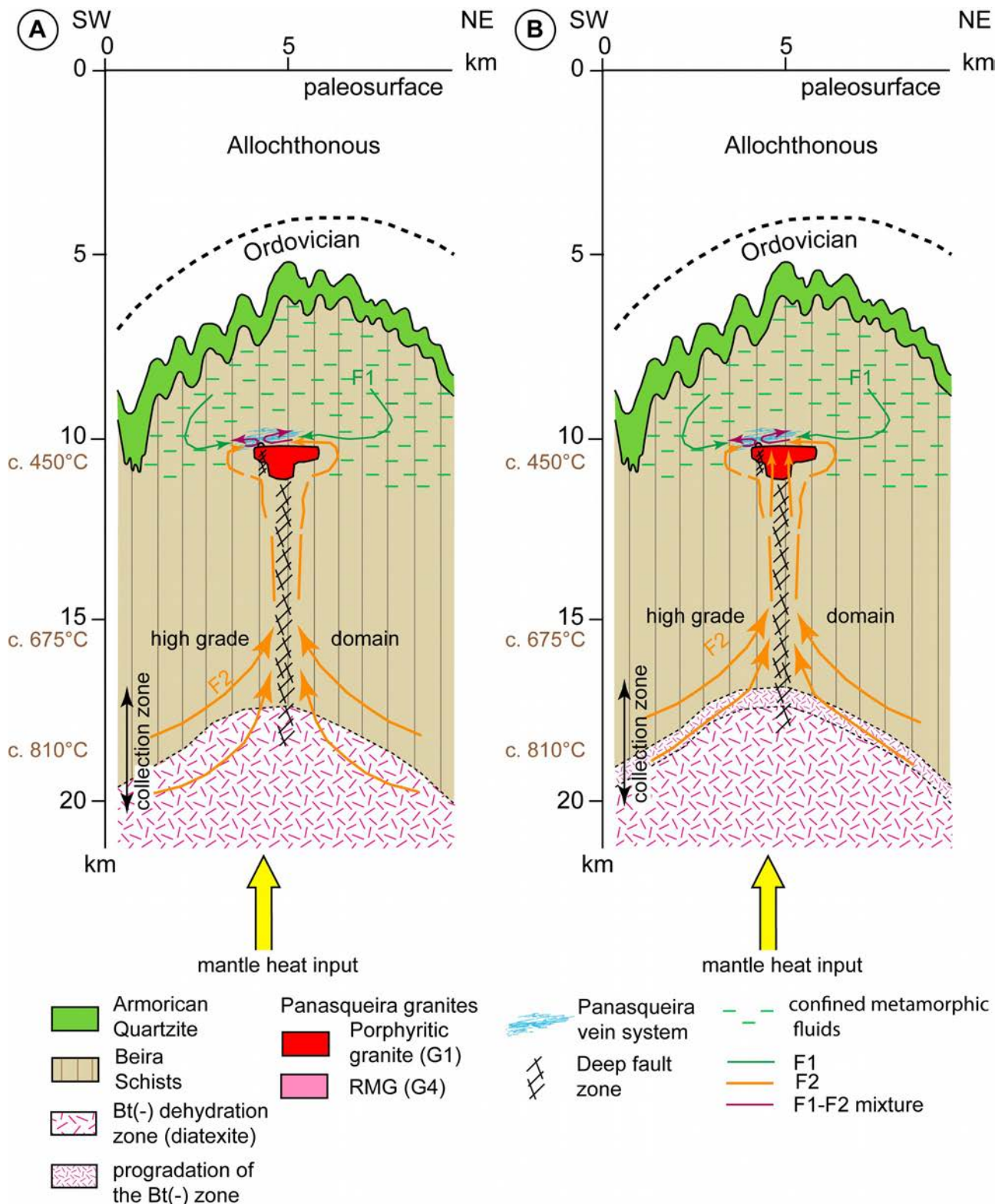


Fig. 6.1: Conceptual models for the first stages of evolution of the Panasqueira metallogenic (mineral) system. **A.** At 305 Ma, main tourmalinization stage and incipient wolframite deposition (see Chapter 1). **B.** At 305±t Ma ($t \ll 1$ Ma), main stage of wolframite deposition. The same kind of fluids are implied, with the important difference that the deep L2 fluid is now allowed to permeate and alter the G1 granite, adding a new (potentially W-bearing) fluid to the hydrothermal mix. Minor interactions in the G4 cupola are also possible (not represented but see Fig. 5.9).

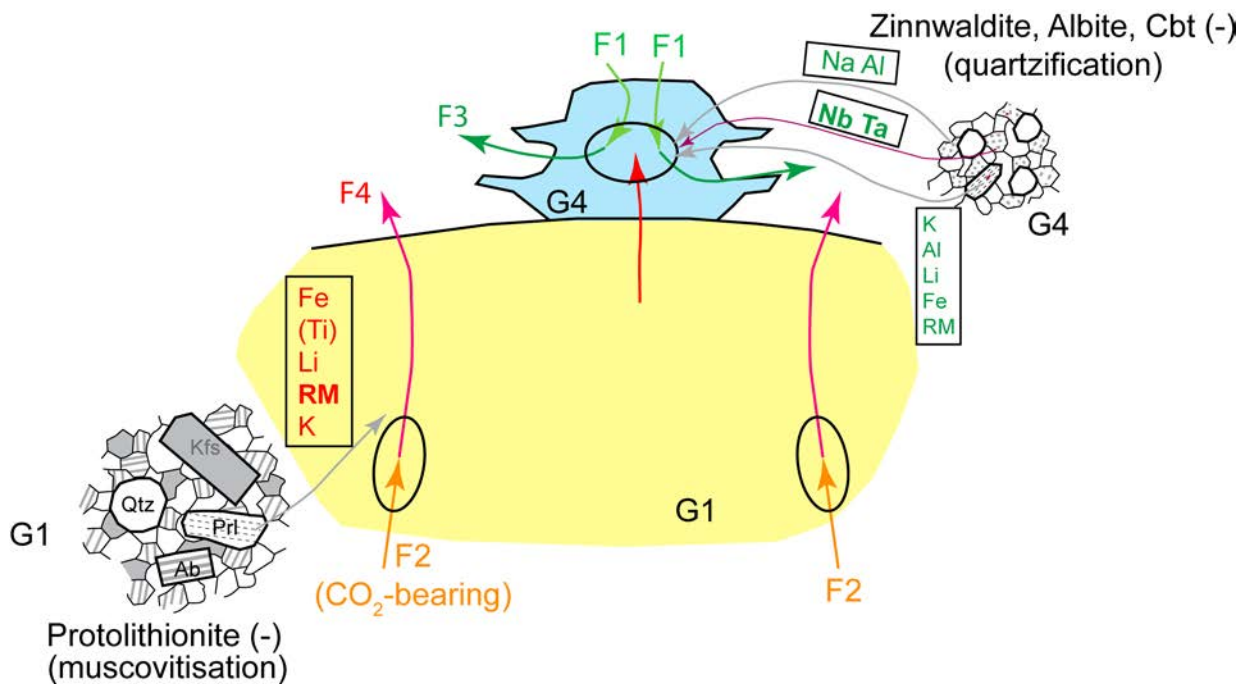


Fig. 6.2: Conceptual scheme of the fluid-rock interactions in the upper part of the Panasqueira granite body. Deep F2 fluids may interact with the G1 porphyritic facies and transform protolithionite into muscovite, releasing in particular W, a potential source for the main stage of wolframite deposition. A part of the reacted fluids may translate through the higher level cupola where their mixing with the F1 metamorphic fluids allow oversaturation in quartz and the development of the quartzification process in the G4 facies. The released Nb-Ta from columbo-tantalite may contribute to the episodic Nb enrichments observed in the mainstage wolframite (see text for explanations). Ab albite; Cbt columbo-tantalite; Kfs K-feldspar; Prl protolithionite; RM rare metals; Qtz quartz.

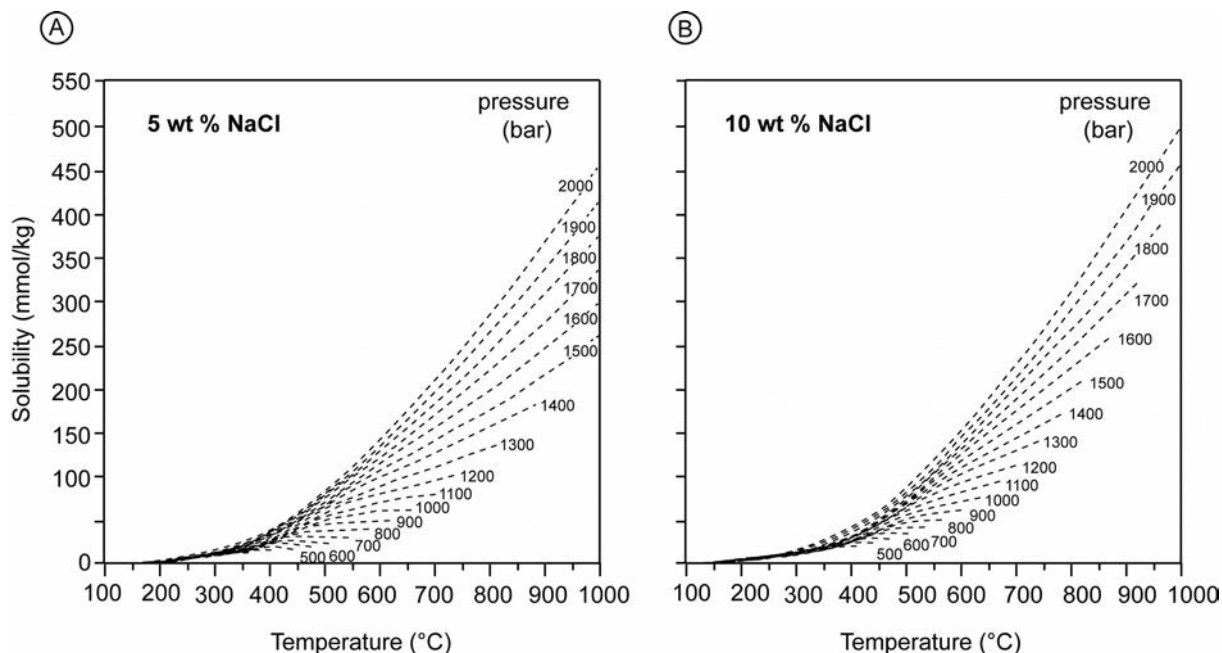


Fig. 6.3: Pressure-salinity dependence of quartz solubility in the single-phase field of the H₂O-NaCl system, for salinities of 5 and 10 wt% NaCl, and pressures varying from 50 to 200 MPa (redrawn from Monecke et al. 2018). These relations allow a modelling of the quartzification process in the G4 cupola (see text for explanation).

5.2 A protracted hydrothermal system

Fluid inclusions data yielded to a new P-T path (Figure 6.4 and Figure 6.5), by far different of the literature P-T estimates. This path is characterized by exhumation at rather constant temperature until the end. According to the recent geochronological data and the subsequent new time chart, this process lasts at least 9 Ma (from ca.305 Ma to c-a. 296 Ma). Two main stages are distinguished:

- Stage I-III: the exhumation is a limited and therefore slow (0.1 mm/yr), the main W(Sn) mineral system being deep seated around 9-12 km depth.
- Stage IV: the structural level is much shallower (*around 3 km depth*).

Yet, the fluid nature does change significantly during the whole history, even at the late stage, meaning that the contribution of surficial fluids remained limited. This, in turn, may be correlated to the persisting existence of an impermeable cap materialized by the Ordovician quartzites. Main aqueous-carbonic fluids seem to have been trapped and produced until the very end of the system.

From stage II to stage IV, a rather quick exhumation occurred from around 9-10 km at 303 Ma to ca. 3 km at 296 Ma implies an exhumation of 6-7 km in 7 Ma, and an exhumation rate of 1 mm/yr.

These findings modify considerably the concept of formation of the deposit which has been considered during more than 40 years as formed close to the surface, as an epithermal deposit. The latter hypothesis was formulated on the basis of the "boiling" of fluids, based on fluid inclusions which are more probably related to stage IV and not to the main W stage (Qtz I and II).

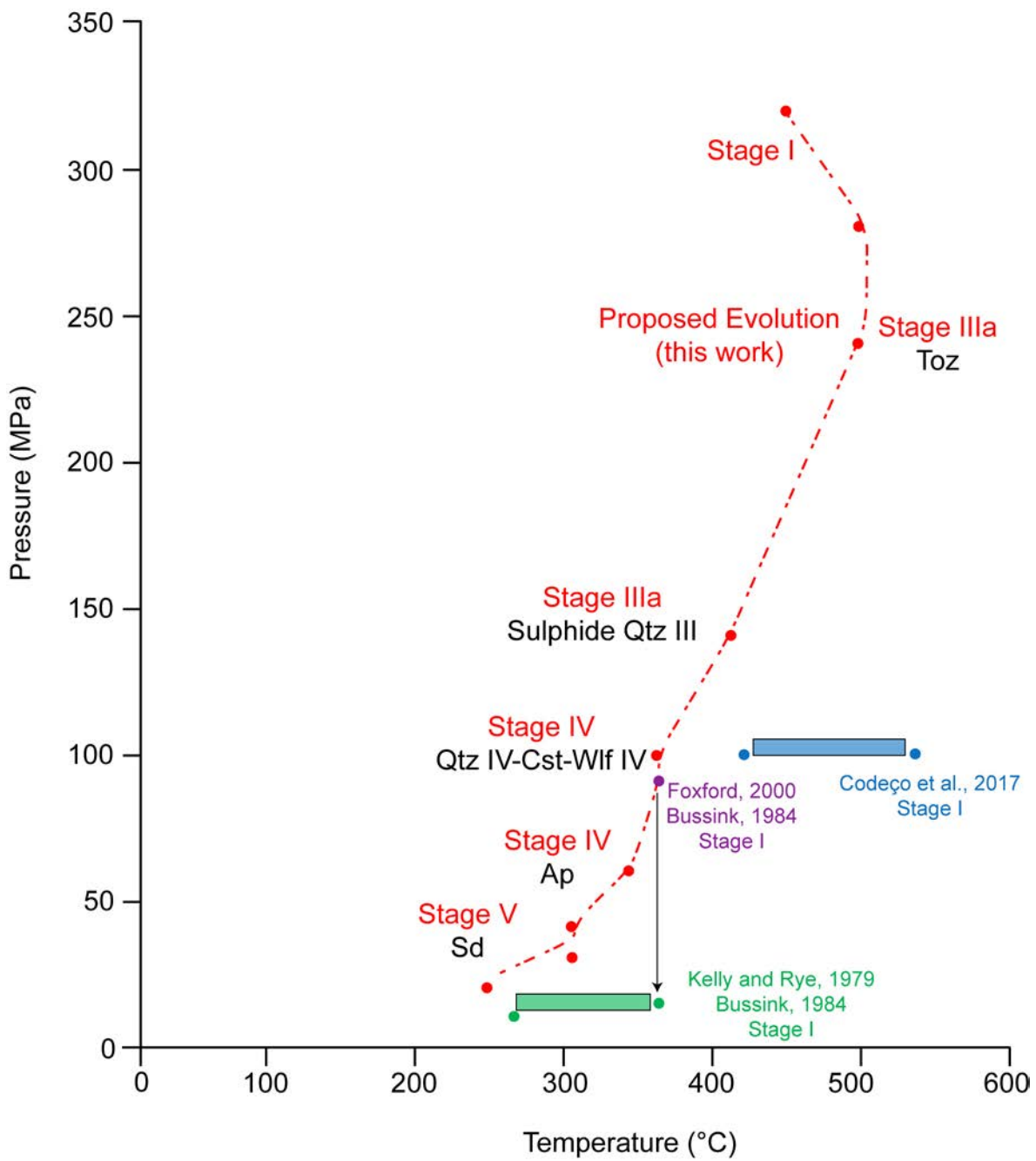


Fig. 6.4: P-T-t path for the Panasqueira FI from stage I to stage V displaying strong pressure decrease at constantly high temperatures. Prior estimates by previous workers are shown. Note the small temperature increase at stage III. Transition from dominantly lithostatic pressure conditions to dominantly hydrostatic likely occurred between Stage III and Stage IV.

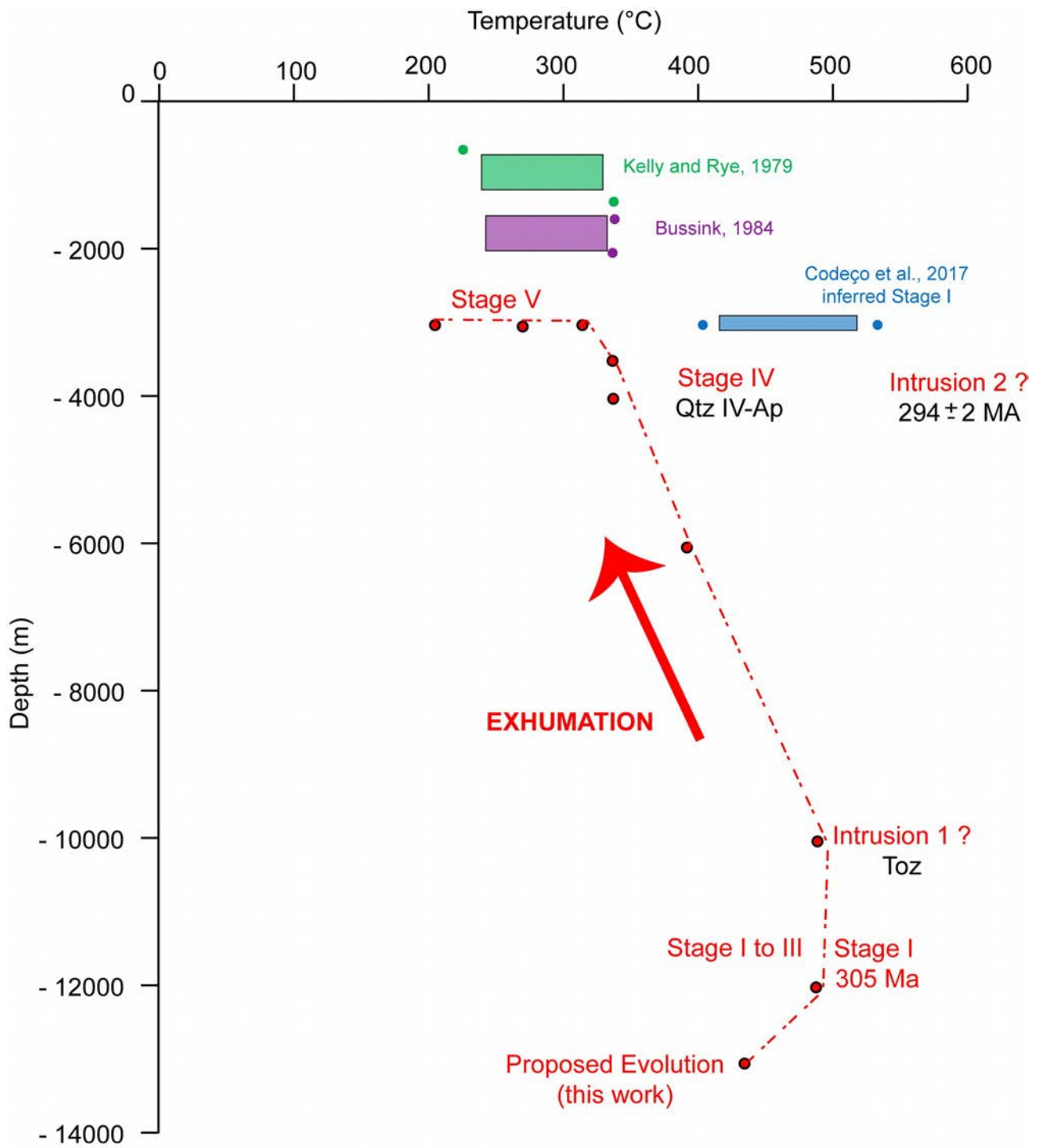


Fig. 6.5: Temperature-depth evolution of Panasqueira fluids showing a two-stage exhumation process, first slow from stage I to stage III, and then accelerating from Stage III to Stage V.

5.3. A long-lived crustal scale system

From the beginning and for all its life, the main features of the Panasqueira system are depicted in Fig. 6.1:

- Multiple sources of fluids and metals. Fluids of metamorphic derivation are constantly involved, some of them being inferred to have been produced in deep migmatitic zones (biotite dehydration melting). Fluids of magmatic origin are less evident, but their presence is inferred from the paragenetic succession (stages III and IV). Fluid-rock interaction with either metamorphic or magmatic (granite) rocks are involved in the metal sources. Mixing between fluids of various origin is a constant all along the history.

- Several magmatic contributions, involving evolved granite melts (RMG family). The earliest (G1-G4 suite) preceded the inception of the hydrothermal system. At least two other RMG emplacement events (concealed bodies, until now not found in drill holes) were involved in stage III (Toz-Cst) and stage IV (Ms2-Cst).

- Long-lived hydrothermal system (at least 10 Ma, possibly more), with temperatures constrained to a narrow HT range (350-550°C) until the end. Therefore, renewed heat inputs, at depth (mantle-crust interactions, migmatitic domains) and transferred through fluid and melt (granites) heat advection. Early lamprophyre dykes (overprinted by the veins) attest for the antiquity of mantle involvement in the area.

- Location controlled by a NW-SE lineament, favouring successive granite intrusions and long-time fluid draining.

- Structural control at the mineralization level. The thick impermeable cap formed by the Ordovician quartzite served as a long-duration trap for all the fluids arriving or produced at the Panasqueira structural level, hence the periodic overpressuring and crack-seal phenomena. Vein system localized in a damaged zone draining fluid migration, multiple deformational stages affecting the same area. A pre-mineralization hydrothermalism, marked by the seixo-bravo system is also indication of long-lived fluid system.

Finally, the quartz-wolframite events, as well as the other mineralizing events (Sn, Cu), appear localized in time and space as privileged moments in the overall history of the metallogenic system. The optimal conditions developed from time to time in the upper reaches of the concealed G1 granite, ultimately depend of events developed at a far larger time and space scale. Finally, Panasqueira deposit experienced the same history as that of several other mineralized areas (Au, W, As) in the West European Variscan belt (northern Portugal, French Massif Central) in the course of the Late Carboniferous. All these zones underwent late magmatism coupled with significant exhumation and flow of metamorphic fluids, following a P-T trajectory very similar to that of Panasqueira, e.g., a significant pressure decrease at nearly constant high temperature. These trajectories were described in northern Portugal in several places such as Castromil (Vallance et al., 2003) and Tres Minas which are known for their Au(As) deposits. This is not a surprise that

W districts experienced similar P-T-X history than Au districts. It can be noted finally, that this depth-time evolution ends, at the last stage of exhumation, with P-T conditions similar to those of geothermal fields such as Geysers (California) or Larderello (Tuscan area) where both granite intrusions and mantle heat anomalies are proven.

References

- Arnek, R., & Sasaki, Y. (1974). Equilibrium Studies of Polyanions. 20. A Recalculation of Emf Data on the Reactions of H⁺ and WO₄²⁻ in 3 M Na (ClO₄) at 25 C. *Acta Chemica Scandinavica*, 28(1).
- Audtat, A., Gröther, D., & Heinrich, C. A. (2000). Magmatic-hydrothermal evolution in a fractionating granite: A microchemical study of the Sn-WF-mineralized Mole Granite (Australia). *Geochimica et Cosmochimica Acta*, 64(19), 3373-3393.
- Aveston, J. (1964). Hydrolysis of tungsten (VI): ultracentrifugation, acidity measurements, and Raman spectra of polytungstates. *Inorganic Chemistry*, 3(7), 981-986.
- Barabanov, V. F. (1971). Geochemistry of tungsten. *International Geology Review*, 13(3), 332-344.
- Barré, T., Arurault, L., & Sauvage, F. X. (2005). Chemical behavior of tungstate solutions: Part 1. A spectroscopic survey of the species involved. *Spectrochimica Acta Part A: Molecular and Biomolecular Spectroscopy*, 61(4), 551-557.
- Bebout, G. E., Cooper, D. C., Bradley, A. D., & Sadofsky, S. J. (1999). Nitrogen-isotope record of fluid-rock interactions in the Skiddaw aureole and granite, English Lake District. *American Mineralogist*, 84(10), 1495-1505.
- Bilal, B. A., Haufe, P., & Möller, P. (1986). Raman spectroscopic and electrochemical study of polymerization of tungsten (VI) in a hydrothermal solution up to 1 kbar and 200 C. *Physica B+ C*, 139, 721-724.
- Boiron, M.-C., Cathelineau, M., Banks, D. A., Fourcade, S. & Vallance, J. (2003) Mixing of metamorphic and surficial fluids during the uplift of the Hercynian upper crust: consequences for gold deposition. *Chemical Geology*, 194, 119-141.
- Bussink R. W. (1984). Geochemistry of the Panasqueira tungsten-tin deposit, Portugal. *Geol. Ultraiectina*. 33, 170p.
- Černý, P., Blevin, P. L., Cuney, M., & London, D. (2005). Granite-related ore deposits. *Society of Economic Geologists*, 100, 337-370.
- Codeço, M. S., Weis, P., Trumbull, R. B., Glodny, J., Wiedenbeck, M., & Romer, R. L. (2019). Boron Isotope Muscovite-Tourmaline Geothermometry Indicates Fluid Cooling During Magmatic-Hydrothermal W-Sn Ore Formation. *Economic Geology*, 114(1), 153-163.
- Cox, S.F., Wall, V.J., Etheridge, M.A., Potter, T.F. (1991). Deformational and metamorphic processes in the formation of mesothermal gold deposits. Examples from Lachlan Fold Belt in central Victoria, Australia. *Ore Geol. Rev.* 6, 391– 423.
- Cruywagen, J. J., & Van Der Merwe, I. F. (1987). Tungsten (VI) equilibria: a potentiometric and calorimetric investigation. *Journal of the Chemical Society, Dalton Transactions*, (7), 1701-1705.
- Cuney, M., Marignac, C., & Weisbrod, A. (1992). The Beauvoir topaz-lepidolite albite granite (Massif Central, France); the disseminated magmatic Sn-Li-Ta-Nb-Be mineralization. *Economic Geology*, 87(7), 1766-1794.

- De Amorin, A. (2017). Pétrographie géochimie des granitoides de la mine de W de Panasqueira (Portugal): Rôle dans la genèse des minéralisations: Unpublished M.Sc. thesis, Université de Lorraine (France), Laboratoire Géoressources, 37 p.
- De La Roche, H., Leterrier, J., Grandclaude, P., & Marchal, M. (1980). A classification of volcanic and plutonic rocks using R1R2-diagram and major-element analyses-its relationships with current nomenclature. *Chemical geology*, 29, 183-210.
- Dugdale, A.L., Hagemann, S.G. (2001). The Bronzewing lode-gold deposit, Western Australia: P-T-X evidence for fluid immiscibility caused by cyclic decompression in gold-bearing quartz veins. *Chem. Geol.* 173, 59–90.
- Duit, W., Jansen, J. B. H., van Breemen, A., & Bos, A. (1986). Ammonium micas in metamorphic rocks as exemplified by Dome de l'Agout (France). *American Journal of Science*, 286(9), 702-732.
- Duncan, J. F., & Kepert, D. L. (1961). 1050. Polyanion equilibria in aqueous solution. Part I. The quantitative analysis of acidified tungstate solutions. *Journal of the Chemical Society (Resumed)*, 5317-5325.
- Eugster H. P. and Wilson G. A. (1985). Transport and deposition of ore-forming elements in hydrothermal systems associated with granites. In *High Heat Production Granites, Hydrothermal Circulation and Ore Genesis. Inst. Min. Metall., London*, pp. 87-98.
- Gibert, F., Moine, B., Schott, J., & Dandurand, J. L. (1992). Modeling of the transport and deposition of tungsten in the scheelite-bearing calc-silicate gneisses of the Montagne Noire, France. *Contributions to Mineralogy and Petrology*, 112(2-3), 371-384.
- Groves, D.I., Goldfarb, R.J., Gebre-Mariam, M., Hagemann, S.G., Robert, F. (1998). Orogenic gold deposits, a proposed classification in the context of their crustal distribution and relationship to other gold deposit types. *Ore Geol. Rev.* 13, 7 –27.
- Guillot, B., Marteau, P., & Obriot, J. (1988). Far-infrared absorption in nitrogen-rare gas compressed mixtures: an experimental and theoretical survey. *Molecular Physics*, 65(4), 765-784.
- Guillot, C., & Moine, B. (1989). Relationships between N₂ in the fluid inclusions and NH₃ in rocks (and micas) in the Dôme de Montredon, Montagne Noire, France. *ECROFI X abst, London*, 41.
- Gundlach, H. (1967). Transport und Abscheidungsbedingungen von Wolframerzen aus Wasserigenlösungen. *Pegmatische Lagerstätten und Ihre Wirtschaftliche Bedeutung*, H.19, Clausthal-Zellerfeld.
- Harlaux, M. (2016). *Tungsten and rare-metal (Nb, Ta, Sn) hydrothermal metallogenic systems in the late-variscan orogenic context: example of the French Massif Central* (Doctoral dissertation).
- Harlaux, M., Mercadier, J., Marignac, C., Peiffert, C., Cloquet, C., & Cuney, M. (2018). Tracing metal sources in peribatholithic hydrothermal W deposits based on the chemical composition of wolframite: The example of the Variscan French Massif Central. *Chemical Geology*, 479, 58-85.
- Harlaux, M., Kouzmanov, K., Gialli, S., Fontboté, L., Marger, K., Bouvier, A. S., ... & Kalinaj, M. (2019). Cassiterite deposition triggered by fluid mixing: Evidence from in-situ $\delta^{18}\text{O}$ - $\delta^{11}\text{B}$ analysis of tourmaline from the San Rafael tin deposit, Peru. In *15th Biennial SGA Meeting*
- Häufe, P. (1982). Raman-spectrophotometric determination of the tungstate anion and its isopolyanions in aqueous systems. *Fresenius' Zeitschrift für analytische Chemie*, 310(5), 388-391.
- Heinrich, C. A. (1990). The chemistry of hydrothermal tin (-tungsten) ore deposition. *Economic Geology*, 85(3), 457-481.

- Higgins, N. C. (1980). Fluid inclusion evidence for the transport of tungsten by carbonate complexes in hydrothermal solutions. *Canadian Journal of Earth Sciences*, 17(7), 823-830.
- Ivanova, G. F. (1966). Thermodynamic evaluation of possibility of tungsten transport as halogen compounds. *Geochemistry International Ussr*, 3(5), 964.
- Jaques, L., & Pascal, C. (2017). Full paleostress tensor reconstruction using quartz veins of Panasqueira Mine, central Portugal; part I: Paleopressure determination. *Journal of Structural Geology*, 102, 58-74.
- Keggin, J. F. (1934). The structure and formula of 12-phosphotungstic acid. *Proceedings of the Royal Society of London. Series A, Containing Papers of a Mathematical and Physical Character*, 144(851), 75-100.
- Kepert, D. L. (1973). Isopolyanions and heteropolyanions. *Comprehensive inorganic chemistry*, 4, 607-672.
- Kreulen, R., & Schuiling, R. D. (1982). N₂ - CH₄z. sbnd; CO₂ fluids during formation of the Dôme de l'Agout, France. *Geochimica et Cosmochimica Acta*, 46(2), 193-203.
- Launay, G., Sizaret, S., Guillou-Frottier, L., Gloaguen, E., & Pinto, F. (2018). Deciphering fluid flow at the magmatic-hydrothermal transition: A case study from the world-class Panasqueira W-Sn-(Cu) ore deposit (Portugal). *Earth and Planetary Science Letters*, 499, 1-12.
- Lourenço, A. (2002). Paleofluidos e mineralizações associadas às fases tardias da Orogenia Hercínica. Thèse de doctorat, Université de Porto. 303p.
- Lourenço, A. (2006). Granito da Panasqueira (Cúpula da Barroca Grande). Estudo de um sistema granítico associado a mineralizações de estanho The Panasqueira granite (Barroca Grande cupola). Study of a Granite system associated with tin lodes.
- Manning, D. (1984). Volatile control of tungsten partitioning in granitic melt-vapour systems. *Institution of Mining and Metallurgy Transactions*, 93.
- Manning, D. A., & Henderson, P. (1984). The behaviour of tungsten in granitic melt-vapour systems. *Contributions to Mineralogy and Petrology*, 86(3), 286-293.
- Marignac, C. (2004). Comment on "Formation and evolution processes of the Salanfe W-Au-As-skarns (Aiguilles Rouges Massif, western Swiss Alps)" by Chiaradia M (*Mineralium Deposita* 38: 154-168). *Mineralium Deposita*, 39(3), 396-398.
- Marignac, C., & Cathelineau, M. (2009). The nature of ore-forming fluids in peri-batholithic Sn-W deposits and a classification. In *Smart science for exploration and mining, Proceedings Xth Biennial SGA Meeting, Townsville* (pp. 245-247).
- Melleton, J., Gloaguen, E., Frei, D., & Lima, A. (2011, August). U-Pb dating of columbite-tantalite from Variscan rare-elements granites and pegmatites.
- Ni, P., Wang, X. D., Wang, G. G., Huang, J. B., Pan, J. Y., & Wang, T. G. (2015). An infrared microthermometric study of fluid inclusions in coexisting quartz and wolframite from Late Mesozoic tungsten deposits in the Gannan metallogenic belt, South China. *Ore Geology Reviews*, 65, 1062-1077.
- Ng, K. Y. S., & Gulari, E. (1984). Spectroscopic and scattering investigation of isopoly-molybdate and tungstate solutions. *Polyhedron*, 3(8), 1001-1011.
- Noronha, F., Cathelineau, M., Boiron, M.C., Banks, D., Doria, A., Ribeiro, M.A., Nogueira, P., Guedes, A. (2000). A three-fluid stage model for Au metallogenesis in granites and their metamorphic host rocks in Northern Portugal. *J. Explor. Geochem.* 71, 209- 224.

- Palmer D. A., Wesolowski D. and Mesmer R. E. (1987). A potentiometric investigation of the hydrolysis of chromate (VI) ion in NaCl media to 175°C. *Journal of solution chemistry*, 16, 443-463.
- Pearson, R. G. (1963). Hard and soft acids and bases. *Journal of the American Chemical society*, 85(22), 3533-3539.
- Polya, D. A. (1988). Efficiency of hydrothermal ore formation and the Panasqueira W-Cu (Ag)-Sn vein deposit. *Nature*, 333(6176), 838.
- Polya, D. A. (1989). Chemistry of the main-stage ore-forming fluids of the Panasqueira W-Cu (Ag)-Sn deposit, Portugal; implications for models of ore genesis. *Economic Geology*, 84(5), 1134-1152.
- Raimbault, L., Cuney, M., Azencott, C., Duthou, J. L., & Joron, J. L. (1995). Geochemical evidence for a multistage magmatic genesis of Ta-Sn-Li mineralization in the granite at Beauvoir, French Massif Central. *Economic Geology*, 90(3), 548-576.
- Redkin, A. F., & Bondarenko, G. V. (2010). Raman spectra of tungsten-bearing solutions. *Journal of solution chemistry*, 39(10), 1549-1561.
- Ribeiro, R. F. (2017). Gravimetric Modelling and Geological Interpretation of Argemela-Panasqueira Area.
- Rollinson C.L. (1973). Chromium, molybdenum and tungsten. In: Bailar JC, Emeleus H J, Nyholm S, Trotman-Dickenson AF (eds). *Comprehensive inorganic chemistry*, 3, 742-769, Pergamon Press, Oxford.
- Štemprok, M., Holub, F. V., & Novák, J. K. (2003). Multiple magmatic pulses of the Eastern Volcano-Plutonic Complex, Krušné hory/Erzgebirge batholith, and their phosphorus contents. *Bull Geosci*, 78(3), 277-296.
- Taylor, B. E. (2007). Epithermal gold deposits. Mineral deposits of Canada: a synthesis of major deposit-types, district metallogeny, the evolution of geological provinces, and exploration methods. *Geological Association of Canada, Mineral Deposits Division, Special Publication*, 5, 113-139.
- Vallance J., Cathelineau M., Boiron M.C., Shepherd T.J., Naden J. (2003) - Fluid-rock interactions and the role of late Hercynian aplite intrusion in the genesis of the Castromil gold deposit, northern Portugal. *Chemical Geology*, 194, 201-224.
- Walther, J.V., Helgeson, H.C. (1977). Calculation of the thermodynamic properties of aqueous silica and the solubility of quartz and its polymorph at high temperatures and pressures. *Am. J. Sci.* 277, 1315-1351.
- Wesolowski, D., Drummond, S. E., Mesmer, R. E., & Ohmoto, H. (1984). Hydrolysis equilibria of tungsten (VI) in aqueous sodium chloride solutions to 300. degree. C. *Inorganic Chemistry*, 23(8), 1120-1132.
- Wood, S. A., & Vlassopoulos, D. (1989). Experimental determination of the hydrothermal solubility and speciation of tungsten at 500° C and 1 kbar, 2. *Geochimica et Cosmochimica Acta*, 53(2), 303-312.
- Wood, S. A. (1990). The aqueous geochemistry of the rare-earth elements and yttrium: 2. Theoretical predictions of speciation in hydrothermal solutions to 350 C at saturation water vapor pressure. *Chemical Geology*, 88(1-2), 99-125.
- Wood, S. A. (1992). Experimental determination of the solubility of WO₃ (s) and the thermodynamic properties of H₂WO₄ (aq) in the range 300-600 C at 1 kbar: calculation of scheelite solubility. *Geochimica et Cosmochimica Acta*, 56(5), 1827-1836.
- Wood, S. A., & Samson, I. M. (2000). The hydrothermal geochemistry of tungsten in granitoid environments: I. Relative solubilities of ferberite and scheelite as a function of T, P, pH, and m NaCl. *Economic Geology*, 95(1), 143-182.

- Zhang RQ, Ramos V, Leal S, Noronha F, Pinto F. 2019. U-Pb geochronology of cassiterites from primary Sn mineralizations in Sn-W Variscan Metallogenic Province, Portugal. SGA Meeting 357-360
- Zouhair, M., & Marignac, C. (1990). Evolution des systèmes hydrothermaux stériles du massif granitique du Ment (Maroc central). *Réunion annuelle des sciences de la terre*, (13).

Appendix

APPENDIX PART ONE: CHAPTER ONE

Table A1: Operating conditions for the LA-ICP-MS equipment

Laboratory & Sample Preparation	
Laboratory name	Géosciences Rennes, UMR CNRS 6118, Rennes, France
Sample type/mineral	Rutile
Sample preparation	Rutile grains in context in thin-sections
Imaging	JEOL J7600F scanning electron microscope (SEM)
Laser ablation system	
Make, Model & type	ESI NWR193UC, Excimer
Ablation cell	ESI NWR TwoVol2
Laser wavelength	193 nm
Pulse width	< 5 ns
Fluence	8.0 J/cm ²
Repetition rate	5 Hz
Spot size	45 μm (round spot)
Sampling mode / pattern	Single spot
Carrier gas	100% He, Ar make-up gas and N ₂ (3 ml/min) combined using in-house smoothing device
Background collection	20 seconds
Ablation duration	60 seconds
Wash-out delay	15 seconds
Cell carrier gas flow (He)	0.75 l/min
ICP-MS Instrument	
Make, Model & type	Agilent 7700x, Q-ICP-MS
Sample introduction	Via conventional tubing
RF power	1350W
Sampler, skimmer cones	Ni
Extraction lenses	X type
Make-up gas flow (Ar)	0.87 l/min
Detection system	Single collector secondary electron multiplier
Data acquisition protocol	Time-resolved analysis
Scanning mode	Peak hopping, one point per peak
Detector mode	Pulse counting, dead time correction applied, and analog mode when signal intensity > ~ 10 ⁶ cps
Masses measured	²⁰⁴ (Hg + Pb), ²⁰⁶ Pb, ²⁰⁷ Pb, ²⁰⁸ Pb, ²³² Th, ²³⁸ U
Integration time per peak	10-30 ms
Sensitivity / Efficiency	25000 cps/ppm Pb (50μm, 10Hz)
Dwell time per isotope	5-70 ms depending on the masses
Data Processing	
Gas blank	20 seconds on-peak
Calibration strategy	R10 Rutile used as primary reference material, R19 rutile used as secondary reference material (quality control)
Reference Material info	R10 (Luvizotto et al., 2009) R19 (Zack et al., 2011)
Data processing package used	Iolite (Paton et al., 2010), VizualAge_UcomPbine (Chew et al., 2014)
Quality control / Validation	R19: Apr 2016: 490 ± 3.4 Ma (MSWD=1.11; N=13) Dec 2017 : 493 ± 12 Ma (MSWD=2; N=12)

Appendix A2: Ar-Ar dating of muscovite (methodology)

Argon isotopes (from mass 40 to 37) were measured using Faraday detectors with low noise 1×10^{12} Ω resistors and mass 36 was measured using a compact discrete dynode (CDD) detector. The sensitivity for argon measurements is $\sim 6.312 \times 10^{17}$ moles/fA as determined from measured aliquots of Fish Canyon Sanidine (Dazé et al., 2003; Kuiper et al., 2008). Standards and sample were placed in 2 mm deep wells in 18 mm diameter aluminium disks, with standards placed strategically so that the lateral neutron flux gradients across the disk could be evaluated. Planar regressions were fit to the standard data, and the $^{40}\text{Ar}/^{39}\text{Ar}$ neutron fluence parameter (J) interpolated for the unknowns. Uncertainties in J are estimated at 0.1 - 0.2% (1 σ), based on Monte Carlo error analysis of the planar regressions (Best et al., 1995). All specimens were irradiated in the Cadmium-lined, in-core CLICIT facility of the TRIGA reactor at the Oregon State University (USA). The duration of irradiation was 17 hours and using the Fish Canyon sanidine (Kuiper et al., 2008) and GA1550 biotite (Spell and McDougall, 2003) standards. Standards for $^{40}\text{Ar}/^{39}\text{Ar}$ measurements were placed in a Cu sample tray, with a KBr cover slip, in a stainless steel chamber with a differentially pumped ZnS viewport attached to a Thermo Fisher Scientific extraction/purification line and baked with an infrared lamp for 24 hours. Single crystals were fused using the CO₂ laser. The sample selected for the $^{40}\text{Ar}/^{39}\text{Ar}$ dating has been previously investigated by optical microscopy and SEM in order to spot homogeneous areas devoid of alteration, micro-inclusions or internal zoning. Discs of 5 mm in diameter and ~ 150 μm thick were cut from the same polished thick section (150 - 200 μm thick). The discs were mounted using a ceramic adhesive (PELCO) on a quartz slide placed in a stainless steel chamber with a sapphire viewport attached to the same stainless steel high vacuum extraction system as the CO₂ laser, and baked with an infrared lamp for 48 hours. For this study, a raster size of about 100 x 100 μm was used and ablation pits were excavated to an estimated depth of 50 μm . Reactive gases were removed for both the standard and unknown, after 3 minutes, by three GP-50 SAES getters (two at room temperature and one at 450 °C) prior to being admitted to an ARGUS VI mass spectrometer by expansion. Five argon isotopes were measured simultaneously over a period of 6 minutes.

References cited

- Best, M.G., Christiansen, E.H., Deino, A.L., Grommé, C.S., and Tingey, D.G., 1995, Correlation and emplacement of a large, zoned, discontinuously exposed ash-flow sheet: Ar/ Ar 40 39 chronology, paleomagnetism, and petrology of the Pahrnagat Formation, Nevada: *Journal of Geophysical Research*, v. 100, p. 24,593-24,609.
- Dazé, A., Lee, J.K.W., and Villeneuve, M., 2003, An intercalibration study of the Fish Canyon sanidine and biotite $^{40}\text{Ar}/^{39}\text{Ar}$ standards and some comments on the age of the Fish Canyon Tuff: *Chemical Geology*, v. 199, p. 111-127.
- Kuiper, K.F., Deino, A., Hilgen, F.J., Krijgsman, W., Renne, P.R., and Wijbrans, J.R., 2008, Synchronizing the rock clocks of Earth history: *Science*, v. 320, p. 500-504.

Appendix A0:

1. Problems in measuring Tur compositions by EPMA

The Pnq tourmaline crystals from the tourmalinized wall rocks are very small and therefore so are the different zones in the crystals. Owing to the rather low contrasting capacity of back scatter imaging by EPMA in our laboratory, it is usually challenging to assure that a given spot is really located in the desired zone: this is particularly true for the Tur 0 residual cores, that are usually not seen with EPMA. What is more, it is not so easy to retrieve under EPMA the crystals imaged by SEM - given that we ordinary explore the sections at random to find the best crystals.

For all these reasons, it was desirable to make measurements while identifying the zoning features, i.e., to mainly use SEM-EDS. To ensure compatibility of the two approaches, EPMA and SEM measurement were both performed on chosen crystals. Comparison between the results of the two kinds of measurement was thus made possible, and is effected in the following sections.

2. Reality and extent of a Si *apfu* bias in SEM-EDS analyses

As shown in Fig. A0-1, statistics of Si *apfu* from SEM-EDS analyses (calculated on an O, OH, F basis) display a shift towards values higher than 6.00, contrasting with the average 6.00 obtained from EPMA analyses.

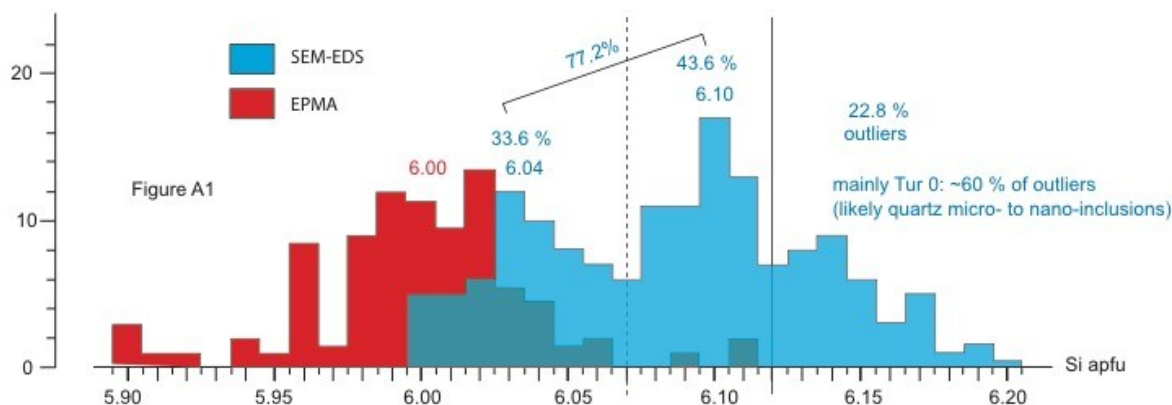


Figure A1. Comparative statistics of Si *apfu* measurements by EPMA or SEM-EDS.

More precisely, the distribution is plurimodal, and ~ 35 % are comprised between 6.0 and 6.06 (averaging 6.04), ~ 45 % are comprised between 6.06 and 6.12 (averaging 6.10) and only ~20 % are higher; the latter are named “outliers” in the following. It may also be noted that there is a consistent overlap between the EPMA

distribution and the first mode of the SEM-EDS distribution: in fact, EPMA distribution could be interpreted as bimodal, with the second mode nearly coincident with the first SEM-EDS mode.

It results that ~ 80 % of the SEM-EDS analyses yield lower than 6.12 Si *apfu* values, and it may be expected that this will cause only small shifts (if any) from the EPMA reference in the various crystal chemistry diagrams: this will be addressed in the following section.

Considering the outliers, it appears that most of them (~ 60 %) come from the Tur0 relict cores. A possible explanation of such deviant analyses could be the presence in the cores of nano-inclusions of quartz crystals: as mentioned in the main text, many tourmaline crystals of the tourmalinized wall-rocks are clouded of quartz inclusions, often concentrated in the core zones. If so, the formula calculation should not affect too much the elemental ratios, and it may be expected that plotting of the analyses in the various diagrams will reveal the same trends as the “cleaner” analyses. This will be examined in a following section.

3. SEM-EPMA comparison

For the comparison, the more suitable crystals, of sufficiently large size, appear to belong to a second generation of tourmaline (Tur2), not addressed in the manuscript, of which two sets of crystals were available, in samples PAN XIX-16-a2-b1 and PAN-III-8-c1/2; in the latter, however, sufficiently contrasted zoned crystals of the first generation (Tur1) found in crack-seal quartz veinlets (see Figure 4 in main text) could also be measured by the two method, as well as late (Tur3) overgrowths on Tur2.

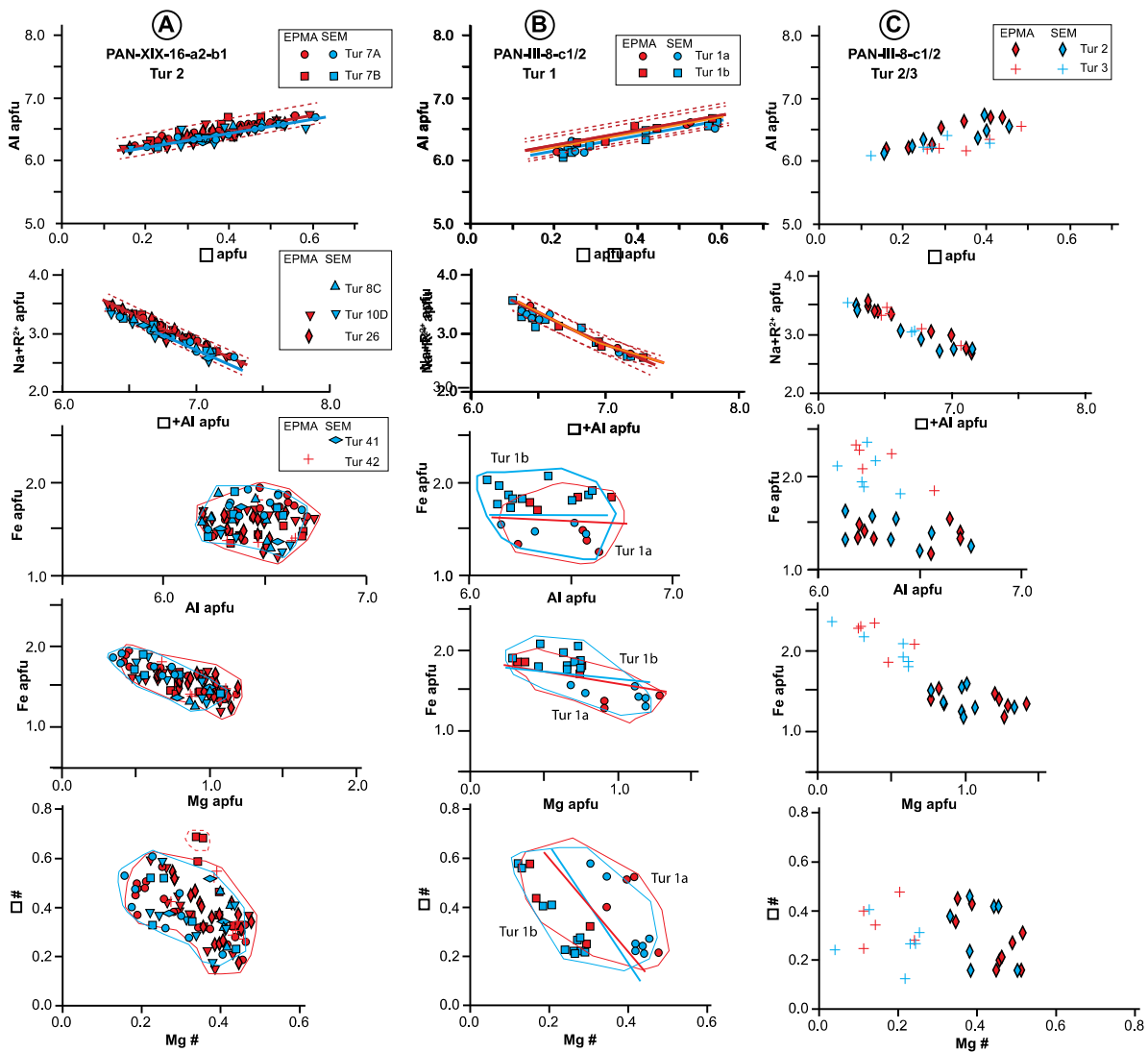


Figure A2. Comparison of EPMA and SEM-EDS measurements on selected sets of tourmaline crystals in two samples (see text).

Comparison is made in a series of diagrams in Fig. A0-2, and results are the following:

- the diagram characteristics (range of values, distribution of Tur types) are basically the same for the two sets of analyses;
- very limited shifts affect the trends in the Al vs [□] and Na+R²⁺ vs Al+[□] diagrams for SEM-EDS analyses relative to EPMA ones: nevertheless, the SEM-EDS trends remain included in the dispersion field of EPMA analyses;
- the Al/Fe/Mg ratios seem in particular identical in the two sets of results; this is confirmed by examination of the AFM diagrams in Fig. A0-3. It is noteworthy that the dispersion of the Al/Fe+Mg ratios is similar whatever the analysis method, thus certifying that this dispersion is real.

It may thus be concluded that use of SEM-EDS analyses in place of EPMA ones for the considered crystals did not affect the restitution of crystal chemistry properties.

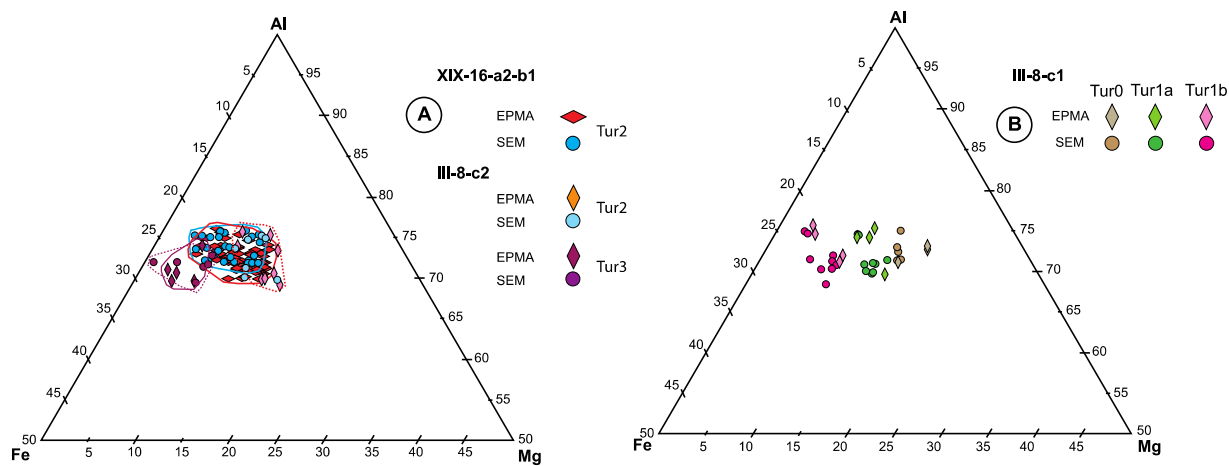


Figure A3. Comparison of EPMA and SEM-EDS analyses in AFM diagrams. **A:** Tur2 (samples PAN-XIX-16-a2-b1 and PAN-III-8-c2) and Tur3 (PAN-III-8-c2; **B:** Tur 0 and Tur 1 (sample PAN-III-8-c1, excepted Tur0-EPMA, taken from other samples).

4. Internal consistency of SEM-EDS analyses

Separating the analyses in three sets corresponding to the three modes in Fig. A0-1 (mode 1 = “low” Si, mode 2 = “high” Si, mode 3 = “outliers”) is done in the diagrams of Fig. A0-4 and A0-5.

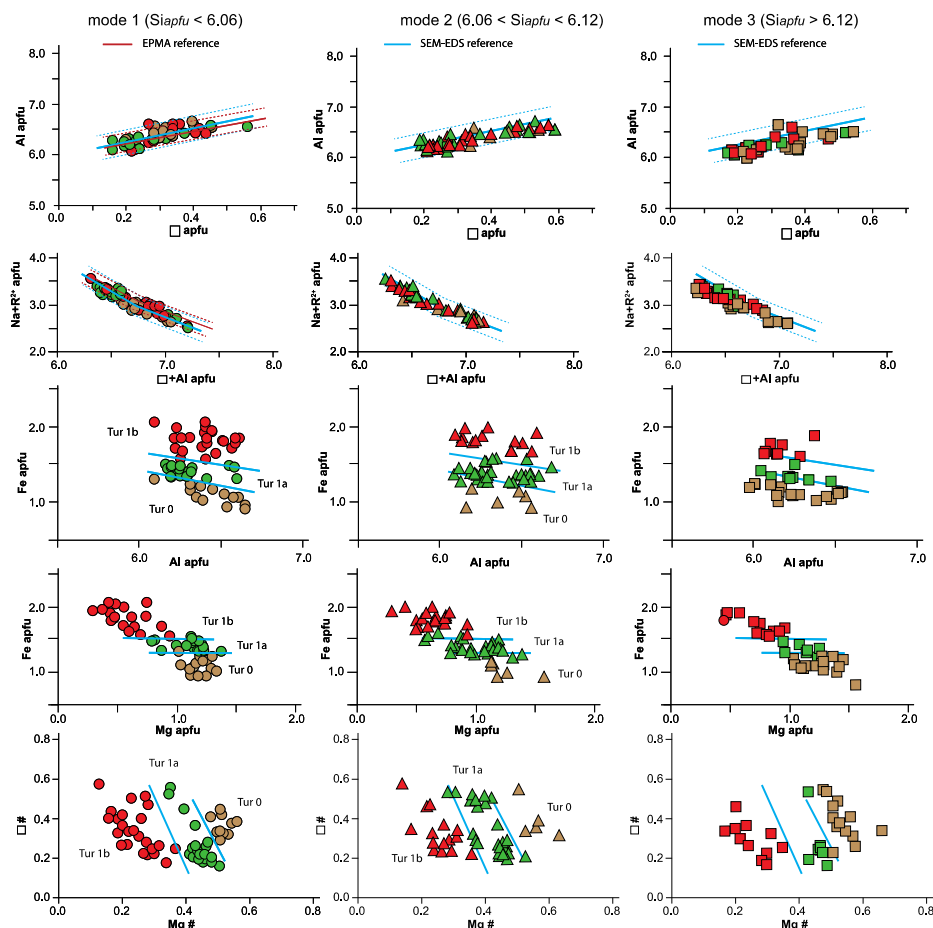


Figure A0-4. Checking the internal consistency of SEM-EDS analyses using classical crystal chemistry diagrams. The domain boundaries are those corresponding to mode 1 in all diagrams. The red lines correspond to EPMA reference.

(i) A first result is that in the Al vs [] and $\text{Na}+\text{R}^{2+}$ vs $\text{Al}+[]$ diagrams, the whole of the mode 1 values behave as the ones in sample III-8-c, as indeed expected. The crystal chemistry diagrams of these mode 1 analyses may thus be in turn used as reference for the other sets of analyses.

(ii) In all the diagrams, the mode 2 values yield basically the same relations, and in particular, the boundaries between “Tur0”, “Tur1a” and “Tur1b” fields are very consistent in the three Fe vs. Al, Fe vs Mg and []# vs. Mg# diagrams in Fig. A0-4, and in the AFM diagrams in Fig. A0-5.

(iii) As expected, the “outlier” values are shifted in the Al vs [] and $\text{Na}+\text{R}^{2+}$ vs $\text{Al}+[]$ diagrams, displaying nevertheless the same characteristics. They however are highly compatible with the preceding sets of values in the other diagrams. This is particularly significant for the Tur0 values.

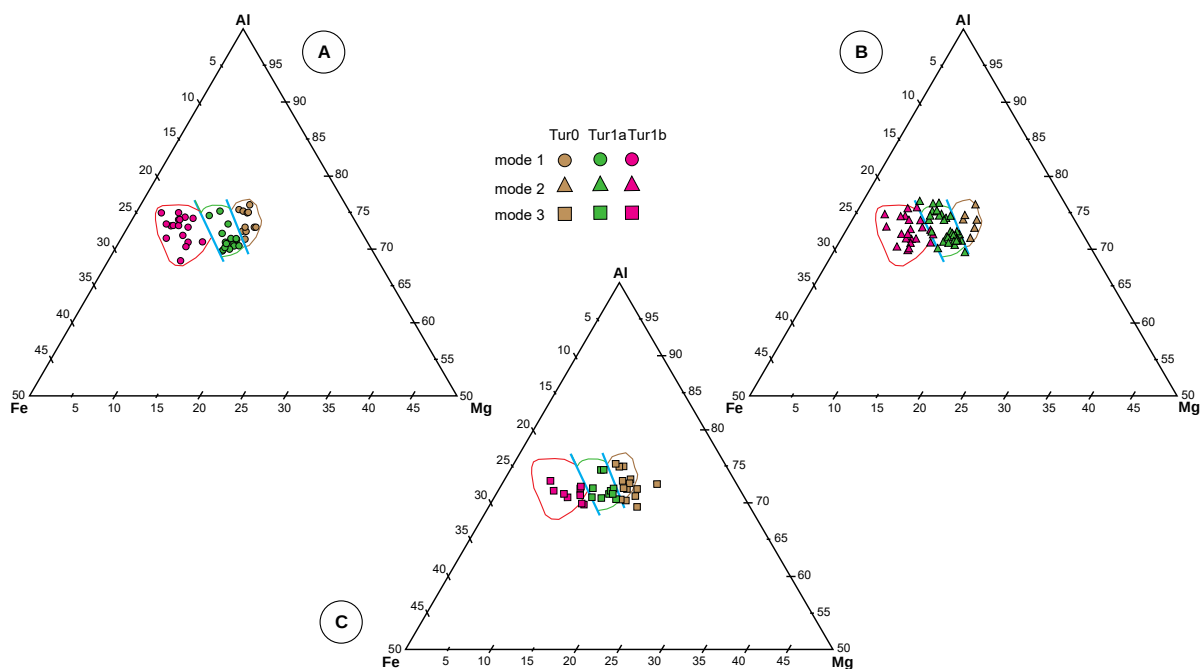


Figure A0-5. Checking the internal consistency of SEM-EDS analyses in the AFM triangle. **A:** mode 1 ("low Si"); **B:** mode 2 ("high" Si); **C:** mode 3 ("outliers"). The domain boundaries are those corresponding to mode 1 in all three diagrams.

5. The case for F

It is known that, in tourmaline, there may be a rough linear relationships between F content and the ionic charge associated with the site X infilling. Consideration of Fig. A0-6 shows that this is indeed the case and that:

(i) there is no significant differences between the SEM-EDS analyses corresponding to either mode 1, or mode 2 or mode 3 of the Si distribution (Fig. A0-6A to C)

(ii) the scarcity of EPMA measurements in Tur 1 prevents a comparison zone by zone, although the rare Tur0 measurements by EPMA confirm that F content in Tur0 id generally low (Fig. A0-6A)

(iii) if therefore EPMA and SEM-EDS analyses are considered as a whole (Fig. A0-6D and E), both sets of analyses display a large dispersion and a very rough linear relationship, with a slight difference between the two sets which nevertheless does not introduce a significant difference for the data interpretation.

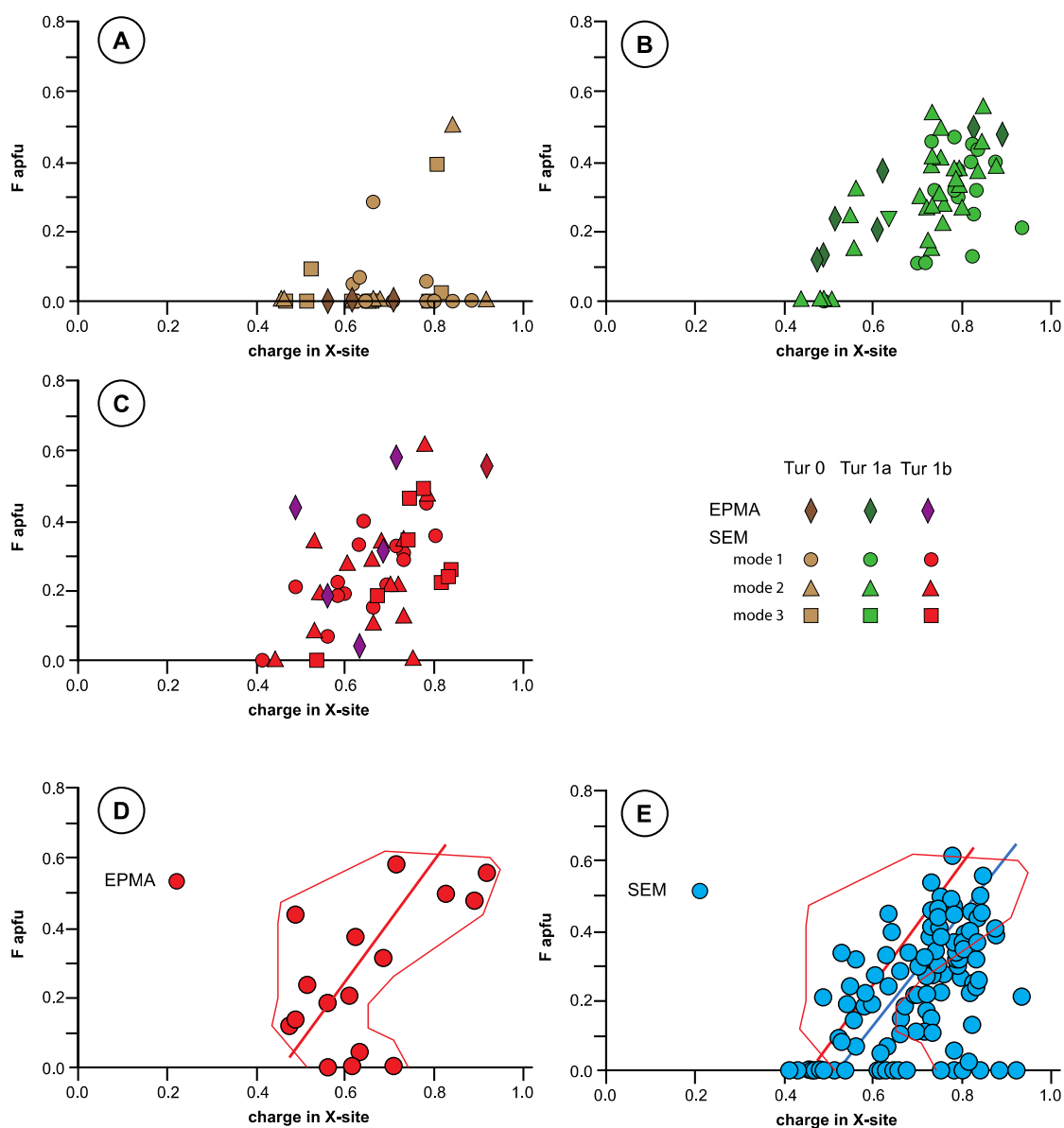


Figure A0-6. Relationships between F and the X-site charge: comparison of EPMA and SEM-EDS results. A to C: comparison zone by zone (A: Tur0; B: Tur 1a; C: Tur 1b); D-E: bulk comparison. Contours in E: from D

6. Conclusion

It results from the preceding that the SEM-EDS analyses may be safely used for the crystal chemistry characterization of the Panasqueira tourmaline, provided that analyses from mode 3 group be discarded. Finally, 117 spots in 19 samples are taken into consideration in the main text.

Appendix A3-Table A3: Major element analyses of the early tourmaline from Panasqueira

<https://doi.org/10.24396/ORDAR-36>

Appendix A4- Table A4: Major element analyses of the early tourmaline from Panasqueira

<https://doi.org/10.24396/ORDAR-36>

Appendix A6- Table A6: LA-ICP-MS U-Pb data for the Panasqueira Rutile - All errors are listed at 1 sigma

<https://doi.org/10.24396/ORDAR-36>

Appendix A7- Table A7: $^{40}\text{Ar}/^{39}\text{Ar}$ dating of a muscovite selvage from Panasqueira

<https://doi.org/10.24396/ORDAR-36>

Appendix A8:

Boron mass balance calculations

Boron endowment in the granites: It must be emphasized that the greisenized cupola and the subjacent granites layer are typically devoid of tourmaline, meaning that the original melts were not tourmaline saturated. This raises the question of these granites being a boron source for the Panasqueira system. In any case, these granites being of the RMG family, and their solidus temperature being accordingly in the c. 600°-650°C range (Aksyuk and Konyshov, 2011), their boron content could not have been higher than the equilibrium B content in equilibrium with tourmaline in the melt at these temperatures, i.e., no more than 0.5 wt% B₂O₃ (London, 2011; and references therein). The volume of the cupola itself (approximated by a cone, high 150 m, diameter 250 m) being of $\sim 2.5 \cdot 10^6 \text{ m}^3$, it could not contain more than $\sim 9 \text{ kt B}$ (with a melt density of 2.3 t.m^{-3} : Dingwell et al., 1993). The subjacent RMG sheet-like body, made of several separate intrusions (De Amorin, 2017), may be approximated as a 100 m thick body with about 1 km^2 surface (Fig. 2), yielding a $\sim 10^8 \text{ m}^3$ volume and a maximal content of 360 kt B. Thus, the total possible boron yield by the evolved granites could not have exceeded 370 kt B.

Boron required for the wall-rock tourmalinization: These values must be compared with the B content in the tourmalinized wall-rock. (i) At the single vein scale, we consider an average vein system based onto the description by Foxford et al. (2000, their Fig.8): an elliptical area (minor axis ~100 m, major axis ~300 m), a total width of the tourmalinized margins of 0.45 m (i.e., 15 cm on one side of the vein and 30 cm on the other) and an averaged 50 volume % of tourmaline in the altered zones. This yields a unitary volume of the altered zone of $\sim 1.1 \cdot 10^4 \text{ m}^3$. Adopting an average density of 3.1 t.m^{-3} , and a boron content of 3.3% for the tourmaline, this unitary volume contains $\sim 540 \text{ t B}$. (ii) The number of elementary veins may be estimated using the published values for the total volume of the vein system, between 3 and $6 \cdot 10^3 \text{ km}^3$ (Polya, 1989), and assuming an average vein thickness of 0.2 m (Foxford et al., 2000). This yields an estimated number of elementary veins comprised between 750 and 1500. (iii) Finally, the total B content of the tourmalinized wall rocks may be bracketed between 410 and 810 kt. These values are clearly higher than the maximum boron tonnage possibly delivered by the Panasqueira RMG.

Volume of magmatic water required for boron transportation

At the elementary vein scale, and at any time of the tourmalinization process, the effective volume of fluid present in the V_0 volume of altered rocks (estimated at $1.2 \cdot 10^4 \text{ m}^3$, see above) is controlled by rock porosity. If ϕ is the porosity, this effective volume is only $\phi \cdot V_0$. The porosity of metamorphic rocks is generally considered to be in the 10^{-1} to 10^{-2} range (Bickle and McKenzie 1987), and was for instance estimated at 0.08 in the Tinos schists (Breeding et al., 2003). Here, we take $\phi=0.1$. The effective $\phi \cdot V_0$ volume contains a boron mass $m_0 = \phi \cdot V_0 \cdot \rho_w \cdot X$, with ρ_w the fluid density and X the boron content in the fluid. For a magmatic fluid equilibrated with tourmaline at the solidus temperature, the boron content X will be close to 1 wt % B_2O_3 (Weisbrod et al., 1986) and the fluid density will be in the 0.62 - 0.68 t.m^{-3} range, depending on salinity between ~ 10 and $\sim 20 \text{ wt\% NaCl}$ (Sakuma and Ichiki, 2016); taking an average 0.65 yields $m_0= 2 \text{ t B}$. Therefore, to attain the 540 t B accumulated in the tourmalinized wall rock, the $\phi \cdot V_0$ volume must be renewed $540/2=270$ times, i.e., a total flow of $270 \cdot \phi \cdot V_0= 2.9 \cdot 10^6 \text{ m}^3$ of fluid must be channelled through the transforming schist. At the deposit scale, this in turn means that a volume of fluid comprised between $2.2 \cdot 10^9$ and $4.3 \cdot 10^9 \text{ m}^3$ was required for the tourmalinization be effective.

Possible water yield by the granite system

The water content of a RMG melt is $\sim 5 \text{ wt\%}$. Thus, the Panasqueira RMG sheet-like body, with a volume of 10^8 m^3 and a melt density of 2.3 t.m^{-3} , contained about $1.2 \cdot 10^7 \text{ t}$ water, i.e. (with a water density of 0.65 t.m^{-3}) could have expelled $\sim 1.8 \cdot 10^7 \text{ m}^3$ of fluid. This is clearly two orders of magnitude below the required fluid quantity. It must be noted that it is the same for the main wolframite deposition stage, as already stated by Polya (1989), who estimated a several 100 km^3 (up to 1000) flow to produce the deposit.

This was however based on a 0.2 ppm W content in the fluid, which was clearly underestimated: owing to the data of Wood and Vlassopoulos (1989), a content of ~ 500 ppm W is more realistic, and would demand a volume of $\sim 5 \cdot 10^8 \text{ m}^3$ to yield the c. 150 kt of W of the deposit, one order of magnitude larger than the granite water endowment.

References cited

- Bickle, M.J., and McKenzie, D., 1987, The transport of heat and matter by fluids during metamorphism: *Contributions to Mineralogy and Petrology*, v. 95, p. 384-392.
- Breeding, C.M., Ague, J.J., Brocker, M., and Bolton, E.W., 2003, Blueschist preservation in a retrograded, high-pressure, low-temperature metamorphic terrane, Tinos, Greece: implications for fluid flow paths in subduction zones: *Geochemistry Geophysics Geosystems*, v. 4, 1: 9002, doi: 10.1029/2002GC000380.
- De Amorin, A., 2017, Pétrographie géochimie des granitoides de la mine de W de Panasqueira (Portugal): Rôle dans la genèse des minéralisations: Unpublished M.Sc. thesis, Université de Lorraine (France), Laboratoire Géoressources, 37 p.
- Dingwell, D.B., Knoche, R., and Webb, S.L., 1993, The effect of F on the density of haplogranite melt: *American Mineralogist*, v. 78, p. 325-330.
- Foxford, K.A., Nicholson, R., Polya, D.A., and Hebblethwaite, R.P.B., 2000, Extensional failure and hydraulic valving at Minas da Panasqueira, Portugal: evidence from vein spatial distributions, displacements and geometries: *Journal of Structural Geology*, v. 22, p. 1065–1086, [http://dx.doi.org/10.1016/S0191-8141\(00\)00029-8](http://dx.doi.org/10.1016/S0191-8141(00)00029-8).
- Polya, D.A., 1989, Chemistry of the main-stage ore-forming fluids of the Panasqueira W–Cu(Ag)–Sn deposit, Portugal: implications for models of ore genesis: *ECONOMIC GEOLOGY*, v. 84, p. 1134–1152.
- Sakuma, H., and Ichiki, M., 2016, Density and isothermal compressibility of supercritical H₂O–NaCl fluids: molecular dynamics study from 673 to 2000 K, 0.2 to 2 GPa, and 0 to 22 wt% NaCl: *Geofluids*, v. 16, p. 89-102.
- Weisbrod, A., Polak, C., and Roy, D., 1986, Experimental study of tourmaline solubility in the system Na–Mg–Al–Si–B–O–H. Applications to the boron content of natural hydrothermal fluids and tourmalinization processes: *International Symposium on Experimental Mineralogy and Geochemistry (Nancy), Abstracts*, v. 140-141.
- Wood, S.A., and Vlassopoulos, D., 1989, Experimental determination of the solubility and speciation of tungsten at 500 °C and 1 kbar: *Geochimica et Cosmochimica Acta*, v. 53, p. 303–312.

Appendix A9: Oscillatory zoning: a (micro)seismic connection?

For a large spectrum of mineral species, and in a large temperature (25°-450°C) and pressure (0.1-200 MPa) range, experimentally measured crystal growth rates are comprised between a few 10^{-1} nm.s⁻¹ and 10-20 (up to 100) nm.s⁻¹ (e.g., Laudise et al 1964, Nielsen and Toft 1984, Yanagisawa et al. 1996, Teng et al. 2000, Lander et al. 2008). As a rule, the rates increase with the concentration of the solution and the temperature of crystallization. For the Panasqueira rutile, growing at c. 450°C, it seems then reasonable to bracket the growth rates between 1 and 10 nm.s⁻¹, as a first order of magnitude. With such values, the time growth of a 20 µm-large band in a rutile crystal would be in the order of $2 \cdot 10^3$ to $2 \cdot 10^5$ s, i.e., from less than 1 h to ~2 days, meaning that it should be also the time scale for the turning over of the flow feeding at the doublet growth scale.

It is known that seismic events have the capacity to activate micropermeability in the affected rock volume, allowing the incorporation of otherwise captive fluids in the circulating fluid flow (Charmoille, 2005; Charmoille et al., 2005). The time constant of the process is in the order of a few hours to a few days, consistent with the estimated growth rates for the rutile. Thus, the formation of a doublet could be understood as the result of seismic activity. A(micro)seismic event would allow in a first time the influx in the growing environment of the main fluid circulating at this time at the deposit scale, which, accordingly to the previous discussion, should be a F2-dominated, W-rich, F1-F2 mixture, and a "light band" would grow. After a short time-lag, a new fluid (F3), coming from a low permeability reservoir, would in turn invade the growing environment, provoking the growth of the succeeding "dark band".

References cited

- Charmoille, A., 2005, Traçage hydrochimique des interactions hydrauliques et mécaniques entre les volumes perméables et peu perméables au sein des aquifères fracturés carbonatés: Aquifère karstique de Fourbanne (Avant-pays jurassien, 25), Laboratoire naturel de Coaraze (Alpes Méridionales, 06): PhD thesis, Besançon University (France), 271 p.
- Charmoille, A., Fabbri, O., Mudry, J., Guglielmi, Y., and Bertrand, C., 2005, Post-seismic permeability change in a shallow fractured aquifer following a ML 5.1 earthquake (Fourbanne karst aquifer, Jura outermost thrust unit, eastern France): *Geophysical Research Letters*, v. 32: LA8406, doi:10.1029/2005GL023859.
- Lander, R.H., Bonnell, L.M., and Larese, R.E., 2008, Toward more accurate quartz cement models: The importance of euhedral versus noneuhedral growth rates: *Association of American Petroleum Geologists Bulletin*, v. 92, p. 1537–1563, doi:10.1306/07160808037.
- Laudise, R.A., Kolb, E.D., and Caporaso, A.J., 1964, Hydrothermal growth of large sound crystals of zinc oxide: *Journal of the American Ceramic Society*, v. 47, p. 9-12.
- Nielsen A.E., and Toft, J.M., 1984, Electrolyte crystal growth kinetics: *Journal of Crystal Growth*, v. 67, p. 278-288.
- Teng, H.H., Dove, P.M., and De Yoreo, J.J., 2000, Kinetics of calcite growth: Surface processes and relationships to macroscopic rate laws: *Geochimica et Cosmochimica Acta*, v. 64, p. 2255-2266.

Yanagisawa, K., Feng, Q., Ioku, K., Yamasaki, N., 1996, Hydrothermal single crystal growth of calcite in ammonium acetate solution: *Journal of Crystal Growth*, v. 163, p. 285-294.

APPENDIX PART ONE: CHAPTER TWO

Supplementary Data: Table S1

<https://doi.org/10.24396/ORDAR-36>

APPENDIX PART THREE: CHAPTER FOUR

Annex 2: Table 1, k calibration, Table 3, Table 4

<https://doi.org/10.24396/ORDAR-36>

Annex 1: Table 5, Table 6, Table 7

<https://doi.org/10.24396/ORDAR-36>

Acknowledgments

I am grateful to my supervisors, Michel Cathelineau and Laurent Truche, for the opportunity, for all the help to continue and finish this manuscript. I am grateful to the director of the laboratory GeoRessources Jacques Pironon as well. Thank you to the jury of my thesis discussion: thank you, Maria Mercedes Fuertes Fuente, Johann Raith, Jean-Louis Hazemann and Cécile Fabre for your touching words after my discussion, to be there (or almost, in videoconference), and to have discussed with me upon 4 years of work.

Christian Marignac, thank you so much to teach me the hard work! You taught me to have patience, to look at the data in every possible way, how to interpret results, and most of all: *ordre et méthode!* It has been a pleasure and an honor working beside you! Thank you so much also for the very interesting conversations especially about politics, philosophy and science, and for spending some time in refreshing my geological knowledge, when I ignored it, without judging me. Thank you for all your precious help!

It's been many years before I sit here refreshing my head about everyone who crossed my path during the rugged, hard, exasperating, but also marvelous, amazing and astonishingly moving experience that was my Ph.D. I would like to say thank you to all of you who stayed and always stay by my side, even when I've been the first to see all dark and blue... yes me, who usually never give up or try to see the light through the deepest abysses. You are going to last in my heart, forever! Let's start from the beginning.

Cristian Montanaro. You are the first of the list because it's you who inspired me to undertake this memorable adventure. Thanks to your human being example and your rock-philosophical life style, you gave me the hope and the straightness to go on wherever, whenever, however despite everything! You are a nature force! Thank you for all your insulting to make me react, for all the music which make me dream, for all the cuddle to make me feel warm. Thank you, my dear friend, for your love!

Diego González García, thank you so much to you too, for always encouraging me, from the very beginning to the end and more! For all your suggestions, for sharing the ups and the downs of this life as researchers and for your precious friendship, all around Europe. Thank you for listening all my crazy stories, I got nothing to scold you... just you must improve your tiramisú, ehheheh!

Jeanne Rivière and Miha Založnik, thank you for welcoming me as part of your friends, you helped me a lot in what was my new life in Nancy, and it has been a pleasure to meet you. Your always green spirits relieved me of the burden of the most difficult period. I will never forget it!

Ilaria Lucardesi and Léonard Monsaingeon, thank you for your friendship, I love you! It was great hanging out in Nancy with you guys. After work, have a beer at the Royal with you, it will remain my favorite beer! Auuuuu!!

Thanks to my colleagues: Marah, Yoram, Raphaël, Hélène, Roland, Francois, Jérémy, Christof, Pierre, Julien B., Héloïse, Julien P., Hoan, Max, Camilo, Elena, Rodrigue, Régine, Marie-Camille, Marie-Christine, Jerome, Karine, Pascal, Aurélien G., Aurélien R., Filipe, Antonin, Julien M., Marc, Antoine, Alexy, Hilaire, Ottone, Francesca, Isabelle, Patrick, Agnese, Camille, Véronique, Aurélie... and sorry if I forget somebody... It was great working and growing up with you around! Thank you for all the moments spent together!

Among all the staff of Georessources, some special thanks go to Matthieu Harlaux. Thank you for all your suggestions and presence, you are the one who, always with a smile, helped me, also in distance! Thank you so much, for all your messages and inputs! I am lucky to have you by my side!

And again, thanks to Joséphine Gigon, you are one of the best scientific woman I have never met! You have been an inspiration to me, I like your strength of spirit! It was a pleasure share with you the final period of the PhD, all the emotions and thank you again for your administration help!!

Thanks to Dimitris Rallakis, our Mediterranean connection relieved me a lot during the darkest period, speaking with you and sharing our troubles made me feel not alone.

Jessica Strydom, I am such a lucky girl to have met you! Thank you to put on the table the same dubs and questions as mine! Thank you for your deep and comprehensive soul! Thank you for sharing the humanity, that is often put apart in the scientific world! "You may say I am a dreamer, but I'm not the only one!!" Jessica is a dreamer too!!!

Maria Kokh, thank you for your precious help, for all brilliant scientific discussions, and your patience during my rough explications! You are an inspiration to me as well!

Outside the lab, thanks to Alexis, Alizé, Charles, Daishi, Dafne, Guilherme, Hatice, Ioannis, Maria, Mari, Ornella, Paolo, Sény, Tanya, Tayeb, Valia, Vasillis and Vitalis for the pleasant time passed together!

I would like to say a special thank you to:

Antoine Crémades, for sharing the same political ideas, beer and the good food, I loved your company.

Alvaro Ebuelto and Sara Brennan, for the short trip to Munich, and your energy. We must redo it!

Ario Fahimi, for your lightness optimism, which gave me a new speed during the last year of work. Thank you for your tenacity, your modesty and your lovely personality, most of all thank you for your friendship!

Axel Denis, you know... it is because of people like you that this world is beautiful. Thank you for the dinner, and the digeridoo concert in my apartment, I will never forget it!

Becca Wiltshire, for the short week together, rich of promises for a long and brilliant friendship! Thank you for sharing your passion for geology, you are one of the scientific woman inspiring me!

Bertrand Tinoco, for your friendship and the funny moments together, I love Nancy also because of you!

Elisa Ruiz, for everything. Thank you really for your friendship, that saved me from... you know! Ahah

Guillaume Barré, to be not just a colleague. Hahahah!! I'm already laughing if I think back to us preparing capillaries! Thank you Gui Gui to be my friend, like two children playing all the time! Thank you for every single moment spend together! All the laughs, all the nights out and the day trip, they will last forever!

Iordan Iordanov, for being one of the most important people I met in Nancy, and it does not matter in which part of the globe you are, I'll be there for you. Thank you for recognizing in me what I could not see, to accept me as a friend, as a part of your life!

Isabella Pignatelli, for sharing your experience, that has later been mine. Thank you for all the warnings and suggestions, for being my friend, for passing time together in the sign of what we miss most of our country: food!! Thank you for your company and honesty.

Joa Paredes Mariño and Kathrin Laeger, for your energy and friendship!

Loïc and Adèle Mangin, for making me feel at home, every time. Thank you for your friendship and love!

Lorenzo Cavallina, for sharing good food, good conversation and good alcohol (W la Svania).

Loup, for the beautiful moments together.

Stefano Baldini, for sharing the passion of freedom on the magic seal boat!

Sylvia Duprat-Oualid for your solar company, I will never forget our trip to Italy together!

Thèò Leduc, for never making me feel like a foreigner, but with patience you always explained me everything. Thank you to share with me all the break time outside the office, your life and all the PhD!!! It has been an honor!

Vladimir Latocha, for your friendship, it was great discussing with you!

I am going to switch a little in Italian, to express my gratitude to my family which does not speak a word of English.

Tanto lo so che è inutile dirlo, che si sa, ma stigrancarri, vi voglio un mondo di bene, ed è comunque solo grazie a voi se respiro su sta benedetta terra. Cari genitori miei, Tiziana Minelli e Luciano Carocci, nonostante mi fate a volte sbuffare vi sono molta grata di tuttissimo, della forza che mi avete sempre trasmesso, soprattutto quella di mollare mai. E con voi al mio fianco è davvero impossibile mollare. Durante questa nuova vita mi siete stati accanto anche di più, mi avete sempre sostenuta, con non poca preoccupazione! Grazie mille, spero che siate felici per me, io lo sono davvero tanto. E se volessi pareggiare i conti, non mi basterebbero 10000 vite.

Simona Carocci, come non ringraziarti di tutto il sollievo che mi dai ad ogni telefonata? Grazie davvero di cuore, di farmi da specchio di vedere in te tante cose di me, di farmi ridere di gusto come nessuno riesce a fare! Grazie di esserci stata, senza di te, sarebbe stata durissima. Grazie per essere non solo una sorella, ma uno splendido esempio da seguire, un'amica con la quale posso parlare di tutto, alla quale non devo dare molte spiegazioni, per farmi capire. A noi due basta uno sguardo, per tornare ad essere complici di tutte le malfatte, in tutti gli scherzi della vita. Ti voglio tanto tanto bene!

Voglio ringraziare la mia famiglia al completo, ma soprattutto Lucia Carbonari, Mario Carocci e Matteo Carocci, che in questi 4 anni è diventato un uomo! Grazie per la vostra presenza incondizionata, per tutto il sostegno e per il vostro amore! Sapervi nel mio cuore mi rassicura non sapete quanto! Vi amo!

Grazie all'amore delle mie nonne, Gianna Casciari e Linda Grelli, perché sarà pure banale fare un piatto di pasta, ma senza di loro io non saprei proprio come si cucina, quindi grazie di cuore perché la cucina

significa convivialità, significa calore, significa piacere, ma soprattutto significa amore ed è una dote che porto con me ovunque io vada!

Finally, at last but not for importance, thanks to:

Ilaria Buttarazzi, for being always by my side, for being my soulmate. I will never forget all the hard time spent together in each increasingly difficult test of our life! I should be more present in your day life, though! I am so grateful to have you in my life, and to be a part of your beautiful family!

Benjamin Descharmes, for being the one who hates "The Science", but still loves me. I love you too.

*Tungsten transport and deposition in magmatic-hydrothermal environments: the example of Panasqueira
(Portugal)*

Panasqueira W-Cu-Sn deposit (Portugal) consists of sub-horizontal mineralized veins of Qtz-Wfm-Cst-Ms-Toz-sulfurs. Qtz dissolution-recrystallization is the rule, complicating the setting up of the paragenetic sequence and the study of earliest stages over later superimposition. A considerable part of this thesis is devoted to the mineralogical study of the first wolframite (Wfm) depositional stage, which is the most valuable in terms of ore (W)-quantity. It is preceded by a tourmalinization coeval with W-rich rutile (305.2±5.7Ma). Studies on rutile have shown that oscillatory zoning is the result of the successive mixing between a W-rich, Nb + Ta poor fluid, with a Nb+Ta-rich and W-poor fluid. Also, Tur crystal composition (good recorder of the ore-fluid chemistry) has confirmed a multi-sources origin for W-transport and Wfm deposition. However, the hydrothermal transport and deposition of W are not well constrained. Here we use Raman spectroscopy coupled to the fused silica glass capillary technic to define the stability of the tungsten-polymers at different temperatures (up to 400°C) and pH. As a result, tungsten has a strong tendency to form complexes characterized by Kegging structures in acidic conditions which precipitate at high T, while its solubility increase with the pH increment. Fluid inclusion studies have been taken in consideration in this work, to evaluate the evolution of Panasqueira hydrothermal system. FI on quartz belonging to latest depositional stages have been examined and results have shown that trapping conditions are characterized by lower pressure and elevated temperatures. This allows to conclude that high geothermal gradient affected the studied zones at several stages and are related to heat advection produced by concealed granites from 305 to 295 Ma.

KEY WORDS: HYDROTHERMAL SYSTEMS, DATING, PATHFINDERS, FLUID INCLUSIONS, TUNGSTEN SPECIATION

*Transport et dépôt du tungstène dans les environnements magmatiques-hydrothermaux : exemple de
Panasqueira (Portugal)*

Le gisement de Panasqueira W-Cu-Sn (Portugal) est constitué de veines minéralisées sous-horizontales de Qtz-Wfm-Cst-Ms-Toz-sulfurs. La dissolution-recristallisation de Qtz est la règle, compliquant la mise en place de la séquence paragenétique et l'étude des premiers stades sur la superposition ultérieure. Une grande partie de cette thèse est consacrée à l'étude minéralogique du premier stade de dépôt de la wolframite (Wfm), qui est le plus précieux en termes de quantité de W. Il est précédé d'une tourmalinisation coeval avec rutile riche en W (305.2 ± 5.7Ma). Des études sur le rutile ont montré que le zonage oscillatoire est le résultat du mélange successif entre un fluide riche en W, et pauvre en Nb+Ta, avec un fluide riche en Nb+Ta et pauvre en W. De plus, la composition du cristal de Tur (bon enregistreur de la chimie du fluide) a confirmé une origine multi-sources pour le transport de W et le dépôt de la Wfm. Cependant, le transport hydrothermal et le dépôt de W ne sont pas bien construits. Ici, nous utilisons la spectroscopie Raman couplée à la technologie capillaire pour définir la stabilité des polymères de tungstène à différentes températures (jusqu'à 400 °C) et pH. En conséquence, tungstène a une forte tendance à former des complexes caractérisés par des structures Kegging dans des conditions acides qui précipitent à T élevé, tandis que sa solubilité augmente avec l'incrément de pH. Des études d'inclusion de fluides ont été prises en considération dans ce travail, pour évaluer l'évolution du système hydrothermal de Panasqueira. FI sur le quartz appartenant aux derniers stades de dépôt ont été examinés et les résultats ont montré que les conditions de piégeage sont caractérisées par une pression plus faible et des températures élevées. Ceci permet de conclure que le gradient géothermique élevé a affecté les zones étudiées à plusieurs stades et est lié à l'advection thermique produite par les granites cachés de 305 à 295 Ma.

MOTS-CLÉS : SYSTEM HYDROTHERMAL, DATATION, TRACEURES, INCLUSION FLUIDES, SPÉCIATION DU TUNGSTÉN

